PACIFIC EARTHQUAKE ENGINEERING RESEARCH CENTER

Shake Table Tests and Analytical Studies on the Gravity Load Collapse of Reinforced Concrete Frames

Kenneth John Elwood

and

Jack P. Moehle
University of California, Berkeley

PEER 2003/01
NOV. 2003

Shake Table Tests and Analytical Studies on the Gravity Load Collapse of Reinforced Concrete Frames

Kenneth John Elwood
Graduate Student Researcher
Department of Civil and Environmental Engineering
University of California, Berkeley

and

Jack P. Moehle
Professor
Department of Civil and Environmental Engineering
University of California, Berkeley

PEER Report 2003/01
Pacific Earthquake Engineering Research Center
College of Engineering
University of California, Berkeley

November 2003

ABSTRACT

The collapse vulnerability of reinforced concrete building frames constructed before the introduction of modern seismic codes has been well documented by earthquake reconnaissance, but the mechanisms that lead to collapse are not yet well understood. The collapse of a structure can occur only if the structure loses its ability to support gravity loads. Among other causes, the loss of gravity load capacity can result from column buckling, unseating of the supported beam, P-δ instability, or degradation of axial capacity due to column shear failure. This last cause and the effect of the axial load failure on the rest of the building frame are the focus of the study presented in this report.

An empirical model, based on the evaluation of results from an experimental database, is developed to estimate the drift at shear failure of existing reinforced concrete building columns. A shear-friction model is also developed to represent the general observation from experimental tests that the drift at axial failure of a shear-damaged column is directly proportional to the amount of transverse reinforcement and is inversely proportional to the magnitude of the axial load. The two drift capacity models are incorporated in a nonlinear uniaxial constitutive model implemented in a structural analysis platform to allow for the evaluation of the influence of shear and axial load column failures on the response of a building.

Shake table tests were designed to observe the process of dynamic shear and axial load failures in reinforced concrete columns when an alternative load path is provided for load redistribution. The results from these tests provide data on the dynamic shear strength and the hysteretic behavior of columns failing in shear, the loss of axial load capacity after shear failure, the redistribution of loads in a frame after shear and axial failures of a single column, and the influence of axial load on each of the above-mentioned variables. An analytical model of the shake table specimens, incorporating the proposed drift capacity models to capture the observed shear and axial load failures, provides a good estimate of the measured response of the specimens.

ACKNOWLEDGMENTS

This work was supported in part by the Pacific Earthquake Engineering Research Center through the Earthquake Engineering Research Centers Program of the National Science Foundation under award number EEC-9701568. This support is gratefully acknowledged.

Many people deserve our thanks for the contributions they have provided during the course of this research. The advise of Professors Stephen Mahin, Gregory Fenves, and Filip Filippou is gratefully acknowledged. The authors are particularly indebted to the OpenSees developers, Dr. Frank McKenna and Michael Scott, without whom the analysis presented herein would not have been possible. Dr. Gilberto Mosqueda greatly profited this research by his immeasurable kindness and intellectually stimulating exchanges.

The help provided by staff at the Pacific Earthquake Engineering Research Center, University of California, Berkeley, is gratefully appreciated. In particular, the experimental phase of this research, conducted in the research laboratories of PEER, benefited considerably from the advice and hard work of Don Clyde, David McLam, and Wesley Neighbour. Our gratitude also extends to Janine Hannel for her assistance with editing.

CONTENTS

LIST OF FIGURES

LIST OF TABLES

1 Introduction

1.1 BACKGROUND

Experimental research and post-earthquake reconnaissance have demonstrated that reinforced concrete columns with light or widely spaced transverse reinforcement are vulnerable to shear failure during earthquakes. Such damage can also lead to a reduction in axial load capacity, although this process is not well understood. As the axial capacity diminishes, the gravity loads carried by the column must be transferred to neighboring elements, possibly leading to a progression of damage, and in turn, collapse of the building.

Current methodologies for the evaluation of existing structures (ASCE, 2000) only consider the damage to individual components when evaluating a building for the collapse limit state. Reconnaissance of recent earthquakes (Sezen et al., 2000) provides evidence that components can experience significant damage, including column shear failures and loss of axial load capacity, without collapse of the building system, indicating that the entire system should be considered when evaluating the collapse limit state. To implement a system-based capacity assessment method, analytical models incorporating the shear and axial load failure of reinforced concrete columns are required.

Engineers involved in the seismic retrofit of buildings in California have found that, given the current state of knowledge, it is frequently not economically feasible to protect all columns in an existing reinforced concrete building from shear failure during strong ground motion. Given the lack of understanding of how the axial loads will be supported after shear failure, some engineers have resorted to installing secondary gravity load support systems to ensure that shear failure of individual columns does not lead to collapse of the building (Holmes, 2000). Hence, a better understanding of column axial load capacity after shear failure may lead to a significant reduction in seismic retrofit costs.

The gravity load collapse of structures during earthquakes involves a complicated interaction between the lateral demands imposed by the ground motion, the vertical demands imposed by the weight of the structure and by overturning, the lateral capacity of the structural system, and the vertical capacity of the structure to support the gravity loads. Collapse of the structural system can result if the lateral demands cause a degradation in the lateral capacity that in turn leads to the vertical capacity degrading below the level of the vertical demands. The lack of adequate models capturing the interaction between the lateral and vertical capacity of building frames has been identified as a critical deficiency of current methods used to assess the collapse potential of reinforced concrete buildings (Comartin, 2001).

Research is required to develop practical shear and axial-load-capacity models for existing reinforced concrete columns that can be implemented in an analytical model. Furthermore, experimental research is required to validate the ability of analytical models to capture the critical response characteristics of existing reinforced concrete building frames. After a review of pertinent existing research, the scope and objectives of the current study will be defined in an effort to address the issues discussed above.

1.2 PREVIOUS RESEARCH

1.2.1 Shear Response of Existing Reinforced Concrete Columns

A vast amount of research, both experimental and analytical, has been conducted to investigate the shear behavior of reinforced concrete elements. Only a small subset of this research, however, is applicable to existing reinforced concrete columns with wide spacing of the transverse reinforcement. Sezen (2002) provides a thorough review of experimental research on existing reinforced concrete columns experiencing flexural yielding before shear failure. Most of these studies are included in the database described in Section 2.2.

Several models have been developed to estimate the degradation of column shear strength with increasing inelastic deformations (Watanabe and Ichinose, 1992; Aschheim and Moehle, 1992; Priestley et al. 1994; Sezen, 2002). These models are useful for estimating the maximum shear demand a column can withstand, however, they do not provide a reliable estimate of the drift capacity at shear failure. Only a limited number of drift capacity models have been developed for columns experiencing flexural yielding before shear failure (Pujol et al., 1999; Pujol et al., 2000; Pujol, 2002; and Kato and Ohnishi, 2002). Each of these models are described in detail in Section 2.3.

1.2.2 Axial Load Failure of Existing Reinforced Concrete Columns

A major obstacle to studying the response of building frames at the point of incipient collapse is the lack of experimental data at this extreme performance level. Most structural testing for earthquake engineering to date has concentrated on the lateral resistance of the structural elements. With the recent effort to develop performance-based seismic design methodologies, researchers have begun to recognize the need to understand not just the shear capacity of older reinforced concrete columns but also the capacity to sustain axial loads after shear failure. Full-scale shear-critical reinforced concrete building columns were tested at UC Berkeley under cyclic lateral loads until the column could no longer sustain the applied axial load. These tests have demonstrated that the loss of axial load capacity does not necessarily follow immediately after a loss of lateral load capacity (Lynn, 2001; Sezen, 2002). The results suggest that the drift at which axial failure occurs is dependent on the axial stress on the column and the amount of transverse reinforcement (refer to Section 3.2 for more details on these tests).

Several pseudo-static tests have been performed in Japan to investigate the axial capacity of shear-damaged columns (Yoshimura and Yamanaka, 2000; Nakamura and Yoshimura, 2002; Tasai, 1999; Tasai, 2000; Kato and Ohnishi, 2002; Kabeyasawa et al., 2002). Based on the results from six columns (three experiencing shear failure before flexural yielding and three failing after flexural yielding) subjected to a variety of lateral loading routines while under constant axial stress, Yoshimura and Yamanaka (2000) found that the deformation increment ratio (defined as the ratio of the vertical deformation increment to the lateral deformation increment) was approximately constant at axial failure for all six columns, regardless of the loading routine. This conclusion was also supported by four column tests performed by Nakamura and Yoshimura (2002) where the principle variables were the applied axial stress and type of unidirectional loading (i.e., cyclic or monotonic). These tests also suggested that axial failure occurred when the shear capacity was reduced to approximately zero, and that the drift at axial failure decreased with increasing axial stress.

Tasai (2000) reported results from five pseudo-static tests on columns designed with approximately equal shear and flexural strengths. Each column, subjected to a constant axial stress, was tested under unidirectional cyclic lateral loads to different levels of damage beyond the peak shear strength. To determine the residual axial strength, the columns were returned to plumb vertical, and then subjected to increasing axial compression until failure. Sliding along the diagonal shear cracks was observed before axial failure. The results indicated that the residual axial capacity decreased proportionally with the an increase in the maximum lateral drift and the amount of shear-strength degradation. Tasai (2000) proposed that the residual axial strength could be estimated by summing the axial load carried by a truss mechanism, an arch mechanism, and the longitudinal reinforcement:

$$P_{res} = {}_c\sigma_t b_e \lambda j_e + {}_c\sigma_a bD + \sigma_y A_s \tag{1.1}$$

where ${}_c\sigma_t$ is the concrete compressive stress in a strut of a truss mechanism selected based on the AIJ Guidelines (1999), $b_e\lambda j_e$ is the effective area of the strut according to the AIJ Guidelines, ${}_c\sigma_a$ is the concrete compressive stress determined based on an arch mechanism, bD is the gross cross-sectional area of the column, and σ_y and A_s are the yield stress and area of the longitudinal reinforcement, respectively. By summing the three components together, as shown in Equation 1.1, any differences in the orientation of the three forces has been ignored. Tasai concluded that the deterioration of the residual axial capacity with increasing drift demand was related to the deterioration of ${}_c\sigma_t$.

Based on the results from 32 column specimens tested in Japan, Kato and Ohnishi (2002) calibrated a drift capacity model to estimate both the drift at shear failure and at axial failure. Details of the model are presented in Section 2.3.4.

1.2.3 Shake Table Tests

Only limited dynamic tests have been conducted to investigate the shear and axial load failure of existing reinforced concrete columns during earthquakes. Minowa, et al. (1995) performed shake table tests to investigate the loss of axial load capacity after shear failure of reinforced concrete columns with different hoop spacing. The test specimens were composed of four similar columns connected by a rigid mass and, hence, did not incorporate redundancy expected in ordinary building frames. The results showed that columns with smaller hoop spacing can maintain the gravity loads at larger drifts than columns with larger hoop spacing. The shake table test results were compared with the results from pseudo-static tests on the same type of specimen, finding that the strength and deformation capacities of the two types of tests were very close, even though the damage patterns were different.

Inoue, et al. (2000) compared the results of shake table and pseudo-static tests on shear-critical columns. The displacement routine for the pseudo-static tests was selected based on the recorded displacements from the shake table tests. The results suggested that the columns tested under pseudo-static conditions may experience shear failures at lower drifts than those tested on a shake table. No results beyond shear failure were presented.

1.2.4 Analytical Models for Shear-Critical Columns

The majority of analytical models for the response prediction of reinforced concrete members have been developed to capture the flexural response of the component when subjected to seismic demands (Otani and Sozen, 1972; Chen and Powell, 1982; Zeris and Mahin, 1991; Spacone et al., 1996). Such models have been used to estimate the point of shear failure through a post-processing comparison of the calculated flexural response with a shear-strength model, such as those described in Section 1.2.1 (An and Maekawa, 1998; Browning et al., 2000; Tsuchiya et al., 2001; Yoshikawa and Miyagi, 2001). To determine the response of a structure with sufficient accuracy as it approaches the collapse limit state it is necessary to not only detect the occurrence of shear failures, but also the influence of shear failure, and subsequent degradation of shear strength, on the response of the structure.

Several detailed models involving the discretization of a single column into many finite elements, capable of capturing the degrading behavior after shear failure, have been developed (Kaneko et al., 2001; Ozbolt et al., 2001; Shing and Spencer, 2001). Although such models provide insight into the complex stress and strain distributions during shear failure, the computational effort required makes these models impractical for the analysis of larger structural systems such as building frames.

Analytical models for shear-critical columns have also been developed using multiple uniaxial elements in a lattice or truss system (Kim and Mander, 1999; Niwa et al., 2001). The models capture interaction between flexure and shear, while explicitly modeling the critical force-

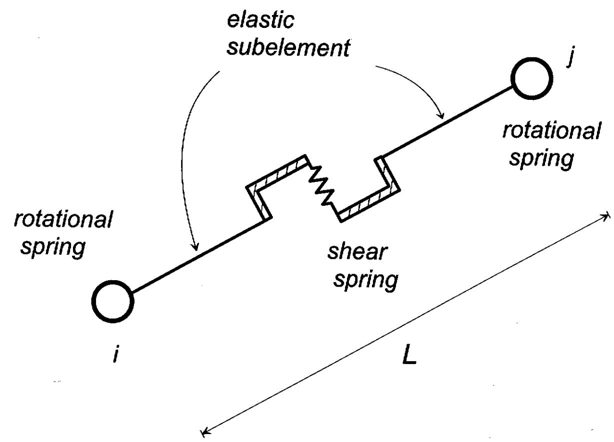

Figure 1-1. Illustration of macro-element model based on a frame element with lumped plasticity flexural springs (Pincheira et al., 1999)

resisting components (i.e., the longitudinal and transverse reinforcement, diagonal compression struts, and compression struts due to arch action). Similar to the finite-element mesh models, however, the large number of elements and nodes required to model a single column does not facilitate the use of lattice or truss models for the analysis of large structural systems. Macro-elements, incorporating all of the column response into one or two elements, are preferred for frame analysis.

Several macro-elements incorporating the effects of shear failure have been developed based on a frame element with lumped-plasticity at the element ends and an elastic interior (Figure 1-1). Pincheira and Jirsa (1992) accounted for shear failure by eliminating the lateral strength of the column element after the shear demand exceeded a specified shear strength. A column element developed by Li and Jirsa (1998) allows for a residual shear capacity after failure by incorporating two subelements in parallel. Once a specified shear strength is exceeded, one of the parallel subelements is converted to a truss element, while the other continues to deform laterally, and resist load, through yielding of its plastic hinges.

Pincheira et al. (1999) developed a column element incorporating nonlinear shear and rotational springs in series as shown in Figure 1-1. The backbone of the nonlinear shear spring allowed for strength degradation and was selected based on the Modified Compression Field Theory (Vecchio and Collins, 1986). The solution strategy, however, required the use of a small fictitious positive slope when on the descending branch of the backbone curve, resulting in a force unbalance which was applied to the model in the next time step. The procedure can be very computationally intensive and may not capture the dynamic characteristics of a softening structure.

Each of the macro-element column models discussed above determine the point of shear-strength degradation based on the column shear force exceeding a specified shear strength or the peak in the shear spring backbone. These models do not account for the degradation of shear strength with inelastic flexural deformations and, hence, may not accurately predict the point of shear failure for columns experiencing flexural yielding before shear failure. Ricles et al. (1998) used the shear-strength model by Priestley et al. (1994) to initiate the shear-strength degradation of a macro-element column model. The Priestley model accounts for degradation of the shear strength with increasing displacement ductility demand and, hence, its incorporation into the macro-element model allows for flexural yielding before shear failure. Several deficiencies of using a shear-strength model to detect the point of shear failure will be discussed in Section 2.3.1.

Macro-element models based on a fiber element, and incorporating shear deformations, have also been developed to capture the influence of the axial-flexural coupling response of reinforced concrete elements (Ranzo and Petrangeli, 1998; Petrangeli, 1999; and Shirai et al., 2001). For the elements by Ranzo and Petrangeli, and Shirai et al., a shear model acts in series with the fiber section, but no explicit coupling exists between the response of the shear model and the flexural or axial deformations. The model proposed by Petrangeli (1999) allows for coupling between the shear response and the flexural and axial behavior. The shear deformations are determined by requiring equilibrium between the concrete and transverse reinforcement. The load-displacement behavior for each of the models based on a fiber element is dependent on the concrete and steel models employed for the fibers.

None of the column models discussed above are capable of representing the axial failure of shear-critical columns. Little or no attention has been given to incorporating the influence of axial failures in analytical models. Casciati and Faravelli (1984) considered column axial failures in a building frame analysis by removing a column element entirely if failure was detected. (Failure of a component was defined by damage indices, determined based on the flexural response, exceeding specified values.) Casciati and Faravelli found that, in general, axial failure of a single column led to global failure of the system.

For the investigation of intermediate-story collapses of existing reinforced concrete buildings, Yoshimura and Nakamura (2002) concluded that a frame analysis was impractical, since “it is impossible at present to represent the column axial behavior at and after the collapse realistically.” Instead, an equivalent shear building model was used with the story-drift at collapse (i.e., when the story-shear capacity has degraded to zero) defined by an estimate of the story-drift at axial failure based on experimental data (Nakamura and Yoshimura, 2002).

1.3 OBJECTIVES AND SCOPE

The overall objective of this research is to quantify the ability of a structural system to resist collapse. (Note that for the current study, collapse of a building frame is defined as the loss of the capacity to sustain the gravity loads from the floors above.) Such a broad objective requires some definition of scope. The project described herein is limited to the study of two-dimensional frames. Obviously, out-of-plane frames and slab systems will contribute to the capacity of a building to resist collapse; however, the response of two-dimensional building frames must be well understood before the whole building system can be realistically considered.

This study is further limited to reinforced concrete frames with columns that can be characterized by a low ductility capacity and a shear-failure mode. The shear failure is accompanied by significant lateral strength degradation, and may be followed by a loss of axial load capacity. “Short” columns or piers, characterized by a shear failure before yielding of the longitudinal reinforcement, are not directly considered in this study, although, some of the general theory regarding loss of axial load capacity after shear failure (Chapter 3) may be extended to this class of elements.

The behavior of the component (column) must be well defined before useful results can be obtained for the system (building frame). Hence, a primary objective of this study is the development and validation of an analytical model for shear-critical columns. In contrast to existing models described in Section 1.2.4, the model presented here incorporates both shear and axial load failures in a general purpose macro-element model for building frame analysis. Given such a model, engineers will be better equipped to not only evaluate the capacity of vulnerable columns, but also determine the influence of shear and axial load failures on the rest of the structural system.

As discussed in Section 1.2.3, very few dynamic tests have been conducted to investigate the gravity load collapse of reinforced concrete frames. In an attempt to fill this gap and provide benchmark data for analytical modeling, shake table tests of a reinforced concrete frame incorporating a shear-critical column have been conducted as part of this study. The objectives of the shake table tests were as follows:

1. to obtain data on the dynamic shear strength and the hysteretic behavior of columns failing in shear,
2. to observe the process by which the axial load may be lost in a shear-damaged column,
3. to observe the redistribution of loads due to the shear and axial load failure of a single column in a simplified reinforced concrete frame, and
4. to observe the influence of axial load on each of the above mentioned variables.

1.4 ORGANIZATION

This report has been organized in the following manner: the development of the capacity and analytical models for shear-critical columns; a presentation of the response of the shake table test specimens; and a validation of the analytical model through a comparison with the shake table test results.

Chapter 2, "Drift at Shear Failure," evaluates several existing models for the drift at shear failure based on a database of 49 pseudo-static column tests. In an effort to reduce the wide dispersion of predicted drift capacities based on the existing models, two empirical drift capacity models are proposed based on an evaluation of the critical parameters influencing the database results.

Chapter 3, "Axial Capacity Model," describes a model to estimate the drift at axial failure for a shear-damaged column. The model evaluates the capacity to resist sliding along the shear-failure plane based on shear-friction concepts. The accuracy of the model is evaluated based on the observed drift capacity at axial failure for twelve pseudo-static column tests.

Chapter 4, "Limit State Failure Model," describes the implementation of the capacity models from Chapters 2 and 3 in a uniaxial material model for the OpenSees analytical platform (OpenSees, 2002). The material model can be used in series with a beam-column element to model the shear and axial load failure of shear-critical columns in a building frame analysis. The object-oriented code written to implement the Limit State Failure model is described in Appendix D.

Chapter 5, "Design of Shake Table Tests," describes the design, construction, instrumentation, and shake table testing of two one-half scale reinforced concrete frame specimens, differing only by the axial load applied to the shear-critical center column. The test specimens were composed of three columns fixed at their base and interconnected by a beam at the upper level. The center column had wide transverse reinforcement spacing making it vulnerable to shear failure and subsequent axial failure during testing. A scaled ground motion record from the 1985 Chile earthquake was used as the input table motion. More details on the design, construction, and experimental setup are provided in Appendices A and B.

Chapter 6, “Shake Table Test Results,” presents and discusses the results from the shake table tests. The results from the two specimens are compared to evaluate the influence of the axial load on the center column. The focus of the discussion is on the response of the shear-critical center column and the redistribution of loads during shear and axial failure. Videos of the tests, synchronized with data plots, are included on a compact disk as part of Appendix E.

Chapter 7, “Comparison of Test Data with Predictive Models,” evaluates the accuracy of models commonly used in practice to predict the yield displacement, elastic stiffness, and flexural strength of the center and outside columns of the test specimens. The test results are also compared with the drift capacity models for shear and axial load failure from Chapters 2 and 3, and a simple model is used to represent the response of the beam during axial load redistribution.

Chapter 8, “Analysis of Shake Table Test Specimens,” compares the response of the shake table specimens with the results from an analytical model incorporating the capacity models from Chapters 2 and 3 using the uniaxial material model developed in Chapter 4. The comparison allows for an evaluation of the ability of the macro-element column model to represent the response of shear-critical columns during shear and axial load failure. The influence of several model parameters on the accuracy of the predicted response is also investigated.

Finally, Chapter 9, “Conclusions and Future Work,” will summarize the critical results from the report and recommend topics in need of further investigation to achieve the overall objective of this research: to quantify the ability of a structural system to resist collapse.

2 Drift at Shear Failure

2.1 INTRODUCTION

It has been well established by experimental evidence that many existing reinforced concrete columns are vulnerable to shear failure after flexural yielding (Kokusho, 1964; Ikeda, 1968; Umemuro and Endo, 1970; Wight and Sozen, 1973; Ohue et al., 1985; among others). Several models have been developed to represent the degradation of shear strength with increasing inelastic deformations (Watanabe and Ichinose, 1992; Aschheim and Moehle, 1992; Priestley et al. 1994; Sezen, 2002). Although these shear-strength models are useful for estimating the column capacity for conventional strength-based design and assessment, the recent move toward displacement-based design and assessment methods (ATC, 1996; ASCE, 2000) requires a model for the drift beyond which shear failure is expected. Furthermore, after flexural yielding the force demand on a column will be approximately constant, while the displacement demand will increase substantially, suggesting that a drift capacity model is more useful for columns experiencing flexural-shear failures such as those considered in this study. Although the shear-strength models relate the degradation of shear strength to displacement ductility, these models may not be appropriate for assessing the drift at shear failure.

Three drift capacity models have been proposed by Pujol et al. (1999), Pujol et al. (2000), and Pujol (2002). The first is based only on statistical evaluation of experimental test results. The second model is based on the Coulomb failure criterion and uses experimental test data to relate the degradation of the cohesion coefficient to the drift at shear failure. The final model endeavors to incorporate the effect of displacement history on the drift capacity. Considering the additional complexities of implementing the final model in a general-purpose analytical code, this model has not been evaluated in this study.

This chapter will use a database of 50 shear-critical reinforced concrete columns to evaluate the drift capacity at shear failure calculated by the following models:

- The shear-strength model by Sezen (2002)
- The statistical drift capacity model by Pujol et al. (1999)
- A model based on Coulomb's criterion by Pujol et al. (2000)
- A plastic drift capacity model by Kato and Ohnishi (2002)
- Two empirical models based on observations from the shear-critical column database

2.2 EXPERIMENTAL DATABASE

With the goal of selecting a capacity model to be used in the analysis of shear-critical columns (see Chapter 4), the applicability of the models described above to existing reinforced concrete building columns will be evaluated using a database of 50 experimental tests. The database, compiled by Sezen (2002), consists of column specimens with observed shear distress at failure and tested under unidirectional lateral load in single or double curvature with the following range of properties:

- shear span to depth ratio: $2.0 \le \frac{a}{d} \le 4.0$
- concrete compressive strength: $2500 \le f_c' \le 6500$ psi
- longitudinal reinforcement nominal yield stress: $40 \le f_{yl} \le 80$ ksi
- longitudinal reinforcement ratio: $0.01 \le \rho_l \le 0.08$
- transverse reinforcement ratio: $0.01 \le \frac{\rho'' f_{yt}}{f_c'} \le 0.12$
- maximum shear stress: $2.0 \le \frac{v}{\sqrt{f_c'}} \le 9.0$ (psi units)

The specimen properties and selected response quantities are presented in Tables 2-1 and 2-2. Note that all displacements are given for an equivalent column in double curvature (i.e., for those specimens tested in single curvature the displacements in Tables 2-1 and 2-2 are twice those recorded during the experiment). The yield displacement and the displacement at shear failure were determined based on the backbone curve from the test data as shown in Figure 2-1. For this pur-

Table 2-1. Database of shear-critical column tests[1](double-curvature specimens)

Specimen	b	h	d	a	s	ρ_{long}	ρ'	f_{yl}	f_{yt}	f'_c	P	Δ_y	Δ_s	V_{test}
	in.	in.	in.	in.	in.			ksi	ksi	ksi	kips	in.	in.	kips
Sezen (2002)														
2CLD12	18	18	15.5	58	12	0.025	0.0017	64	68	3.06	150	1.04	2.97	70.8
2CHD12	18	18	15.5	58	12	0.025	0.0017	64	68	3.06	600	0.57	1.02	80.7
2CVD12[2]	18	18	15.5	58	12	0.025	0.0017	64	68	3.03	500	0.76	2.23	67.6
2CLD12M	18	18	15.5	58	12	0.025	0.0017	64	68	3.16	150	1.11	3.33	66.2
Lynn (2001)														
3CLH18	18	18	15	58	18	0.03	0.001	48	58	3.71	113	0.78	1.2	61.0
3SLH18	18	18	15	58	18	0.03	0.001	48	58	3.71	113	0.61	1.15	60.0
2CLH18	18	18	15	58	18	0.02	0.001	48	58	4.8	113	0.72	3	54.0
2SLH18	18	18	15	58	18	0.02	0.001	48	58	4.8	113	0.63	2.4	52.0
2CMH18	18	18	15	58	18	0.02	0.001	48	58	3.73	340	0.61	1.2	71.0
3CMH18	18	18	15	58	18	0.03	0.001	48	58	4.01	340	0.61	1.2	76.0
3CMD12	18	18	15	58	12	0.03	0.0017	48	58	4.01	340	0.74	1.8	80.0
3SMD12	18	18	15	58	12	0.03	0.0017	48	58	3.73	340	0.86	1.8	85.0
Ohue Morimoto, Fujii, and Morita (1985)														
2D16RS	7.87	7.87	6.89	15.7	1.97	0.02	0.0057	54	46	4.65	41.1	0.3	1.08	22.9
4D13RS	7.87	7.87	6.89	15.7	1.97	0.027	0.0057	54	46	4.34	41.1	0.26	0.58	24.9
Esaki (1996)														
H-2-1/5	7.87	7.87	6.89	15.7	1.97	0.025	0.0052	52	53	3.34	36.2	0.16	0.79	23.2
HT-2-1/5	7.87	7.87	6.89	15.7	2.95	0.025	0.0052	52	53	2.93	31.8	0.19	0.82	22.9
H-2-1/3	7.87	7.87	6.89	15.7	1.57	0.025	0.0065	52	53	3.34	60.4	0.14	0.63	27.1
HT-2-1/3	7.87	7.87	6.89	15.7	2.36	0.025	0.0065	52	53	2.93	53	0.19	0.79	25.1

1. **Notation:** b = column section width; h = column section height; d = depth to centerline of tension reinforcement; a = shear span; s = tie spacing; ρ_{long} = longitudinal reinforcement ratio (A_{sl}/bh); ρ'' = transverse reinforcement ratio (A_{st}/bs); f_{yl} = longitudinal steel yield strength; f_{yt} = transverse steel yield strength; f'_c = concrete strength; P = axial load (at time of shear failure for variable axial load test); Δ_y = yield displacement; Δ_s = displacement at shear failure (at 20% loss in peak shear); V_{test} = peak shear recorded (see Figure 2-1 for definition of Δ_y, Δ_s, and V_{test}).

2. Variable axial load test. All data given for compression cycles (i.e., direction in which shear failure was initiated.

Table 2-2. Database of shear-critical column tests (single-curvature specimens)

Specimen	b	h	d	a	s	ρ_{long}	ρ''	f_{yl}	f_{yt}	f'_c	P	Δ_y	Δ_s	V_{test}
	in.	in.	in.	in.	in.			ksi	ksi	ksi	kips	in.	in.	kips
Li, Park, and Tanaka (1995)														
U-7	15.8	15.8	14.8	39.4	4.7	0.024	0.0047	64.7	55.4	4.21	104	0.7	2.8	73.7
U-8	15.8	15.8	14.8	39.4	4.7	0.024	0.0052	64.7	55.4	4.86	241	0.66	1.66	88.3
U-9	15.8	15.8	14.8	39.4	4.7	0.024	0.0057	64.7	55.4	4.95	368	0.6	2.4	96.6

Table 2-2. ***(Continued)*** **Database of shear-critical column tests (single-curvature specimens)**

Specimen	b in.	h in.	d in.	a in.	s in.	ρ_{long}	ρ''	f_{yl} ksi	f_{yt} ksi	f'_c ksi	P kips	Δ_y in.	Δ_s in.	V_{test} kips
Saatcioglu and Ozebe (1989)														
U1	13.8	13.8	12	39.4	5.9	0.033	0.003	62.4	68.2	6.32	0	1.34	4.18	61.8
U2	13.8	13.8	12	39.4	5.9	0.033	0.003	65.7	68.2	4.38	135	1.18	3.38	60.7
U3	13.8	13.8	12	39.4	3	0.033	0.006	62.4	68.2	5.05	135	1.26	3.54	60.3
Yalcin (1997)														
BR-S1	21.7	21.7	19	58.5	11.8	0.02	0.001	64.5	61.6	6.5	469	0.64	1.82	130.0
Ikeda (1968)														
43	7.87	7.87	6.81	19.7	3.9	0.02	0.0028	63	81	2.84	18	0.26	1.04	16.6
44	7.87	7.87	6.81	19.7	3.9	0.02	0.0028	63	81	2.84	18	0.26	0.64	17.2
45	7.87	7.87	6.81	19.7	3.9	0.02	0.0028	63	81	2.84	35	0.38	0.64	18.5
46	7.87	7.87	6.81	19.7	3.9	0.02	0.0028	63	81	2.84	35	0.38	0.48	18.1
62	7.87	7.87	6.81	19.7	3.9	0.02	0.0028	50	69	2.84	18	0.24	1.46	13.0
63	7.87	7.87	6.81	19.7	3.9	0.02	0.0028	50	69	2.84	35	0.24	1.1	15.4
64	7.87	7.87	6.81	19.7	3.9	0.02	0.0028	50	69	2.84	35	0.28	1.32	15.4
Umemura and Endo (1970)														
205	7.87	7.87	7.09	23.6	3.9	0.02	0.0028	67	47	2.55	35	0.38	0.98	16.0
207	7.87	7.87	7.09	15.8	3.9	0.02	0.0028	67	47	2.55	35	0.32	0.5	23.8
214	7.87	7.87	7.09	23.6	7.9	0.02	0.0014	67	47	2.55	88	0.48	0.82	18.6
220	7.87	7.87	7.09	15.8	4.7	0.01	0.0011	55	94	4.77	35	0.12	0.94	17.6
231	7.87	7.87	7.09	15.8	3.9	0.01	0.0013	47	76	2.14	35	0.08	0.64	11.4
232	7.87	7.87	7.09	15.8	3.9	0.01	0.0013	47	76	1.9	35	0.1	0.64	13.1
233	7.87	7.87	7.09	15.8	3.9	0.01	0.0013	54	76	2.02	35	0.12	0.54	15.5
234	7.87	7.87	7.09	15.8	3.9	0.01	0.0013	54	76	1.9	35	0.12	0.64	15.1
Kokusho (1964)														
372	7.87	7.87	6.69	19.7	3.9	0.01	0.0031	76	51	2.88	35	0.2	0.84	16.7
373	7.87	7.87	6.69	19.7	3.9	0.02	0.0031	76	51	2.96	35	0.28	0.78	19.8
Kokusho and Fukuhara (1965)														
452	7.87	7.87	6.69	19.7	3.9	0.03	0.0031	52	88	3.18	88	0.24	0.6	24.8
454	7.87	7.87	6.69	19.7	3.9	0.04	0.0031	52	88	3.18	88	0.18	0.4	24.8
Wight and Sozen (1973)														
40.033a	6	12	10.5	34.5	5	0.024	0.0033	72	50	5.03	42.5	0.6	2.5	22.3
40.033	6	12	10.5	34.5	5	0.024	0.0033	72	50	4.87	40	0.96	3.46	22.8
25.033	6	12	10.5	34.5	5	0.024	0.0033	72	50	4.88	25	0.94	2.48	23.5
0.033	6	12	10.5	34.5	5	0.024	0.0033	72	50	4.64	0	0.6	2.2	22.1
40.048	6	12	10.5	34.5	3.5	0.024	0.0048	72	50	3.78	40	1.14	3.82	21.2
0.048	6	12	10.5	34.5	3.5	0.024	0.0048	72	50	3.75	0	1.06	2.6	23.6

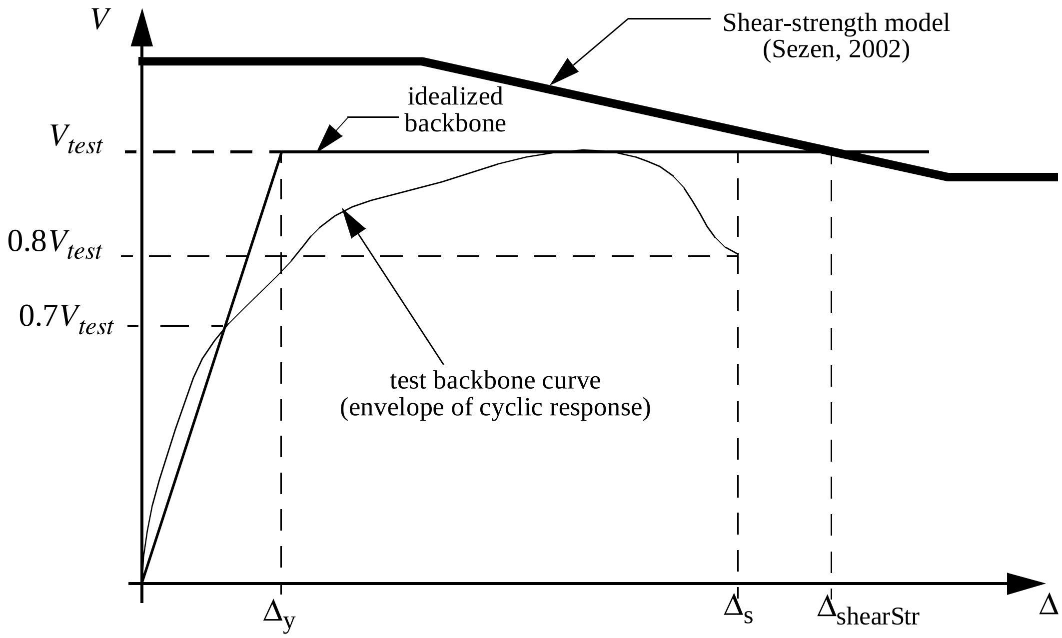

Figure 2-1. Definition of displacements reported in database and calculated by the shear-capacity model (Section 2.3.1)

pose, the backbone curve was defined as the force-deformation response which enveloped the entire cyclic response. For approximately 20% of the specimens the shear strength did not drop below 80% of the maximum shear strength recorded. In such cases, Δ_s was taken as the maximum displacement reported, and as such, represents a lower bound to the true displacement at shear failure. Response histories and specimen details are provided in Sezen (2002).

Figure 2-2 compares the drift ratio at shear failure (i.e., the displacement at shear failure divided by the height of the column) with several key parameters. It is apparent from the plots that there is considerable variability in the results and no clear relationship with any one parameter. The data in Figure 2-2 suggest that the maximum nominal shear stress (in psi) recorded during the tests ($v = V_{test}/(bd)$), expressed as a fraction of $\sqrt{f_c'}$ (psi), is not strongly correlated with the drift at shear failure. However, the plots do suggest that for columns with high axial loads, the maximum drift ratio at shear failure tends to be less than the median for columns with low axial loads. Furthermore, columns with higher transverse reinforcement ratios, ρ'', tended to achieve larger drifts at shear failure compared with columns with lower transverse reinforcement ratios. In contrast, there is no discernible relationship between $\frac{\rho'' f_{yt}}{f_c'}$ and the drift ratio at shear failure, suggesting that for the specimens included in the database, the drift ratio may be better related to the *amount* of

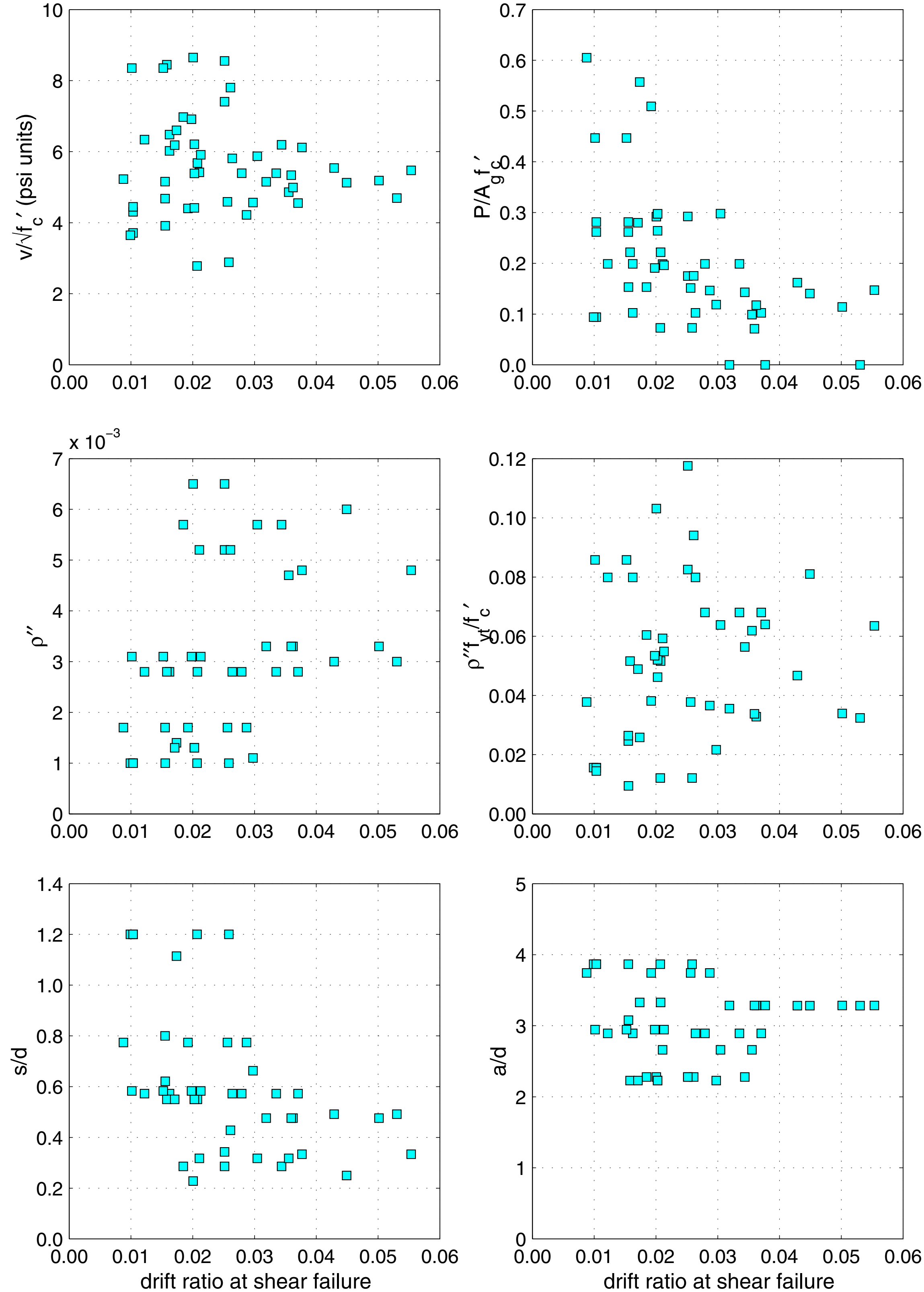

Figure 2-2. Effect of key parameters on drift ratio at shear failure

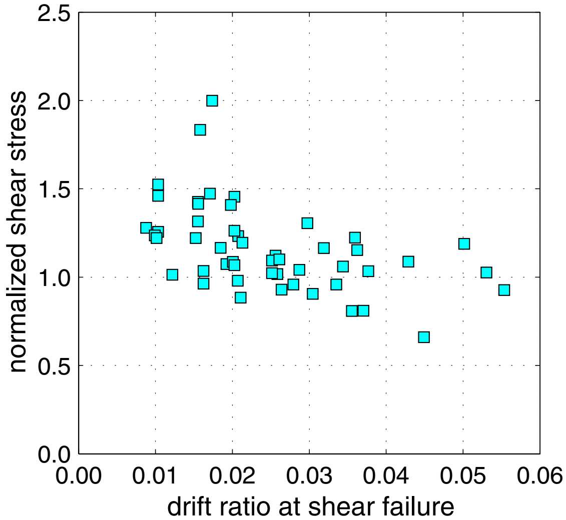

Figure 2-3. Variation of normalized shear stress with drift ratio at shear failure (Normalized shear stress = $\frac{V_{test}}{bd} / (2\sqrt{f_c'} + \rho'' f_{yt})$ in psi units)

transverse reinforcement, rather than to the *strength*. This conclusion is also supported by the apparent inverse relationship between the spacing of the hoops (s/d) and the drift at shear failure. Based on the data, the aspect ratio, *a*/*d*, has no clear relationship with the drift ratio at shear failure.

When the maximum shear stress is normalized by $2\sqrt{f_c'} + \rho'' f_{yt}$ (in psi units), as shown in Figure 2-3, a slight degradation of the shear strength with increasing drift can be observed. This general observation has led to the degrading shear-strength models proposed in the literature (Wantanabe and Ichinose, 1992; Aschheim and Moehle, 1992; Priestley et al. 1994; Sezen, 2002). The nearly horizontal slope of the apparent relationship between the normalized shear stress and the drift ratio at shear failure suggests that any small change in the shear strength would result in a large change in the drift ratio at failure. Given the uncertainty in determining the shear strength, this may not be an appropriate relationship to be used for estimating the drift ratio at shear failure. The difficulties of using shear-strength models to predict the drift at shear failure will be discussed further in the next section.

2.3 MODELS FOR DRIFT RATIO AT SHEAR FAILURE

Most models for estimating the drift capacity of reinforced concrete columns are based on the performance of columns with good seismic detailing. Such models assume that the response is domi-

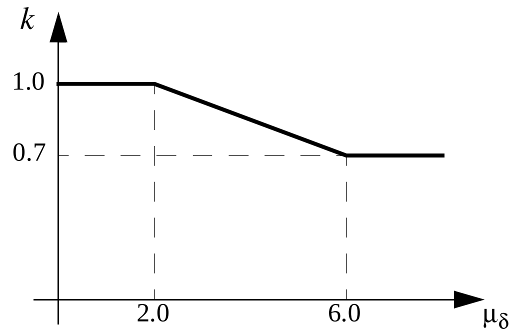

Figure 2-4. Variation of degradation coefficient *k* with displacement ductility

nated by flexural deformations, and use estimates of the ultimate concrete and steel strains to determine the ultimate curvatures the section can withstand. These models are not applicable to older reinforced concrete columns with limited transverse reinforcement, since the degradation of the shear strength begins before the flexural deformation capacity can be achieved. Furthermore, the calculation of ultimate strains assumes good crack control, provided by reasonably distributed reinforcement, such that deformations can be averaged over finite distances. Experimental studies and earthquake reconnaissance have shown, however, that the shear failure of older reinforced concrete columns often is associated with deformations concentrated along a limited number of primary cracks (Pantazopoulou, 2003). Hence, such models based on flexural mechanics will not be considered in this chapter.

2.3.1 Shear-Strength Model (Sezen, 2002)

Similar to other shear-strength models by Aschheim and Moehle (1992) and Priestley (1994), the model proposed by Sezen (2002) relates the column shear strength to the displacement ductility demand. The model divides the shear strength into two terms: the shear carried by the concrete, V_c; and the shear carried by the reinforcement through a $45°$ truss model, V_s.

$$V_n = k(V_c + V_s) = k\frac{6\sqrt{f_c'}}{a/d}\sqrt{1 + \frac{P}{6\sqrt{f_c'}A_g}}0.8A_g + k\frac{A_{st}f_{yt}d}{s} \tag{2.1}$$

The coefficient k defines the degradation of shear strength with increasing displacement ductility, as shown in Figure 2-4. The degradation coefficient is applied to both V_c and V_s under the assumption that the concrete component will diminish due to increased cracking and degrada-

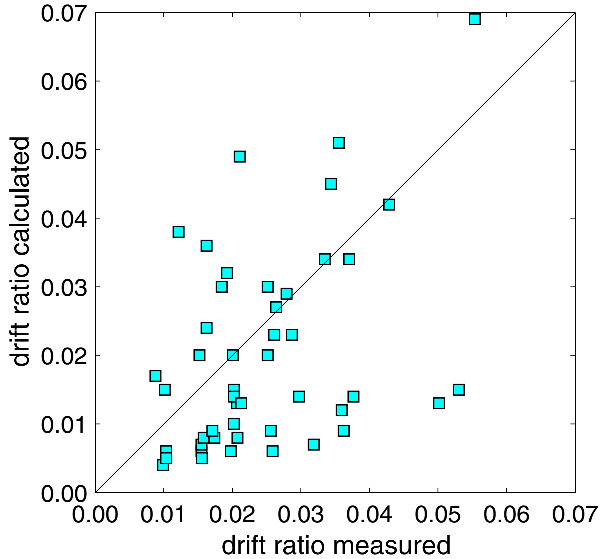

Figure 2-5. Comparison of calculated[1] and measured drifts for Sezen (2002) shear-strength model

1. The idealized backbone for two of the columns passed below the shear-failure surface, indicating that the shear-strength model would not predict shear failure for these specimens. These columns are not included in Figure 2-5.

tion of the aggregate interlock mechanism, while the steel component is assumed to drop due to a reduction in the bond stress capacity required for an effective truss mechanism. Derivation of the V_c term in Equation 2.1 and further details of the shear-strength model can be found in Sezen (2002).

For a given column with a known yield displacement, the shear-strength model ideally can be used to estimate the drift at shear failure. As shown in Figure 2-1, the displacement at shear failure based on the shear-strength model, $\Delta_{shearStr}$, is the displacement at which the idealized backbone curve intercepts the shear-failure surface given by Equation 2.1 and Figure 2-4. Based on this method, the drift ratio at shear failure can be calculated for each of the columns in the experimental database. A comparison of the results with the measured drift ratios (Figure 2-5) indicates that the shear-strength model does not adequately predict the drift ratio at shear failure for the selected database. (The mean of the measured drift ratio at shear failure divided by the calculated drift ratio is 1.78; the coefficient of variation is 0.63.)

Sezen (2002) recommends against using the shear-strength model to estimate the drift ratio at shear failure, since a small variation in the shear strength (or flexural strength) corresponds to a large change in the estimated drift ratio at shear failure. If the variability in the shear strength is

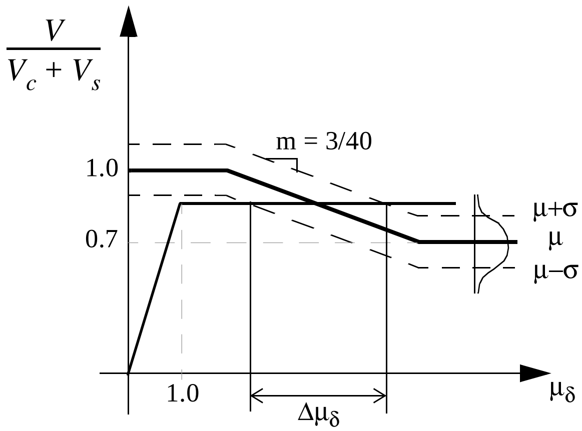

Figure 2-6. Variation in displacement ductility for columns within one standard deviation, σ, of the mean shear strength, μ, defined by Equation 2.1

assumed to be adequately represented by a normal distribution with a mean, μ, given by Equation 2.1 and a standard deviation, σ, and the response of the column is assumed to be elastic-perfectly-plastic before shear failure, then for the case illustrated in Figure 2-6, the variation in the displacement ductility demand required to cause shear failure for columns within $\pm\sigma$ of the mean shear strength is $(80/3)\sigma$. For example, if $\sigma = 0.16$ (determined by Sezen (2002) using the same experimental database discussed above), the variation in the ductility demand, $\Delta\mu_\delta$, in Figure 2-6, is 4.3.

Furthermore, the shear-strength model of Sezen (2002) could be interpreted to suggest that the column drift ratio at shear failure should increase for an increase in the axial load (Figure 2-7). In contrast, the experimental database (Figure 2-2) suggests that an increase in the axial load may, in some cases, reduce the drift ratio at shear failure.

Considering the deficiencies outlined above, the shear-strength model will not be used to estimate the drift ratio at shear failure.

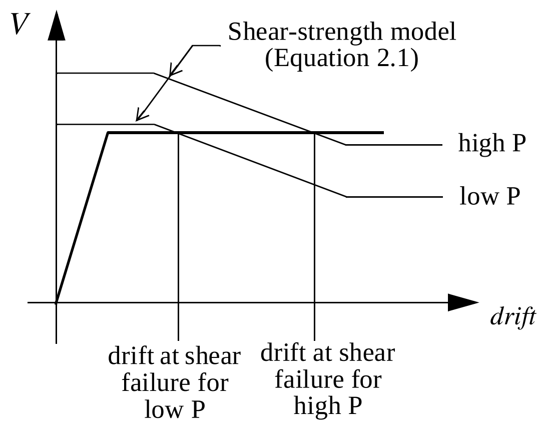

Figure 2-7. Change in drift ratio at shear failure due to change in axial load according to the shear-strength model

2.3.2 Pujol et al. (1999)

Pujol et al. (1999) used a database of 92 columns to establish a conservative estimate of the maximum drift ratio[1]. The database included both circular and rectangular cross-section columns with the following ranges of experimental parameters:

- shear span to depth ratio: $1.3 \le \frac{a}{d} \le 5.0$
- concrete compressive strength: $3000 \le f_c' \le 12500$ psi
- longitudinal reinforcement ratio: $0.005 \le \rho_l \le 0.051$
- transverse reinforcement ratio: $0.0 \le \rho'' \le 0.0164$
- maximum shear stress: $2.0 < \frac{v}{\sqrt{f_c'}}$ (psi units)
- axial load ratio: $0.0 \le \frac{P}{A_g f_c'} \le 0.2$

The most significant differences with the database introduced in Section 2.2 include the consideration of columns with transverse reinforcement ratios greater than 1%, the relatively low limit placed on the axial load ratio, and the inclusion of circular cross-section columns representative of bridge columns.

1. The maximum drift ratio was defined the same as was the drift ratio at shear failure for the database presented in Section 2.2 (drift ratio at a 20% loss in the maximum column shear strength), although the failure mode for some of the columns was described as flexural.

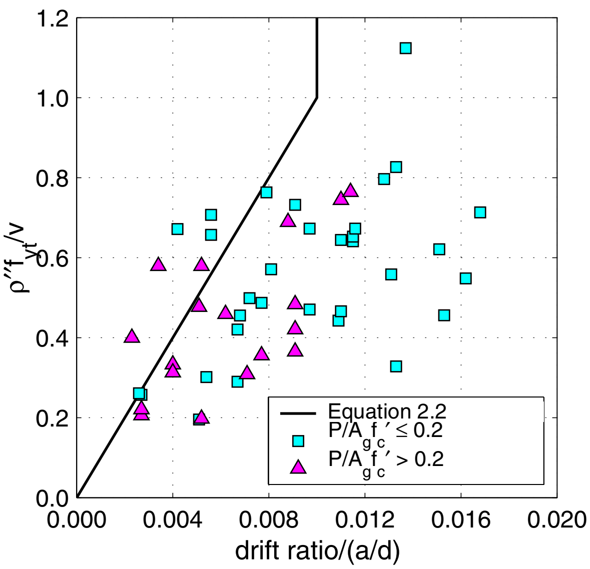

Figure 2-8. Pujol et al. (1999) model compared with database from Section 2.2

Pujol et al. (1999) observed that the ratio of the maximum drift ratio to the column aspect ratio, *a/d*, tended to increase with an increase in the reinforcement index $\frac{\rho'' f_{yt}}{v}$. Based only on statistical evaluation of the database results, and in an effort to establish a conservative estimate of the maximum drift ratio, Pujol et al. recommended the following relationship:

$$100\frac{\Delta_{max}}{L} = \frac{\rho'' f_{yt}}{v}\frac{a}{d} \le \begin{cases} \frac{a}{d} \\ 4 \end{cases} \tag{2.2}$$

As shown in Figures 2-8 and 2-9, the maximum drift-ratio model (Equation 2.2) is not conservative for six of the columns in the database from Section 2.2. Three of those columns were subjected to axial loads in excess of the axial loads considered in the development of the model.

The mean of the measured drift ratio at shear failure divided by the drift ratio calculated according to Equation 2.2 is 1.71; the coefficient of variation is 0.42. Since a drift capacity model providing an estimate of the mean response is preferred for use in a performance-based design methodology, the model by Pujol et al. (1999) will not be used in this study. Similar empirical models providing better estimates of the mean drift ratio at shear failure are developed in Section 2.3.5.

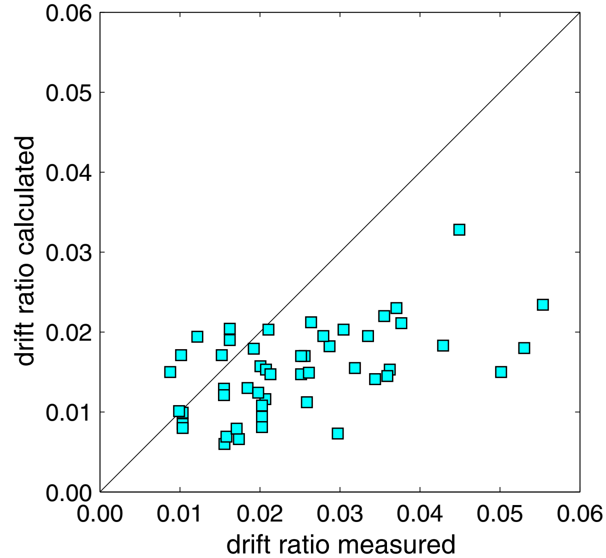

Figure 2-9. Comparison of calculated and measured drifts for Pujol et al. (1999) model

2.3.3 Pujol et al. (2000)

In an effort to determine the amount of transverse reinforcement required for columns subjected to seismic loads, Pujol et al. (2000) developed a model based on Coulomb's criterion and calibrated to a database of 29 columns. The model can also be used to estimate the maximum drift capacity of a reinforced concrete column (where the maximum drift capacity is defined the same as that used by Pujol et al. (1999), see Section 2.3.2).

Pujol et al. (2000) used the following expression, attributed to Richart et al. (1929), that expresses the cohesion term in Coulomb's criterion in terms of the concrete strength:

$$v_u = k_1 f_c' + k_2 \sigma_n \tag{2.3}$$

where v_u is the average ultimate shear stress capacity and σ_n is the average stress normal to the potential failure plane. Richart et al. (1929) estimated the coefficients k_1 and k_2 to be $1/4$ and $3/4$, respectively. Pujol et al. (2000) hypothesized that only the cohesion coefficient, k_1, varied depending on the seismic demands, and selected k_2=3/4.

The coefficient k_1 was related to the maximum drift capacity using a database of columns with the following ranges for the experimental parameters:

- shear span to depth ratio: $1.9 \le \frac{a}{d} \le 3.5$
- concrete compressive strength: $3700 \le f_c' \le 14000$ psi
- longitudinal reinforcement ratio: $0.02 \le \rho_l \le 0.036$
- transverse reinforcement ratio: $240 \le \rho'' f_{yt} \le 1400$ psi
- maximum shear stress: $6.0 \le \frac{v}{\sqrt{f_c'}} \le 13.0$ (psi units)
- axial load ratio: $0.07 \le \frac{P}{A_g f_c'} \le 0.35$

The most significant differences with the database introduced in Section 2.2 include the consideration of columns with higher transverse reinforcement ratios and relatively higher shear stresses.

Pujol et al. (2000) determined the cohesion coefficient k_1 for each of the columns in their database using Equation 2.3 to define Coulomb's criterion and the average axial, confining, and shear stresses based on the column core dimension. Pujol et al. (2000) found that k_1 tended to decrease with increasing drift ratio, and proposed the following expression as an approximate lower bound to their database results:

$$k_1 = \frac{1}{7}\left(1 - \frac{100}{3}\frac{(\Delta_{max}/L)}{(a/d)}\right) \ge 0 \tag{2.4}$$

Figure 2-10 compares the cohesion coefficients determined for each of the columns in the database from Section 2.2 with Equation 2.4. (The average stresses on the column core were determined by assuming $A_g/A_{core} = 1.6$ for each of the columns in the database.) The results from the database from Section 2.2 also suggest that k_1 tends to decrease with increasing drift ratio. Although Equation 2.4 was selected as a lower bound to the database used by Pujol et al. (2000), the model appears close to the mean for the database from Section 2.2.

Given the k_1 coefficient calculated for each of the columns in the database from Section 2.2 (Figure 2-10), the maximum drift ratio can be estimated using Equation 2.4. For any of the columns where $k_1 > 0.14$, Equation 2.4 will give a meaningless negative maximum drift ratio. However, observing that the drift ratio for the columns included in the database appears to be limited to greater than 1% (see Figure 2-2), it is proposed that the maximum drift ratio calculated using Equation 2.4 should also be limited to greater than 1%. Hence the maximum drift ratio can be calculated as follows:

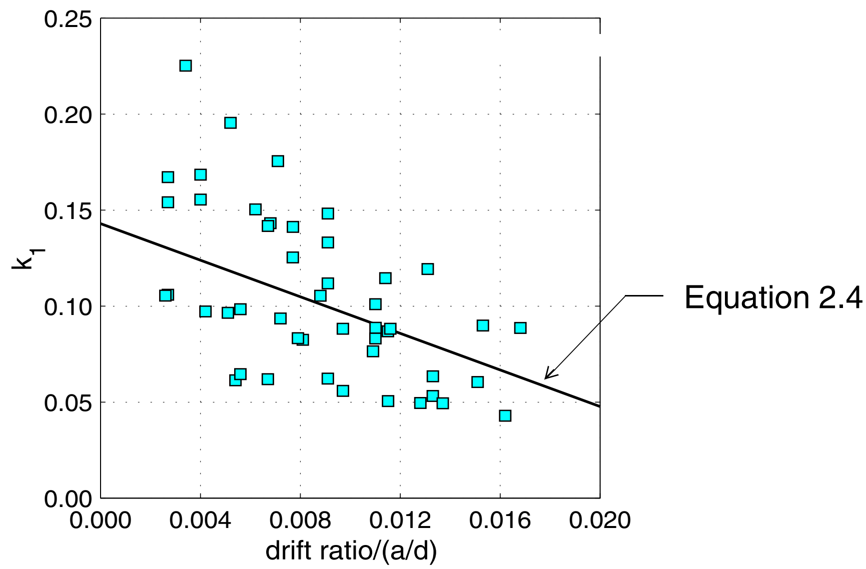

Figure 2-10. Comparison of cohesion coefficient from Pujol et al. (2000) with database from Section 2.2

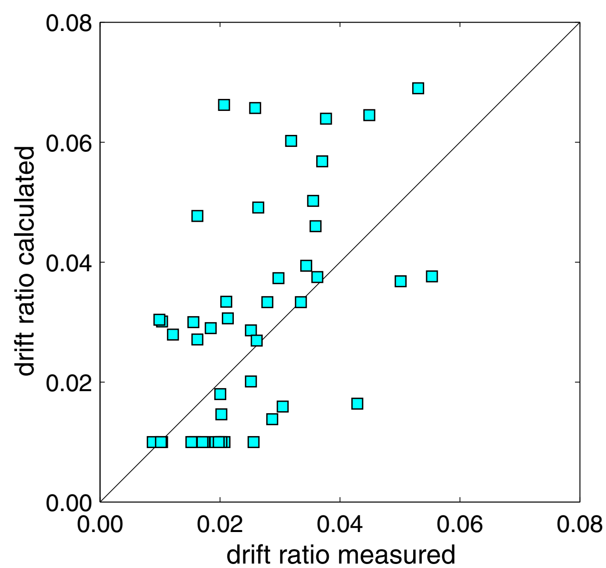

Figure 2-11. Comparison of calculated and measured drifts for Pujol et al. (2000) model

$$\frac{\Delta_{max}}{L} = \frac{3}{100}\left(\frac{a}{d}\right)(1-7k_1) \geq \frac{1}{100} \tag{2.5}$$

Figure 2-11 compares the calculated and measured drift ratios for the columns in the database from Section 2.2. The mean of the measured drift ratio divided by the calculated drift ratio is 1.12; the coefficient of variation is 0.55. Although the mechanics of this model are transparent to

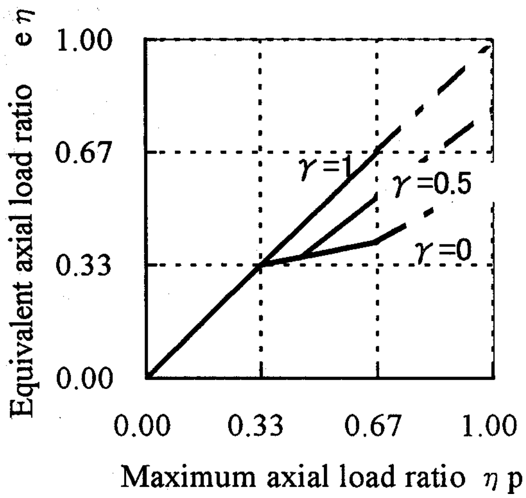

Figure 2-12. Equivalent axial load ratio (from Kato and Ohnishi, 2002)
(γ = minimum axial load / maximum axial load > 0)

the user, the relatively large coefficient of variation suggests that parameters not considered in the model may influence the maximum drift ratio for shear-critical columns.

2.3.4 Kato and Ohnishi (2002)

Kato and Ohnishi proposed that the plastic drift capacity can be estimated based on the maximum edge strain in the core concrete, the axial load ratio, and the cross-section dimensions. The total drift ratio is given by the sum of the drift ratio at yielding of the longitudinal reinforcement and the calculated plastic drift ratio:

$$\frac{\Delta}{L} = \frac{\Delta_y}{L} + \frac{\Delta_p}{L} \tag{2.6}$$

$$\text{where } \frac{\Delta_p}{L} = \begin{cases} D\left(\dfrac{m\varepsilon_{cp}}{j_e}\right)\left(\dfrac{2}{3}\Big/e_\eta\right) & \left(0 < e_\eta < \dfrac{1}{3}\right) \\ D\left(\dfrac{m\varepsilon_{cp}}{j_e}\right)\left(\dfrac{2}{3}\Big/\left(5e_\eta - \dfrac{4}{3}\right)\right) & \left(\dfrac{1}{3} \le e_\eta < \dfrac{2}{3}\right) \end{cases} \tag{2.7}$$

where D is the full depth of the gross cross section, j_e is the depth of the core, ε_{cp} is the strain at maximum stress for the core concrete, m is the ratio of the concrete strain at the edge of the core concrete to ε_{cp}, and e_η is an equivalent axial load ratio accounting for the effect of variable axial loads (Figure 2-12). The coefficient m was selected to achieve a good agreement between

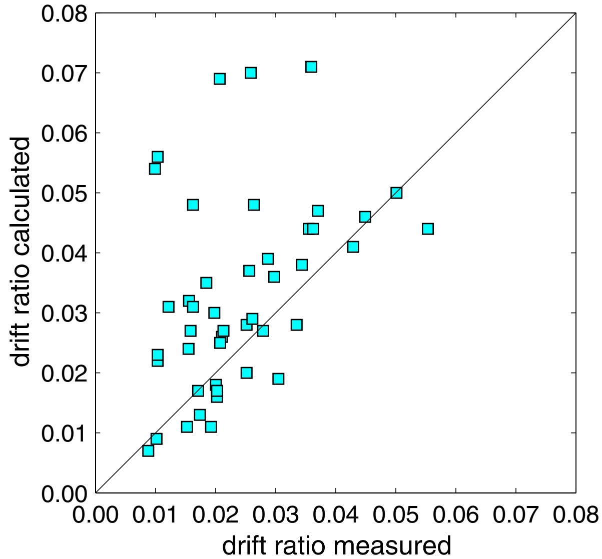

Figure 2-13. Comparison of calculated and measured drifts for Kato and Ohnishi (2002) model

Equation 2.6 and measured drifts ratios from 36 pseudo-static column tests. For the drift at shear failure (also defined as the drift at 20% loss in shear capacity), Kato and Ohnishi (2002) recommend m = 2.3. For the drift at axial failure, Kato and Ohnishi (2002) recommend m = 3.6 (this model will be evaluated in Chapter 3).

Figure 2-13 compares the calculated drift ratios at shear failure based on Equation 2.6 with the measured drift ratios for the columns in the database from Section 2.2. To avoid introducing additional errors into the model, the drift ratio at yielding of the longitudinal reinforcement, used in Equation 2.6, was determined based on the experimental data (Table 2-1). The core concrete was assumed to be unconfined for each of the column specimens, hence, ε_{cp} was set equal to 0.002. Columns with zero axial load could not be evaluated using the model, and do not appear in Figure 2-13. The mean of the measured drift ratio divided by the calculated drift ratio is 0.84; the coefficient of variation is 0.44. Although the model provides a better estimate of the measured drift at shear failure compared with the models by Pujol and Sezen, Equation 2.6 relies on an accurate estimate of the drift at yielding of the longitudinal reinforcement and significantly overestimates the drift at shear failure for many of the columns with low axial loads.

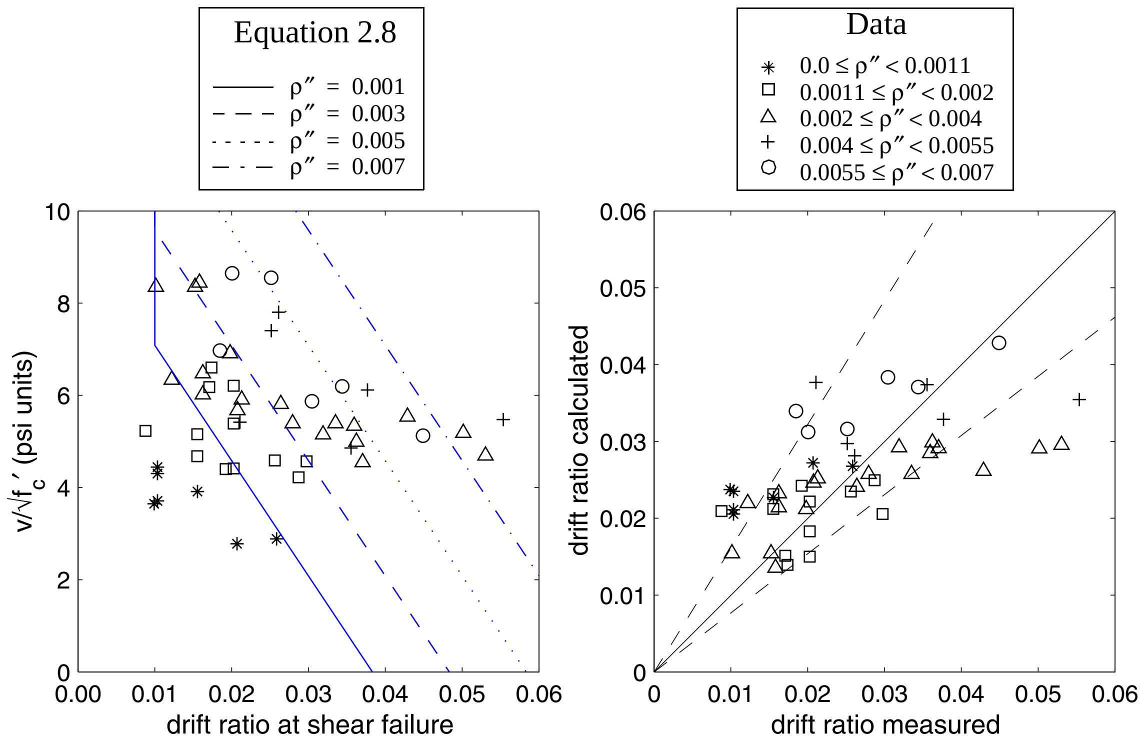

Figure 2-14. Comparison of calculated drift ratio at shear failure using Equation 2.8 with database from Section 2.2. (Dashed lines in right plot are +/− one standard deviation from the mean.)

2.3.5 Proposed Empirical Drift Capacity Models

The models for the drift ratio at shear failure presented in the previous sections do not adequately capture the behavior of the shear-critical columns included in the experimental database from Section 2.2. This section will introduce an empirical model based on observations from the experimental database. As such, the model may not be applicable to columns with parameters outside the ranges included in the database. The goal of developing a new model is to reduce the coefficient of variation and provide a simple relationship that identifies the critical parameters influencing the drift at shear failure for shear-critical building columns.

If the data shown in the upper left plot of Figure 2-2 are sorted by transverse reinforcement ratio (Figure 2-14), then, for a given transverse reinforcement ratio, the maximum shear stress can be seen to degrade with increasing drift at shear failure. The “bins” used in Figure 2-14 to sort the data by transverse reinforcement ratio were chosen to group the data points close to $\rho'' =$

0.001, 0.0015, 0.003, 0.005, and 0.006. Based on this observation, the following empirical expression is proposed to estimate the drift ratio at shear failure:

$$\frac{\Delta_s}{L} = \frac{1}{30} + 5\rho'' - \frac{4}{1000}\frac{v}{\sqrt{f_c'}} \geq \frac{1}{100} \text{ (psi units)} \tag{2.8}$$

The coefficients in Equation 2.8 were chosen based on a least-squares fit to the data. The mean of the measured drift ratio divided by the calculated drift ratio is 0.96; the coefficient of variation is 0.35. Refinement of the coefficients using more significant figures could reduce the coefficient of variation and improve the mean; however, such refinements would imply a higher degree of accuracy than the model should be expected to produce. The relatively large scatter suggests that other parameters not included in Equation 2.8, such as axial load ratio, likely influence the drift ratio at shear failure.

The influence of axial load on the drift ratio at shear failure was incorporated into the empirical model by including the variable $P/(A_g f_c')$ in the least-squares fit to the data, resulting in the following expression for the drift ratio at shear failure:

$$\frac{\Delta_s}{L} = \frac{3}{100} + 4\rho'' - \frac{1}{500}\frac{v}{\sqrt{f_c'}} - \frac{1}{40}\frac{P}{A_g f_c'} \geq \frac{1}{100} \text{ (psi units)} \tag{2.9}$$

Figure 2-15 compares Equation 2.9 with the results from the database. The mean of the measured drift ratio divided by the calculated drift ratio is 0.97, the coefficient of variation is 0.34; indicating that the incorporation of the axial load ratio results in only a slight improvement over Equation 2.8.

The left-hand plot of Figure 2-15 compares Equation 2.9, using the mean value of $v/\sqrt{f_c'}$ from the database, with the axial load and transverse-reinforcement ratios for each of the column tests. The results from the database suggest that for columns with low levels of transverse reinforcement, say $\rho''<0.004$, an increase in the axial load ratio tends to result in a decrease in the drift ratio at shear failure. For columns with $\rho''>0.004$, a relationship between the axial load ratio and drift ratio at shear failure is not as clear, suggesting that Equation 2.8, which ignores the influence of axial load, may be more appropriate for such columns.

Note that the empirical drift capacity models are less sensitive to variability in the shear strength or flexural strength compared with the Sezen (2002) shear-strength model due to the rel-

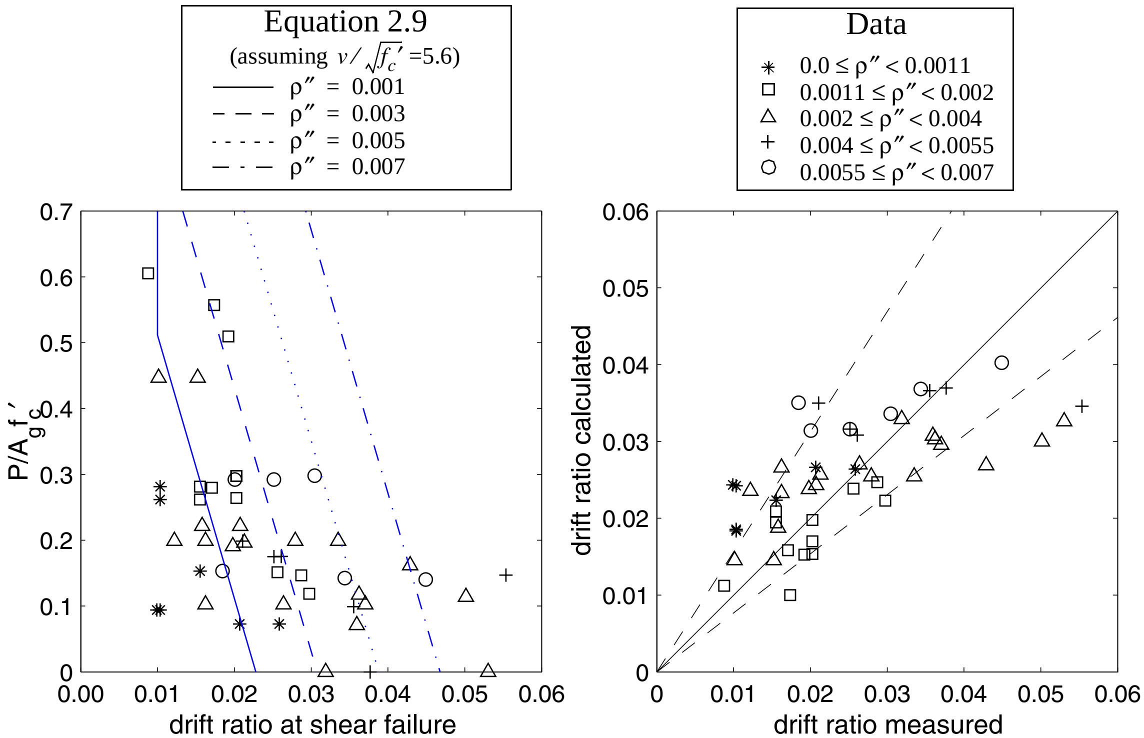

Figure 2-15. Comparison of calculated drift ratio at shear failure using Equation 2.9 with database from Section 2.2. (Dashed lines in right plot are +/− one standard deviation from the mean.)

atively steep slope of the relationship between shear stress and drift ratio at shear failure resulting from Equations 2.8 and 2.9 (e.g., see left-hand plot of Figure 2-14). The steeper lines result from grouping the data by transverse reinforcement ratio.

The application of the proposed empirical drift capacity models should be limited to columns representative of those included in the database from Section 2.2. In particular, Equations 2.8 and 2.9 should be used only if the shear capacity defined by an appropriate shear-strength model (e.g., Equation 2.1 (Sezen, 2002)) is exceeded by the shear demand calculated according to accepted analytical procedures. Further study is required to account for variability in both the demand and capacity, and the influence of the variability on the selection of an appropriate drift capacity model.

Equations 2.8 and 2.9 can be considered limit state surfaces defining the point of shear failure for a column representative of those included in the database. For Equation 2.8, each of the lines shown in the left-hand plot of Figure 2-14 define the shear-failure surface for a column with a given transverse reinforcement ratio. As shown in Figure 2-16, the predicted flexural response of

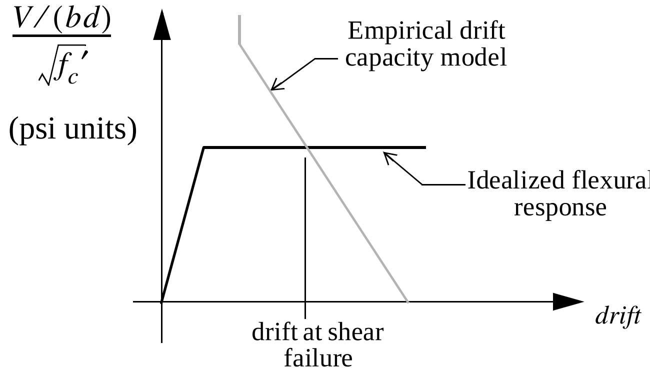

Figure 2-16. Evaluation of drift at shear failure

a column can be plotted along with the line defined by either Equation 2.8 or 2.9, and the intercept provides an estimate of the state of the column at the point of shear failure.

Earthquake reconnaissance has shown that columns in reinforced concrete buildings constructed before the introduction of details for seismic resistance (e.g., closely spaced ties and 135° hooks) in the early 1970s in the western United States are particularly vulnerable to shear failure. Such columns typically experience maximum shear stresses greater than $2\sqrt{f_c'}$ (psi units) and have transverse reinforcement ratios less than 0.002. Equations 2.8 and 2.9 suggest that the drift ratio at shear failure for such columns could range from 0.01 to 0.035.

Figure 2-17 compares the accuracy of the shear-strength and drift-ratio capacity models for the database from Section 2.2. The plots clearly illustrate that the shear strength can be estimated more accurately than the at shear failure. For both Equations 2.8 and 2.9, approximately 60% of the data points fall within the lower-left and upper-right quadrants, indicating that if the shear-strength model underestimates (or overestimates) the shear strength of the column, then the drift capacity model will not necessarily underestimate (or overestimate) the drift capacity as well.

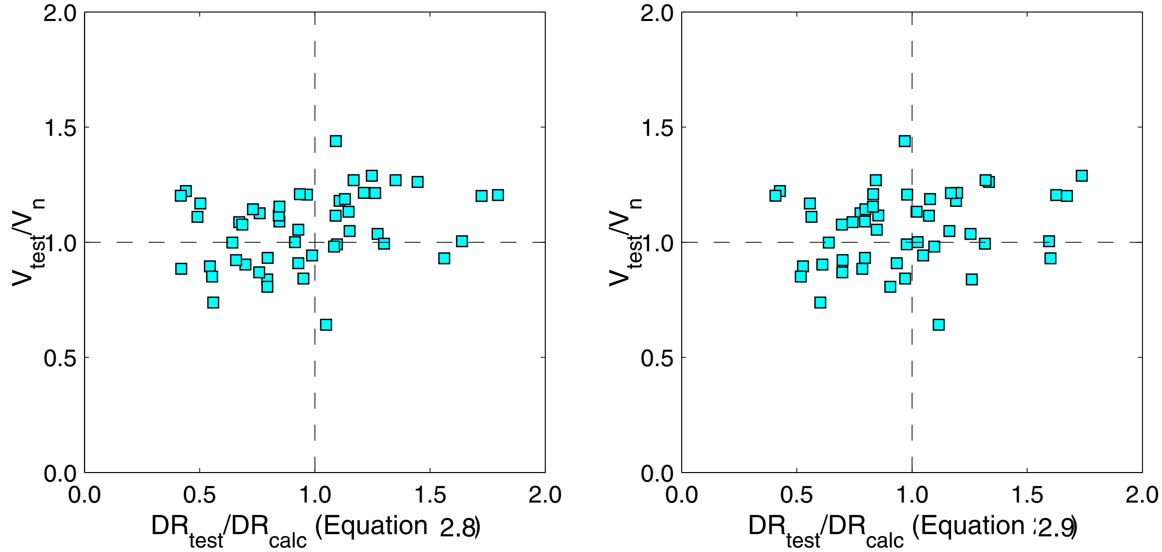

Figure 2-17. Comparison of Sezen (2002) shear-strength capacity model (Equation 2.1) and drift-ratio capacity models (Equations 2.8 and 2.9)

3 Axial Capacity Model

3.1 INTRODUCTION

A method to calculate the axial capacity of a column that has previously failed in shear will be introduced in this chapter. Given such a method, engineers involved in seismic retrofits will be better equipped to evaluate whether shear-critical elements, unable to withstand the expected lateral deformations without shear failure, will be able to maintain their axial loads. The method will also help to determine how much axial load must be transferred to neighboring elements after a column shear failure and to aid in quantifying the ability of a structural system to resist collapse.

3.2 EXPERIMENTAL EVIDENCE

Most tests of reinforced concrete columns under seismic load conditions have been terminated shortly after the loss of lateral load capacity. The resulting data are useful for columns considered as part of the lateral-force-resisting system. Considering traditional notions of safety (i.e., once shear failure begins, axial load collapse cannot be far behind), the data also probably define a practical upper-bound displacement capacity even for columns not considered part of the lateral-force-resisting system in new building designs. For existing buildings, whether being evaluated for seismic resistance or for seismic retrofit, a less conservative approach may be required by economic and functionality considerations. If a column can reliably carry gravity load after its lateral strength degradation begins, it may be possible to achieve considerable savings by considering the column as a secondary component.

For this reason pseudo-static tests on full-scale shear-critical reinforced concrete columns were conducted by Lynn (2001) and Sezen (2002) up to the point of axial failure. These tests were

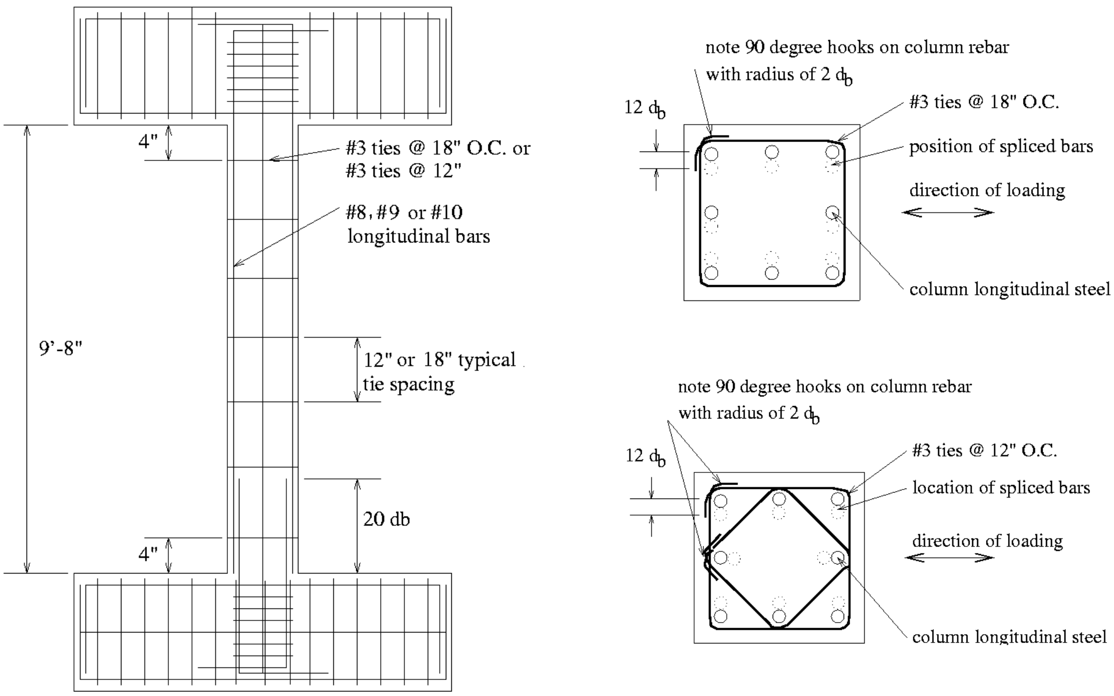

Figure 3-1. Typical column test specimen (Lynn, 2001; Sezen, 2002)

also included in the larger database used to develop a model for the drift at shear failure (see Section 2.2). Figure 3-1 illustrates a typical test column configuration. Table 3-1 summarizes the specific column characteristics, material properties, and measured responses. The loading routine subjected a column to nominally constant axial compression and maintained nominally zero rotation between column ends while the column was subjected to a series of lateral displacements at increasing amplitude, with three cycles at each amplitude. The two exceptions were Column 2CVD12, which had variable axial load ranging from 56 kips tension to 600 kips compression (with an axial load of 331 kips just before axial failure), and Column 2CLD12M, which, after cycles below the yield displacement, was subjected to monotonic lateral loading until axial failure. Since the test setup did not allow for any redistribution of the applied axial load, once axial failure was initiated the tests were terminated.

Owing to the limited size of the database of tests providing axial failure data, it is difficult to draw conclusions; however, some trends can be observed. Figure 3-2 plots drift ratios corresponding to significant events for the 12 columns reported by Lynn and Sezen. For columns having lower axial loads, the tendency is for axial load failure to occur at relatively large drifts,

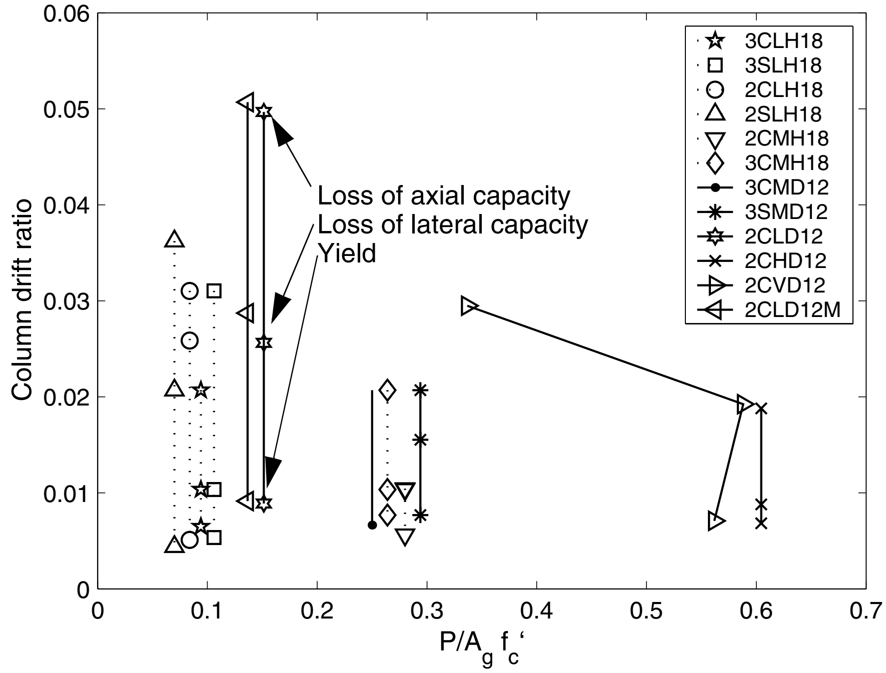

Figure 3-2. Column drift ratios as a function of axial load for columns tested by Lynn (2001) and Sezen (2002). (Dashed and solid lines indicate columns with transverse reinforcement spacing of 18″ and 12″, respectively.)

regardless of whether shear failure had just occurred or whether shear failure had occurred at much smaller drift ratios. For columns with larger axial loads, axial load failure tended to occur at smaller drift ratios, and might occur almost immediately after loss of lateral load capacity. Note also that the drift ratios at axial load failure tend to be lower for columns with larger spacing of the transverse reinforcement (dashed lines). The next section presents a shear-friction model that can be used to represent the general observation from Figure 3-2 that the drift at axial load failure is inversely related to the magnitude of axial load, and directly related to the amount of the transverse reinforcement.

3.3 A SHEAR-FRICTION MODEL

3.3.1 Equilibrium Equations

The column shown in Figure 3-3 was damaged during the 1999 Kocaeli, Turkey, earthquake. Any axial load supported by the damaged column must be transferred across the obvious shear failure plane. Such transfer of load can be modeled by a mechanism known as shear friction. Shear-fric-

Table 3-1 Database of columns with axial failure data

Specimen	b (in.)	d (in.)	cover (in.)	a (in.)	l_{splice} (in.)	No. bars	d_b (in.)	$\rho_{long.}$	A_{st} (in.^{2})	s (in.)	Tie type	f'_c (ksi)	f_{yl} (ksi)	f_{yt} (ksi)	P (kips)	V_{test} (kips)	Δ_y (in.)	Δ_s (in.)	Δ_a (in.)
Lynn (2001)																			
3CLH18	18	15.49	1.5	58	None	8	1.27	0.03	0.22	18	r90	3.71	48	58	113	61	0.75	1.2	2.4
2CLH18	18	15.625	1.5	58	None	8	1	0.02	0.22	18	r90	4.80	48	58	113	54	0.59	3.0	3.6
3SLH18	18	15.49	1.5	58	25	8	1.27	0.03	0.22	18	r90	3.71	48	58	113	60	0.62	1.2	3.6
2SLH18	18	15.625	1.5	58	20	8	1	0.02	0.22	18	r90	4.80	48	58	113	52	0.51	2.4	4.2
2CMH18	18	15.625	1.5	58	None	8	1	0.02	0.22	18	r90	3.73	48	58	340	71	0.65	1.2	1.2
3CMH18	18	15.49	1.5	58	None	8	1.27	0.03	0.22	18	r90	4.01	48	58	340	76	0.89	1.2	2.4
3CMD12	18	15.49	1.5	58	None	8	1.27	0.03	0.38	12	d90	4.01	48	58	340	80	0.77	1.8	2.4
3SMD12	18	15.49	1.5	58	25	8	1.27	0.03	0.38	12	d90	3.73	48	58	340	85	0.89	1.8	2.4
Sezen (2002)																			
2CLD12	18	15.436	1.625	58	None	8	1.128	0.025	0.38	12	d90	3.06	64	68	150	73	1.03	3.0	5.8
2CHD12	18	15.436	1.625	58	None	8	1.128	0.025	0.38	12	d90	3.06	64	68	600	78	0.79	1.0	2.2
2CVD12	18	15.436	1.625	58	None	8	1.128	0.025	0.38	12	d90	3.03	64	68	Var.	70	0.82	2.2	3.4
2CLD12M	18	15.436	1.625	58	None	8	1.128	0.025	0.38	12	d90	3.16	64	68	150	67	1.06	3.3	5.9

Notation: b = square column width; d = depth to centerline of tension reinforcement; cover = clear cover to transverse steel; a = shear span (half of column height); l_{splice} = splice length; d_b = diameter of longitudinal reinforcement; ρ_{long} = longitudinal reinforcement ratio; A_{st} = area of tie steel; s = tie spacing; f'_c = concrete strength; f_{yl} = longitudinal steel yield strength; f_{yt} = transverse steel yield strength; P = axial load (Var. = variable axial load); V_{test} = peak shear recorded; Δ_y = yield displacement (based on strain gage data); Δ_s = displacement at shear failure (at 20% loss in peak shear); Δ_a = displacement at axial failure. Tie types: r90 = rectangular hoop with 90° hooks; d90 = rectangular and diamond hoops with 90° hooks.

Figure 3-3. Damaged column from 1999 Kocaeli, Turkey, earthquake

tion models evaluate the shear stress that can be transferred across a crack as a function of the normal stress on the crack surface. The normal stress results from the elongation of reinforcement crossing the crack and/or applied forces normal to the crack surface. For the column shown in Figure 3-3, the transverse reinforcement crossing the shear failure plane and the axial load carried by the column combine to provide a normal force and, hence, a shear transfer across the shear failure plane.

Figure 3-4 shows the free-body diagram for the upper portion of the column from Figure 3-3. The external moment vector at the top of the column is not shown and will not enter the equilibrium equations written here. The inclined free surface at the bottom of the free-body diagram is assumed to follow a critical inclined crack associated with shear damage. In this presentation, the "critical" crack is one that, according to the idealized model, results in axial load failure as the shear-friction demand exceeds the shear-friction resistance along the crack. The dowel forces from the transverse reinforcement crossing the inclined crack are not shown; instead, the dowel forces are assumed to be included implicitly in the shear-friction force, V_{sf}, along the inclined plane. Equilibrium of the forces shown in the free-body diagram results in the following equations:

$$\Sigma F_x \rightarrow N\sin\theta + V = V_{sf}\cos\theta + \frac{A_{st}f_{yt}d_c}{s}\tan\theta + n_{bars}V_d \qquad (3.1)$$

$$\Sigma F_y \rightarrow P = N\cos\theta + V_{sf}\sin\theta + n_{bars}P_s \qquad (3.2)$$

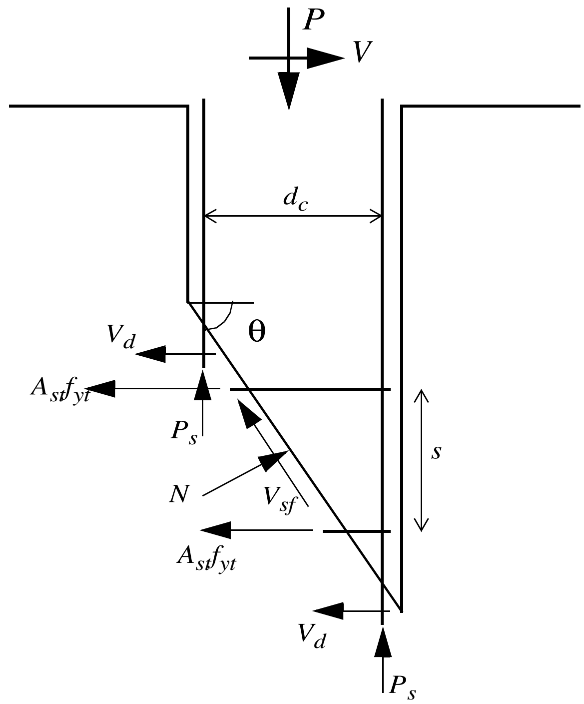

Figure 3-4. Free-body diagram of column after shear failure

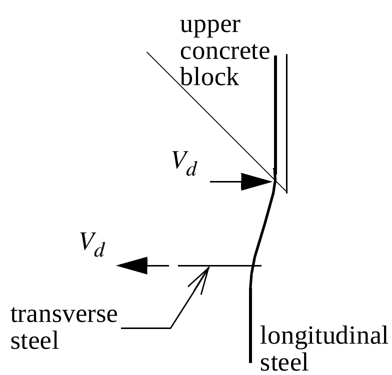

Figure 3-5. Dowel action in longitudinal bars

where n_{bars} is the number of longitudinal bars crossing the shear failure plane, d_c is the depth of the column core from center line to center line of the ties, s is the spacing between the transverse reinforcement, A_{st} and f_{yt} are the area and yield strength, respectively, of the transverse reinforcement, and the forces P, V, N, V_{sf}, P_s, and V_d are shown in Figure 3-4.

The shear resistance due to the dowel action of the longitudinal bars, V_d, is dependent on the spacing of the transverse reinforcement. As shown in Figure 3-5, the upper concrete block will bear against the longitudinal bar on one side of the crack and the transverse steel will restrain the bar on the other side. As the distance between these forces increases, the effectiveness of the dowel action will diminish. Owing to the large spacing of transverse reinforcement in many shear-critical columns of interest in this study, the distance between the forces will most likely be too large to develop any significant dowel action. Note that the dowel action may be more effective for longitudinal reinforcement along the side face of the column (i.e., parallel to the direction of applied shear), since these bars will be restrained by concrete above and below the failure plane. However, any limited resistance to sliding from the dowel action can be considered as incorporated in the shear due to shear-friction, V_{sf}, acting on the shear failure plane. Hence, the forces due to the dowel action will be ignored in the derivation of the axial capacity model. In addition, when considering the stage of axial load failure, the external shear force V can be set equal to zero, under the assumption that the column has lost most of its lateral load resistance due to shear failure.

In light of the above discussion, Equation 3.1 can be rewritten as follows:

$$N\sin\theta = V_{sf}\cos\theta + \frac{A_{st}f_{yt}d_c}{s}\tan\theta \qquad (3.3)$$

Further development of an axial capacity model using Equations 3.2 and 3.3 requires models for the critical crack angle, θ, the axial capacity of the longitudinal reinforcement, P_s, and the relationship between N and V_{sf}. Each of these models will be discussed in turn in the following sections.

3.3.2 Critical Crack Angle

Few reliable models exist for estimating the inclination θ of the shear failure plane. A basic principles approach is to define θ as the angle of the nominal principal tension stress at the instant when it reaches the tensile capacity of concrete under combined shear and axial load, using a Mohr's circle representation of the state of stress. This approach, however, invariably results in an angle steeper than that observed in tests.

A model proposed by Kim and Mander (1999) estimates the crack angle based on minimizing the external work due to a unit shear force. For the columns tested by Lynn and Sezen, the critical crack angle estimated by the model ranges from 65° to 71°, with an average of 68°.

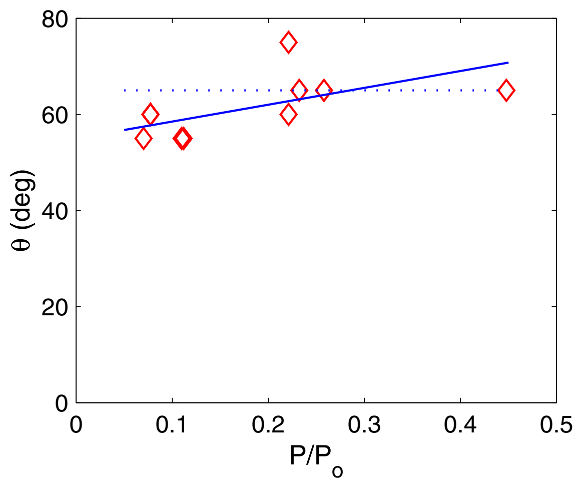

Figure 3-6. Relation between observed angles of critical cracks and axial load

Figure 3-6 plots the observed average angle of critical shear cracks from the tests. (The angles were subjectively estimated from photographs.) The angle could be approximated as 65° relative to horizontal (the dashed line in the figure), or could have the linear variation suggested by the solid line in the figure, that is:

$$\theta = 55 + 35P/P_o \tag{3.4}$$

P_o is the axial capacity of the undamaged column given by $P_o = 0.85f_c(A_g - A_{sl}) + f_{yl}A_{sl}$ where f'_c is the concrete compressive strength, A_g is the gross concrete area, A_{sl} is the area of longitudinal steel, and f_{yl} is the yield strength of the longitudinal reinforcement. (The outlying datum in Figure 3-6 at $P/P_o \approx 0.21$ was for Column 3CMH18. That column had a critical crack that was somewhat less steep over most of its length, with a vertical segment near column mid-depth, resulting in the relatively large reported critical crack angle.) Considering the difficulties of accurately determining the critical crack angle given the state of many of the columns at the end of the tests, and the lack of improvement observed in the prediction of the drift at axial failure when Equation 3.4 is used in place of a constant crack angle of 65°, only the constant crack angle model will be used in the development of the axial failure model presented here.

All of the columns tested by Lynn and Sezen had a height to width ratio greater than 6.0. For columns with low height to width ratio, it is expected that the maximum crack angle will be limited by the aspect ratio of the column (i.e., $\theta_{max} = \tan^{-1}(height/width)$). This may be considerably less than 65°.

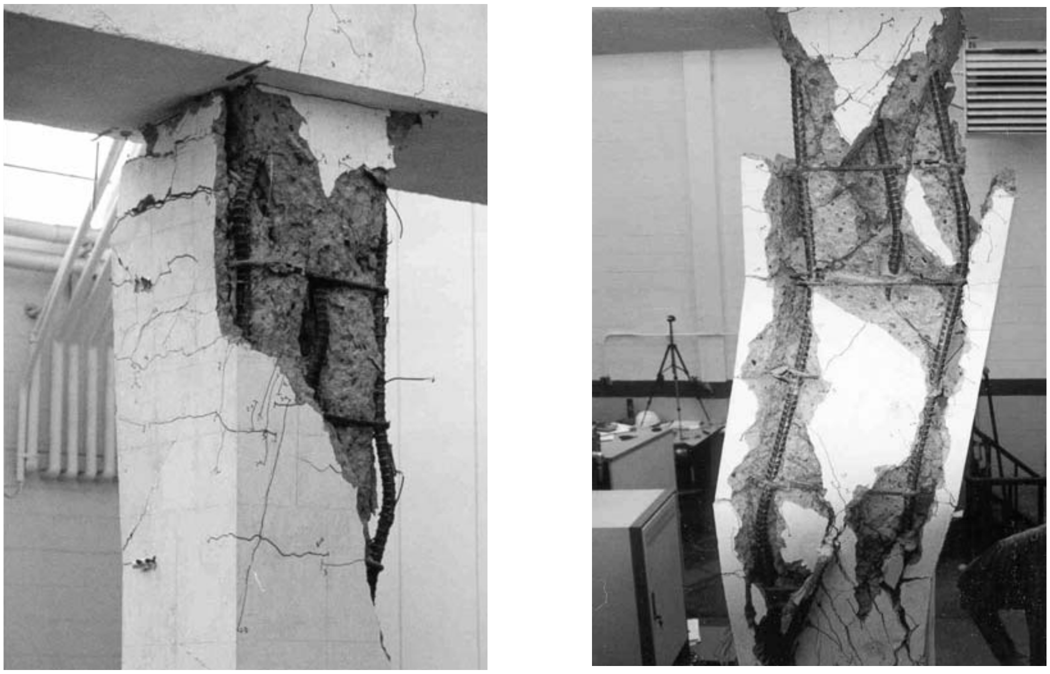

(a) (b)

Figure 3-7. Deformed shape for longitudinal bars at loss of axial load capacity for column with (a) high axial load and (b) low axial load (Sezen, 2002)

3.3.3 Longitudinal Reinforcement Axial Capacity

Based on observations of the final state of the column longitudinal reinforcement from the static tests by Lynn (2001) and Sezen (2002), it is assumed that the longitudinal reinforcement will support a portion of the axial load, $n_{bars}P_s$, up to a maximum load defined by either the buckling or the plastic capacity of the reinforcing bars. Columns with an axial load greater than the pure axial plastic capacity of the longitudinal reinforcement ($A_{sl}f_{yl}$) experienced a deformed shape of the longitudinal reinforcement after axial failure indicative of a buckling failure (e.g., Figure 3-7a). In contrast, most of the columns with an axial load less than $A_{sl}f_{yl}$ experienced a deformed shape of the longitudinal reinforcement after axial failure that did not suggest a buckling failure of the longitudinal reinforcement (Figure 3-7b). Note that the elastic buckling capacity of the longitudinal reinforcement, calculated using a buckling length equal to the spacing of the ties and assuming full rotational fixity at the bar ends, is greater than $A_{sl}f_{yl}$, suggesting that the lightly loaded columns in the test series will not experience buckling of the longitudinal reinforcement upon axial failure.

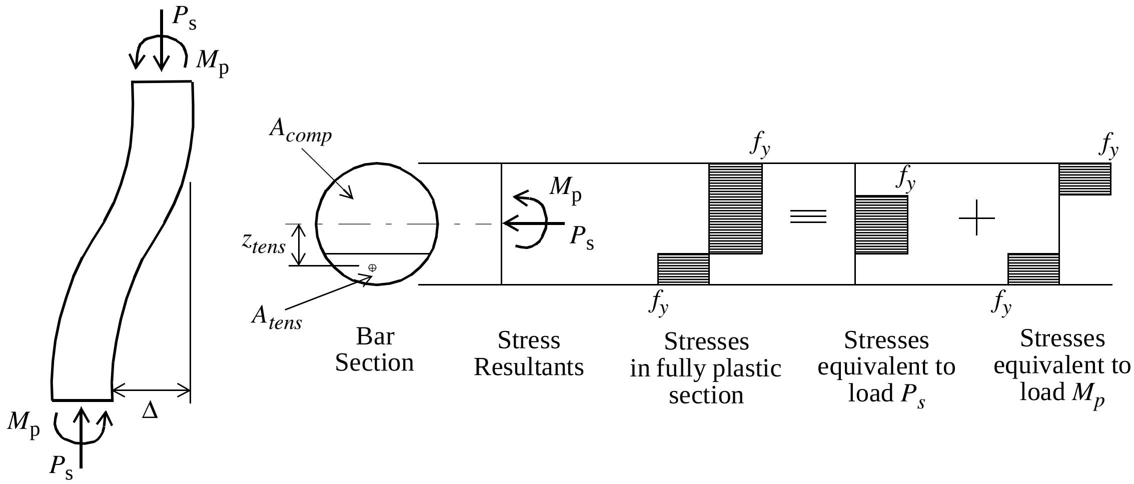

Figure 3-8. Plastic strength of longitudinal reinforcement in deformed configuration

Based on these observations the longitudinal reinforcement axial capacity was evaluated as follows:

- for columns where $P < A_{sl}f_{yl}$, P_s is based on the plastic axial load strength of the longitudinal reinforcement in the deformed configuration.
- for columns where $P \geq A_{sl}f_{yl}$, P_s is based on the plastic strength in the deformed configuration, but limited by the plastic buckling capacity.

The following paragraphs discuss each of these cases in turn.

The plastic strength of the longitudinal reinforcement in the deformed configuration is illustrated in Figure 3-8. Assuming there is no dowel force, the plastic moment capacity of the reinforcing bar and the axial capacity are related by:

$$P_s\Delta = 2M_p \tag{3.5}$$

By using the decomposition of the stresses in the fully plastic section of a reinforcing bar shown in Figure 3-8, the plastic moment can be determined as follows:

$$M_p = 2A_{tens}f_{yl}z_{tens} \tag{3.6}$$

where A_{tens} is the area of the reinforcing bar in tension, and z_{tens} is the distance from the centroid of A_{tens} to the centroid of the bar section. Given an axial load in the reinforcing bar, A_{tens} can be determined as follows:

$$A_{tens} = \frac{1}{2}\left(A_{bar} - \frac{P_s}{f_{yl}}\right) \tag{3.7}$$

where A_{bar} is the cross-sectional area of one longitudinal reinforcing bar. Equations 3.5 through 3.7 can be used to determine a theoretical relation between the axial load, P_s, and the lateral displacement at which the plastic capacity of a reinforcing bar is fully developed. The results for the three bars used as longitudinal reinforcement in the tests by Sezen (2002) and Lynn (2001) are shown in Figure 3-9.

The curves shown in Figure 3-9 must be determined by iteration due to the nonlinear moment-axial load interaction diagram that results from solving Equations 3.6 and 3.7. If the linear conservative approximation to the interaction diagram shown in Figure 3-10 is used with Equation 3.5, the axial plastic capacity of the longitudinal reinforcement can be related directly to the story drift, without iteration, as follows:

$$\frac{P_s}{A_{bar}f_{yl}} = \frac{d_b/L}{\frac{3}{4}\pi\frac{\Delta}{L} + \frac{d_b}{L}} \tag{3.8}$$

where L is the clear height of the column, and d_b is the diameter of the longitudinal reinforcing bars. Equation 3.8, shown in Figure 3-11, provides a conservative approximation of the axial plastic capacity of the longitudinal reinforcement without iteration and will be used in the further development of the axial capacity model.

For heavily loaded columns ($P \geq A_{sl}f_{yl}$), the axial capacity of the longitudinal reinforcement given by Equation 3.8 will be limited by the plastic buckling capacity. Evaluation of the plastic buckling capacity requires estimation of the tangent modulus of the reinforcement and the effective buckling length. Based on tensile coupon tests of typical reinforcing bars, the tangent modulus is estimated as $0.07E_s$, where E_s is the elastic modulus of the reinforcement. (Alternatively, an equivalent modulus model could be used to estimate the material stiffness (Pantazopoulou, 1998); however, such a model predicts that the plastic buckling load does not control the axial capacity of the longitudinal reinforcement for any of the columns in the database. Considering the observed buckled deformed shape of the longitudinal reinforcement for two of the tests (Figure 3-7a), the equivalent modulus model was not adopted for this study.) Based on the observed deformed shape of the longitudinal reinforcement shown in Figure 3-7a, the effective buckling

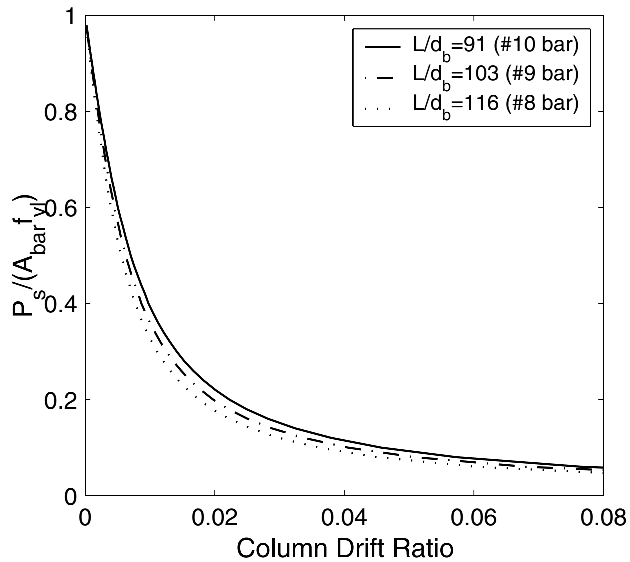

Figure 3-9. Longitudinal reinforcing bar axial plastic capacity using Equations 3.5 through 3.7

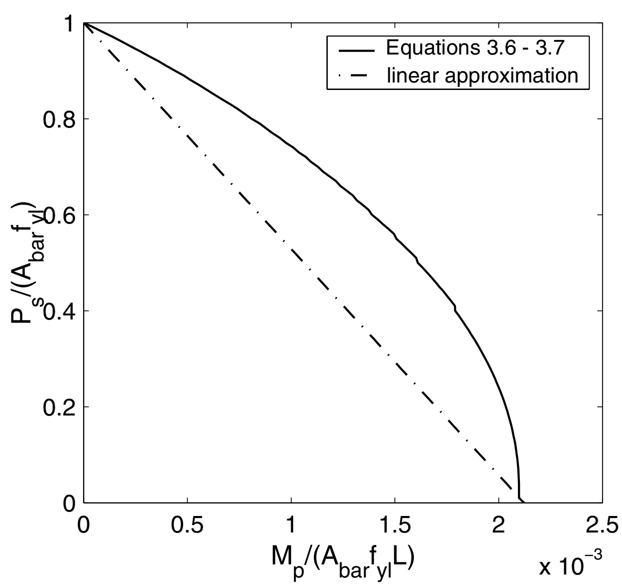

Figure 3-10. Axial load-moment interaction diagram for reinforcing bar (L/d_b = 100)

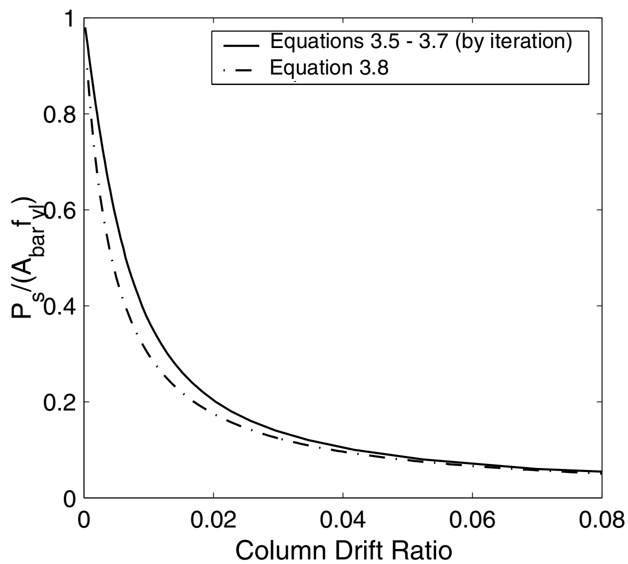

Figure 3-11. Longitudinal reinforcing bar axial plastic capacity. Comparison of iterative method and approximation of Equation 3.8. (L/d_b = 100)

length should be $1.0s < L_{eff} < 0.7s$ (i.e., shorter than a pinned-pinned condition at the ties and longer than a fixed-fixed condition at the ties). An effective buckling length of 0.8*s* is selected for this investigation. Based on these assumptions, the axial capacity of the longitudinal reinforcement is given by:

$$\frac{P_s}{A_{bar}f_{yl}} = \frac{d_b/L}{\frac{3}{4}\pi\frac{\Delta}{L}+\frac{d_b}{L}} \qquad \text{if } P < A_{sl}f_{yl} \tag{3.9}$$

$$= \frac{d_b/L}{\frac{3}{4}\pi\frac{\Delta}{L}+\frac{d_b}{L}} < 0.1\frac{\pi^2 E_s I_{bar}}{s^2}\frac{n_{bars}}{A_{sl}f_{yl}} \qquad \text{if } P \geq A_{sl}f_{yl}$$

Table 3-2 gives the axial capacity of the longitudinal reinforcement at axial failure of the column, estimated based on Equation 3.9, for the columns tested by Lynn and Sezen. The values in Table 3-2 were calculated based on the total measured column drift ratio at axial failure. Note that only 2CMH18 is controlled by the plastic buckling load. For most of the columns the above formulation results in approximately 25% of the axial load being carried by the longitudinal reinforcement at the point of axial failure. For two of the columns with a low axial load (P=0.09$A_g f'_c$) and a relatively high longitudinal reinforcement ratio of 3%, Equation 3.9 estimates that the longitudinal bars are supporting over 50% of the axial load. Owing to the relatively low axial stiffness

Table 3-2. Calculated longitudinal reinforcement axial capacity for columns in database from Section 3.2

Specimen	$P_s/(A_{bar}f_{yl})$	$P_s n_{bars}/P$
3CLH18	0.18 (0.12)	0.76 (0.50)
2CLH18	0.11	0.29
3SLH18	0.13 (0.12)	0.54 (0.50)
2SLH18	0.09	0.25
2CMH18	0.11[a]	0.10
3CMH18	0.18	0.25
3CMD12	0.18	0.25
3SMD12	0.18	0.25
2CLD12	0.08	0.27
2CHD12	0.18	0.16
2CVD12	0.12	0.19
2CLD12M	0.08	0.26

a. Controlled by plastic buckling capacity

of the longitudinal bars, this seems unreasonably high and suggests that a limit on the fraction of axial load supported by the longitudinal bars may be appropriate. As shown in Figure 3-4, the axial load supported by shear friction and the axial load supported by the longitudinal reinforcement act in parallel. By using the ultimate axial capacity of the longitudinal reinforcing bars in the equilibrium equation (Equation 3.1), it is assumed that the ultimate shear-friction capacity and the ultimate capacity of the longitudinal reinforcement are reached at the same time. The ultimate shear-friction capacity may be exceeded before full development of the longitudinal reinforcement axial capacity, thereby transferring axial load to the longitudinal reinforcement as sliding occurs on the shear failure plane. This may lead to development of the ultimate axial capacity of the reinforcement and, subsequently, to axial failure of the column. In this case, axial failure should be defined by exceeding the shear-friction capacity, and the load carried by the longitudinal reinforcement should be limited to some fraction of the total axial load. A limit of $P_s n_{bars}/P < 50\%$ was selected, since this improved the correlation of the model with test data. Considering this limit, the axial load supported by the longitudinal reinforcement for specimens 3CLH18 and 3SLH18 is reduced to $0.12A_{sl}f_{yl}$. (These latter reduced values are shown in parentheses in Table 3-2.)

3.3.4 Maximum and Total Capacity Models

Considering the expected transfer of the axial load from the shear failure plane to the longitudinal reinforcement after the shear-friction capacity is exceeded, it may be appropriate to consider the axial load support from the longitudinal reinforcement independently of that for shear friction. In such a model, the load carried by the longitudinal bars is removed from the equilibrium equation (Equation 3.2) and the capacity curves for the longitudinal reinforcement (Figure 3-11) are superimposed on the capacity curves to be developed in the next section for the shear-friction capacity. The axial capacity of the column is taken as the maximum of the capacity from the longitudinal reinforcement and the capacity from the shear-friction model. This model, referred to as the *maximum* capacity model, will be developed further in the following sections. The model based on summing the ultimate capacity from the longitudinal reinforcement and the ultimate capacity from shear-friction, in accordance with the equilibrium equations, will be referred to as the *total* capacity model.

3.3.5 Shear-Friction Models

The literature documents several shear-friction models which relate V_{sf} and N (Mattock and Hawkins, 1972; Mattock, 1988; Mau and Hsu, 1988). Two of the models will be used, in conjunction with Equations 3.2 and 3.3, to develop an expression for the axial capacity of a column after shear failure.

3.3.5.1 Classical Shear-Friction Model

The classical shear-friction model, included in ACI 318 since 1977, idealizes the crack across which shear must be transferred as a flat plane with an effective coefficient of friction, μ. The shear capacity is defined as:

$$V_{sf} = N\mu \tag{3.10}$$

where N is the compression force acting normal to the crack, as shown in Figure 3-4. Since the shear transfer mechanism includes aggregate interlock and dowel action in addition to pure friction, values for μ must be higher than that for pure friction across a concrete interface in order to match Equation 3.10 with test data.

Substitution of Equation 3.10 into Equations 3.2 and 3.3, and eliminating the case where $\mu = \tan\theta$, gives the following expression for the axial capacity of the column illustrated in Figure 3-4:

$$P = \frac{A_{st} f_{yt} d_c}{s} \tan\theta \frac{1 + \mu \tan\theta}{\tan\theta - \mu} + n_{bars} P_s \tag{3.11}$$

The first term in Equation 3.11 is the axial load carried through shear friction, while the second term is the axial load carried by the longitudinal reinforcement (given by Equation 3.9). Note that values of μ greater than $\tan(\theta = 65°)$ will result in a meaningless negative shear-friction capacity. For μ equal to zero, the shear-friction term in Equation 3.11 reduces to the same form as the 45° truss model.

Recall that for the total capacity model, the shear-friction and longitudinal reinforcement terms are summed, as shown in Equation 3.11, while for the maximum capacity model only the maximum of the two terms is considered. Equation 3.11 can be rearranged to give the following expression for the effective coefficient of friction for the total capacity model:

$$\mu_t = \frac{P - n_{bars} P_s - \frac{A_{st} f_{yt} d_c}{s}}{\frac{(P - n_{bars} P_s)}{\tan\theta} + \frac{A_{st} f_{yt} d_c}{s} \tan\theta} \tag{3.12}$$

where the subscript t refers to the total capacity model. By using a constant crack angle of 65° and the longitudinal reinforcement axial capacity given in Table 3-2 (but limited to less than 50% of the axial load on the column, as discussed previously), the effective coefficient of friction for each of the test columns can be calculated using Equation 3.12. Figure 3-13 plots the calculated values for each column as a function of the lateral drift ratio at which the column could no longer sustain the applied axial load. The data apparently follow a trend that can be approximated by:

$$\mu_t = \tan\theta - \frac{100}{3}\left(\frac{\Delta}{L}\right)_{axial} \geq 0 \tag{3.13}$$

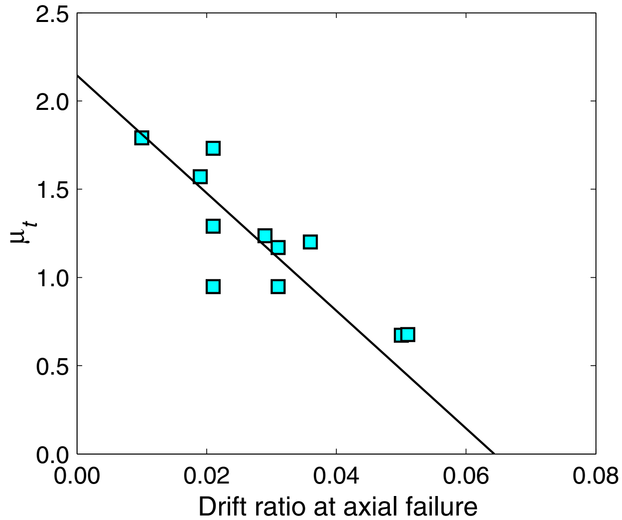

Figure 3-12. Relation between effective coefficient of friction and the drift ratio at axial failure for the total capacity model

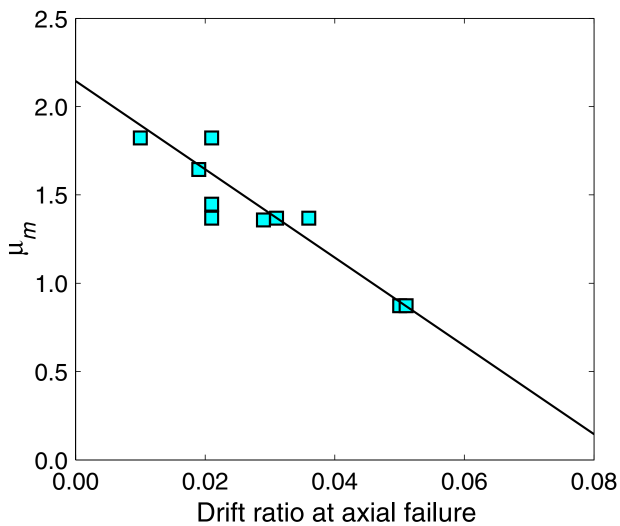

Figure 3-13. Relation between effective coefficient of friction and the drift ratio at axial failure for the maximum capacity model

In selecting Equation 3.13, the effective coefficient of friction was set equal to tan(65°) at zero drift to ensure that the shear-friction capacity remained positive for all valid drifts.

A plot similar to that shown in Figure 3-13 can be developed for the maximum capacity model by omitting the $n_{bars}P_s$ term from Equation 3.12 and recalculating the effective coefficient of friction (Figure 3-12). The data appear to have less scatter when the capacity of the longitudinal reinforcement is omitted. Based on Figure 3-12, the drift ratio at axial failure appears to follow a straight-line trend that can be approximated by:

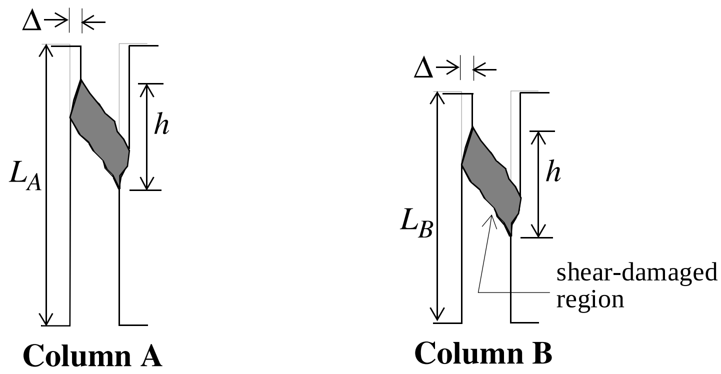

concentrated drift ratio (CDR) = $\dfrac{\Delta}{h} \approx \dfrac{\Delta}{d_c \tan\theta}$

interstory drift ratio (IDR) = $\dfrac{\Delta}{L}$

Figure 3-14. Concentrated versus interstory drift ratio

$$\mu_m = \tan\theta - \frac{100}{4}\left(\frac{\Delta}{L}\right)_{axial} \geq 0 \tag{3.14}$$

The data of Figures 3-13 and 3-12 suggest that the effective shear-friction coefficient is a function of the drift angle at axial failure. This relation is plausible considering that increased deformation (and increased sliding along the critical shear plane) degrades the roughness of the shear plane and reduces the effective friction. It is worth recalling that the increased deformation capacities are associated with reduced axial loads and increased amount of transverse reinforcement (Figure 3-2).

It is expected that the shear-friction coefficient will also be inversely proportional to other parameters related to the amount of sliding along the critical shear plane. Among others, such parameters may include the displacement ductility, the number of cycles past the yield displacement, and a drift ratio based on the height of the damaged region of the column. The interstory drift ratio (IDR) (based on the clear height of the column) was selected for this investigation to be consistent with research by other investigators into the use of the maximum IDR as an appropriate *engineering demand parameter* in a performance-based design methodology (Krawinkler et al., 2003). Axial failure may be more closely related to a drift ratio based on the height of the damaged region, or the concentrated drift ratio (CDR), as defined in Figure 3-14 (d_c is the depth of the column core from center line to center line of the ties). After shear failure, most of the column deformations are concentrated in the shear-damaged region of height h. As suggested by Figure 3-14, two columns of length L_A and L_B that experience the same displacement will have different IDRs, but may have the same CDR. For columns shorter than $d_c \tan 65°$, the height of the damaged region will be constrained by the height of the column and the IDR will be equal to the CDR. Since all of the columns tested by Lynn and Sezen have the same height to width ratio and a critical crack angle of approximately $65°$ is assumed for all specimens, the CDRs for this database will be approximately equal to the IDRs times a constant factor. For a more extensive database the CDR should be used to distinguish between columns such as those illustrated in Figure 3-14.

3.3.5.2 Modified Shear-Friction Model

The modified shear-friction model (Mattock and Hawkins, 1972; Mattock, 1988) separates the shear transferred across a crack into two terms: one representing the friction on the crack surface; and another representing the resistance of both shearing the local asperities along the crack surface and the dowel action from reinforcement crossing the crack. Mattock (1988) proposed the following form to the model based on static, monotonic, tests:

$$v_u = 4.5 f_c'^{0.545} + 0.8\sigma_n \tag{3.15}$$

where v_u is the ultimate shear stress that can be transferred across the crack through shear-friction, and σ_n is the normal stress on the crack.

A similar model was proposed by Richart et al. (1929) to define the strength of concrete:

$$v_u = k_1 f_c' + k_2 \sigma_n \tag{3.16}$$

where k_1 and k_2 were estimated to be 1/4 and 3/4, respectively, based on monotonic tests of concrete confined by hydraulic pressure. Pujol et al. (2000) used Equation 3.16 and $k_2 = 3/4$ to determine the amount of transverse reinforcement required for columns subjected to seismic loads. Using Coulomb's criterion, Pujol et al. (2000) related the constant k_1 to the drift at shear failure, and determined that k_1 tends to decrease with increasing drift ratio.

Equation 3.16, with $k_2 = 3/4$, can be converted to forces and substituted into Equations 3.2 and 3.3, giving the following expression for the axial capacity of the column illustrated in Figure 3-4:

$$P = \frac{1 + (\tan\theta)^2}{\tan\theta - 0.75} k_1 f_c' A_{core} + \frac{1 + 0.75\tan\theta}{\tan\theta - 0.75}\left(\frac{A_{st} f_{yt} d_c}{s}\right)\tan\theta + n_{bars} P_s \qquad (3.17)$$

where A_{core} is the area of the concrete core measured to the center line of the transverse reinforcement. By using $\theta = 65°$, Equation 3.17 simplifies to:

$$P = 4k_1 f_c' A_{core} + 4\frac{A_{st} f_{yt} d_c}{s} + n_{bars} P_s \qquad (3.18)$$

The terms of Equation 3.18 may be interpreted as follows: the first term gives the axial load carried by the core concrete through direct bearing across the shear failure plane; the second term gives the axial load carried through shear friction due to yielding of the transverse reinforcement; and the last term is the axial load carried by the longitudinal reinforcement. Again, recall that for the total capacity model, all the terms are summed, as shown in Equation 3.18, while for the maximum capacity model only the maximum of $4\left(k_1 f_c' A_{core} + \frac{A_{st} f_{yt} d_c}{s}\right)$ and $n_{bars} P_s$ are considered.

Similar to the classical shear-friction model, Equation 3.18 can be rearranged to solve for the constant k_1 for the total capacity model:

$$k_{1t} = \frac{P - \left(4\frac{A_{st} f_{yt} d_c}{s} + n_{bars} P_s\right)}{4 f_c' A_{core}} \qquad (3.19)$$

where the subscript t refers to the total capacity model upon which Equation 3.19 is based. As with the effective coefficient of friction for the classical shear-friction model, k_{1t} can be determined for each specimen in Table 3-1 by using Equation 3.19, and related to the drift ratio at axial failure, as shown in Figure 3-15. The data do not follow a clear linear trend, although k_{1t} appears to decrease with increasing drift ratio. The data points are clearly grouped by the axial stress on the column core. The relatively large scatter in Figure 3-15 suggests that the model does not represent the test data very well.

For the maximum capacity model, k_{1m} is determined for each specimen by using Equation 3.19 with the term $n_{bars} P_s$ omitted. The data, plotted in Figure 3-16, show even more scatter than shown in Figure 3-15 for the total capacity model, and are clearly divided into groupings based on the axial stress. Owing to the poor correlation with the test data, the modified shear-friction method will not be used in the development of the drift capacity models presented in the next section.

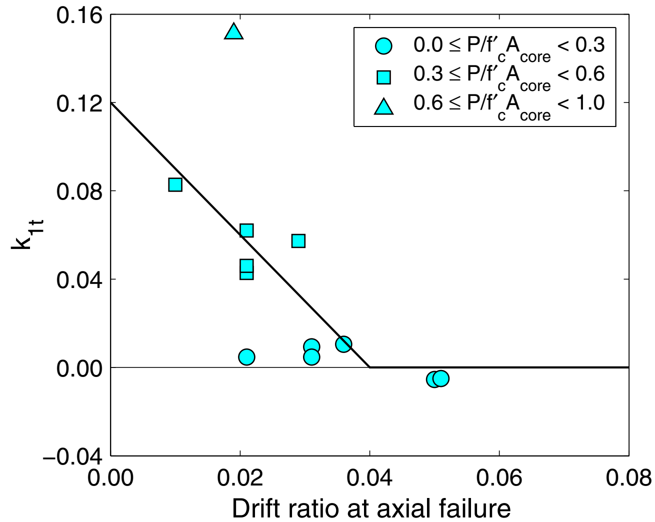

Figure 3-15. Relation between k_{1t} and the drift ratio at axial failure for the total capacity model

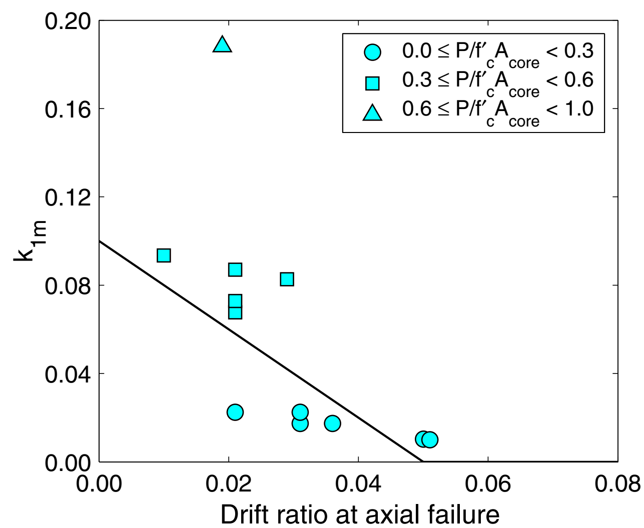

Figure 3-16. Relation between k_{1m} and the drift ratio at axial failure for the maximum capacity model

3.3.6 Drift Capacities

The preceding sections presented the expressions that can be used to establish relationships for the drift ratio at axial failure in terms of the axial load, the transverse reinforcement, and the longitudinal reinforcement. Only the total and maximum capacity models based on classical shear friction will be used to develop the drift capacity relationships.

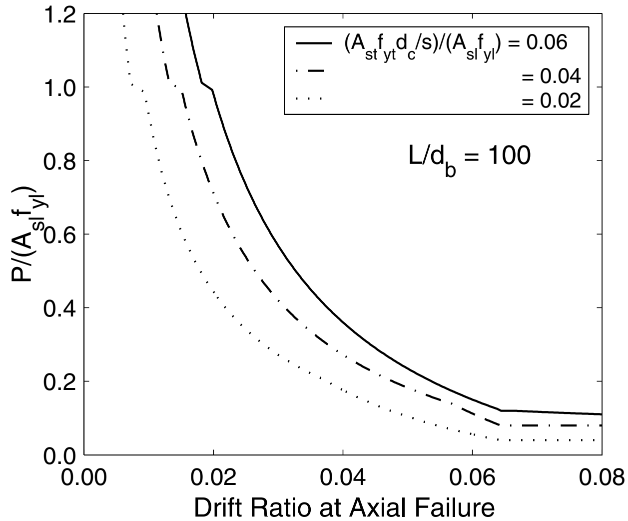

Figure 3-17. Drift capacity curves based on the total capacity model and the classical shear-friction model. (Reduced drift capacity for $P > A_{sl}f_{yl}$ due to consideration of buckling of longitudinal reinforcement. $P_{cr} = 0.1A_{sl}f_{yl}$ shown here.)

For the total capacity model, Equations 3.9, 3.11 (with $\theta = 65°$), and 3.13 are combined to give the drift capacity curves shown in Figure 3-17. For low axial loads the drift capacity curves approach horizontal, suggesting that a lower-bound axial load exists below which axial failure is not expected to occur. Based on this model, the lower-bound axial load capacity is the sum of the axial load supported by the 45° truss model and the longitudinal bar capacity at large drifts. For high axial loads, the buckling capacity of the longitudinal reinforcement is assumed to govern according to Equation 3.9, resulting in the sudden reduction in drift capacity seen in Figure 3-17.

Figure 3-18 shows the plastic capacity curve for the longitudinal reinforcement (from Figure 3-11) plotted with the drift capacity curves based only on the shear-friction capacity (i.e., the first term of Equation 3.11, with $\theta = 65°$, and Equation 3.14). The maximum capacity model, shown in Figure 3-19, takes the maximum axial load from either the longitudinal bar capacity or the shear-friction capacity. Note that longitudinal bar buckling does not influence this model, since the buckling capacity of the longitudinal reinforcement will always be less than the shear-friction capacity at low drifts. For the parameters shown, the longitudinal bar capacity governs only for large column drifts and low amounts of transverse reinforcement. Given that the longitudinal bar capacity has such little effect on the maximum capacity model, and that no data exist beyond a drift ratio of 0.06 to support the claim that the longitudinal bars will govern the capacity, the additional complexity of including the longitudinal bar capacity may not be warranted.

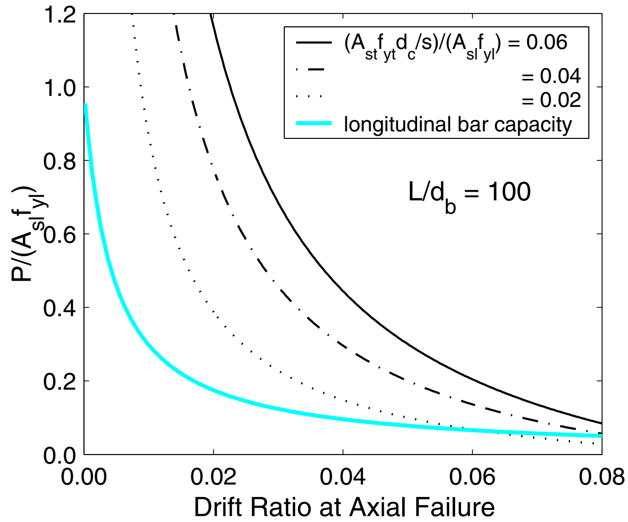

Figure 3-18. Drift capacity curves for shear friction and longitudinal reinforcement shown separately. (Used to find curves for maximum capacity model shown in Figure 3-19.)

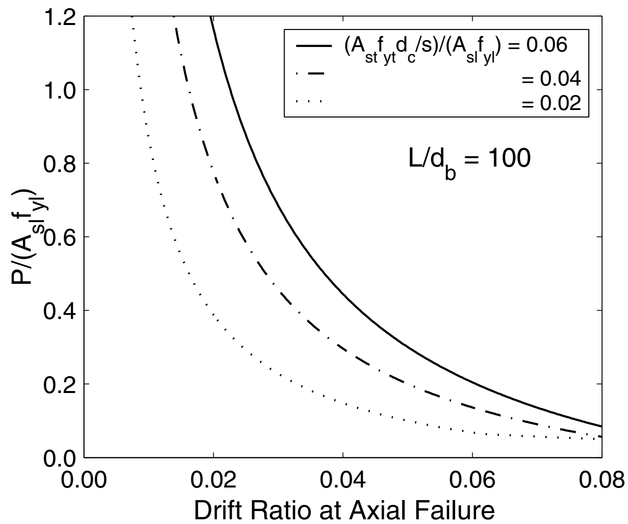

Figure 3-19. Drift capacity curves based on the maximum capacity model and the classical shear-friction model

All of the plotted relations in Figures 3-17 through 3-19 suggest the intuitive result that drift capacity increases with increasing transverse reinforcement and decreasing axial load. This is consistent with the experimental observations discussed in Section 3.2.

Figure 3-20 compares the drift capacity curves based on the total and maximum capacity models. The very close agreement between the two models is a result of selecting the relations between the effective coefficient of friction and the drift ratio at axial failure based on the same

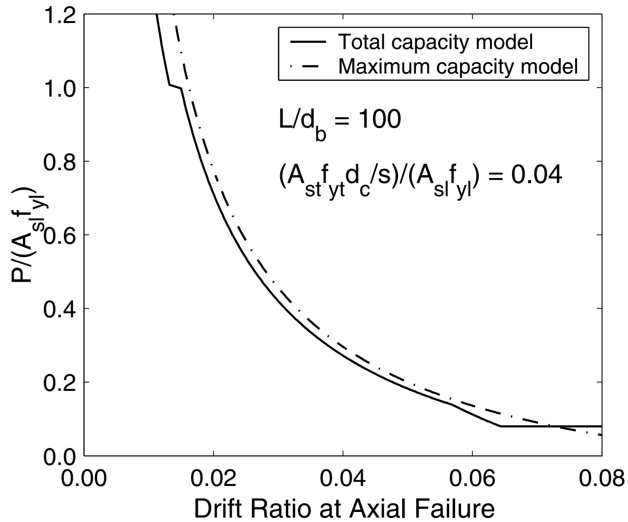

Figure 3-20. Comparison of total and maximum capacity models

data (Figures 3-12 and 3-13). The variation between the two models at low and high drifts is due to the changes in the longitudinal reinforcement capacity, which influences only the total capacity model.

To convey a sense of the accuracy implicit in the relations of Figures 3-17 and 3-19, those relations were used to estimate the drift capacity of the columns tested by Lynn and Sezen. The results are plotted in Figure 3-21 for the total capacity model, and Figure 3-22 for the maximum capacity model. The mean ratios of the measured to calculated drift at axial load failure based on the total and maximum capacity models are 1.02 and 0.97, respectively; the coefficients of variation are 0.22 and 0.26, respectively.

Given the close agreement between the models (Figure 3-20), the lack of influence from the longitudinal reinforcement on the maximum capacity model (Figure 3-18), and the reasonable accuracy of the two models (Figures 3-21 and 3-22), it is recommended that the maximum capacity model based on the shear-friction capacity alone should be used to assess the drift ratio at which axial failure is expected to occur. Based on the test data, the accuracy of such a model is equivalent to that shown in Figure 3-22 for the maximum capacity model, since the longitudinal reinforcement capacity did not control at the drift ratios recorded in the tests. Such a model requires information only on the transverse reinforcement and the axial load, and can be expressed as follows:

$$\left(\frac{\Delta}{L}\right)_{axial} = \frac{4}{100}\frac{1+(\tan\theta)^2}{\tan\theta + P\left(\frac{s}{A_{st}f_{yt}d_c\tan\theta}\right)} \tag{3.20}$$

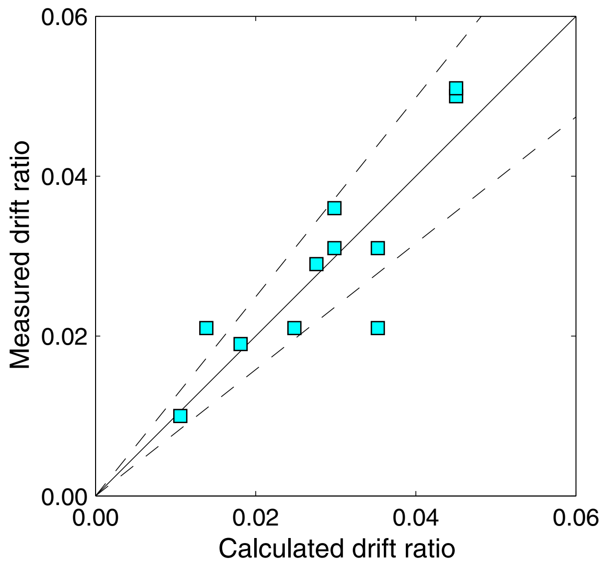

Figure 3-21. Comparison of measured to calculated drift ratios for tests by Lynn and Sezen based on total capacity model. (Dashed lines are +/− one standard deviation from the mean.)

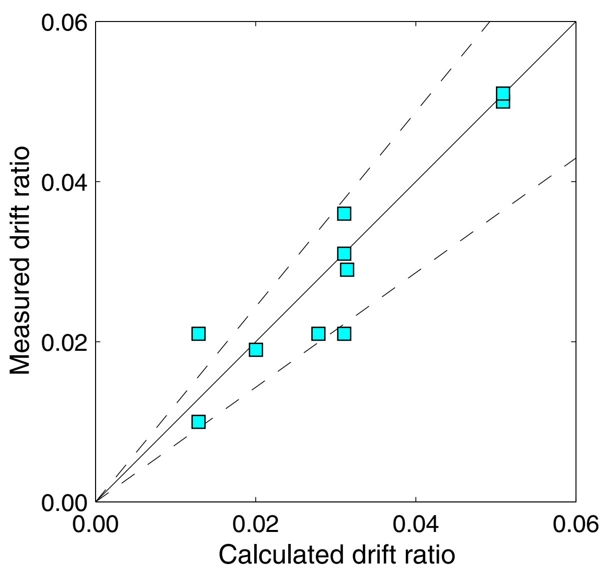

Figure 3-22. Comparison of measured to calculated drift ratios for tests by Lynn and Sezen based on maximum capacity model. (Dashed lines are +/− one standard deviation from the mean.)

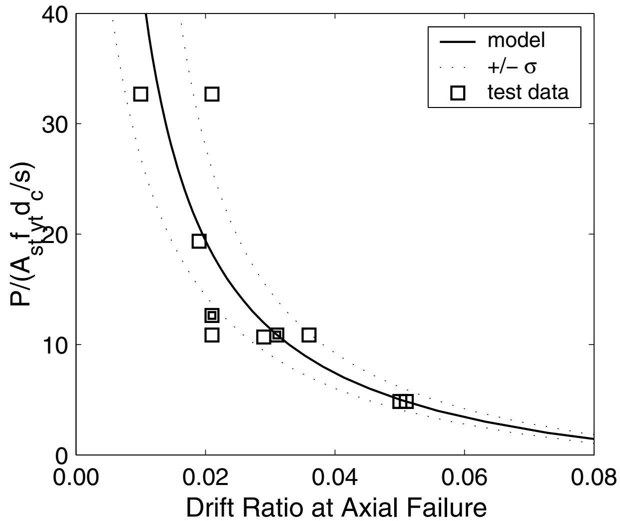

Figure 3-23. Axial capacity model (Equation 3.20) plotted with test data from Lynn (2001) and Sezen (2002)

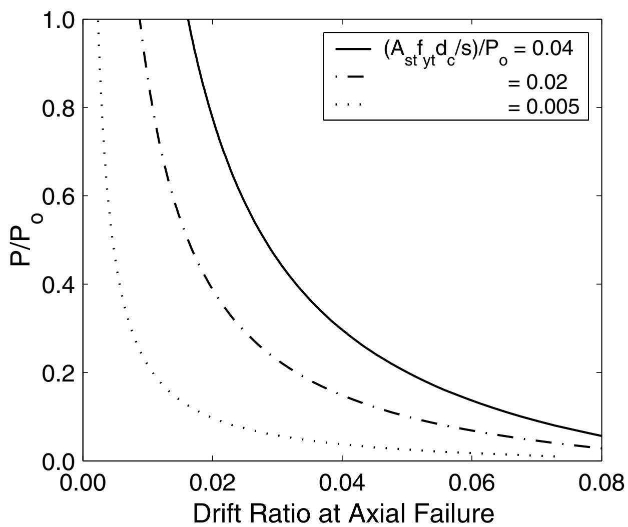

Figure 3-24. Axial capacity model normalized to undamaged axial capacity, P_o

where θ was assumed to be 65° is the derivation of the model. The axial capacity model can be plotted as a single curve, as shown in Figure 3-23, although the influence of the transverse reinforcement is not immediately obvious, as it is in Figure 3-24.

Note that the uppermost data points (2CMH18 and 3CMH18) in Figure 3-23 differ only by the amount of longitudinal reinforcement. Based on the longitudinal reinforcement capacity model presented in Section 3.3.3, the column with the lower drift ratio at axial failure and lower longitudinal reinforcement ratio (2CMH18) is expected to experience buckling of the longitudinal rein-

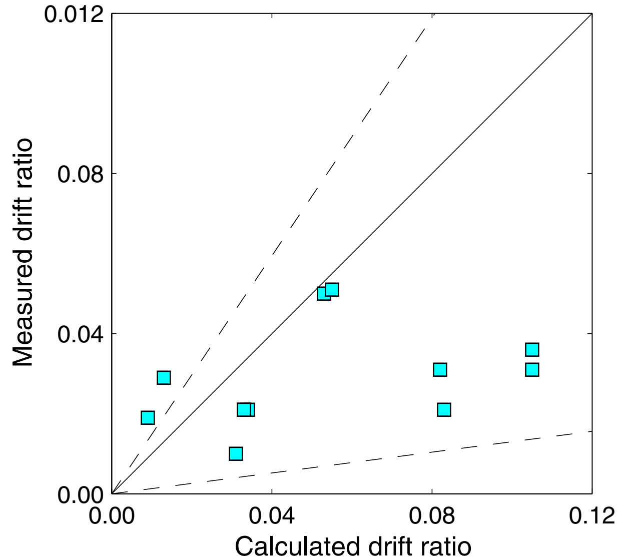

Figure 3-25. Comparison of measured to calculated drift ratios for tests by Lynn and Sezen based on model by Kato and Ohnishi (2002). (Dashed lines are +/− one standard deviation from the mean.)

forcement. Therefore, the difference in measured drifts at axial failure for the two specimens may be explained by the reduction in drift capacity for columns susceptible to longitudinal bar buckling according to the total capacity model (Figure 3-17).

Although useful as a design chart for determining drift capacities, Figure 3-23 should be used only with full understanding that a significant number of columns are likely to fail at drifts below the calculated quantities. The relatively large scatter may be a product of inherent randomness associated with the complicated failure mechanism. Additional data and analyses may well improve our ability to predict the onset of axial load failure of columns.

3.4 KATO AND OHNISHI (2002) MODEL

The drift capacity model by Kato and Ohnishi (2002) presented in Section 2.3.4 (Equations 2.6 and 2.7) can be used to predict the drift ratio at axial failure. Based on a database of 36 columns subjected to cyclic lateral loads, Kato and Ohnishi (2002) recommend using m = 3.6 to estimate the drift at axial failure. Figure 3-25 clearly shows that the model does not adequately represent the measured drifts at axial failure for the column tests by Lynn and Sezen. The mean ratio of the measured to calculated drift at axial failure is 0.81; the coefficient of variation is 0.84.

3.5 EXTENSION OF SHEAR-FRICTION MODEL

The degrading slope of the shear-drift backbone after shear failure is a key parameter influencing the response of shear-critical columns before axial failure. The shear-friction model can be extended to provide an estimate of the degrading slope.

Considering the column illustrated in Figure 3-4 just before the total loss of shear capacity, and ignoring the dowel action and axial capacity of the longitudinal reinforcement as done for the drift capacity model above, the equilibrium equations can be written as follows:

$$\Sigma F_x \rightarrow N\sin\theta + V = V_{sf}\cos\theta + \frac{A_{st}f_{yt}d_c}{s}\tan\theta \tag{3.21}$$

$$\Sigma F_y \rightarrow P = N\cos\theta + V_{sf}\sin\theta \tag{3.22}$$

By using the classical shear-friction model (Equation 3.10) and the relationship between drift and the effective coefficient of friction for the maximum capacity model (Equation 3.14), the equilibrium equations can be combined to give the following expression for the shear force:

$$V = \frac{A_{st}f_{yt}d_c}{s}\tan\theta - P\left(\frac{25\frac{\Delta}{L}}{1 + \tan^2\theta - 25\tan\theta\frac{\Delta}{L}}\right) \tag{3.23}$$

To find the degrading slope of the shear-drift backbone, Equation 3.23 is differentiated with respect to the drift ratio:

$$\frac{dV}{d\left(\frac{\Delta}{L}\right)} = \frac{-25P}{1 + \tan^2\theta}\frac{1}{\left(1 - \frac{25\tan\theta}{1 + \tan^2\theta}\frac{\Delta}{L}\right)^2} \tag{3.24}$$

Finally, using Equation 3.20 to express the drift ratio as a function of the axial load and the transverse reinforcement, the following expression provides an estimate of the degrading slope of the shear-drift backbone:

$$\frac{dV}{d\left(\frac{\Delta}{L}\right)} = \frac{-25P}{1 + \tan^2\theta}\left(\frac{A_{st}f_{yt}d_c}{Ps}\tan^2\theta + 1\right)^2 \quad \text{where } \theta = 65^\circ \tag{3.25}$$

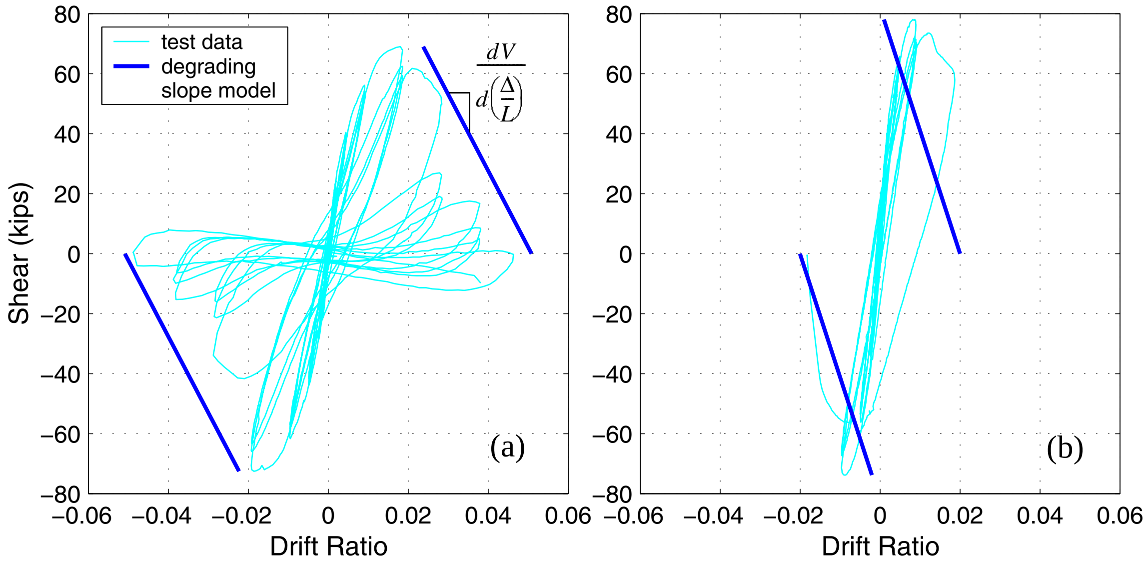

Figure 3-26. Comparison of degrading slope model (Equation 3.25) with hysteretic response from specimens (a) 2CLD12 and (b) 2CHD12

Unfortunately, Equation 3.25 does not agree well with the response for many of the columns in the database. Figure 3-26(a) shows good agreement between the degrading slope model (Equation 3.25) and the response of specimen 2CLD12; however, Figure 3-26(b) shows that the model can significantly underestimate the degrading slope for columns with higher axial load (e.g., specimen 2CHD12). The degrading slope model shown in Figure 3-26 is assumed to intersect the x-axis at the drift ratio at axial failure given by Equation 3.20.

Given the poor agreement with test data, Equation 3.25 requires further refinement before it can be used with confidence to estimate the degrading slope of the shear-drift backbone. If the model can be improved to provide a better estimate of the degrading slope, then it may be possible to use the same model to predict the drift at shear failure by finding the intercept between the degrading slope and the column plastic capacity.

3.6 MODEL DEFICIENCIES

The shear-friction model described above significantly simplifies a very complex problem**;** hence, several deficiencies in the model can be expected. Some of the deficiencies include the reliance on full anchorage of the transverse reinforcement, not accounting for direct bearing of concrete

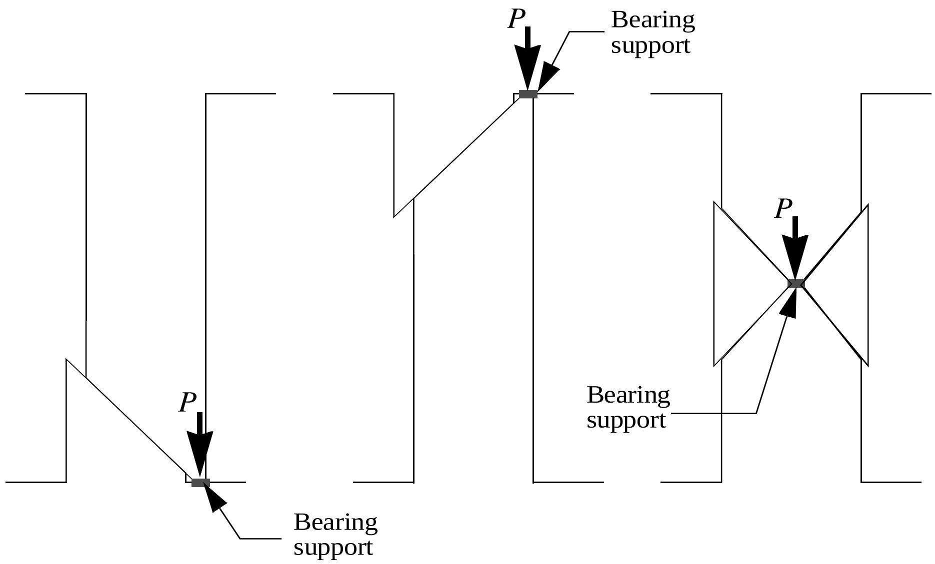

Figure 3-27. Shear failure modes with bearing support for axial loads

components, the dependence on a distinct shear failure plane, and the limited data set upon which the model is based.

The shear-friction model assumes that the full yield capacity of the transverse reinforcement can be achieved and maintained after shear failure of the column. This assumption is valid only if the transverse reinforcement has sufficient anchorage. Since 90° hooks are common for the ties of older reinforced concrete columns, such anchorage cannot always be relied upon. It is recommended that future modifications to the model include a coefficient that reduces the contribution of the transverse reinforcement. Such a reduction factor has been proposed for the calculation of the shear capacity of older reinforced concrete columns (Moehle et al., 2001).

Several shear failure modes, illustrated in Figure 3-27, result in axial support provided by the bearing of concrete against concrete across a shear failure plane. This mechanism of axial load support is not considered in the shear-friction model. However, there are currently no methods by which the formation of a failure mode resulting in this additional axial support can be predicted. Hence, it would be unconservative to rely upon the bearing of concrete against concrete to support the axial loads after shear failure.

The shear-friction model assumes that the shear failure plane is continuous and distinct. However, the complex behavior of a column during shear failure can result in a disjointed failure plane where the principle sliding surface is intercepted by multiple cracks at various angles. Owing

Figure 3-28. Damaged column from 1971 San Fernando earthquake, Olive View Hospital (Steinbrugge K. V., NISEE database)

to damage to the column core, the failure "surface" may in fact consist of several blocks of concrete bearing against one another as shown in Figure 3-28. The shear-friction model would most likely not provide a good estimate of the axial load capacity of such a column.

It must be recognized that the axial failure model derived in this chapter is based on data from only 12 columns. All of the columns were constructed of normal strength concrete, had the same height to width ratio, and were designed to yield the longitudinal reinforcement before shear failure. Only limited variation in the spacing and type of transverse reinforcement was possible. The axial failure model presented here may not be appropriate for columns for which the test specimens are not representative.

Furthermore, all of the columns in the database were tested under unidirectional lateral loading parallel to the one face of the column. With the exception of two tests, the loading routine was standardized, with each column subjected to nominally constant axial compression and a series of lateral displacements at increasing amplitude (three cycles at each amplitude). During earthquake excitation columns can experience bidirectional loading and a wide variety of loading histories, which may consist of a single large pulse or many smaller cycles before shear and axial load failure. It has been demonstrated that an increase in the number of cycles past the yield displacement can result in a decrease in the drift capacity at shear failure (Pujol, 2002). Although it is anticipated that an increase in the number of cycles has a similar impact on the drift capacity at axial failure, not enough test data are available to support or refute this hypothesis. Further testing of existing reinforced concrete columns to the stage of axial failure is needed to supplement the current database.

4 Limit State Failure Model

4.1 INTRODUCTION

Analytical models capable of representing the different failure modes of structural components are required to evaluate the response of a structure as it approaches the collapse limit state. For the evaluation of existing reinforced concrete buildings subjected to earthquake ground motion, there exists a need for analytical models that incorporate the initiation of column shear and axial load failures, in addition to the subsequent strength degradation. Given such a model, an engineer could evaluate the influence of column shear and axial load failures on the response of the building frame system. This chapter will describe how the drift capacity models for shear and axial load failures presented in the previous chapters can be incorporated in an analytical model to detect and initiate strength degradation of column elements.

Section 2.3 evaluates several capacity models, or limit state surfaces, which can be used to define the onset of shear failure. The proposed empirical models, introduced in Section 2.3.5, relate the shear demand to the drift at shear failure based on the transverse reinforcement and axial load ratios. As shown in Figure 4-1, the point of shear failure, according to the model, is determined by the intersection of the load-deformation curve for the column and the limit surface defined by the empirical drift capacity model. Although it is known that the shear strength will degrade after failure, the shape of the load-deformation curve after intersection with the limit surface is not well understood. Analytical models allowing for a user-defined degrading slope after failure will enable the investigation of the influence of the rate of shear strength degradation on the behavior of the structural system.

As described in Section 3.2, experimental research has shown that axial failure of a shear-damaged column is related to several variables including the axial stress on the column, the amount

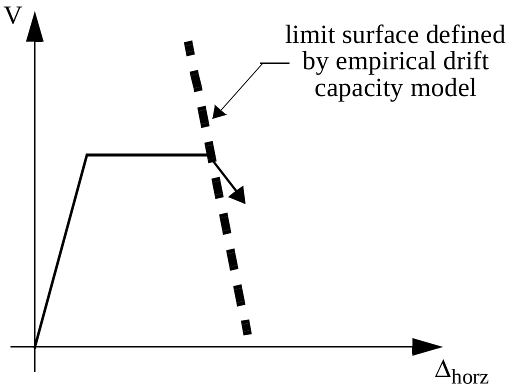

Figure 4-1. Shear failure defined by proposed drift capacity model

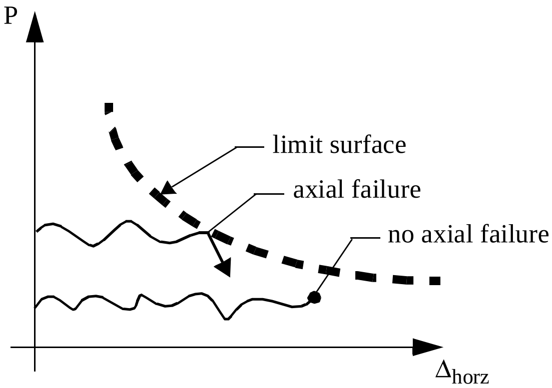

Figure 4-2. Axial failure model

of transverse reinforcement, and the drift demand. Based on these observations, the onset of axial failure has been described using a shear-friction model (see Section 3.3). Similar to the shear-failure model described above, this capacity model defines a limit surface at which axial failure is expected to occur, as shown in Figure 4-2. According to this model, columns with a low axial load or drift demand would not be expected to experience axial failure. As with the shear-failure model, column behavior after the onset of axial failure is not well understood; however, it is reasonable to expect that the axial load-horizontal deflection relation for the damaged column will remain on or below the limit surface after failure is detected.

Although describing different phenomenon, the shear and axial models described above both take on the same general form. Both models define a limit surface and trigger a change in the hysteretic behavior once the appropriate load-deformation relation for the column intersects the limit surface. This similarity allows both failure models to be implemented in one uniaxial material model for structural analysis. The material model requires a user-defined ordinate, abscissa, and limit surface function.

This chapter will describe the implementation of the general material model in OpenSees, a finite-element analysis platform designed for earthquake engineering simulation (OpenSees, 2002). First, the concept of material models, as they are applied in OpenSees, will be introduced. Then, in an effort to improve on available shear-critical column models, the new material model, described above, will be developed. Finally, three applications of the material model will be discussed. The performance of the new material model will be demonstrated in Chapter 8 for the analysis of the shake table tests performed as part of this study. The C++ implementation and the user interface for the new material model are presented in Appendix D.

4.2 UNIAXIAL MATERIAL MODELS IN OpenSees

Uniaxial material models in OpenSees define a constitutive relationship. Depending on the application, the material could define a relation between stress and strain, force and displacement, moment and curvature, or moment and rotation.

Uniaxial materials are the lowest level of objects that compose elements in OpenSees. The relationship between elements and materials is illustrated in Figure 4-3. One-dimensional elements, such as springs and trusses, have only one uniaxial material associated with them. For a truss, the uniaxial material defines the stress-strain relationship and is converted to force-displacement by the element kinematic and equilibrium relationships. For a zero-length spring, the uniaxial material defines the force-displacement (or moment-rotation) relationship directly. Multi-dimensional elements, such as beam-column elements, have multiple uniaxial materials associated with them. For beam-column elements, the uniaxial materials are grouped together to form sections. Sections can be located at integration points along the element length or at its ends, depending on the element formulation. At the section level, uniaxial materials can be used to define the stress-strain relationship for fibers, and a standard section analysis (assuming plane sections remain plane) is performed to determine the force resultants on the section, as shown in Figure 4-3. Alternatively, uniaxial materials could be used to define the moment-curvature and axial load-axial strain relationships directly, eliminating the need for a section analysis but omitting any coupling between the force resultants. Note that a uniaxial material defining a shear-shear strain relationship

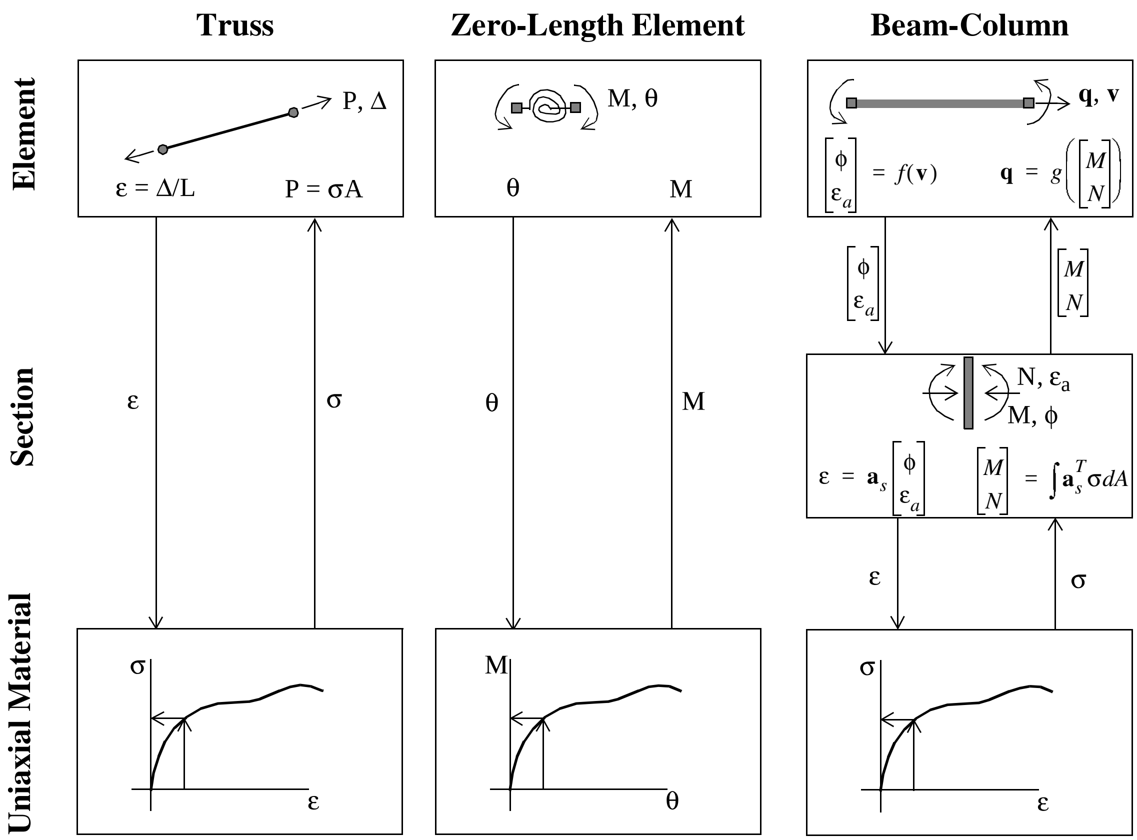

Figure 4-3. Examples of relationship between a material and an element in OpenSees

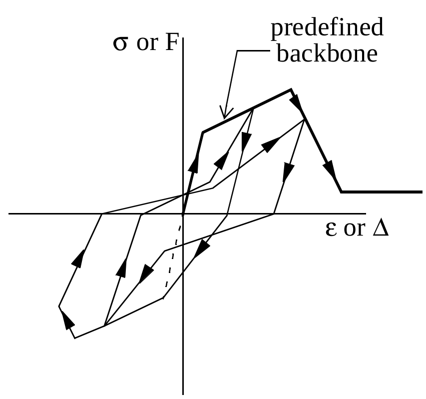

Figure 4-4. Example of capabilities of Hysteretic uniaxial material

can be aggregated with any section, allowing uncoupled shear deformations to be included in the element response.

The uniaxial material developed in this chapter is based on the Hysteretic uniaxial material available in OpenSees. The Hysteretic material has a predefined trilinear backbone and five parameters to define the hysteretic behavior, including pinching and stiffness degradation. As shown in

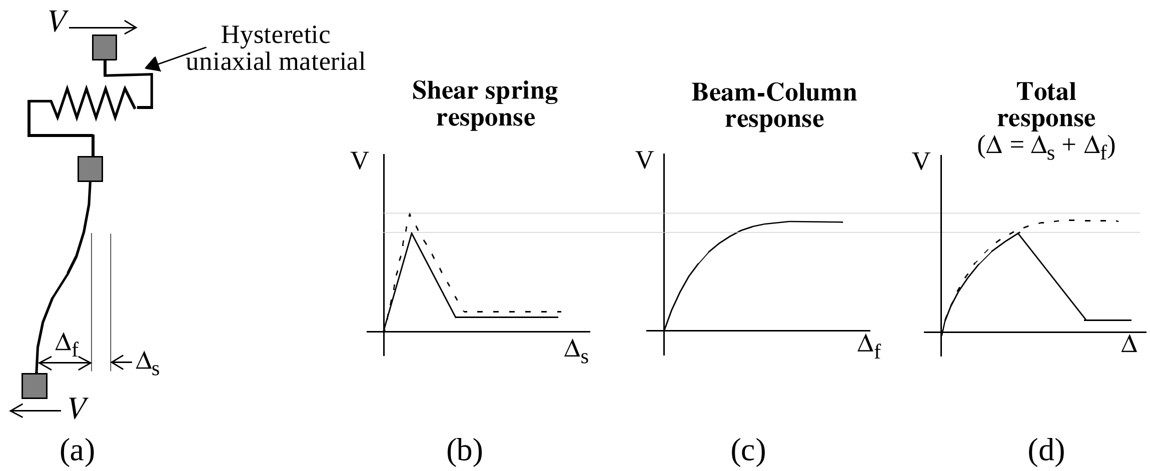

Figure 4-5. Shear spring in series model using Hysteretic material

Figure 4-4, the backbone can include strength degradation, a necessary feature for modeling the behavior of shear-critical columns. A more detailed description of the Hysteretic material model is provided in Section D.4.

4.3 A COLUMN MODEL

To motivate the development of a new uniaxial material model, the example of a shear spring in series with a beam-column element, as shown in Figure 4-5, is considered for modeling the shear strength degradation of shear-critical columns. The shear spring could be a separate zero-length element, or could be aggregated into any of the sections of the beam-column element as discussed above. The Hysteretic uniaxial material model, with strength degradation, can be used to define the constitutive relationship for the shear spring. Any beam-column element capable of modeling the flexural deformations can be used. For the following discussion it will be assumed that the flexural deformations modeled by the beam-column element include both the deformations due to curvatures over the column height and those due to concentrated rotations at the column ends resulting from anchorage bar slip.

Similar models have been proposed previously for modeling the post-peak behavior of existing reinforced concrete columns (Pincheira et al., 1999; Shirai et al., 2001). In such a model, all of the flexural deformations are concentrated in the beam-column element and the shear deformations are modeled by the shear spring. If the shear strength (i.e., the peak in the shear spring response backbone) is less than the flexural yield strength of the column, then the model will be able to capture the degrading shear behavior, as shown by the solid line for the total response of the column in Figure 4-5(d). If, however, the shear strength is estimated to be higher than the flexural yield strength of the column, then, given limited strain hardening in the flexural response, the model will not capture any shear degradation, as shown by the dashed line for the total response of the column in Figure 4-5(d). Several studies have shown, however, that the shear strength decays with increased inelastic deformation (Watanabe and Ichinose, 1991; Aschheim and Moehle, 1992; Priestley et al., 1994). Hence, the total response behavior depicted by the dashed curve in Figure 4-5(d) is not realistic for columns that yield in flexure close to their estimated shear strength. The point of shear failure (i.e., the start of the degrading behavior in the total response backbone) should be determined by considering both force and deformation. The model in Figure 4-5(a) determines the point of shear failure based only on the column shear.

The behavior of the series model can be improved by using a uniaxial material for the shear spring that will degrade only after shear failure has been detected. The detection of shear failure should be based on the column shear and the total deformation of the column. Calculation of the total deformation requires a coupling of the shear spring and beam-column element. This can be achieved by a new uniaxial material that traces the behavior of the beam-column element and changes its backbone to include strength degradation once the response of the beam-column element exceeds a predefined limit state surface as described in the next section.

4.4 LIMIT STATE UNIAXIAL MATERIAL

The Limit State uniaxial material was developed based on the existing Hysteretic material in OpenSees. The following inputs are required for Limit State material:

- all of the inputs required for Hysteretic material to define the response before failure (i.e., the corner points of the initial backbone, the pinching parameters (2), the stiffness and strength degradation parameters (2), and the unloading slope parameter)
- an identifying tag for the beam-column element that the uniaxial material will be monitoring to detect the point of failure
- identifying tags for the two nodes whose displacements will be used to determine the interstory drift
- parameters used to determine the limit state surface that defines the point of failure

- the degrading slope to be used for the backbone after failure is detected (or the unloading slope for the beam-column element as discussed in Section 4.5.1)
- the residual capacity of the uniaxial material

The limit state surface used by the uniaxial material is referred to as a “limit curve,” since it is defined in only two dimensions. The choice of these two dimensions, or the ordinate and abscissa on which the limit curve is defined, depends on the application. Three limit curves have been implemented: one to define shear failure (Figure 4-1), another to define axial failure (Figure 4-2), and a trilinear general purpose limit curve. As shown in Figures 4-1 and 4-2, the shear force is used for the ordinate of the shear-failure limit curve and the axial force is used for the ordinate of the axial failure limit curve. The abscissa is assumed to be a deformation measure, such as maximum chord rotation or interstory drift.

In an analytical model of a frame structure, where the column ends are not fully restrained against rotation, the computed interstory drift (i.e., the displacement of floor $i+1$ minus the displacement of floor i, divided by the height of the story) will include a rigid body rotation component not present in the experiments used to develop the shear and axial capacity models. To remove the effect of rigid body rotations, deformation measures based on the local behavior of the beam-column element, such as the maximum chord rotation, can be used. (For a fixed-fixed column, the chord rotation is equal to the drift ratio, and for any column with equal end rotations, the chord rotation will be equal to the drift ratio minus the rigid body rotation.) However, for most low- or moderate-height building frames, the rigid body rotations do not contribute significantly to the interstory drift. The interstory drift is calculated using node displacements, while the chord rotations are determined based on the beam-column element response. If chord rotations are used to define the abscissa of the limit curve, then all of the deformations expected before failure must be included in the response of the beam-column element.

Before failure, Limit State material follows the same hysteretic rules as defined for Hysteretic material (Figure 4-4). The corner points for the pre-failure backbone can be defined such that the response of the uniaxial material remains linear or is allowed to yield. After each converged step the uniaxial material queries the beam-column element for its force and deformation and then checks to see if the response has exceeded the selected limit curve. If the limit curve has not been exceeded, then the analysis continues to the next step without any change to the backbone. If the limit curve has been exceeded, then the backbone is redefined to include the degrading slope, K_{deg},

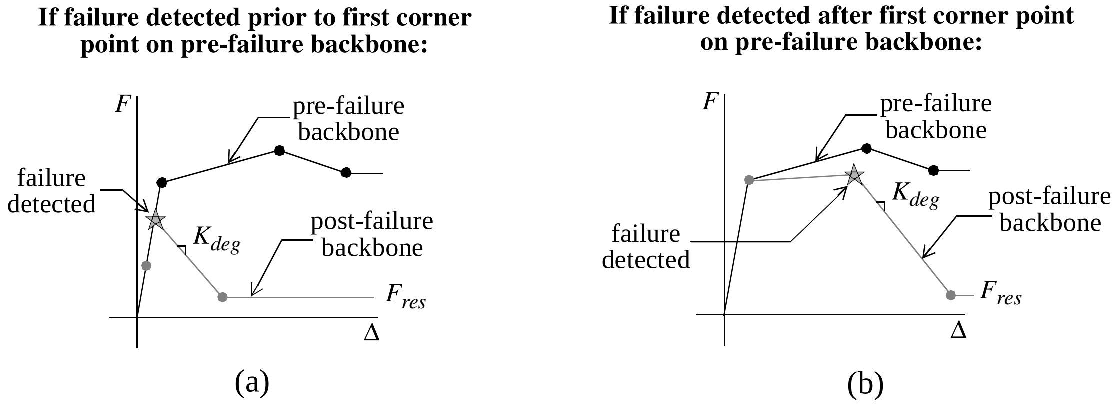

Figure 4-6. Redefinition of backbone after failure is detected

and residual strength, F_{res}. Figure 4-6 illustrates how the backbone for the force-deformation relation of the Limit State material is redefined upon failure. Note that since the limit curve can be defined using an ordinate and abscissa that are uncoupled from the force-deformation relation of the uniaxial material, the point at which failure is detected (marked by a star in Figure 4-6) may not necessarily occur at a peak in the deformation response of the uniaxial material. For such a case, the point at which failure is detected will not lie on the pre-failure backbone, as shown in Figure 4-6b. Exceedance of the limit curve is checked only after each converged load step to avoid “flip-flopping” between the pre- and post-failure states within a single load step. Consequently, small load steps (or time steps for dynamic analysis) are required to accurately determine when the limit curve is exceeded.

4.5 THREE APPLICATIONS OF LIMIT STATE MATERIAL

Three examples of how the Limit State material model can be used will be presented in the following sections. The first two examples demonstrate how the uniaxial material can be used to model column shear failures, while the third demonstrates its application to column axial failures. When used to model axial failure, the Limit State material incorporates coupling between shear and axial load after failure is detected. This coupling will be discussed in Section 4.5.3.

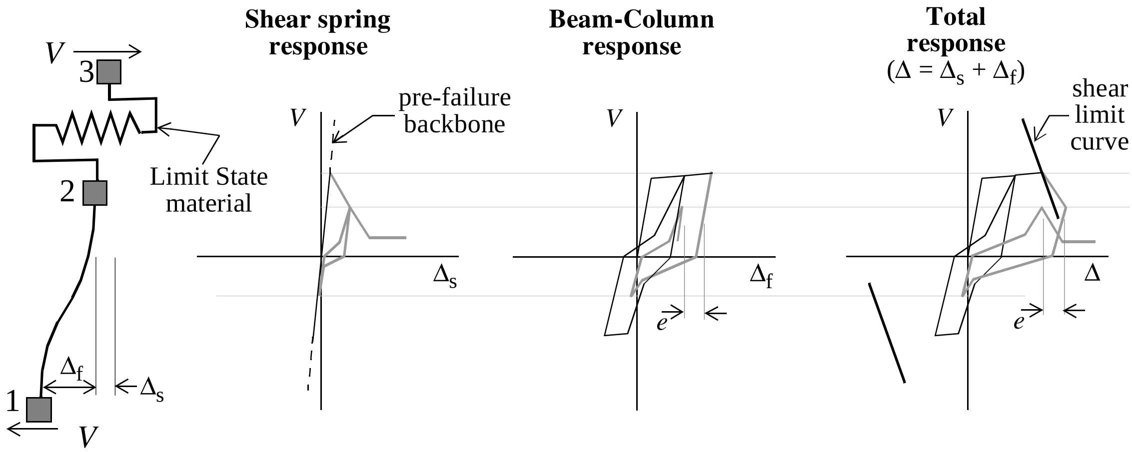

Figure 4-7. Shear spring in series model using Limit State uniaxial material

4.5.1 Shear Spring in Series

The shear spring in series model was introduced in Section 4.3. Here the Limit State material model is used to define the force-deformation relationship of the shear spring. The uniaxial material monitors the response of the beam-column element which is connected in series with the shear spring. As shown in Figure 4-7, the limit curve is defined based on the column shear, V, and the total displacement, Δ (or the interstory drift).

If the column is vulnerable to shear failure after flexural yielding, then the empirical drift capacity model from Section 2.3.5 can be used to define the limit curve. The pre-failure backbone for the Limit State material is selected as linear with a steep slope equal to the shear stiffness of an uncracked column. Note that by defining the limit curve based on the total displacement, the shear deformations are included in the displacements monitored by the uniaxial material, and shear failure is based on the sum of the flexure and shear deformations.

When the beam-column response hits the limit curve for the first time, the backbone of the shear spring is redefined, as shown in Figure 4-6, to include the degrading slope, K_{deg}, and residual strength, F_{res}. Since shear failure will influence the strength of the column in both directions, the backbone is redefined for cycles in either direction, regardless of the direction of failure. Note that for the current implementation of the Limit State material, the backbone after failure is assumed to be symmetric about the origin. This assumption is valid for columns with approximately equal flexural strengths in positive and negative bending (e.g., interior columns with symmetric longitudinal reinforcement). For columns with different flexural strengths in positive and negative bend-

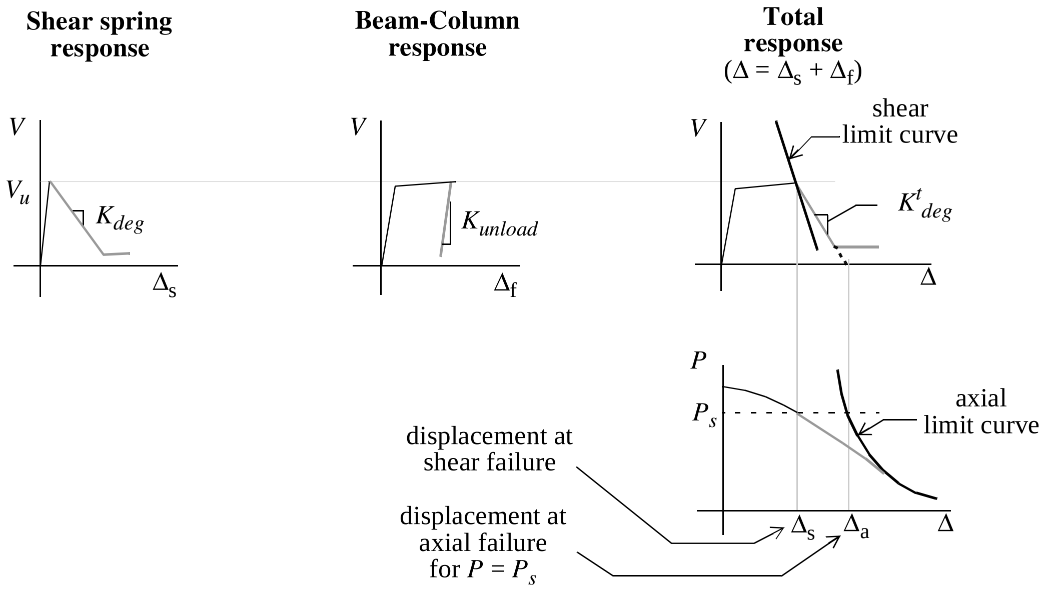

Figure 4-8. Determination of degrading slope, K_{deg}

ing (e.g., outside columns in a building frame), the backbone should be redefined such that the peak shear in each direction does not exceed the flexural strength in the respective direction.

After failure is detected, the response follows the gray hysteretic curves shown in Figure 4-7. Additional lateral demands will result in strength degradation of the shear spring and an increase in the shear deformations, accompanied by unloading of the beam-column element, and therefore, a slight reduction in the flexural deformations. (Experimental results suggest that the shear deformations increase significantly after shear failure, but do not conclusively show whether the flexural deformations increase or decrease (Sezen, 2002).)

Experimental studies have shown that axial failure tends to occur when the shear strength degrades to approximately zero (Nakamura and Yoshimura, 2002). Hence, K_{deg} can be estimated using the calculated drift at axial failure as illustrated in Figure 4-8.When shear failure is detected, based on the intersection of the total response and the shear limit curve, the degrading slope for the total response, K^t_{deg}, can be estimated as follows:

$$K^t_{deg} = \frac{V_u}{(\Delta_a - \Delta_s)} \tag{4.1}$$

where V_u is the ultimate shear capacity of the column, Δ_s is the calculated displacement at shear failure, and Δ_a is the calculated displacement at axial failure for the axial load at the time of shear failure, P_s. (Note that since the column axial load can change during the analysis, Δ_a is not necessarily equal to the displacement at which axial failure is detected.) Since the shear spring and beam-column element are in series, the total flexibility is equal to the sum of the flexibilities of the shear spring and the beam-column element. Hence, K_{deg} can be determined as follows:

$$K_{deg} = \left(\frac{1}{K^t_{deg}} - \frac{1}{K_{unload}}\right)^{-1} \tag{4.2}$$

Note that K_{unload} must be provided in the input parameters for the Limit State material. To investigate the influence of different rates of shear-strength degradation on the behavior of the structural system, the material model also allows the analyst the option of specifying K_{deg} directly before running the analysis.

If the shear spring unloads and reloads before reaching F_{res}, as shown in Figure 4-7, then a weakness of this model becomes apparent. When the shear strength begins degrading again after reloading, the flexural displacements will be less than they were when unloading of the shear spring began (as noted by displacement e in Figure 4-7). This discrepancy will result in the peak of the total response hysteresis occurring at a displacement e from the point where unloading began. Experimental results suggest that the peak should occur at a displacement close to where the unloading began. This weakness can be overcome by concentrating both the shear and flexural deformations in rotational springs as described in the next section.

The beam-column element response must have a positive slope when shear failure is detected; without a positive slope there is not a unique solution for an increase in the total displacement. Figure 4-9 illustrates the response of the column model for monotonically increasing total displacements. In Case 1, the beam-column response has a positive slope at shear failure, while for Case 2, a negative slope at shear failure is considered. The softening force-displacement relation for the shear spring requires that an increase in the total displacement after shear failure be accompanied by a decrease in the applied shear. For Case 1, the beam column is forced to unload to achieve the required reduction in shear. The reduction in Δ_f requires an increase in Δ_s to achieve the desired increase in the total displacement; hence, only one solution is possible. In contrast, for Case 2, the beam-column element can either unload or continue softening to achieve the required reduction in shear. This leads to three possible solutions for an increase in the total displacements: the shear spring can soften while the beam-column unloads (b+A), the shear spring can unload while the beam-column softens (a+B), or both the shear spring and the beam-column can soften (b+B). Although all three solutions satisfy equilibrium, only the (b+A) solution exhibits the

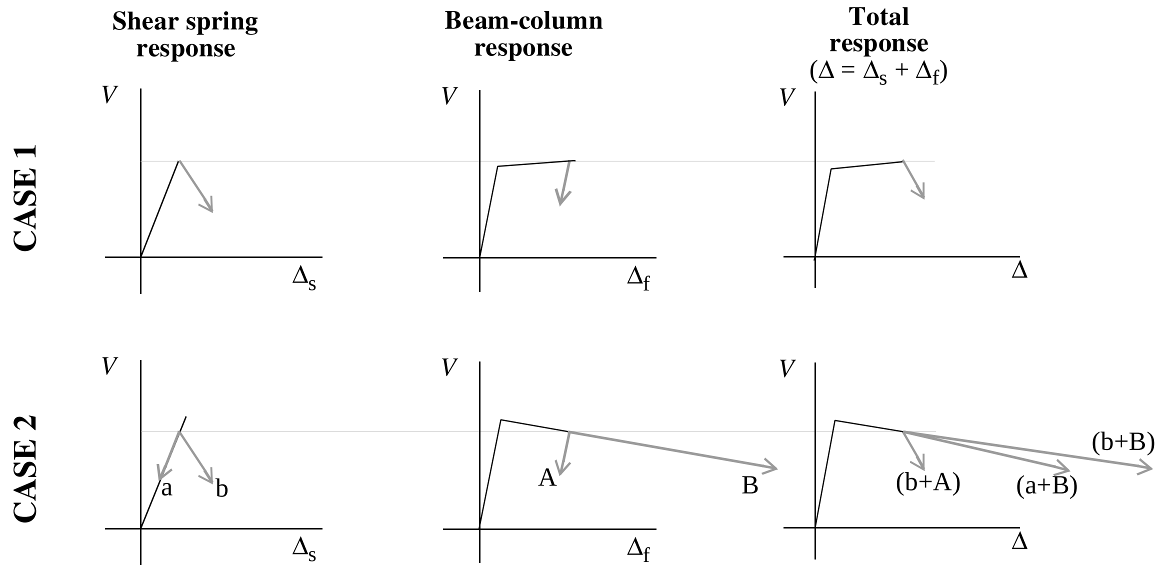

Figure 4-9. Comparison of response given positive and negative strain hardening slopes at shear failure

expected localization of damage in the shear spring. Crisfield and Wills (1988) have shown that the equilibrium state upon which the solution will converge depends on the step size and the selected iterative technique. To avoid numerical convergence problems and ensure a localization of damage in the shear spring, it is recommended that the beam-column response always maintain a positive slope. (Note that a softening beam-column element will also cause numerical problems for the model described in Section 4.3.)

A similar model for shear-critical bridge columns was developed by Ricles et al. (1998) by incorporating the shear-strength model by Priestley et al. (1994) to initiate shear failure. However, as discussed in Section 2.3.1, the use of a shear-strength model to predict the point at which shear failure occurs can result in an unacceptably large variability in the predicted drift at shear failure for shear-critical building columns.

4.5.2 Rotational Springs Including Flexural and Shear Deformations

An alternative model for representing shear failure is illustrated in Figure 4-10. The Limit State material is used to describe the constitutive relationship for the rotational springs. Either a concentrated moment-rotation relationship or a moment-curvature relation integrated over a specified plastic hinge length can be used. The following assumes that the uniaxial material describes a con-

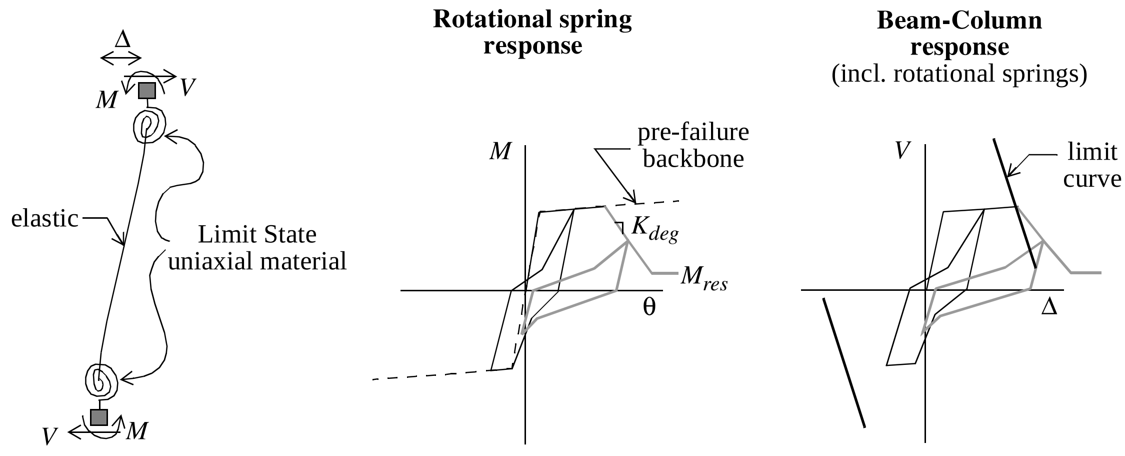

Figure 4-10. Rotational spring model

centrated moment-rotation relationship incorporating all of the nonlinear response of the column. The internal portion of the column element between the rotational springs remains linear elastic. The rotational springs are incorporated in the beam-column element such that the beam-column displacement, Δ, is equal to the sum of the flexural and shear components.

The pre-failure backbone for the Limit State material allows flexural yielding before failure. The initial slope of the pre-failure backbone allows for concentrated rotation at the column ends due to bar slip. If bar slip displacements were not significant, a rigid slope before yielding would be required.

Although the Limit State material is used here to define the M-θ relation for a rotational spring, as shown in Figure 4-10, the limit curve is defined based on the column *shear* and the total beam-column displacement. Once the response of the beam-column element exceeds the limit curve, the backbone of the rotational spring is redefined to include the degrading slope, K_{deg}, and residual strength, M_{res}. After failure, the response follows the gray lines in Figure 4-10. Since all of the inelastic deformation is concentrated in the rotational springs, upon displacement reversals, the total beam-column response does not exhibit the displacement offset *e* observed in the shear spring in series model (see Figure 4-7).

In addition to the improved hysteretic behavior, the rotational spring model has better numerical stability compared with the shear spring in series model. Since all of the sources of nonlinearity are concentrated in the rotational springs, convergence is achieved with fewer iterations. However, the series model is conceptually more appealing because the deformations due to flexure

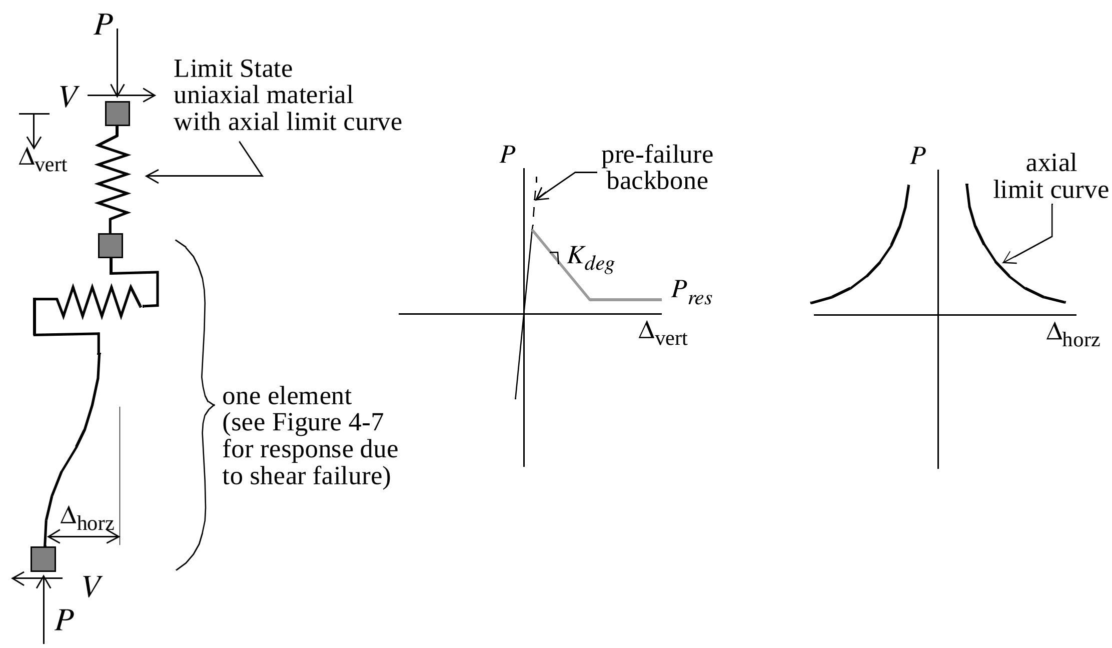

Figure 4-11. Axial spring in series model

and shear can be determined separately by the beam-column element and the shear spring, respectively.

Figure 4-10 assumes that both rotational springs use the same uniaxial material model, and hence for a fixed-fixed column, the rotational springs will both detect failure at the same time and degrade the moment capacity at the same time. This will result in a degradation of the shear capacity to a residual level of $2M_{res}/L$. If only one rotational spring was defined using the Limit State material model, then the shear capacity of the beam-column element would not degrade below $(M_{res}+M_p)/L$, where M_p is the plastic moment capacity of the column section.

4.5.3 Axial Spring in Series Model

The Limit State uniaxial material can also be used to model axial failure where the limit curve is defined by the shear-friction model described in Chapter 3. Since the shear-friction model assumes that shear failure has already occurred, the axial failure spring must be used in conjunction with one of the shear-failure models described above. The model described here, and illustrated in Figure 4-11, assumes that shear failure is modeled by a shear spring in series. The shear limit curve should be defined using the interstory drift, or the column chord rotations (with the shear spring aggregated into one of the column sections), to ensure that the displacements monitored by the axial spring include both flexural and shear deformations. After any analysis, postprocessing should be used to confirm that shear failure was detected before axial failure.

As shown in Figure 4-11, the axial failure limit curve is defined on a plot of axial load versus total lateral drift, and requires only a term describing the strength of the transverse reinforcement ($((A_{st}f_{yt}d_c)/s)$) to define its shape. If the beam-column element includes the axial flexibility of the column, the pre-failure backbone for the axial spring should be defined by a steep straight line to ensure that the spring does not add any axial flexibility to the model. If, on the other hand, the beam-column element is considered to be axially rigid, then the slope of the pre-failure backbone for the axial spring should be set equal to the initial axial stiffness of the column. After axial failure, the backbone will be redefined to include the degrading slope, K_{deg}, and the residual strength, P_{res}. Since the shear-friction model describes only compression failure, the backbone is only redefined for compressive axial loads (shown as positive in Figure 4-11).

Shear-axial coupling should be included in any model in which the behavior after the onset of axial failure is of interest. Although very little experimental data have been collected after the onset of axial failure, shake table tests performed as part of this study (see Chapter 6), and large-scale pseudo-static tests by Lynn (2001) and Sezen (2002), suggest that an increase in lateral shear deformations may lead to an increase in axial deformations, and a loss of axial load. Based on this general observation, the coupling model illustrated in Figure 4-12 has been developed to approximate the shear-axial coupling after axial failure. The response after axial failure is shown as a gray line in Figure 4-12. For any increase in lateral displacement after axial failure is detected, the P-Δ_{horz} relationship is assumed to follow the axial limit curve defined by the shear-friction model. As the earthquake imposes lateral deformations on the damaged column beyond the point of axial failure, the P-Δ_{horz} relationship will result in a loss of axial load, which will in turn lead to an increase in axial deformations due to the P-Δ_{vert} relationship defined by the post-failure backbone of the axial spring. When the P-Δ_{horz} response is on the limit curve, the stiffness of the axial spring is set to K_{deg} to ensure that the spring does not unload elastically. When the earthquake reverses the direction of motion of the structure, it is assumed that the critical shear failure crack will partially close and that sliding along the crack will be arrested, resulting in temporary support of the axial load. Since the column has sustained significant damage, the axial stiffness of the column can be assumed to be less than the elastic axial stiffness. To account for this behavior when the P-Δ_{horz}

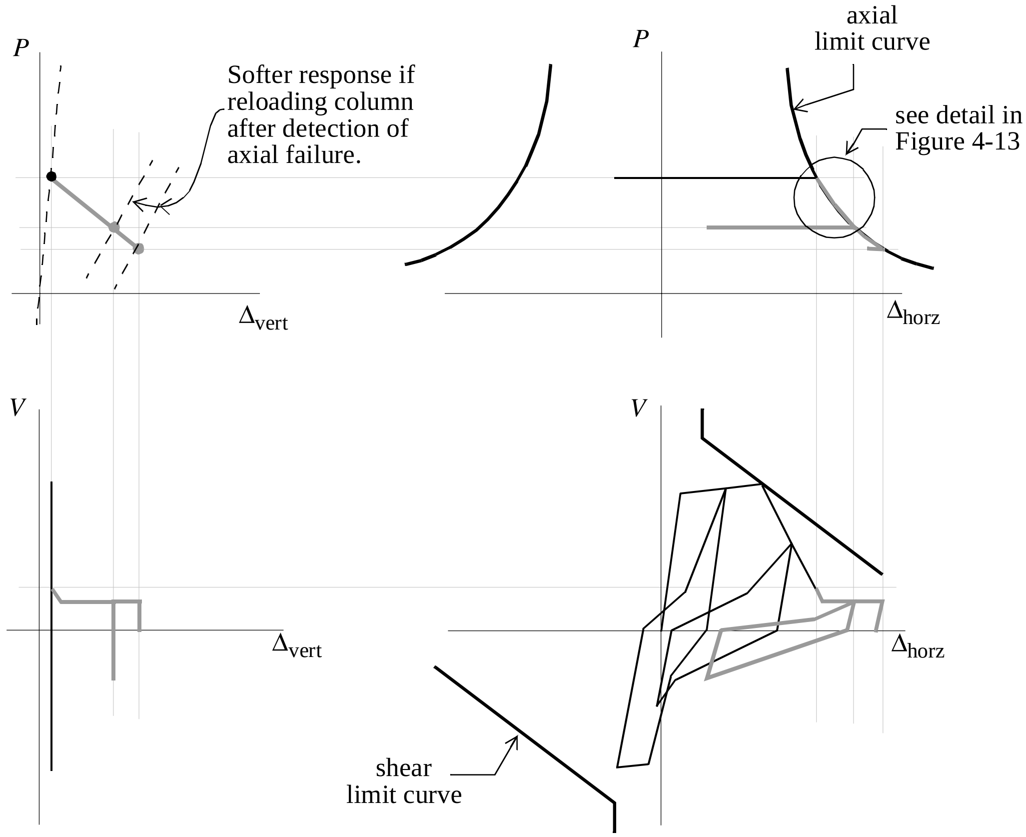

Figure 4-12. Shear-axial coupling after axial failure of the model shown in Figure 4-11

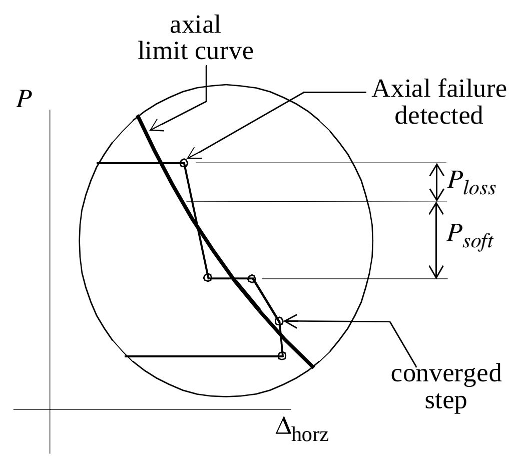

Figure 4-13. Detail of axial load loss from Figure 4-12

response leaves the axial limit curve, the backbone of the axial spring is redefined such that the stiffness of the spring is equal to 1/100 times the elastic axial stiffness of the column, temporarily stopping the decay along the P-Δ_{vert} backbone. Sliding along the critical shear-failure plane, and hence, decay along the P-Δ_{vert} backbone will resume if the P-Δ_{horz} response hits the limit curve again.

The 1/100 factor applied to the axial spring stiffness was selected to approximately represent the damage to the column core. Furthermore, if the original elastic axial stiffness of the column was used, numerical convergence was frequently not achieved when the P-Δ_{horz} response left the axial limit curve due to the sudden change in stiffness.

Figure 4-13 provides a closer look at how the material response is forced to follow the axial limit curve after failure. Recall that exceedance of the limit curve is only checked after each converged load step to avoid "flip-flopping" between the pre- and post-failure states within a single load step. For each converged step beyond the limit surface there exists an unbalance force, P_{loss}, required to return the material to the limit curve at the same deformation. As shown in Figure 4-13, the axial load lost after each converged step beyond the limit curve is the sum of P_{loss} and axial load lost due to softening of the damaged column, P_{soft}. The total, $P_{loss}+P_{soft}$, is equal to the gravity load which must be redistributed to neighboring elements within one time step.

The lengthening of columns due to flexural cracking will result in some coupling between Δ_{horz} and Δ_{vert} not shown in Figure 4-12. For clarity, the response illustrated here assumes there is no coupling except on the axial limit curve, resulting in the horizontal and vertical lines seen on the P-Δ_{horz} and the V-Δ_{vert} plots, respectively, and the stationary points marked by solid circles on the P-Δ_{vert} plot.

4.6 EFFECT OF VARIABILITY ON THE LIMIT STATE FAILURE MODEL

The accuracy of any analysis using the limit state failure model described in this chapter is limited by the accuracy of the capacity models used to define the limit curves and the ability of the hysteretic rules to represent the behavior after failure. Although further study is required to improve estimates of the limit curves and the degrading behavior after shear and axial failure, significant variability in the estimates is expected to remain due to the extent of damage expected at the points of shear and axial failure. Limited experimental studies on the response of reinforced concrete columns after shear failure, and particularly after axial failure, make reliable assessment of the variability difficult.

Owing to the significant change in the response of the structure once a limit curve is reached, the limit state failure model is particularly sensitive to any variability in the limit curves. For example, if a conservative estimate of the axial capacity limit curve is used and failure is detected in a column, then the additional gravity load redistributed to other columns may lead to their failure and a progressive collapse of the structure. If, on the other hand, a limit curve representing the mean axial capacity is used, then failure of the first column may not be detected and no collapse would ensue. The sensitivity of the system response to the variability of the limit curves must be accounted for directly when evaluating the results from any analysis using the limit state failure model.

Research by other investigators may enable the use of the limit state failure model in a probabilistic assessment of the structural response. Work by Gardoni (2002) can be used to construct probabilistic capacity models based on the deterministic limit curves presented here. Work by Haukaas (2003) will allow the probabilistic capacity models to be included in a finite element analysis using the limit state failure model and OpenSees, resulting in the assessment of the probability of collapse.

5 Design of Shake Table Tests

5.1 INTRODUCTION

Shake table tests were designed to observe the process of dynamic shear and axial load failures in reinforced concrete columns when an alternative load path is provided for load redistribution. This chapter provides an overview of the design, construction, instrumentation, and testing of the reinforced concrete frame specimens. More details can be found in Appendices A and B.

5.2 SPECIMEN DESIGN AND CONSTRUCTION

The test specimens were composed of three columns fixed at their bases and interconnected by a beam at the upper level (Figure 5-1). The central column had wide spacing of transverse reinforcement making it vulnerable to shear failure, and subsequent axial load failure, during testing. As the central column failed, shear and the axial load would be redistributed to the adjacent ductile columns.

Two test specimens were constructed and tested. The first specimen supported a mass of 67 kips (the maximum mass that the shake table could reliably control at a height of 7 to 8 feet off the table surface), producing column axial load stresses roughly equivalent to those expected for a seven-story building. The second specimen also supported a mass of 67 kips, but pneumatic jacks were added to increase the axial load carried by the central column from 28.7 kips ($0.10 f'_c A_g$) to 68.2 kips ($0.24 f'_c A_g$), thereby amplifying the demands for redistribution of the axial load when the central column began to fail.

The shear-critical center column was designed as a one-half scale reproduction of the 9'-8" tall, 18"x18" square columns tested by Sezen (2002) (see Figure 3-1). From those previous tests, it was expected that the center column would sustain flexural yielding before developing shear fail-

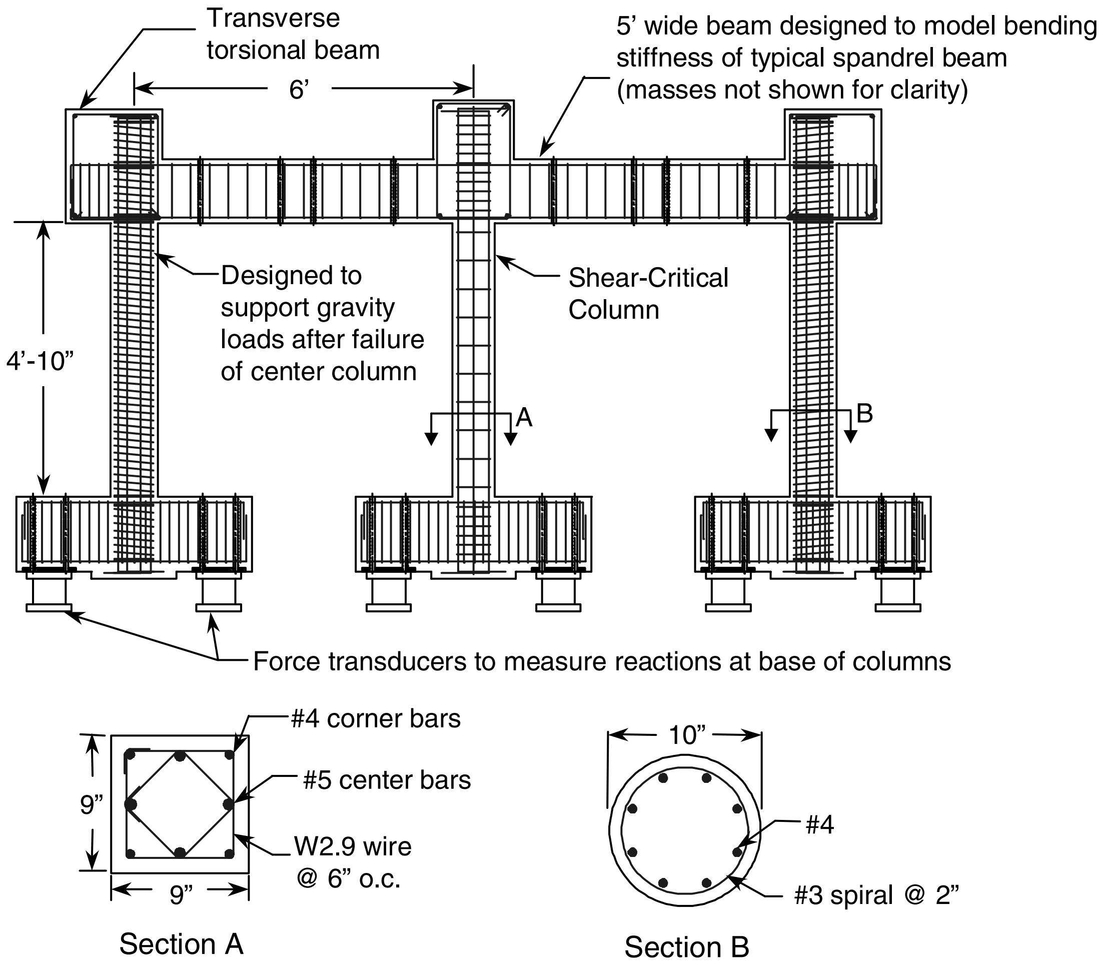

Figure 5-1. Shake table test specimen (see Appendix A for as-built drawings)

ure. Axial load failure was expected to be more gradual for the column with low axial load and more sudden for the column with higher axial load.

The test specimens were constructed in an upright position in a casting site adjacent to the earthquake simulator laboratory. Reinforcement cages were assembled and instrumented with strain gages. Normal-weight aggregate concrete (nominal maximum aggregate size of 10 mm) was cast in two lifts. Specimens were wet-cured for 14 days and then stored in the laboratory until testing (age at testing was 151 days for Specimen 1 and 184 days for Specimen 2). Companion cylinders were stored with the specimens and were tested near the day of the shaking table tests according to ASTM procedures. Table 5-1 summarizes the critical properties of the frame specimens illustrated in Figure 5-1. More material property and construction details are provided in Appendix A. The following sections describe selected aspects of the final design.

Table 5-1. Properties for the shake table test specimens

f'_c (columns and beam, Specimen 1)	3.56 ksi
f'_c (columns and beam, Specimen 2)	3.47 ksi
f_y (center column longitudinal bars)	69.5 ksi
f_y (outside column longitudinal bars)	61.5 ksi
f_y (center column transverse bars)	100 ksi
Mass	67 kips
Center column axial load (Specimen 1)	28.7 kips
Center column axial load (Specimen 2)	67.2 kips
ρ_l (center column)	2.5%
ρ_l (outside column)	2.0%
ρ_h (center column)	0.18%

5.2.1 Design Approach

The specimen design began with the selection of the reinforcement for the half-scale center column. The center column details were scaled from the full-scale columns tested by Sezen (2002) according to standard similitude rules (Krawinkler and Moncarz, 1982). Reinforcing wire with a nominal cross-sectional area of 0.029 in.^{2} was used to model the #3 reinforcing bars used by Sezen (2002) for transverse reinforcement. Although the yield stress of the reinforcing wire was significantly higher than that of full-scale reinforcing bars, the wire was selected to achieve the appropriate scaled elastic stiffness. One #5 and two #4 reinforcing bars were used as longitudinal reinforcement on each face of the center column to achieve, as close as possible, the scaled area for three #9 reinforcing bars used by Sezen (2002) on each face of the full-scale column. A concrete design strength of 3000 psi was selected to maintain consistency with the full-scale tests.

After the design of the center column, the remaining frame elements (i.e., the beams, outside columns, and footings) were not scaled from prototype designs, but instead were designed to achieve the desired response. For example, the beams were designed to be much stronger than the columns in bending (similar to spandrel beams found in 1960s buildings), and provide the bending stiffness of a beam spanning over a column which has lost its axial load capacity (see Section 5.2.3).

Once the strength and stiffness of the outside columns were chosen (see Section 5.2.2), capacity design procedures were used to design the beams and footings. Pushover analyses were conducted up to displacements corresponding to three levels of damage to the center column (i.e., just before shear failure, just after shear failure, and after axial load failure) to determine the critical demands for the beams. Owing to the lack of analytical tools to accurately model the shear failure of reinforced concrete components, the shear failure was crudely modeled by removing the lateral stiffness of the center column once a specified shear demand (corresponding to shear failure) was reached. The demands after axial failure of the center column were roughly determined by "pushing" the frame, modeled without a center column, to a displacement ductility greater than 6 (equal to the maximum displacement ductility observed to cause axial load failure in the columns tested by Sezen (2002)). To ensure that all of the damage was concentrated in the columns, the estimated column strengths were multiplied by 1.5 for the pushover analyses (resulting in higher demands in the beams), and a very conservative strength reduction factor of 0.5 was used in the design of the beams and footings.

5.2.2 Outside Columns

For a building containing columns susceptible to combined flexure-shear-axial load failure, as considered in this study, it is reasonable to expect that some components would experience limited yielding before the columns failed in shear. Hence, the outside columns of the frame were designed to yield before shear failure of the center column. Furthermore, preliminary analysis of the frame showed that if the outside columns were allowed to remain elastic, or nearly elastic, then the lateral response of the frame following shear failure of the center column would entail only elastic vibration of the remaining intact elements. This response did not seem reasonable for such an extreme loading condition and was not of interest to the current study. To achieve the desired response, the outside columns were designed to have a yield displacement and yield moment equal to two thirds of the center column.

A circular section with closely spaced spiral reinforcement was chosen for the outside columns in order to ensure that the columns were capable of resisting large ductility demands without

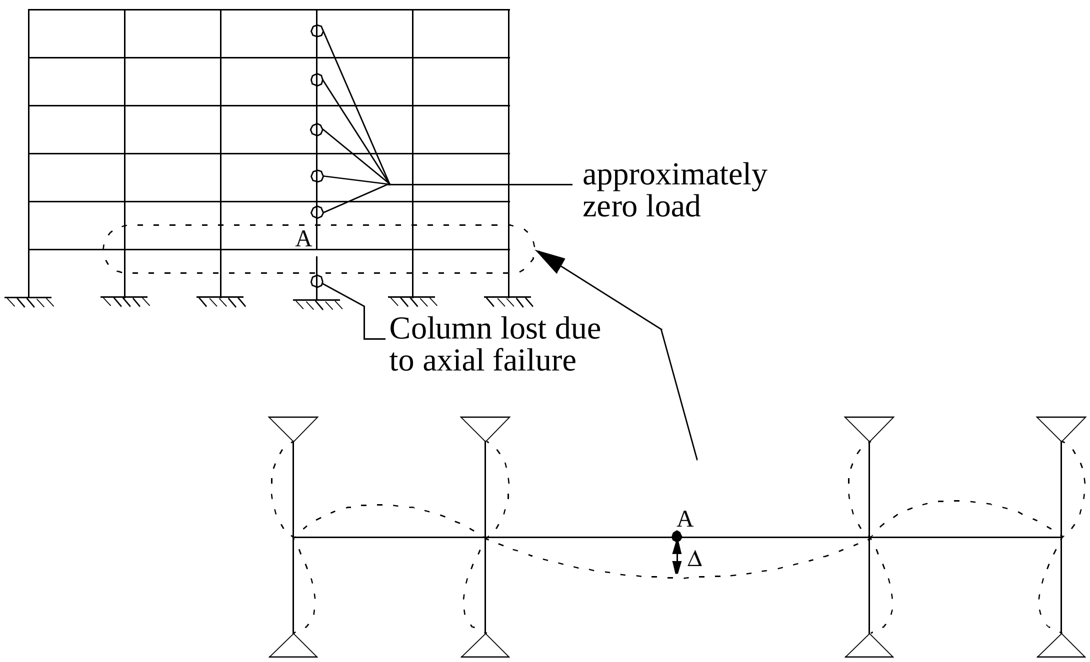

Figure 5-2. Model for determining beam stiffness

any threat of axial failure. This choice of section also provided a more gradually yielding load-displacement relationship compared to a square section, a desirable characteristic, since the three-column frame is intended to represent part of a larger building frame that would also be expected to have a gradually yielding load-displacement relationship.

5.2.3 Beam Stiffness and Strength

Since the bending stiffness of the beam will influence the shedding of the axial load after failure of the center column, the beam stiffness must be appropriately chosen. For this purpose, a seven-story building in Van Nuys, California (described in detail in Browning et al. (2000)) was used as the prototype building. After the axial failure of a first-story column, a longitudinal frame of the building could be approximately modeled as shown in Figure 5-2. If each of the floors is considered identical in stiffness and load, then the columns continuing above the failed column will carry zero axial load and the deflection of the second story at point A can be approximated by considering only the beams, columns, and loads of the second story as shown in Figure 5-2. Using such a model, the deflection at point A due to static gravity loads is approximately 0.18 inches.

The stiffness of the beam in the three-column frame was selected to give a scaled deflection of 0.09 inches (or 0.18 inches at full-scale) after axial failure of the center column for the first test specimen. The width of the beam was chosen as 5 feet to provide support for the 50 kips of lead mass required to achieve the appropriate axial stress in the center column. The beam reinforcement was selected such that at the face of the transverse beam above the center column, the ratio of the yield strength of the beam to the maximum moment demand from plastic analysis after axial failure of the center column was 1.59 for Specimen 1 and 0.82 for Specimen 2.

Figure 5-3. Demands on transverse torsional beams

5.2.4 Transverse Torsional Beams

Particular attention was paid to the connection between the five-foot wide beam and the columns. The moment developed over the width of the wide beam must be transferred to the narrow columns through torque of a beam running transverse to the three-column frame. Sufficiently large transverse beams are required to preclude any reduction in stiffness due to torsional cracking.

Figure 5-3 illustrates the demands on the transverse torsional beams. To avoid any interference with the behavior of the columns, the transverse beams protrude from the top of the wide beam, as shown in Figure 5-1. Since the torsional demands are applied along the side faces of the transverse beams, the resistance to this demand must be calculated from the cracking capacity of the rectangular transverse beam section. The cracking torque capacities were calculated using the skew-bending and plastic theories (Hsu, 1984), and recommendations by Gentry and Wight (1994). The cross-section dimensions of the transverse torsional beams were selected such that the cracking torque exceeded the torsional demands from the pushover analyses discussed in

Section 5.2.1. For further details on the design of the transverse torsional beams, refer to Section A.2.

5.3 EXPERIMENTAL SETUP

Each test specimen was moved to the earthquake simulator before testing. Specimens were aligned with the intended shaking direction on top of six force transducers (two per column) and bolted in place after placement of hydrostone to ensure a level surface. Specimens were shored while lead

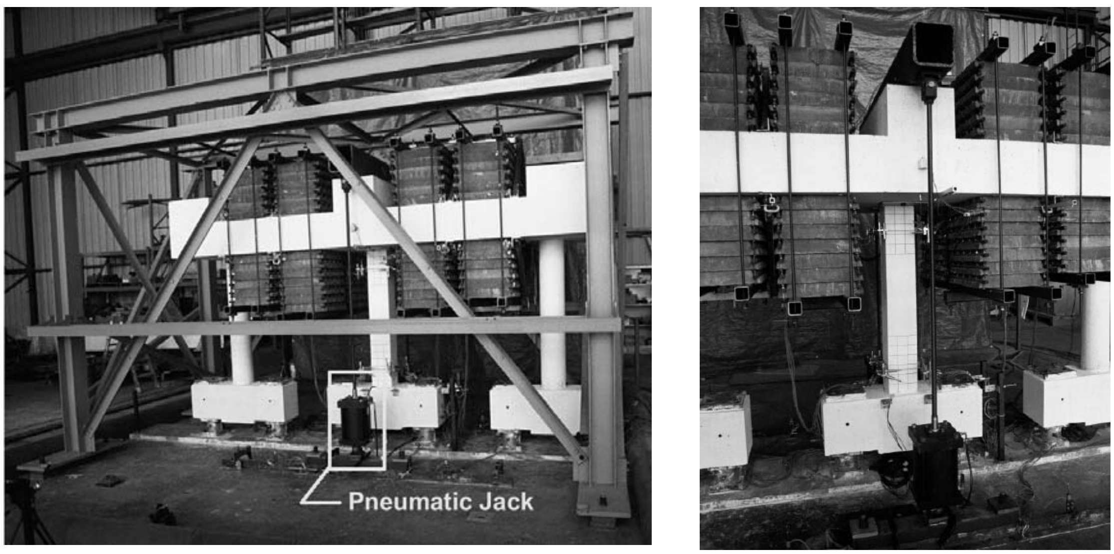

Figure 5-4. Test specimen on the shake table and pneumatic jack for prestressing

weights (total of 67 kips including the mass of the beam) were placed to simulate gravity loads and inertial mass. The lead weights were supported at one end on a steel shim to fix the position and on the other end by a rubber shim to allow deformation of the concrete test specimen beneath the lead weights. The weights were then bolted in position so that they moved in unison with the test specimen.

The two specimens were nominally identical except for the axial load on the columns. Since the shake table could not reliably control a significantly larger mass, the additional axial load for the second test was attained by prestressing using a pneumatic jack on either side of the center column (Figure 5-4). The air cylinder of the pneumatic jacks allows the center column to shorten 1 inch without loosing more than 15% of the prestress load.

The planar frame specimens were subjected to unidirectional horizontal base motions. An out-of-plane bracing system, known as a “pantograph,” was designed to restrain the specimen and ensure essentially unidirectional response.

For more details on the experimental setup, including the performance of the out-of-plane bracing mechanism, see Appendix B.

5.4 INSTRUMENTATION

Instrumentation consisted of force and displacement transducers, accelerometers, and strain gages. This section summarizes the instrumentation setup. More details can be found in Appendix B.

Because it was important to track the redistribution of the horizontal and vertical loads from the center column to the outside columns, the specimens were supported on force transducers that monitored axial load, shear, and moment, as shown in Figure 5-1. The force transducers available at the UC Berkeley Earthquake Simulation Lab had been designed previously for base-isolation projects, and hence, do not have a large moment capacity. This deficiency was overcome by using two transducers per column connected by a stiff footing. The force transducers are very sensitive to the stiffness of the end conditions; the stiffer the connecting elements, the more accurate the measurements. To maximize the stiffness of the connection between the transducer and the shake table, the transducers were located directly over the threadbars used to connect the supporting base plate to the shake table. The threadbars are spaced at 3 feet on center, constraining the column spacing to 6 feet, as shown in Figure 5-1.

Displacement transducers were used to measure the global vertical and horizontal displacements of the mass and local deformations of the center column. The displacement transducers on the center column enabled the observation of deformations along the height of the center column. Owing to the severe damage to the center column during the test, the data from these instruments are valid only before shear failure.

Accelerometers were used to measure vertical and horizontal accelerations of the mass. The accelerometers were mounted on several stacks of lead mass to check that all of the mass was moving in unison. The vertical acceleration of the mass was of particular interest after axial failure of the center column. The horizontal accelerations provided a check on the base shear measured by the force transducers.

Strain gages were mounted on the longitudinal reinforcing bars in the columns and beams, and on the transverse reinforcement in the center column. The strain gages were concentrated in the center column where the local behavior was of particular interest.

Table 5-2. Filter frequencies and scale factors for input table acceleration record

Name	f_{hcut}	f_{hcor}	f_{lcor}	f_{lcut}	*Acc. Scale Factor*[1]	*Time Scale Factor*	*Source*
Chile (Viña del Mar)	0.16	0.2	12	15	0.75	$\sqrt{0.5}$	SAC se32

1) Scale factor only refers to direct scaling of accelerations given in source ground motions. Source motions may have been scaled from original record.

f_{hcut}: high pass cut-off frequency (hertz)
f_{hcor}: high pass corner frequency (hertz)
f_{lcor}: low pass corner frequency (hertz)
f_{lcut}: low pass cut-off frequency (hertz)

Table 5-3. Peak values for table acceleration records

Record	*PGA* *g*	*PGV* *in./sec*	*PGD* *in.*
Filtered Input (Figure 5-5a)	0.66	16.2	1.70
Specimen 1 Recorded (Figure 5-5b)	0.79	15.5	1.61
Specimen 2 Recorded (Figure 5-5c)	0.73	15.2	1.62

5.5 TABLE MOTION

Both specimens were subjected to one horizontal component from a scaled ground motion recorded during the 1985 Chile earthquake (Figure 5-5 and Tables 5-2 and 5-3). Several factors led to the selection of this ground motion record. First, the record needed enough intensity to fail the center column in shear. Secondly, the maximum displacement ductility demand on the frame needed to be limited to avoid failure of the outside columns. Thirdly, a ground motion of long duration was of interest to observe the mechanics of axial failure while the specimen was still subjected to strong ground shaking.

Owing to the lack of accurate analytical models for shear and axial failure of reinforced concrete columns, only approximate analyses, such as displacement ductility spectra, were used to determine if the ground motion achieved the first two criteria listed above. The displacement ductility spectra were developed using stiffness degrading oscillators obeying Clough-type hysteretic

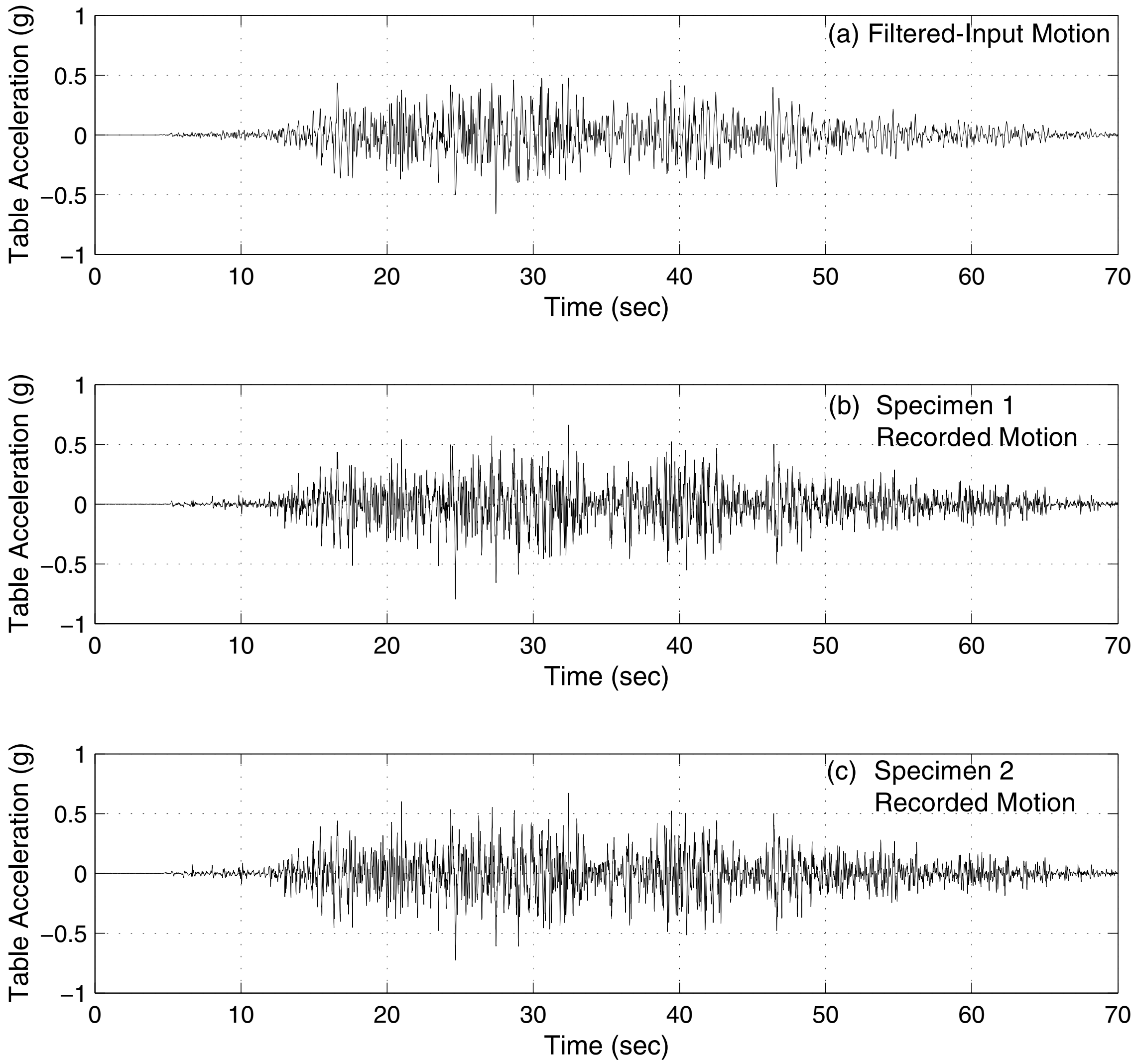

Figure 5-5. Input and recorded table acceleration records

laws (Clough, 1966). The goal was to find a ground motion with a displacement ductility demand that would ensure the shear failure of the center column occurred but did not result in extreme demands on the outside columns after failure of the center column. To this end, ground motions within the range of $3<\mu_\Delta<7$ at the target elastic period (T=0.27 sec) were considered. The selected Chile ground motion resulted in a displacement ductility of 4 at the target period, for a yield strength of 40 kips and 2% damping.

Further restrictions were placed on the choice of ground motions by the capacity of the shake table. The maximum displacement and velocity of the table are 5 inches and 30 in./sec, respectively, as shown in Figure 5-6. Since the length scale factor for the model was 1:2, the

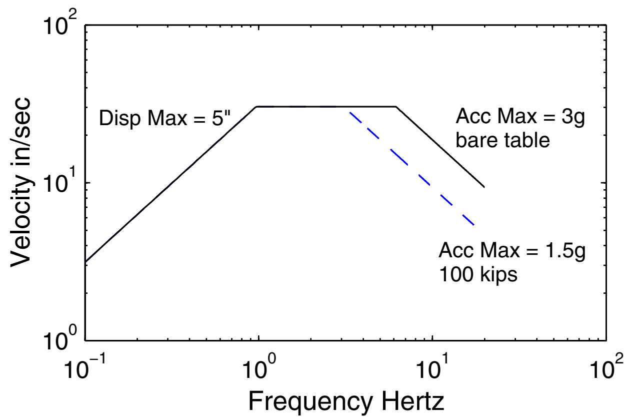

Figure 5-6. UC Berkeley shake table capacities

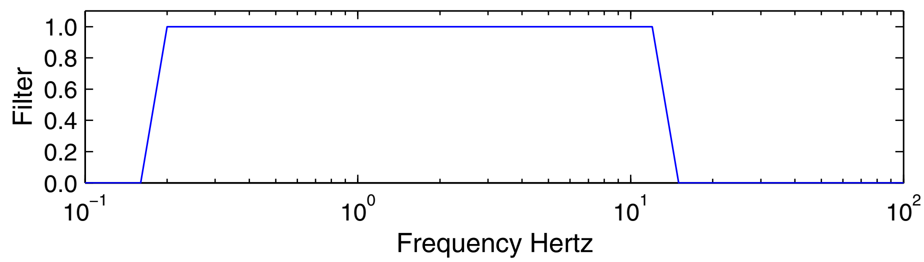

Figure 5-7. Filter used to process the ground motion

ground motions were evaluated using a time scale factor of $\sqrt{0.5}$. Many ground motions used in other shake table tests of smaller scale specimens could not be used in the current study without significant filtering, since the scale reduced the displacements and velocities only by a factor of 0.5 and $\sqrt{0.5}$, respectively.

Filtering of the recorded ground motion was performed to remove the high and low frequencies that were beyond the range of the shake table controller and to reduce the displacements and velocities to within the capabilities described above. The ground motion was filtered by converting the acceleration histories to the frequency domain using a fast Fourier transform, and removing unwanted frequencies using the frequency filter illustrated in Figure 5-7. Then the ground motion was converted back to the time domain by an inverse fast Fourier transform. The filter frequencies used for the chosen ground motion are listed in Table 5-2.

The acceleration records in Figure 5-5 show some discrepancy between the input and recorded table motions due to additional high frequency response of the table. The significance of the differences in the records can be better evaluated by comparing the corresponding response

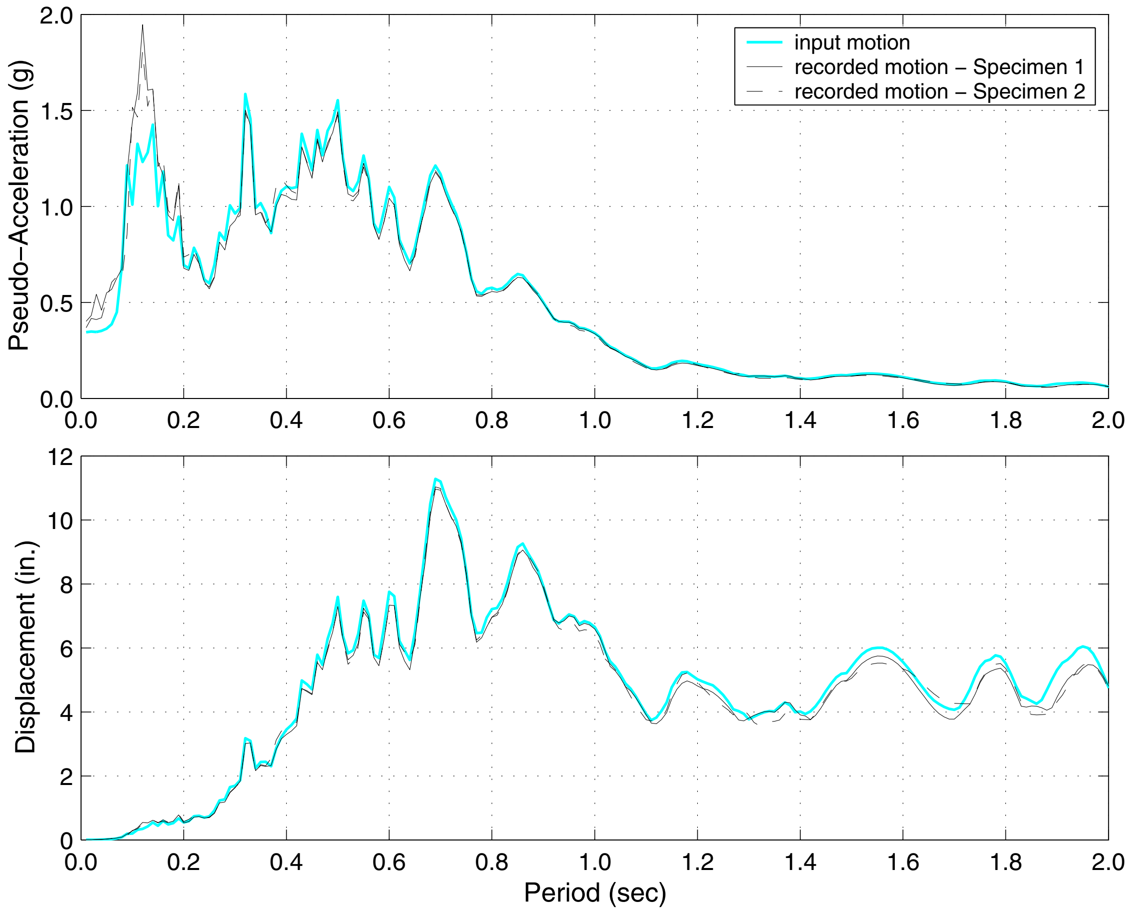

Figure 5-8. Pseudo-acceleration and displacement response spectra for input and recorded table motions (2% damping)

spectra. The displacement and pseudo-acceleration response spectra for the filtered-input motion used to control the shake table, and the recorded motions for the two specimens, are shown in Figure 5-8. The pseudo-acceleration response spectra for the recorded and input motions are in close agreement except around 0.12 seconds. Since the first mode ($T \cong 0.27$ sec) dominates the response of the specimens, this discrepancy did not significantly influence the shake table test results. The displacement response spectra diverge slightly at periods above 1.5 seconds, but show close agreement within the period range of interest (i.e., from T equal to 0.2 to 1.0 sec).

5.6 EXPERIMENTAL PROGRAM

Three types of tests were conducted on the test specimens: free vibration, low level, and shear failure. The chronology of the tests for each specimen is given in Tables 5-4 and 5-5.

The primary test for each specimen, selected to induce shear failure in the center column, was the unidirectional earthquake simulation using the table motion described in Section 5.5. The results from these tests, presented in Section 6.3, are the focus of this experimental study.

Before the shear-failure tests, low-level earthquake simulations were also performed using the table motion from Section 5.5 scaled to a lower intensity such that the maximum relative displacement of the center column remained below the anticipated yield displacement. Results from these tests can be found in Appendix C.

The free-vibration test setup is illustrated in Figure 5-9. The turnbuckle was used to tighten the pull-back cables until the readings from the load cell indicated a tension force of 1100 lbs. (The tension force was chosen to achieve a longitudinal force of 1000 lbs and ensure that the pull-back did not crack the specimen columns.) After the appropriate tension force was achieved, the "dog-bone" steel coupon was cut, resulting in the free-vibration response of the specimen. Free-vibration tests were performed before and after each earthquake simulation test. Measurements from the accelerometers and force transducers were used to determine the natural period and damping of the test specimens.

Table 5-4. Chronology of tests for Specimen 1

Date	*Test Name*	*Table Motion Scaling*[a]
2/16/01	Free-vibration 1	N/A
2/20/01	Low-level	0.13
2/20/01	Free-vibration 2	N/A
2/25/01	Shear-failure	1.0
2/25/01	Free-vibration 3	N/A

Table 5-5. Chronology of tests for Specimen 2

Date	*Test Name*	*Table Motion Scaling*[a]
3/29/01	Free-vibration 1	N/A
3/29/01	Low-level	0.13
3/29/01	Free-vibration 2	N/A
3/30/01	Shear-failure	1.0
4/2/01	Free-vibration 3	N/A

a. Scaling factor applied to the acceleration history shown in Figure 5-5(a).

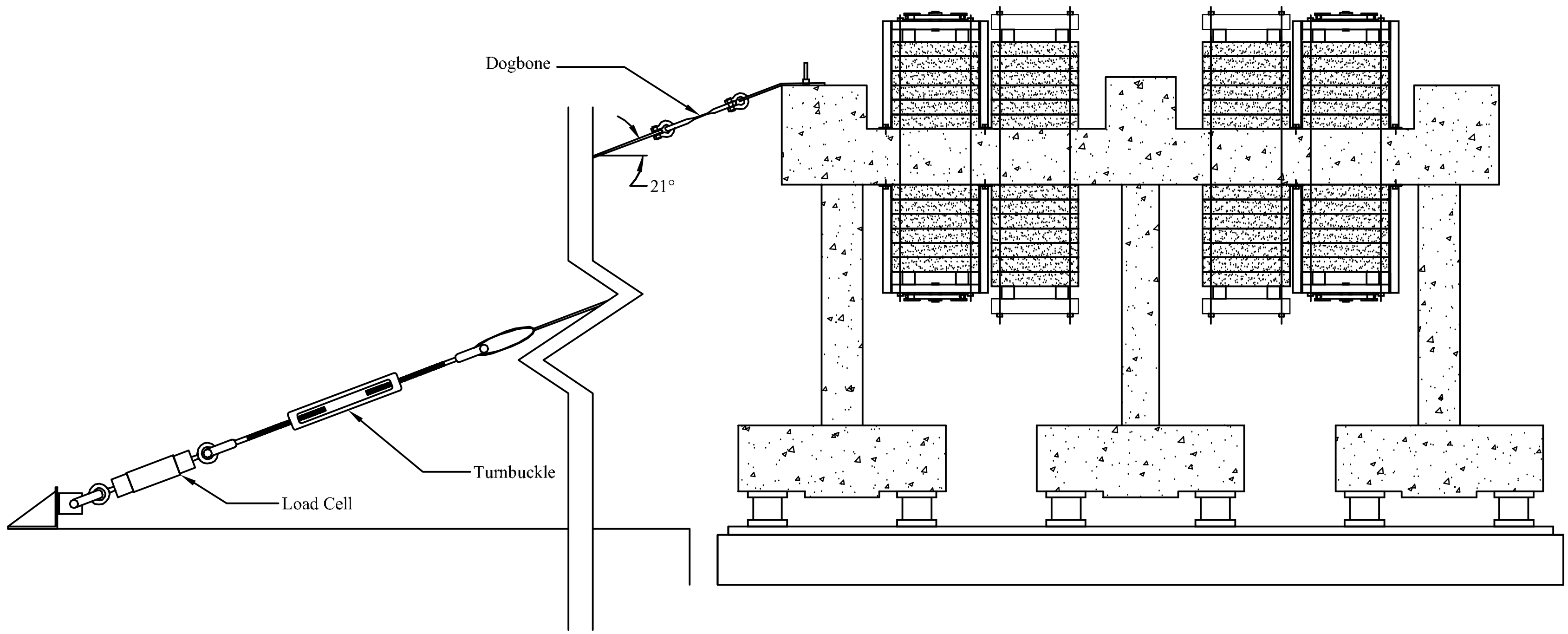

Figure 5-9. Setup for free-vibration tests

6 Shake Table Test Results

6.1 INTRODUCTION

This chapter will document and discuss the results from the free-vibration and shear-failure tests described in Section 5.6. The results from the low-level tests appear in Appendix C. Comparison of the results with predictive models can be found in Chapter 7, while an evaluation of the three-column frame response using nonlinear static and dynamic analyses is presented in Chapter 8.

6.2 FUNDAMENTAL PERIOD AND DAMPING

The apparent fundamental periods and equivalent viscous damping coefficients for both specimens were determined using free-vibration tests described in Section 5.6. The periods and damping coefficients were determined before and after each earthquake simulation test, corresponding to different states of damage. For the first free-vibration test for each specimen, all three columns appeared uncracked. For the second free-vibration test, only a small hairline crack was detected at the base of the center column for each specimen, while the outside columns showed fine cracks distributed over the height of the columns. The Specimen 1 outside columns showed more cracks than observed on the outside columns of Specimen 2. The third and final free-vibration tests were performed after the shear-failure tests, and as such, both specimens had experienced significant damage, including shear failure of the center column and spalling of the concrete cover at the top and base of the outside columns.

For a structure in free-vibration, the equivalent viscous damping ratio can be calculated as follows:

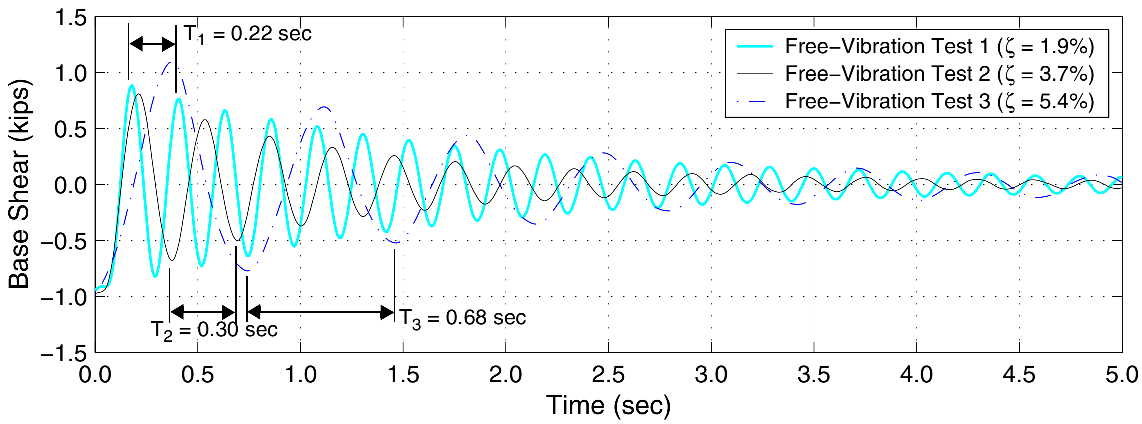

Figure 6-1. Damping ratios and periods from free-vibration tests — Specimen 1

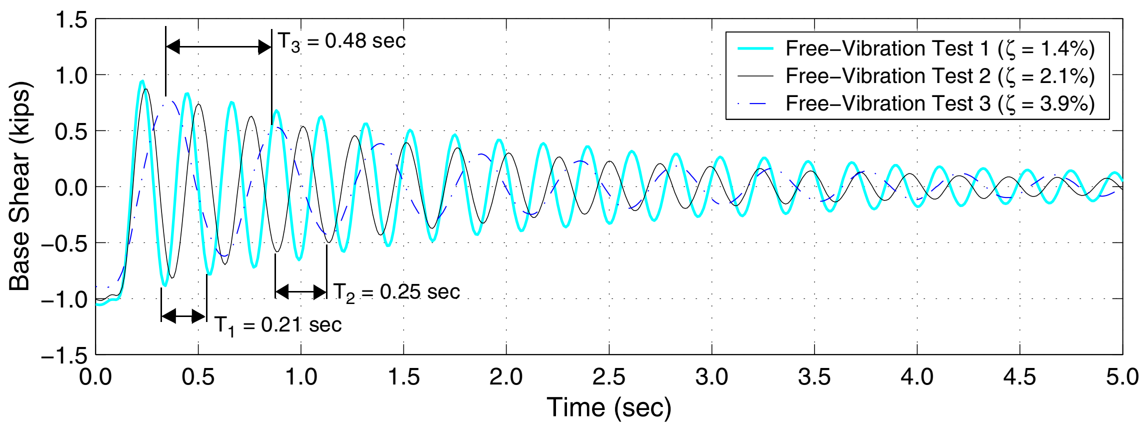

Figure 6-2. Damping ratios and periods from free-vibration tests — Specimen 2

$$\zeta = \frac{\ln\left(\frac{V_1}{V_{n+1}}\right)}{2\pi n} \tag{6.1}$$

where V_1 is the first peak in the base shear response history, V_{n+1} is the (n+1)th peak in the base shear response history, and n is the number of peaks above a base shear of 0.2 kips. (The limiting base shear of 0.2 kips was selected to avoid using base shear measurements below the sensitivity of the force transducers.) The damping ratios calculated using Equation 6.1 and the fundamental periods determined based on a Fourier transform of the base shear response histories are given in Figures 6-1 and 6-2, respectively. The fundamental periods and damping coefficients clearly increase with increasing damage. Although the initial periods of the two specimens are very close, the periods measured after each of the earthquake simulation tests for Specimen 1 are larger than those for Specimen 2. The additional axial load applied by the prestressing equipment for Specimen 2 results in the closure of shear and flexural cracks, thereby increasing the lateral stiffness and decreasing the measured period. The increase in the measured damping coefficients with damage may be a result opening and closing of cracked sections and an increase in the nonlinear response, even for the very low base shear applied in the free-vibration tests.

6.3 SHEAR-FAILURE TESTS

This section presents the results of the shear-failure tests on Specimens 1 and 2. The table motion selected for these tests was presented in Section 5.5. The results from both specimens will be discussed together to enable evaluation of the influence of the center column axial load on the response of the specimens. When comparing the response of Specimens 1 and 2, it is worth recalling that the only difference between the two tests was the axial stress on the columns (Specimen 1 center column: $P = 0.10 f'_c A_g$, Specimen 2 center column: $P = 0.24 f'_c A_g$). The results will be discussed in the following order: global response of the test specimens, response of the center columns, response of the outside columns, and aspects of shear and axial load redistribution.

Videos of the shear-failure tests can be found on the attached compact disk (see Appendix E). The videos include several of the plots discussed in this section. The plots evolve with time and are synchronized with videos of the test specimens allowing for comparison of the damage state of the specimens with measured response quantities. The damage state of the specimens after the tests is shown in Figures 6-3 and 6-4.

To aid in understanding the relationships among the plots in this section, symbols have been placed at significant times in each of the response histories (i.e., at 16.7 sec, 24.9 sec, and 29.8 sec). These times correspond approximately to the following events: the first drop in the center column shear for Specimen 2 relative to Specimen 1, the initiation of axial failure of the center column of Specimen 2, and the end of the sudden drop in the center column axial load for Specimen 2. These events will be discussed in more detail in Section 6.3.2.

6.3.1 Global Response of the Test Specimens

The response histories in Figure 6-5 demonstrate similarities and differences in the global behavior of Specimens 1 and 2.

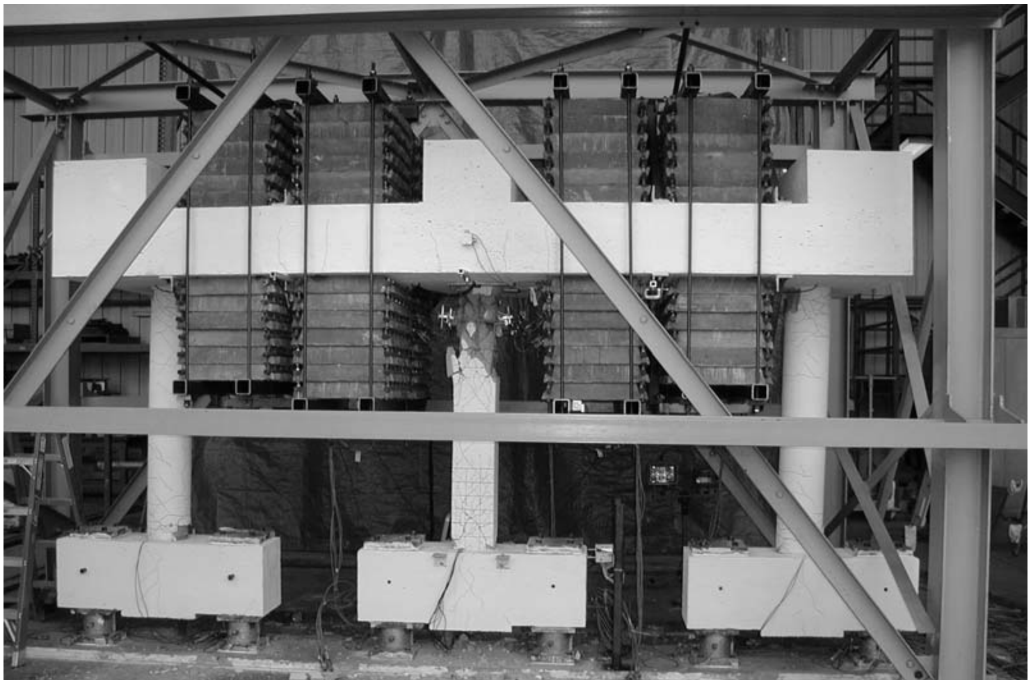

Figure 6-3. Damage state of Specimen 1 after shear-failure test

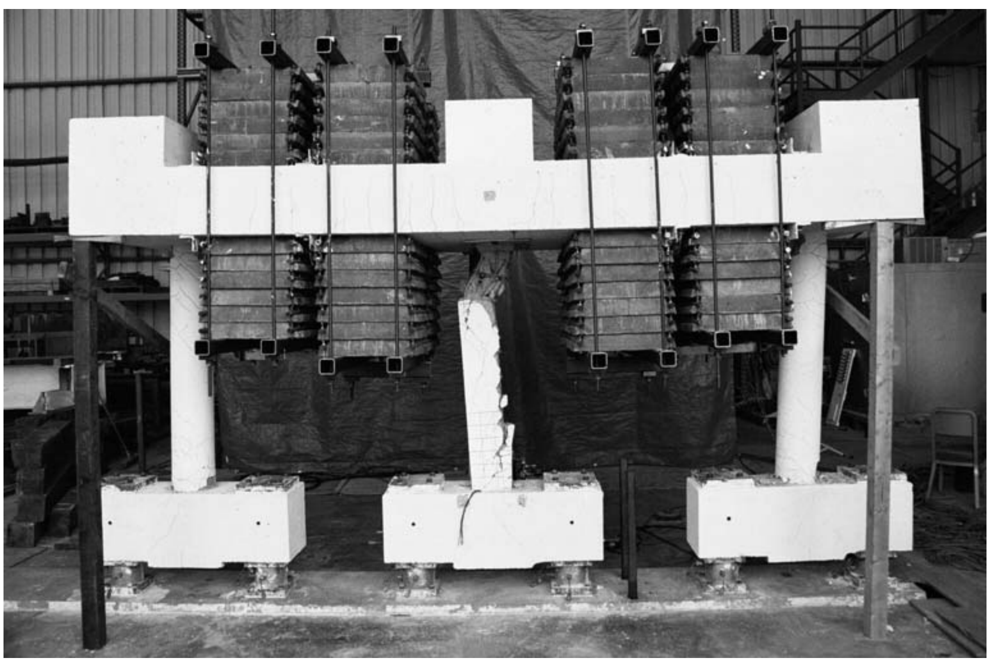

Figure 6-4. Damage state of Specimen 2 after shear-failure test

Early in the ground motion (from t = 10 sec to t = 12 sec), the longitudinal displacements of Specimen 1 appear larger than those of Specimen 2, resulting in a higher base shear and overturning moment for Specimen 1. This difference may result from a slight deviation in the low

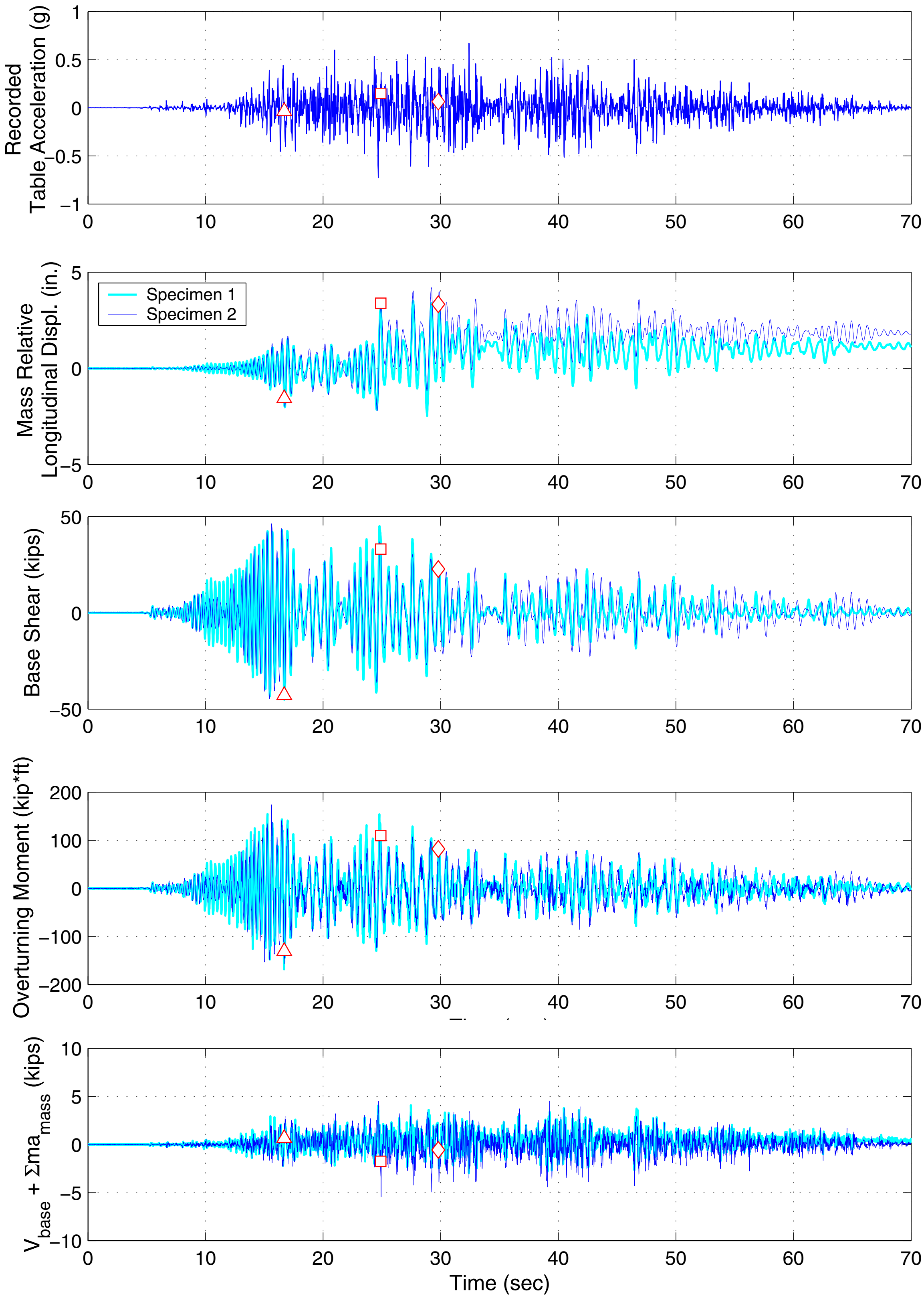

Figure 6-5. Global response histories for Specimens 1 and 2

amplitude control of the shake table for each test, but does not appear to have any influence on the remainder of the test, since both specimens remain linear.

After t = 12 seconds, the longitudinal displacements of the two specimens remain close, with a similar period of response, until the square marker at t = 24.9 seconds. At this point the longitudinal displacements for Specimen 2 increase relative to those of Specimen 1, and begin to oscillate about an offset from the origin of approximately 1.0 inch. Just before the diamond marker at t = 29.8 seconds, the longitudinal displacements for both specimens are further offset from the origin, resulting in a permanent offset of approximately 1.15 inches for Specimen 1 and 1.85 inches for Specimen 2 at the end of the test.

After the triangular marker (at 16.7 sec), the Specimen 2 base shear drops slightly relative to that of Specimen 1. This drop coincides with the development of wide shear cracks in the center column of Specimen 2 (Section 6.3.2).

Figures 6-6 and 6-7 show the base shear hysteretic response of the specimens. The earlier drop in the shear capacity of the center column for Specimen 2 is clearly evident, but otherwise the overall lateral behavior of the frame is not significantly altered by the increase in axial stress on the center column.

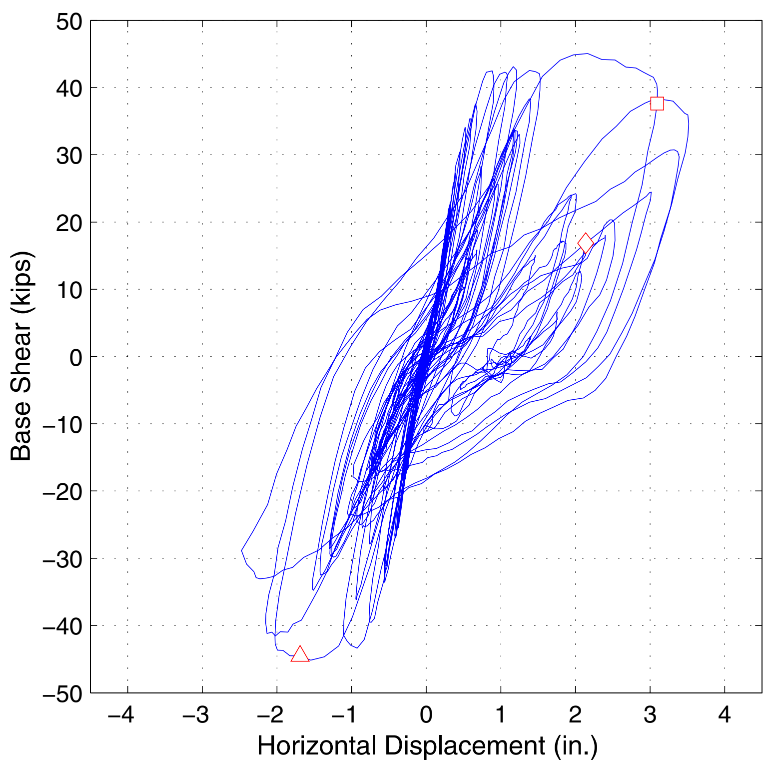

Figure 6-6. Specimen 1 base shear hysteretic response

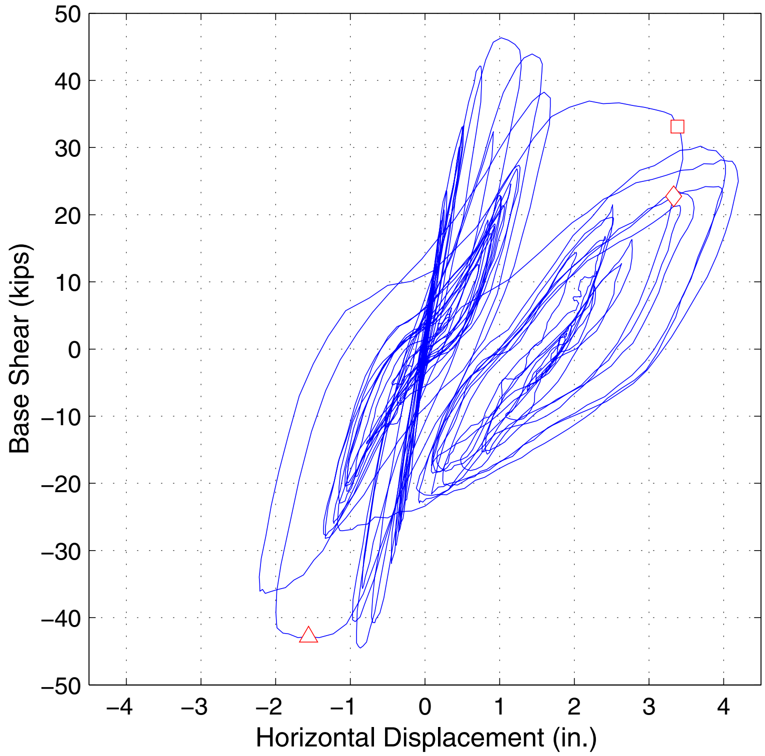

Figure 6-7. Specimen 2 base shear hysteretic response

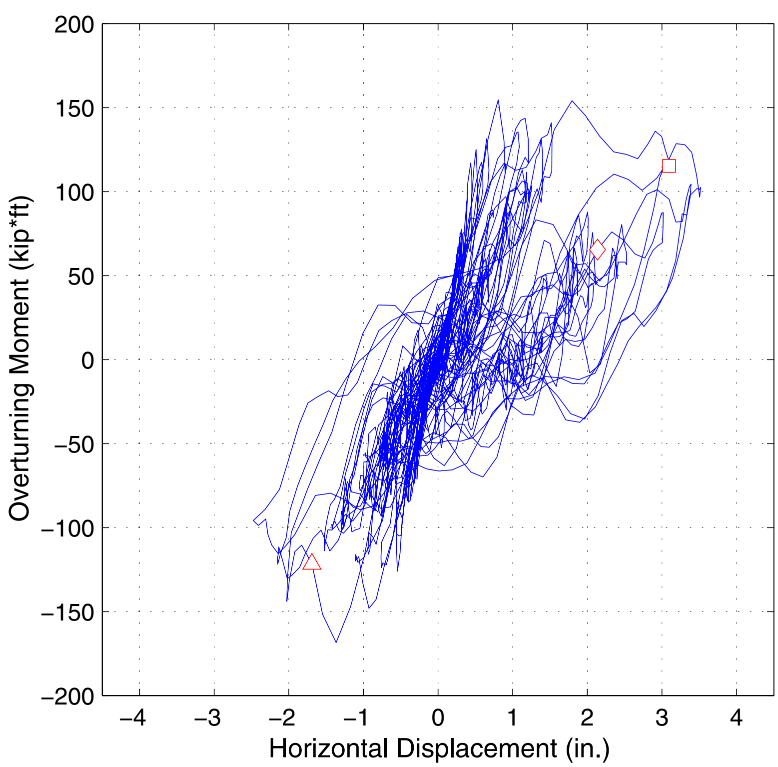

Figure 6-8. Specimen 1 overturning moment hysteretic response

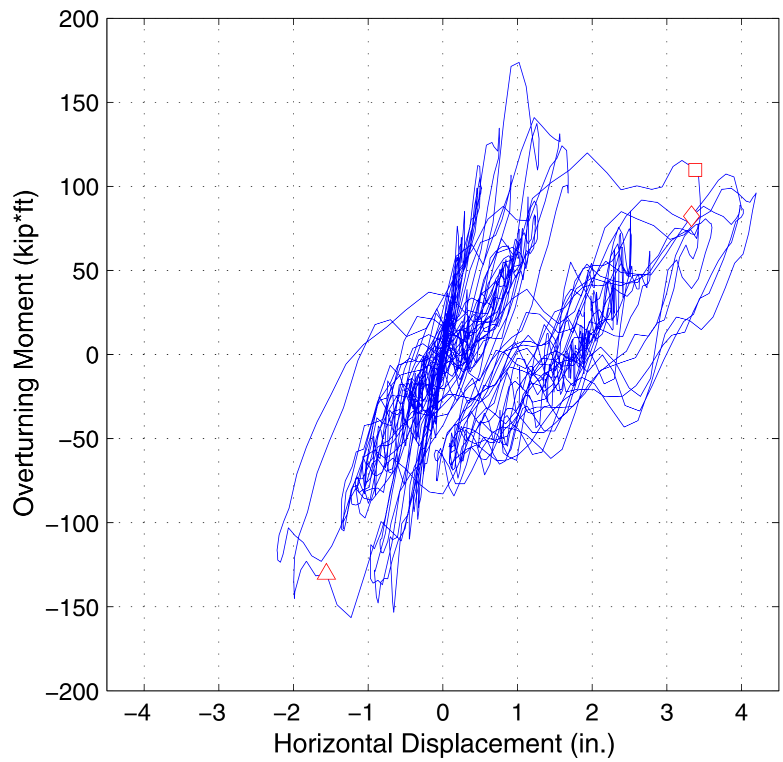

Figure 6-9. Specimen 2 overturning moment hysteretic response

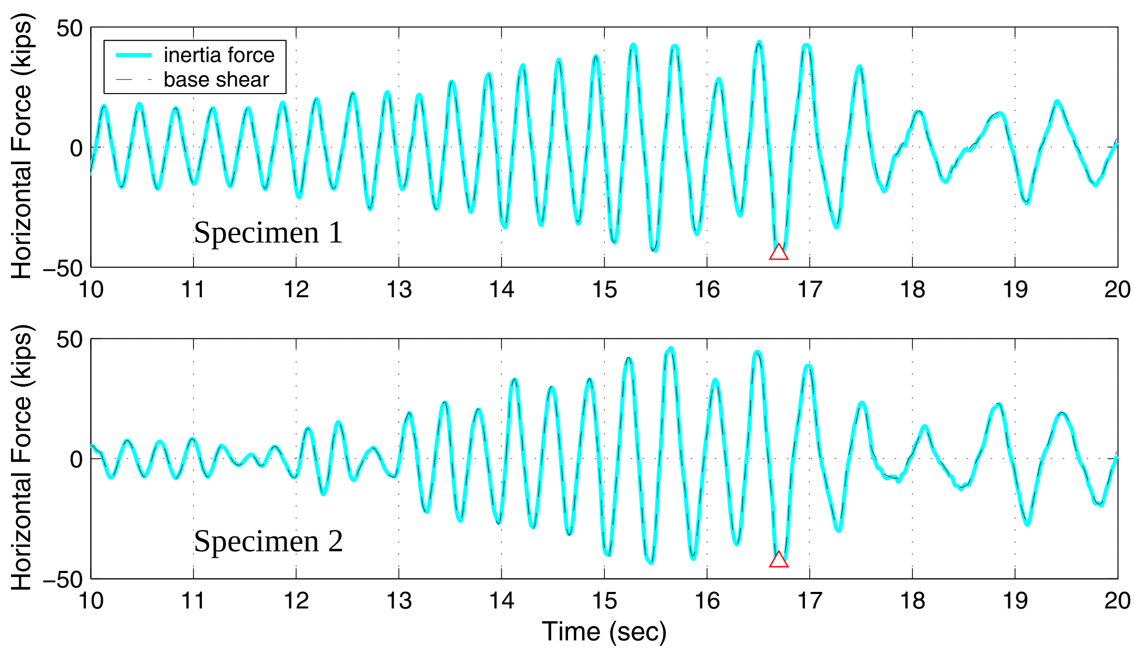

Figure 6-10. Comparison of base shear and inertial force from t = 10 to 20 sec

Figures 6-8 and 6-9 show the overturning moment hysteretic response for the specimens resulting from the inertial forces acting at a height of 64.75 inches above the base of the columns. The chaotic appearance of the overturning moment response can be attributed to imprecision of the shake table controller. Slight pitching of the table at high frequencies (approximately 15 hz) caused vertical acceleration couples, and hence, overturning moments in the specimens. Owing to the high-frequency nature, this controller error did not appear to adversely affect the response the specimens. Further discussion of the overturning moments and how they were derived can be found in Section B.6.

The last response history shown in Figure 6-5 plots the sum of the base shear and the inertial forces (note that the base shear and inertial forces are opposite in sign). From the classical equation of motion for a structure, this sum should give the equivalent viscous damping force. However, in the classical equation of motion viscous damping is used as a mathematical tool to account for various means by which energy is dissipated and the motion of a structure is reduced during (assumed) linear response. With the exception of a limited viscous force due to air resistance, all means of energy dissipation are accounted for in the true force-deformation relationship measured directly by the force and displacement transducers. Figure 6-10 shows very close agreement between the measured inertial force (based on results from accelerometers attached to mass) and the measured base shear (based on the shear forces measured by the force transducers), suggesting that little or no “damping force” exists during the tests. The minor differences can be attributed to high-frequency oscillations of the mass blocks not captured by the force transducers.

6.3.2 Response of the Center Column

The observation of the shear and axial load response of the center column was one of the primary objectives of this experimental study. This section presents response quantities for the center column such as shear, moments, and axial load, in addition to the deformations measured by the center column instrumentation.

The damage states for the top of the center column, for each of the times indicated by the symbols on the plots, are shown in Figures 6-11a through 6-13b. The center column of Specimen 2 experiences more significant damage earlier in the history than the center column of Specimen 1. The videos on the attached compact disk (see Appendix E) provide an excellent visual comparison of the progression of damage during the tests. The following paragraphs discuss the behavior of the center column with reference to the triangle, square, and diamond markers shown in Figures 6-14 through 6-16. Note that the longitudinal displacements for the center column are the same as those shown in Figure 6-5.

The triangular marker indicates the approximate time (16.7 sec) at which the center column shear for Specimen 2 begins to drop off relative to the center column shear for Specimen 1. Also at this time, the center column axial load for both specimens drops by approximately 10 kips. This drop in load coincides with the development of significant cracks in the outside and center columns and, hence, is thought to be caused by redistribution of gravity loads as the lengths of the columns change owing to flexural response. Figures 6-11a and 6-11b show the state of the top of the center column for both specimens at the time indicated by the triangular marker. The diagonal shear cracks appear wider and steeper for Specimen 2.

The square marker indicates the pulse (at 24.9 sec) that initiates the axial failure of the Specimen 2 center column. The continuation beyond this point for Specimen 2 is possible only because an alternative load path was provided and the axial load in the center column could be redistributed to the outside columns. Figures 6-15 and 6-16 demonstrate that by the time indicated by the square marker the center column shear capacity for Specimen 1 has only just begun to degrade, while the center column shear capacity of Specimen 2 has degraded to less than one half of the ultimate center column shear attained. Figures 6-12a and 6-12b show the state of the top of the center columns for both specimens at the time indicated by the square marker. A large shear crack is apparent in the Specimen 1 center column, while the Specimen 2 center column has experienced severe local distortions.

The diamond marker indicates the approximate time (29.8 sec) at which the minimum center column axial load is reached for the first time. By this point the center column shear capacity has all but disappeared for both specimens. The center column axial load for both specimens remains nearly constant after this time despite the continuation of strong ground shaking. Figures 6-13a and 6-13b show the state of the top of the center columns for both specimens at the time indicated by the diamond marker. Cover and core concrete are spalling off the Specimen 1 center column, while the longitudinal reinforcement has clearly buckled in the Specimen 2 center column.

Figures 6-17 and 6-18 show the center column shear hysteresis and an idealized backbone for Specimens 1 and 2, in addition to the point of first yield in the longitudinal reinforcement based

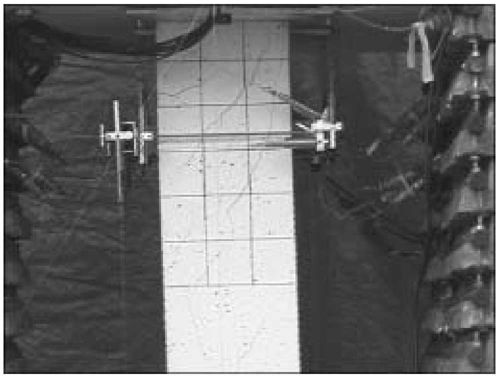

**Figure 6-11a. Top of center column
Specimen 1 at 16.7 sec**

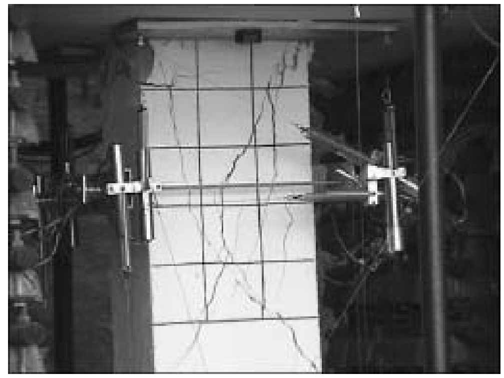

**Figure 6-11b. Top of center column
Specimen 2 at 16.7 sec**

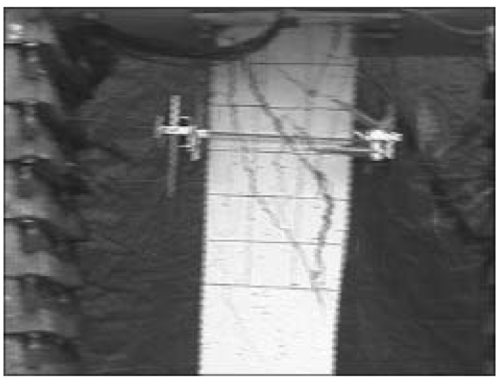

**Figure 6-12a. Top of center column
Specimen 1 at 24.9 sec**

**Figure 6-12b. Top of center column
Specimen 2 at 24.9 sec**

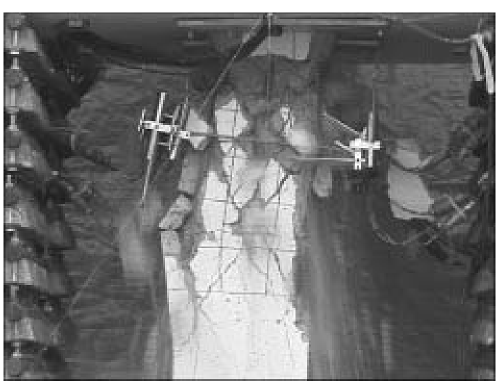

**Figure 6-13a. Top of center column
Specimen 1 at 29.8 sec**

**Figure 6-13b. Top of center column
Specimen 2 at 29.8 sec**

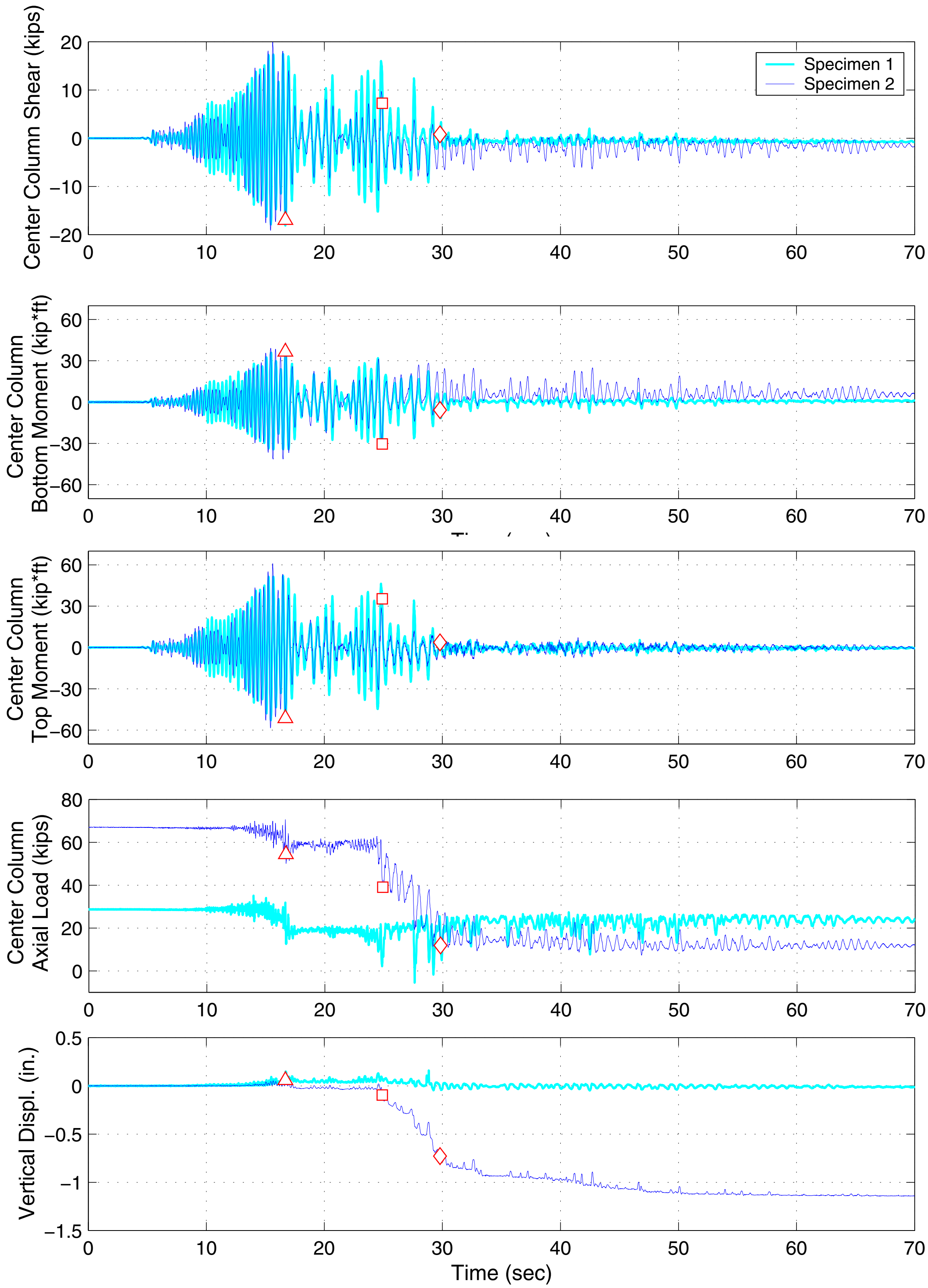

Figure 6-14. Center column response histories (Specimen 1: P = 0.10 f'_cA_g, Specimen 2: P = 0.24 f'_cA_g)

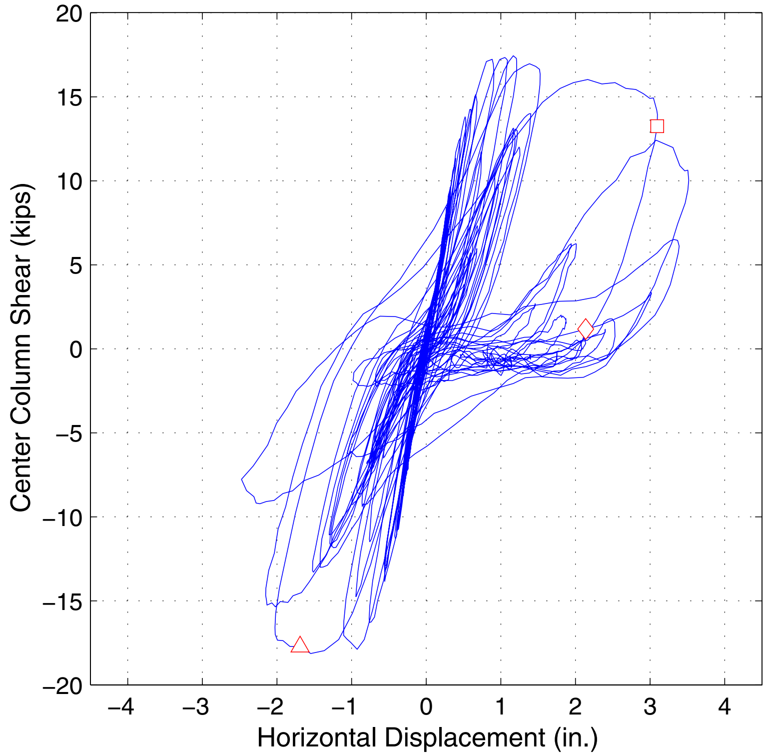

Figure 6-15. Specimen 1 center column shear hysteretic response

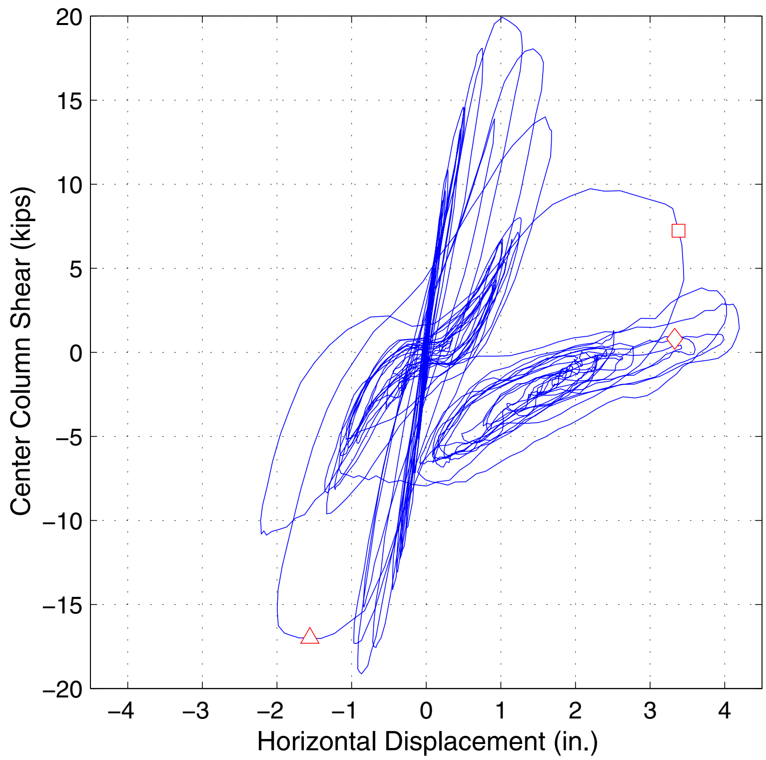

Figure 6-16. Specimen 2 center column shear hysteretic response

on the strain gage data. The idealized backbone in each direction was defined by the following line segments:

- A straight line from the origin through the point on the test data envelope corresponding to 70% of the peak shear recorded in that direction and extended to the peak shear level.
- A flat line at the peak shear level from the end of the previous line to the displacement where there is a loss in the shear resistance of at least 20% of the peak shear recorded in that direction.
- A straight line connecting the end of the previous line with a point on the x-axis at the maximum displacement recorded during the test. This line appears only in the direction of shear failure.

For a backbone representing the full capacity of a column, the last line segment should terminate at zero shear and the displacement at which axial failure occurs. Since axial failure was not observed in Specimen 1, the final line segment is shown as a dashed line. The final line segment in a backbone representing the full capacity of the Specimen 1 center column would be expected to have a flatter slope than the dashed line shown in Figure 6-17.

Since an alternative load path for the gravity loads is provided in the test specimen, the axial load in the failing center column for Specimen 2 is not lost all at once (Figure 6-19). This makes it difficult to establish a single point to be defined as “axial failure.” However, the displacement at axial failure is less than the maximum displacement recorded for Specimen 2. Therefore, the final line segment for a backbone representing the capacity of the Specimen 2 center column should be slightly steeper than that shown in Figure 6-18.

The behavior of the center column during axial failure for Specimen 2 is characterized by the region between the square and the diamond markers in Figure 6-19. The figure suggests that there are two mechanisms by which the vertical displacements increase: first, large pulses that cause a sudden increase in vertical displacement after a critical drift is attained; and second, smaller oscillations that appear to “grind down” the failure plane. It is interesting to note for the first mechanism discussed above that the axial load drops immediately before the sudden increase in vertical displacements, and increases immediately after the increase in vertical displacements. This behavior suggests that the support for gravity loads may be lost suddenly, leading to the sudden drop in axial load, but the inertia of the mass may delay the increase in vertical displacement. After the mass drops, the column suddenly picks up load again, possibly when the top portion of the failure surface hits another support point on the bottom portion of the failure surface or as the horizontal

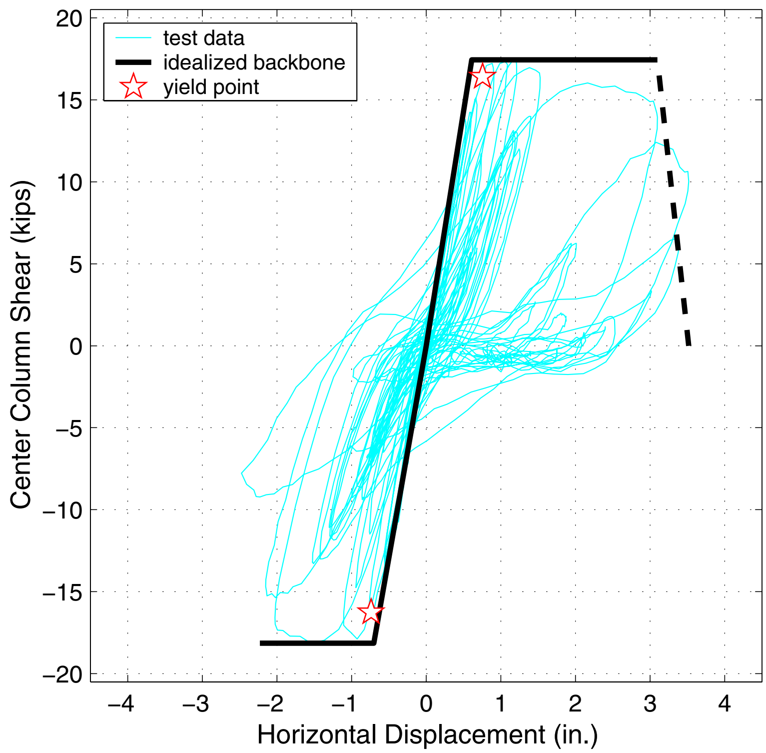

Figure 6-17. Specimen 1 hysteresis with idealized backbone

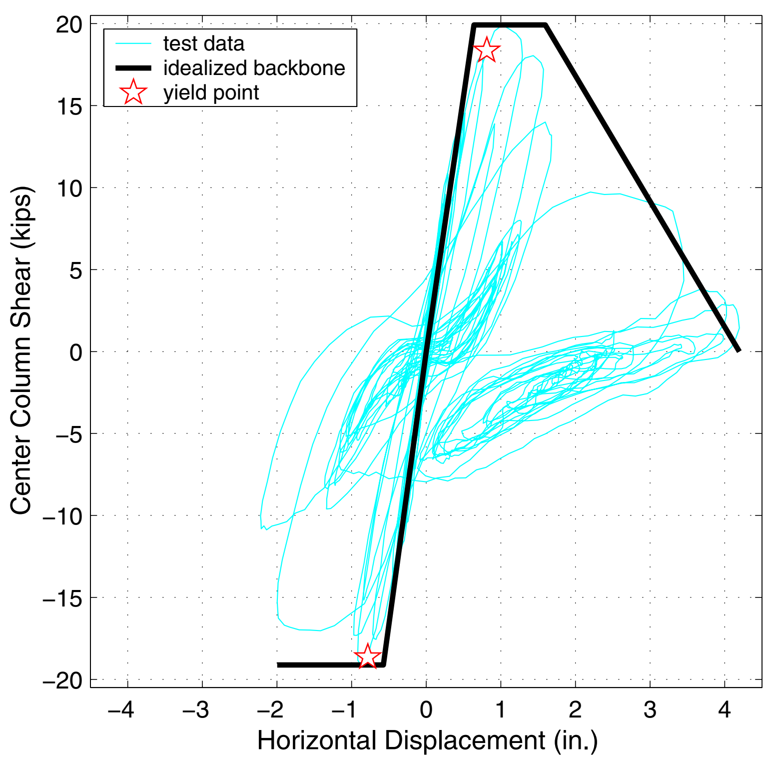

Figure 6-18. Specimen 2 hysteresis with idealized backbone

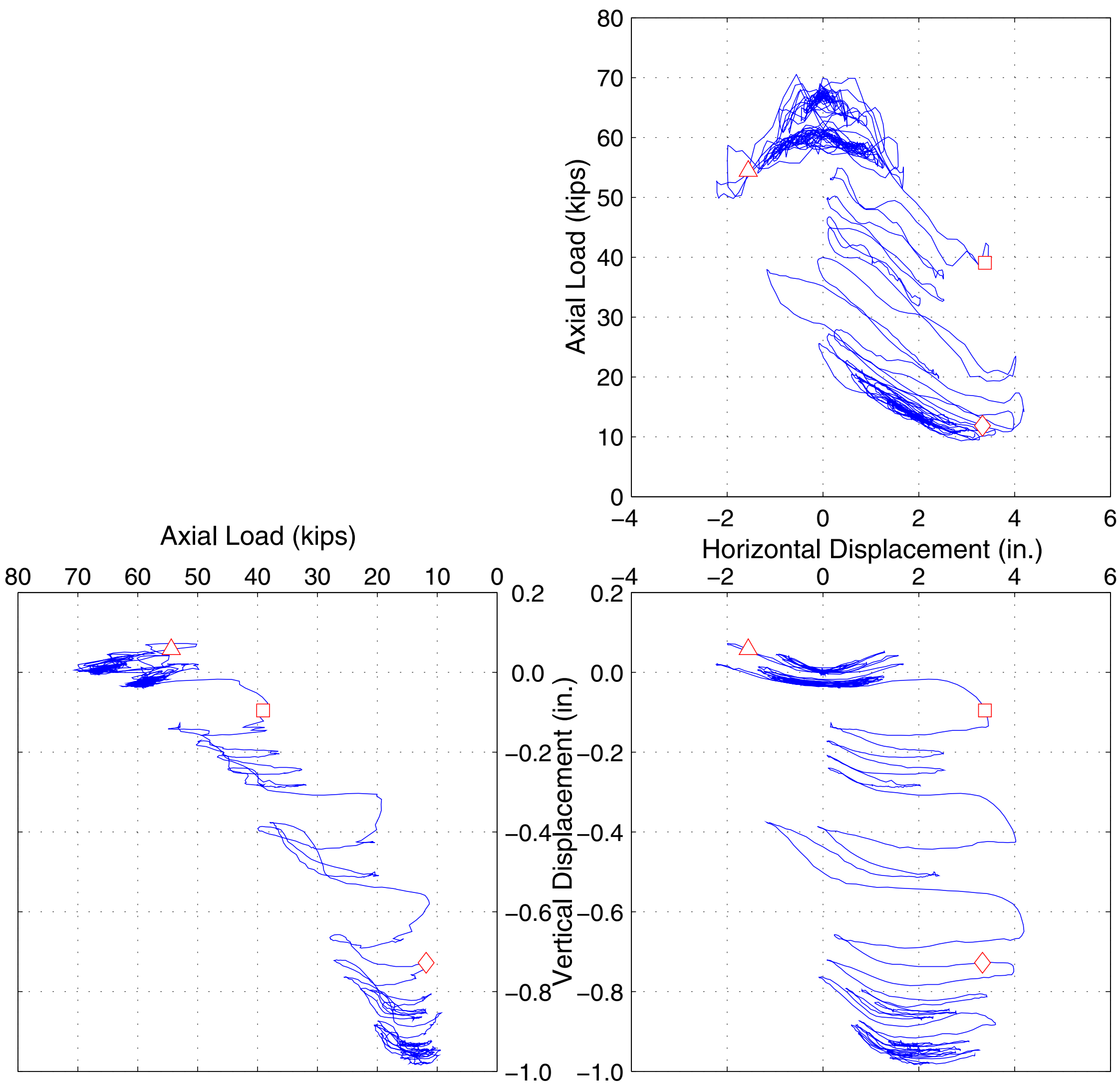

Figure 6-19. Relations between center column axial load, vertical displacement, and horizontal displacement of top of center column for Specimen 2

displacements are reversed by the table motion and the failure surface is partially closed. In Section 7.6, the data from Figure 6-19 will be compared with the axial failure model presented in Chapter 3.

Although the Specimen 1 center column does not experience axial failure, Figure 6-20 indicates that it does exhibit some of the same characteristics as the Specimen 2 center column. The axial load-horizontal displacement response for the Specimen 1 center column, shown in the upper right plot of Figure 6-20, is very similar to that shown in Figure 6-19 for Specimen 2 before the square marker (i.e., before axial failure). The convex shape of this plot for both specimens is con-

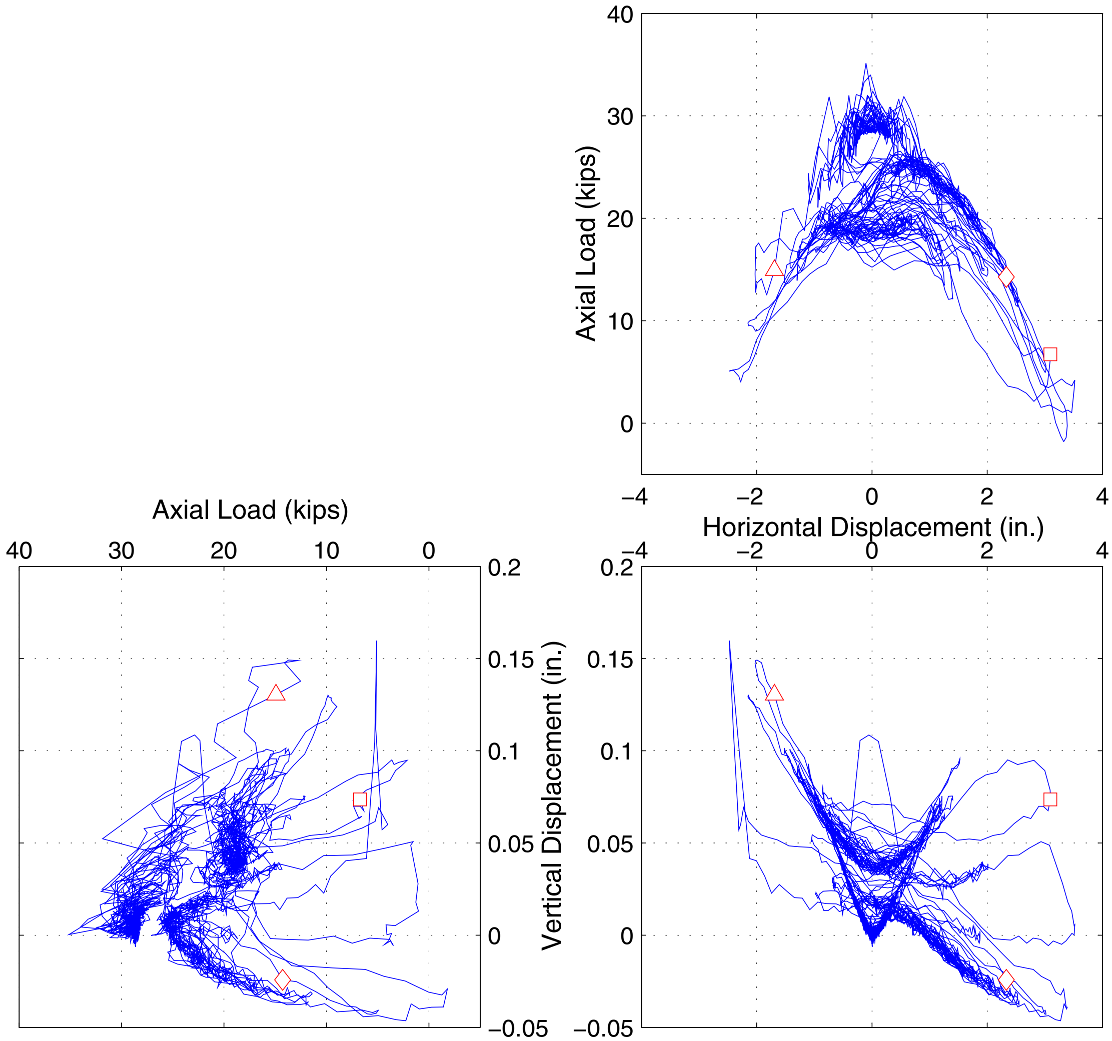

Figure 6-20. Relations between center column axial load, vertical displacement, and horizontal displacement of top of center column for Specimen 1

trolled by the transient redistribution of gravity load to the outside columns due to bending of the beam (discussed in Section 6.3.4.2). Before the square marker (i.e., before shear failure for Specimen 1), the vertical-horizontal displacement plots for both specimens show a lengthening of the center column with increasing horizontal displacements due to an increase in longitudinal strains over the length of the column resulting from flexural cracking. During the pulse indicated by the square marker, and the next large positive horizontal displacement pulse, a sudden drop in the vertical displacement for the Specimen 1 center column can be observed. Although much smaller in magnitude compared with the drops observed in the lower right plot of Figure 6-19 for Specimen 2, this sudden change in vertical displacements also appears to occur once a critical drift is attained.

Since these sudden changes in vertical displacement are not associated with a permanent loss of axial load from the center column, the vertical displacement drops may be due to a shift in the center column axial load support from the core concrete to the longitudinal steel. If the center column axial load is transferred to the longitudinal bars, the vertical strains should increase, while most of the axial load is maintained as long as the buckling capacity of the bars is not exceeded.

After the final free-vibration test for Specimen 1, the loose concrete core at the top of the center column was removed and the longitudinal reinforcement was cut while the axial load in the column was recorded. This procedure demonstrated that approximately 90% of the axial load supported by the center column of Specimen 1 at the end of the test was carried by the longitudinal reinforcement.

Figures 6-21a and 6-21b show the state of the center columns for both specimens at the end of the tests. Note that the distorted shape of the center column of Specimen 2 shown in Figure 6-21b resulted from the upper portion of the column above the shear-failure plane forcing the lower three-quarters of the column to bend to the left as the beam deflected downward. This distorted shape results in the permanent center column shears and base of column bending moments observed at the end of the test (Figure 6-14). At the end of the test, the Specimen 1 center column was supporting 84% of its initial axial load, or 24 kips, while the center column of Specimen 2 was supporting only 18% of its initial axial load, or 12 kips (Figure 6-14).

Figures 6-22 through 6-27 show the center column moment hysteretic response for Specimens 1 and 2. The top and bottom column moments were calculated, accounting for second-order effects, according to the procedures described in Section B.6. Note that according to the plots, the yield strength at the top of the column appears to be approximately 50% higher than that at the bottom of the column. Although some discrepancy in the top and bottom yield strength should be expected due to slight variation in the reinforcement location and pockets of aggregates at the base of the column, one would not expect this discrepancy to be more than approximately 10%. It was concluded, therefore, that an error exists in the force transducer output used to calculate the moments. Section B.6 discusses possible sources of the error; however, in the absence of conclusive proof of the source of the error, the uncorrected data are presented here.

Figures 6-22 and 6-23 plot the moments versus the drift angle, defined as the longitudinal displacement measured by global instruments divided by the height of the column. Figures 6-24 through 6-27 plot the moments versus rotations and curvatures calculated from the center column

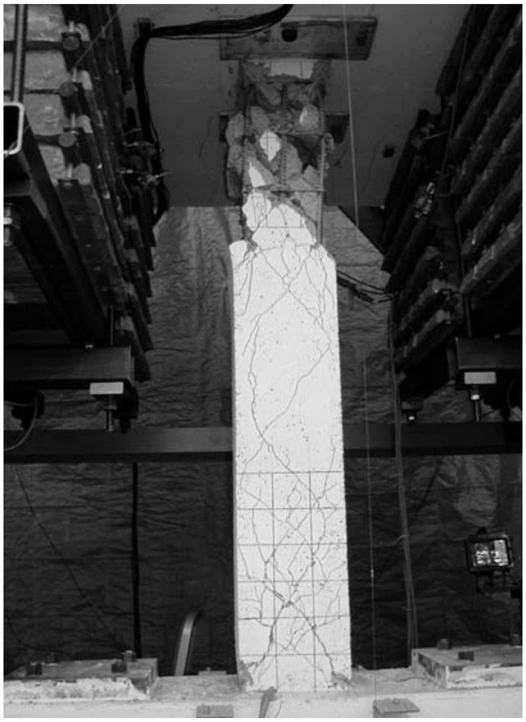

Figure 6-21a. Specimen 1 center column at end of test

Figure 6-21b. Specimen 2 center column at end of test

instruments. Since the spalling cover concrete interferes with instruments mounted on the columns, these data are shown only before t = 27.65 seconds for Specimen 1 and t = 24.90 seconds for Specimen 2. It should be noted that the curvatures and rotations include both slip and flexural deformations. Refer to Section B.6 for a detailed description of how these quantities were calculated from the column instruments.

Figure 6-22 shows the moment at the top of the center column dropping off just before the square marker (at 24.9 sec), and before reduction in the moment at the bottom of the center column. The same degradation at the top of the column before reduction in the moment at the base of the column can seen in Figures 6-23, 6-25, and 6-27 for Specimen 2. The degradation at the top of the column coincides with the opening of diagonal shear cracks at this location (Figure 6-12a). The moment at the bottom of the center column does not appear to degrade significantly within any single cycle; instead the bottom moment reduces upon repeated cycles as the shear resisted by the column reduces. This localization of degrading behavior supports the use of an analytical model that concentrates the degradation in a flexural spring at one end of a column.

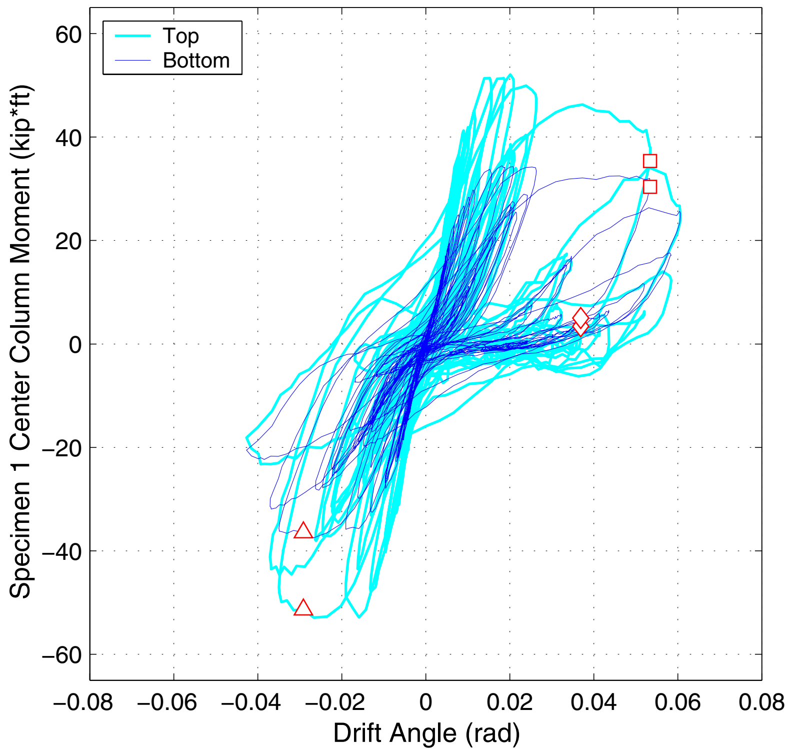

Figure 6-22. Specimen 1 center column moment hysteretic response

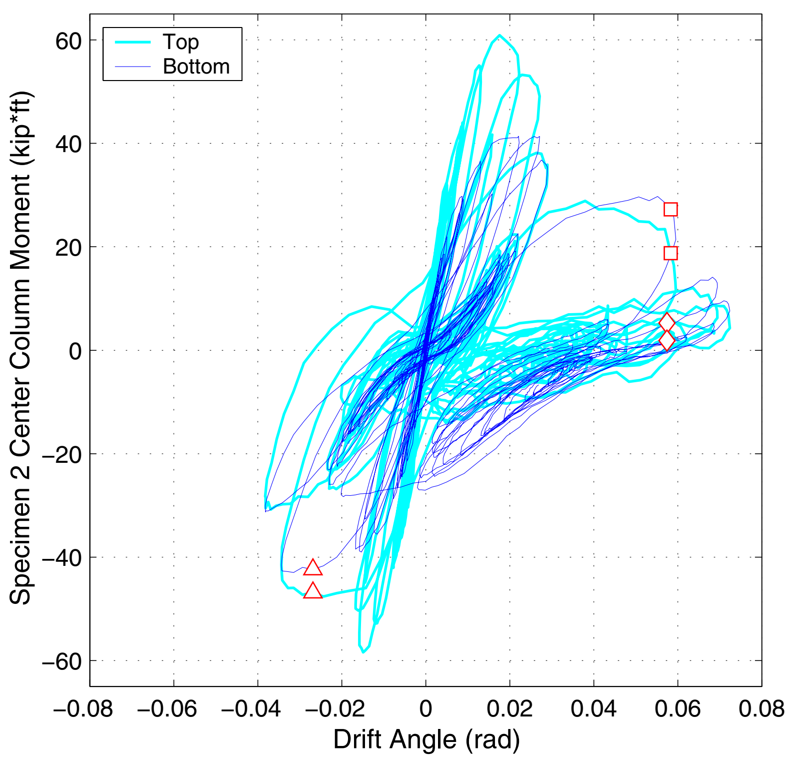

Figure 6-23. Specimen 2 center column moment hysteretic response

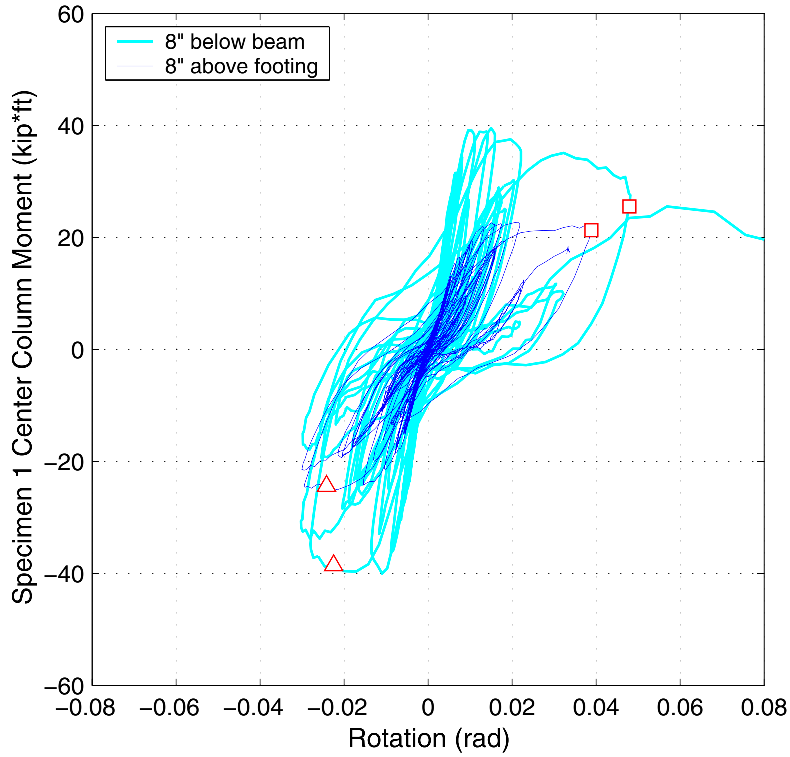

Figure 6-24. Specimen 1 center column moment-rotation hysteretic response

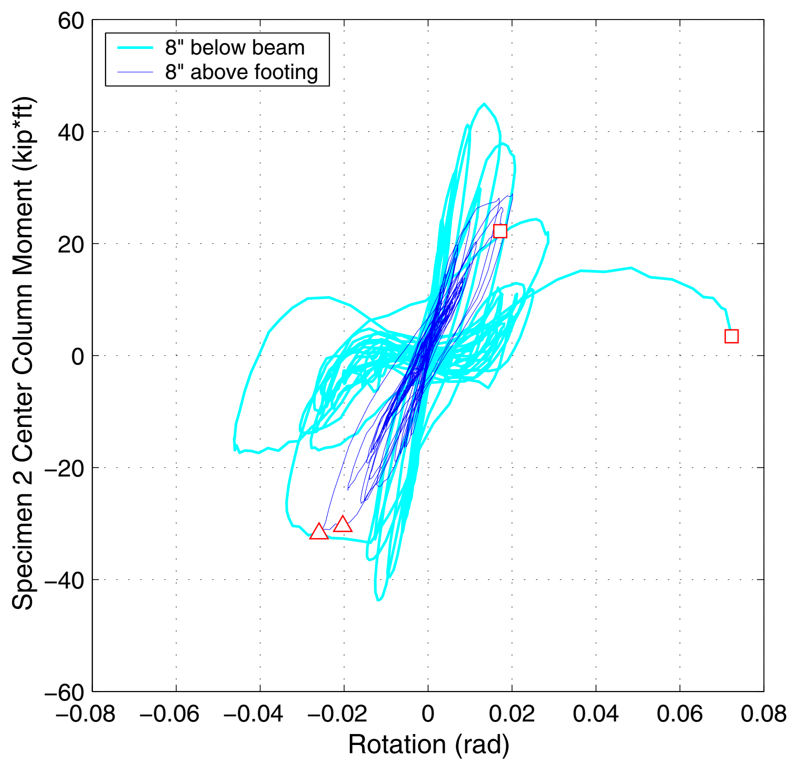

Figure 6-25. Specimen 2 center column moment-rotation hysteretic response

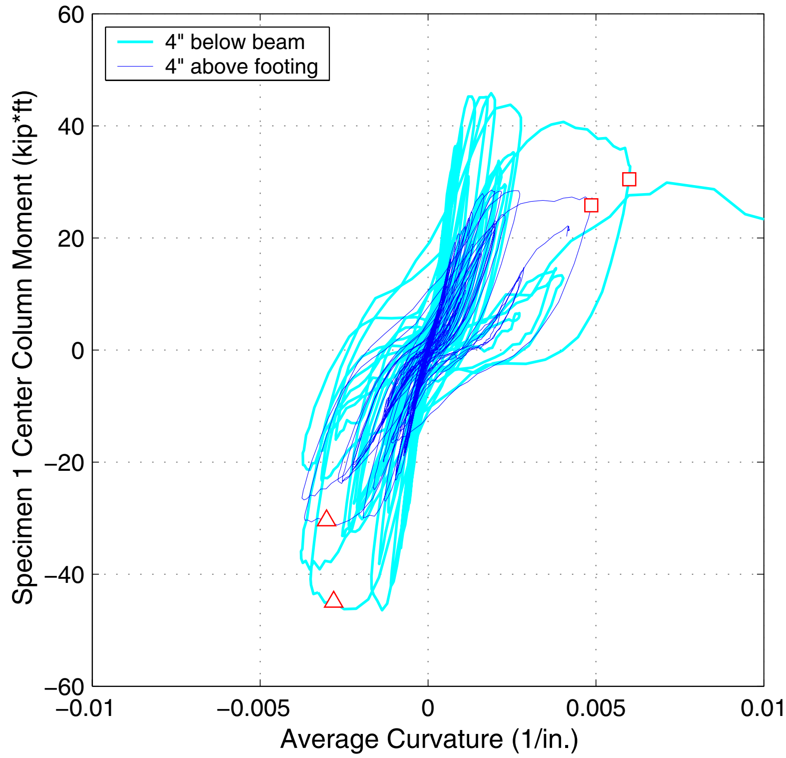

Figure 6-26. Specimen 1 center column moment-curvature hysteretic response

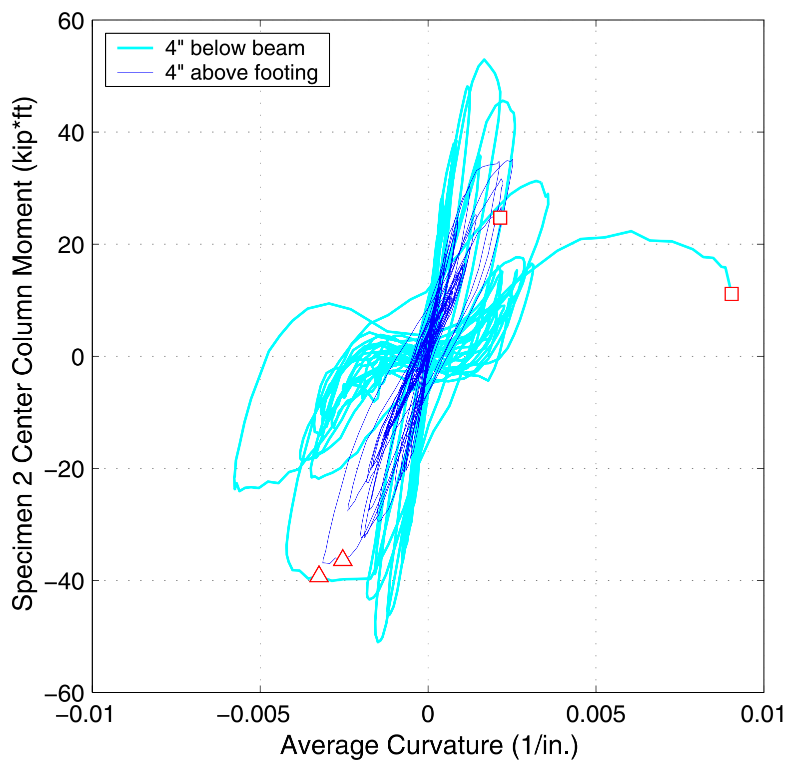

Figure 6-27. Specimen 2 center column moment-curvature hysteretic response

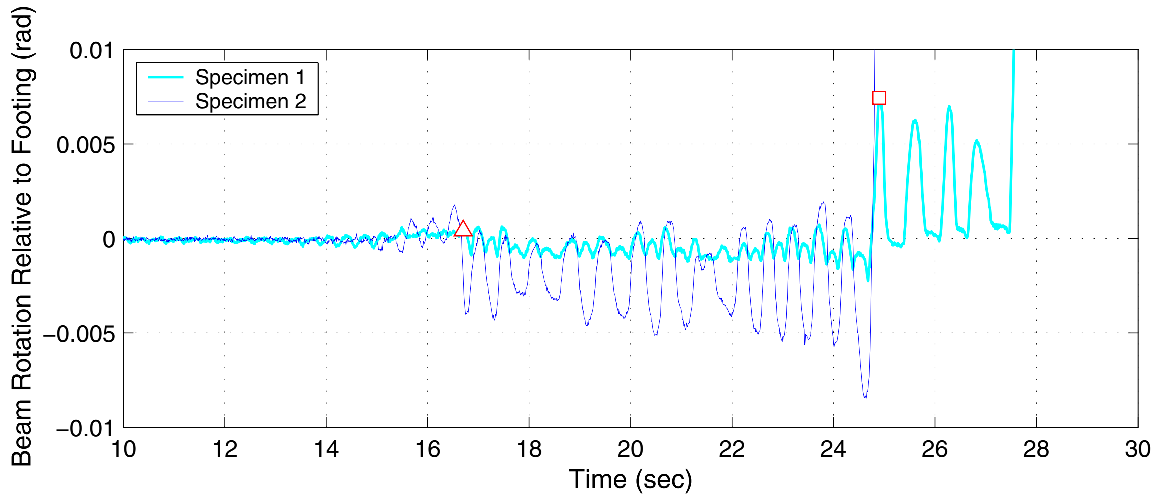

Figure 6-28. Beam rotation relative to footing

The beam rotations at the center column relative to the footing, calculated from the column instruments, are shown in Figure 6-28. Note that the sudden increase in rotations immediately before the square marker for Specimen 1, and at the triangular marker for Specimen 2, coincide with the initial drop in the center column lateral strength for both specimens and the opening of shear cracks at the top of the center column. Since the rotation of the footing was not instrumented, it is not known whether the rotations shown in Figure 6-28 are due to rotation of the footing or rotation of the beam. However, data presented in Figures 6-29 and 6-30 can be used to assess the assumptions of no rotation of the footing or no rotation of the beam.

Figures 6-29(a) and 6-30(a) compare the longitudinal displacements of the center column based on the global instruments (same as that shown in Figure 6-5), with those based on the column instruments assuming there is negligible footing rotation. Similarly, Figures 6-29(b) and 6-30(b) compare the longitudinal displacements based on the global instruments, with those based on the column instruments assuming there is negligible beam rotation. (Refer to Section B.6 for a description of how the data from the column instruments were used to calculate the longitudinal displacements for the two assumptions.) Figures 6-29 and 6-30 show close agreement between the results until t = 27.65 seconds for Specimen 1 and t = 24.90 seconds for Specimen 2, at which point the data from the center column instruments are no longer usable due to severe damage to the column.

The absolute value of errors between the global instrument readings and the column instrument readings at the peaks in the response history are shown in Figures 6-29(c) and 6-30(c). Errors

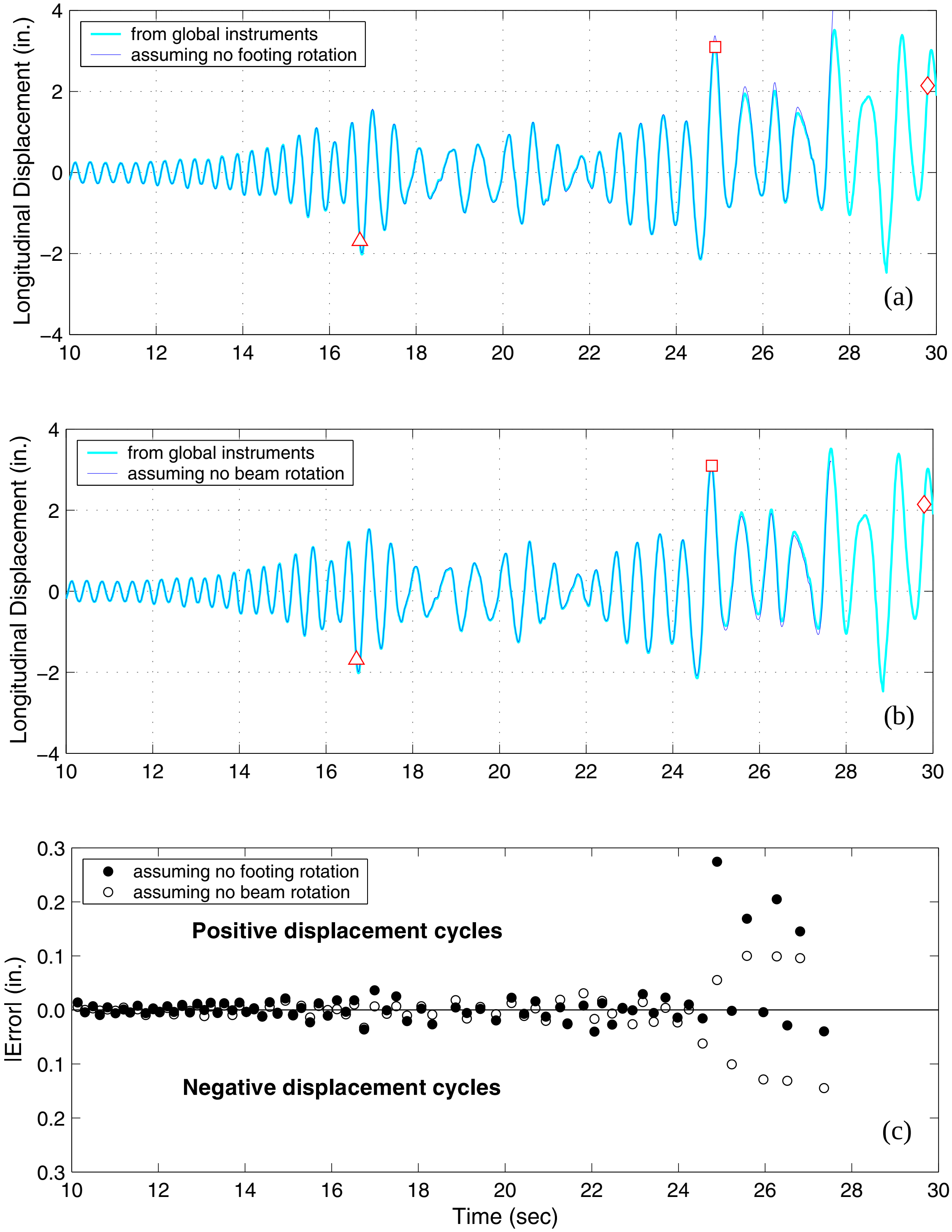

Figure 6-29. Comparison of longitudinal displacements for Specimen 1 measured by global instruments and those calculated from column instruments. In plot (c), points above the line are for positive displacement cycles and points below the line are for negative displacement cycles.

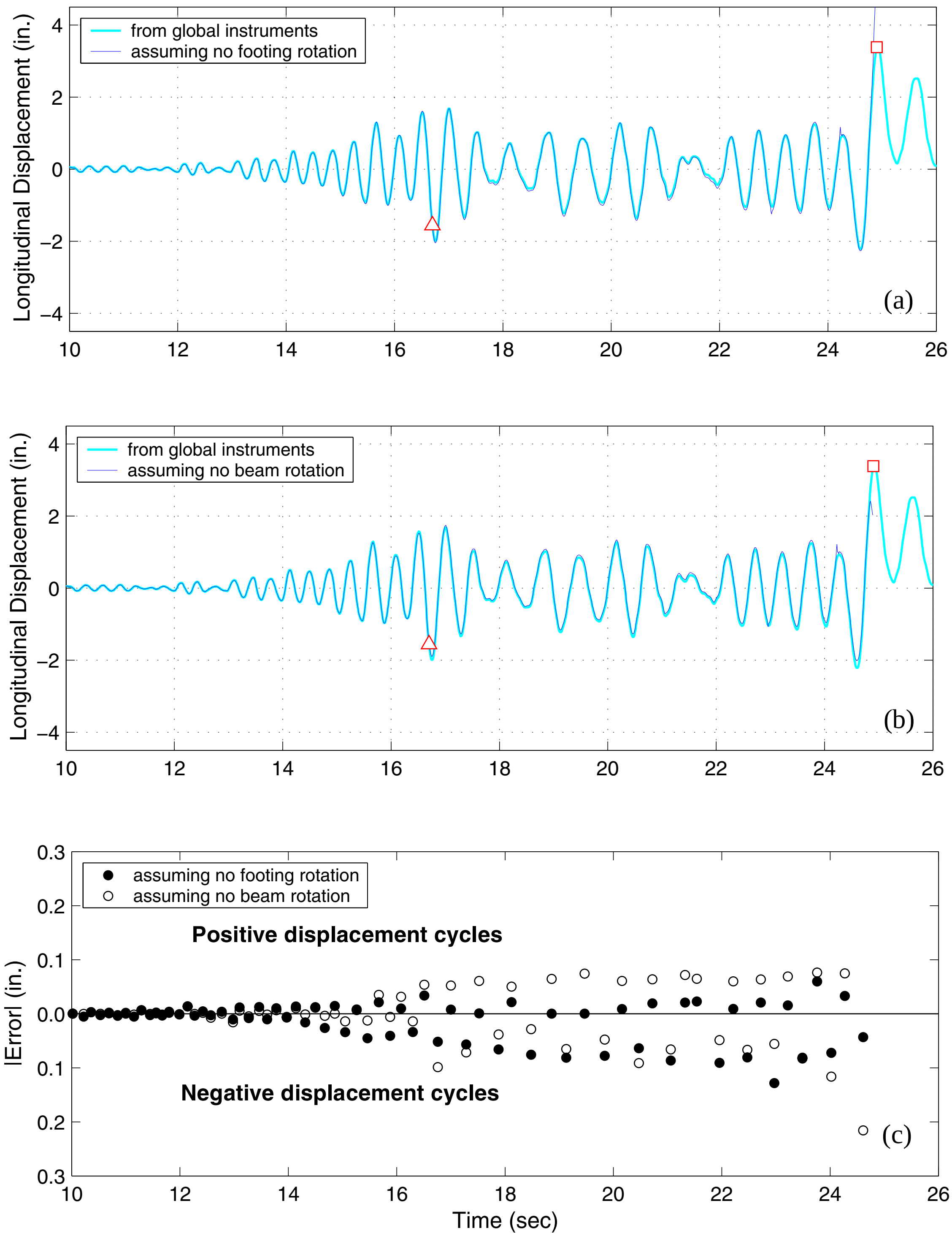

Figure 6-30. Comparison of longitudinal displacements for Specimen 2 measured by global instruments and those calculated from column instruments. In plot (c), points above the line are for positive displacement cycles and points below the line are for negative displacement cycles.

from the peaks in positive displacement cycles are shown above the center line, and errors from peaks in negative displacement cycles are shown below the center line. Considering the extent of cracking experienced by the center column, and vibration of the instrumentation due to the dynamic nature of the test, the minor differences in the readings are likely due to instrumentation error.

If, however, the column instrument readings are assumed to be correct, then Figures 6-29(c) and 6-30(c) can be used to evaluate the influence of footing or beam rotations. If the assumption that there is negligible footing rotation is valid, then the solid circles should plot along the center line, and similarly, if the assumption that there is negligible beam rotation is valid, then the open circles should plot along the center line. Both open and closed circles plotted along the center line suggests that the center column acts as an ideal fixed-fixed column. Figure 6-29(c) suggests that the Specimen 1 center column can be considered as fixed-fixed with negligible beam and footing rotation until t = 24 seconds. After this point, the footing rotations appear to remain negligible for the negative displacement cycles. The errors for all other cases grow after t = 24 seconds, suggesting that the beam rotations may affect the column behavior during negative cycles, and both the beam and footing rotations may influence the response during positive cycles. For the Specimen 2 center column, Figure 6-30(c) indicates that the errors begin to grow earlier in the response history (at approximately t = 15 sec), apparently due to the earlier formation of shear cracks in the center column. For negative displacement cycles after t = 15 seconds, both the beam and footing appear to experience some rotation. For positive displacement cycles, the footing appears to experience limited rotation, while the beam rotations may influence the behavior of the center column.

The center column longitudinal displacements can be separated into deformations that occur within each of the three panels of the column instrumentation frame (i.e., within the bottom 8 in., the middle 42 in., and the top 8 in. of the center column). The longitudinal displacements resulting from these panel deformations are plotted in Figure 6-31 for Specimen 1 and Figure 6-32 for Specimen 2. The panel drift ratios (defined as the longitudinal displacement in the panel divided by the panel height) are shown for four selected times in Figures 6-31 and 6-32. A concentration of deformations within the top panel is clearly seen for positive displacement cycles for both specimens. For Specimen 2, the deformations in the top panel begin earlier in the response history compared with Specimen 1 due to the earlier formation of significant shear cracks observed at the top of the center column. Both specimens show larger middle panel drift ratios for negative displace-

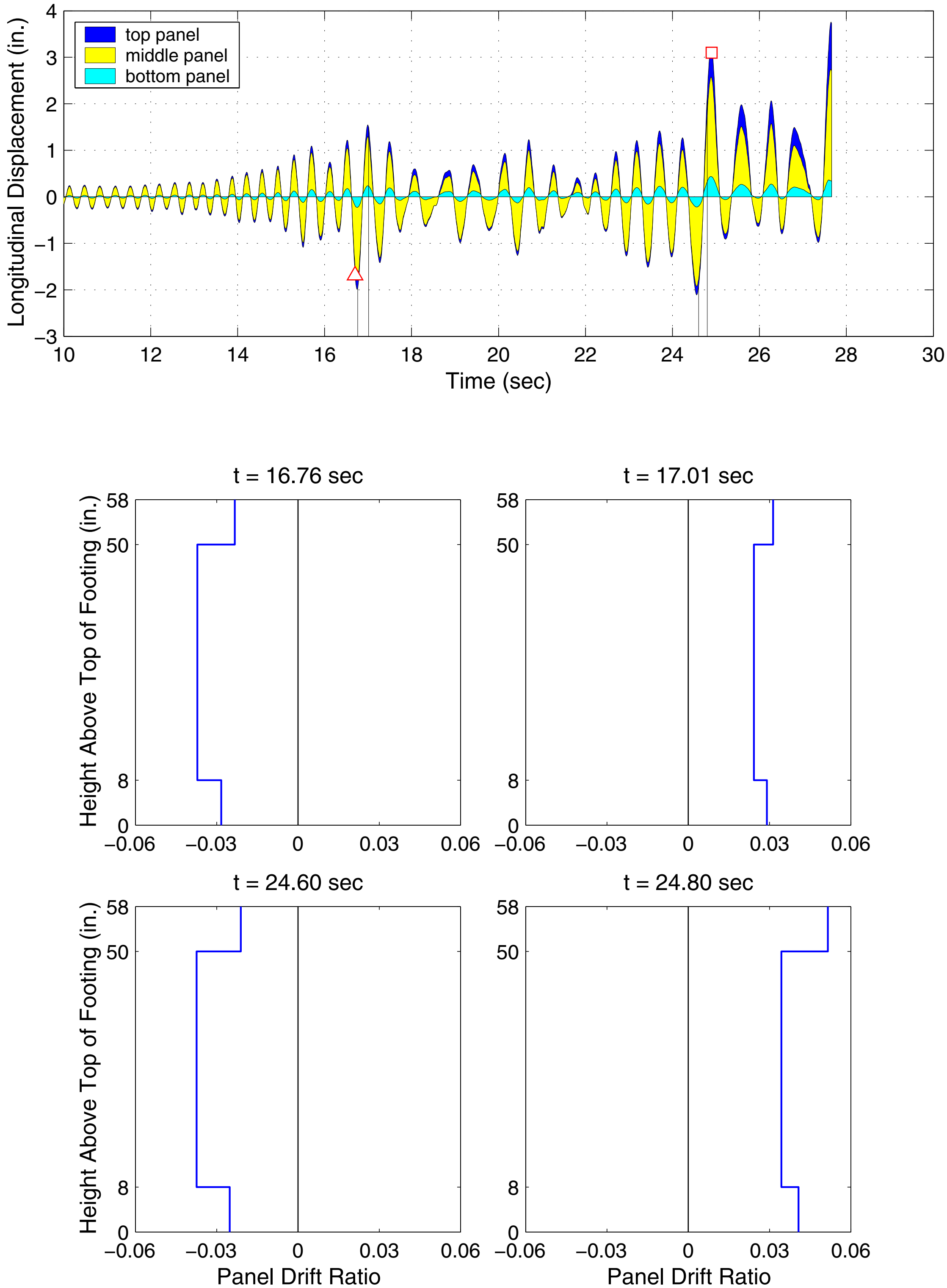

Figure 6-31. Specimen 1 longitudinal displacements for each center column instrumentation panel and panel drift ratios at four selected times

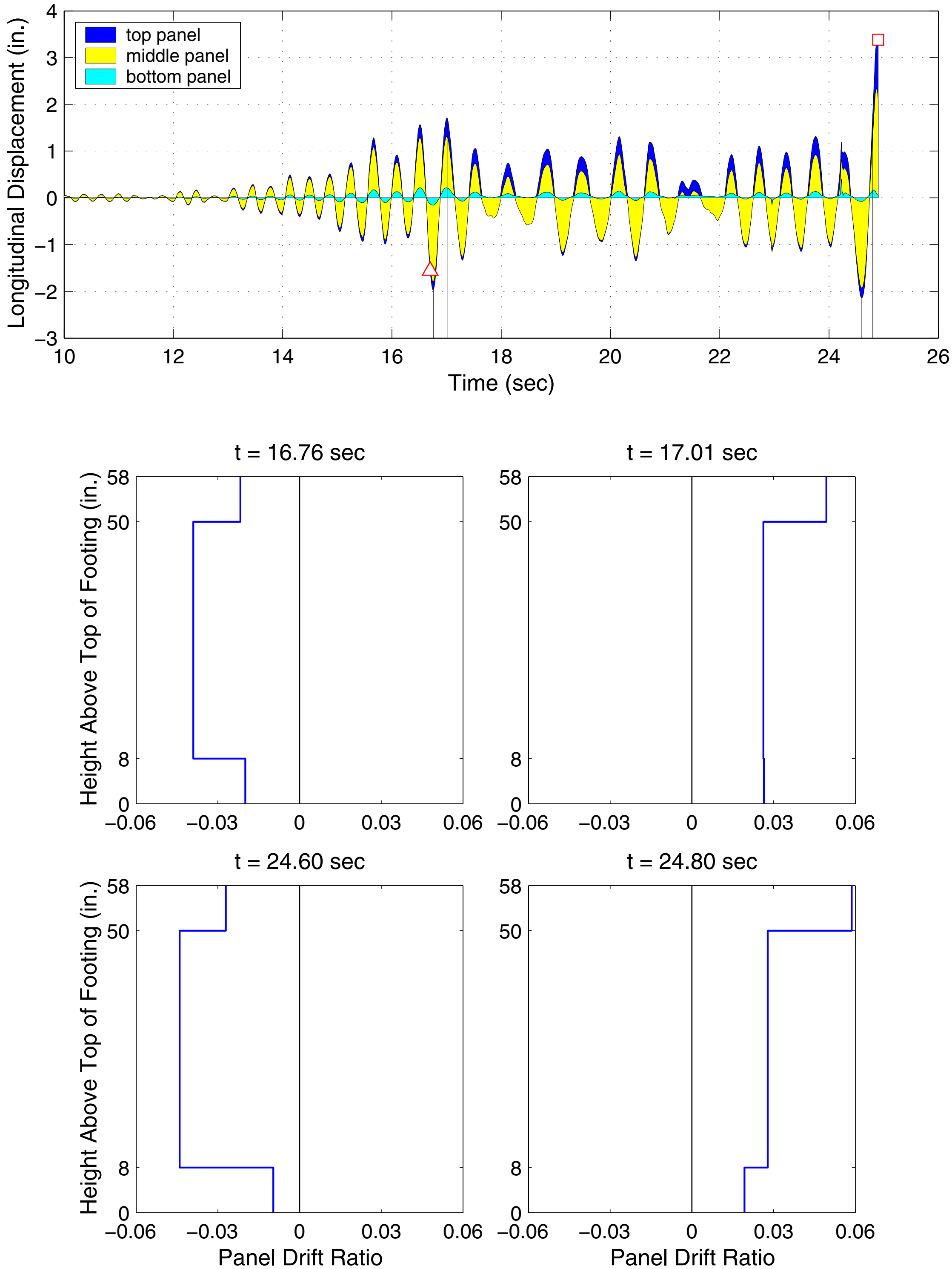

Figure 6-32. Specimen 2 longitudinal displacements for each center column instrumentation panel and panel drift ratios at four selected times

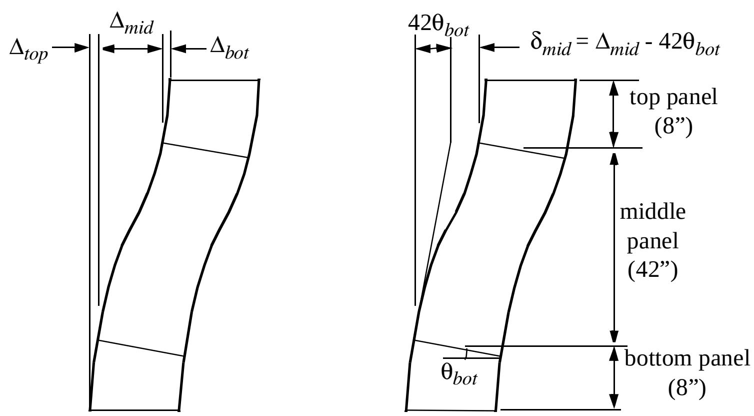

Definition of displacements used in Figures 6-31 and 6-32.

Definition of middle panel deformations used in Figures 6-34 and 6-35.

Figure 6-33. Removal of rigid body rotations from middle panel displacements

ment cycles compared with positive displacement cycles. Also, the deformations in the top and bottom panels appear to contribute less to the overall column displacement for negative displacement cycles. This could be attributed to having to overcome permanent deformations due to demands in the positive displacement cycles before contributing to negative displacements.

Figures 6-31 and 6-32 show middle panel drift ratios on the order of 3% to 5%. A significant portion of this drift results from a rigid body rotation of the middle panel due to the rotation at the top of the bottom panel, as shown in Figure 6-33. As a result, the panel drift ratios are not a good indication of the damage to the middle portion of the column, and hence, the distribution of damage over the height of the column. The panel deformations without rigid body rotations are shown in Figures 6-34 and 6-35. The values for the top and bottom panels are the same as those shown in Figures 6-31 and 6-32, since the footing and beam are assumed not to rotate. The deformations for the middle panel, δ_{mid}, are calculated as shown in Figure 6-33. The panel deformation ratios shown in the lower plots of Figures 6-34 and 6-35 are calculated by dividing the deformations shown in the top plot by the panel height. Note that the middle panel deformations could have been defined using the rotation of the top panel instead of the bottom panel, resulting in somewhat different values. For an ideal fixed-fixed column with symmetric yielding at both ends, both definitions would give the same result. Figures 6-34 and 6-35 clearly show that the damage to the middle panel is not as significant as suggested by Figures 6-31 and 6-32. The panel deformation ratios indicate that, for the times shown, the damage to the Specimen 2 center column spreads fur-

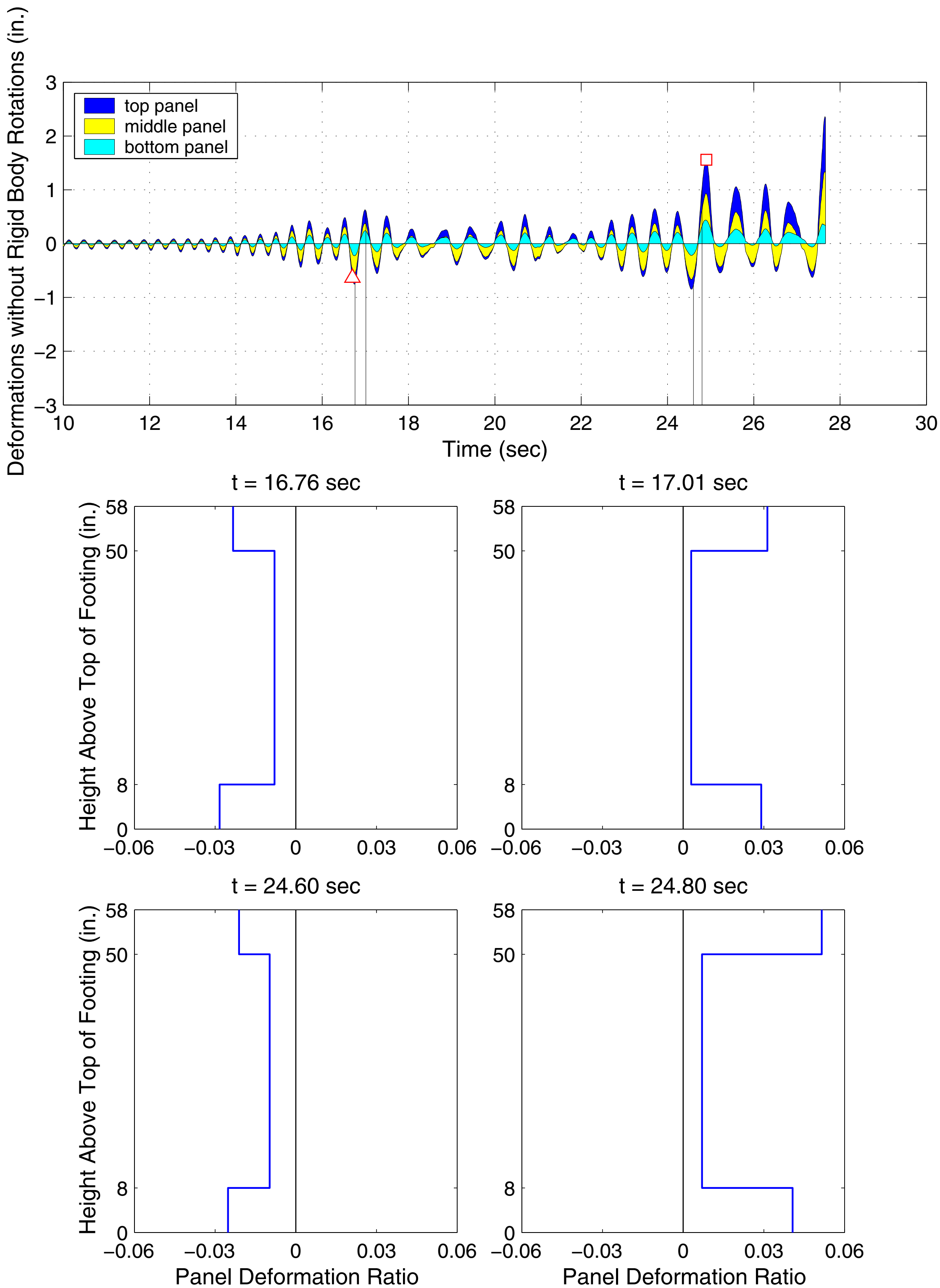

Figure 6-34. Specimen 1 center column deformations for each instrumentation panel and deformations as a fraction of panel height at four selected times

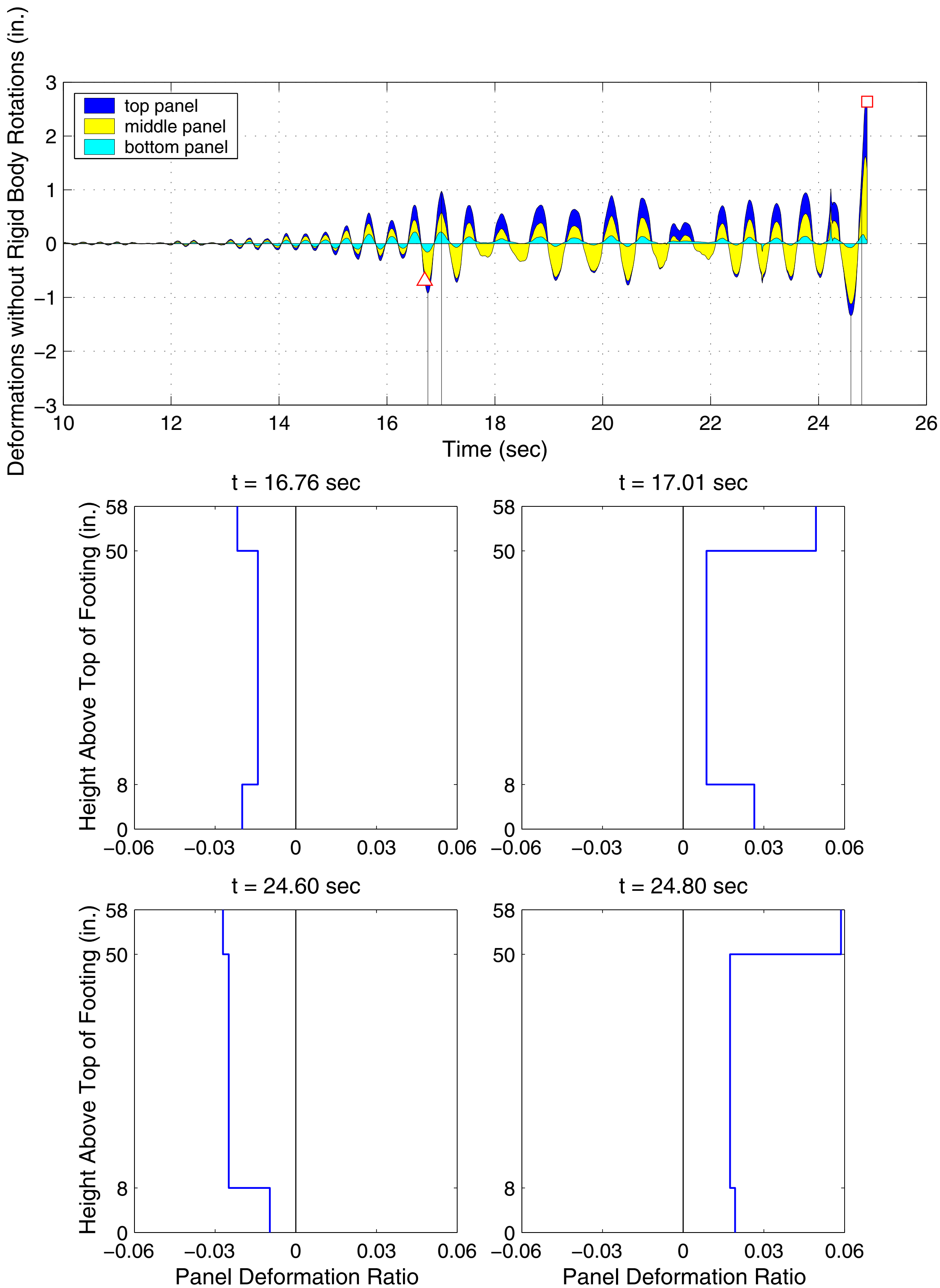

Figure 6-35. Specimen 2 center column deformations for each instrumentation panel and deformations as a fraction of panel height at four selected times

ther into the middle panel than for the Specimen 1 center column. This result is consistent with the extent of cracking observed in Figures 6-11a and 6-11b.

6.3.3 Response of Outside Columns

Figures 6-36 and 6-37 compare the response histories for the west and east columns from both specimens. The column shears and moments begin with an initial offset due to the dead load of the beam and lead weights. The initial shears and moments were determined by analysis as described in Section B.6.

Specimens 1 and 2 exhibit very similar shear and moment response. The maximum positive shear resisted by the west column is approximately 5 kips higher than the maximum positive shear resisted by the east column. This difference can be attributed in part to the direction of the initial shears on the outside columns, and in part to the higher yield moment expected in the west column during cycles in the positive direction (i.e., toward the west) causing increased axial compression due to overturning forces. The opposite is true for negative shear, or cycles in the negative direction.

During axial failure of the Specimen 2 center column (i.e., between the square and diamond markers), the axial load in the Specimen 2 outside columns increases by approximately 25 kips per column. Before the square marker (at 24.9 sec) the axial load response of the east and west columns appears quite similar. After the square marker, the transient axial load variations in the east column are dramatically reduced. This reduction can be observed in both Specimens 1 and 2 (although occurring closer to the diamond marker for the Specimen 1 east column). Comparing the axial load response in Figures 6-14 and 6-37, it can be observed that the transient axial load variations in the center column increase at the same time the decrease is observed for the east column. The shift in the transient axial load variations also coincides with a positive offset in the longitudinal displacements (i.e., displacement to the west). The period of the axial load oscillations approximately matches the period of the shear oscillations. Note that the axial couple resulting from the overturning effect appears to shift from the west and east columns to the west and center columns. Owing to the reduction in moment arm, the magnitude of the axial oscillations must increase to maintain the same overturning moment. The transient axial load redistribution from the center column to the outside columns is believed to result from bending of the beam as the outside columns lengthen

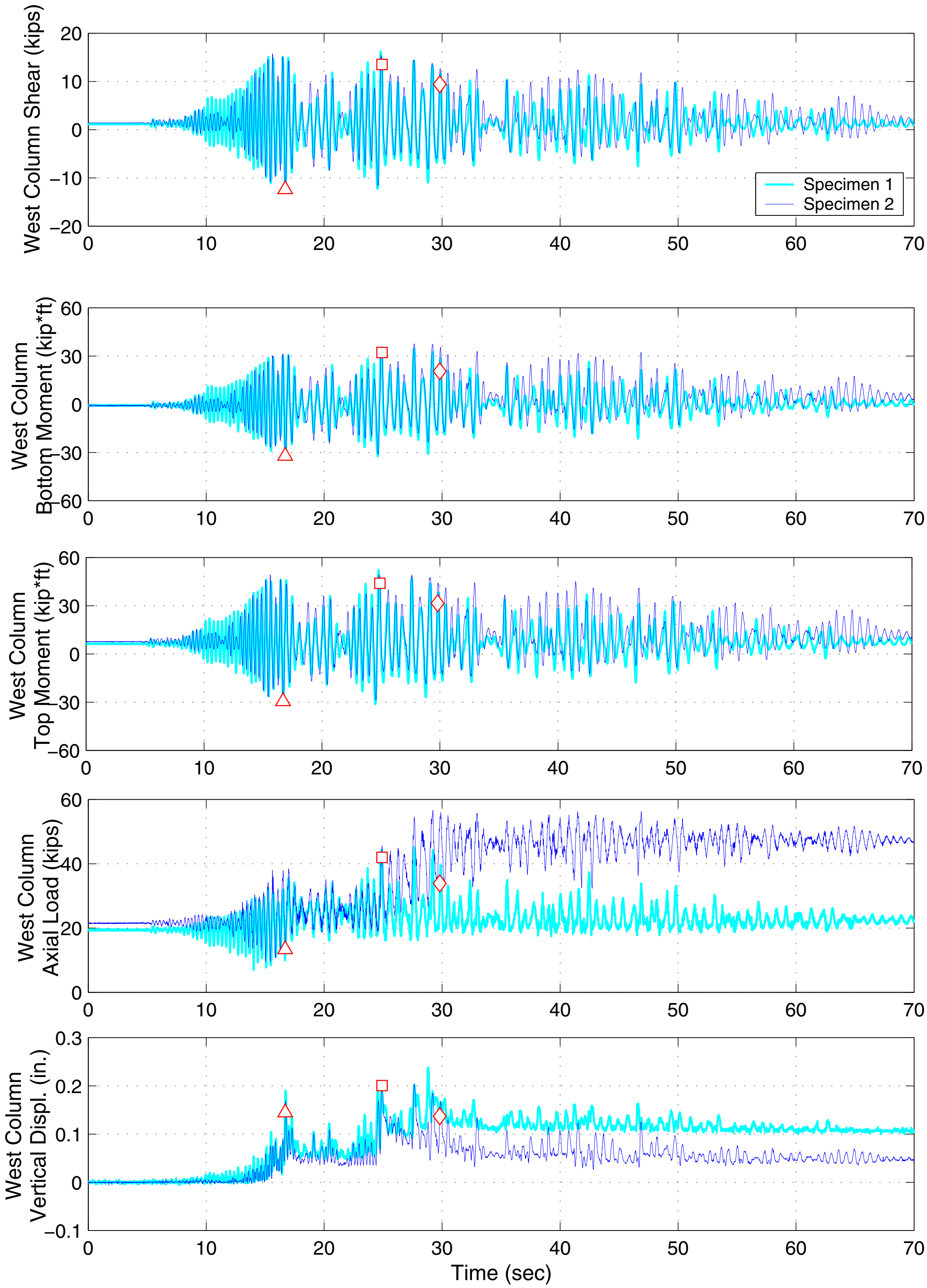

Figure 6-36. West column response histories

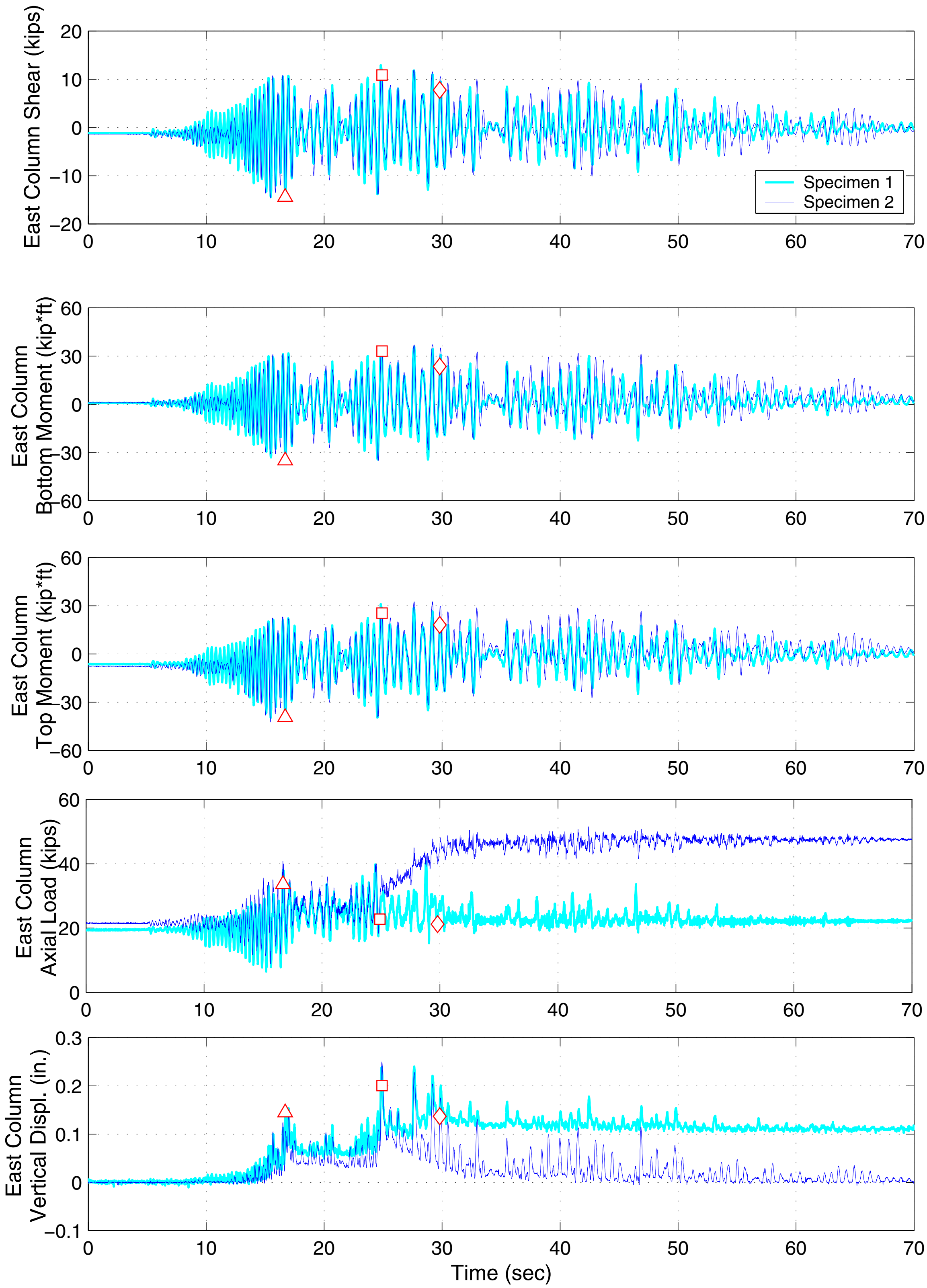

Figure 6-37. East column response histories

during horizontal displacement cycles and the center column shortens due to significant damage to the core concrete (see Section 6.3.4.2 for further discussion).

Both outside columns for Specimens 1 and 2 begin to lengthen at approximately 15 seconds due to opening of flexural cracks upon yielding of the longitudinal reinforcement. This time coincides with the initial redistribution of axial load from the center column (see Figure 6-14). The Specimen 2 outside columns begin to shorten upon increase in the outside column axial load with axial failure of the center column. The Specimen 2 east column returns to its original length, while the west column appears to be 0.05 inches longer at the end of the ground motion. The Specimen 1 outside columns do not see any significant redistribution of gravity loads, and therefore do not shorten upon further damage of the center column.

The shear hystereses of the outside columns for Specimens 1 and 2 are shown in Figures 6-38 through 6-41. The horizontal displacement used in these plots is the same as that shown in Figure 6-5 (i.e., the displacement at the top of the center column corrected for large displacements). Comparison of these data with displacements measured at the end of the beam shows a maximum difference of approximately 0.15 inches after the axial failure of the Specimen 2 center column and yielding of the beam.

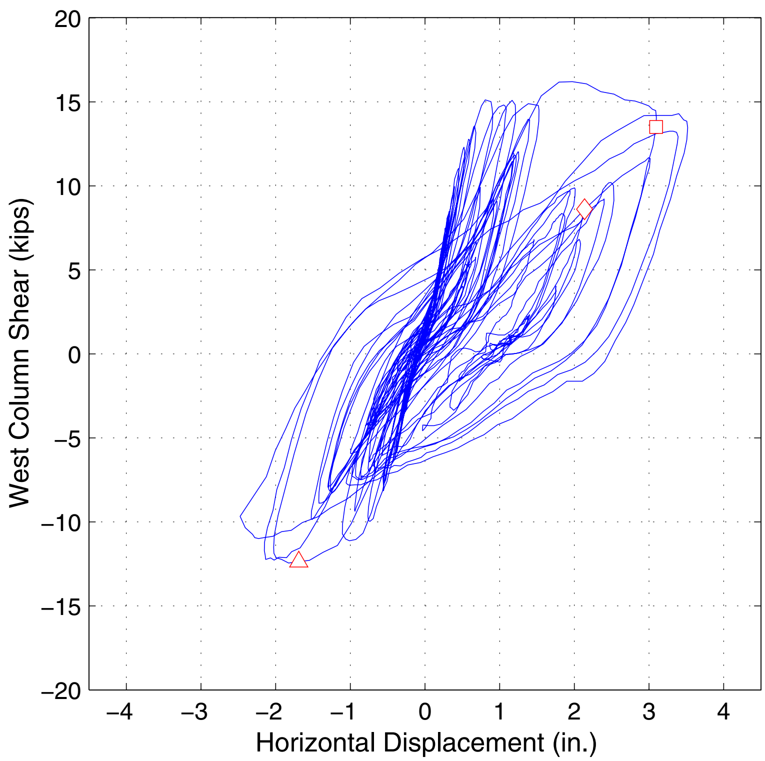

Figure 6-38. Specimen 1 west column shear hysteretic response

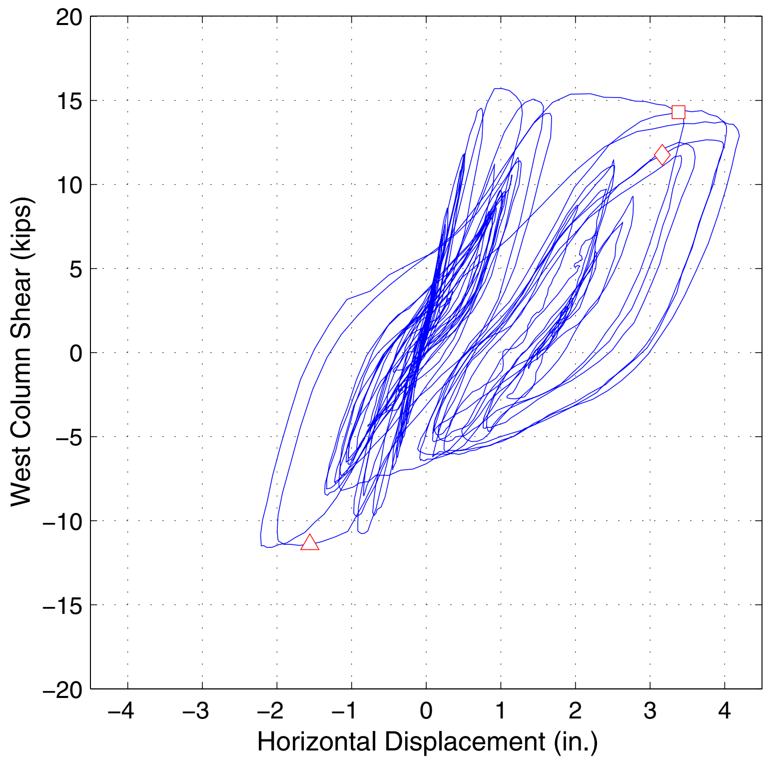

Figure 6-39. Specimen 2 west column shear hysteretic response

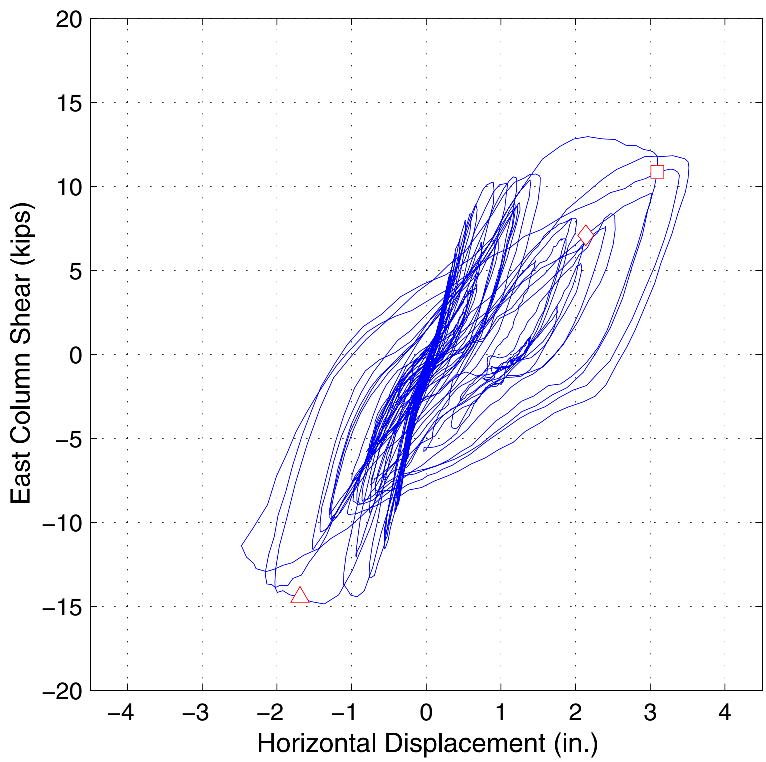

Figure 6-40. Specimen 1 east column shear hysteretic response

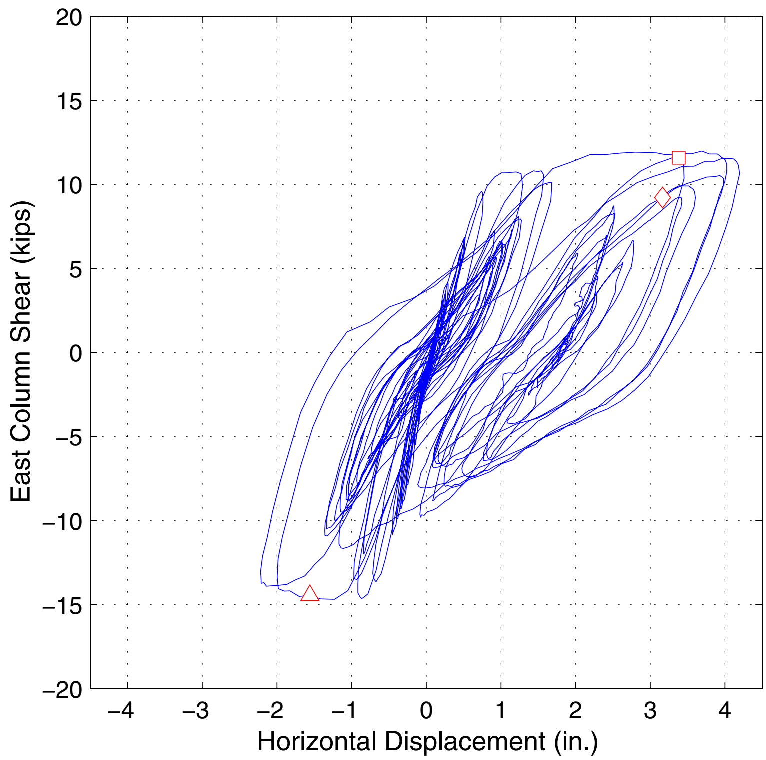

Figure 6-41. Specimen 2 east column shear hysteretic response

The outside column shear hystereses for Specimen 1 in Figures 6-38 and 6-40 show a bulge in the shear capacity just before the square marker. Based on work by Malvar (1998), the high strain rate (approximately 0.2 sec^{-1}) at the time of the observed bulge could result in a 10% to 20% increase in the yield strength of the reinforcement; and therefore a similar increase in the yield strength of the column section. However, since the velocities of the two specimens are similar, this explanation would suggest that a similar bulge should have been observed in Figures 6-39 and 6-41 for Specimen 2. Although no conclusive explanation has been determined based on the available data, the bulge could result from slight rotations at the top of the outside columns due to higher mode effects.

Idealized backbones to the shear hysteresis for each column are shown in Figures 6-42 through 6-45. The backbones are developed using a procedure similar to that described in Section 6.3.2 for the center column, except that the first line segments begin at a shear equal to the initial shear force found from analysis (Figures 6-36 and 6-37) instead of at the origin. The degrading strength line segment shown for the center column does not appear in Figures 6-42 through 6-45, since no significant strength degradation was observed for the outside columns. The star markers on Figures 6-42 through 6-45 indicate the shear and displacement at first yield of the outermost longitudinal reinforcement based on the strain gage data.

The slope of the first line segment of the idealized backbone provides an effective elastic stiffness for the column. The outside columns exhibit roughly a 25% stiffer loading response during quarter cycles in which the axial load increases due to overturning forces, compared with quarter cycles in which the axial load decreases.

Figures 6-46 through 6-49 show the outside column moment hysteretic response for Specimens 1 and 2. The top and bottom column moments were calculated, accounting for second-order effects, according to the procedures described in Section B.6. Similar to the results for the center column, for positive displacement cycles the yield strength at the top of the west column appears to be 50% higher than the yield strength at the bottom of the column. In contrast, the yield strengths at the tops and bottoms of the columns appear similar for the west columns in negative displacement cycles, and for the east columns in either direction. The discrepancy in the yield strength is believed to be due to errors in the force transducer output (see Section B.6).

6.3.4 Load Redistribution

Two forms of load redistribution observed during the shear-failure tests will be discussed in this section: redistribution during shear failure of the center column, and redistribution during axial failure of the center column (Specimen 2 only).

6.3.4.1 Redistribution during Shear Failure

Shear failure reduces the capacity of a column to resist lateral loads. If the lateral load applied to a building frame remains constant during shear failure of a single column, the lateral load initially resisted by the failing column must be redistributed to neighboring elements. However, the equivalent lateral loads resulting from ground motion are caused by the dynamic response of the structure, and hence are not constant. The magnitude and direction of the loads change with time due to variations in the ground motion input and changes in the characteristics of the structure (e.g., lengthening of the fundamental period with increasing damage). Furthermore, formation of a plastic mechanism due to ductile yielding of elements can limit the maximum lateral load resisted by the structure and individual elements. For the three-column frames tested, shear failure of the

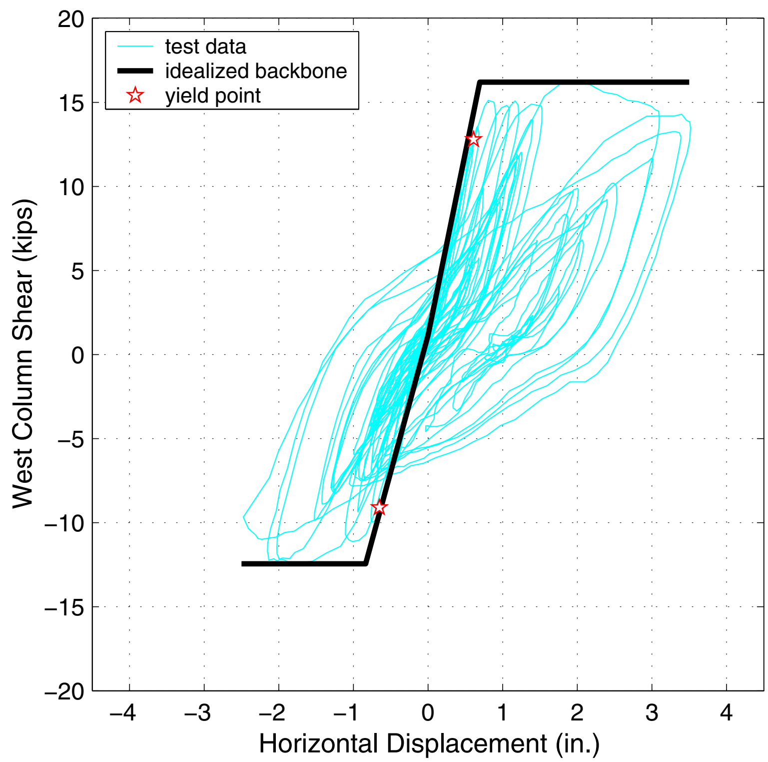

Figure 6-42. Specimen 1 west column hysteresis with idealized backbone

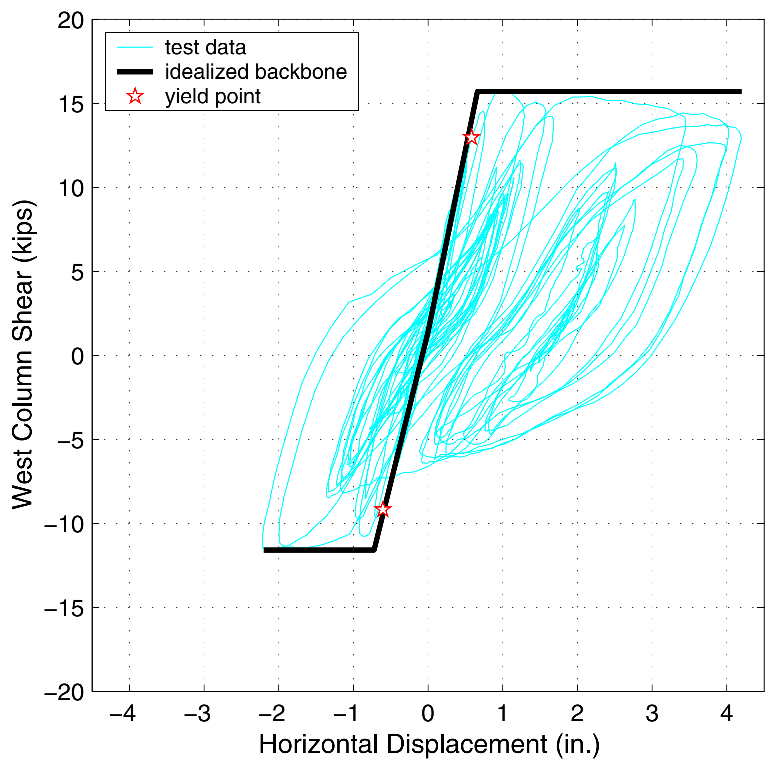

Figure 6-43. Specimen 2 west column hysteresis with idealized backbone

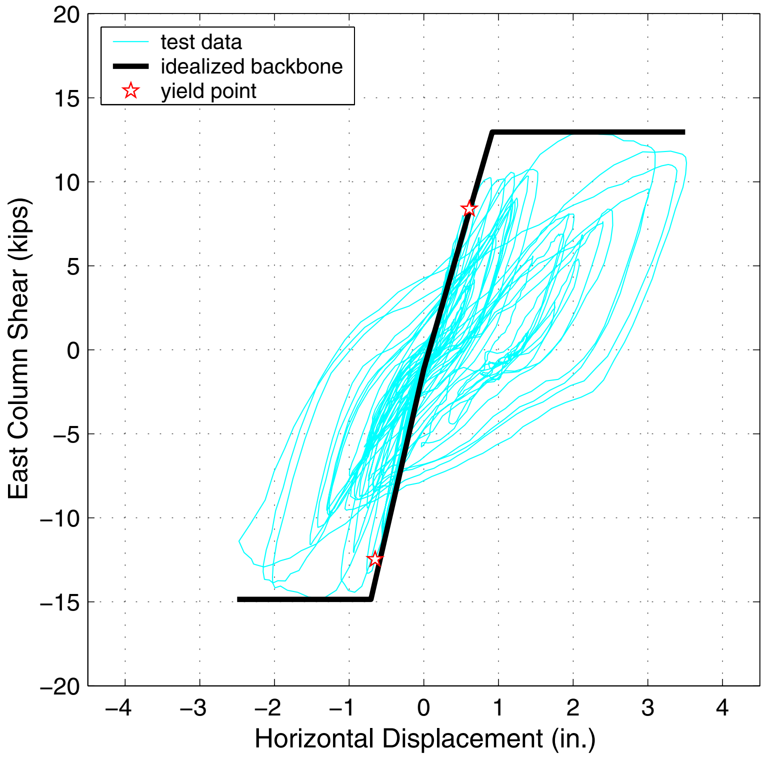

Figure 6-44. Specimen 1 east column hysteresis with idealized backbone

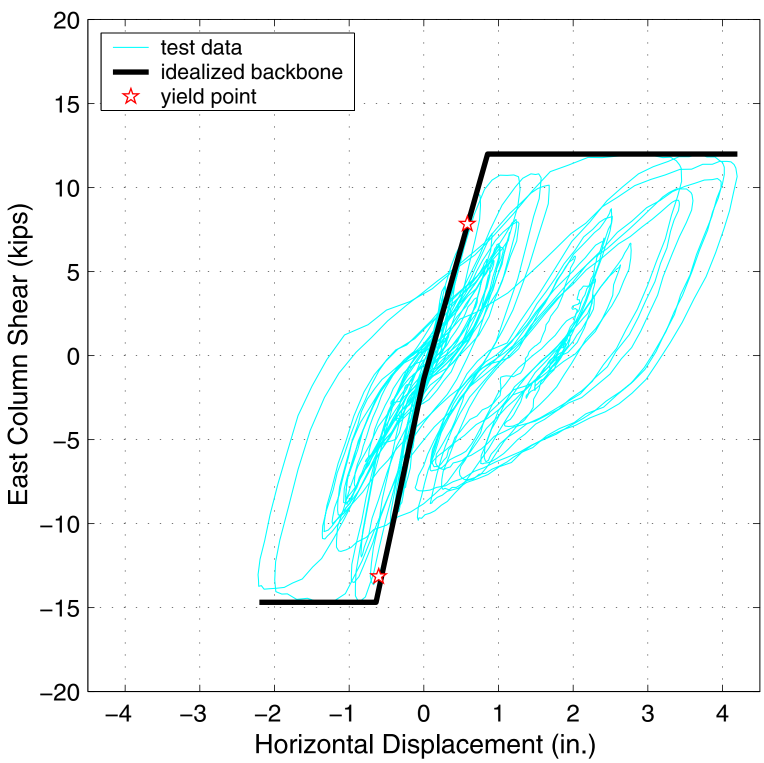

Figure 6-45. Specimen 2 east column hysteresis with idealized backbone

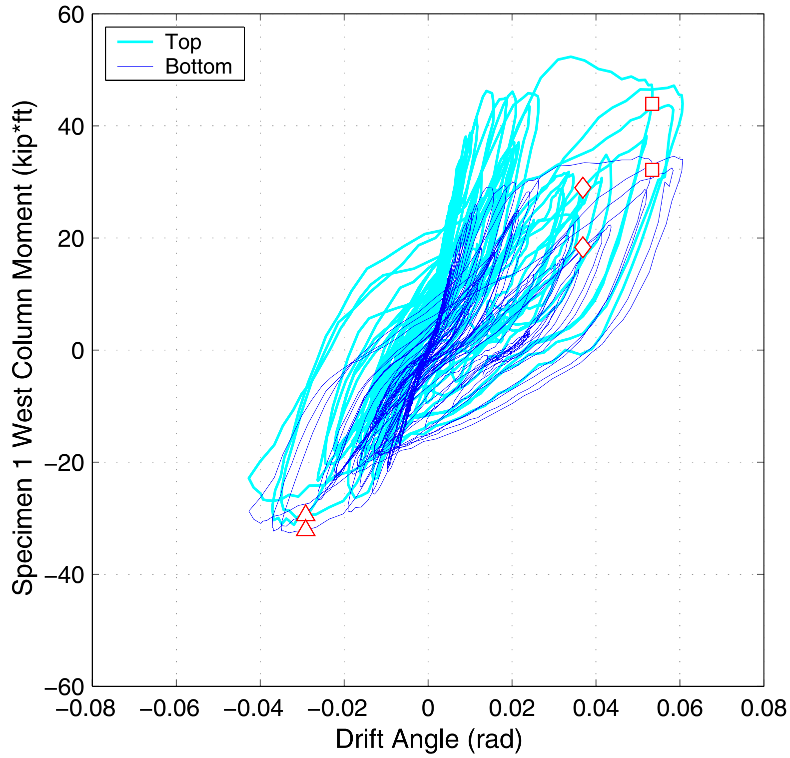

Figure 6-46. Specimen 1 west column moment hysteretic response

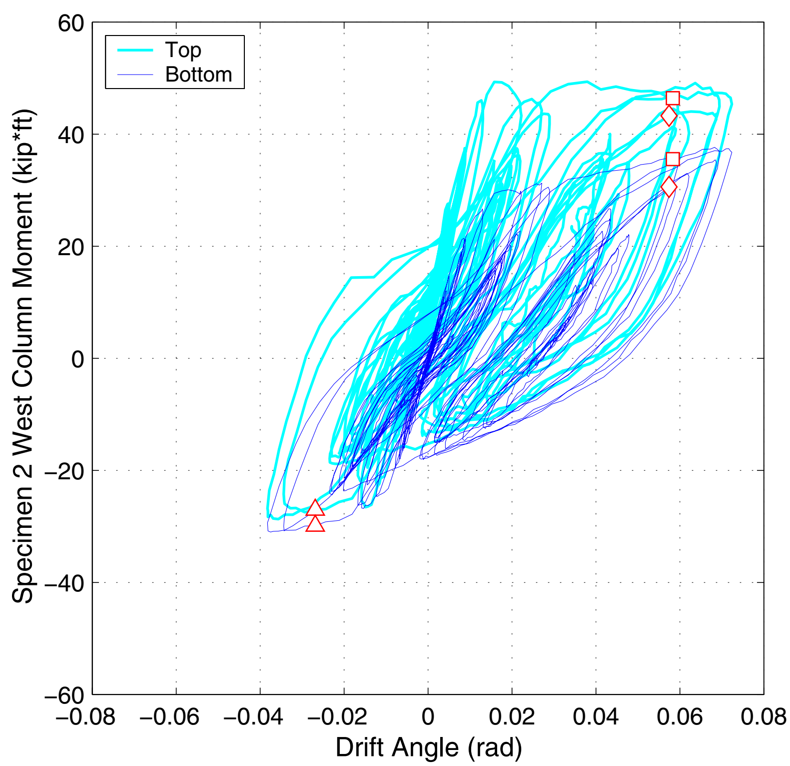

Figure 6-47. Specimen 2 west column moment hysteretic response

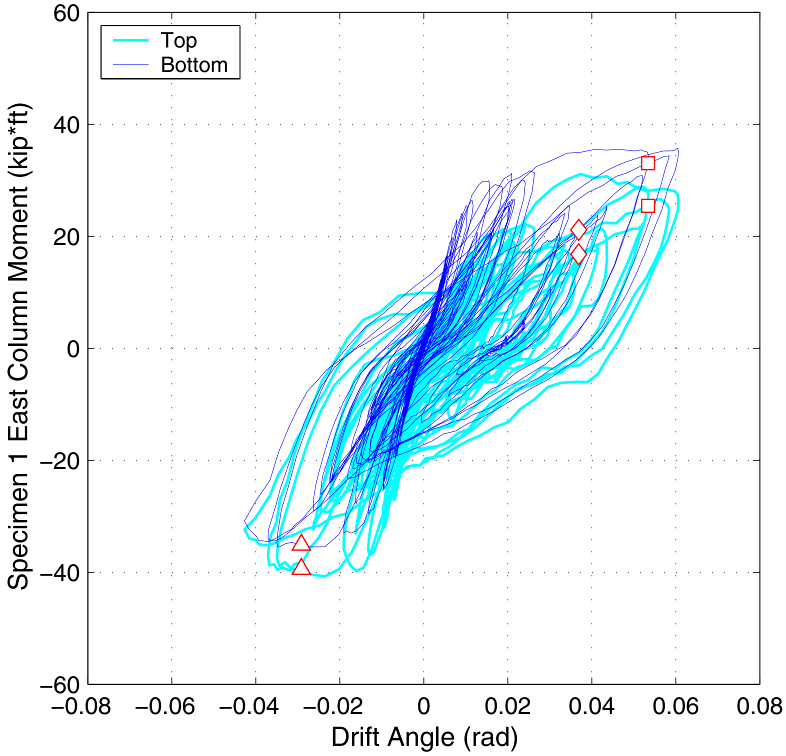

Figure 6-48. Specimen 1 east column moment hysteretic response

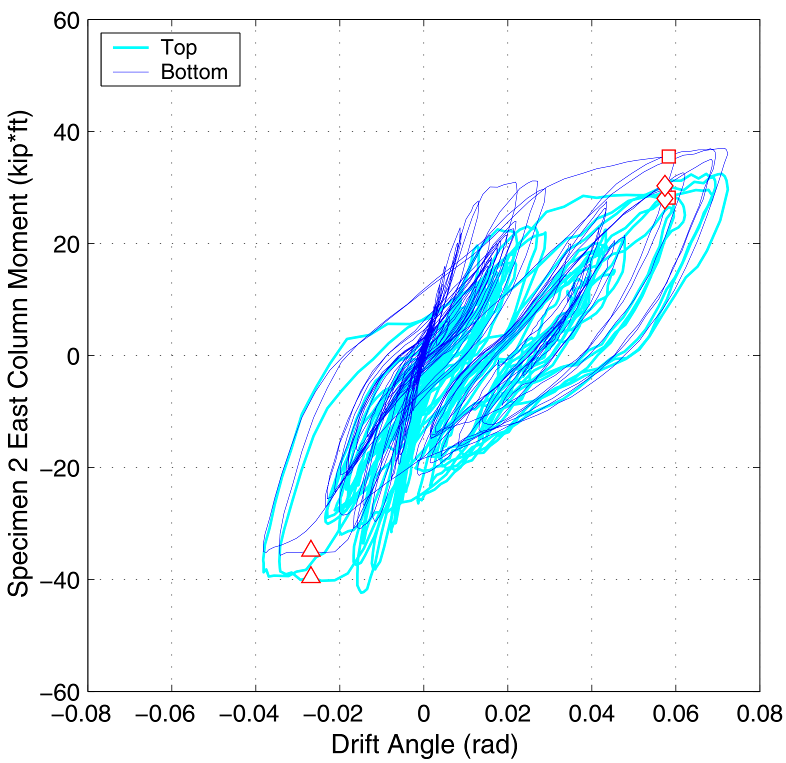

Figure 6-49. Specimen 2 east column moment hysteretic response

center column increases the fundamental period, thereby changing the equivalent lateral load demands. In addition, flexural yielding of the outside columns before shear failure of the center column limits any increase in the lateral load resisted by the outside columns after shear failure of the center column. For these reasons, lateral load redistribution during shear failure did not result in a significant increase in lateral demands on the outside columns. Figures 6-50 through 6-52 illustrate how the lateral loads were distributed before, during, and after shear failure of the center column.

Figure 6-50 shows the fraction of the total base shear resisted by the center column at peaks in the base shear response history. The solid circles represent the fraction of base shear resisted by the center column during positive displacement cycles (i.e., the direction of shear failure for both specimens), and the hollow circles represent the fraction of base shear resisted by the center column during negative displacement cycles. Consistent with the lower stiffness observed in the response of the Specimen 1 center column, this column initially resists a smaller fraction of the total base shear than the Specimen 2 center column. The fraction of the base shear resisted by the center column for Specimen 1 remains nearly constant until the square marker at 24.9 seconds. In contrast, for Specimen 2 redistribution of the base shear can be observed even before the start of significant ground motion at 14 seconds. Immediately following the triangular marker at 16.7 seconds, the fraction of the Specimen 2 base shear resisted by the center column drops by 38%. This coincides with the formation of significant shear cracks in the center column (Figure 6-11b). For positive displacement cycles immediately following the square marker, the fraction of the base shear resisted by the center column drops off to negligible levels within 5.5 seconds for Specimen 1 and 0.5 seconds for Specimen 2. For negative displacement cycles, the fraction of base shear resisted by the Specimen 1 center column drops at approximately the same rate as for positive displacement cycles. The Specimen 2 center column continues to resist approximately 30% of the total base shear for negative displacement cycles after the square and diamond markers. During negative displacement cycles, the upper portion of the failed center column is forced to bear against the lower portion which acts as a cantilever, thereby resisting a portion of the total base shear.

Figures 6-51 and 6-52 show the normalized shear hysteretic response for Specimens 1 and 2 for selected cycles. The hysteresis loops are shown for the center column shear and the sum of the shear resisted by the outside columns. The shear response is normalized by the shear (in either the center or outside columns, depending on the curve) at the star markers which are located just

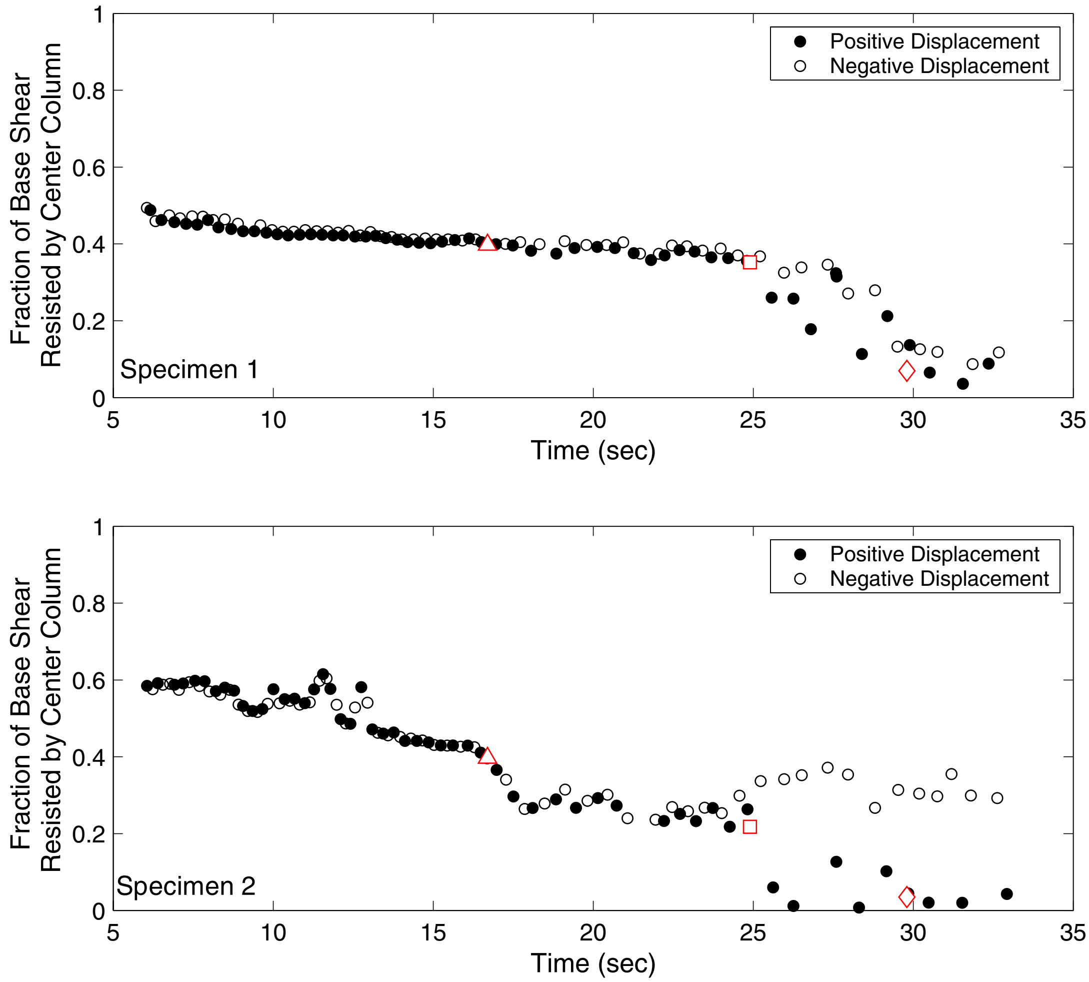

Figure 6-50. Fraction of total base shear resisted by center column

before the first degradation in the center column shear strength. For Specimen 1, Figure 6-51(a) suggests that the shear in the outside columns degrades along with the center column shear immediately after the star marker, but the center column shear drops relative to the outside column shear upon repeated cycles. Figure 6-51(b) shows only a very slight drop in the outside column shear during degradation of the center column shear capacity at the positive peak of the first cycle. In subsequent cycles shown in Figure 6-51(b), the center column shear drops to negligible levels due to degradation of the shear capacity and significantly pinched hysteretic loops. The outside columns maintain stable and wide hysteretic loops during subsequent cycles.

For Specimen 2, Figure 6-52(a) shows no significant difference in the hysteretic response of outside and center columns. With subsequent cycles, shown in Figure 6-52(b), it is clear that the degradation of the center column shear strength has begun. Within two full cycles the normalized

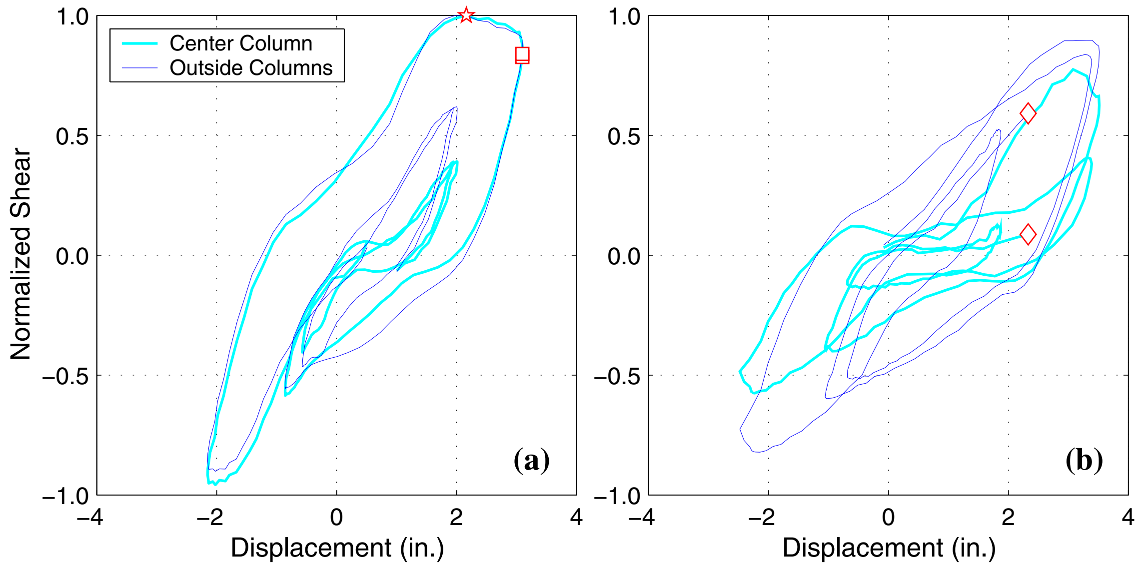

Figure 6-51. Specimen 1 — Shear hysteretic response normalized by shear at star marker. (a) t = 24.33 – 26.38 sec; (b) t = 27.45 – 29.80 sec

shear in the center column is approximately half of the normalized shear in the outside columns. Figures 6-52(c) and 6-52(d) clearly show the shear-strength reduction in the center column relative to the outside columns and the difference in the pinched nature of the hysteretic loops. Note that Figures 6-52(c) and 6-52(d) show the same cycles as those shown for Specimen 1 in Figures 6-51(a) and 6-51(b).

Shear failures and the subsequent degradation in shear capacity are believed to lead to an increase in lateral displacements. If the total shear capacity at a single story-level in a building frame degrades, the inertial forces acting above the damaged story should also decrease. This phenomenon can be observed in the hysteretic loops shown in Figures 6-53 and 6-54; as the base shear capacity of the three-column frame decreases, the inertial force also decreases. The inertial forces retard the motion of the mass, and therefore a decrease in the inertial force should result in an increase in the lateral displacements. Although a control test (without base shear degradation) was not conducted to demonstrate experimentally the influence of the shear failure on the peak displacements, the impact will be demonstrated analytically in Section 8.4.3.

A pulse-type ground motion, resulting in the majority of shear degradation occurring within a single cycle, will likely result in larger displacements than those observed in the shake table tests, since the inertial forces will decrease over a more sustained period of time. Further shake table test-

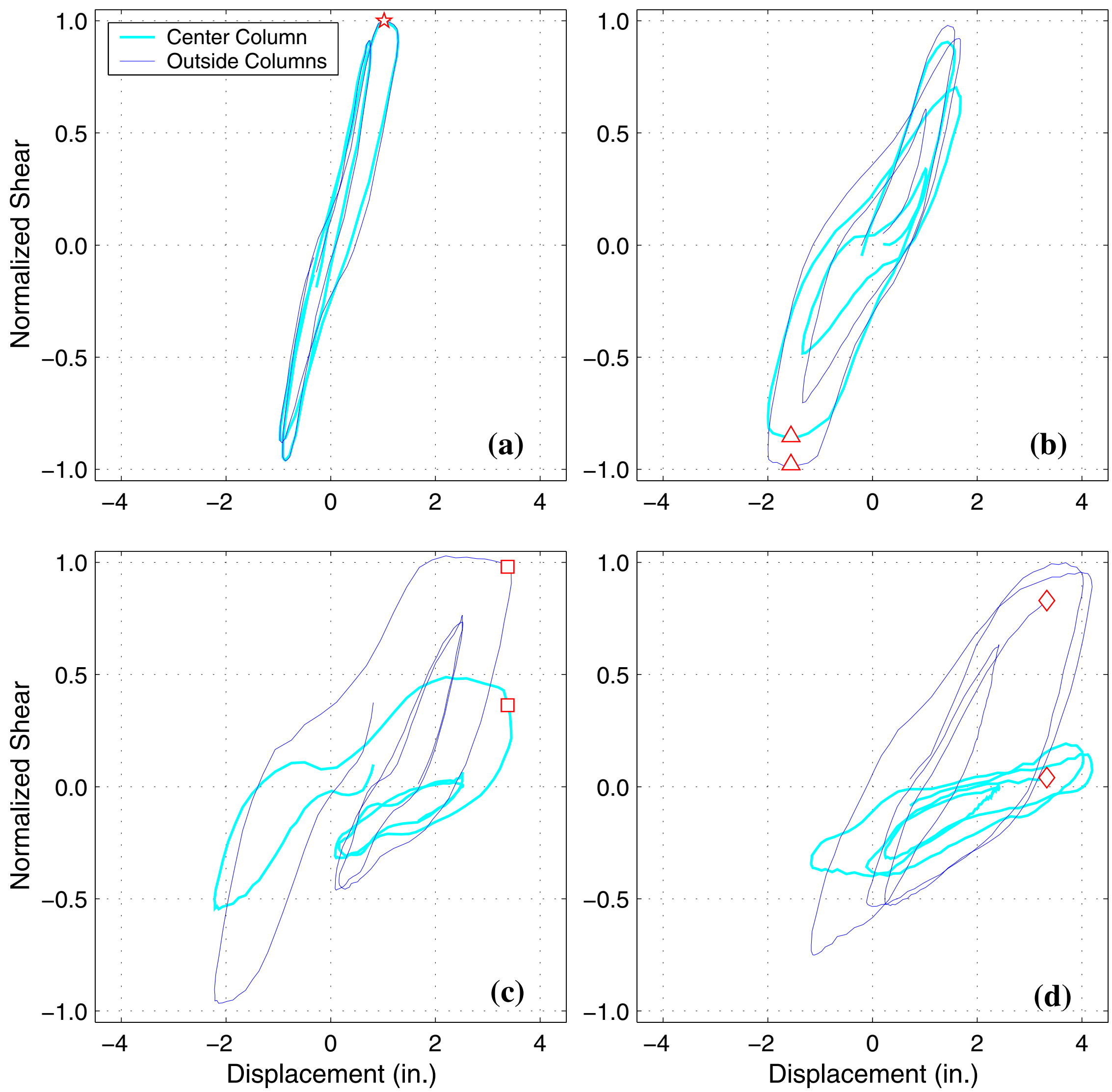

Figure 6-52. Specimen 2 — Shear hysteretic response normalized by shear at star marker. (a) t = 15.12 – 15.96 sec, (b) t = 16.38 – 17.63 sec, (c) t = 24.33 – 26.38 sec, (d) t = 27.45 – 29.80 sec

ing is needed to investigate the influence of the type of ground motion on the response of structures after shear failure.

6.3.4.2 Redistribution during Axial Failure

Unlike seismic loads, gravity loads can never be dissipated through yielding and damage to the structure. In the event of the axial failure of a column, the gravity loads initially supported by the

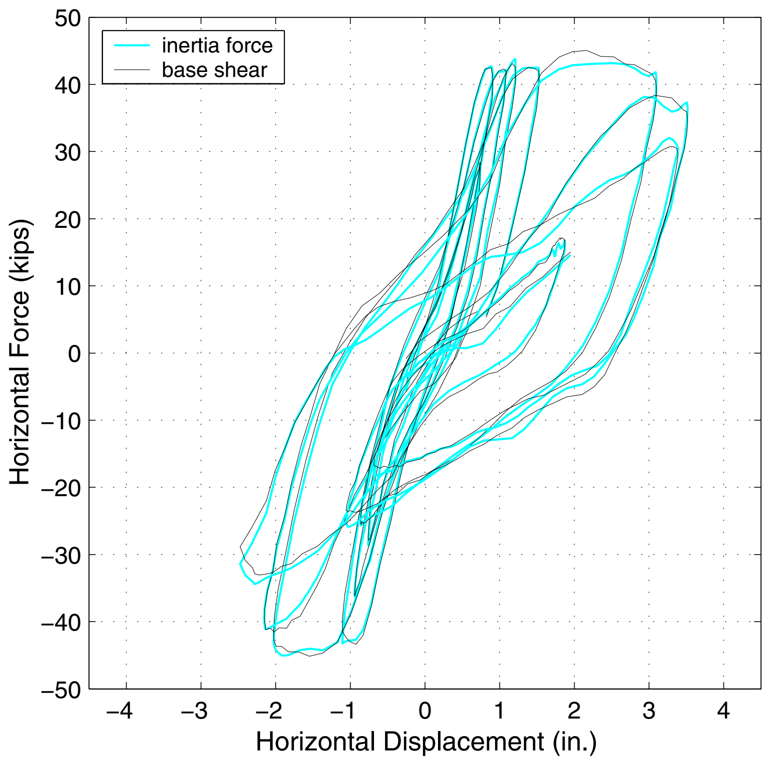

Figure 6-53. Hysteretic response for Specimen 1 (only selected cycles shown)

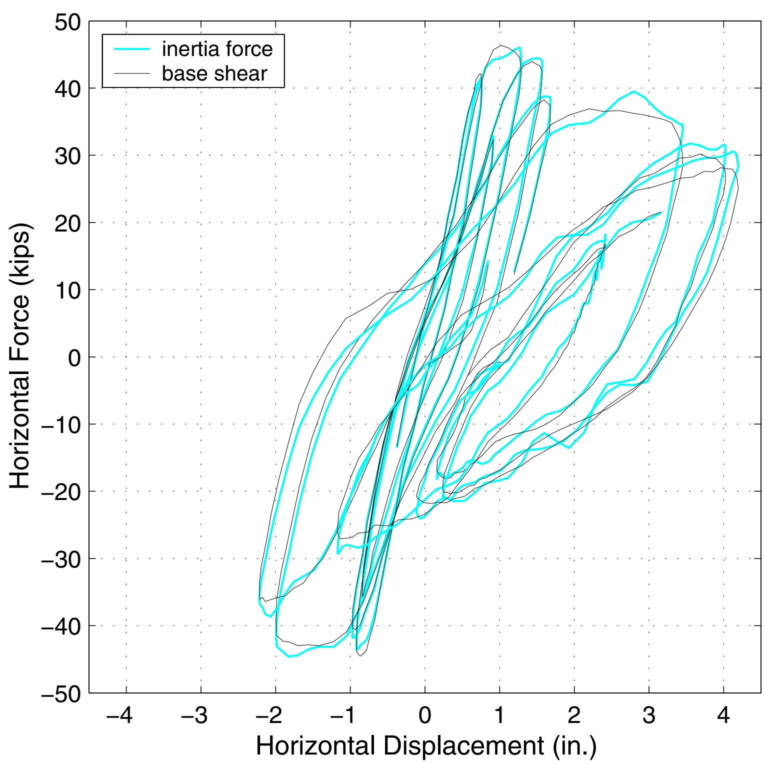

Figure 6-54. Hysteretic response for Specimen 2 (only selected cycles shown)

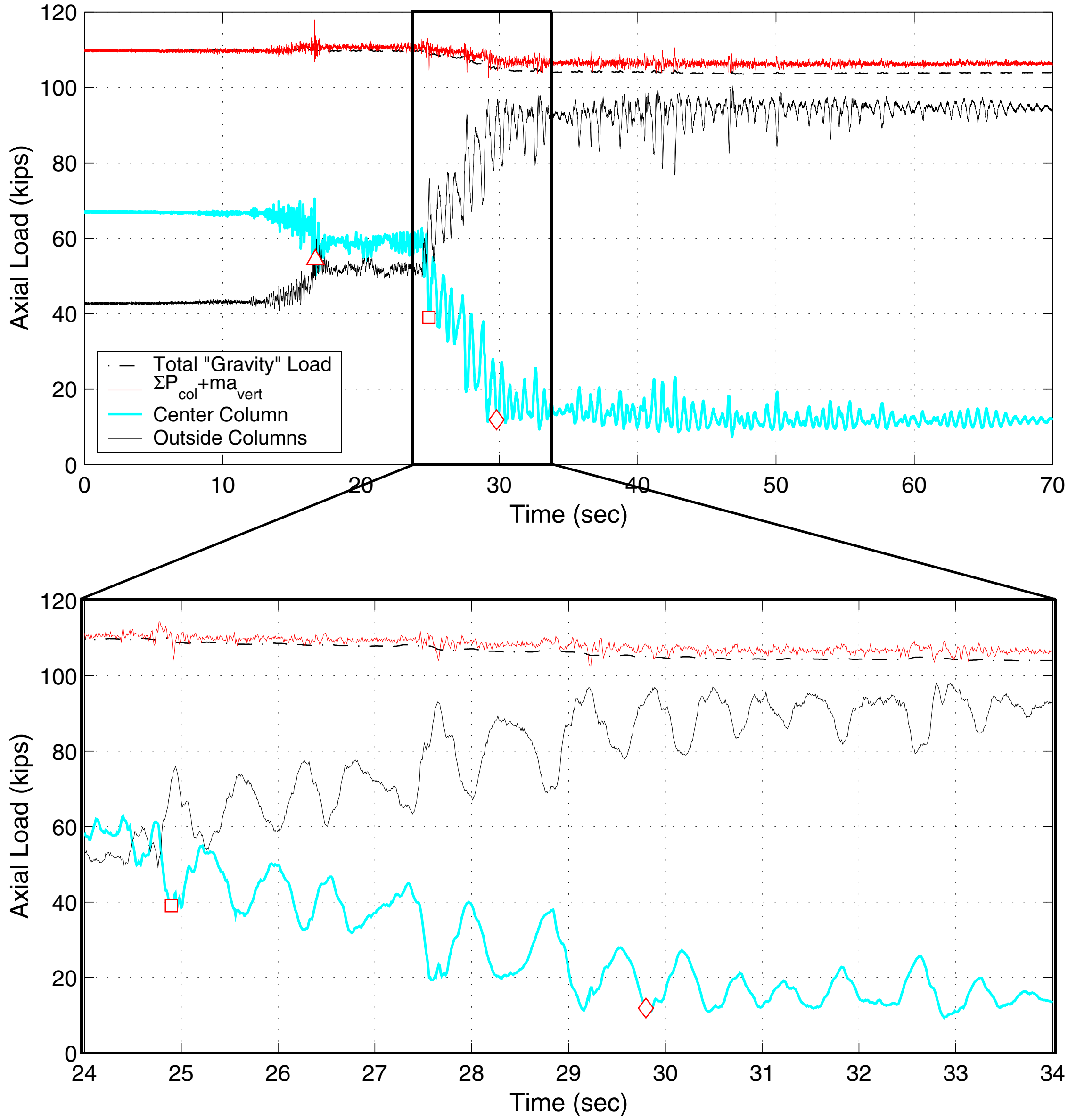

Figure 6-55. Redistribution of axial loads for Specimen 2 (Total “Gravity” Load includes both dead-load and prestress force, ΣPcol+mavert = sum of column axial loads and vertical inertial forces.)

column must be redistributed to neighboring elements. Loss of axial load support will lead to vertical inertial forces resulting from vertical acceleration of the mass above the damaged column. Gravity loads are transferred to neighboring elements through a dynamic process as the vertical inertial forces oscillate. Rapid loss of the axial load support may lead to a dynamic amplification of the transferred axial loads.

Figure 6-55 shows the redistribution of gravity loads during axial failure of the Specimen 2 center column. Note that the Total "Gravity" Load decreases by 6 kips due to relaxation of the prestress force (see Section B.3). The slight difference between the Total "Gravity" Load (calculated based on the measured mass and prestress force) and the sum of the column axial loads and vertical inertial forces suggests that minor errors exist in the column axial load readings (see Section B.6 for further discussion of force transducer errors). At the end of the test there was a difference of 2.5 kips between the Total "Gravity" Loads and the sum of the column axial loads. Agreement between the axial load lost by the center column and the axial load gained by the outside columns during transient cycles suggests that the force transducers were able to capture the variation of loads during axial failure with sufficient accuracy.

The near-total loss of the center column axial load capacity occurs over 5.5 seconds (from 24.5 sec to 30.0 sec), too slow to observe any significant dynamic amplification of the transferred load. Transient cycles caused by the longitudinal movement of the frame during the loss of axial load capacity result in sharp drops in the axial load supported by the center column. For example, at 29 seconds the axial load drops by approximately 25 kips in 0.3 seconds. Figure 6-56(a) shows a detailed view of the loss of center column axial load during the pulse at 29 seconds to illustrate the dynamic process by which the vertical loads are redistributed. The drop in the center column axial load at 28.84 seconds is initially balanced by an increase in the vertical inertial force. When the vertical inertial force peaks at 28.88 seconds, the axial loads in outside columns increase rapidly to balance both the change in the inertial force and the continued loss of axial load from the center column. The process repeats itself starting at the trough in the inertial force response at 28.96 seconds. Note that an increase in the inertial force corresponds to a drop in the center column axial load, with little or no change in the outside column axial loads; while a decrease in the inertial force corresponds to an increase in the outside column axial loads, and a decrease in the rate of axial load loss in the center column. The dynamic process results in a temporary amplification of the axial loads transferred to the outside columns. The dynamic amplification factor (DAF, defined as the change in the outside column axial loads from the start of the pulse divided by the change in the center column axial loads from the start of the pulse) for the pulse shown in Figure 6-56 peaks at 1.5 immediately after the initial transfer of axial load to the outside columns. After the initial transfer of load, the DAF oscillates about 1.0 indicating that little or no dynamic amplification occurs with any further transfer of axial load. (Note that the sum of the column axial loads and the vertical

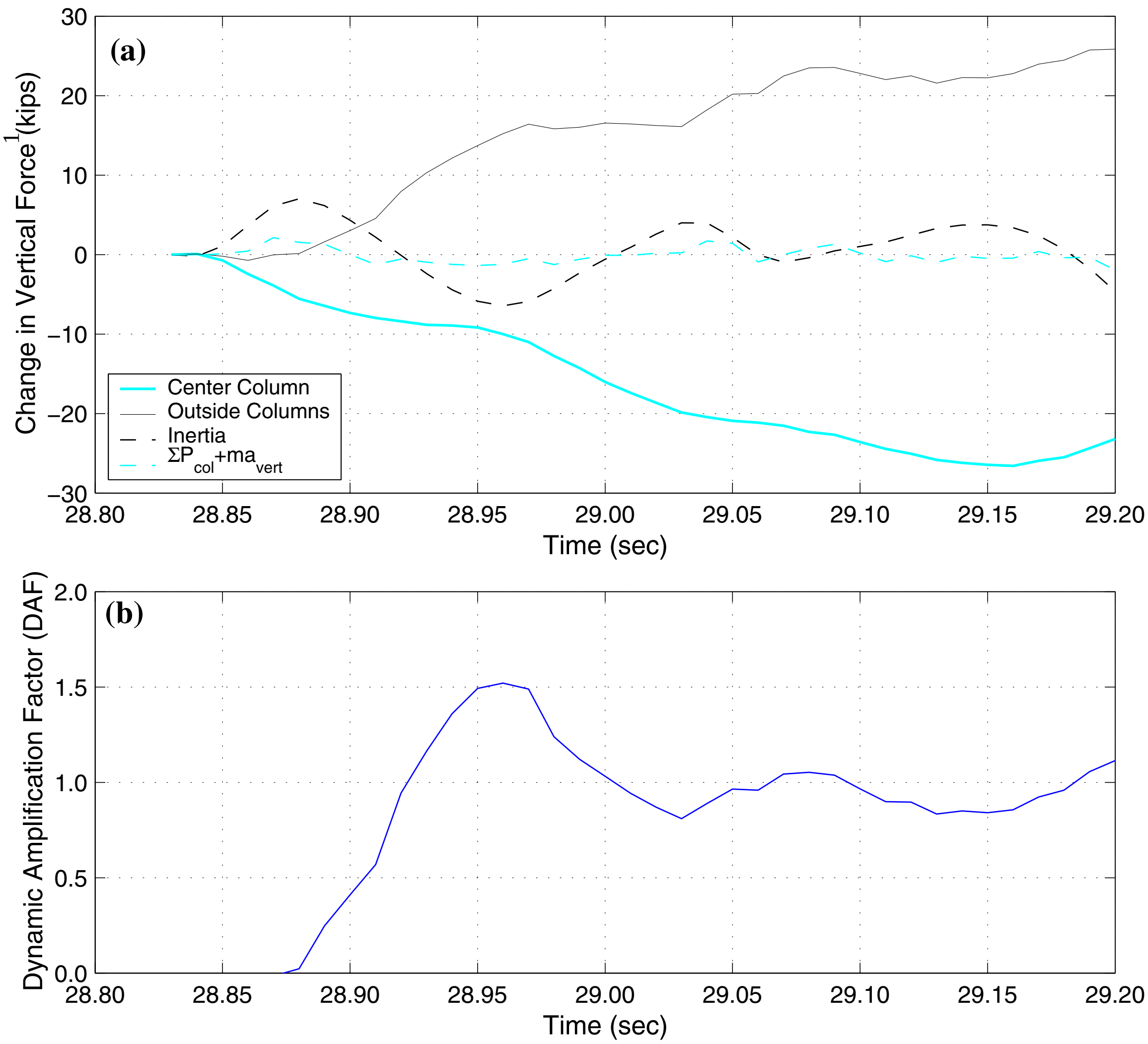

Figure 6-56. (a) Change in axial loads and vertical inertial force. (b) Dynamic amplification of axial loads transferred to outside columns. ([1]Change in forces from those measured at 28.83 seconds) (DAF = quotient of outside and center column axial loads shown in (a))

inertial forces, which should ideally plot along the x-axis, indicates that only slight instrumentation errors exist in the results shown in Figure 6-56.)

Further understanding of the gravity load redistribution during axial failure of the center column can be gained by replotting Figure 6-19 using the difference in the vertical displacement at the center column and the average of the vertical displacements at the outside columns, Δ_{beam}, as shown in Figure 6-57. The beam displacement shows that, before axial failure of the center column, the lengthening of the outside columns due to flexural cracking is greater than the lengthening of the center column (i.e., the beam deflection is negative). The beam deflections during horizontal displacement cycles causes bending of the beam, and hence, transient redistribution of the gravity loads to the outside columns. Changes in the beam deflections with horizontal displacements continue after the onset of axial failure of the center column, resulting in the transient redistribution of gravity loads to the outside columns during failure of the center column (i.e., between the square and diamond markers). In Section 7.7, the stiffness of the beam will be used to predict the slope observed in the upper right plot of Figure 6-57.

The data in the lower left plot of Figure 6-57 can be used to demonstrate the behavior of the beam during axial load redistribution. As shown in Figure 6-58, the beam can be modeled as simply supported between the outside columns with a point load support at the center column equal to the initial axial load of 67 kips. The deflection of the beam at the center column, Δ_{beam} (considering the change in length of both the center and outside columns as shown in Figure 6-57, but defined here as positive for downward displacement at mid span) and the axial load loss in center column, P_{loss}, can be used to define the force-displacement response of the beam during axial failure of the center column as shown in Figure 6-59. The star marker in Figure 6-59 indicates the point of first yield of the beam longitudinal reinforcement based on the strain gage data. Based on the shape of the test data curve, the star marker is likely somewhat past the point of first yield. This inconsistency may be due to the sensitivity of the measured strains to the location of the cracks. If the strain gage is not located at a flexural crack, then the measured steel strains will be less than those at the crack and the displacement at first yield will be overestimated using the strain gage data. The data plotted in Figure 6-59 will be compared with an elastic-perfectly-plastic model of the beam in Section 7.7.

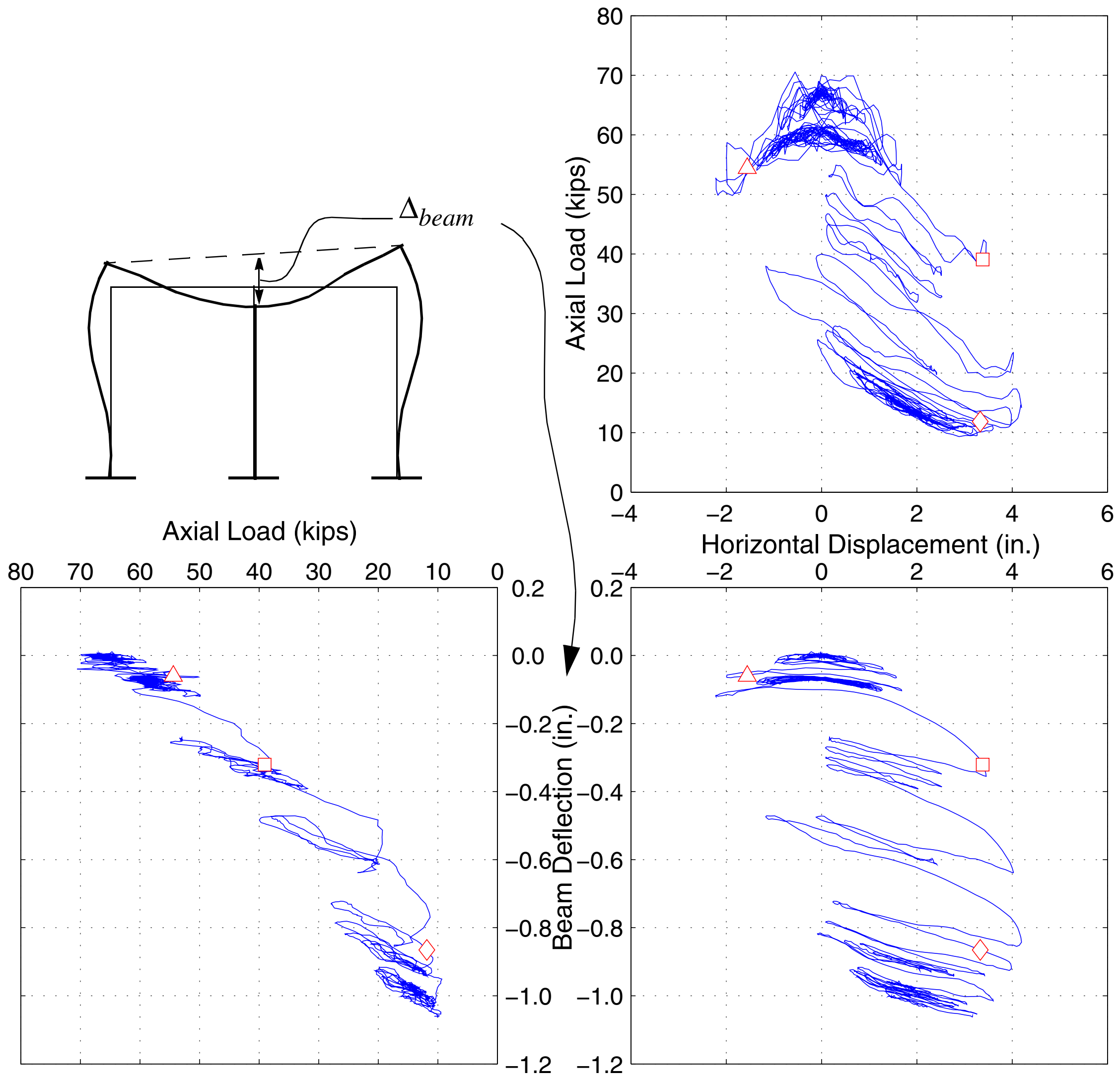

Figure 6-57. Figure 6-19 redrawn using the difference in the vertical displacement at the center column and the outside columns for Specimen 2

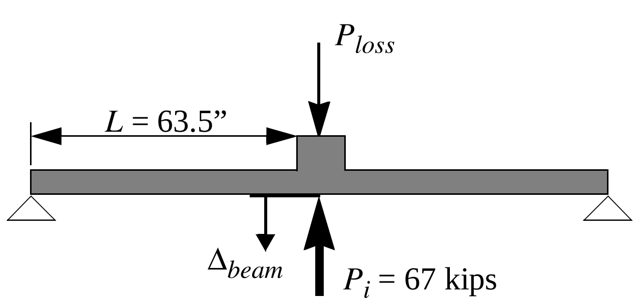

Figure 6-58. Beam modeled as simply supported with point load support from center column. (P_{loss} and Δ_{beam} positive as shown)

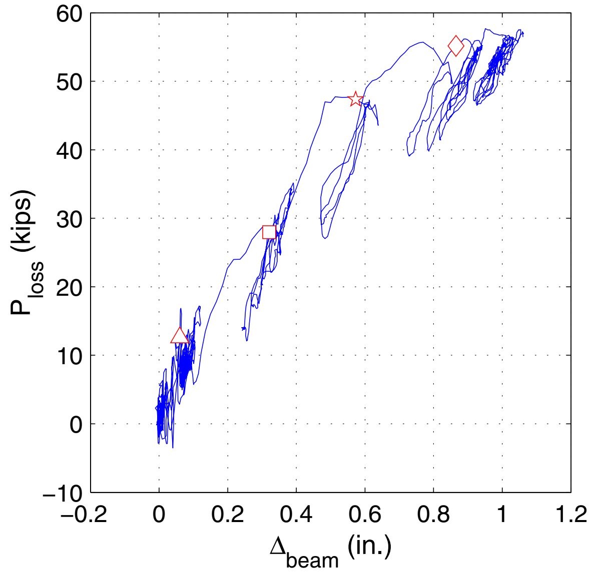

Figure 6-59. Axial load loss in center column versus the beam deflection defined in Figure 6-57.

7 Comparison of Test Data with Predictive Models

7.1 INTRODUCTION

This chapter will compare the test results presented in the previous chapter with results of models to predict yield displacement, elastic stiffness, and flexural strength of the center and outside columns. The predictive models are based on section analysis and are commonly used in practice. The response of the center column is further compared with results of models described in Chapters 2 and 3 to predict the drift at shear and axial load failure. Finally, a simple model for the beam is used to evaluate the observed axial load redistribution.

7.2 YIELD DISPLACEMENT AND STIFFNESS

7.2.1 Center Column

Calculation of the yield displacement and stiffness requires the moment-curvature relationship for the section. The moment-curvature relationships shown in Figure 7-1 were determined using a standard section analysis of the center column (assuming plane sections remain plane), with the concrete and steel models shown in Figure 7-2 (UCFyber, 1999). Note that there was no attempt to predict the ultimate curvature capacity, since shear failure of the column occurred before flexural failure. The idealized bilinear moment-curvature relationships shown in Figure 7-1 were selected to represent the behavior of the center columns before shear failure.

The displacement at first yield of the longitudinal reinforcement can be considered as the sum of the displacements due to flexure, bar slip, and shear:

$$\Delta_y = \Delta_{flex} + \Delta_{slip} + \Delta_{shear} \tag{7.1}$$

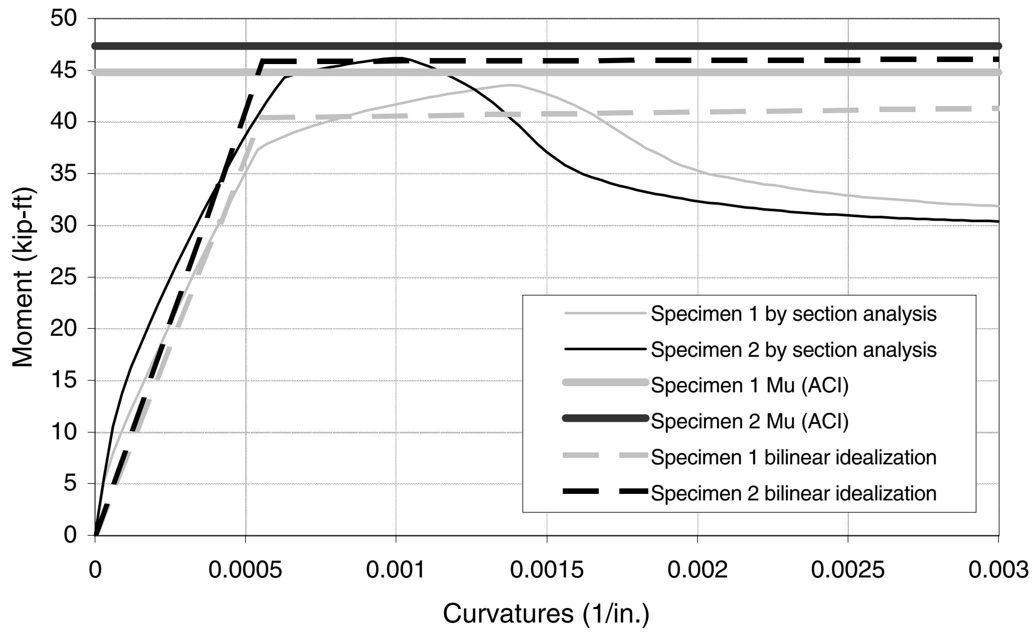

Figure 7-1. Center column moment-curvature relationships

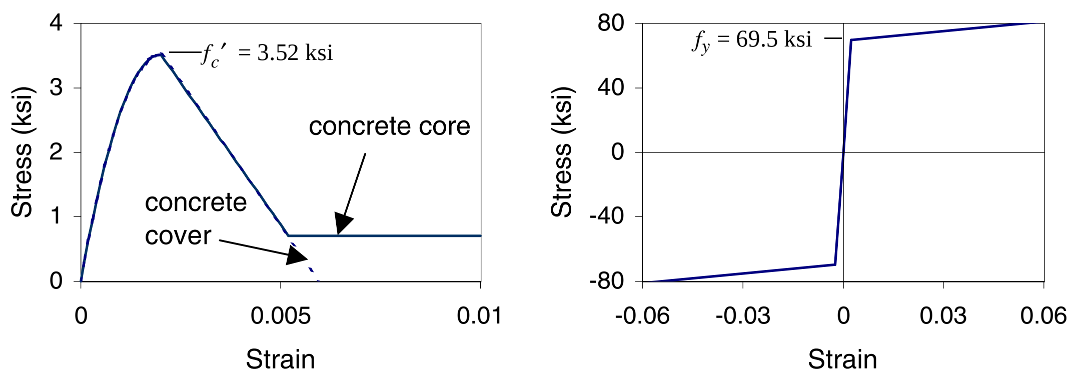

Figure 7-2. Concrete and steel material models used in section analysis of center column

Assuming the column is fixed against rotation at both ends and assuming a linear variation in curvature over the height of the column, the displacement at yield due to flexure can be estimated as follows:

$$\Delta_{flex} = \frac{L^2}{6}\phi_y \tag{7.2}$$

where L is the length of the column and ϕ_y is the curvature at first yield of the longitudinal reinforcement.

As shown in Section B.7, the displacement due to bar slip at first yield can be estimated as follows:

$$\Delta_{slip} = \frac{Ld_b f_y \phi_y}{8u} \tag{7.3}$$

where d_b is the diameter of the longitudinal reinforcement, f_y is the yield stress of the longitudinal reinforcement, and u is the bond stress between the longitudinal reinforcement and the footing or beam concrete. Since both #4 and #5 bars were used as longitudinal reinforcement for the center column, it will be assumed that the smaller bars will limit the slip displacement. A bond stress of $u = 6\sqrt{f_c'}$ (psi units) will be assumed in the following calculations (Sozen et al., 1992).

Assuming the column is fixed against rotation at both ends, the displacement at first yield due to shear deformations can be estimated by idealizing the column as consisting of a homogeneous material with a shear modulus G:

$$\Delta_{shear} = \frac{2M_y}{GA_v} \tag{7.4}$$

where M_y is the moment at first yield of the longitudinal reinforcement, and A_v the shear area of the column section which can be approximated by 5/6 of the gross area of the column section.

For the purpose of estimating the yield displacement, ϕ_y and M_y will be determined from the moment-curvature relationships based on section analysis (Figure 7-1). Table 7-1 compares the calculated yield displacement with the displacement at first yield of the longitudinal reinforcement based on the strain gage data. Note that more than half of the calculated yield displacement is due to bar slip.

Table 7-1. Calculated yield displacement for center column (in.)

Specimen	Δ_{flex}	Δ_{slip}	Δ_{shear}	$\Delta_{y\ calc}$	$\frac{\Delta_{y\ calc}}{\Delta_{y\ test}}$
1	0.30	0.38	0.01	0.69	0.93
2	0.35	0.45	0.01	0.81	1.04

For the purpose of building an analytical model to predict the ultimate behavior of the frame, the response of the center column before yielding of the longitudinal reinforcement can be approximated as linear-elastic. For flexural deformations, the effective elastic stiffness can be expressed as a fraction of the gross moment of inertia of the column section, I_g. The calculated effective flexural stiffness of the center column, $I_{eff\,flex\,calc}$, based on the bilinear idealization of the moment-curvature relationships shown in Figure 7-1, is given in Table 7-2.

If the total displacement before yielding is assumed to be due only to flexure, as is convenient for most analytical models used in practice, the effective stiffness, $I_{eff\,total}$, can be estimated as follows:

$$I_{eff\ total} = \frac{M_y L^2}{6\Delta_y E_c} \qquad (7.5)$$

where E_c is the approximate Young's modulus of concrete ($57,000\sqrt{f_c'}$ in psi units) and it is assumed that the column is fixed against rotation at both ends. Table 7-2 lists the effective stiffnesses determined based on the test results ($I_{eff\,total\,test}$) and based on the calculated moment-curvature relationships and yield displacements for the center column ($I_{eff\,total\,calc}$). For $I_{eff\,total\,test}$, the yield moment, M_y, and the yield displacement, Δ_y, are determined based on the idealized backbone relations shown in Figures 6-17 and 6-18. The stiffnesses from positive and negative displacements are averaged to determine $I_{eff\,total\,test}$. For $I_{eff\,total\,calc}$, M_y is based on the bilinear idealization of the moment-curvature relationships and Δ_y is calculated from Equations 7.2 and 7.3 using the yield curvature from the bilinear idealization of the moment-curvature relationships shown in Figure 7-1. Note that the $I_{eff\,total}$ values are approximately half of $I_{eff\,flex\,calc}$ due to the influence of slip deformations, and considerably less than values such as $0.5I_g$ or $0.7I_g$ commonly used in practice (ASCE, 2000).

Table 7-2. Effective center column stiffness as a fraction of I_g

Specimen	$I_{eff\,flex\,calc}$	$I_{eff\,total\,calc}$	$I_{eff\,total\,test}$
1	$0.47I_g$	$0.22I_g$	$0.24I_g$
2	$0.53I_g$	$0.25I_g$	$0.28I_g$

7.2.2 Outside Columns

The moment-curvature relationships shown in Figures 7-3 through 7-5 were determined using a standard section analysis of the outside columns with the concrete and steel material models shown in Figure 7-6. The confined concrete model by Mander et al. (1988) was used to determine the stress-strain relationship for the concrete core. The moment-curvature relationships were computed at three axial loads, selected based on the range of axial loads observed during the tests (see

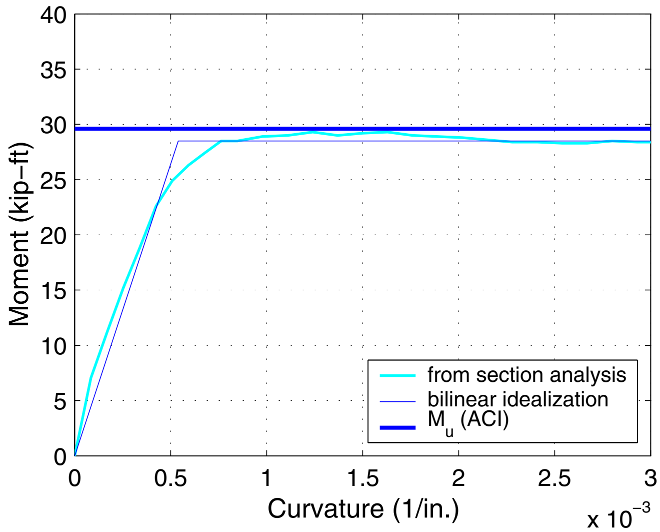

Figure 7-3. Calculated moment-curvature relationship for outside columns with initial axial load (P=20 kips)

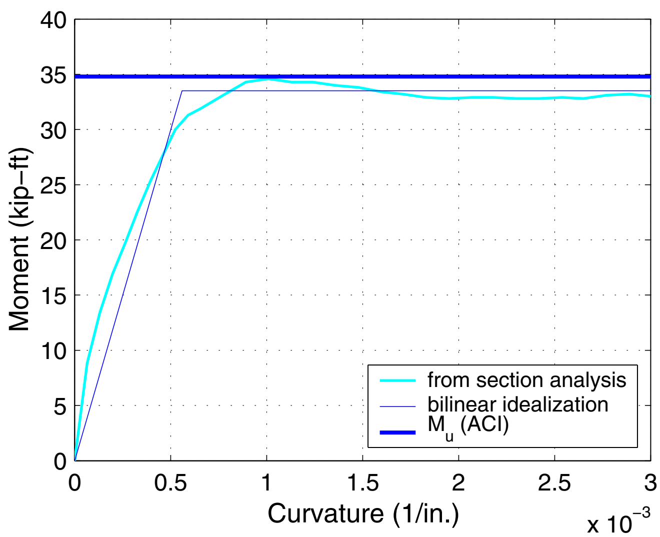

Figure 7-4. Calculated moment-curvature relationship for outside columns with upper-bound axial load (P=55 kips)

Figures 6-36 and 6-37): the initial axial load of 20 kips, an upper-bound axial load of 55 kips, and a lower-bound axial load of 8 kips. This range of axial loads was chosen to enable the calculation of bounds on the yield displacement, stiffness, and flexural strength of the outside columns.

Similar to the center column, the yield displacement can be expressed as the sum of displacements due to flexure, bar slip, and shear deformations. As shown for the center column, the displacements due to elastic shear deformations are very small and will be ignored for the outside

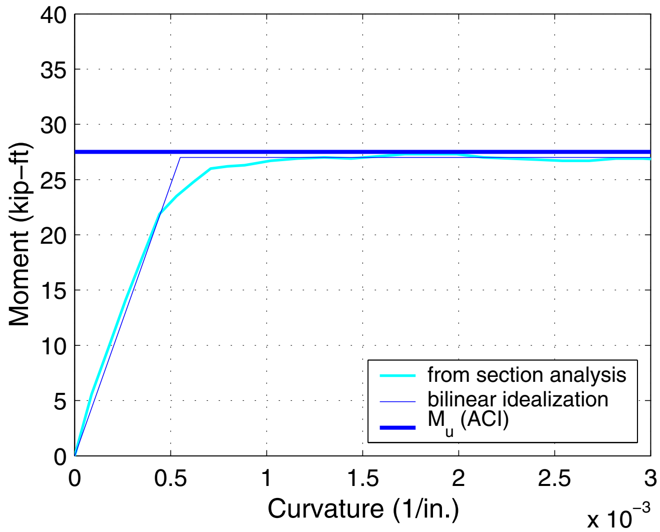

Figure 7-5. Calculated moment-curvature relationship for outside columns with lower-bound axial load (P=8 kips)

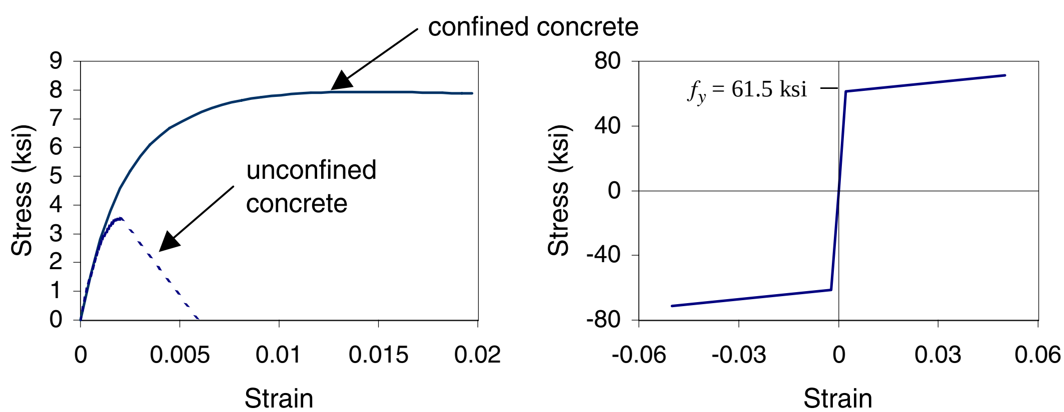

Figure 7-6. Material models used in section analysis of outside columns

columns. Adopting similar assumptions as outlined for the center column in Section 7.2.1, the displacements due to flexure and slip deformations can be approximated by Equations 7.2 and 7.3, respectively. Table 7-3 compares the calculated yield displacement for the initial axial load of 20 kips, with the displacement at first yield of the longitudinal reinforcement based on the strain gage data. Owing to the location of strain gages in the outside columns, the values in Table 7-3 are for first yielding of the outermost reinforcing bars.

As noted in the previous chapter, the outside columns exhibit a stiffer response during cycles in which the axial load increases due to overturning forces. Such cycles are referred to as *compression cycles*. Likewise, the outside columns exhibit a softer response during cycles in which

Table 7-3. Calculated displacement for outside columns at first yield of outermost reinforcement (in.)

Specimen	Δ_{flex}	Δ_{slip}	$\Delta_{y\ calc}$	$\dfrac{\Delta_{y\ calc}}{\Delta_{y\ test}}$
1	0.29	0.32	0.60	0.98
2	0.29	0.32	0.60	1.02

the axial load decreases (or *tension cycles*). Table 7-4 compares the stiffness observed during compression cycles with the calculated stiffness using the upper-bound bilinear moment-curvature relationship from Figure 7-4, and the stiffness observed during the tension cycles with the calculated stiffness using the lower-bound bilinear moment-curvature relationship from Figure 7-5. Similar to the center column, the observed stiffnesses are determined based on the idealized backbones in Figures 6-42, 6-43, 6-44, and 6-45, and assuming that both ends of the columns are fixed against rotation, a reasonable assumption before axial failure of the center column. Owing to the similar axial loads experienced by the outside columns for both specimens during low-level cycles, the observed stiffnesses, $I_{eff\ flex\ test}$ and $I_{eff\ total\ test}$, are determined by averaging the stiffnesses for all four outside columns (two columns per specimen). In Table 7-4 the effective stiffness is expressed as a fraction of the gross moment of inertia of the column, I_g. The procedure for calculating each of the terms is given in Section 7.2.1. As with the results for the center column, the influence of slip deformations reduces the total effective stiffness for the outside columns to values that are considerably less than those typically used in practice.

Table 7-4. Effective stiffness for outside columns as a fraction of I_g

Cycle Type	$I_{eff\ flex\ calc}$	$I_{eff\ total\ calc}$	$I_{eff\ total\ test}$
Compression	$0.43I_g$	$0.21I_g$	$0.20I_g$
Tension	$0.36I_g$	$0.17I_g$	$0.16I_g$

7.3 FLEXURAL STRENGTH

7.3.1 Center Column

Table 7-5 compares the calculated and measured yield moments and ultimate flexural strengths for the center column. Owing to inaccuracies in the measured moments from the force transducer data (see Section B.6), the measured values were determined using the measured shears and assuming that the column was fixed against rotation at both ends ($M = V(L/2)$). The terms listed in Table 7-5 are defined as follows:

- $M_{y\ test}$ = measured moment at first yield of the longitudinal reinforcement.
- $M_{u\ test}$ = maximum moment measured during the test.
- $M_{y\ calc}$ = calculated yield moment based on section analysis.
- $M_{u\ calc}$ = calculated ultimate moment based on section analysis.
- $M_{u\ ACI}$ = calculated ultimate moment using a standard rectangular stress block with ultimate concrete strain of 0.004, concrete strength based on concrete cylinder tests (Appendix A), bilinear steel model from Figure 7-2, and a strength reduction factor of unity.

Table 7-5 shows a close agreement between the calculated and measured results. Note that the ultimate moment achieved in the tests, particularly for the Specimen 2, may be governed by the shear strength of the column. Shear strength is not considered in the calculated ultimate flexural strengths.

Table 7-5. Measured and calculated flexural strengths for center column (kip-ft)

Specimen	$M_{y\ test}$	$M_{u\ test}$	$M_{y\ calc}$	$M_{u\ calc}$	$M_{u\ ACI}$
1	39.3	43.8	37.3	43.6	44.8
2	45.1	48.1	44.3	46.2	47.4

Table 7-6. Measured and calculated flexural capacities for outside column (kip-ft)

Cycle Type	$M_{y\ test}$	$M_{u\ test}$	$M_{y\ calc}$	$M_{u\ calc}$	$M_{u\ ACI}$
Compression	33.8	39.9	31.2	34.6	34.8
Tension	18.1	26.8	21.9	27.3	27.5

7.3.2 Outside Columns

The flexural strengths for the outside columns are listed in Table 7-6. As for the measured effective stiffnesses, the measured flexural strengths were determined by averaging the moments from the four outside columns during the appropriate cycle. As for the center column, the measured moments were determined based on the measured shears and assuming that the columns remain fixed against rotation at both ends. This assumption is not valid for Specimen 2 after axial failure of the center column and vertical deflection of the beam leads to rotations at the beam ends, and, hence, rotation of the top of the outside columns. However, the maximum shear in the outside columns of Specimen 2 is recorded before axial failure of the center column.

The calculated values overestimate the measured values during tension cycles, and underestimate the measured values during compression cycles. The discrepancies may be a result of the assumption that the column ends remain fixed against rotation.

7.4 SHEAR STRENGTH

The center column for both specimens appeared to fail in shear as suggested by the characteristic diagonal failure plane observed during the test. As described in Chapter 2, several predictive models exist for calculating the shear strength of reinforced concrete columns. Models proposed by Sezen (2002) and Priestley et al. (1994), in addition to the equations from ACI318-02, are compared with the test results in Table 7-7. The maximum center column shear measured during the tests was 18.1 kips and 19.9 kips for Specimens 1 and 2, respectively.

The shear-strength models proposed by Sezen (2002) and Priestley et al. (1994) require the displacement ductility demand on the column. To remove further uncertainty from the evaluation of the shear-strength models, the displacement ductility, μ_δ, was determined based on the test data by using the following expression:

$$\mu_\delta = \frac{\Delta_u}{\Delta_y} \tag{7.6}$$

where Δ_y is the displacement (in the positive direction) at first yield of the longitudinal reinforcement based on the strain gage data, and Δ_u is defined as the displacement (in the positive direction) at which the backbone of the test data first drops below 80 percent of the maximum recorded center column shear. (Priestley et al. (1994) determined the measured yield displacement by extrapolating a line from the origin, through the displacement at first yield, to the theoretical flexural strength based on measured material properties. Where available, Sezen (2002) used the reported yield displacement based on strain gage data; otherwise, the yield displacement was determined by extrapolating a line from the origin, through the backbone of the test data at 70% of the maximum lateral load, to the maximum measured lateral load.) Only the displacements in the positive direction are considered, since the degradation in shear strength is initiated in this direction. Given this definition, the observed maximum displacement ductilities are 4.08 and 1.96 for Specimens 1 and 2, respectively.

Table 7-7. Predicted shear strengths as a fraction of the maximum measured shear

Shear-Strength Model	*Specimen 1*	*Specimen 2*
ACI318-02	22.5 kips / 18.1 kips = **1.24**	24.5 kips / 19.9 kips = **1.23**
Priestley et al. (1994)	26.2 kips / 18.1 kips = **1.45**	38.2 kips / 19.9 kips = **1.92**
Sezen (2002)	18.1 kips / 18.1 kips = **1.00**	24.0 kips / 19.9 kips = **1.21**

The results from this very limited data set suggest that the model proposed by Sezen (2002) provides good accuracy for the columns tested in this study. A detailed comparison of the models using a database of 51 columns can be found in Sezen (2002).

Figures 7-7 and 7-8 compare the shear-strength models by Sezen (2002) and Priestley et al. (1994) (based on the calculated yield displacement from Table 7-1) with the center column shear hysteresis for Specimens 1 and 2. Elastic-perfectly-plastic (EPP) backbone models, based on the calculated yield displacements from Table 7-1 and the yield moment from the idealized moment curvature relationships shown in Figure 7-1, are also included on the plots. The intercepts of the EPP model and the shear-strength model indicate the displacements at which the model would predict shear failure (or shear-strength degradation of approximately 20%). The EPP model does not intercept the Priestley shear-strength model for either specimen, indicating that this shear model would not predict shear failure for such a column. As discussed in Section 2.3.1, the shear-strength models do not provide a reliable estimate of the displacement at shear failure, and this assertion is supported by the results shown in Figures 7-7 and 7-8.

7.5 SHEAR-DRIFT BACKBONE

The backbone of the shear-drift hysteretic response for a column expected to experience flexural yielding before shear failure can be approximated as shown in Figure 7-9. Each coordinate of the backbone can be determined using models discussed previously. The flexural strength, V_u, can be determined based on an idealization of the calculated moment-curvature response (Figure 7-1); the drift ratio at flexural yielding, Δ_y/L, can be calculated as discussed in Section 7.2; the drift ratio at shear failure, Δ_s/L, can be calculated using models discussed in Section 2.3; and the drift ratio at axial failure, Δ_a/L, can be calculated using the shear-friction model from Section 3.3.6. The calcu-

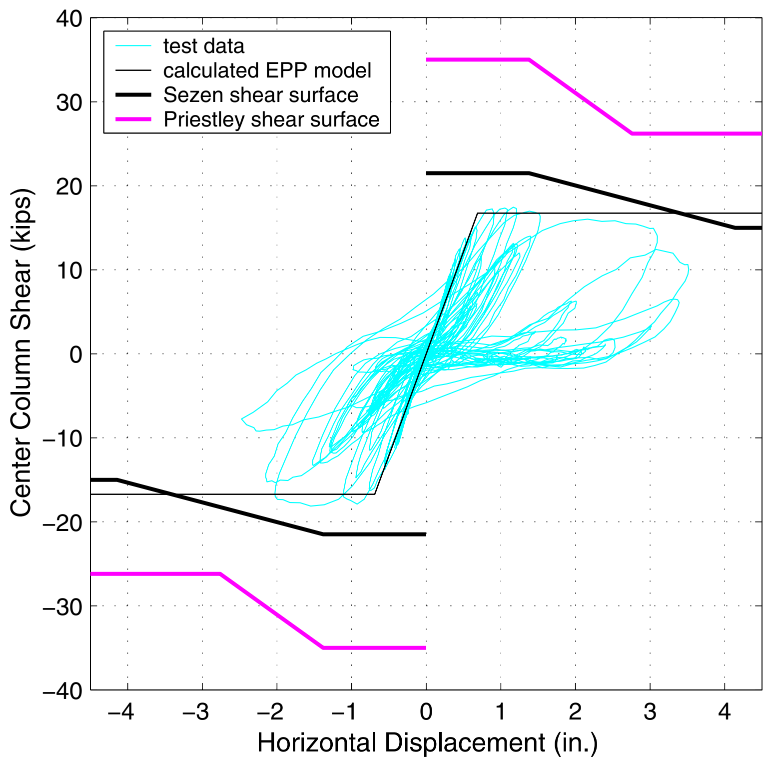

Figure 7-7. Comparison of shear-failure surfaces with Specimen 1 test data

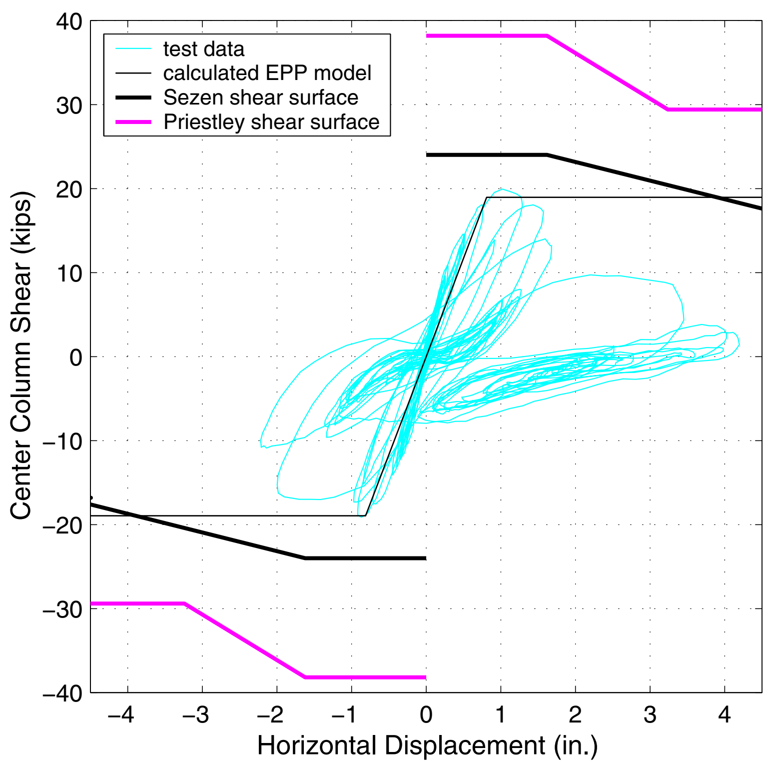

Figure 7-8. Comparison of shear-failure surfaces with Specimen 2 test data

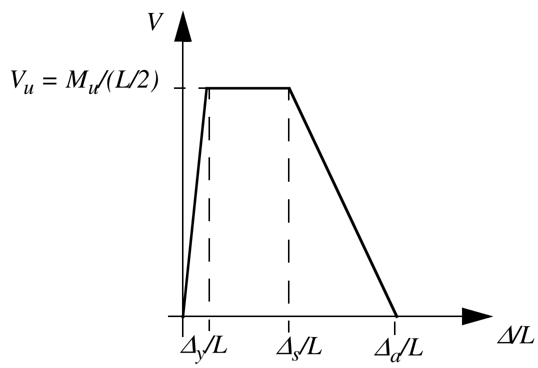

Figure 7-9. Idealized shear-drift backbone for shear-critical columns

lated backbones for the center column response, using the six models for Δ_s/L from Section 2.3, are shown in Figures 7-10 through 7-15. (Equation 3.20 was used to calculate Δ_d/L for all plots except Figure 7-15, where the model by Kato and Ohnishi (2002) discussed in Section 3.4 was used.) For all cases the axial load was taken as the initial axial load supported by the center column.

The empirical drift capacity models (Equations 2.8 and 2.9) and the model by Pujol et al. (1999) provide very similar estimates of the shear-drift backbone for both specimens. The models underestimate the drift at shear failure for Specimen 1, but provide a good estimate of the drift at shear failure for Specimen 2. These results suggest that the drift capacity models may underestimate the influence of the axial load on the drift ratio at shear failure.

The model by Pujol et al. (2000) provides a good estimate of the shear-drift backbone for Specimen 1, but significantly underestimates the drift at shear failure for Specimen 2. The calculated drift at shear failure for Specimen 2 was less than the calculated drift at flexural yielding, resulting in the backbone shown in Figure 7-13.

As noted previously, the shear strength model by Sezen (2002) does not provide a reliable estimate of the drift at shear failure. For Specimen 2, the shear strength model predicts a drift at shear failure which is larger than the calculated drift at axial failure, resulting in the erroneous predicted shear-drift backbone shown in Figure 7-14. Note that, contrary to all of the other models presented for the drift at shear failure, the shear strength model incorrectly predicts that the higher axial load for Specimen 2 will result in an increase in the drift at shear failure compared with Specimen 1.

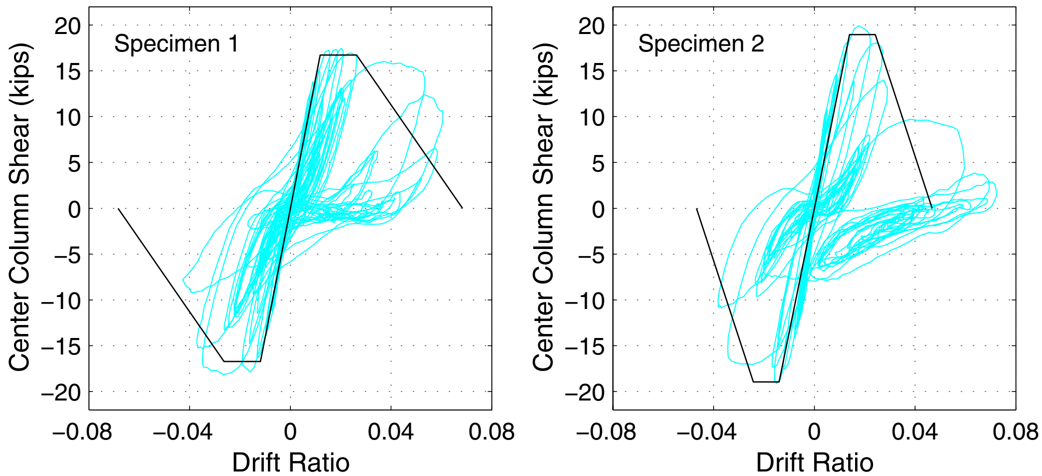

Figure 7-10. Calculated backbone using Equation 2.8

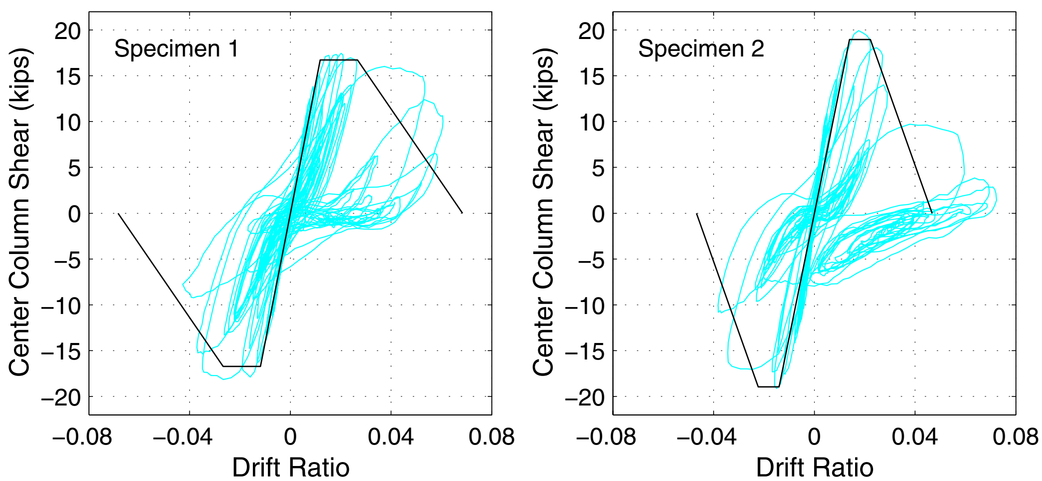

Figure 7-11. Calculated backbone using Equation 2.9

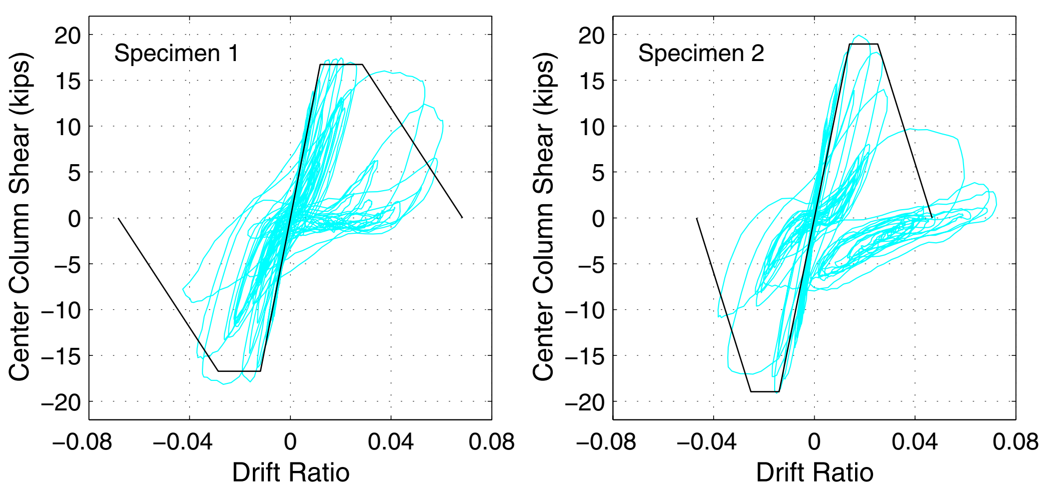

Figure 7-12. Calculated backbone using Pujol et al. (1999) (Equation 2.2)

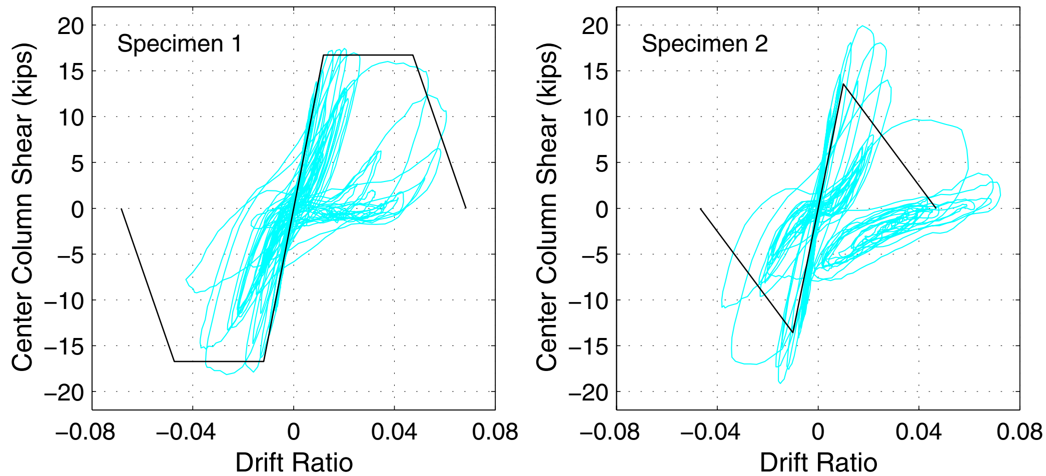

Figure 7-13. Calculated backbone using Pujol et al. (2000) (Equation 2.5)

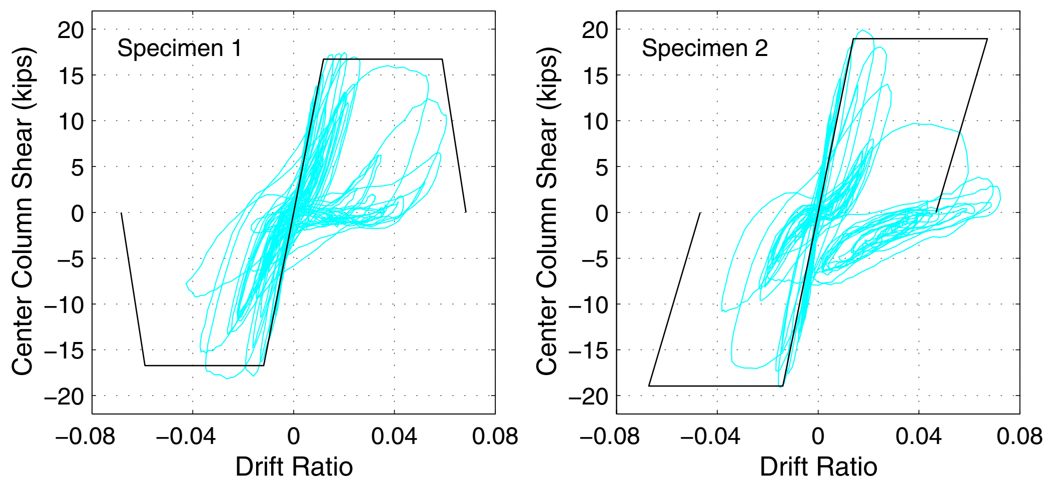

Figure 7-14. Calculated backbone using Sezen (2002) (see Figures 7-7 and 7-8)

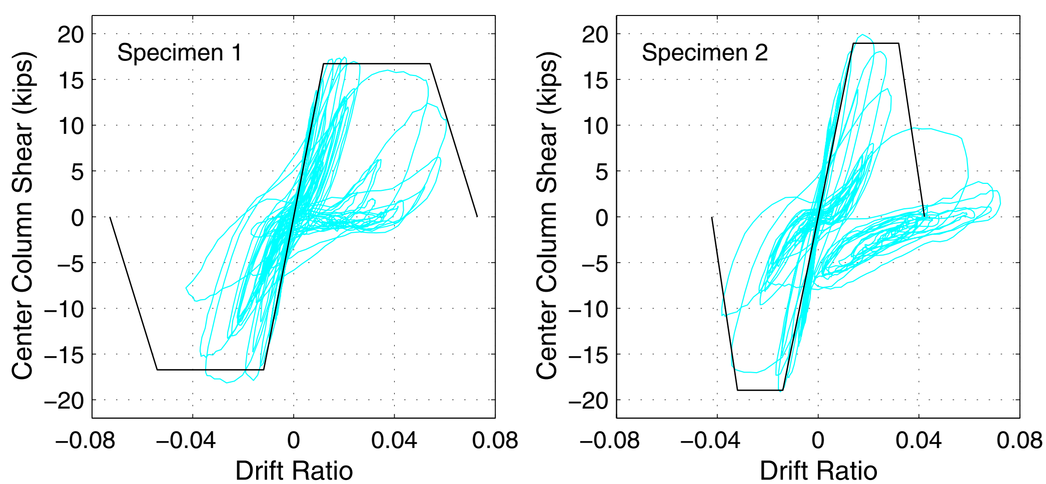

Figure 7-15. Calculated backbone using Kato and Ohnishi (2002) (Equation 2.6)

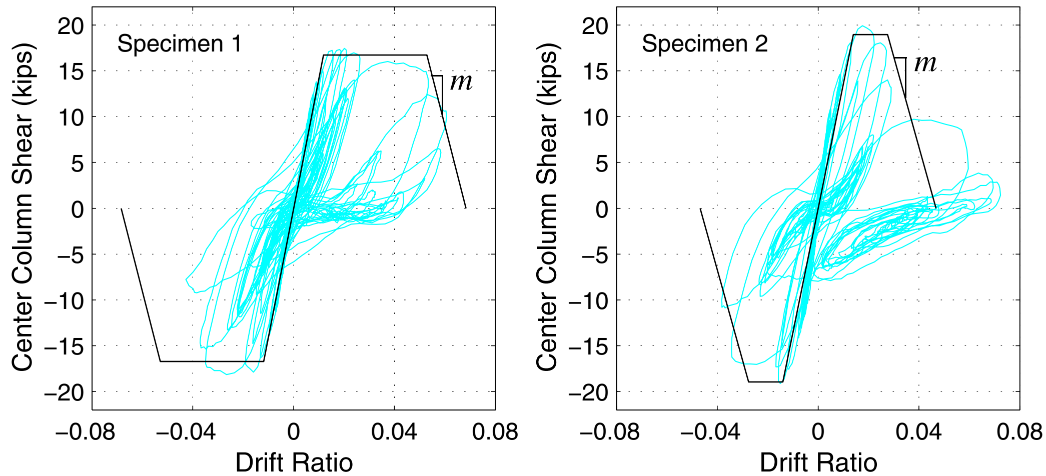

Figure 7-16. Calculated backbone using degrading slope model (slope *m* given by Equation 3.25)

The model for the drift at shear and axial load failure by Kato and Ohnishi (2002) shows close agreement with the center column hysteretic response for both specimens. By using one expression (Equation 2.6) with different coefficients for shear and axial failure, the model by Kato and Ohnishi (2002) ensures that the calculated drift at axial failure will always exceed the calculated drift at shear failure.

As described in Section 3.5, the degrading slope after shear failure and the displacement at which significant shear strength degradation first occurs can be estimated using a shear-friction model (Equation 3.25). Figure 7-16 uses the degrading slope model to construct the shear-drift backbone for the center column of each specimen. The intercept of the degrading slope model and the $V = 0$ axis in Figure 7-16 are assumed to be given by the axial-failure model (Equation 3.20) using the initial axial load on the center column. Although the model provides a good estimate of the degrading slope and the displacement at which degradation begins for the columns tested in this study, it must be noted that the degrading slope model does not agree well with the results from the pseudo-static tests in the database from Section 3.2.

7.6 AXIAL RESPONSE

Figures 7-17 and 7-18 show the axial-load lateral-drift response of the center column for each specimen compared with the axial failure surface based on Equation 3.20. The response of the center column for Specimen 1 remains below the failure surface, indicating that the model predicts no

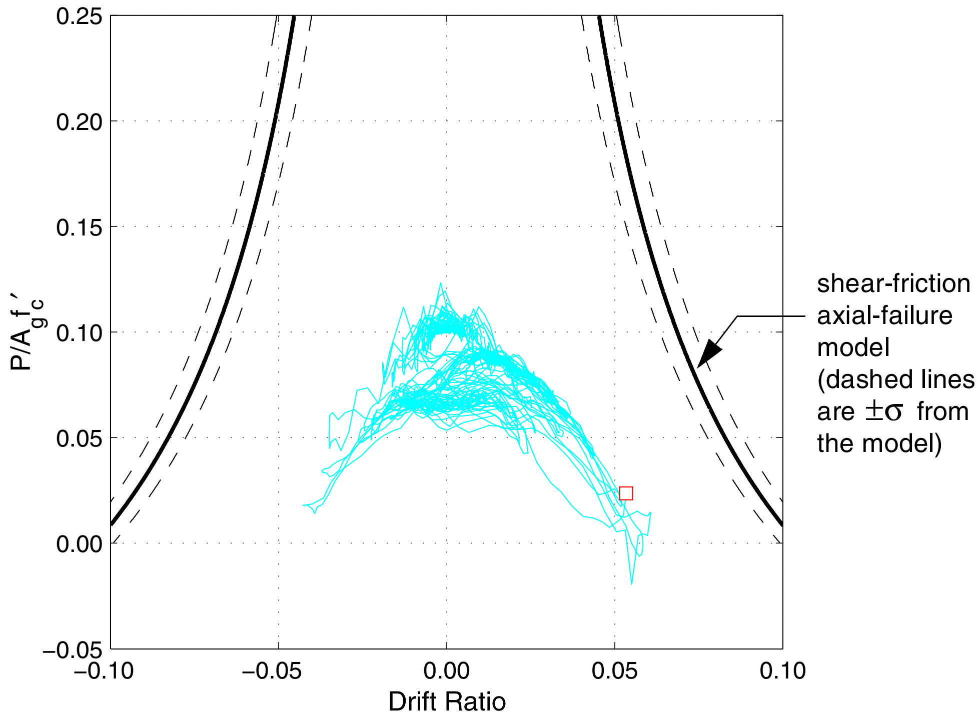

Figure 7-17. Comparison of center column response from Specimen 1 to shear-friction axial-failure model (Equation 3.20)

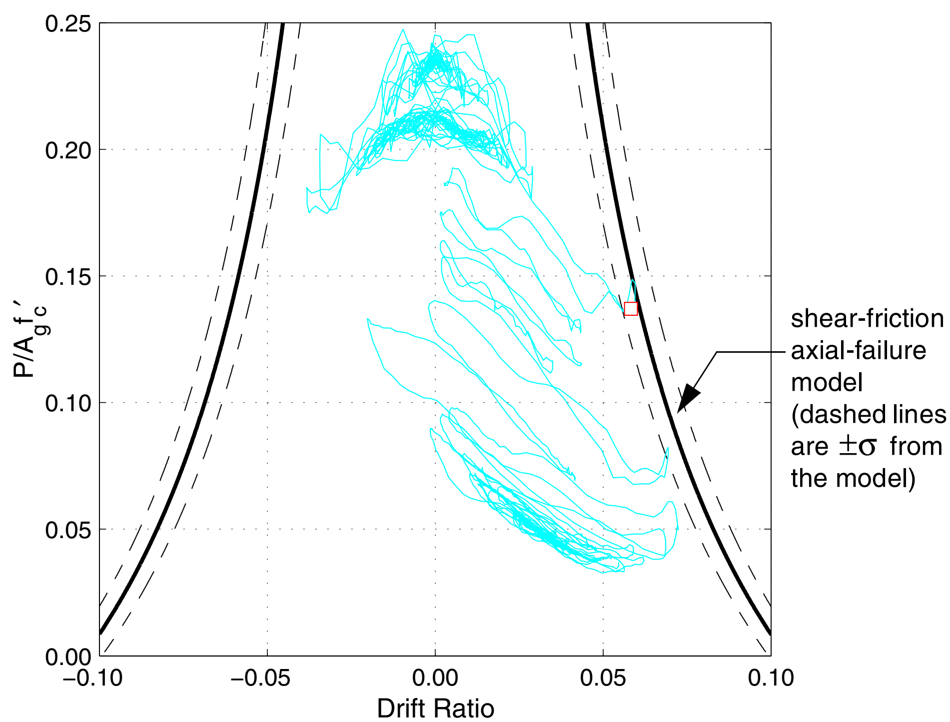

Figure 7-18. Comparison of center column response from Specimen 2 to shear-friction axial-failure model (Equation 3.20)

axial failure for the test with low axial load. The response of the center column for Specimen 2 touches the failure surface, indicating that the model predicts that axial failure can be expected for the test with a moderate axial load. These results are consistent with the observed behavior during the tests.

The intercept of the center column response from Specimen 2 and the failure surface occurs at approximately 24.9 seconds, as indicated by the square marker (the same square marker appears in the plots of Chapter 6). At 24.9 seconds significant distortion of the top of the center column, possibly due to sliding along the diagonal shear-failure plane, could be observed visually, as shown in Figure 6-12b.

7.7 BEAM RESPONSE AND LOAD REDISTRIBUTION

As discussed in Section 6.3.4, the beam stiffness influences the redistribution of gravity loads observed during the tests. Estimates of the yield displacement and the flexural strength of the beam can be used to model the beam stiffness and the transient redistribution of gravity loads.

Owing to the flexibility of the outside columns compared with that of the beam, the beam can be approximately modeled as simply-supported between the outside columns with a point load support at midspan equal to the initial axial load in the center column (as shown in Figure 6-58). The yield deflection at midspan due to P_{loss} (the drop in the center column axial load capacity) can be estimated by adding the deflection due to flexure and the deflection due to slip of the longitudinal bars from the center transverse beam.

$$\Delta_{beam\ y} = \Delta_{beam\ flex} + \Delta_{beam\ slip} \tag{7.7}$$

Note that all calculations are done for deflections at the face of the center transverse beam. Owing to the increased stiffness from the center transverse beam, these deflections should provide a good estimate of the midspan deflections.

Considering half of the beam as a cantilever, the yield deflection due to flexural deformations resulting from P_{loss} can be estimated as follows:

$$\Delta_{beam\ flex} = \frac{L^2}{3}(\phi_y - \phi_{DL}) \tag{7.8}$$

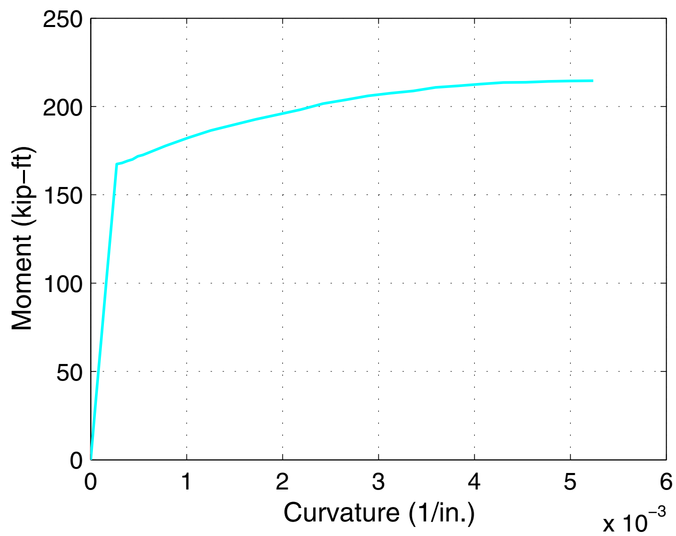

Figure 7-19. Moment-curvature relationship for beam section

where ϕ_{DL} is the curvature at the face of the transverse beam based on the simply-supported model subjected to dead loads (including prestress forces) and the initial axial load in the center column, ϕ_y is the yield curvature of the beam, and L is the distance between the center line of the outside columns and the face of the center-column transverse beam. The yield curvature was based on the moment-curvature relationship calculated from a standard section analysis as shown in Figure 7-19. The flexural displacement of the beam at yield, based on Equation 7.8, is 0.31 inches.

Since the center transverse beam acts as an anchorage block for the beam longitudinal reinforcement, the slip of the beam longitudinal bars within the center transverse beam must be considered when evaluating the yield deflection. As shown in Figure 7-20, the slip of the longitudinal bars, δ_{slip}, can be estimated by integrating the strains in the reinforcing bars within half of the center transverse beam. Given δ_{slip}, the deflection at midspan due to the reinforcement slip at yield can be estimated as follows:

$$\Delta_{beam\ slip} = \frac{\delta_{slip}}{c}L \tag{7.9}$$

where c is the distance from the neutral axis to the reinforcement at yield based on section analysis, and L is the length from the center line of the outside column to the face of the center transverse beam.

Based on Figure 7-20 and Equation 7.9, the beam deflection at yield due to slip of the reinforcing bars from the center transverse beam is approximately 0.11 inches. Therefore, based on

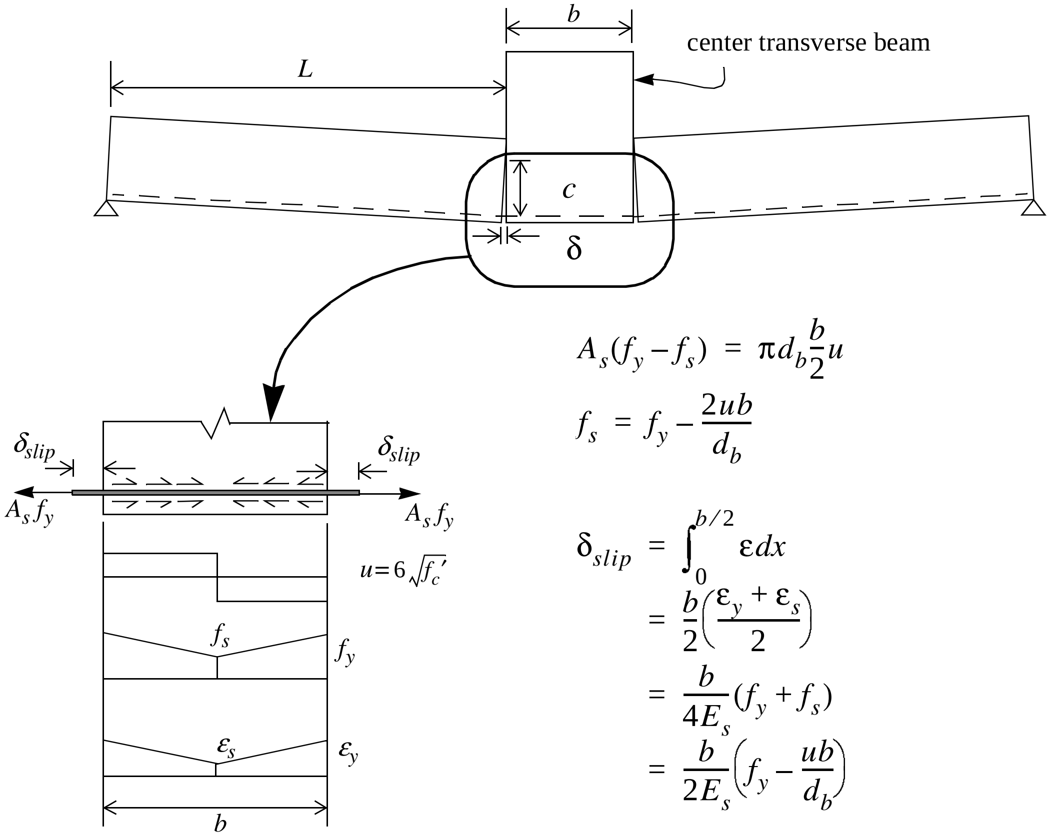

$$\delta_{slip} = \int_0^{b/2} \varepsilon dx = \frac{b}{2}\left(\frac{\varepsilon_y + \varepsilon_s}{2}\right) = \frac{b}{4E_s}(f_y + f_s) = \frac{b}{2E_s}\left(f_y - \frac{ub}{d_b}\right)$$

Figure 7-20. Slip of beam longitudinal reinforcement from center transverse beam

Equation 7.7, the total deflection of the beam at yield of the longitudinal reinforcing bars is approximately 0.42 inches. Based on the simplified model shown in Figure 6-58, including the dead load and applied prestress force, P_{loss} = 53 kips produces a moment at the face of the transverse beam equal to the yield moment from section analysis.

Figure 7-21 compares the measured response of the beam from Specimen 2 shown in Figure 6-59 with an elastic-perfectly-plastic model based on the yield deflection and yield moment discussed above. The calculated yield displacement and stiffness appear consistent with the recorded results, although the test data suggest that the beam yields more gradually than the EPP model would indicate.

Figure 7-22 shows relations between the center column axial load, horizontal displacements, and beam displacements for Specimen 2. The slope of the bold line shown on the lower right plot of Figure 7-22, and the stiffness of the beam, can be used to estimate the loss in the center column axial load at the time of the square marker. (Note that the test data are used in place of a

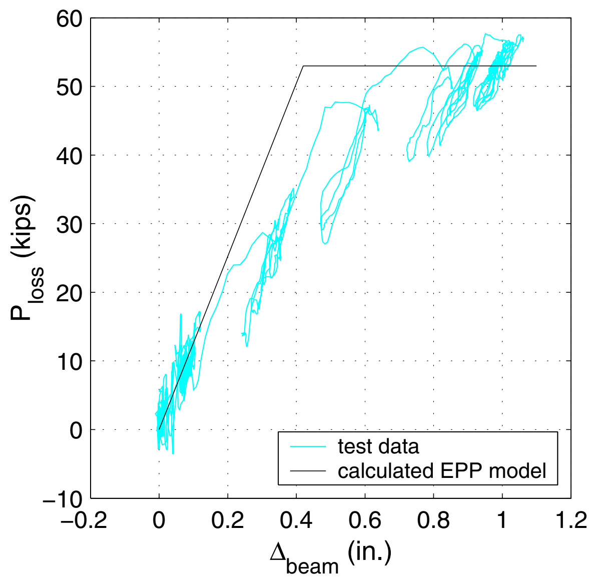

Figure 7-21. Measured and calculated response of the beam from Specimen 2

model for the horizontal versus beam displacement relationship, since a simplified model of the axial shortening of a column after shear failure is not currently available.) The bold line, at a slope of 0.08, is approximately tangent to the response of the column during the pulse initiating axial failure. By using this linear approximation to the axial response of the columns, the difference in the vertical displacements at a horizontal displacement of 3.4 inches (at the square marker) can be calculated as -0.08*3.4 = -0.27 inches. The elastic stiffness of the beam, based on the EPP model shown in Figure 7-21, is such that lifting the outside columns by 0.27 inches relative to the center column will result in relieving the center column axial load by 29 kips. Since the initial axial load in the center column was 67 kips, a horizontal displacement of 3.4 inches should result in a center column axial load of approximately 38 kips. This result is consistent with the location of the square marker in the upper-right plot of Figure 7-22.

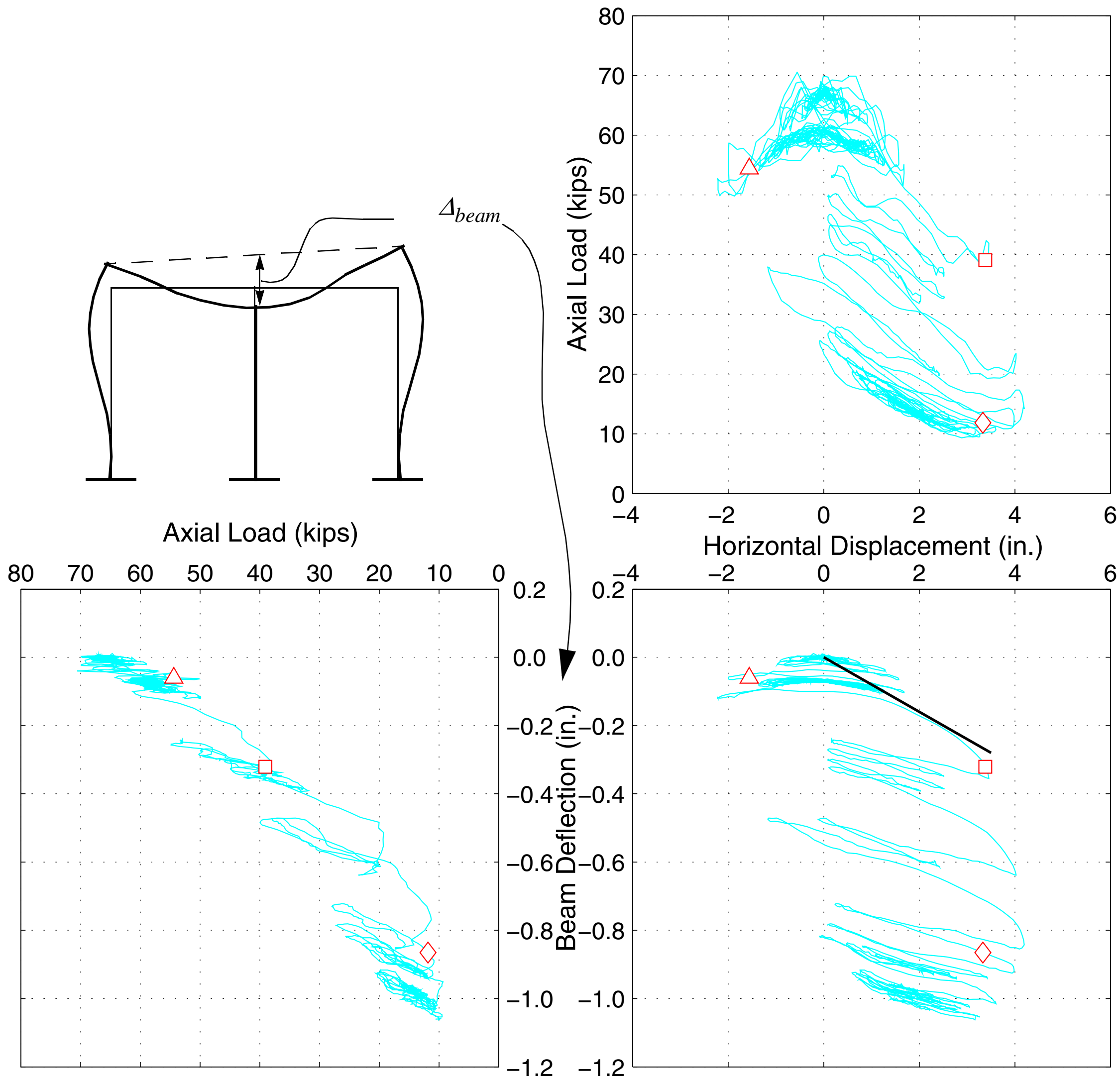

Figure 7-22. Relations between the center column axial load, the horizontal displacement and the beam displacement for Specimen 2, with a linear approximation to the horizontal versus beam displacement relationship. (Same as data plotted in Figure 6-57)

8 Analysis of Shake Table Test Specimens

8.1 INTRODUCTION

This chapter will describe an analytical model for the shake table test specimens developed using OpenSees, a finite-element analysis platform designed for earthquake engineering simulation (OpenSees, 2002). The behavior of the model under both static and dynamic loading conditions will be investigated. The goal of the static analyses is to evaluate the ability of the model to reproduce the observed hysteretic behavior of the specimen components if the lateral drifts are predicted exactly. The goal of the dynamic analyses is to evaluate the ability of the model to reproduce the observed response of the specimens as described in Chapter 6. The sensitivity of the results to changes in several parameters will also be investigated.

The analysis described herein will use the models presented in Chapters 2 through 4 in an effort to reproduce the observed response of the shake table test specimens described in Chapter 6. The proposed model for the drift capacity at shear failure (Equation 2.9) and the axial failure model (Equation 3.20), both implemented in OpenSees using the limit state failure model introduced in Chapter 4, will be used to identify the initiation of shear- and axial-strength degradation, respectively, for the center columns. The sensitivity of the analytical results to the accuracy of the failure models will be investigated.

8.2 DESCRIPTION OF THE ANALYTICAL MODEL

The layout of the nodes and elements for the analytical model is shown in Figure 8-1. The following sections describe the models used for the frame components and the loading for the dead-load model.

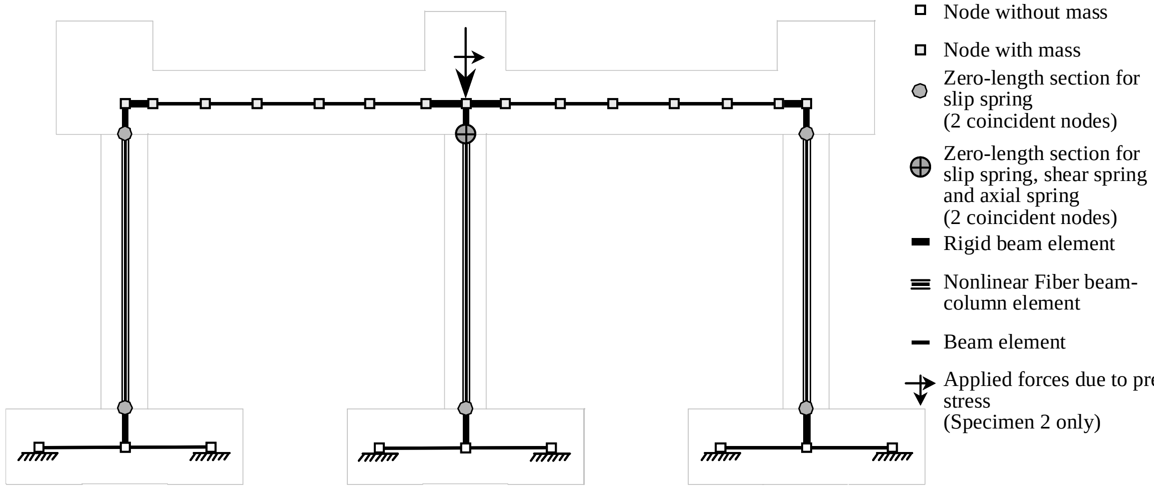

Figure 8-1. Model of shake table specimen

8.2.1 Beam and Footing Models

The calculated moment-curvature and slip response for the beam, presented in Section 7.7, was used to determine the stiffness and flexural yield strength of the beam elements. Although the beam was modeled as nonlinear (with moments and axial load uncoupled) for the dynamic analyses, it was necessary to use a linear-elastic beam model for the static analyses to maintain static equilibrium. Figure 8-2 shows the loads acting on the beam node at the top of the center column. During axial failure, the center column axial load, P, decreases with increasing lateral drift (as described in Section 4.5.3). If the beam is yielding in positive bending due to axial shortening of the center column, then the beam shear forces, V_1 and V_2, are approximately equal and constant. For static analysis, nodal equilibrium cannot be achieved with a yielding beam, since W+V_1+V_2 remains constant while P decreases. For dynamic analysis, however, the inertial force due to the downward

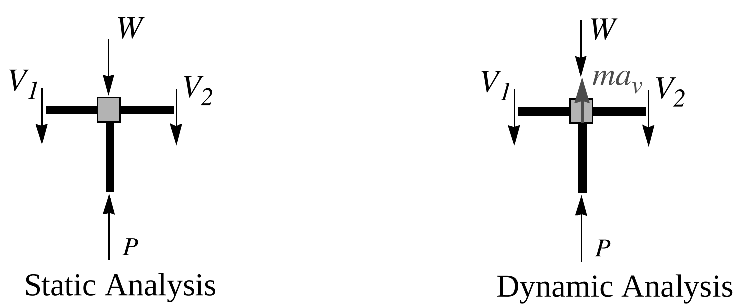

Figure 8-2. Nodal equilibrium at top of the center column

acceleration of the beam mass, ma_v, will increase as P decreases, thereby maintaining nodal equilibrium. Lengthening of the beam due to cracking was not considered.

The footings were modeled as linear-elastic with the flexural stiffness approximated by 80% of the gross moment of inertia. The force transducers were not included in the model, since their shear stiffness (approximately 6000 kips/in.) was considered high enough to be considered a fixed end condition.

8.2.2 Column Models

Zero-length sections located at the top and bottom of each of the columns attached the nonlinear beam-column elements to the beam and footings. The zero-length sections were defined by three uncoupled material models describing the moment-rotation relationship, the shear-longitudinal displacement relationship, and the axial load-vertical displacement relationship between two coincident nodes (one attached to the end of the nonlinear beam-column element, and one attached to the rigid beam element). Each material model could be interpreted as a spring in series with the nonlinear beam-column element.

As noted in Chapter 7, displacements due to slip of the longitudinal reinforcing bars from the footing and beam accounted for approximately half of the yield displacement and significantly influenced the observed stiffness of the columns. To account for this additional flexibility, elastic slip springs, based on the calculated slip displacements from Section 7.2, were included in zero-length sections at the ends of each of the column elements.

The zero-length section at the top of the center column element included material models to represent the shear and axial-load failure of the center column. The limit state failure model described in Section 4.5.1 was used to define the shear-longitudinal displacement relationship (shear spring), while the limit state failure model described in Section 4.5.3 was used define the axial load-vertical displacement relationship (axial spring) for the zero-length section. The limit curve for the shear spring was defined using the empirical drift capacity model incorporating the influence of axial load from Section 2.3.5 (Equation 2.9), while the limit curve for the axial spring was defined by the axial failure model from Section 3.3.6 (Equation 3.20). The initial slope for the shear spring (i.e., the slope of the pre-failure backbone from Figure 4-7) was chosen based on the shear stiffness of the uncracked column (i.e., GA_v/L = 1700 kips/in., where effective shear area, A_v, is approximated by $(6/5)A_g$). As discussed in Section 4.5.1, the degrading slope for the shear spring after shear failure is detected (K_{deg} from Figure 4-8) was determined based on achieving the calculated drift at axial failure (per Equation 3.20) once the shear strength has degraded to zero. The initial slope for the axial spring (i.e., the slope of the pre-failure backbone from Figure 4-11) was selected as 100 times stiffer than the axial stiffness of the column to ensure that no additional axial flexibility was introduced into the model. The degrading slope of the axial spring (K_{deg} from Figure 4-11) was selected as -90 kips/in. based on a linear approximation to test data from Specimen 2.

Rigid shear and axial springs, with negligible deformations under the anticipated loads, were included in the zero-length sections at the tops and bottoms of the outside columns and the bottom of the center column.

All three columns were modeled using nonlinear fiber beam-column elements with five sections defining the moment-axial load interaction. Based on the flexibility method, the beam-column elements determine the section forces (moment and axial load) from interpolation of the element end forces and integrate the resulting section deformations (curvatures and axial strains) over the length of the element to determine the element end deformations (rotations and axial lengthening). By capturing the moment-axial load interaction, the fiber elements are able to model the axial lengthening of the columns resulting from lateral displacements. The influence of large displacements on the column response is also incorporated in the element formulation. For a complete description of the nonlinear fiber beam-column elements refer to Spacone et al. (1996a and 1996b). For the development of the specific nonlinear beam-column element available in OpenSees, and used for the analyses described here, refer to Souza (2000).

Each nonlinear fiber beam-column element was composed of five sections located at Gauss-Lobatto integration points along the length of the element for optimum integration of the section deformations, while still providing the critical section forces and deformations at the ends of the element. The sections were subdivided into concrete and steel fibers. The cyclic response of the concrete material models used to define the behavior of the concrete fibers for the outside and center columns is shown in Figure 8-3. Two concrete models were used for the outside columns: one, based on the confined concrete strength of 7900 psi calculated according to Mander et al. (1988), was used to define the response of the confined core; while an unconfined concrete model, with a compressive strength equal to the test day cylinder strength of 3520 psi, was used to define

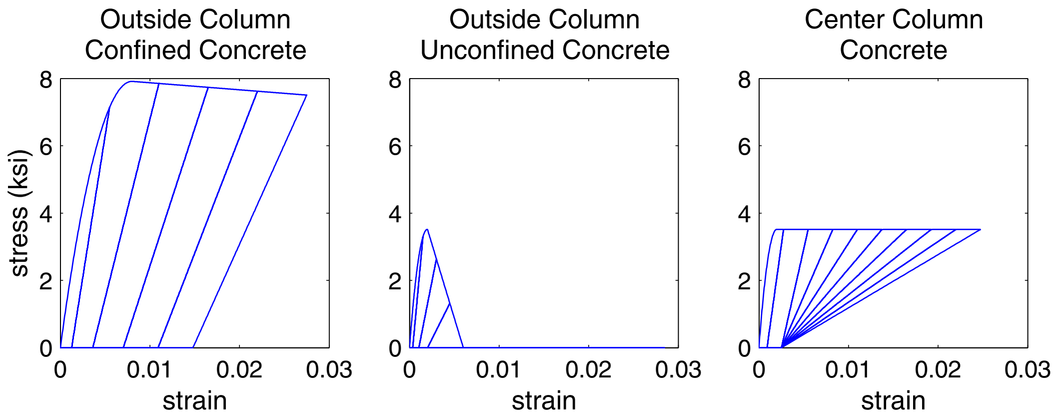

Figure 8-3. Concrete material models for fiber sections

the response of the cover concrete. As shown in Figure 8-3, the tensile capacity of the concrete was ignored.

As discussed in Section 4.5.1, for a column using the limit state failure model to define shear failure, computational issues require that the flexural response always maintains a positive slope prior to shear failure. Although the concrete for the center column could be considered unconfined due to the wide spacing of the transverse reinforcement, to avoid a negative slope in the flexural response, the selected concrete material model did not allow for strength degradation after reaching the unconfined concrete compressive strength of 3520 psi. The reinforcing steel material model for the center column used a strain-hardening modulus of $0.015E_s$ (where E_s = 29,000 ksi), approximately twice that observed in the coupon tests, to ensure that the P-delta effects did not result in a negative slope in the flexural response. Since strength degradation due to shear failure, modeled by the shear spring in the zero-length section, governed the strength degrading behavior of the center column, the altered concrete and steel material model did not significantly impact the calculated column response.

The steel material model has a significant impact on the calculated cyclic response of the column element. Three steel models available in OpenSees, and the associated moment-curvature response for the outside column section subjected to an axial load of 20 kips, are shown in Figure 8-4. Since the bilinear model does not capture the stiffness degradation observed even in well-confined reinforced concrete elements, this material model will not be used for the analyses presented in this chapter. The base model presented in Sections 8.3 and 8.4 uses the Clough-type hysteretic steel model for the outside and center columns. The influence of the choice of steel model on the response of the shake table specimens is discussed in Section 8.3.2.2.

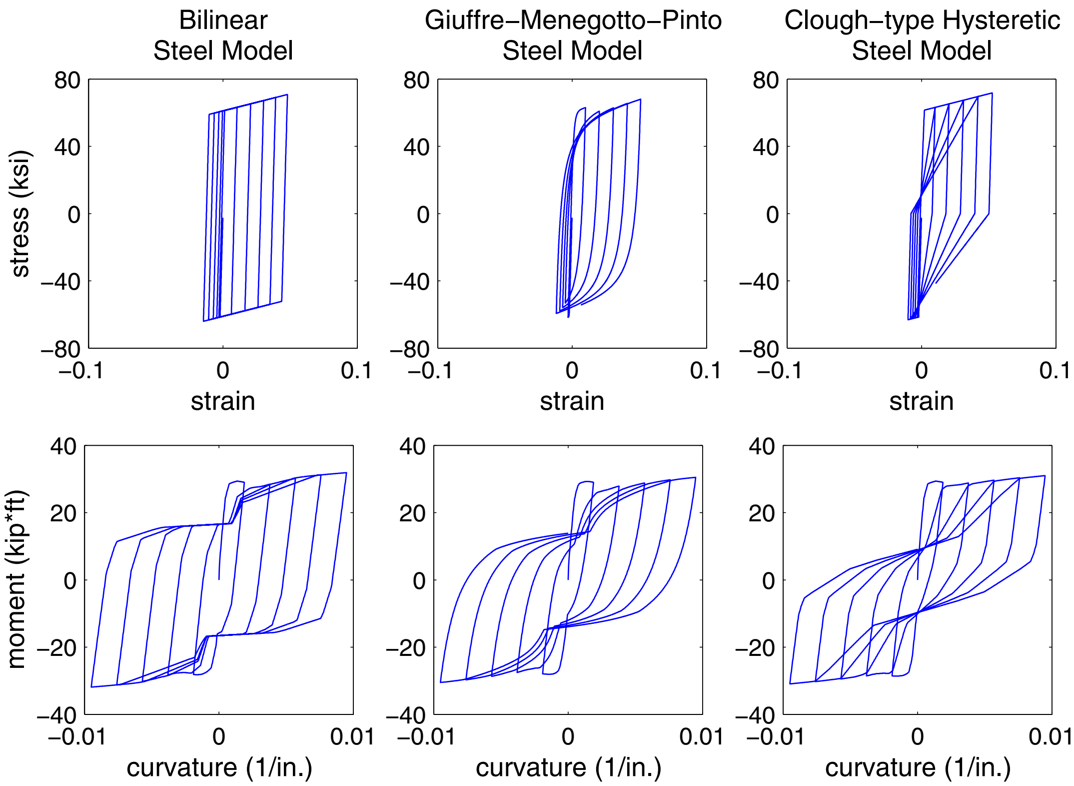

Figure 8-4. Steel material models and moment-curvature response for outside column fiber sections

8.2.3 Dead-Load Model

All of the mass was modeled at the center of the mass of the beam and lead packets (i.e., 6.75 inches above the beam soffit). The dead loads were distributed according to the measured weight of the lead and the calculated weight of the beam, and applied to the beam elements at the location of the shims supporting the lead packets (see Appendix B). For Specimen 2, both the horizontal and vertical components of the prestress force applied to the specimen by the pneumatic cylinders were applied to the beam node over the center column. The components of the prestress force were determined using the measured prestress load (see Figure B-9) and the measured displacement at the top of the center column. The maximum horizontal component of the prestress force was 1.6 kips.

The initial distribution of the gravity loads to the three columns, as determined by the model described above, resulted in a center column axial load that was higher than that recorded by the force transducers. The discrepancy was likely a result of the method used to support the dead load during casting of the hydrostone between the force transducers and the specimen. The specimen was supported on screw-jacks under each of the footings and stabilized by straps attached to the overhead crane, while the hydrostone was cast. Owing to the high stiffness of the beam, a slight discrepancy in the height of the screw jacks, or in the level of the footings, would result in a different dead-load distribution than determined by the analysis. To achieve agreement between the measured and calculated center column axial loads, the bottom nodes of the outside columns in the analytical model were “lifted” by 0.09 inches for Specimen 1 and 0.11 inches for Specimen 2, thereby shifting more gravity load to the outside columns. A more detailed description of the dead-load analysis and the resulting initial loads on the outside columns can be found in Section B.6.

8.3 STATIC ANALYSIS

Static nonlinear analyses are used increasingly by practicing engineers to evaluate the capacity of structures subjected to earthquakes; however, few analysis tools exist to include the influence of column shear and axial load failures. Static monotonic and cyclic analyses of the shake table specimens are presented in the following sections to demonstrate the capability of the center column model described in Section 8.2 to model shear and axial load failures, and the influence of the failures on the response of the shake table specimens.

8.3.1 Static Monotonic Analysis

The monotonic analysis results illustrate the behavior of the column elements under a simplified loading condition. The analyses were performed by linearly increasing a horizontal displacement imposed on the beam node above the center column, up to a maximum displacement of 5 inches (or a column drift of 8.6%). All other degrees of freedom (including the vertical and rotational degrees of freedom where the horizontal displacements were imposed) were free to move according to the response of the structure. A prestress force of 42 kips applied to the beam node above the center column was maintained throughout the analysis. The column axial loads were the same as those measured before the shake table test for Specimen 2.

The shear response of the center column is shown in Figure 8-5. The column drift has been decomposed into the flexural component, based on the horizontal displacements of the center column nonlinear fiber element (including the slip springs attached to the top and bottom of the element), and the shear component, based on the displacements of the shear spring in the zero-

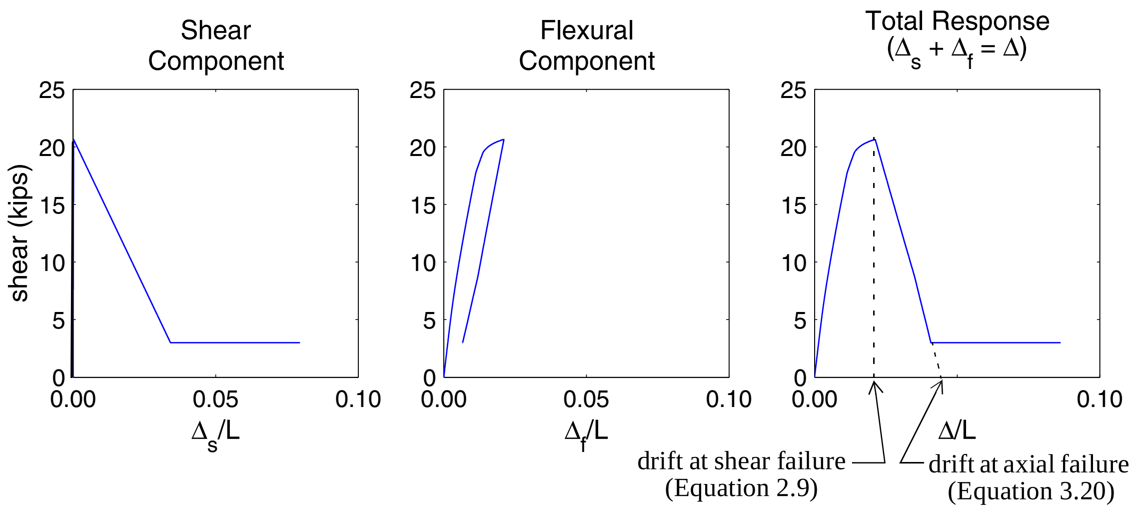

Figure 8-5. Shear response of center column during monotonic analysis

length section at the top of the center column element. As expected, before shear failure, the total response of the center column is dominated by the flexural (including slip) displacements. After the total response exceeds the calculated drift at shear failure, the capacity of the shear spring degrades such that the total drift, after full degradation of the center column strength, will be equal to the calculated drift at axial failure (Figure 8-5). The shear-strength degradation forces the fiber element to unload, resulting in a decrease in the flexural displacements and an increase in the shear displacements after shear failure. This response is consistent with the increase in the shear deformation component after shear failure that is observed in large-scale pseudo-static tests (Sezen, 2002; Lynn, 2001).

The shear response of the entire frame and of the outside columns are shown in Figure 8-6. The imposed displacements moved the beam toward the west, resulting in additional axial compression in the west column due to overturning moments. The slightly higher axial loads resulted in a higher yield strength for the west column as shown in Figure 8-6. The initial shear forces in the outside columns from the dead-load model resulted in the west column yielding at a lower drift compared with the east column.

A column supporting an axial load and subjected to transverse deformations producing curvatures along the length of the column, as shown in Figure 8-7, will experience axial lengthening due to the increase in the axial strain at the centroid of the section, ε_a. The nonlinear fiber elements are capable of capturing this axial lengthening experienced by reinforced concrete elements sub-

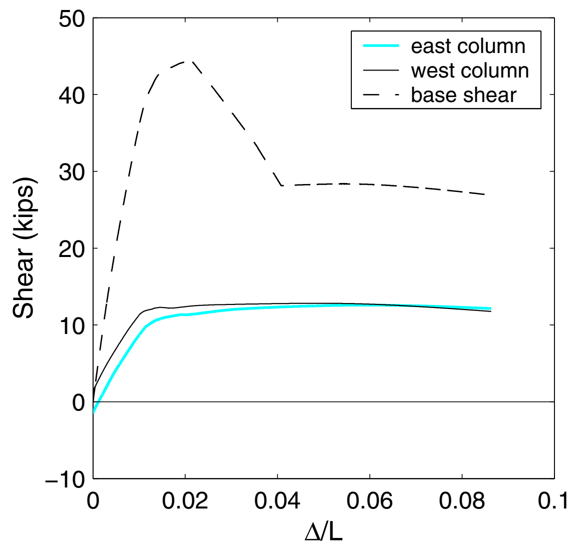

Figure 8-6. Shear response of outside columns and entire frame for monotonic analysis

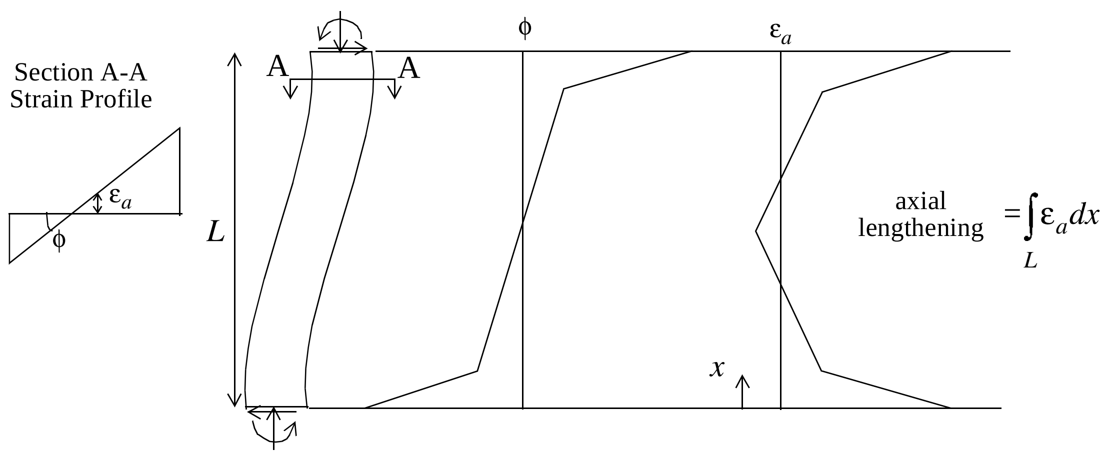

Figure 8-7. Axial lengthening due to applied transverse displacements

jected to transverse deformations. Additional axial lengthening due to cyclic deformations will be discussed in Section 8.3.2.

The vertical deformations experienced by the outside and center columns during the monotonic analysis are shown in Figure 8-8. Before shear failure of the center column at a drift ratio of 2.1%, all three columns experience axial lengthening. The higher transverse stiffness of the center column results in a slower increase in vertical displacements compared with the response of the outside columns. After shear failure, the center column flexural deformations (i.e., the curvatures) decrease, resulting in a decrease in ε_a, and therefore a decrease in the axial lengthening of the center column. At a drift of 5.2%, axial failure is detected by the axial spring attached in series with the

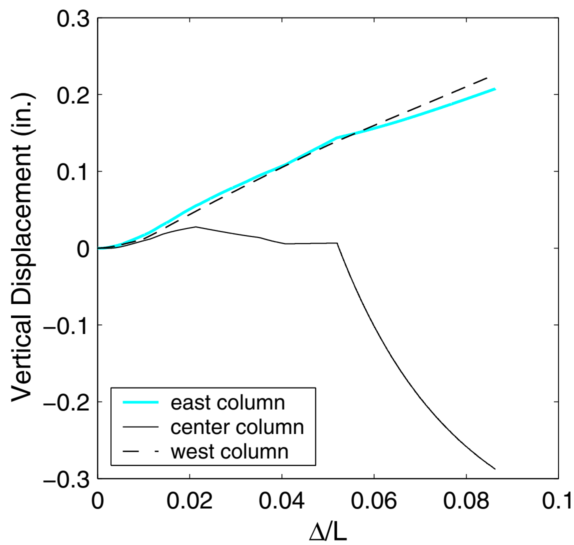

Figure 8-8. Column vertical displacements during monotonic analysis

center column fiber element, resulting in a sudden increase in the vertical displacements in the downward direction.

The column axial load response during the monotonic analysis is shown in Figure 8-9. Initially, overturning moments cause a decrease in the east column and an increase in the west column axial loads. As the west column yields before the east column, the shear in the west beam drops relative to the shear in the east beam, resulting in a slight increase in the center column axial load at a drift ratio of 1%. As noted in Figure 8-8, upon shear failure of the center column ($\Delta/L = 2.1\%$), the vertical displacements of the outside and center columns begin to diverge. The difference between the vertical displacements results in bending of the beam, and in turn, transfer of gravity load from the center column to the outside columns even before axial failure of the center column. Hence, the decrease in the center column axial load from a drift ratio of 2.1% to 5.2% can be attributed to the stiffness of the beam in bending as the center column shortens and the outside columns lengthen. As shown in Figure 8-9, at a drift ratio of 5.2% the center column response intersects the axial limit curve defined by Equation 3.20 and axial failure of the center column is initiated. According to the shear-axial coupling model described in Section 4.5.3, once axial failure is detected, the axial load-lateral drift response remains on the limit curve, thereby forcing the redistribution of the gravity loads to the outside columns with continued lateral drift.

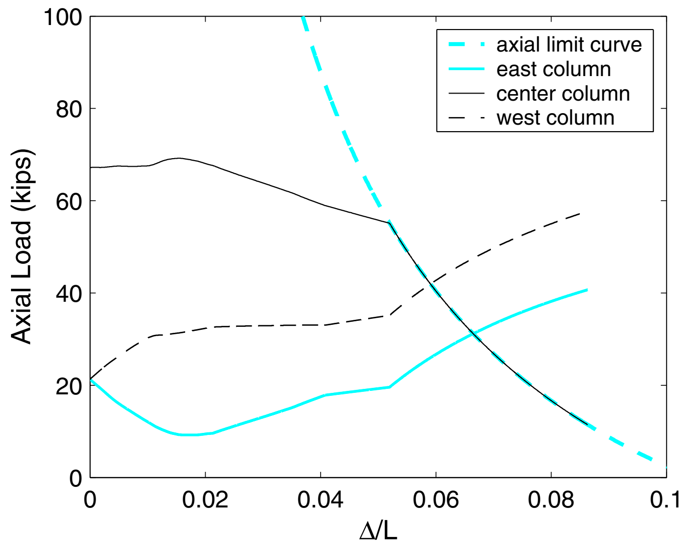

Figure 8-9. Column axial load response during monotonic analysis

8.3.2 Static Cyclic Analysis

Static cyclic analyses were performed by applying the recorded longitudinal displacements for both specimens (second plot in Figure 6-5) to the beam node at the top of the center column. Such analyses are similar to those performed to validate analytical models using static test data (e.g., Pincheira et al., 1999). The results demonstrate the capability of the analytical model to reproduce the hysteretic behavior observed during the test. As will be demonstrated in Section 8.4, close agreement between the static analysis results and the recorded response may not necessarily result in sufficiently accurate dynamic analysis results.

8.3.2.1 Shear Response — Center Column

Figure 8-10 compares the results from the static cyclic analysis with the measured shear hysteretic response for the center columns of both specimens. Recall that the empirical drift capacity model at shear failure (Equation 2.9) was used to initiate the shear-strength degradation clearly seen in the calculated center column response for both specimens, and that the degrading slope of the calculated shear response was determined based on achieving the drift at axial failure (Equation 3.20) after full degradation of the shear strength.

The analytical model adequately represents the measured response in terms of the initial and degraded column stiffness. Prior to shear failure, stiffness degradation results from the hyster-

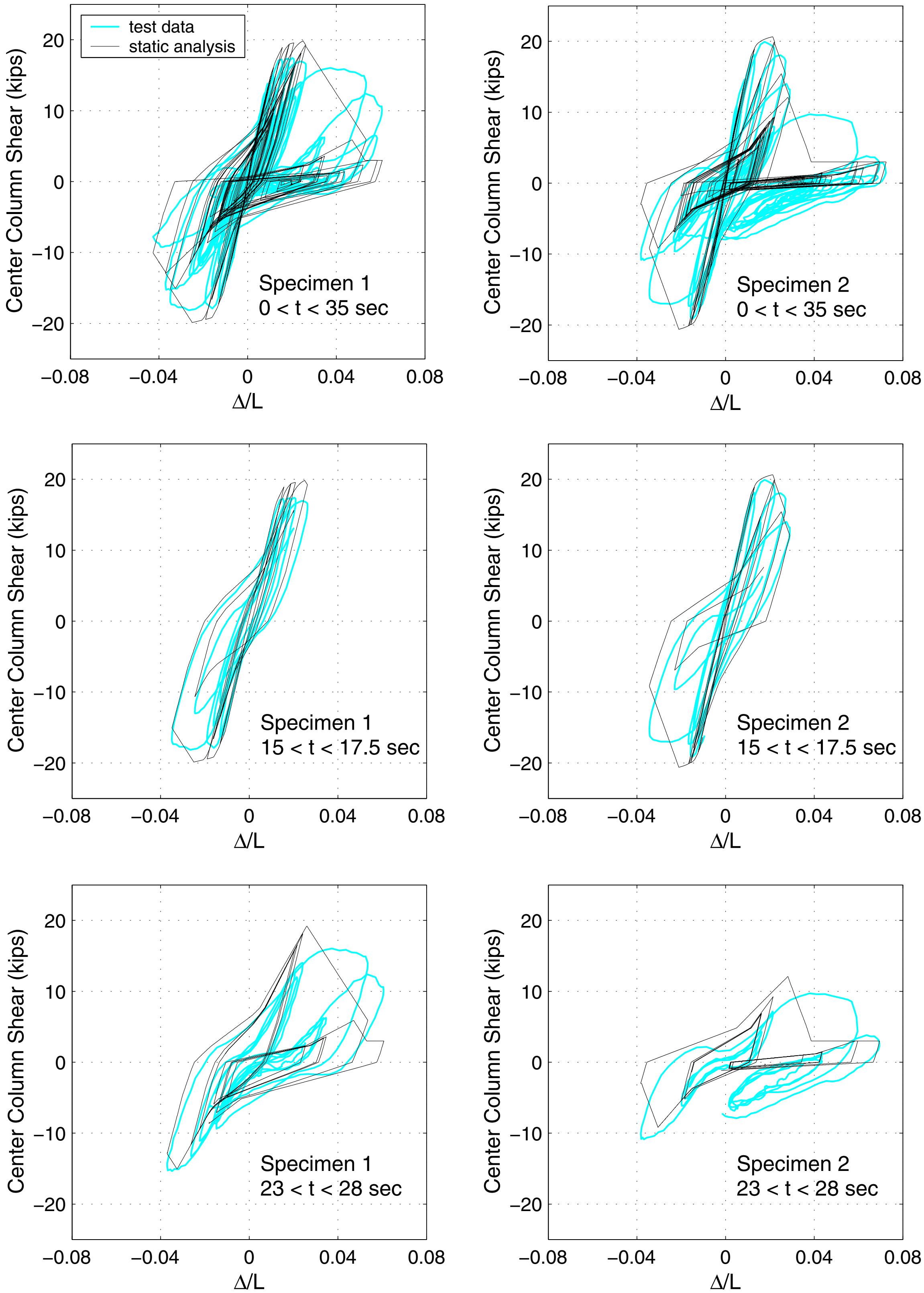

Figure 8-10. Center column shear hysteretic response using static cyclic analysis

etic behavior of the concrete and steel models used to define the fiber element sections (Figures 8-3 and 8-4) and the flexural response of the fiber element. After shear failure, the shear deformations modeled by the shear spring dominate the response of the analytical model (Figure 8-11). The pinched hysteretic response of the shear spring material model provides the additional stiffness degradation observed after shear failure.

The fiber element, with the selected material properties, overestimates the flexural strength for Specimen 1 (with $P = 0.10A_g f_c'$), but adequately reproduces that observed for Specimen 2 (with $P = 0.24A_g f_c'$). The apparent overestimation of the flexural strength for Specimen 1 is partially a result of the high strain-hardening for the steel model and the lack of concrete strength degradation used to avoid a strength-degrading flexural response before shear failure (see Section 8.2.2).

For Specimen 1, the analytical model detects that shear strength degradation begins during a negative displacement cycle at a drift ratio of -2.5%, while for Specimen 2, shear strength degradation is first detected during a positive displacement cycle at a drift ratio of 2.1%. This response is consistent with the observed behavior for both specimens.

The bottom plots in Figure 8-10 indicate that the measured shear strength degradation did not occur as rapidly as indicated by the analytical results. In particular, the measured shears for both specimens beyond a drift ratio of 4% for the large positive displacement cycles at 25 seconds are as much as twice those estimated by the analysis. Regardless of overestimating the rate of shear strength degradation, the model adequately represents the near-complete loss of shear strength after 28 seconds for Specimen 1 and 25 seconds for Specimen 2.

As shown in the lower right plot of Figure 8-10, the negative shear forces measured during the final cycles for Specimen 2 are not captured by the analytical model. These shear forces result from the lateral deformation of the center column, as shown in Figure 6-21b, resulting from axial failure. The analytical model does not attempt to represent such effects.

In Figure 8-11, the response of the analytical model from 15 to 17.5 seconds is decomposed into the shear and flexural (including slip) deformation components. Although the flexural deformations estimated by the model are similar for the two specimens, the estimated shear deformations for Specimen 2 are considerably greater than those for Specimen 1. The larger shear deformations result in the greater loss of shear strength for Specimen 2 during the cycles shown in

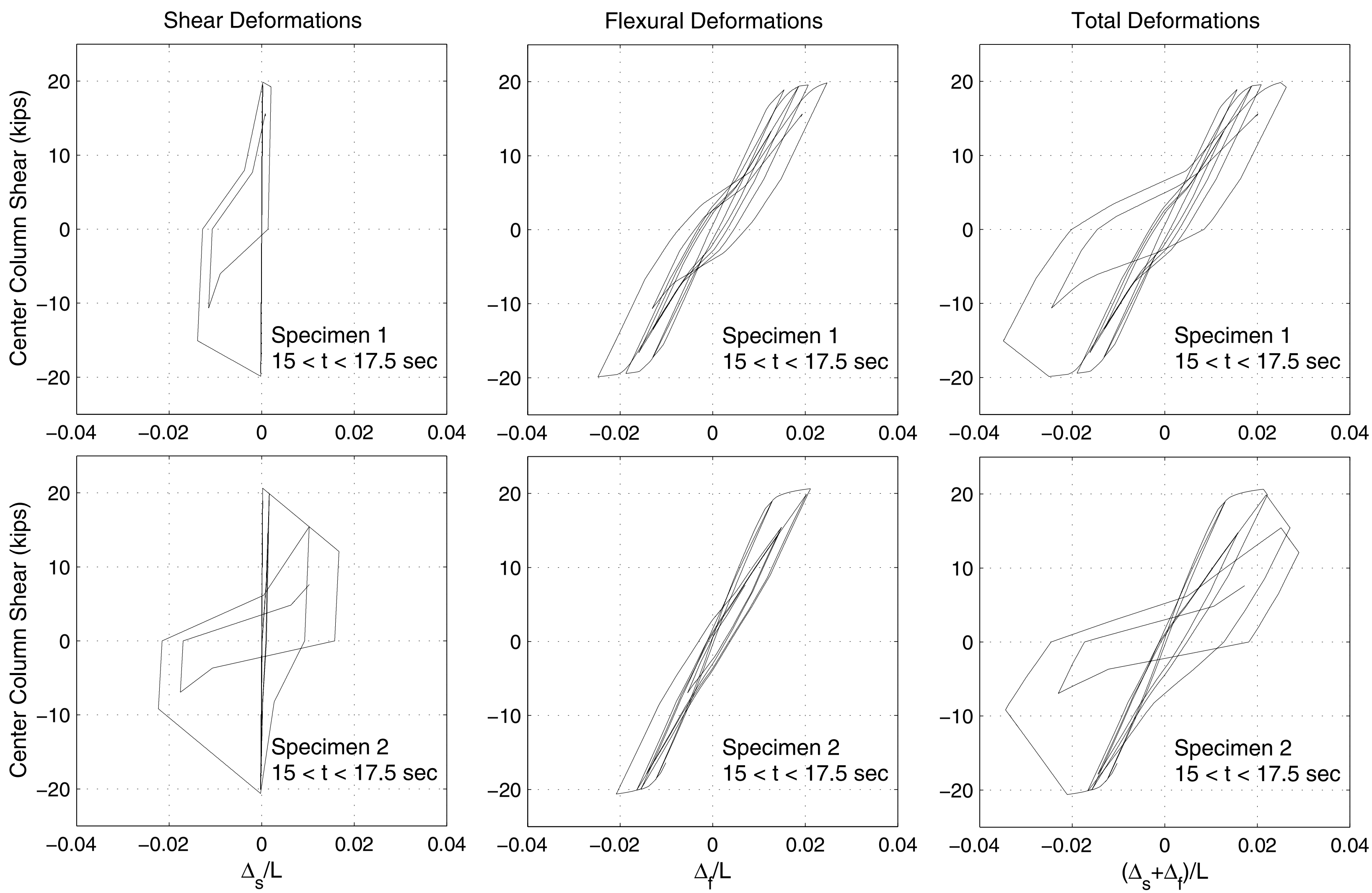

Figure 8-11. Shear and flexural deformations for the center column model (static cyclic analysis)

Figure 8-11. The earlier influence of shear deformations and loss of shear strength for Specimen 2 is one of the fundamental differences between the observed response of the two specimens.

8.3.2.2 Shear Response — Outside Columns

The shear hysteretic response for the outside columns is shown in Figures 8-12 and 8-13. Since the initial shear forces acting on the outside columns could not be measured before the tests, the reactions from the dead-load model were used to determine the initial shear forces for the test data shown in Figures 8-12 and 8-13 (see Section B.6 for more details). The model adequately represents the stiffness and flexural strength of the columns for cycles in which the overturning forces reduce the axial compression acting on the column (i.e., positive displacement cycles for the east column and negative displacement cycles for the west column). In contrast, the model underestimates the stiffness and flexural strength for cycles in which the overturning forces increase the axial compression acting on the outside columns (i.e., negative displacement cycles for the east column and positive displacement cycles for the west column).

The measured yield strength during compression cycles is approximately 35% higher than the measured yield strength during tension cycles. Considering that the axial load on the outside columns remains well below the balance point, an increase in strength and stiffness due to higher compression is expected. This effect is accounted for by the fiber beam-column elements, and results in approximately a 15% increase in the yield strength for the compression cycles compared with the tension cycles as indicated by the static analysis results shown in Figures 8-12 and 8-13. A high strain rate can also cause an increase in strength; however, the strain rate should influence the strength for both tension and compression cycles, and therefore does not explain the observed discrepancy. Notwithstanding any errors in the measured shears due to cross talk with the axial load channels (not anticipated due to the close agreement between the base shear and inertial forces shown in Figure 6-5), the considerably higher measured yield strength for the compression cycles compared with the tension cycles shown in Figures 8-12 and 8-13 is likely a result of an inaccurate estimate of the initial shear forces acting on the outside columns based on the dead-load model.

The hysteresis loops from the static analysis shown in Figures 8-12 and 8-13 are more pinched than the hysteresis loops from the test data. Most of the pinching captured by the fiber beam-column elements can be attributed to the pinching characteristics of the steel material model

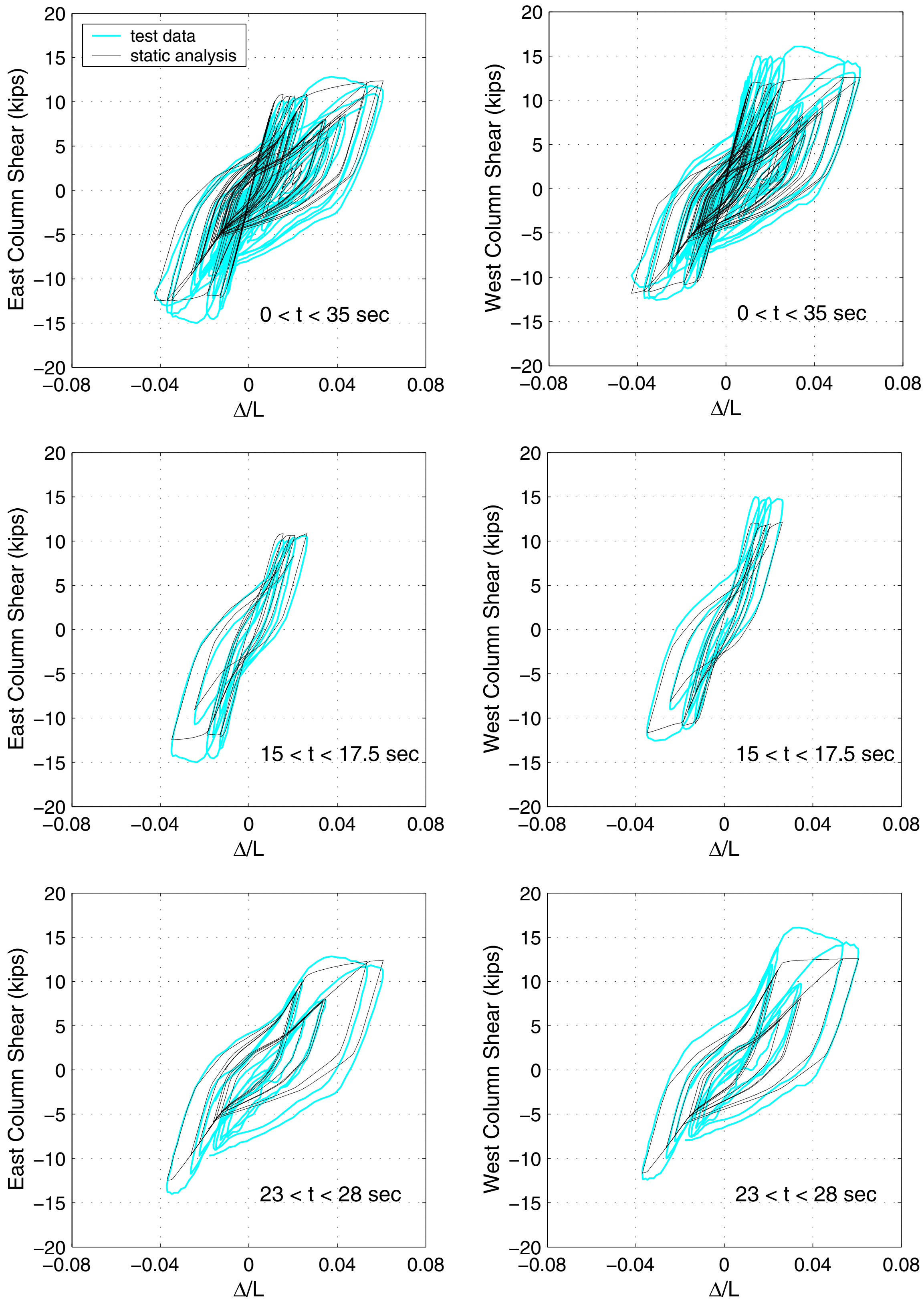

Figure 8-12. Specimen 1 outside column shear hysteretic response from static cyclic analysis

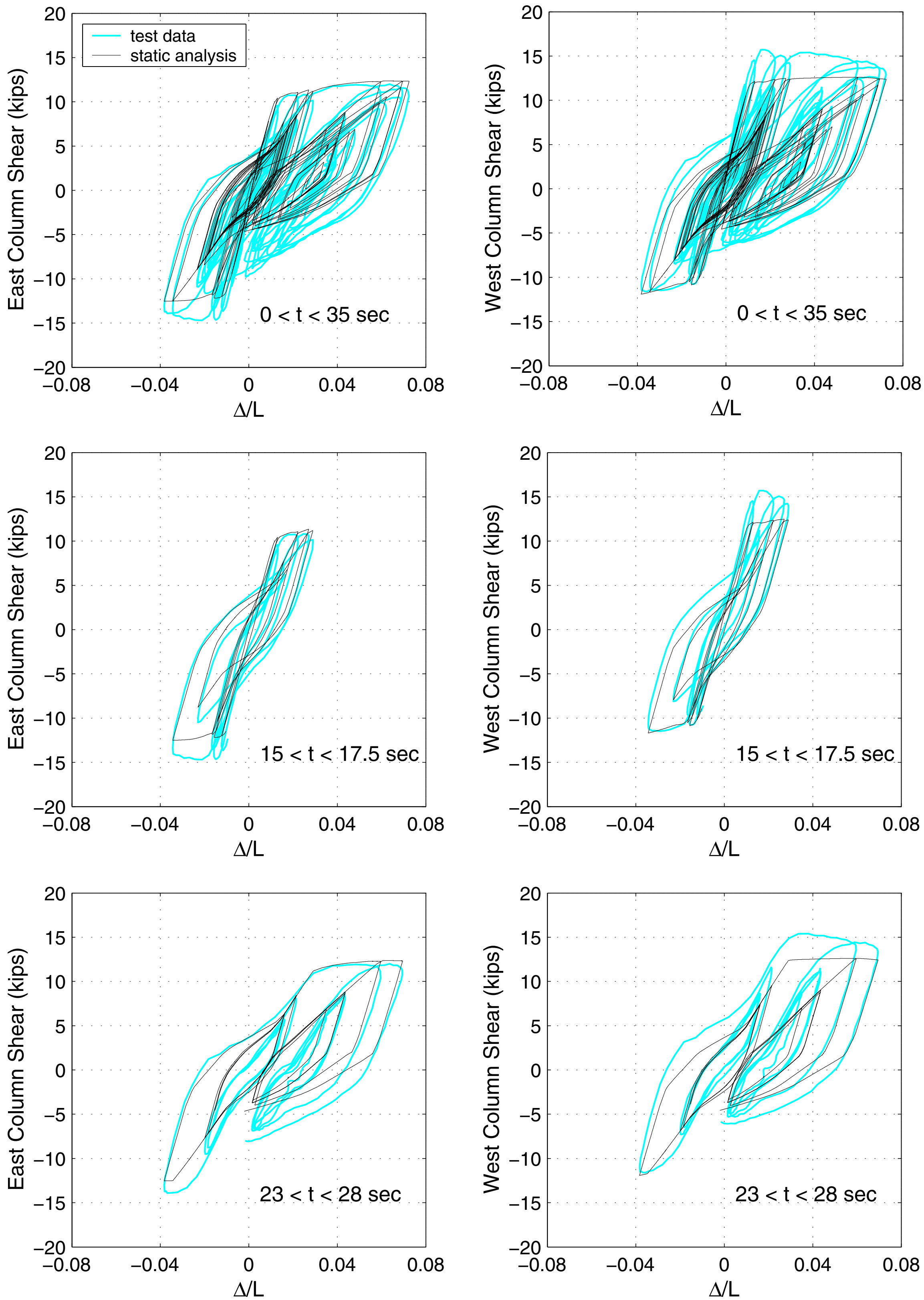

Figure 8-13. Specimen 2 outside column shear hysteretic response from static cyclic analysis

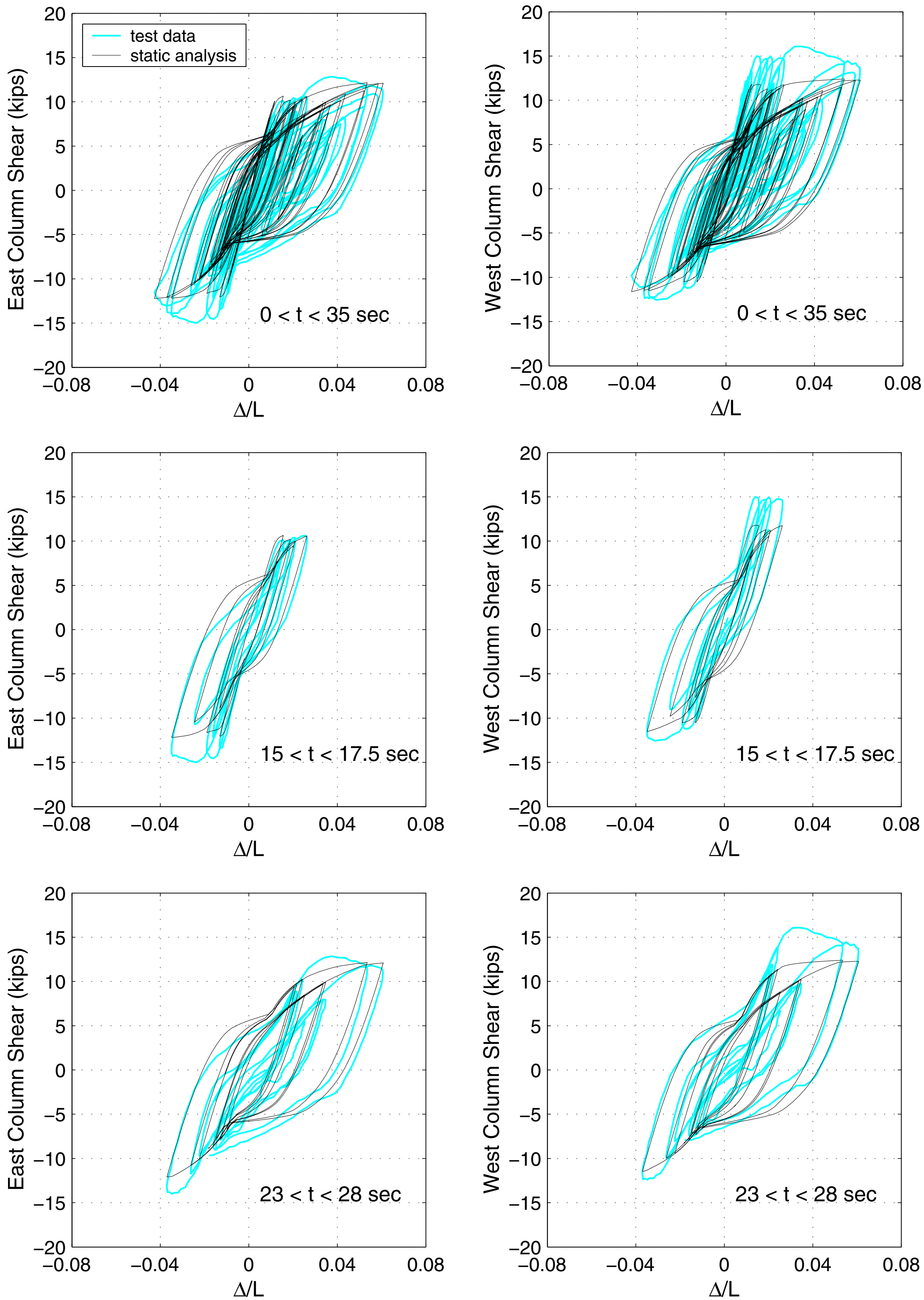

Figure 8-14. Specimen 1 outside column shear hysteretic response from static cyclic analysis using Giuffre-Menegotto-Pinto steel material model

used for the reinforcing bars. As shown in Figure 8-4, the Giuffre-Menegotto-Pinto (GMP) steel model results in less pinching than the Clough-type hysteretic steel model used for the analysis shown in Figures 8-12 and 8-13. The response of the Specimen 1 outside columns using the GMP steel model is shown in Figure 8-14. Although the envelope of response is better estimated by using the GMP steel model, the Clough-type hysteretic steel model provides a better estimate of the stiffness for the smaller cycles. Based on comparing the results using the two steel models for the significant cycles from 15 to 17.5 seconds and 23 to 28 seconds, it was concluded that the hysteretic steel model provided a better estimate of the measured response.

8.3.2.3 Axial Response

The axial response of the shake table specimen was influenced by three primary factors: the axial lengthening of the outside columns, the initial axial lengthening and subsequent axial shortening of the center column, and the bending of the beam resulting from the change in the column lengths. Although the nonlinear response of the beam cannot be included in the static analysis (see Section 8.2.1), the analytical model does incorporate the mechanisms leading to column lengthening and shortening. The monotonic analysis, discussed in Section 8.3.1, demonstrated the lengthening of the outside columns associated with increasing lateral displacement, and the shortening of the center column relative to the outside columns beginning at the point of shear failure and increasing rapidly at the point of axial failure (Figure 8-8). Since Specimen 1 did not experience axial failure of the center column, only the vertical response of Specimen 2 will be considered here.

Figure 8-15 shows the vertical lengthening of the outside columns resulting from the lateral displacements measured during the shake table test. Although the estimate of the vertical displacements provided by the fiber beam-column elements is in better agreement with the test data for compression cycles compared with tension cycles, both are sufficiently accurate given other uncertainties in the model. The cyclic response results in additional axial lengthening of the columns not seen in the monotonic analysis. After reaching a peak in lateral (and vertical) displacement resulting in yielding of the tension reinforcement, and upon unloading, the flexural demands on the column sections will reduce and the reinforcing steel will unload with approximately its elastic stiffness. The steep, nearly-elastic response during unloading will result in less shortening of the reinforcement compared with the lengthening of the reinforcement experienced during yielding,

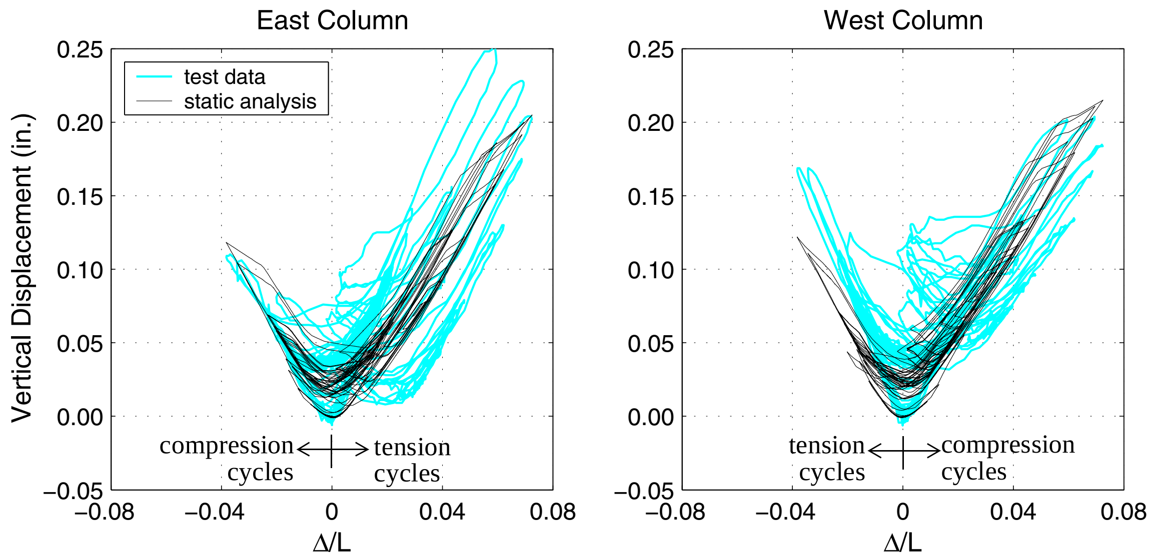

Figure 8-15. Coupling of horizontal and vertical displacements at top of outside columns for Specimen 2

which will in turn lead to limited axial shortening of the column during unloading until the reinforcement reloads in compression. This response results in the flatter slope observed at the peaks in displacement for the calculated vertical versus lateral displacement plots shown in Figure 8-15.

The vertical displacements and axial load response for the center column is shown in Figures 8-16 through 8-18. Similar to the monotonic analysis, the center column lengthens with increasing lateral displacement prior to shear failure. After shear failure but before axial failure, the influence of the lateral displacements on the calculated vertical response diminishes as the shear demand on the center column drops. The analytical model does not capture the 0.02 inches of downward vertical displacement accompanying shear failure (at 17 sec) as seen in the test data shown in the right-hand plot of Figure 8-16.

After axial failure is detected, the vertical displacements at the center column increase rapidly in the downward direction. As shown in Figure 8-17, the downward vertical displacements given by the analytical model only increase, while the calculated response follows the axial limit curve. Although the analytical model captures some of the general characteristics of the measured axial load-vertical displacement response for the center column (left-hand plot of Figure 8-17) and correctly determines the timing of the first increase in downward vertical displacements (bottom plot of Figure 8-18), the model underestimates the increase in vertical displacements, in part due

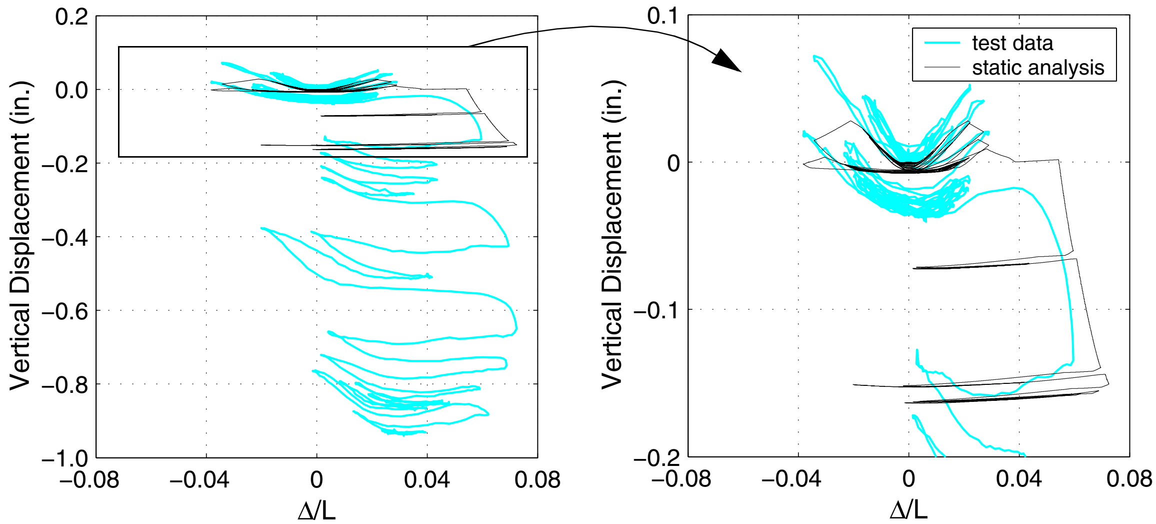

Figure 8-16. Coupling of horizontal and vertical displacements at the Specimen 2 center column

to the position of the axial limit curve. The influence of the position of the axial limit curve will be discussed in more detail below.

Similar to the monotonic analysis, Figure 8-17 shows that the axial load in the center column decreases with increasing lateral displacement due to the difference in the vertical displacements at the center and outside columns and the accompanying bending of the beam. Since the slight downward movement of the beam at shear failure of the center column (at 17 sec) is not captured by the analytical model, the accompanying 7 kip drop in the center column axial load is also not observed in the calculated results. Once the calculated results intersect the axial failure limit curve, according to the shear-axial coupling model described in Section 4.5.3, the axial load in the center column is forced to follow the limit curve until the direction of motion reverses and the column begins to pick up load again as the outside columns shorten with decreasing lateral displacement. The analytical results indicate a minimum axial load of 24 kips, compared with a measured minimum axial load of 10 kips. Although underestimating the total axial load lost, the analytical model reproduces many of the critical characteristics of the center column axial load response history, as shown in Figure 8-18.

As noted in Chapter 3, there is considerable uncertainty in the estimation of the axial limit curve defining axial failure of the center column. Based on the database from Chapter 3, the standard deviation for the axial failure model, σ_a, is equivalent to a drift ratio of 0.5% (the subscript *a*

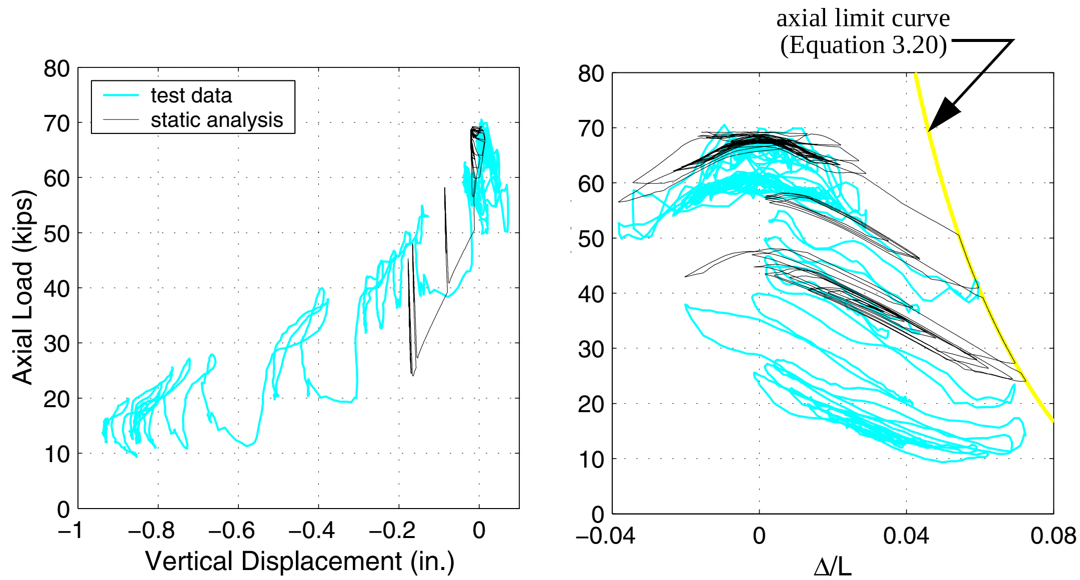

Figure 8-17. Variation of Specimen 2 center column axial load with vertical displacement and drift ratio

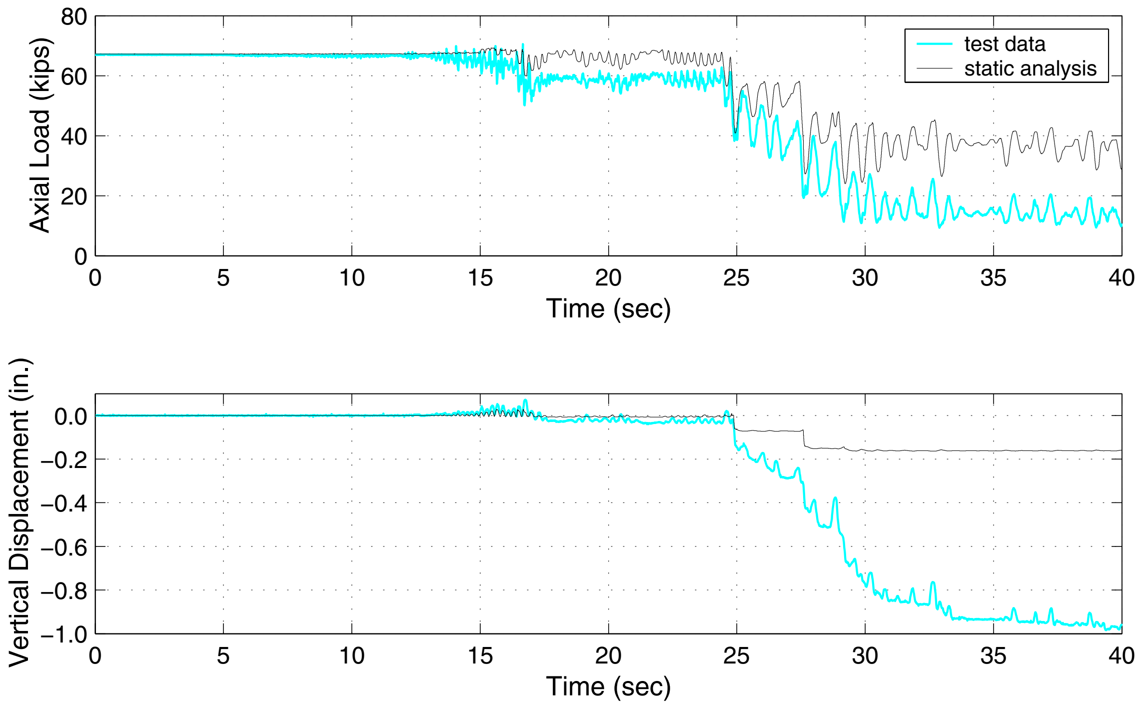

Figure 8-18. Axial load and vertical displacement response histories for Specimen 2 center column

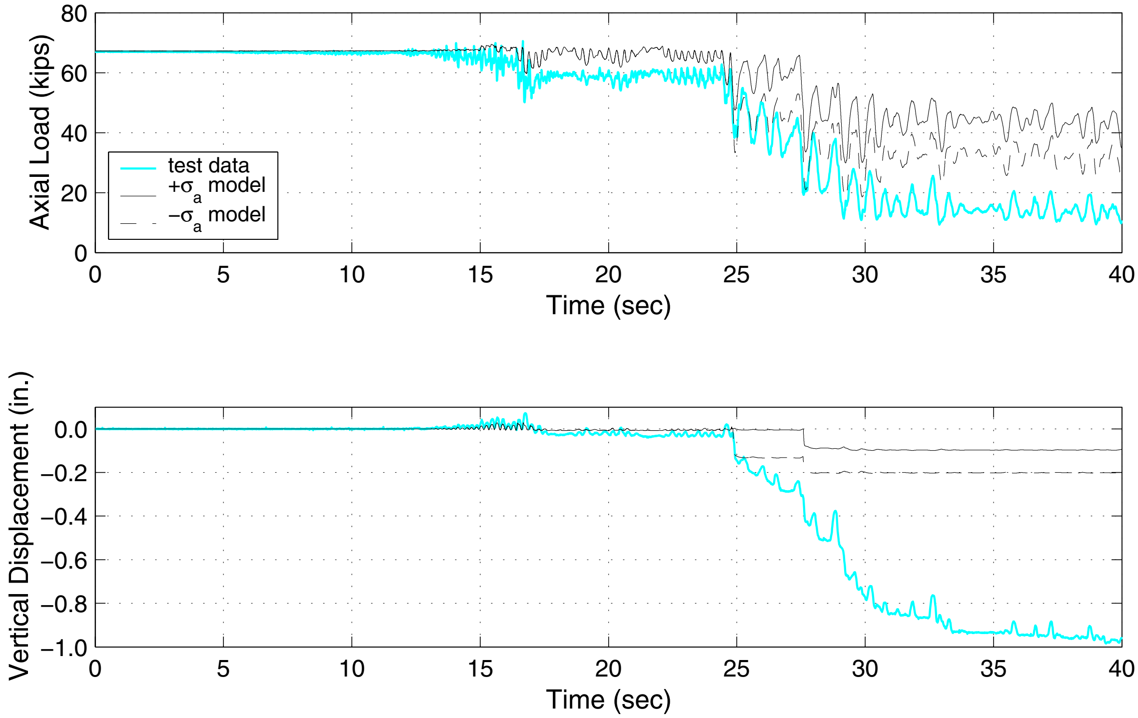

Figure 8-19. Calculated axial response for the center column for the +/- σ_a models

denoting the standard deviation of the drift at *axial* failure). Figure 8-19 shows the calculated axial load response for the center column using an axial limit curve based on Equation 3.20 plus σ_a, and minus σ_a (referred to as the $+\sigma_a$ model and $-\sigma_a$ model, respectively). The $+\sigma_a$ model estimates a minimum axial load of 30 kips and a vertical displacement of 0.10 inches, while the $-\sigma_a$ model estimates a minimum axial load of 18 kips and a vertical displacement of 0.20 inches. The difference in the axial load results illustrates the importance of accounting for the uncertainty in the position of the axial limit curve. The vertical displacements for the $-\sigma_a$ model are still well below those observed during the test (maximum of -1.0 inches). The difference between the calculated and measured vertical displacements and axial loads suggests that the assumed coupling model between axial load and lateral drift described in Section 4.5.3 may underestimate the rate at which the axial load is lost with increasing lateral drift. The discrepancy is also likely a result of not accounting for the axial load lost (and therefore the increasing vertical displacements) due to repeated lateral cycles, after the initiation of axial failure, causing a “grinding down” of the shear failure plane. Note that the calculated minimum center column axial load was not sufficient to cause yielding of the beam; hence the linear beam model used for the static analyses did not impact the results shown in Figure 8-19. The significant increase in the vertical displacements after beam yielding will be illustrated in Section 8.4.1.

8.4 DYNAMIC ANALYSIS

Dynamic analyses of the shake table specimens were conducted using the same model used for the static analyses described in the previous section. The analytical models for the two specimens varied only by the applied prestress load on the center column and the slight increase in mass due to the prestressing equipment for Specimen 2. Regardless of these differences, the calculated fundamental periods for both specimens were the same, 0.30 seconds. The calculated fundamental period is the same as the period measured just prior to the shake table test for Specimen 1, but overestimates the measured period of 0.25 seconds for Specimen 2 (see Figures 6-1 and 6-2).

By using mass-proportional damping, the equivalent viscous damping was set at 2% of critical for the fundamental mode of the frame. Stiffness-proportional damping could not be used in this model because the sudden change in response at shear and axial failure of the zero-length springs resulted in a large increase in velocity and, hence, unrealistically large damping forces at the node connecting the springs to the beam-column element. Since no mass was modeled at this node, the increase in velocity did not influence the mass-proportional damping forces.

The mass matrix included lumped masses for each of the horizontal and vertical degrees of freedom at the beam nodes, m_x and m_y, respectively. Rigidly connecting the m_y masses to the beam nodes resulted in high-frequency (25 Hz) beam oscillations after the sudden shortening of the center column due to shear failure. The beam oscillations led to vertical inertial forces and fluctuations in the center column axial loads. Such high-frequency oscillations were not observed in the test data shown in Figure 6-14. To avoid the spurious axial load oscillations the m_y masses were isolated from the beam by soft vertical springs, as illustrated in Figure 8-20. For the recorded table motion analyses, the stiffness of the spring, k, was selected as 1.5 kips/in. such that the minimum period of the vertical mass-spring system at each beam node was longer than the period of the beam vertical displacements resulting from the lengthening and shortening of the fiber column elements. For the pulse motion analysis described in the next section, a higher spring stiffness of 10 kips/in. could be used, since the beam does not oscillate during the short duration of the analysis. The stiffer spring permitted the development of the vertical inertial forces necessary for nodal equilibrium in the event of beam yielding (Figure 8-2).

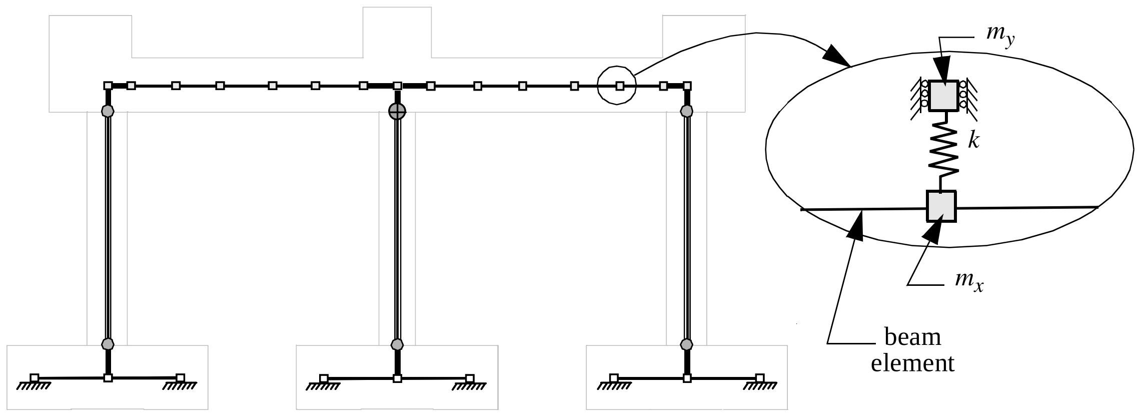

Figure 8-20. Isolation of vertical mass

8.4.1 Pulse Input Motion

The analytical model for Specimen 2 was subjected to the horizontal ground acceleration shown in Figure 8-21. The response to this pulse motion, shown in Figure 8-22, demonstrates the key stages of behavior, including column yielding, shear failure, axial failure, and beam yielding. Although the maximum drifts from the analysis are larger than those experienced by the shake table specimens, the pulse motion illustrates the process by which the analytical model will shed nearly all gravity load supported by the center column to the outside columns.

Similar to the monotonic analysis results from Section 8.3.1, the west column yields first, leading to a slight increase in the center column axial load. Shear failure of the center column is detected at a drift of 2.1% as defined by the empirical drift capacity model from Section 2.3.5. After shear failure, the vertical displacements at the center column begin to drop off, while the out-

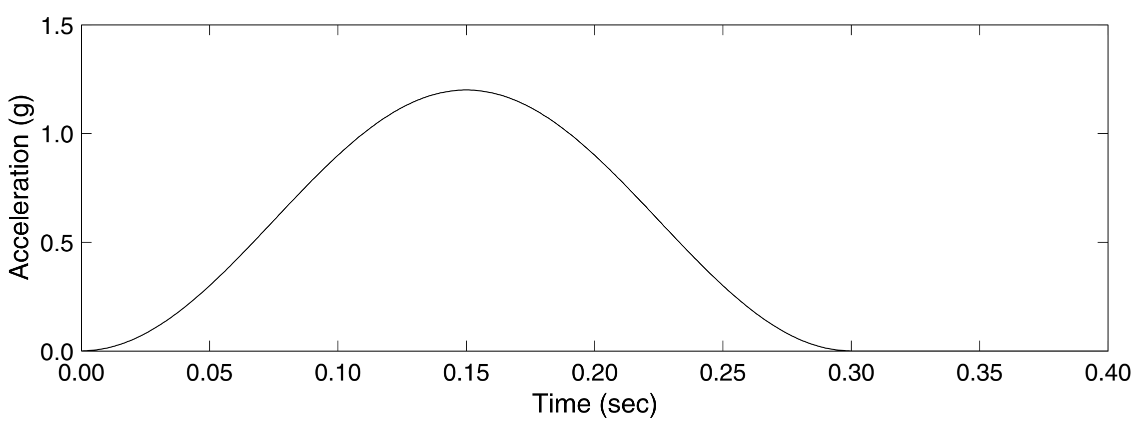

Figure 8-21. Pulse input motion

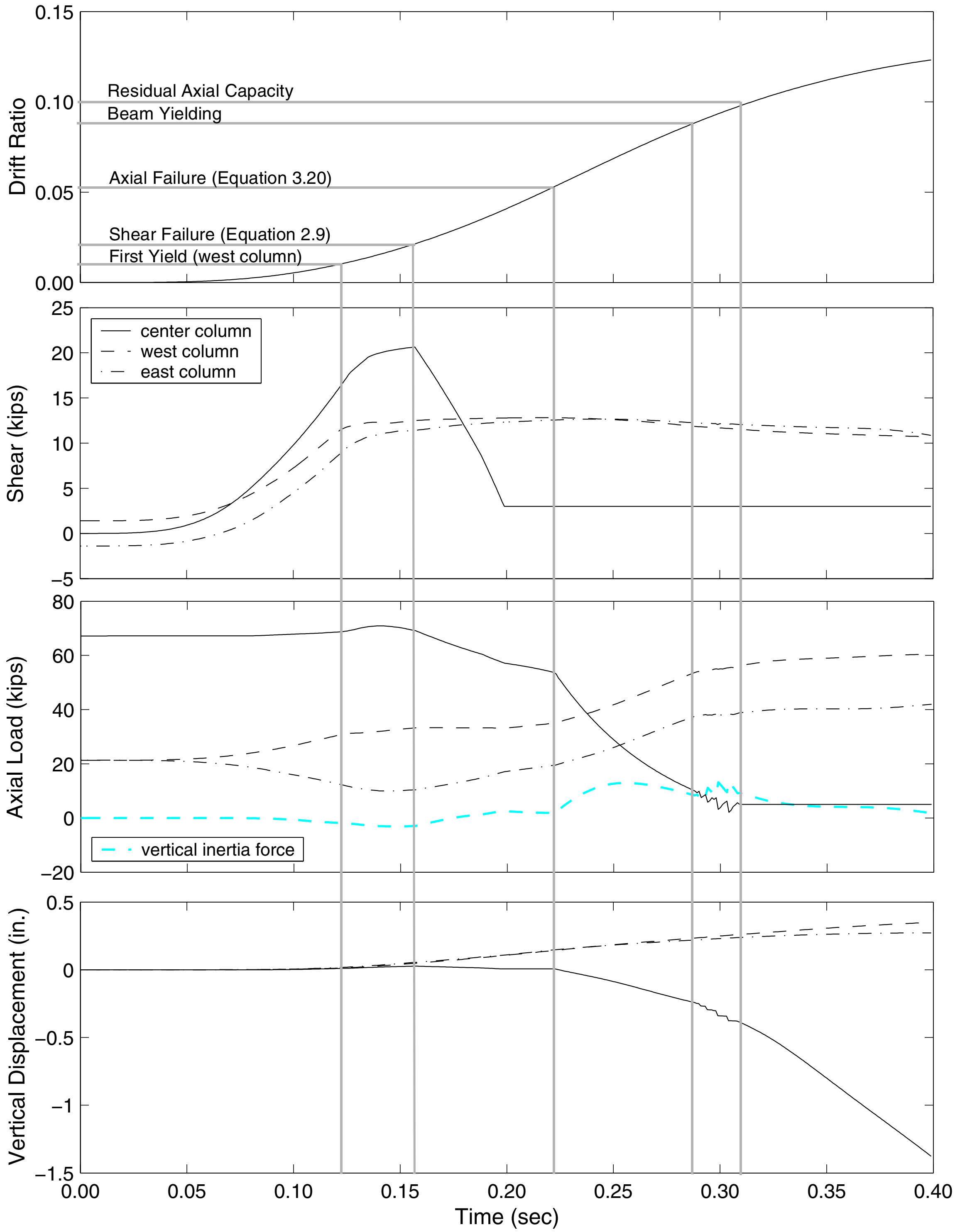

Figure 8-22. Response due to pulse input motion

side columns continue to lengthen with increasing lateral drift. The difference in the vertical displacements causes bending of the beam and a reduction of the axial load on the center column.

The axial failure of the center column is detected at a drift of 5.2% as defined by the axial failure model of Section 3.3.6. Axial failure has very little influence on the shear demand, since the outside columns have yielded and the center column shear has been reduced to its residual capacity. After axial failure is detected, the center column axial load response is forced to follow the axial limit curve defined by the Equation 3.20. The sudden drop of the beam with the axial failure of the center column results in an increase in vertical accelerations and vertical inertial forces distributed along the beam.

At a drift of 9.0% the beam yields in positive bending at the face of the transverse beam above the center column. Yielding of the beam results in a sudden increase in vertical displacements, and therefore a sudden drop in the axial load in the center column. The change in the axial load causes the response of the center column to drop below the axial limit curve. As described in Section 4.5.3, the stiffness of the axial spring is redefined after each converged step if the response crosses the axial limit curve. This procedure results in the jagged appearance of the center column axial load and vertical displacement response histories immediately following the yielding of the beam.

At a drift of 9.5% the center column reaches the preselected residual axial load capacity of 5 kips. Owing to yielding of the beam, the vertical displacements at the center and outside columns diverge rapidly with little change in the column axial loads. At this stage the structure is unstable without strain hardening in the beam response, or a change in the ground motion causing a reversal in the horizontal displacements.

Note that the analytical model overestimates the drift required to cause yielding of the beam by approximately 2%. The higher estimate is due to the assumption that the axial response of the center column must follow the axial limit curve after axial failure is detected. In part owing to the influence of repeated cycles, the measured center column axial load drops off more rapidly with increasing drift than the axial limit curve would suggest (see Figure 8-17).

8.4.2 Recorded Table Input Motion — Specimen 1

The analytical model for the shake table specimen was subjected to the unidirectional horizontal table acceleration recorded during the shear failure test for Specimen 1 (Figure 6-5). Although slight pitching of the table was recorded, analyses using the recorded table displacements and rotations confirmed that this did not significantly influence the response of the specimens, and hence, was not included in the analyses presented here. The test data and the response of the analytical model are compared in Figures 8-23 through 8-26**.** For a closer look at the critical period of response, the response histories shown in Figure 8-23 show only the data from 5 to 35 seconds.

There is poor agreement between the analytical model response and the test results before approximately 13 seconds. The analysis is slightly out-of-phase with the test results, suggesting that the analytical model does not capture the lengthening of the natural period of response of the specimen due to cracking of the columns. The recorded shears and displacements are significantly underestimated by the analysis between 10 and 13 seconds. (Recall that this same difference is observed when comparing the response of Specimen 1 to that of Specimen 2.) This result might be expected, since the period of the analytical model (0.30 sec) falls at a “valley” in the jagged response spectrum, while the apparent period of the specimen based on the measured response between 10 and 13 seconds (0.35 sec) falls close to a “peak” (see Figure 5-8). Note that the apparent period of the specimen from the measured response is longer than the period based on the free-vibration test.

Despite the lack of agreement early in the response histories, the analytical model provides a reasonable estimate during the critical periods of response. As observed during the test, the analytical model detects shear failure of the center column, but not axial failure. Shear failure is first detected, and shear strength degradation begins, during a negative displacement cycle at approximately 17 seconds. The initial shear strength degradation decreases the stiffness of the center column in the analytical model, resulting in a close agreement between the predominant period of response in the analytical model and that of the test data. The analytical model accurately identifies that the positive displacement pulse at 25 seconds causes significant shear damage to the center column, although the loss of shear strength during the pulse is overestimated. The analytical model, however, does not capture the complete shear strength degradation observed during the test, result-

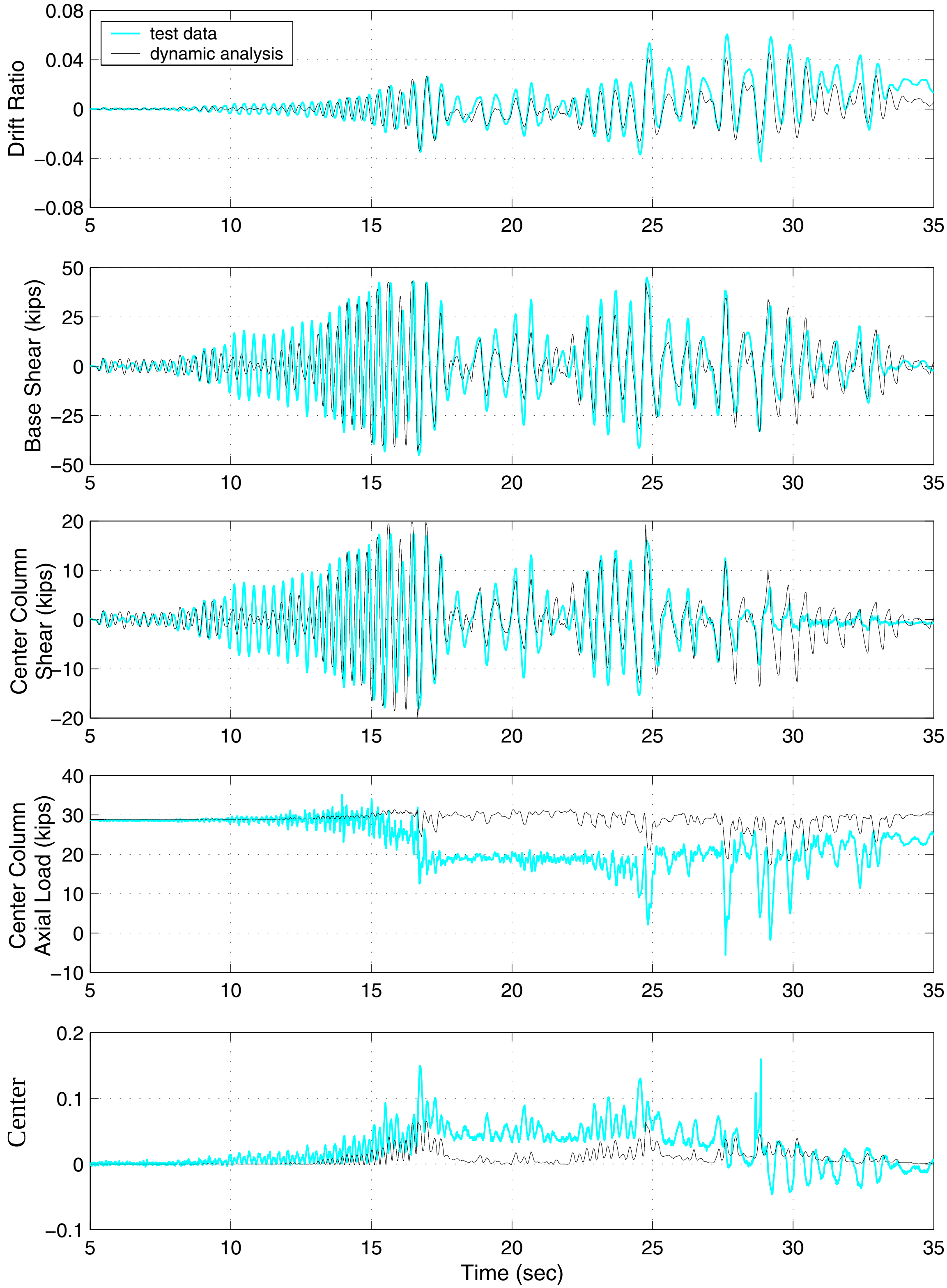

Figure 8-23. Response histories for Specimen 1

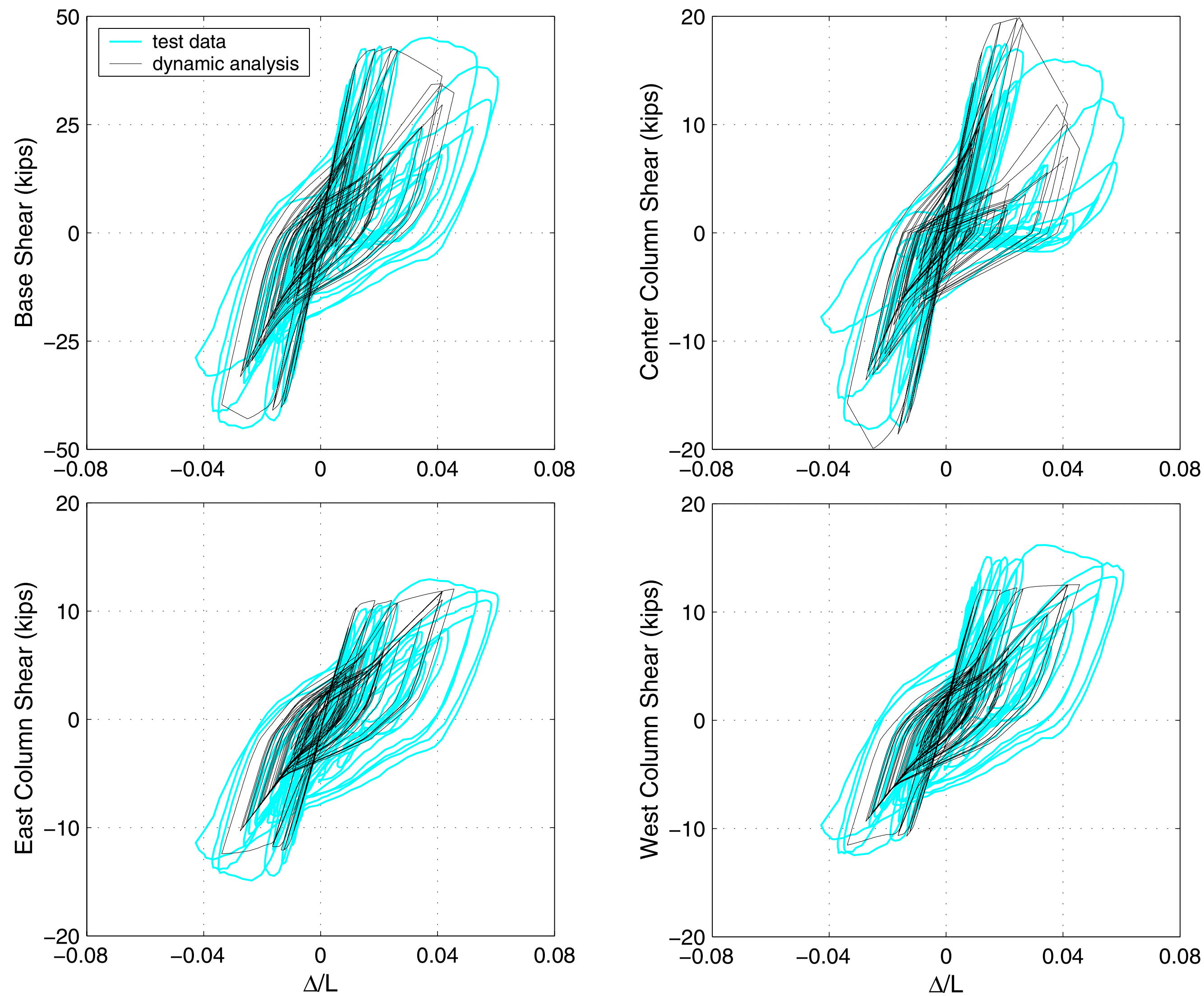

Figure 8-24. Shear hysteretic response for Specimen 1 (0 – 35 sec)

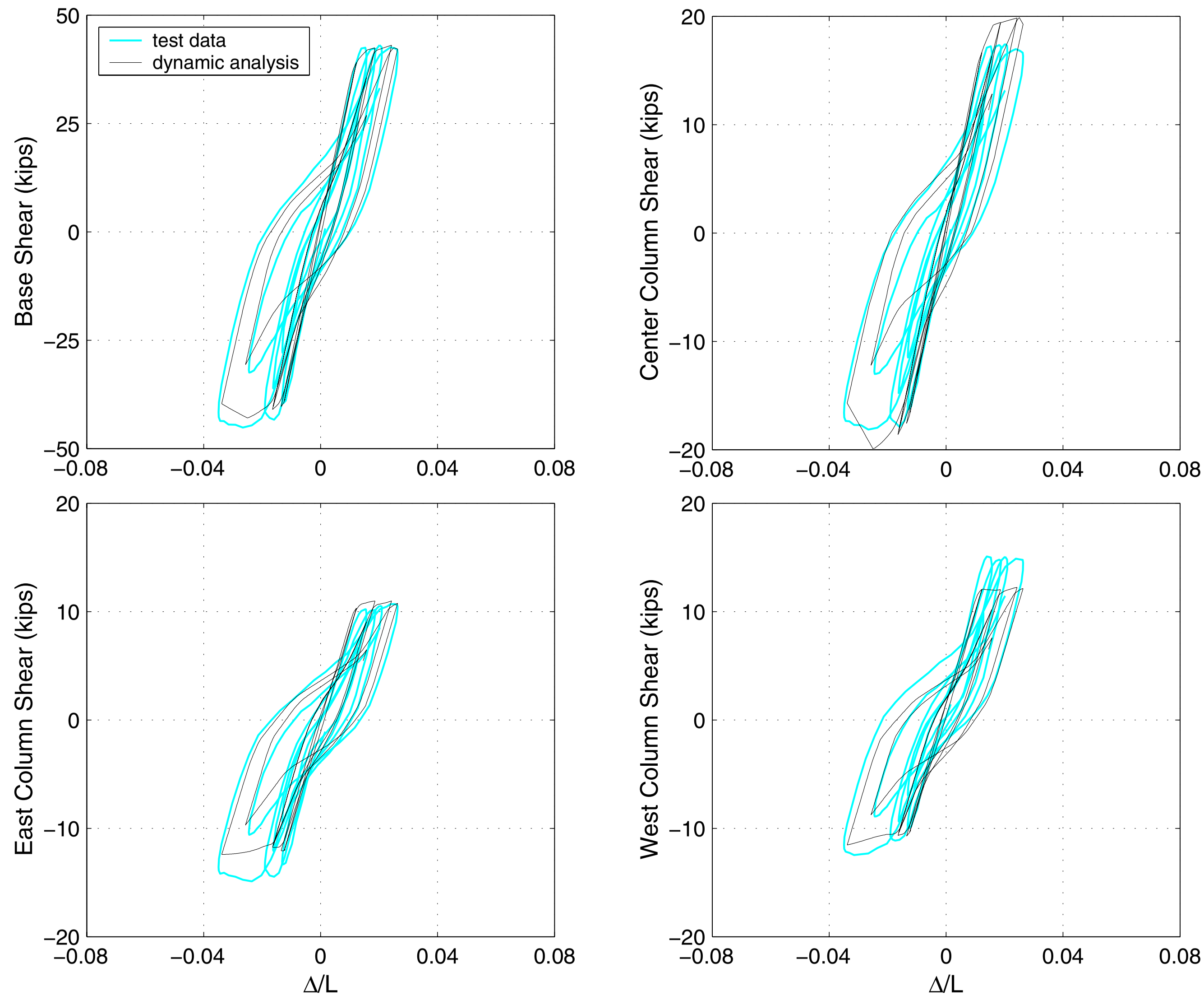

Figure 8-25. Shear hysteretic response for Specimen 1 (15 – 17.5 sec)

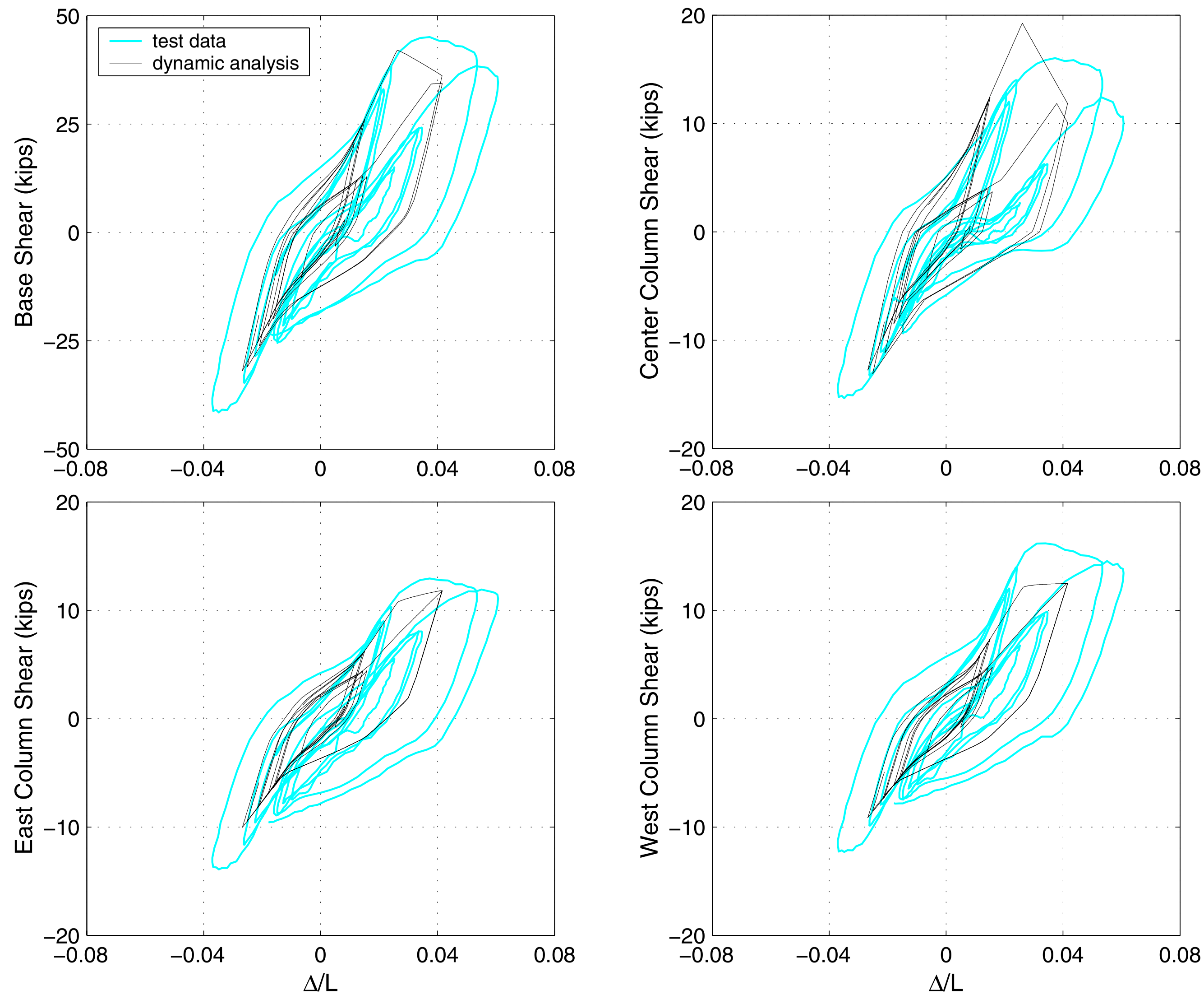

Figure 8-26. Shear hysteretic response for Specimen 1 (23 – 28 sec)

ing in an overestimation of the center column shear strength and stiffness late in the response history.

As noted for the static cyclic analysis, the hysteresis plots of Figures 8-24 through 8-26 indicate that the flexural strength of the outside columns during the compression cycles is underestimated, while the flexural strength of the center column is overestimated by the analytical model. Coincidently, these off-setting errors result in a close agreement for the overall strength of the specimen. The hysteresis plots in Figure 8-25 show that the stiffness of the analytical model agrees well with the test data at the time when shear failure is first detected. The hysteresis plots in Figure 8-26 illustrate the influence of the underestimation of the drift demand on the response of the analytical model.

The center column axial loads and vertical displacements are shown in the bottom two plots of Figure 8-23. The analytical model is unable to capture the 10-kip loss in the axial load observed to coincide with the initial shear cracking of the center column and the permanent axial lengthening of the outside columns at 17 seconds. This indicates that although the outside column models capture some permanent lengthening due to yielding of the longitudinal reinforcement, they do not capture enough to relieve the axial load from the center column. Although lengthening of the center column is underestimated by the analytical model, the dynamic analysis does capture the reduction in the center column elongation after shear failure. The detection of shear failure of the center column at 17 seconds, together with the subsequent decrease in the analytical estimate of the flexural deformations, results in only limited elongations of the center column after shear failure.

To investigate the influence of uncertainty in the drift at which shear failure is initiated, the analysis of the base model described above was repeated using a shear limit curve shifted by +/- one standard deviation, σ_s (the subscript *s* denoting the standard deviation of the drift at *shear* failure). Based on the database of Section 2.2, and the drift capacity model of Equation 2.9, σ_s is equivalent to a drift ratio of 0.9%. The $-\sigma_s$ model represents those columns that experience shear strength degradation prior to the drift given by the drift capacity model, while the $+\sigma_s$ model represents those columns capable of maintaining their shear strength until drift ratios past that given by the drift capacity model. Although Specimen 1 belongs to the latter category, the $-\sigma_s$ model provides a better estimate of the observed drifts, while the response of the $+\sigma_s$ model is very similar to that of the base model. The response of the $+/-\sigma_s$ models are compared with the test data in Figures 8-27 through 8-30. As expected, the $-\sigma_s$ model experiences shear strength degradation earlier

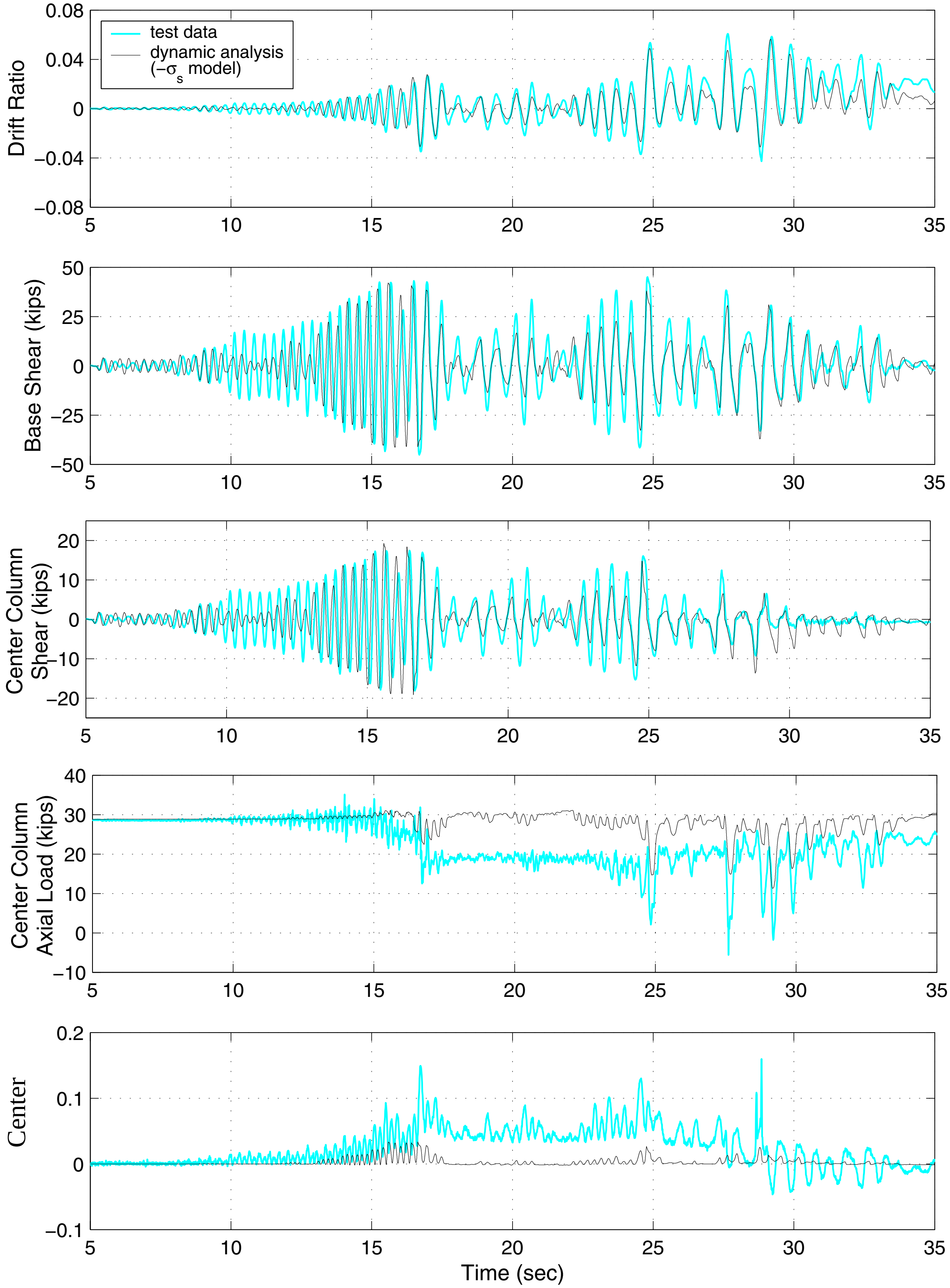

Figure 8-27. Response histories for -σ_s model, Specimen 1

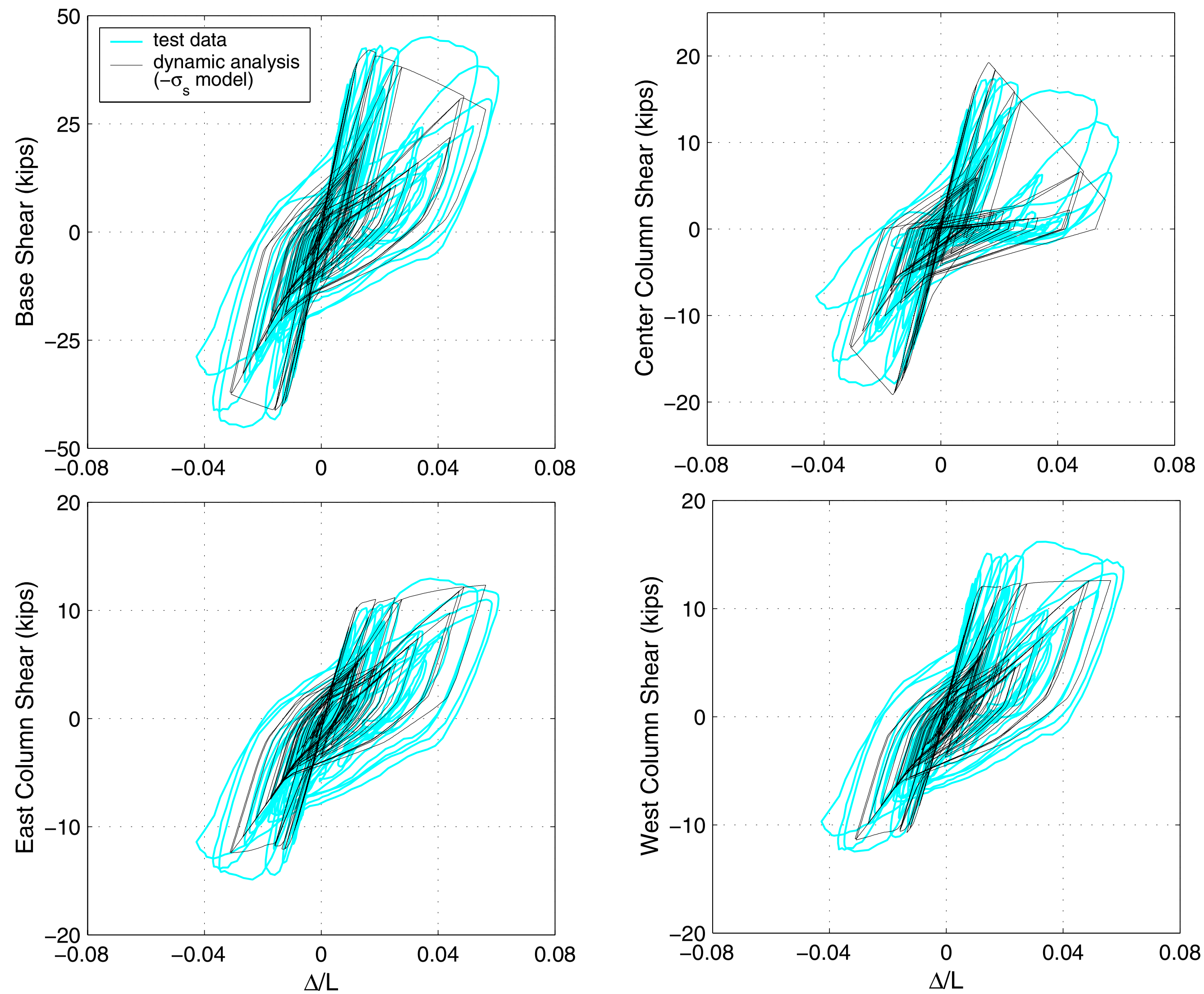

Figure 8-28. Shear hysteretic response for $-\sigma_s$ model, Specimen 1 (0 – 35 sec)

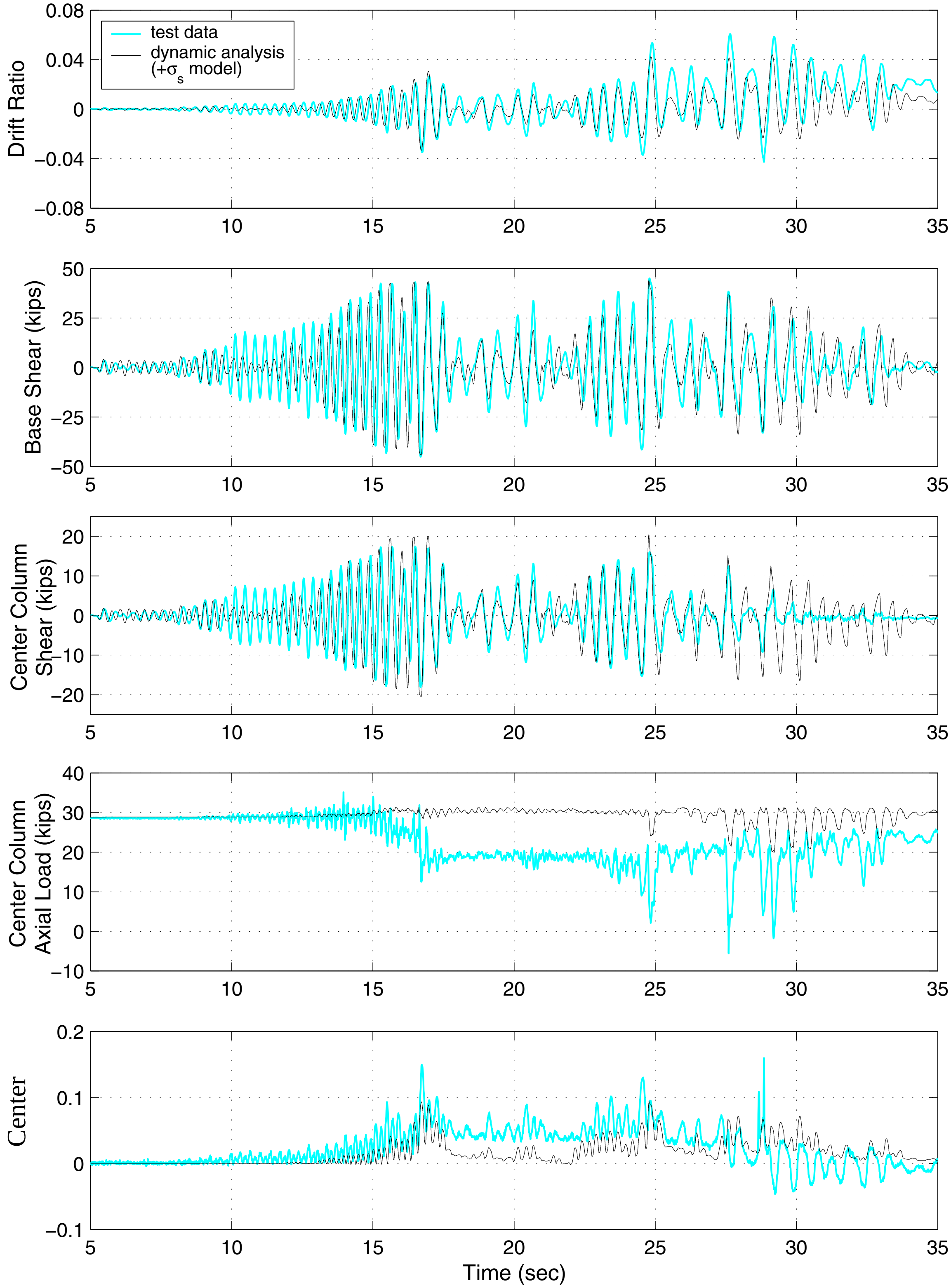

Figure 8-29. Response histories for +σ_s model, Specimen 1

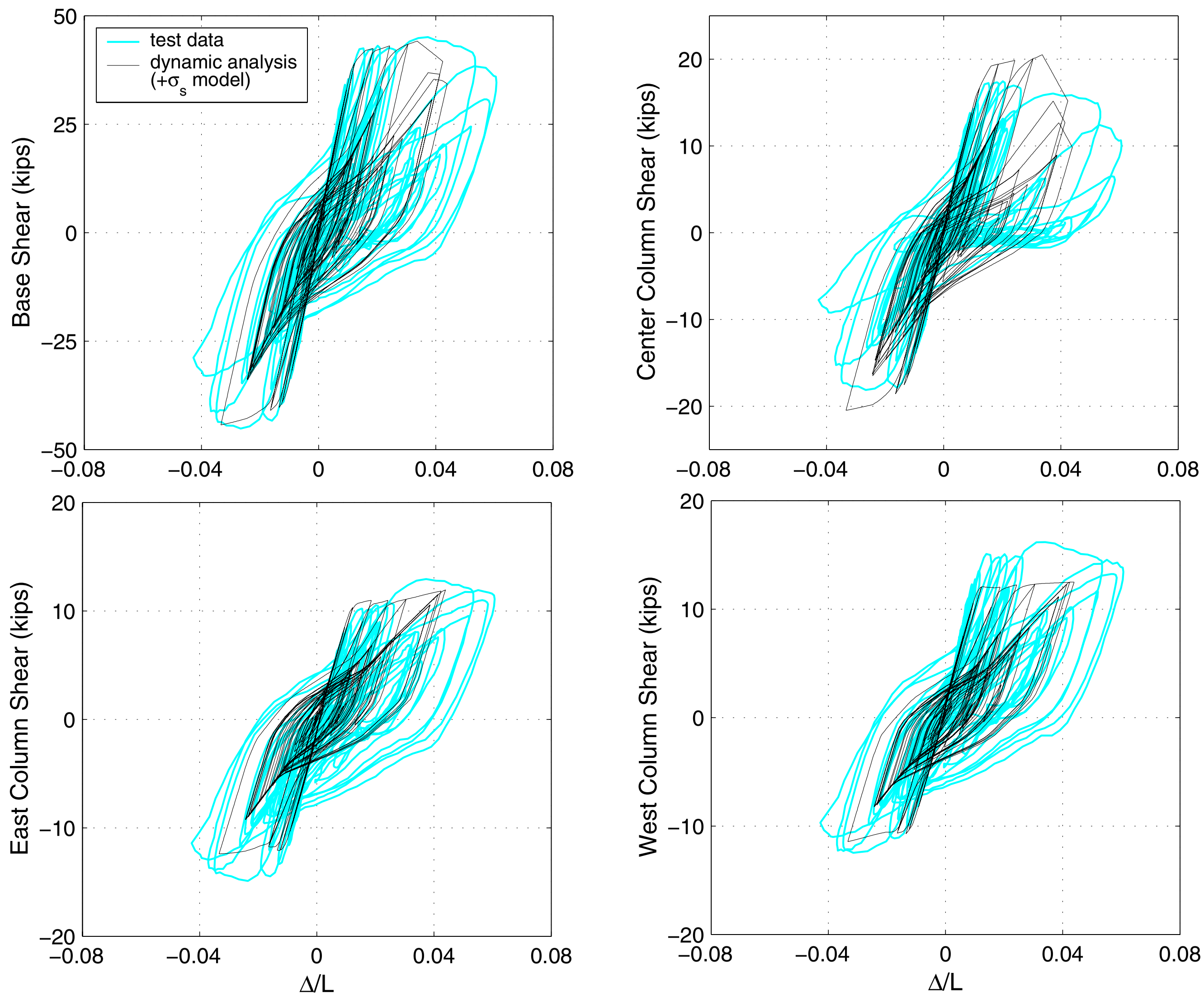

Figure 8-30. Shear hysteretic response for +σ_s model, Specimen 1 (0 – 35 sec)

than the base model and earlier than observed during the test. The effect, however, is a better estimate of the damaged column stiffness and a very good approximation of the drift response. Recall that a good estimate of the interstory drifts is necessary for the prediction of axial failure and for the evaluation of various damage states for performance-based seismic design.

Although the hysteretic response observed during the test does not indicate that the response is dominated by a degrading shear strength behavior, the increase in the influence of shear strength degradation behavior for the -σ_s model clearly results in an improved estimate of the drifts compared with the base and +σ_s models. Although a conclusion cannot be drawn based on a single analysis, the results suggest that the drift at which shear failure should be initiated to achieve the best estimate of the drift response may not correspond to the "drift at shear failure" as defined in Chapter 2 (i.e., the drift at which the observed shear strength first drops below 80% of the maximum shear recorded). Note that an increase in the contribution of the shear deformations to the total lateral drift prior to the "drift at shear failure" has also been observed in pseudo-static column tests (Sezen, 2002). Further study is required to improve the criteria for determining the drift at which shear failure should be initiated.

8.4.3 Recorded Table Input Motion — Specimen 2

As done for Specimen 1, the analytical model for Specimen 2 was subjected to the unidirectional horizontal table acceleration recorded during the shear failure test. The test data and the response of the analytical model are compared in Figures 8-31 through 8-34.

The analytical model adequately represents the measured response in terms of apparent vibration period and force amplitude throughout the test. The model provides a very good estimate of the drifts up to the point of axial failure (at approximately 25 sec), at which point the permanent offset in the drifts observed in the test is not captured by the analysis. The lack of residual drifts in the analytical results suggests that the fiber model does not capture the extent of the damage sustained by the outside columns during the test. Poor agreement between measured and calculated residual drifts has also been observed in shake table studies of reinforced concrete bridge columns (Hachem, 2002).

The shear hysteretic response is well represented by the analytical model. Figure 8-33 indicates that the analytical model adequately captures the column stiffnesses at yield and just after the

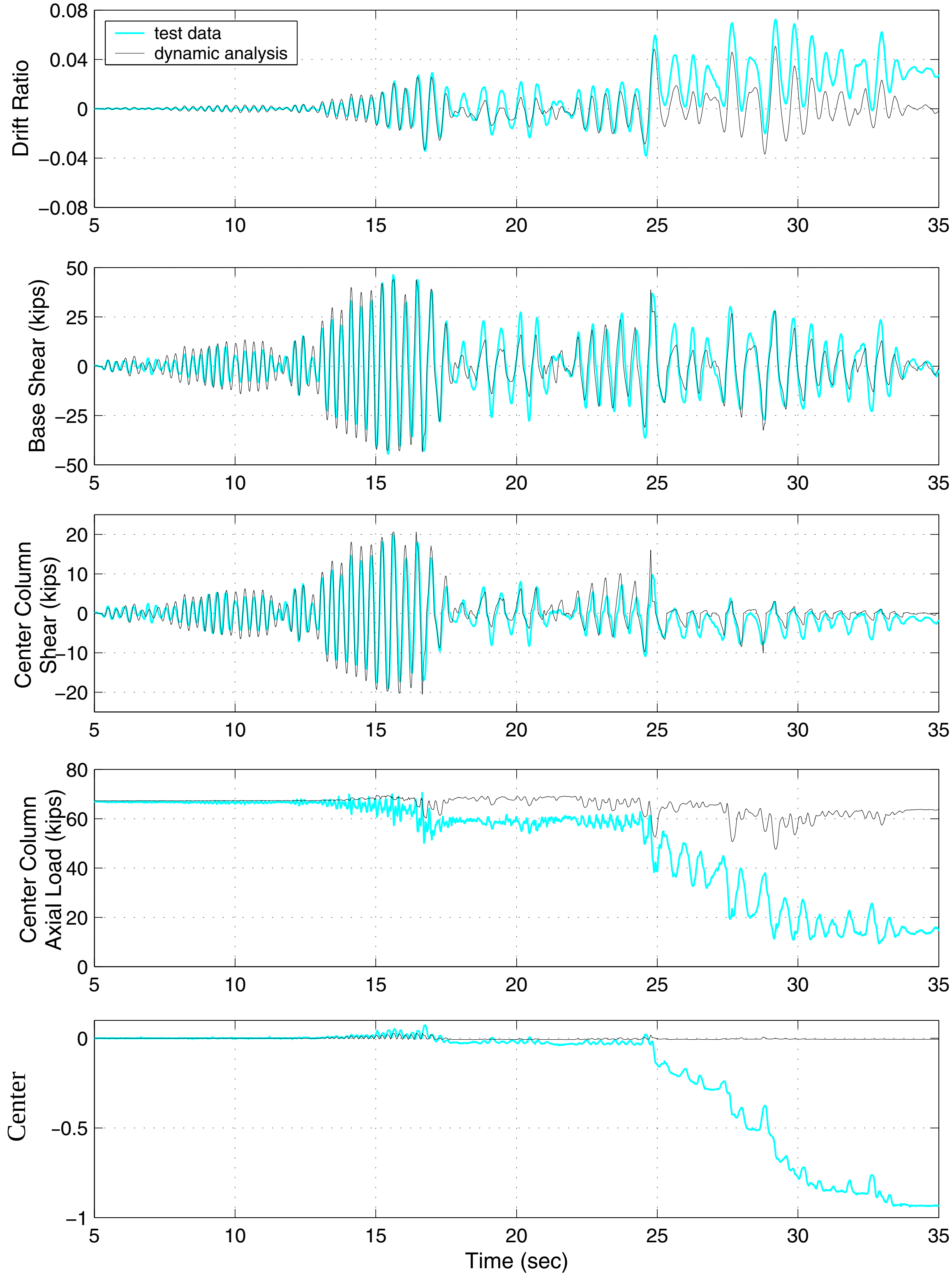

Figure 8-31. Response histories for Specimen 2

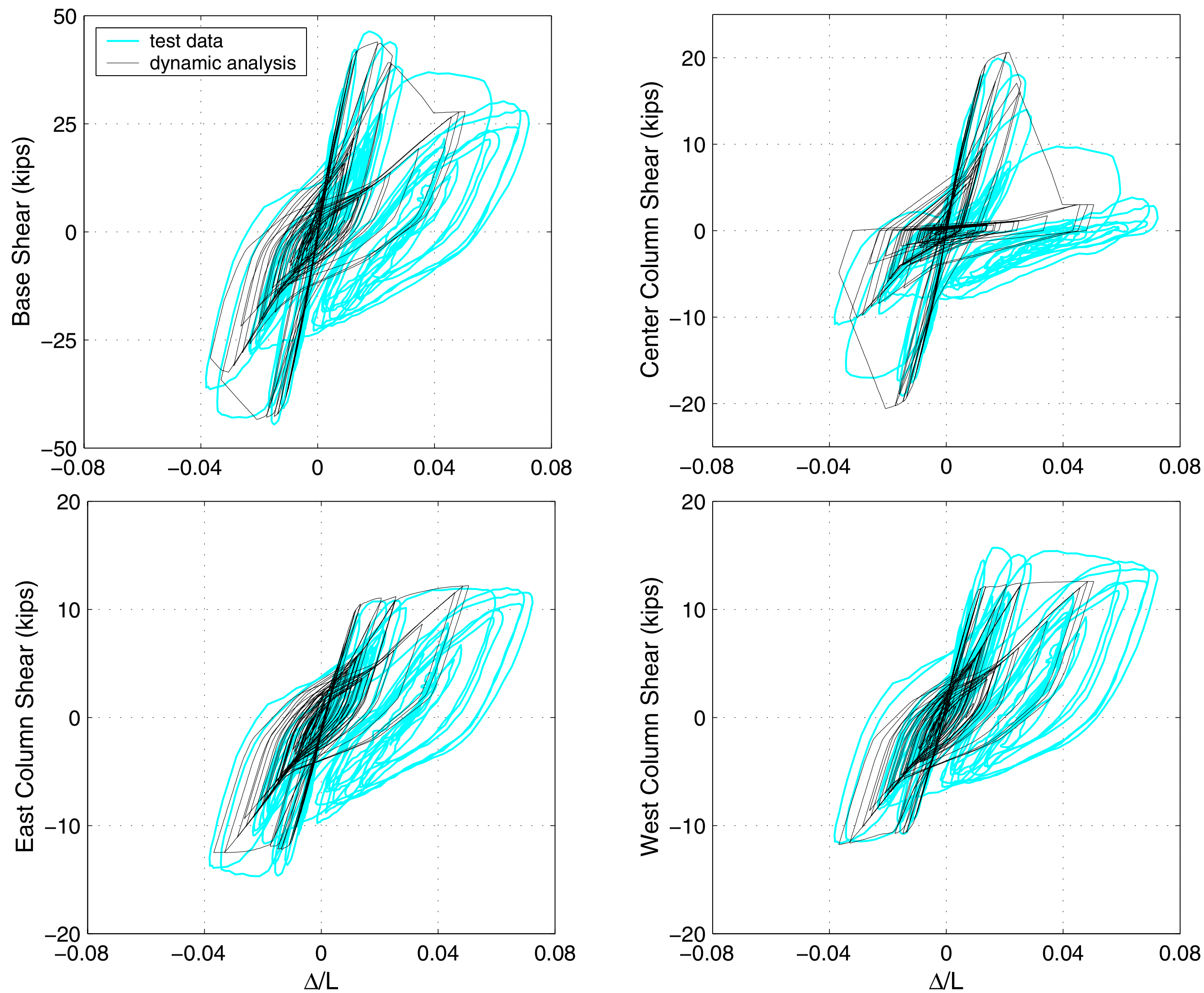

Figure 8-32. Shear hysteretic response for Specimen 2 (0 – 35 sec)

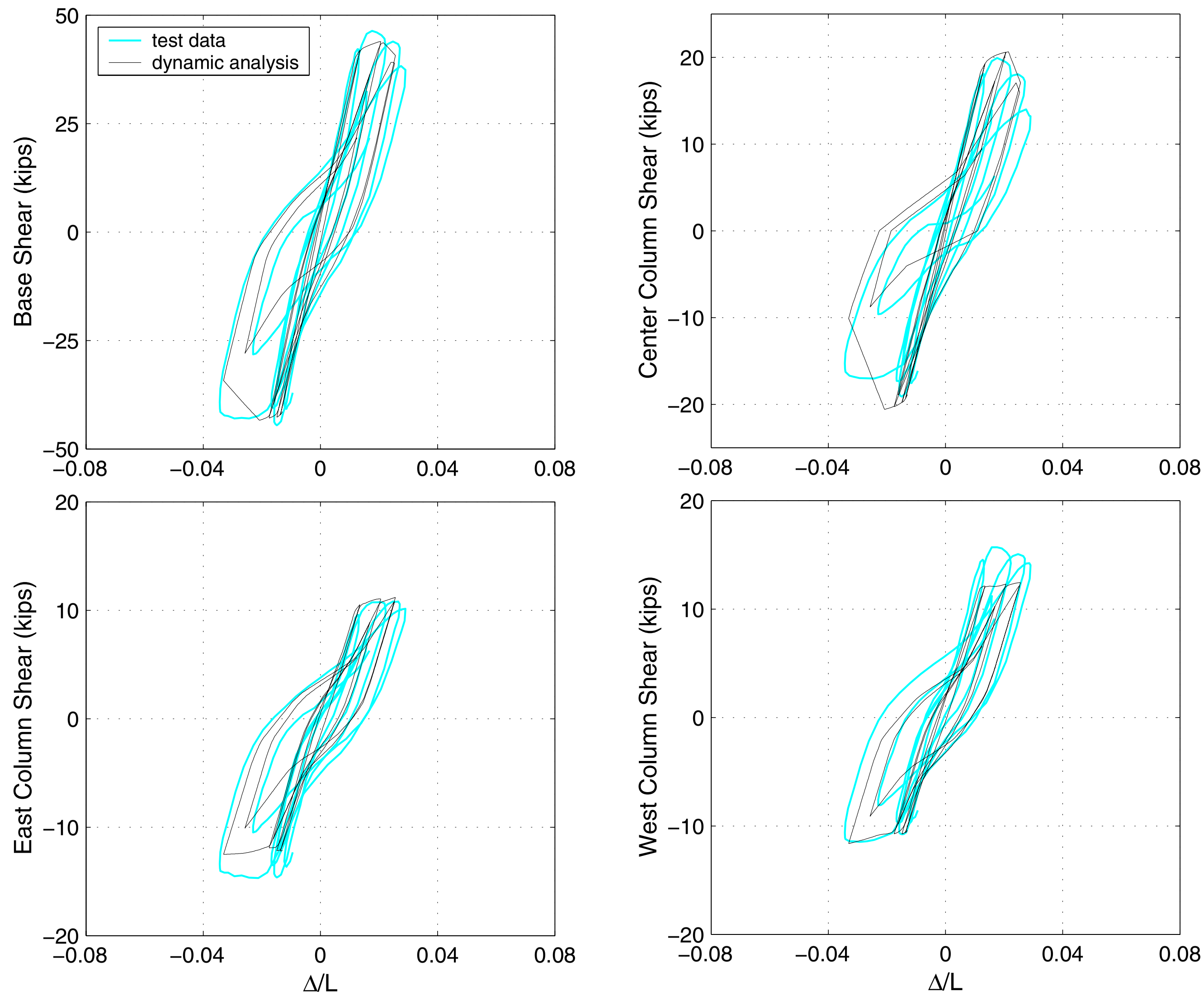

Figure 8-33. Shear hysteretic response for Specimen 2 (15 – 17.5 sec)

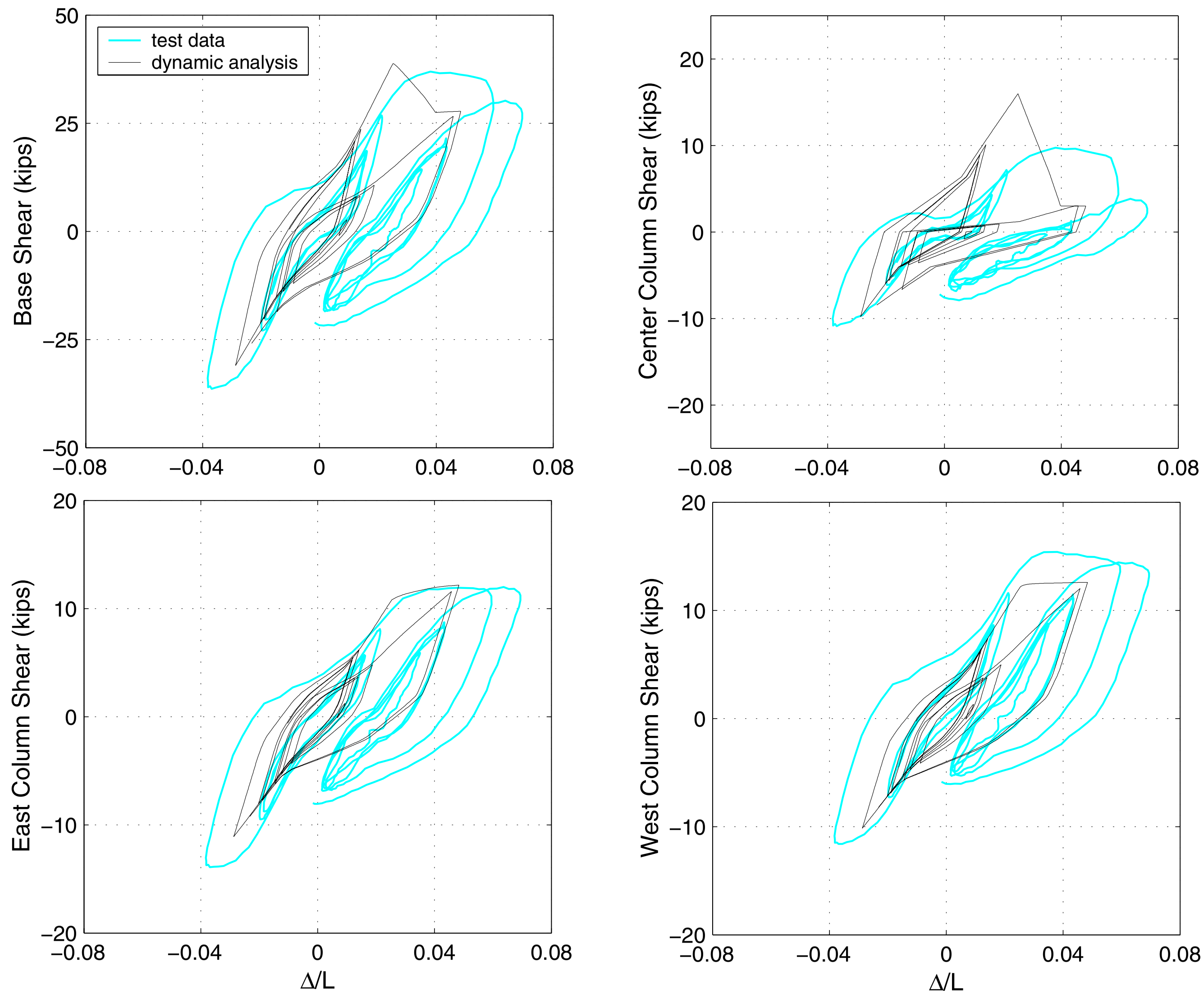

Figure 8-34. Shear hysteretic response for Specimen 2 (23 – 28 sec)

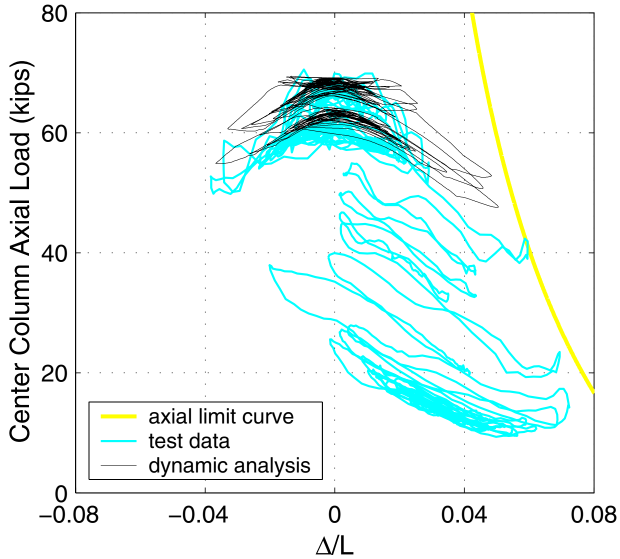

Figure 8-35. Axial response for Specimen 2

initiation of shear failure, and correctly detects the cycles in which the center column shear strength degradation begins. Figure 8-34 clearly shows that the analytical model does not capture the full extent of the significant pinching observed in the center column response prior to the large pulse at 25 seconds. The resulting overestimation of the center column stiffness may contribute to the underestimation of the drifts during and after the pulse.

Figure 8-35 shows that the axial load response of the center column based on the dynamic analysis does not cross the axial limit curve defined by Equation 3.20. As a result the analytical model failed to detect the axial failure of the center column. In this case, the lack of axial failure in the analytical results is primarily a result of the underestimation of the lateral drifts, rather than an error in the position of the axial limit curve.

The results from the analytical model discussed above are based on the shear and axial limit curves determined from the measured properties of the center column. Considering the uncertainty in the models used to define the limit curves, it is useful to evaluate the extent to which the analytical response changes with variation in the shear and axial limit curves. The following sections discuss the influence of the position of the shear and axial limit curves and the rate of shear strength degradation (i.e., the post-failure slope of the shear spring) on the response of the shake table specimen. In particular, the discussion concentrates on the drift response of the analytical models.

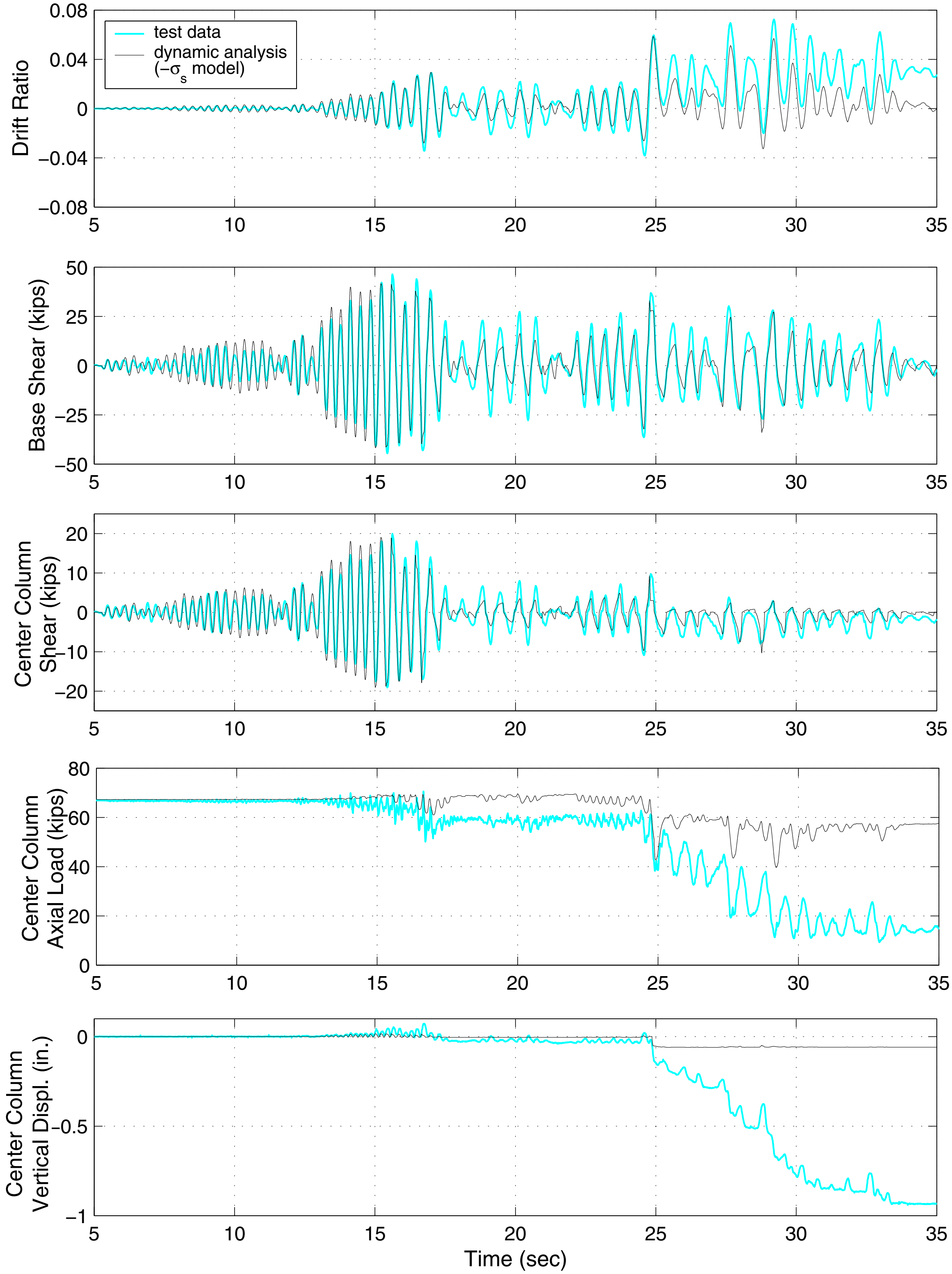

Figure 8-36. Response histories for -σ_s model, Specimen 2

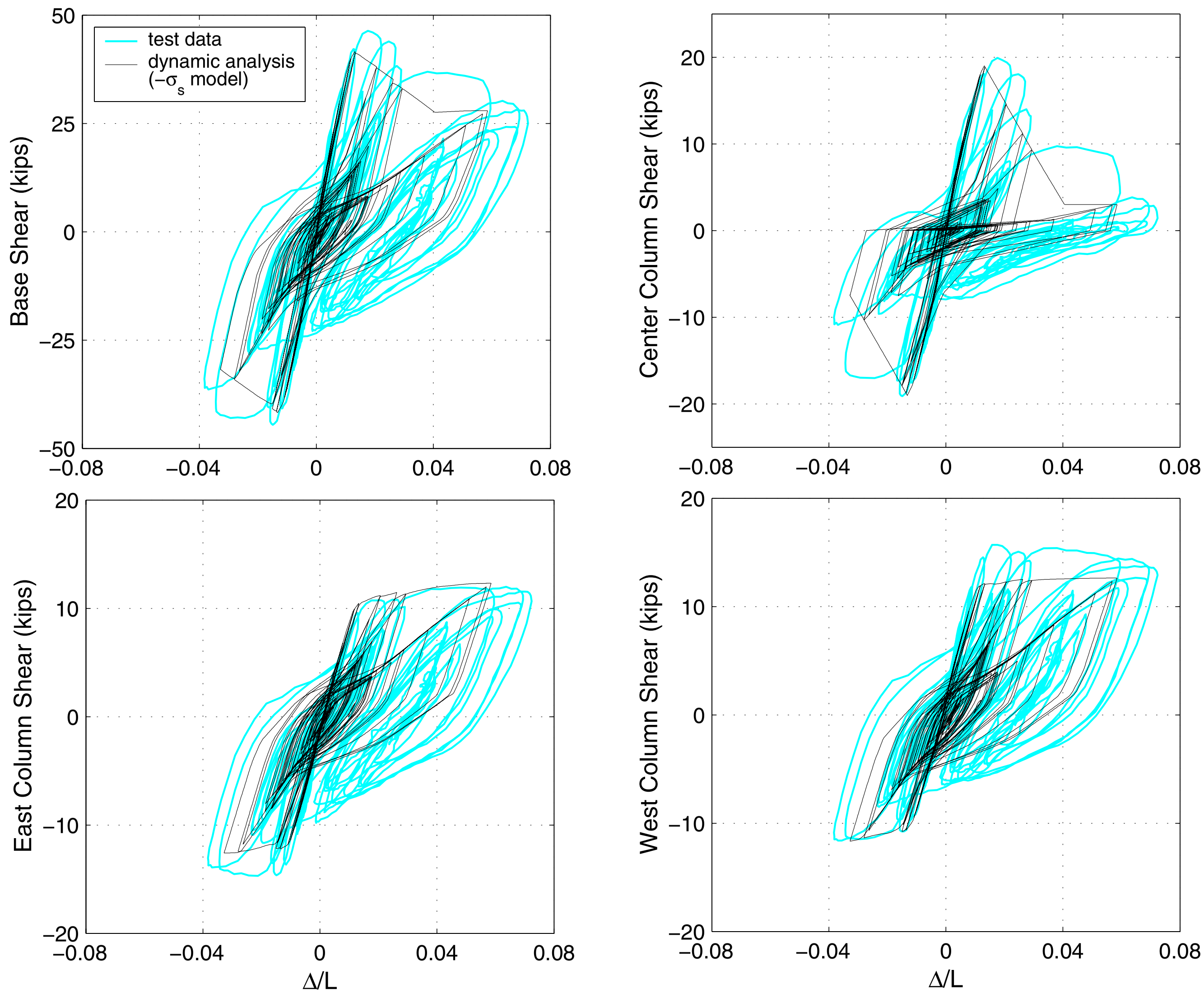

Figure 8-37. Shear hysteretic response for -σ_s model, Specimen 2 (0 – 35 sec)

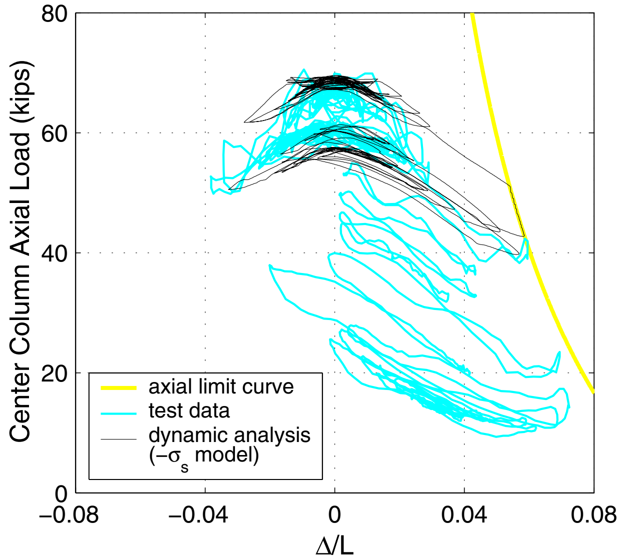

Figure 8-38. Axial response for -σ_s model, Specimen 2

8.4.3.1 Influence of Position of Shear Limit Curve

As done for Specimen 1, the shear limit curve was shifted +/- σ_s to investigate the influence of the position of the shear limit curve on the response of the shake table specimen. (Recall that σ_s is equivalent to a drift ratio of 0.9%.) As shown in Figures 8-36 through 8-40, and similar to the results for Specimen 1, the -σ_s model provides a better estimate of the measured drift response compared with either the base model or the +σ_s model. The drift during the critical pulse at 25 seconds is well represented by the -σ_s model, although the model does not capture the permanent offset in the drifts that appears to be initiated during this pulse, resulting in an underestimation of the drifts during subsequent cycles. Axial failure of the center column is correctly detected during the pulse at 25 seconds. However, as a result of the underestimation of the drifts during subsequent cycles, the response of the center column does not remain on the axial limit curve, as shown in Figure 8-38, and the amount of axial load lost is significantly underestimated.

By shifting the shear limit curve toward higher drifts, the +σ_s model does not correctly detect the cycle in which shear strength degradation begins. For positive displacements, shear strength degradation was first observed in the test data during a cycle at approximately 16 seconds, while the +σ_s model indicated that shear degradation would not begin until 25 seconds. This delay results in a slightly shorter period of response for the +σ_s model compared with the test data prior to the detection of shear failure at 25 seconds. The axial response of the center column for the +σ_s

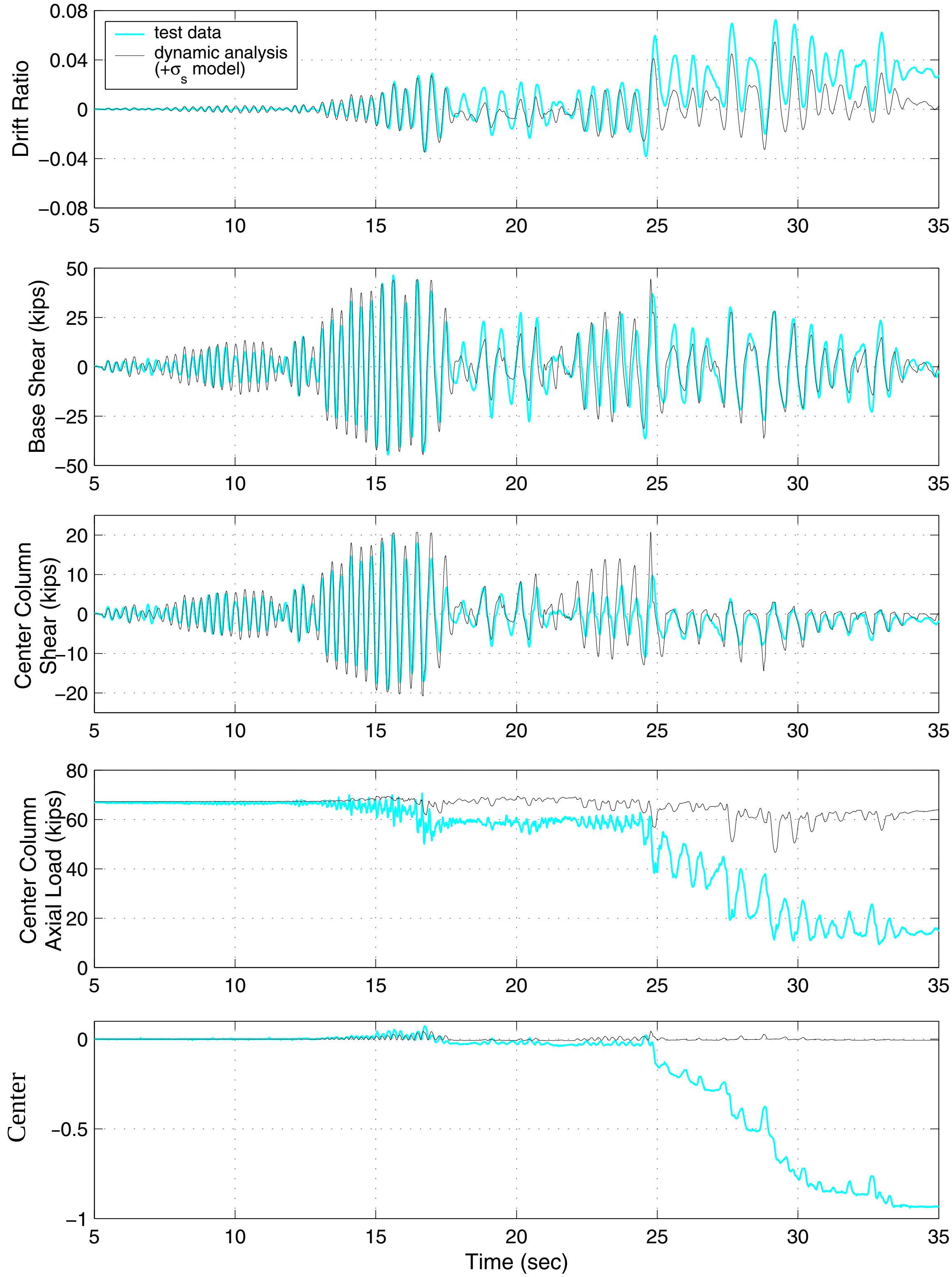

Figure 8-39. Response histories for +σ_s model, Specimen 2

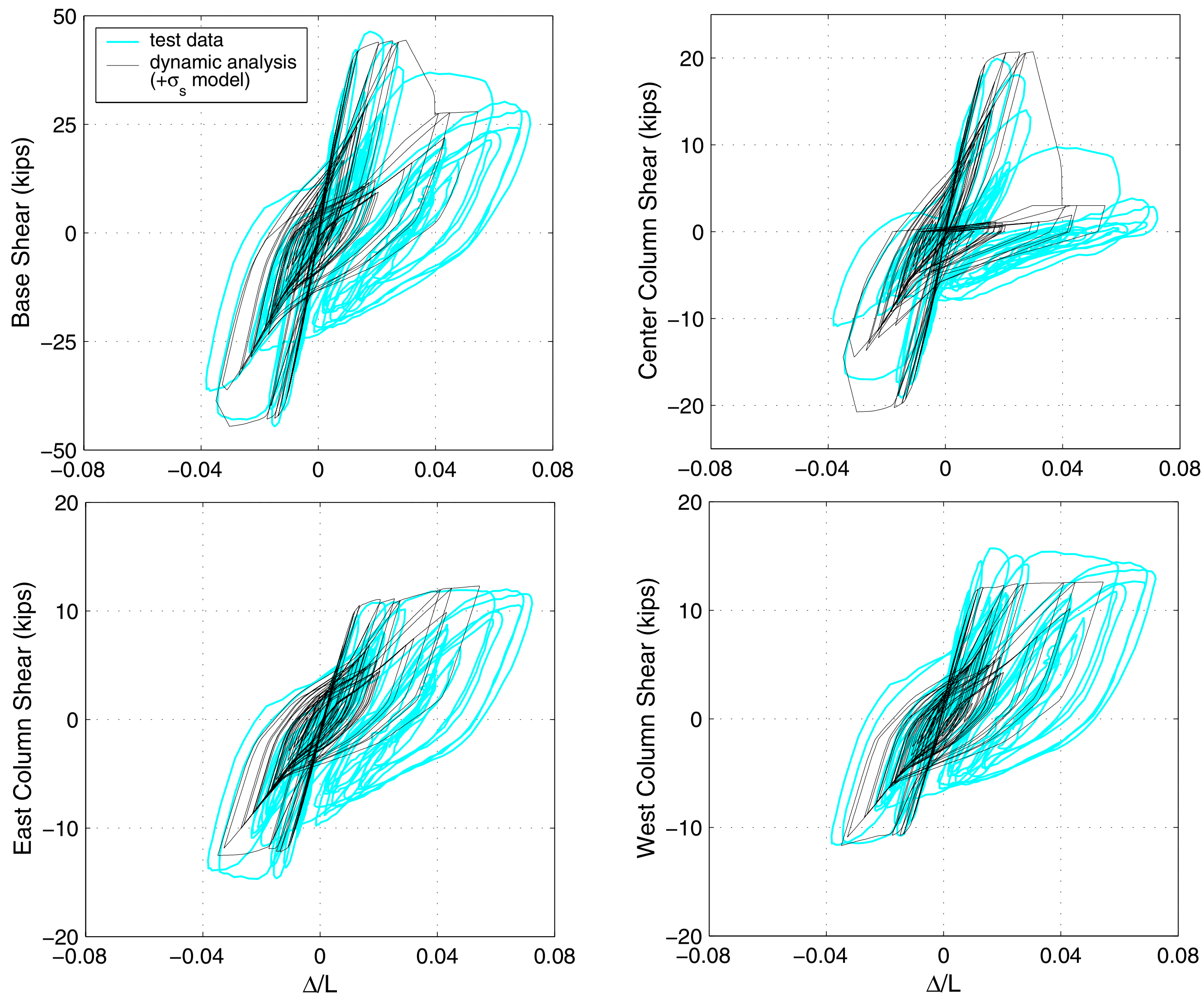

Figure 8-40. Shear hysteretic response for $+\sigma_s$ model, Specimen 2 (0 – 35 sec)

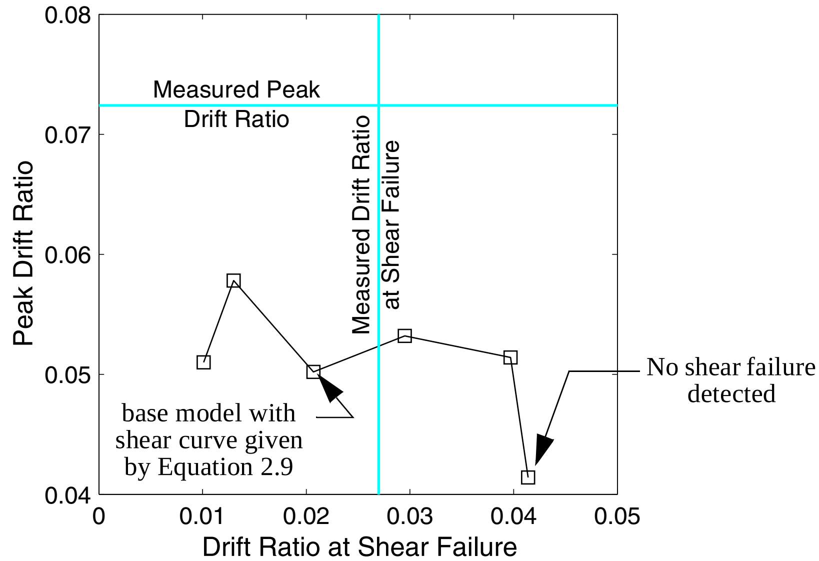

Figure 8-41. Influence of drift ratio at shear failure on the calculated peak drift ratio, Specimen 2

model did not intersect the axial limit curve, and hence, the model failed to detect the axial failure of the center column.

Figures 8-36 and 8-40 show that the peak drift response changes with the position of the shear limit curve. The peak drift is an important demand parameter commonly used in performance-based seismic design, and a good estimate is required for an accurate prediction of axial failure. Figure 8-41 illustrates the influence of the position of the shear limit curve on the peak drift determined from the analysis. The drift at which shear failure is detected, or the drift at which the shear-drift response intersects the shear limit curve, is plotted on the x-axis. The measured peak drift is underestimated by the analysis regardless of the position of the shear limit curve. The largest calculated peak drifts result if shear failure is initiated in the analysis at drifts below that determined by the drift capacity model (Equation 2.9), but after flexural yielding. For all cases where shear failure is detected in the analysis, the peak drift is approximately 1% larger than the calculated peak drift ratio when shear failure is not detected.

The results shown in Figure 8-41 suggest that the peak drift ratio from the analytical model results is not very sensitive to the position of the shear limit curve; however, this result may be dependent on the assumptions used to select the degrading slope after shear failure. Recall that the degrading slope after shear failure is determined based on the calculated displacement at axial failure, which remains approximately constant for each of the analyses shown in Figure 8-41. This results in a steeper shear strength degradation response as the drift ratio at shear failure increases, and likely leads to the lack of decay in the peak response as the drift ratio at shear failure increases above 2%.

8.4.3.2 Influence of Degrading Slope after Shear Failure

This section will consider the influence of the degrading slope on the drift response of the center column. As noted above, and described in detail in Section 4.5.1, for the analyses presented thus far the degrading slope of the shear spring, K_{deg}, has been determined based on achieving the calculated drift at axial failure after full degradation of the shear strength. (See Figure 4-8 for a definition of K_{deg}.) K_{deg} can also be specified directly by the analyst. Figure 8-42 shows the drift response for five models with different K_{deg} values specified for the center column. Only slight variations in the drift response after shear failure are apparent from the results. Although a steeper degrading slope generally results in a better estimate of the drifts during the large pulse at 25 seconds, there is no improvement in the estimation of the permanent drift offset observed at the end of the test. Figure 8-43 indicates that the calculated peak drift ratio is insensitive to the degrading slope selected for the response of the center column after shear failure. It is likely that the lack of sensitivity to the degrading slope is due to the ductile response of the outside columns. After shear failure of the center column, the lateral response of the frame is dominated by the stable hysteretic response of the outside columns.

Although further study is required to generalize the results shown here for building frame structures, the lack of sensitivity of the peak response to the drift at shear failure (Figure 8-41) and the degrading slope (Figure 8-43) suggest that for a structure similar to the shake table specimens with both shear-critical and ductile components, and subjected to a long duration ground motion, the peak response may not be particularly sensitive to the selection of the parameters for the shear-critical components. This result is encouraging for designers considering the significant uncertainty in determining the drift at shear failure and lack of data on the rate of shear strength degradation. It is anticipated that the peak drift response will be more sensitive to the parameters for the shear-critical components if the structure is subjected to a pulse-type ground motion where the

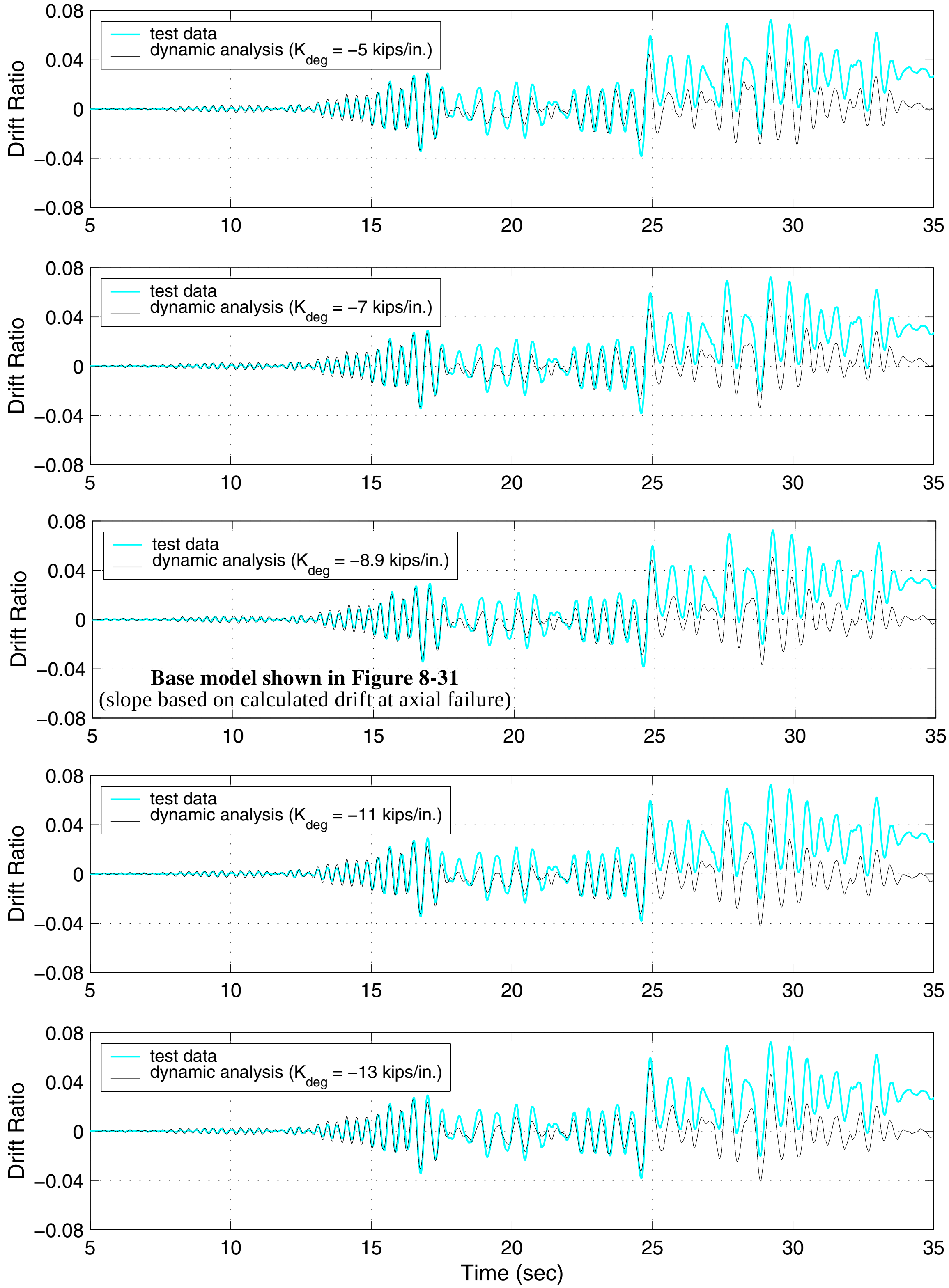

Figure 8-42. Drift response histories for analytical model using different degrading slopes, Specimen 2

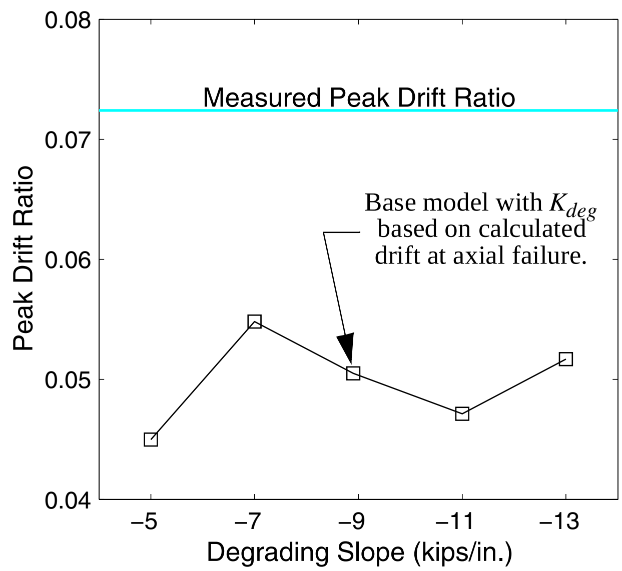

Figure 8-43. Influence of degrading slope on the calculated peak drift ratio, Specimen 2

majority of damage occurs during one cycle, or if multiple columns sustain shear failures. The latter case is considered in Section 8.4.4.

8.4.3.3 Influence of Position of Axial Limit Curve

To investigate the influence of the position of the axial limit curve on the calculated response of Specimen 2, analyses were conducted with the limit curve shifted to lower drifts by one standard deviation ($-\sigma_a$ model) and two standard deviations ($-2\sigma_a$ model). (Recall that σ_a is equivalent to a drift ratio of 0.5%.) Since axial failure was not detected in the base model (Figure 8-35), shifting the axial limit curve by $+\sigma_a$ would result in the same response discussed above for the base model. Apart from minor increases in the drifts after the shear strength of the center column has fully degraded, the $-\sigma_a$ and $-2\sigma_a$ models have very little influence on the lateral response of the analytical model. Figures 8-44 through 8-48 show the axial response of the center column for the $-\sigma_a$ and $-2\sigma_a$ models.

The $-\sigma_a$ model correctly determines the timing of the axial failure of the center column, but does not remain on the limit curve long enough to result in any significant loss of axial load. The $-2\sigma_a$ model adequately represents the loss of axial load during the pulse at 25 seconds and experiences gravity load redistribution of 15 kips. This underestimates the load redistribution observed during the test and results in only 0.1 inches of downward vertical displacement at the center col-

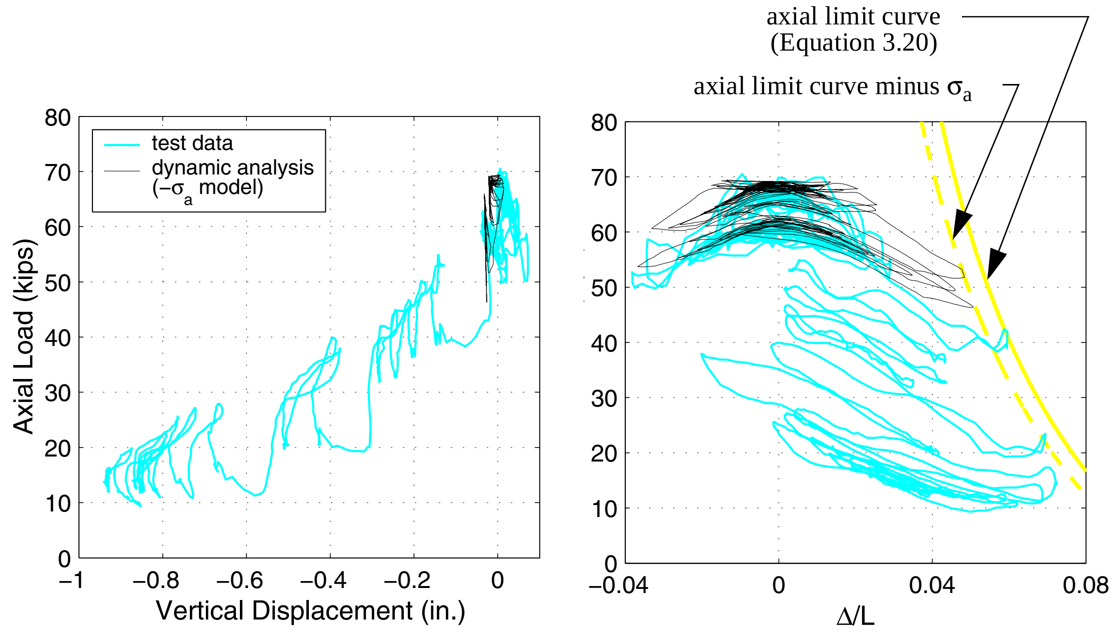

Figure 8-44. Variation of Specimen 2 center column axial load with vertical displacement and drift ratio for the -σ_a model

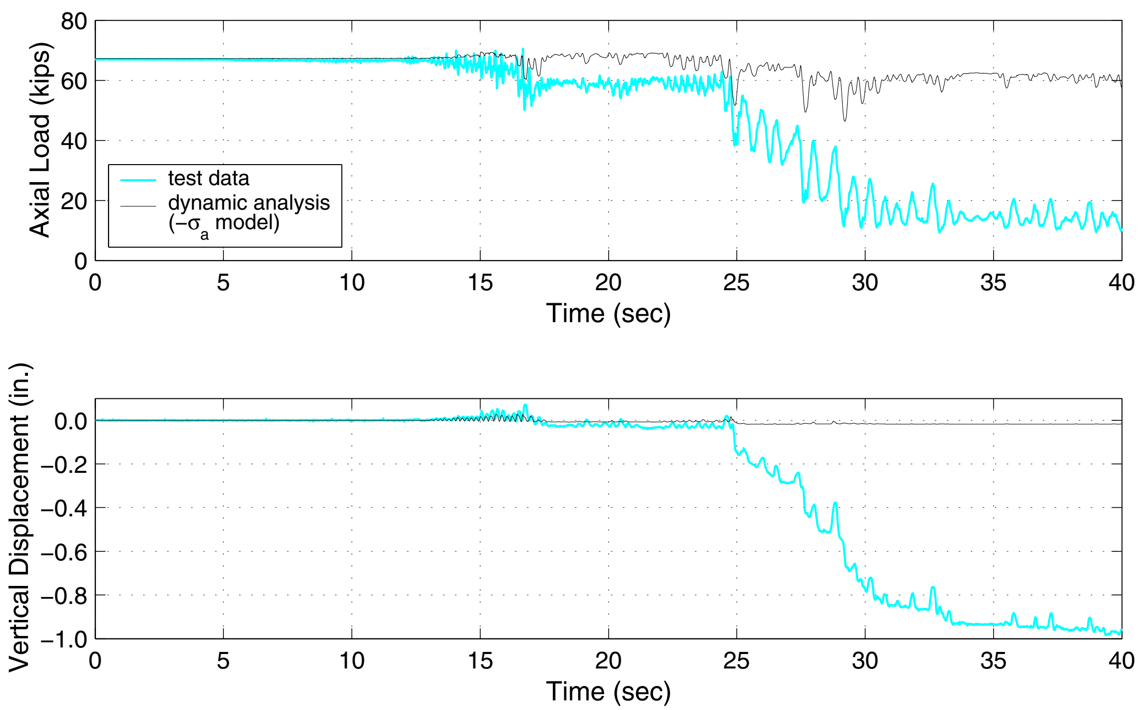

Figure 8-45. Axial load and vertical displacement response histories for Specimen 2 center column for the -σ_a model

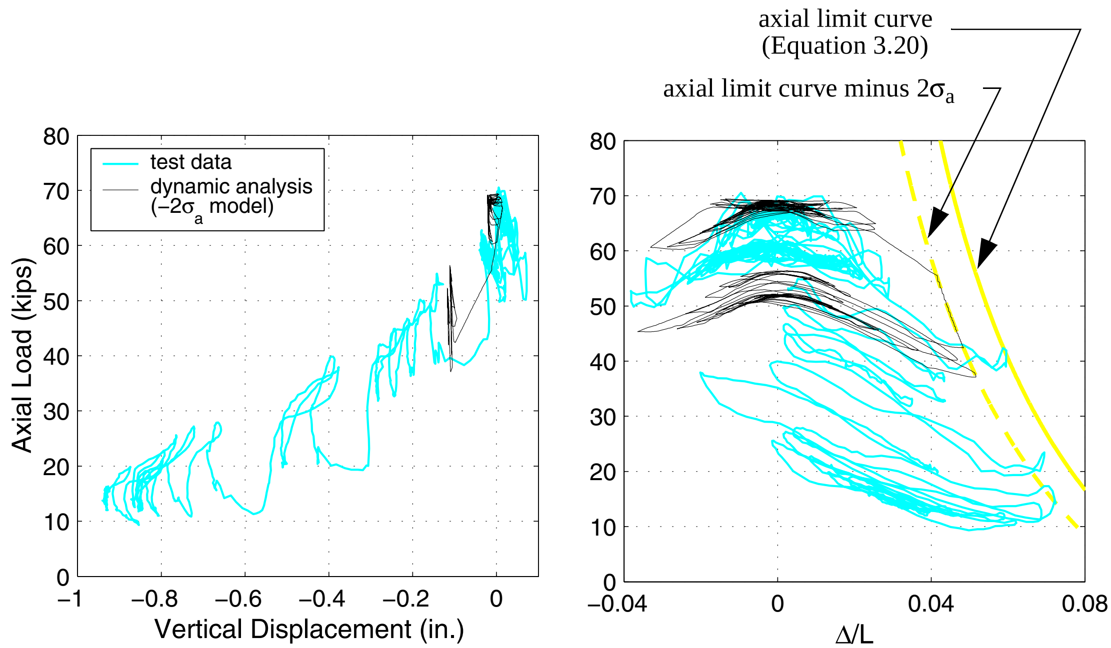

Figure 8-46. Variation of Specimen 2 center column axial load with vertical displacement and drift ratio for the -2σ_a model

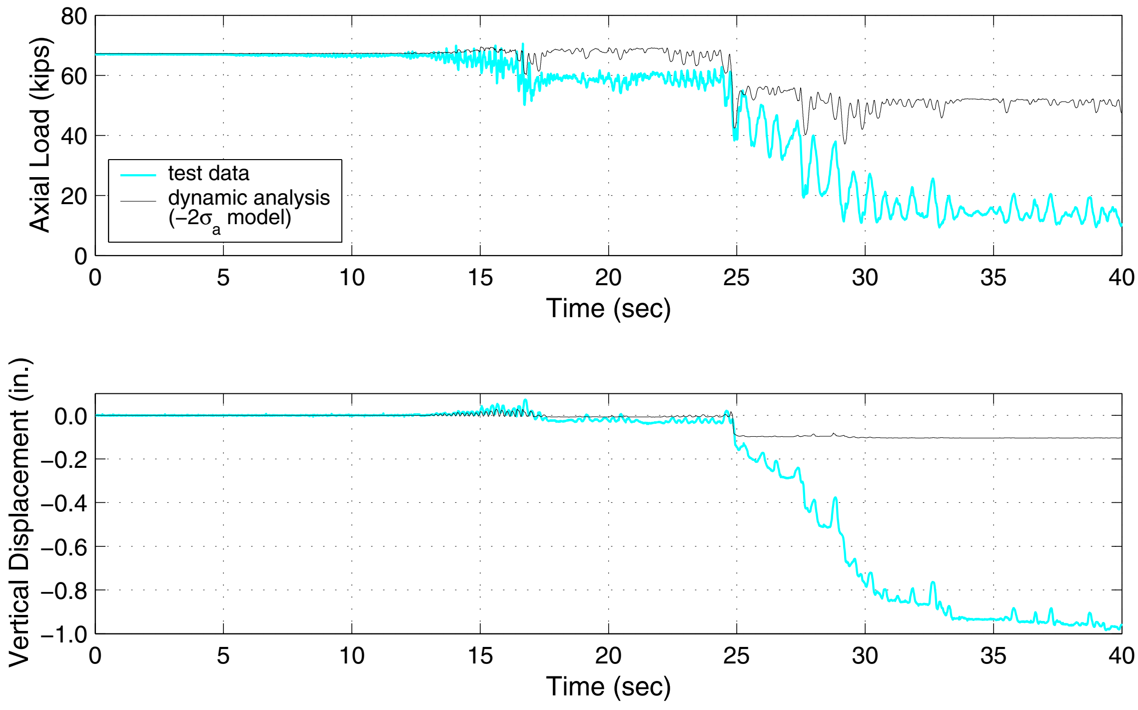

Figure 8-47. Axial load and vertical displacement response histories for Specimen 2 center column for the -2σ_a model

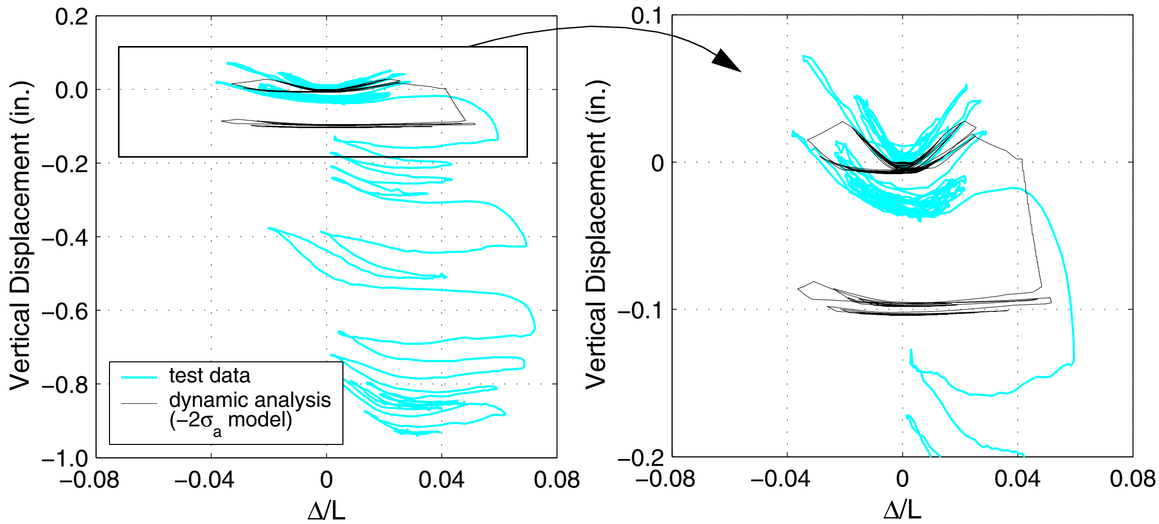

Figure 8-48. Coupling of vertical and horizontal displacements at Specimen 2 center column for the -2σ_a model

umn. Figure 8-48 shows that although the vertical displacements are underestimated, the model does reasonably represent the sudden increase in vertical displacements that occur after achieving a critical drift limit.

Better estimates of the axial load loss and vertical displacements would be achieved if the axial curve were moved inward (i.e., to smaller drifts) or steepened with increasing damage. Such a model would require the selection of rules to determine the movement or change in slope of the axial limit curve, and perhaps the development of a damage index considering the axial capacity of the column. The development of such rules and damage indices is not currently feasible given the limited data available on the axial response of a column after shear failure.

It is worth repeating that the base model would have detected axial failure of the center column if the model were able to capture the larger lateral drifts observed during the test. A proper estimate of the drifts would have also resulted in a significantly higher loss of axial load for the -σ_a and -2σ_a models. Hence, the effect of shifting the axial limit curve is highly dependent on the ability of the analytical model to achieve a good estimate of the lateral drifts.

8.4.4 Three-Column Frame with All Shear-Critical Columns

To illustrate the stabilizing influence of the outside columns on the response of the shake table specimens, an analysis of the three-column frame model was conducted with the outside column

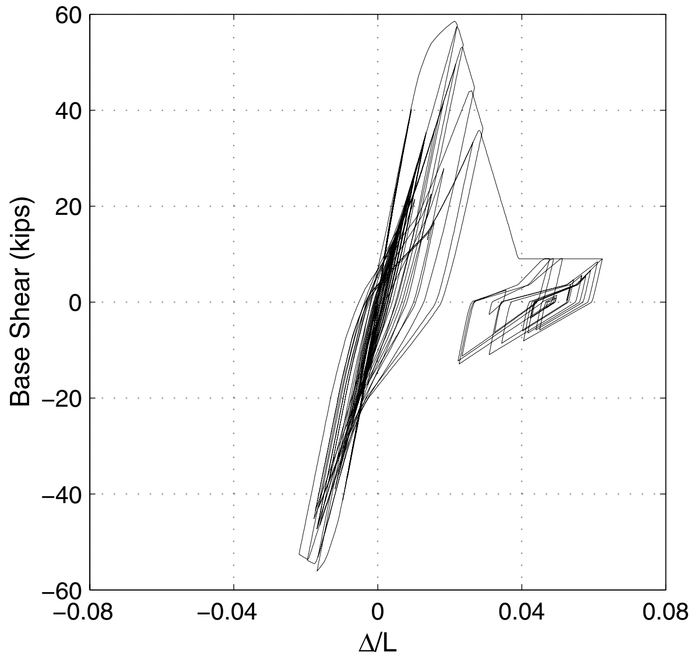

Figure 8-49. Base shear hysteretic response for three-column frame with all shear-critical columns

model replaced by the shear-critical center column model. The calculated response of the new model when subjected to the table motion from Specimen 2 is shown in Figures 8-50 through 8-52. All three columns experience shear failures, resulting in nearly full degradation of the base-shear capacity as shown in Figure 8-49. Without the stable response of the well-confined outside columns, the new model experiences permanent drifts of approximately 4.0%.

Figure 8-50 shows the variation in the axial-load demand and capacity for each of the columns during the analysis. The capacity shown is the lesser of the axial capacity of the undamaged column according to ACI 318-02 (with a strength reduction factor of unity) and the axial capacity according to Equation 3.20 using the column drifts from the analysis. For large drifts the axial capacity based on Equation 3.20 will govern, resulting in a decrease in the axial capacity. At 32.5 and 33.0 seconds, the axial-load demand on the center column is limited by the axial-load capacity, as response of the center column follows the axial limit curve (Figure 8-51). The drop in the center column axial load results in sharp increases in the center column vertical displacements (Figure 8-52) and the outside column axial loads (Figure 8-51). The large drifts which accompany axial failure of the center column also result in a decrease in the outside column axial-load capacities. The increase in demand and drop in capacity very nearly result in axial failure of the west column at

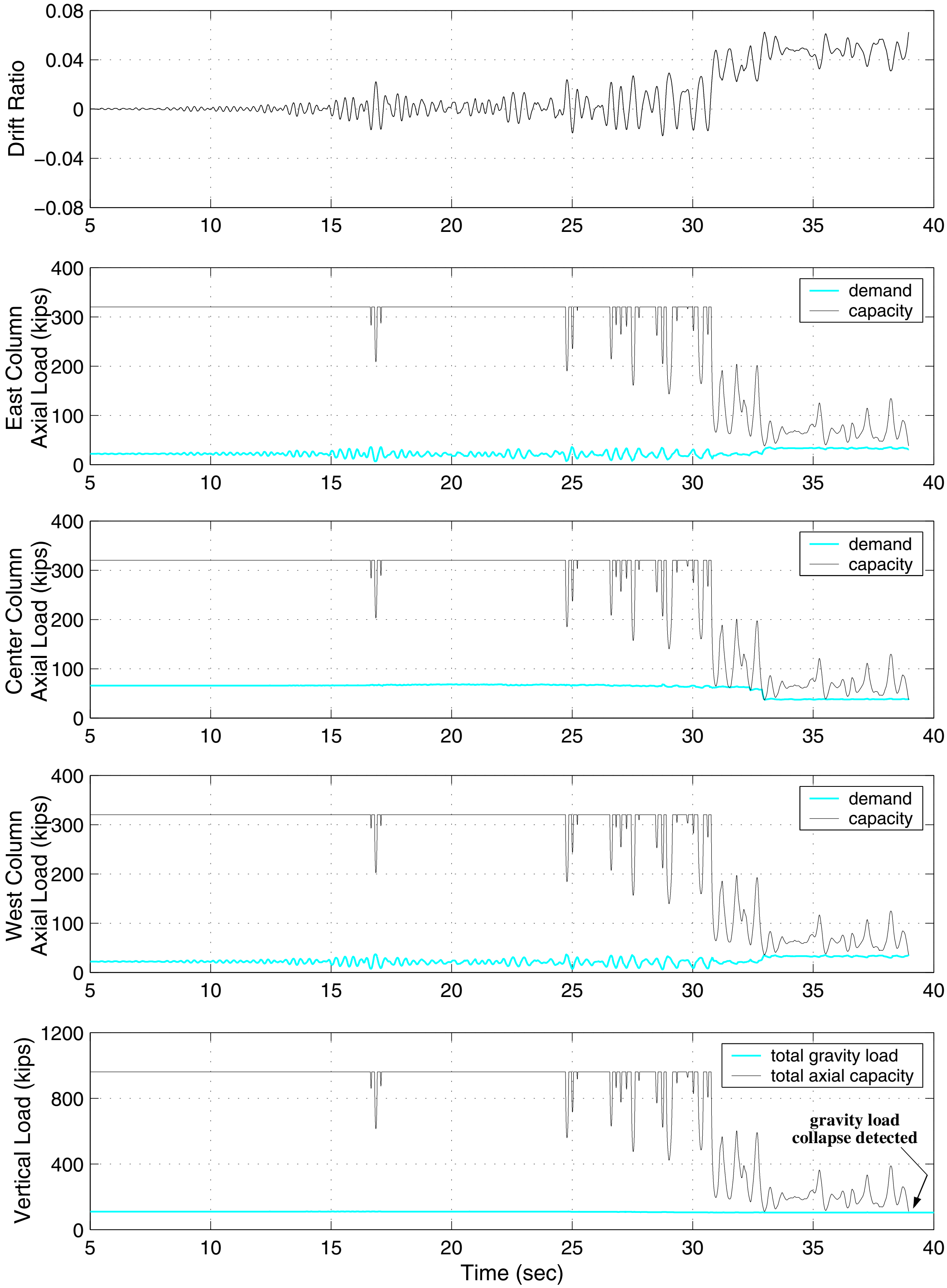

Figure 8-50. Drift and axial load response histories for three-column frame with all shear-critical columns

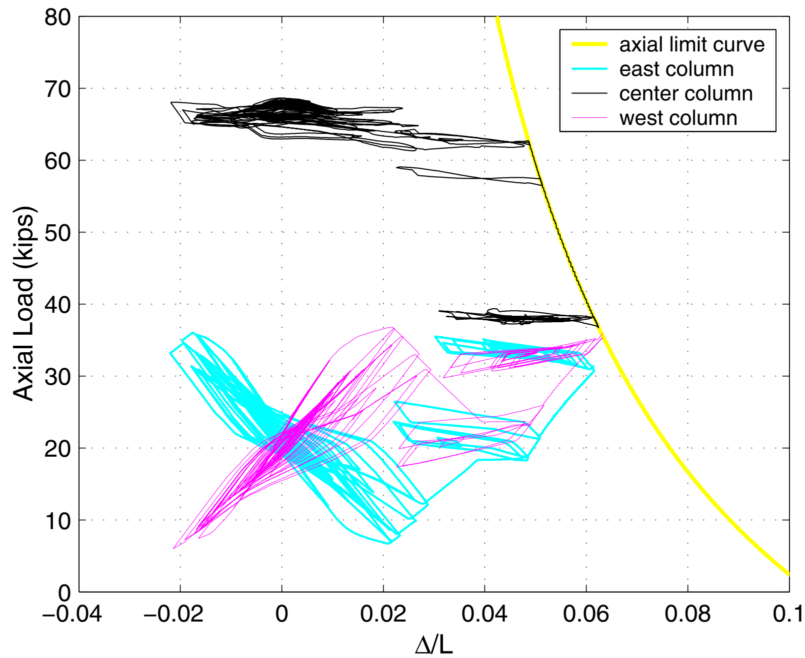

Figure 8-51. Axial load response for three-column frame with all shear-critical columns

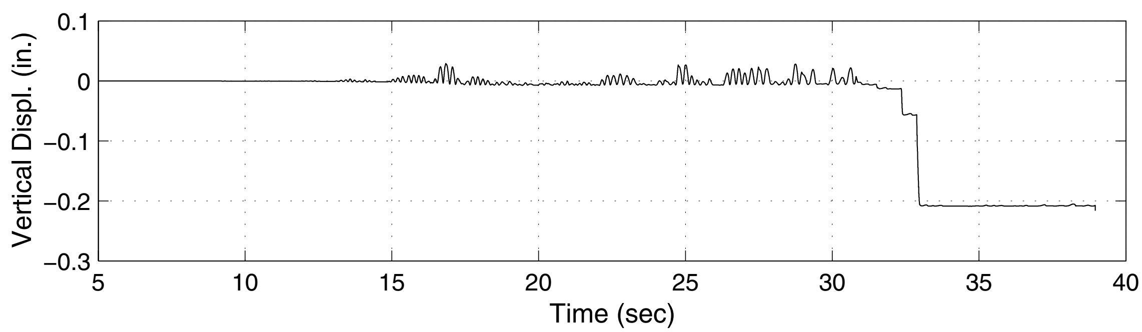

Figure 8-52. Vertical displacement of beam above center column for three-column frame with all shear-critical columns

33.0 and 35.5 seconds. At 39.0 seconds axial failure is detected in the west column. At the same time, the sum of the column axial-load capacities approaches the total gravity load supported by the frame, as shown in the bottom plot of Figure 8-50. As the total axial capacity drops below the total gravity load, inertial forces due to vertical acceleration of the mass are needed to maintain equilibrium. The analysis does not capture significant vertical inertial forces due to the soft springs used to isolate the vertical mass to avoid spurious column axial loads (see Section 8.4). Hence, gravity load collapse of the frame is detected when the analysis fails to converge as the total axial capacity drops below the total gravity load supported by the frame.

The near-failure of the frame at 33.0 seconds illustrates the need to account for the uncertainty in the position of the axial limit curves. A slight shift toward smaller drifts for the west column axial limit curve would have resulted in an earlier prediction of gravity load collapse. Correspondingly, a shift of the axial limit curve toward higher drifts may have resulted in the total axial capacity never dropping below the total gravity load, and, hence, no collapse of the three-column frame.

9 Conclusions and Future Work

9.1 SUMMARY AND CONCLUSIONS

The analytical and experimental studies described in this report were undertaken to investigate the shear and axial load failure of columns leading to the gravity load collapse of reinforced concrete building frames during earthquakes.

Given the lack of agreement between existing models for the drift at shear failure and results from an experimental database of shear-critical building columns, two empirical models were developed to provide a more reliable estimate of the drift at shear failure for existing reinforced concrete columns:

$$\frac{\Delta_s}{L} = \frac{1}{30} + 5\rho'' - \frac{4}{1000}\frac{v}{\sqrt{f_c'}} \geq \frac{1}{100} \text{ (psi units)} \tag{9.1}$$

$$\frac{\Delta_s}{L} = \frac{3}{100} + 4\rho'' - \frac{1}{500}\frac{v}{\sqrt{f_c'}} - \frac{1}{40}\frac{P}{A_g f_c'} \geq \frac{1}{100} \text{ (psi units)} \tag{9.2}$$

Based on the experimental database and Equation 9.1, the mean and coefficient of variation for the measured drift at shear failure divided by the calculated drift are 0.96 and 0.35, respectively. For Equation 9.2, the mean and the coefficient of variation are 0.97 and 0.34, respectively. The models indicate that the drift at shear failure is proportional to the amount of transverse reinforcement, and inversely proportional to the applied shear stress and axial load. The application of the proposed empirical drift capacity models should be limited to columns representative of those included in the database.

Based on shear-friction concepts and the results from 12 columns tested to axial failure, a model was also developed to estimate the drift at axial failure for a shear-damaged column:

$$\frac{\Delta_a}{L} = \frac{4}{100}\frac{1 + (\tan\theta)^2}{\tan\theta + P\left(\frac{s}{A_{st} f_{yt} d_c \tan\theta}\right)} \quad \text{where } \theta = 65° \tag{9.3}$$

The mean ratio of the measured to calculated drift at axial load failure based on Equation 9.3 is 0.97; the coefficient of variation is 0.26. The model is consistent with the general observation from experimental tests that the drift at axial failure is directly proportional to the amount of transverse reinforcement and inversely proportional to the magnitude of the axial load.

The capacity models for the drift at shear and axial load failure were used to initiate the strength degradation of a uniaxial material model implemented in the OpenSees analytical platform (OpenSees, 2002). When attached in series with a beam-column element, the material model can be used to model either shear or axial failure, or both if two materials are used in series. Based on experimental evidence suggesting that an increase in lateral shear deformations may lead to an increase in axial deformations and a loss of axial load, shear-axial coupling was incorporated in the material model to approximate the response of a column after the onset of axial failure.

Shake table tests were designed to provide data on the degradation of axial load capacity after shear failure of a reinforced concrete column, and the resulting redistribution of shear and axial loads to the rest of the building system. The test specimens consisted of a three-column frame with a shear-critical center column. Care was taken in selecting appropriate member sizes and strengths to achieve the desired behavior (including shear and possibly axial failure of the center column, yielding of the outside columns before failure of the center column, appropriate beam deflections after axial failure of the center column, and controlled transfer of loads from the wide beam to the columns). Two specimens were tested, differing only by the axial stress on the center column. Both specimens were subjected to one horizontal component from a scaled ground motion recorded during the 1985 Chile earthquake.

The results from the shake table tests have been presented. A comparison of the results from the two specimens indicates that the behavior of the frame is dependent on the initial axial stress on the center column. The specimen with a lower axial load failed in shear, but maintained most of its initial axial load. For the specimen with a higher axial load, shear failure of the center column occurred at lower drifts and earlier in the ground motion record, and was followed by axial failure of the center column. Displacement data from immediately after the onset of axial failure suggest that there are two mechanisms by which the center column shortens during axial failure: First, by large pulses that cause a sudden increase in vertical displacement after a critical drift is attained; and second, by smaller oscillations that appear to “grind down” the shear-failure plane. Dynamic amplification of axial loads transferred from the center column to the outside columns was observed during axial failure of the center column.

A comparison of the test data with predictive models indicated that the yield displacement, stiffness, and flexural strength of the columns could be adequately estimated by models commonly used in engineering practice. The comparison also indicated that slip of the longitudinal reinforcement accounted for over half of the total displacement at first yield of the longitudinal reinforcement. The shear strength model by Sezen (2002) provided a good estimate of the shear strength of the center column for both specimens, but significantly overestimated the displacement at shear failure for the second specimen. The proposed models for the drift at shear and axial load failure (Equations 9.1, 9.2, and 9.3), along with the predicted yield displacement and flexural strength, provided a reasonable backbone to the measured shear-drift response for the center column. A comparison of the axial capacity model with the measured axial-load-drift response indicated that, as observed during the tests, axial failure of the center column should occur only for the specimen with higher axial load.

The measured response of the test specimens was also compared with results from an analytical model incorporating the proposed models for the drift at shear and axial load failure. Nonlinear static and dynamic analyses were performed. The static analyses accurately determined the timing of the shear and axial load failures, and captured the variation in center column axial load during axial failure. The total loss of axial load and the vertical shortening of the center column was underestimated by the static analyses. The dynamic analyses adequately represented the measured response in terms of the apparent period of vibration and the lateral force amplitude throughout the test. The analytical model provided a good estimate of the measured drifts through the point of shear failure; however, large displacements after shear failure, resulting in a permanent offset at the end of the tests, were not captured by the analysis. Axial failure of the center column for Specimen 2 was not detected by the analysis due to the underestimation of the lateral drifts. The sensitivity of the analytical results to the accuracy of the shear and axial failure models was also investigated. The analytical results did not appear particularly sensitive to changes in the shear failure model; however, all analyses underestimated the measured peak drifts. Since the axial failure model is based on a relationship between the axial load and the lateral drift experienced by a column, the analytical estimate of the peak lateral drifts must be improved to achieve an accurate representation of axial failure and the subsequent load redistribution. An analytical model of a frame with three shear-critical columns demonstrated that the proposed column model can be used to assess the gravity load collapse potential of a reinforced concrete frame.

9.2 FUTURE RESEARCH

Several topics requiring further study were identified during the course of this research.

1. More test data are required to refine the models for the drift at shear and axial load failure. The axial failure model, in particular, is based on a small database of static column tests. Additional data and analyses may well improve the capability to predict the onset of axial load failure of columns.

2. A more refined definition of the drift at shear failure based on measured shear deformations may reduce the relatively large coefficient of variation associated with the model for the drift at shear failure.

3. Further study is required to investigate the influence of the variability in the seismic demand and column capacity on the selection of an appropriate drift capacity model.

4. The drift capacity models should be extended to account for the effects of bidirectional bending, variable axial loads, and the lateral loading history. The latter has been investigated by Pujol (2002).

5. Shake table studies using different ground motions, particularly near-fault motions incorporating fling and directivity effects, are required to investigate the influence of the type of ground motion on the shear and axial load failure of columns, and the response of the building frame before gravity load collapse.

6. Shake table tests of specimens with multiple shear-critical columns are needed to provide data on the influence of multiple-column failures on the drift response and gravity load collapse of building frames. Furthermore, tests on multistory building frames are needed to investigate the causes of story-wide column failures.

7. Experimental and analytical studies are needed to investigate the contribution of floor systems and out-of-plane frames to the capacity of a building to resist gravity load collapse. The redistribution of forces within a three-dimensional building frame system should also be considered.

8. The current shear spring model assumes that the flexural capacity of the column is nearly equal for deformations in both directions along the same axis, and may not be appropriate for outside columns in a building frame where the flexural capacity can be significantly different depending on the direction of motion. Furthermore, the limit state failure model should be refined to account for the influence of shear failure in one direction on the shear capacity in the opposite direction. In general, the robustness of the limit state failure model implemented in OpenSees should be improved such that it can be used with confidence in a building frame analysis.

9. Since the shear-axial interaction after axial failure is not well understood, the axial spring model should be adapted to allow for the entire removal of the column element after axial failure is detected. This would provide an upper bound on the redistribution of forces within the building frame.

10. Improvements to nonlinear analytical models are necessary to achieve a better prediction of the drift demands. Without an accurate prediction of the drift demands, the drift capacity models will not be able to accurately predict the point of shear and axial load failure.

11. Refinements to fiber models are necessary to achieve better agreement between axial load oscillations observed during dynamic analysis and measured axial loads from shake table tests.

12. Rayleigh damping, based on linear theory, is commonly used for both linear and nonlinear analysis. Damping models should be developed specifically for nonlinear dynamic analysis.

13. Research is required to account for all significant sources of uncertainty affecting the outcome of a gravity load collapse analysis. Uncertainty in the position and shape of the shear and axial load failure surfaces is expected to have a significant impact on the probabilistic assessment of structural response.

REFERENCES

American Concrete Institute (ACI) Committee 318, 1999, *Building Code Requirements for Structural Concrete (318-99) and Commentary (318R-99)*, American Concrete Institute, Farmington Hills, Michigan.

American Society of Civil Engineers (ASCE), 2000, *Prestandard and Commentary for the Seismic Rehabilitation of Buildings*, *FEMA 356*, Federal Emergency Management Agency, Washington DC, November 2000.

An, X., and Maekawa, K., 1998, Shear Resistance and Ductility of RC Columns after Yield of Main Reinforcement, *Concrete Library of JSCE*, No. 32, December, pp. 99-118.

Applied Technology Council (ATC), 1981, *Seismic design guidelines for highway bridges, ATC-6*, Applied Technology Council, Berkeley, California.

Applied Technology Council (ATC), 1996, *Seismic evaluation and retrofit of concrete buildings, ATC-40*, California Seismic Safety Commission (SSC 96-01), Sacramento, California.

Architectural Institute of Japan (AIJ), 1999, *Design guidelines for earthquake resistant reinforced concrete buildings on inelastic displacement concept*, Architectural Institute of Japan, Tokyo, Japan.

Aschheim, M., and Moehle, J. P., 1992, Shear strength and deformability of RC bridge columns subjected to inelastic displacements, *UCB/EERC 92/04*, University of California, Berkeley.

Browning, J., Li, Y. R., Lynn, A. C., and Moehle, J. P., 2000, Performance Assessment of a Reinforced Concrete Frame Building, *Earthquake Spectra*, Vol. 16, No. 3, pp. 541-555.

Casciati, F., and Faravelli, L., 1984, Progressive Failure for Seismic Reliability Analysis, *Engineering Structures*, Vol. 6, April, pp. 97-103.

Chen, P.F., and Powell, G.H., 1982, Generalized plastic hinge concept for 3D beam-column elements, *UCB/EERC 82/20*, University of California, Berkeley.

Clough, R.W., 1966, Effect of Stiffness Degradation on Earthquake Ductility Requirements, *Report 66-16*, Structural and Materials Research, Structural Engineering Laboratory, UC Berkeley.

Comartin, C.D., 2001, PBEE Needs, Buildings Perspective: Critical Needs throughout the Performance Spectrum, *2001 PEER Annual Meeting*, Oakland, California.

Crisfield, M.A., and Wills, J., 1988, Solution Strategies and Softening Materials, *Computer Methods in Applied Mechanics and Engineering*, Vol. 66, pp. 267-289.

Esaki, F., 1996, Reinforcing Effect of Steel Plate Hoops on Ductility of R/C square Columns, *Proceedings of the Eleventh World Conference on Earthquake Engineering*, Pergamon, Elsevier Science Ltd., Oxford, England, Disc 3, Paper No. 196.

Filippou, F.C., and Spacone, E., 1996, FEDEAS: Nonlinear Analysis for Structural Evaluation, *Proceedings of the Eleventh World Conference on Earthquake Engineering*, Pergamon, Elsevier Science Ltd., Oxford, England, Disc 3, Paper No. 1664

Gardoni, P., 2002, Bayesian analysis for constructing structural capacity models, *Ph.D. Dissertation*, Department of Civil and Environmental Engineering, University of California, Berkeley.

Gentry, T.R., and Wight, J.K., 1994, Wide Beam-Column Connections under Earthquake-type Loading, *Earthquake Spectra*, Vol. 10, No. 4, pp. 675-703.

Hachem, M.M., 2002, Seismic Performance of Circular Reinforced Concrete Bridge Columns under Bidirectional Earthquake Loading, *Ph.D. Dissertation*, Department of Civil and Environmental Engineering, University of California, Berkeley.

Hatamoto, H., Bessho, S., and Matsuzaki, Y. 1991, Reinforced Concrete Wide-Beam-to-Column Subassemblages Subjected to Lateral Load, *Design of Beam-Column Joints for Seismic Resistance, SP-123,* American Concrete Institute, Farmington Hills, Michigan, pp. 291-316.

Haukaas, T., 2003, Finite Element Reliability and Sensitivity Analysis of Hysteretic Degrading Structures, *Ph.D. Dissertation*, Department of Civil and Environmental Engineering, University of California, Berkeley (to be submitted).

Holmes, W.T., 2000, Risk Assessment and Retrofit of Existing Buildings, *Proceedings of the 12th World Conference on Earthquake Engineering,* New Zealand Society for Earthquake Engineering, Upper Hutt, New Zealand, Paper No. 2826.

Hsu, T,T.C. 1984, *Torsion of Reinforced Concrete*, Van Nostrand Reinhold, New York.

Ikeda A., 1968, Report of the Training Institute for Engineering Teachers. Yokohama National University. Japan. Also in "A List of Past Experimental Results of Reinforced Concrete Columns" by Masaya H. Building Research Institute, Ministry of Construction. Japan.

Inoue, N., Inai, E., Wada, A., Kuramoto, H., Fujimoto, I., and Iiba, M., 2000, A Shaking Table Test of Reinforced Concrete Frames Designed Under Old Seismic Regulations in Japan, *Proceedings of the 12th World Conference on Earthquake Engineering,* New Zealand Society for Earthquake Engineering, Upper Hutt, New Zealand, Paper No. 1783.

Kabeyasawa, T., Tasai, A., and Igarashi, S., 2002, An Economical and Efficient Method of Strengthening Reinforced Concrete Columns Against Axial Load Collapse during Major Earthquake, *Third US-Japan Workshop on Performance-Based Earthquake Engineering Methodology for Reinforced Concrete Building Structures*, Seattle, WA, PEER report 2002/02. Berkeley, Calif.: Pacific Earthquake Engineering Research Center, University of California, pp. 399-412.

Kaneko, Y., Mihashi, H., and Ishihara, S., 2001, Entire Load-Displacement Characteristics for Direct Shear Failure of Concrete, *Modeling of Inelastic Behavior of RC Structures under Seismic Load*, American Society of Civil Engineers, Reston, Virginia, pp. 175-192.

Kato, D., and Ohnishi, K., 2002, Axial Load Carrying Capacity of R/C Columns under Lateral Load Reversals, *Third US-Japan Workshop on Performance-Based Earthquake Engineering Methodology for Reinforced Concrete Building Structures*, Seattle, WA, PEER report 2002/02. Berkeley, Calif.: Pacific Earthquake Engineering Research Center, University of California, pp. 247-255.

Kim, J.H., and Mander, J.B., 1999, Truss Modeling of Reinforced Concrete Shear-Flexure Behavior, *MCEER-99-0005*, Multidisciplinary Center for Earthquake Engineering Research, Buffalo, N.Y.

Kokusho, S., 1964, Report by Building Research Institute, Tsukuba, Japan. Also in "A List of Past Experimental Results of Reinforced Concrete Columns" by Masaya H. Building Research Institute, Ministry of Construction. Japan.

Kokusho, S., and Fukuhara, M., 1965, Report by Kokusho Lab., Tokyo Industrial University. Also in "A List of Past Experimental Results of Reinforced Concrete Columns" by Masaya H. Building Research Institute, Ministry of Construction. Japan.

Krawinkler, H., and Moncarz, P. D., 1982, Similitude requirements for dynamic models, *Dynamic Modeling of Concrete Structures SP 73-1*, American Concrete Institute, Detroit, Michigan, pp. 1-22.

Krawinkler, H., Medina, R., and Alavi, B., 2003, Seismic Drift and Ductiltity Demands and their dependence on Ground Motions, *Engineering Structures*,Vol. 25, No. 5, pp. 637-653.

Li, Y.R., and Jirsa, J.O., 1998, Nonlinear Analysis of an Instrumented Structure Damaged in the 1994 Northridge Earthquake, *Earthquake Spectra*, Vol. 14, No. 2, pp. 265-283.

Li, X., Park, R., and Tanaka, H., 1991, Effects of variations in axial load level on the strength and ductility of reinforced concrete columns, *Proceedings of Pacific Conference on Earthquake Engineering*, New Zealand, pp.147-158, Vol. 1.

Lynn, A.C., 2001, Seismic Evaluation of Existing Reinforced Concrete Building Columns, *Ph.D. Dissertation*, Department of Civil and Environmental Engineering, University of California, Berkeley.

Malvar, L.J., 1998, Review of Static and Dynamic Properties of Steel Reinforcing Bars, *ACI Materials Journal*, Vol. 95, No. 5, pp. 609-616.

Mander J.B., Priestley M.J.N., and Park, R., 1988, Theoretical Stress-Strain Model for Confined Concrete, *Journal of Structural Engineering*, Vol. 114, No. 8, pp. 1804-1826.

Mattock, A.H., and Hawkins, N., 1972, Shear Transfer in Reinforced Concrete - Recent Research, *Journal of Prestressed Concrete Institute*, Vol. 17, No. 2, pp. 55-75.

Mattock, 1988, Discussion, *PCI Journal*, Vol. 33, No. 1, pp. 165-166.

Mau, S.T., and Hsu, T.T.C., 1988, Discussion, *PCI Journal*, Vol. 33, No. 1, pp. 166-168.

McKenna, F.T., 1997, Object-oriented finite element programming: Frameworks for analysis, algorithms and parallel computing, *Ph.D. Dissertation*, Department of Civil and Environmental Engineering, University of California, Berkeley.

Minowa, C., Ogawa, N., Hayashida, T., Kogoma, I., and Okada, T., 1995, Dynamic and Static Collapse Tests of Reinforced-Concrete Columns, *Nuclear Engineering and Design*, Vol. 156, pp. 269-276.

Moehle, J. P., Elwood, K. J., and Sezen, H., 2002, Gravity Load Collapse of Building Frames during Earthquakes, *S.M. Uzumeri Symposium: Behavior and Design of Concrete Structures for Seismic Performance, ACI SP-197*, American Concrete Institute, Farmington Hills, Michigan, pp. 215-238.

Nakamura, T., and Yoshimura, M., 2002, Gravity Load Collapse of Reinforced Concrete Columns with Brittle Failure Modes, *Journal of Asian Architecture and Building Engineering*, Vol. 1, No. 1, pp. 21-27.

Niwa, J., Ito, A., Tanabe, T., 2001, Lattice Model Prediction for Ultimate Deformation of RC Columns Subjected to Cyclic Loading, *Modeling of Inelastic Behavior of RC Structures under Seismic Load*, American Society of Civil Engineers, Reston, Virginia, pp. 384-402.

Ohue, M., Morimoto, H., Fujii, S., and Morita, S., 1985, The Behavior of R.C. Short Columns Failing in Splitting Bond-Shear Under Dynamic Lateral Loading, *Transactions of the Japan Concrete Institute*. Vol. 7, pp. 293-300.

OpenSees, 2002, *Open System for Earthquake Engineering Simulation*, (opensees.berkeley.edu), Berkeley, Calif.: Pacific Earthquake Engineering Research Center, University of California.

Otani, S., and Sozen, M. A., 1972, Behavior of Multistory Reinforced Concrete Frames During Earthquakes, *Structural Research Series No. 392*, University of Illinois, Urbana.

Ozbolt, J., Mayer, U., and Vocke, H., 2001, Smeared Fracture FE-Analysis of Reinforced Concrete Structures - Theory and Examples, *Modeling of Inelastic Behavior of RC Structures under Seismic Load*, American Society of Civil Engineers, Reston, Virginia, pp. 234-256.

Pantazopoulou, S.J., 1998, Detailing for Reinforcement Stability in RC Members, *Journal of Structural Engineering*, Vol. 124, No. 6, pp. 623-632.

Pantazopoulou, S.J., 2003, Deformation Capacity of Old Components, Chapter 4, in *Deformation Controlled Assessment of Existing Structures*, State of the Art Report of WG1, Seismic Commission of fib (Commission 7), fib bulletin, to appear.

Petrangeli, M., 1999, Fiber Element for Cyclic Bending and Shear of RC Structures. II: Verification, *Journal of Engineering Mechanics*, Vol. 125, No. 9, pp. 1002-1009.

Pincheira, J.A., and Jirsa, J.O., 1992, Seismic Strengthening of Reinforced Concrete Frames using Post-Tensioned Bracing Systems, *Phil M. Furguson Structural Engineering Lab Report N. 92-3*, University of Texas at Austin.

Pincheira, J.A., Dotiwala, F.S., and D'Souza, J.T., 1999, Seismic Analysis of Older Reinforced Concrete Columns, *Earthquake Spectra*, Vol. 15, No. 2, pp. 245-272.

Popov, E.P., Cohen, J.M., Koso-Thomas, K., and Kasai, K., 1992, Behavior of Interior Narrow and Wide Beams, *ACI Structural Journal*, Vol. 89, No. 6, pp. 607-616.

Priestley, M.J.N., Verma, R., and Xiao, Y., 1994, Seismic Shear Strength of Reinforced Concrete Columns, *Journal of Structural Engineering*, Vol. 120, No. 8, pp. 2310-2329.

Pujol, S., and Ramirez, J.A., Sozen, M.A., 1999, Drift Capacity of Reinforced Concrete Columns Subjected to Cyclic Shear Reversals, *Seismic Response of Concrete Bridges, SP-187*, American Concrete Institute, Farmington Hills, Michigan, pp. 255-274.

Pujol, S. Sozen, M.A., and Ramirez, J.A., 2000, Transverse Reinforcement for Columns of RC Frames to Resist Earthquakes, *Journal of Structural Engineering*, Vol. 126, No. 4, pp. 461-466.

Pujol, S., 2002, Drift Capacity of Reinforced Concrete Columns Subjected to Displacement Reversals, *Ph.D. Thesis*, School of Civil Engineering, Purdue University.

Ranzo, G., and Petrangeli, M., 1998, A fibre finite beam element with section shear modelling for seismic analysis of RC structures, *Journal of Earthquake Engineering*, Vol. 2, No. 3, pp. 443-473.

Richart, F.E., Brandtzaeg, A., and Brown, R.L., 1929, The failure of plain and spirally reinforced concrete in compression, *Bulletin No. 190*, University of Illinois Engineering Experiment Station, Vol. 26, No. 31.

Ricles, J.M., Yang, Y.-S., and Priestley, M.J.N., 1998, Modelling Nonductile R/C Columns for Seismic Analysis of Bridges, *Journal of Structural Engineering*, Vol. 124, No. 4, pp. 415-425.

Saatcioglu, M., and Ozcebe, G., 1989, Response of Reinforced Concrete Columns to Simulated Seismic Load, *ACI Structural Journal*, Vol. 86, No.1, pp. 3-12.

Scott, M., 2003, *Ph.D. Dissertation*, Department of Civil and Environmental Engineering, University of California, Berkeley.

Sezen, H., 2002, Seismic Response and Modeling of Reinforced Concrete Building Columns, *Ph.D. Dissertation*, Department of Civil and Environmental Engineering, University of California, Berkeley.

Sezen, H., Elwood, K.J., Whittaker, A.S., Mosalam, K.M., Wallace, J.W., and Stanton, J.F., 2000, *Structural Engineering Reconnaissance of the August 17, 1999 Earthquake: Kocaeli (Izmit), Turkey*, PEER report 2000/09.Berkeley, Calif.: Pacific Earthquake Engineering Research Center, University of California.

Shing, P.B., and Spencer, B., 2001, Modeling of Shear Behavior of RC Bridge Structures, *Modeling of Inelastic Behavior of RC Structures under Seismic Load*, American Society of Civil Engineers, Reston, Virginia, pp. 315-333.

Shirai N., Moriizumi, K., and Terasawa, K., 2001, Cyclic Analysis of Reinforced Concrete Columns: Macro-Element Approach, *Modeling of Inelastic Behavior of RC Structures under Seismic Load*, American Society of Civil Engineers, Reston, Virginia, pp. 435-453.

Souza, R.M.d., 2000, Force-based Finite Element for Large Displacement Inelastic Analysis of Frames, *Ph.D. Dissertation*, Department of Civil and Environmental Engineering, University of California, Berkeley.

Sozen, M.A., Monteiro, P., Moehle, J.P., and Tang, H.T., 1992, Effects of Cracking and Age on Stiffness of Reinforced Concrete Walls Resisting In-Plane Shear, *Proceedings*, 4th Symposium on Current Issues Related to Nuclear Power Plant Structures, Equipment and Piping, Orlando, Florida.

Spacone, E., Filippou, F.C., and Taucer, F.F., 1996a, Fibre beam-column model for non-linear analysis of R/C frames: part I. formulation, *Earthquake Engineering & Structural Dynamics*, Vol. 25, No. 7, pp. 711-725.

Spacone, E., Filippou, F.C., and Taucer, F.F., 1996b, Fibre beam-column model for non-linear analysis of R/C frames: part II. applications, *Earthquake Engineering & Structural Dynamics*, Vol. 25, No. 7, pp. 727-742.

Tasai, A., 1999, Residual Axial Capacity and Restorability of Reinforced Concrete Columns Damaged due to Earthquake, *US-Japan Workshop on Performance-Based Earthquake Engineering Methodology for Reinforced Concrete Building Structures*, Maui, Hawaii, PEER report 1999/10. Berkeley, Calif.: Pacific Earthquake Engineering Research Center, University of California, pp. 191-202.

Tasai, A., 2000, Residual Axial Capacity of Reinforced Concrete Columns during Shear Deterioration, *Second US-Japan Workshop on Performance-Based Earthquake Engineering Methodology for Reinforced Concrete Building Structures*, Sapporo, Japan, PEER report 2000/10. Berkeley, Calif.: Pacific Earthquake Engineering Research Center, University of California, pp. 257-267.

Tsuchiya, S., Ishii, H., and Umehara, H., 2001, Response Analysis of Reinforced Concrete Frames in Railroad Viaducts Damaged by the Hyogo-Ken-Nanby Earthquake, *Modeling of Inelastic Behavior of RC Structures under Seismic Load*, American Society of Civil Engineers, Reston, Virginia, pp. 420-434.

UCFyber, 1999, Cross Section Analysis Structural Software (http://www.zevent.com)

Umemura, H., and Endo, T., 1970, Report by Umemura Lab, Tokyo University. Also in "A List of Past Experimental Results of Reinforced Concrete Columns" by Masaya H., Building Research Institute, Ministry of Construction. Japan.

Vecchio, F.J., and Collins, M.P., 1986, The Modified Compression-Field Theory for Reinforced Concrete Elements Subjected to Shear, *ACI Structures Journal*, pp. 219-231.

Watanabe, F., and Ichinose, T., 1992, Strength and ductility of RC members subjected to combined bending and shear, *Concrete Shear in Earthquake*, Elsevier Applied Science, New York, pp. 429-438

Wight, J.K., and Sozen, M.A., 1973, Shear strength decay in reinforced concrete columns subjected to large deflection reversals, *Structural Research Series No. 403*, University of Illinois, Urbana.

Yalcin, C., 1997, Seismic Evaluation and Retrofit of Existing Reinforced Concrete Bridge Columns, *Ph.D. Dissertation*, Department of Civil Engineering, University of Ottawa.

Yoshikawa, H., and Miyagi, T., 2001, Ductility and Failure Modes of Single Reinforced Concrete Columns, *Modeling of Inelastic Behavior of RC Structures under Seismic Load*, American Society of Civil Engineers, Reston, Virginia, pp. 351-368.

Yoshimura, M., and Nakamura, T., 2002, Intermediate-Story Collapse of Concrete Buildings, *Third US-Japan Workshop on Performance-Based Earthquake Engineering Methodology for Reinforced Concrete Building Structures*, Seattle, WA, PEER report 2002/02. Berkeley, Calif.: Pacific Earthquake Engineering Research Center, University of California, pp. 107-118.

Yoshimura, M., and Yamanaka, N., 2000, Ultimate Limit State of RC Columns, *Second US-Japan Workshop on Performance-Based Earthquake Engineering Methodology for Reinforced Concrete Building Structures*, Sapporo, Japan, PEER report 2000/10. Berkeley, Calif.: Pacific Earthquake Engineering Research Center, University of California, pp. 313-326.

Zeris, C.A., and Mahin, S.A., 1991, Behavior of Reinforced Concrete Structures Subjected to Biaxial Excitation, Journal of Structural Engineering, Vol. 117, No. 9, pp. 2657-2673.

Appendix A: Specimen Drawings, Materials, and Construction

A.1 AS-BUILT SPECIMEN DRAWINGS AND SPECIFICATIONS

Two nominally identical shake table test specimens conforming to the plans shown in Figures A-1 through A-5(b) were constructed. The reinforcement met the following specifications:

- All reinforcement, with the exception of the center column ties and the outside column longitudinal bars, complied with ASTM A706 for grade 60 reinforcement.
- Plain reinforcing wire conforming to ASTM A82 was used for the center column transverse reinforcement.
- Grade 40 bars conforming to ASTM A615 were used for the outside column longitudinal reinforcement.
- All stirrup hooks within the footings and beams were 135° bend plus 6 bar diameters (not less than 3") extension. Consecutive cross ties, with a 90° bend plus 6 bar diameters extension on one end and 135° bend plus 6 bar diameters (not less than 3″) extension on the other, were alternated end for end.
- The center column tie hooks were 90° bend plus 1-1/8 inch extension. The locations of the tie hooks were alternated.
- All bar anchorage hooks were 90° bend plus 12 bar diameters extension, except as noted in the plans.
- The concrete clear cover over the *longitudinal* reinforcement was 1 inch, except as noted in the plans.

Normal-weight aggregate concrete, conforming to the mix design specifications described in Section A.3.1, was cast in two lifts, with the construction joint located at the base of the columns. The specimens were inspected during construction to conform with the tolerances listed in Table A-1.

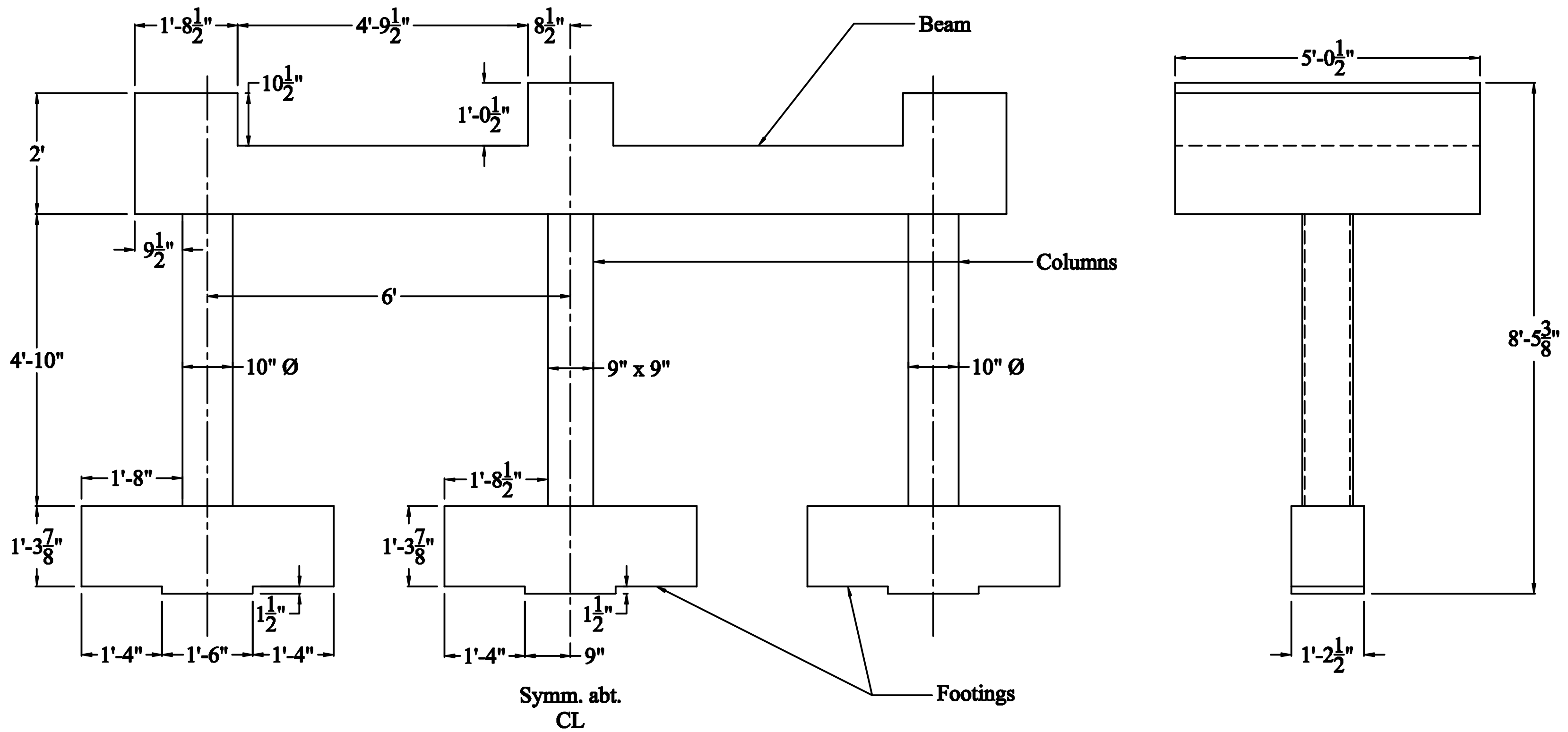

Elevation

Side View

Figure A-1. General plan

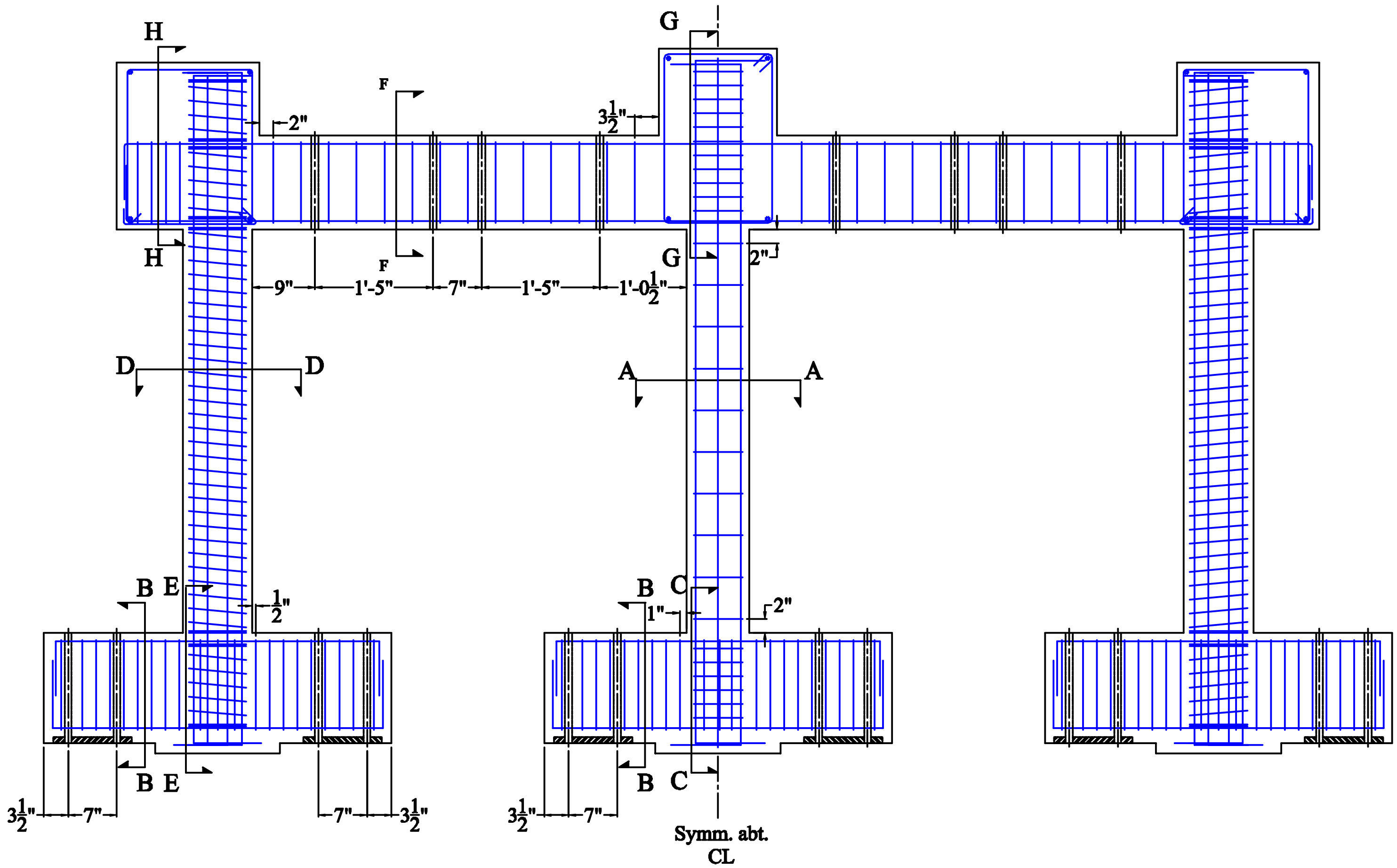

Figure A-2. Reinforcement details — elevation (see Figures A-3 through A-5(b) for section details)

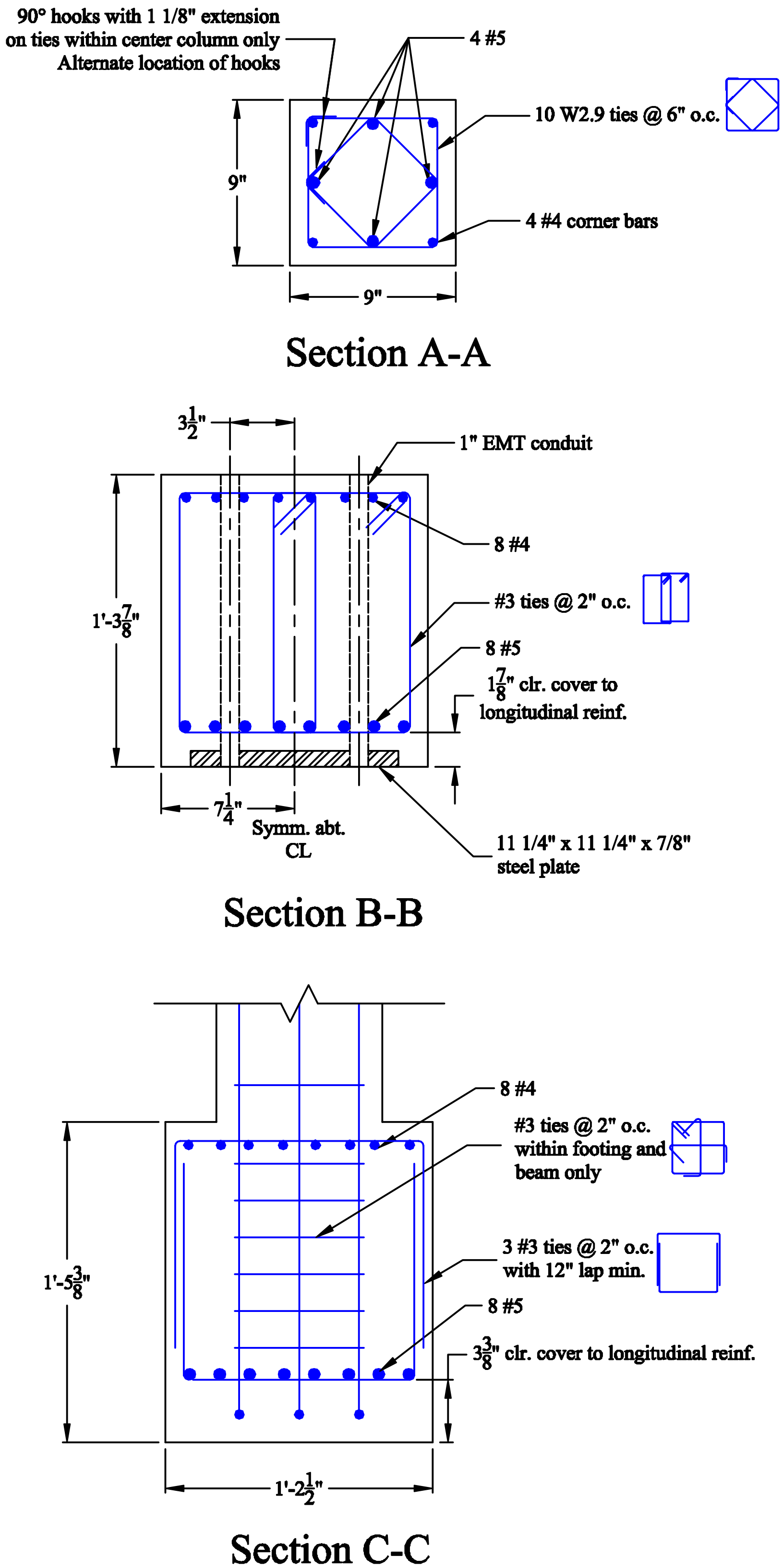

Figure A-3. Reinforcement details — center column

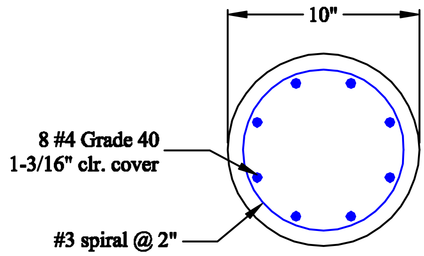

Section D-D

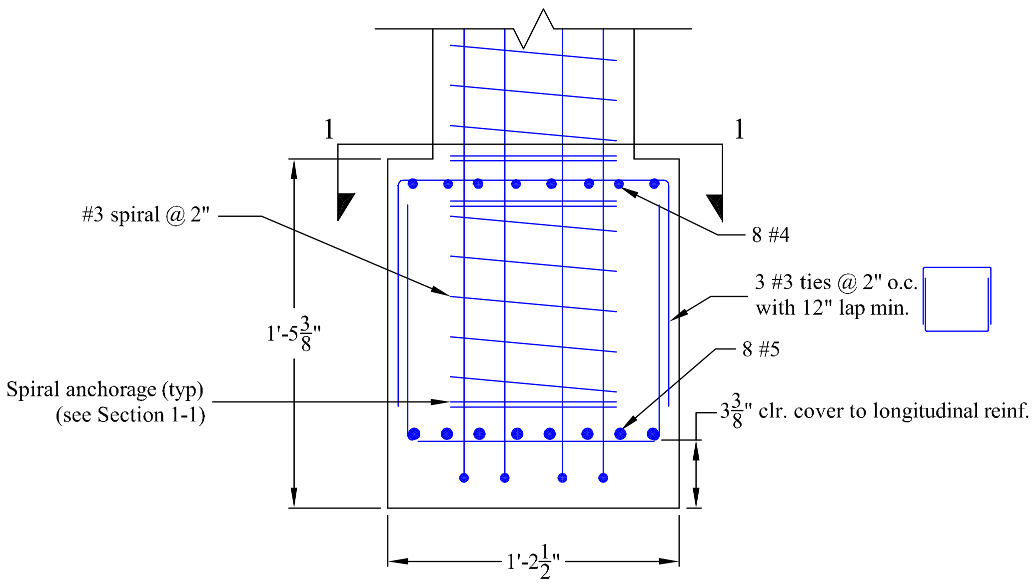

Section E-E

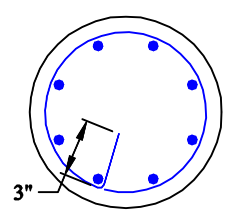

Note: Use an extra 1 1/2 flat turns followed by a 3" hook anchored into column core at ends of each spiral section

Section 1-1

Detail of Spiral Anchorage (typ)

Figure A-4. Reinforcement details — outside columns

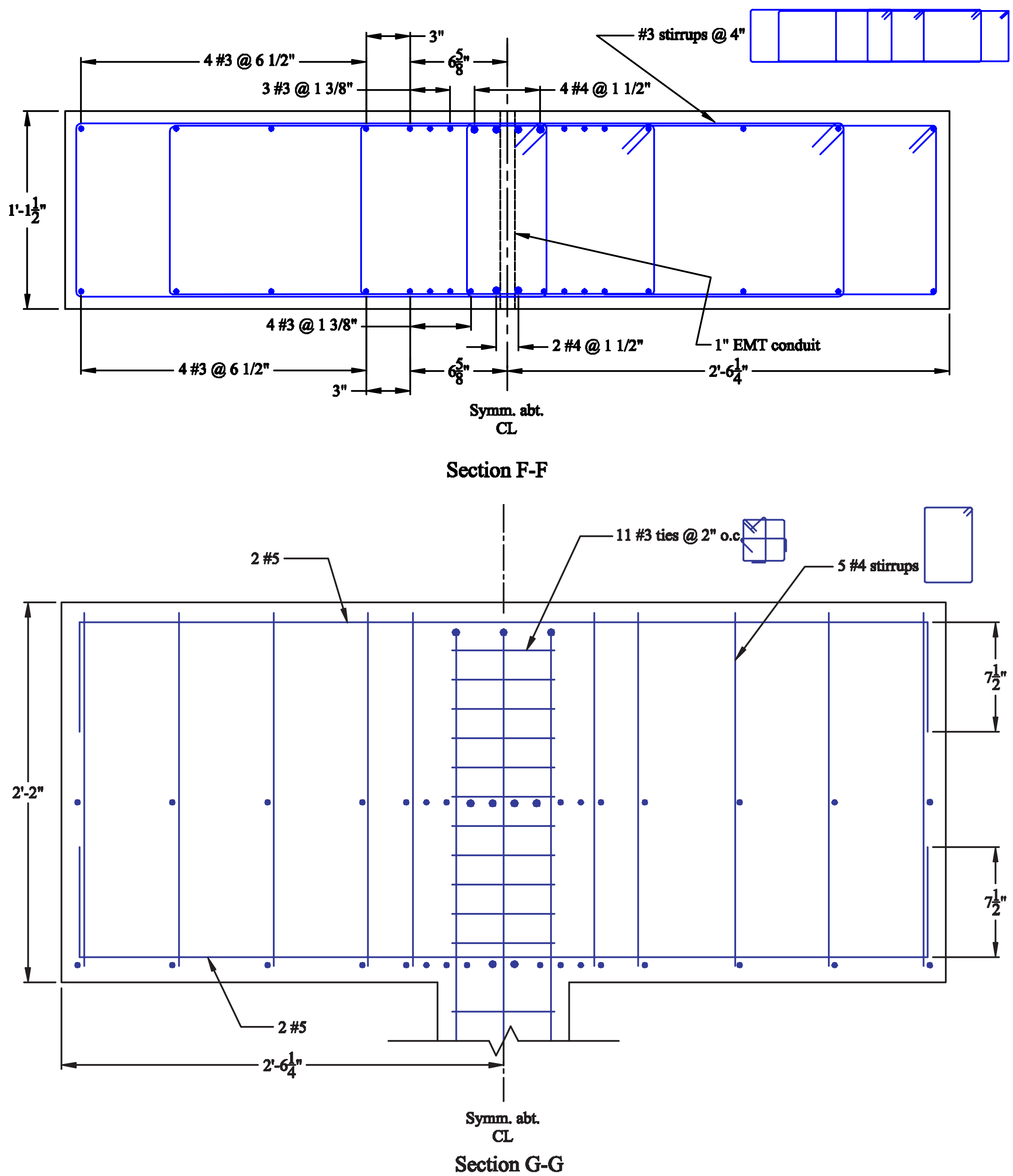

(a)

Figure A-5. Reinforcement details — beam

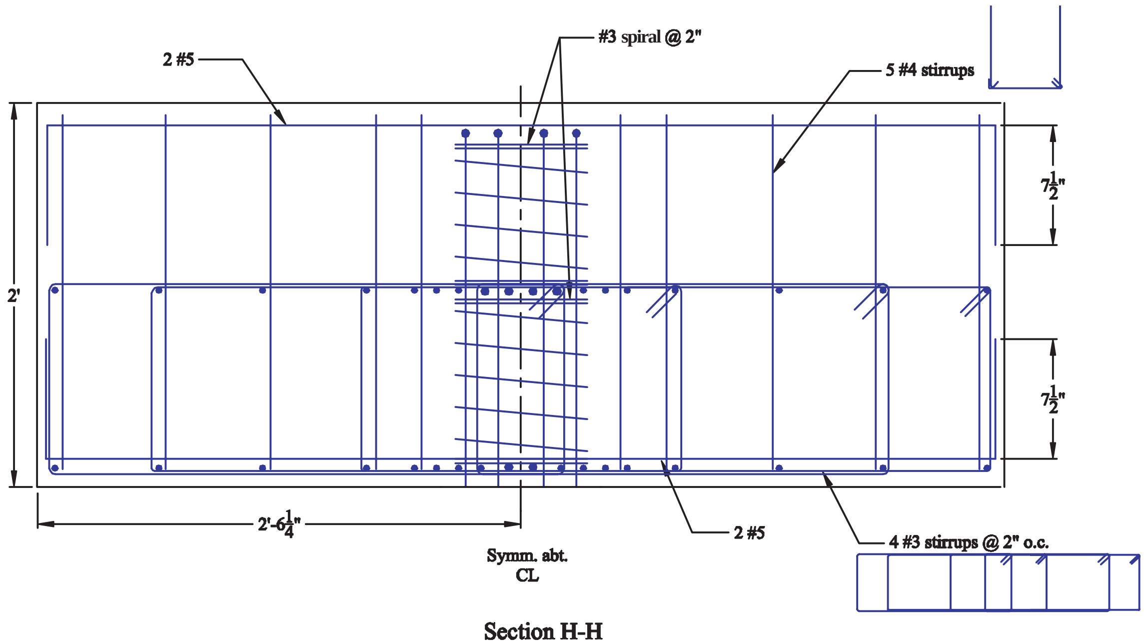

(b)

Figure A-5. ***(Continued)*** **Reinforcement details — beam**

Table A-1. Construction tolerances

Concrete cover	+/- 1/8 in.
Stirrup and tie dimensions	+/- 1/8 in.
Member dimensions	+/- 1/8 in.
Bar cutoff and longitudinal bends	+/- 1/4 in.
Steel placement	+/- 1/8 in.
Conduit locations	+/- 1/8 in.

A.2 DESIGN OF TRANSVERSE TORSIONAL BEAMS

Particular attention was paid to the design of the connection between the 5-foot-wide beam and the columns. The moment developed over the width of the wide beam must be transferred to the narrow columns. A similar condition arises in buildings with wide beams due to restricted story heights or one-way joist systems. Wide beam-column joints from such buildings have been investigated by several researchers (Gentry and Wight, 1994; Popov et al., 1992; Hatamoto et al., 1991). The research indicates that if some of the beam longitudinal bars are anchored significantly outside the joint core, then a transverse beam framing into the joint must be relied upon to carry some of

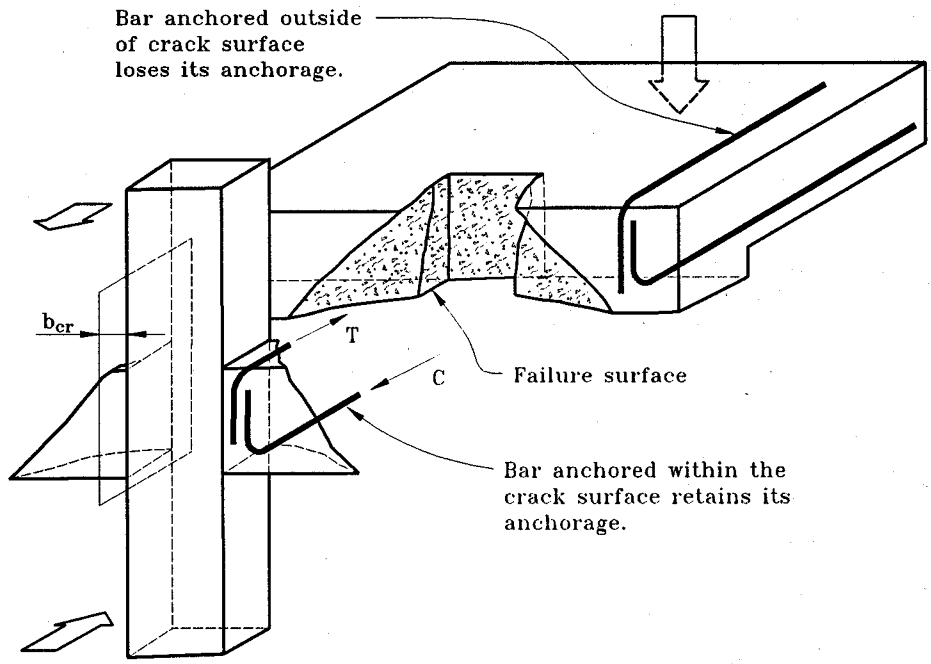

Figure A-6. Failure plane for wide beam-column joints (from Gentry and Wight, 1994)

the beam moment into the column through torsion. If the transverse beam does not have sufficient torsional strength, then it will crack close to the column and any longitudinal bars from the wide beam anchored outside the crack surface will effectively loose their anchorage (Figure A-6). Those researchers have found that exterior wide beam-column joints are particularly vulnerable to this mode of failure.

Gentry and Wight (1994) provide recommendations for the design of wide beam-column joints. Since the stiffness of the transverse torsional beam will decrease significantly after cracking, the recommendations are based on limiting the torque in the transverse beam to less than the cracking torque. Although more accurate expressions exist, the cracking torque can be estimated as:

$$T_{cr} = 2\sqrt{f_c'}x^2y \text{ (psi units)} \tag{A.1}$$

where x and y are the dimensions of the gross cross section (with $x < y$), and f_c' is the concrete compressive strength in psi.

For exterior wide beam-column joints, Gentry and Wight (1994) recommend that the portion of the moment transferred from the wide beam to the column through beam longitudinal bars

Figure A-7. Demands on torsional beams

anchored outside the crack surface should be limited to less than $4\sqrt{f_c'}x^2y$ (psi units). Estimates for the location of the crack surface are provided. Note that the coefficient 4 appears because the resistance provided by the transverse torsional beams on both sides of the column is considered.

Experiments have shown that the torsional strength of transverse beams of interior joints is at least double that of exterior joints due to the confinement provided by the continuous slab. Hence, for interior wide beam-column joints, Gentry and Wight (1994) recommend that the applied torque on the transverse beams be limited to $8\sqrt{f_c'}x^2y$ (psi units).

The skew bending and plastic theories provide the following equations for the cracking torque of a rectangular section (Hsu, 1984):

$$\text{Skew Bending Theory: } T_{cr} = \frac{x^2y}{3}(0.85f_r) \text{ where } f_r = 21\left(1 + \frac{10}{x^2}\right)\sqrt[3]{f_c'} \qquad (A.2)$$

$$\text{Plastic Theory: } T_{cr} = \left(\frac{1}{2} - \frac{x}{6y}\right)x^2yf_c' \qquad (A.3)$$

Equations A.2 and A.3 give lower estimates of the cracking torque than the recommendations by Gentry and Wight (1994).

Since the prototype building for the three-column frame does not include wide beams, sufficiently large transverse beams are required in the three-column frame to preclude any reduction in stiffness due to torsional cracking. The above recommendations and estimates of the cracking torque were used to design the transverse torsional beams for the three-column frame. Figure A-7 illustrates the demands on the transverse torsional beams. (Note that to avoid any interference with the behavior of the columns, the transverse beams protrude from the top of the wide beam.) Since the torsional demands are applied along the side faces of the transverse beams, the resistance to this demand must be calculated from the cracking capacity of the rectangular transverse beam section. This also applies to the transverse beam over the center column, since under side sway of the frame, the torsional demands on either side of the transverse beam act in the same direction (Figure A-7).

For the conventional design of a wide beam-column joint, the demands on the transverse beam are calculated as the ultimate beam moment multiplied by the fraction of longitudinal bars anchored outside the expected torsional crack. For the three-column frame, however, the ultimate beam moment will never be achieved since the columns are designed to yield before the beams. Considering this difference in behavior and the difference in the estimates of the cracking torque discussed above, two demand-capacity ratios were considered in the selection of the appropriate size for the transverse beams:

$$D/C_1 = T_{u\ beam}/T_{cap\ GW} \tag{A.4}$$

$$D/C_2 = max\left[\frac{T_{u\ push}}{T_{cap\ skew}}, \frac{T_{u\ push}}{T_{cap\ plastic}}\right] \tag{A.5}$$

where $T_{u\ beam}$ is the ultimate beam moment multiplied by the fraction of longitudinal bars anchored outside the expected torsional crack, $T_{cap\ GW}$ is torsional capacity recommended by Gentry and Wight (1994), $T_{u\ push}$ is the torsional demand from the pushover analysis, and $T_{cap\ skew}$ and $T_{cap\ plastic}$ are 2 times the cracking torques calculated according to the skew bending and plastic theories, respectively. The torsional capacities were calculated using a strength reduction factor of 0.5. Table A-2 summarizes the demand-capacity ratios for the selected torsional beam sizes.

Table A-2. Demand-capacity ratios for torsional beams

Location	*h (in)*	*b (in)*	D/C_1	D/C_2
Center Column	26	17	0.55	1.02
Outside Column	24	20.5	0.65	0.84

A.3 MATERIAL PROPERTIES

A.3.1 Mix Design

The concrete for the shake table test specimens was delivered to the site. The mix specifications and design are summarized in Tables A-3 and A-4.

Table A-3. Concrete mix specifications

Cement	ASTM C-150 Type II
Water reducer	Pozzolith 322N ASTM C-494 Type A
Minimum 28-day strength	3000 psi
Maximum 28-day strength	3500 psi
Cementitious material	4.52 sacks
Maximum aggregate size	3/8" (pea gravel allowed)
Slump	5" +/- 1"
Water/Cement ratio	0.718

Table A-4. Mix design

Material	*Specific Gravity*	*Absolute Volume (ft^3)*	*SSD Weights (lbs)*
Cement Type II	3.15	2.16	425
Water	1.00	4.89	305
Water Reducer	-	0.41	21.3 fl. oz.
3/8" x #8	2.68	7.47	1250
Regular top sand	2.67	8.75	1460
SR blend sand	2.60	2.16	425
Total		27.00	3980

A.3.2 Concrete Properties

At the time of casting, 6-inch diameter by 12-inch-high standard cylinders were cast according to ASTM C31 requirements. The cylinders were kept in the same environment as the test specimens, and were stripped on the same day the forms were removed. The cylinders were capped with high-strength sulfur mortar and then tested to determine the concrete compressive strength according to ASTM C39. Three cylinders were tested on 7-day intervals until 28 days, and then shortly after the day of the shake table tests. Table A-5 and Figure A-8 summarize the results from the cylinder tests. For the last tests, the stress-strain relationship was determined for each cylinder (Figures A-9 through A-12). Splitting tension tests were performed according to ASTM C496. The calculated tensile stresses at failure are summarized in Table A-6.

Since the cylinder strengths for the footing concrete appeared very low at 14 and 21 days, cores from the same concrete used in the footing were tested at 22 days according to ASTM C42.

Table A-5. Average concrete compressive strengths (each mean based on three cylinder tests)

Days after casting	*Footing (psi)*		*Beam/Column (psi)*	
	mean	*standard deviation*	*mean*	*standard deviation*
7	1240	97	1720	80
14	1500	50	2100	66
21	1790	57	2570	128
28	1920	72	2830	35
165	-	-	3560	76
211	-	-	3470	163
221	3240	112	-	-
267	3150	41	-	-

Table A-6. Splitting tension test results (each mean based on three cylinder tests)

Days after casting	*Type*	*Mean (psi)*	*Standard Deviation (psi)*
221	Footing	336	28
165	Beam/Column	360	52
267	Footing	317	28
211	Beam/Column	323	11

The core strengths were higher than the cylinder strengths, as shown in Figure A-8. The cylinders may have underestimated the true strength of the footing concrete due to exposure to direct sunlight during curing. Cylinders for the beam and column concrete were kept in the shade next to the test specimens during curing.

A.3.3 Reinforcing Steel Properties

For each size of reinforcement used in the test specimens, three steel coupons were machined with a gage length of 2 inches and tested according to ASTM A370. The results are summarized in Table A-7. For the #4 and #5 bars the yield stress, f_y, was taken from the plateau just after first yield, and the yield strain, ε_y, was taken as the strain at the peak at first yield. For the #3 bars the yield stress and strain were defined by the intersection of two straight line approximations, one from before yield and the other just after. The ultimate stress, f_u, was taken as the maximum stress

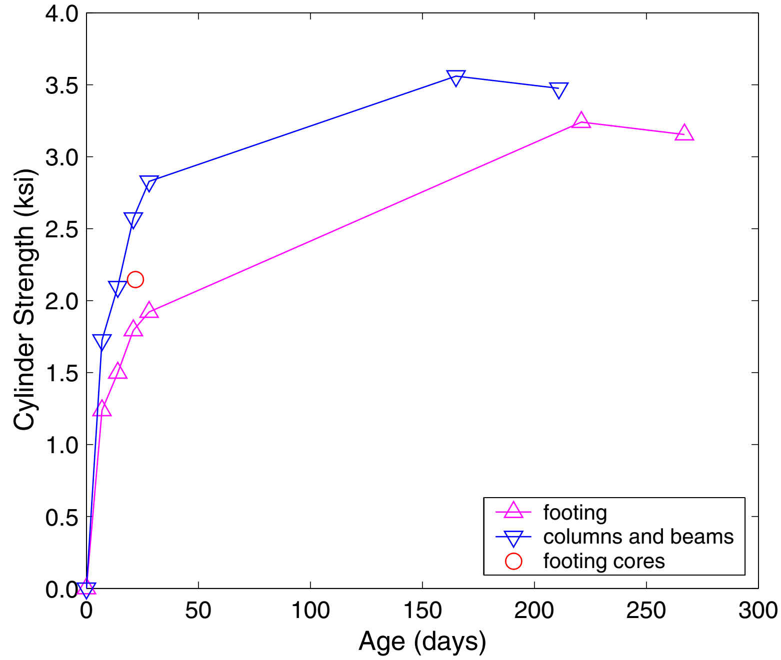

Figure A-8. Concrete strength gain with age (mean of three tests each day)

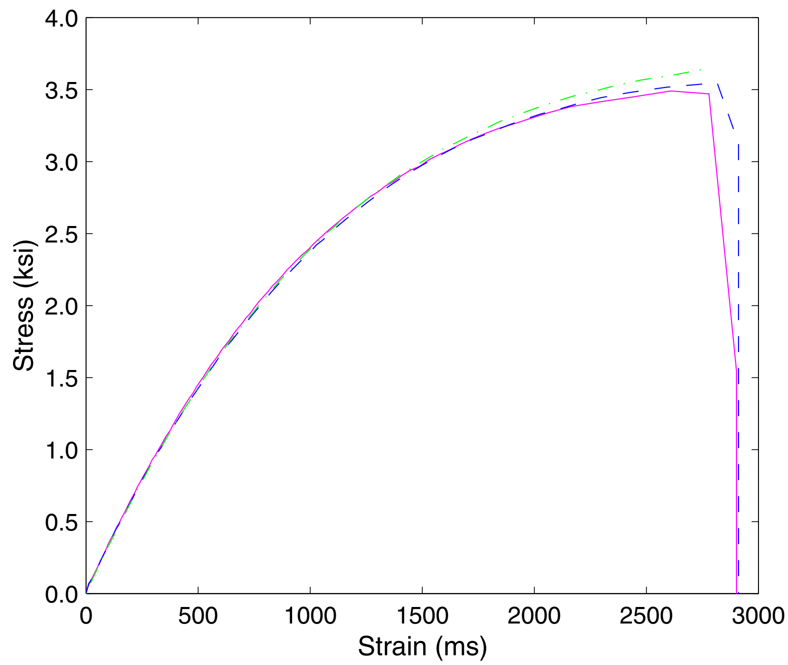

Figure A-9. Concrete stress-strain plots for three cylinders from column and beam concrete (Specimen 1, Day 165)

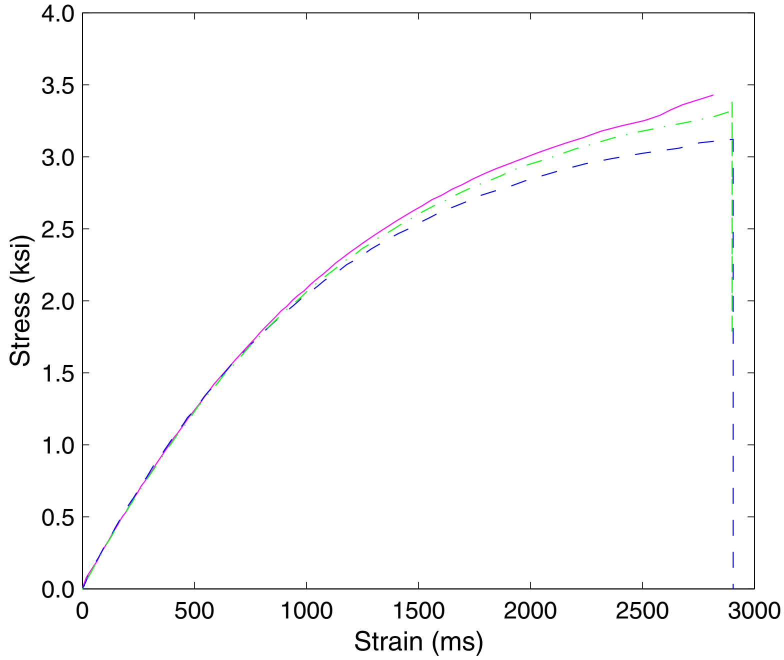

Figure A-10. Concrete stress-strain plots for three cylinders from footing concrete (Specimen 1, Day 221)

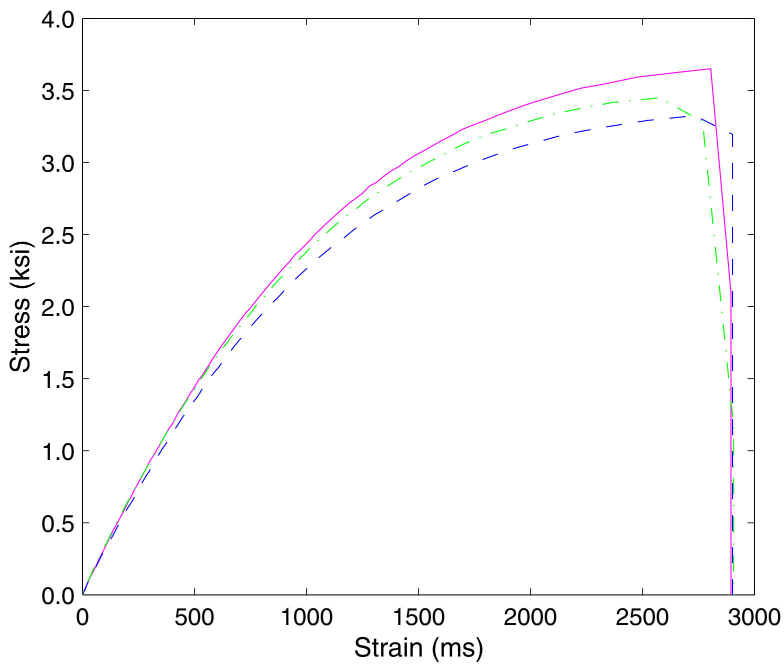

Figure A-11. Concrete stress-strain plots for three cylinders from column and beam concrete (Specimen 2, Day 211)

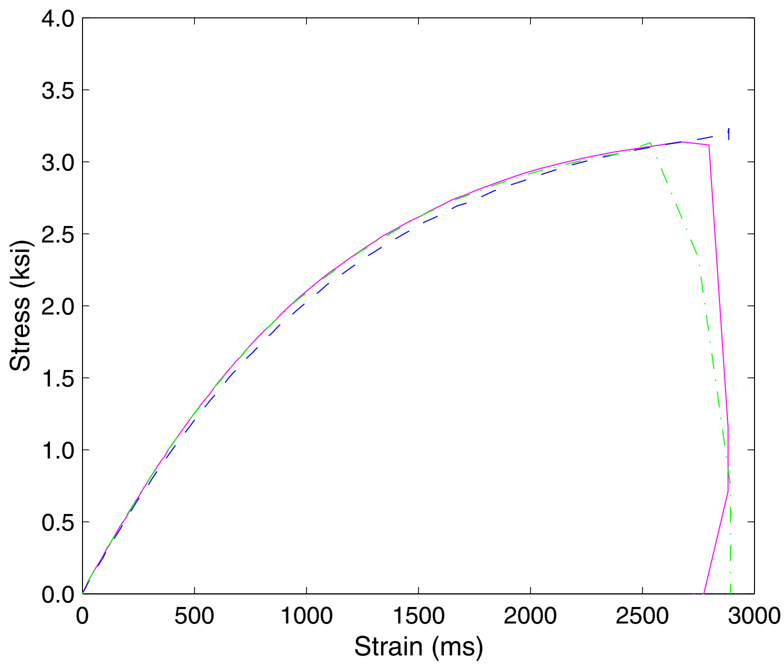

Figure A-12. Concrete stress-strain plots for three cylinders from footing concrete (Specimen 2, Day 267)

recorded during the coupon test; while the ultimate strain, ε_u, reported in Table A-7 was taken as the maximum strain recorded during the coupon test (note that f_u and ε_u do not occur at the same time during coupon test results shown in Figures A-13 – A-17). The modulus of elasticity, E_s, was determined by calculating a linear least-squares fit to the data for strains below 0.002.

.

Table A-7. Averages from reinforcing steel coupon tests

Location and Size	*No. of tests*	f_y *(ksi)*	f_u *(ksi)*	ε_y	ε_u	*maximum elongation*[a] *(in.)*	E_s *(ksi)*
Center column longitudinal (#4 and #5 grade 60)	5[b]	69.5	100	0.0027	0.202	0.51	28940
Outside column longitudinal (#4 grade 40)	2[b]	61.5	95.0	0.0024	0.204	0.48	28950
Beam and outside column transverse (#3 grade 60)	3	79.4	105	0.0028	0.138	0.37	29240
Center column transverse (W2.9 wire)	3	-	104	-	0.022	not measured	29590

a. at 2 inch gage length

b. results from one coupon were ignored (see Figures A-13 and A-14).

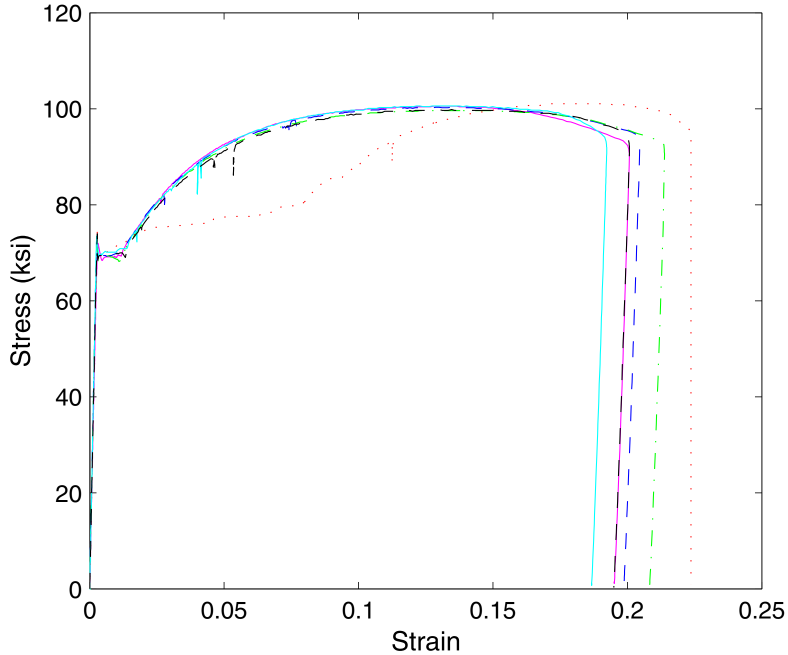

Figure A-13. Reinforcing steel stress-strain plots for center column longitudinal steel (dotted curve ignored)

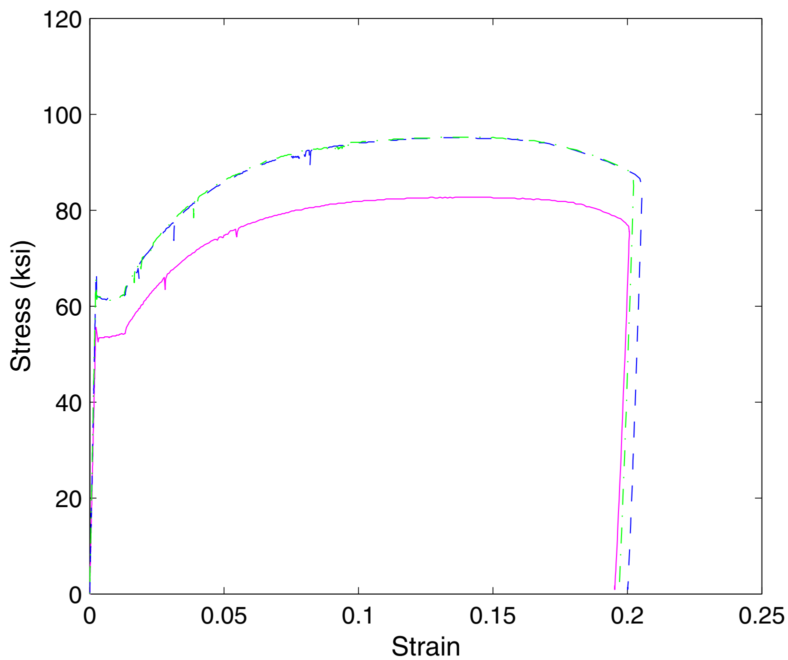

Figure A-14. Reinforcing steel stress-strain plots for outside column longitudinal steel (lower curve ignored, since fracture occurred outside gage length)

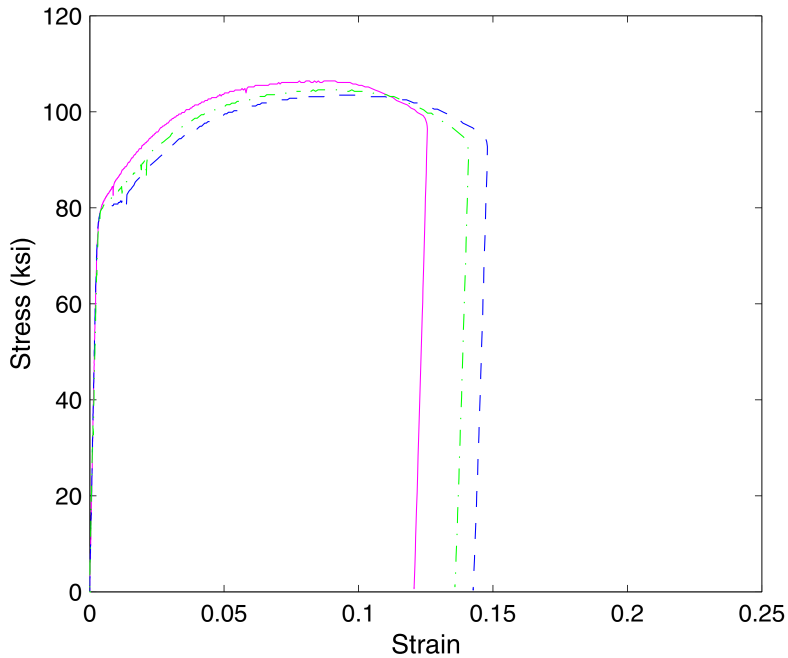

Figure A-15. Reinforcing steel stress-strain plots for beam longitudinal steel

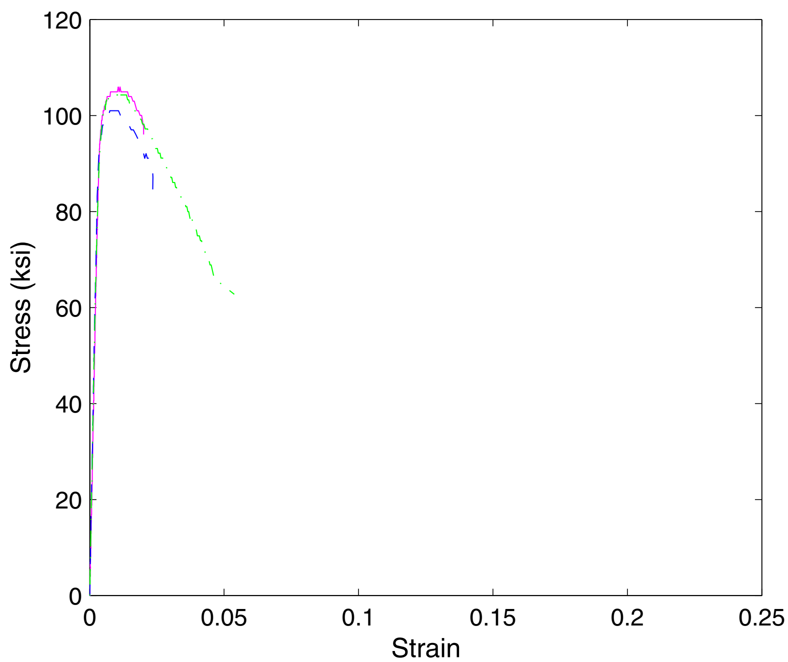

Figure A-16. Reinforcing steel stress-strain plots for center column transverse steel (W2.9 wire)

A.4 CONSTRUCTION PROCEDURES

The specimens were constructed in an upright position at a casting site adjacent to the earthquake simulator laboratory at the Richmond Field Station of the University of California, Berkeley. A local contractor constructed the specimens and supplied the reinforcing steel conforming to the specifications listed in Section A.1. The reinforcement was bent and cut before delivery to the site. The concrete formwork was constructed on-site. The footing cages were fabricated on-site and placed in the forms. After being instrumented with strain gages (see Section B.4.4), the column longitudinal steel was erected and secured (Figure A-17). Concrete was delivered to the site, where a slump test was performed to ensure conformance with the specifications. The footings were cast in one lift with concrete directly from the shoot of the concrete truck (Figure A-18). The column longitudinal reinforcement was cleaned with a wire brush after the footing concrete had cured. The footings were wet-cured for four weeks.

After being instrumented with strain gages, the center column ties were carefully secured to the longitudinal reinforcement. The formwork for the columns and beams was constructed in place (Figure A-19), and the beam steel was erected Figure A-20). Although the beam and column reinforcement was completed within two weeks of the casting of the footings, the concrete pour was delayed seven weeks due to concerns regarding the footing concrete quality (see Section A.3.2). The concrete was again delivered to the site and a slump test was performed. A pump was used to place the column and beam concrete. The column concrete was placed and vibrated prior to the placement of the beam concrete (Figure A-21). The specimens were wet-cured for 14 days and then stripped and transported to the laboratory (Figure A-22) where they were stored until testing (age of the column and beam concrete at testing was 151 days for Specimen 1 and 184 days for Specimen 2).

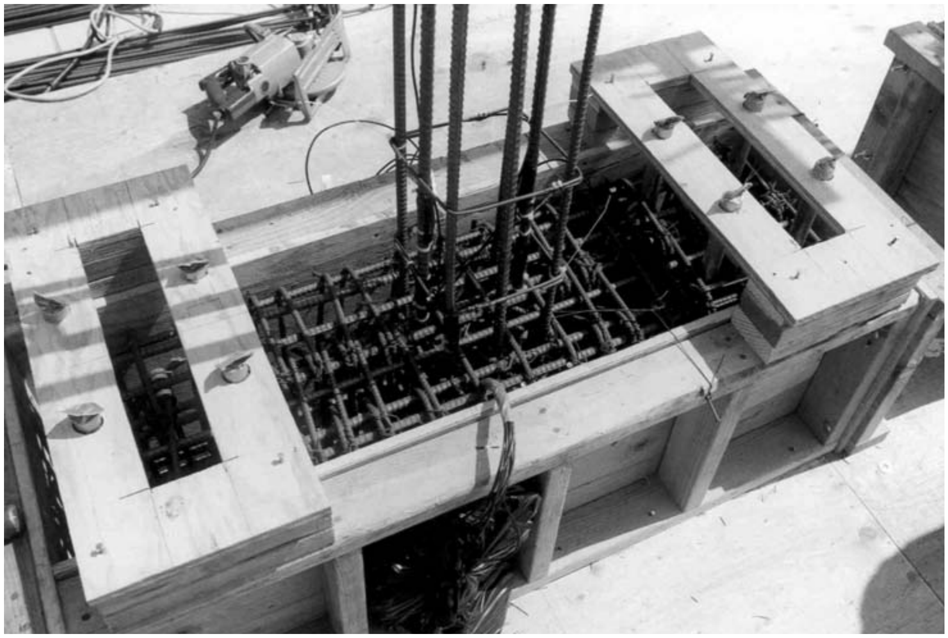

Figure A-17. Reinforcing cage for center column footing in formwork

Figure A-18. Casting footings

Figure A-19. Formwork and wet-curing of footing concrete

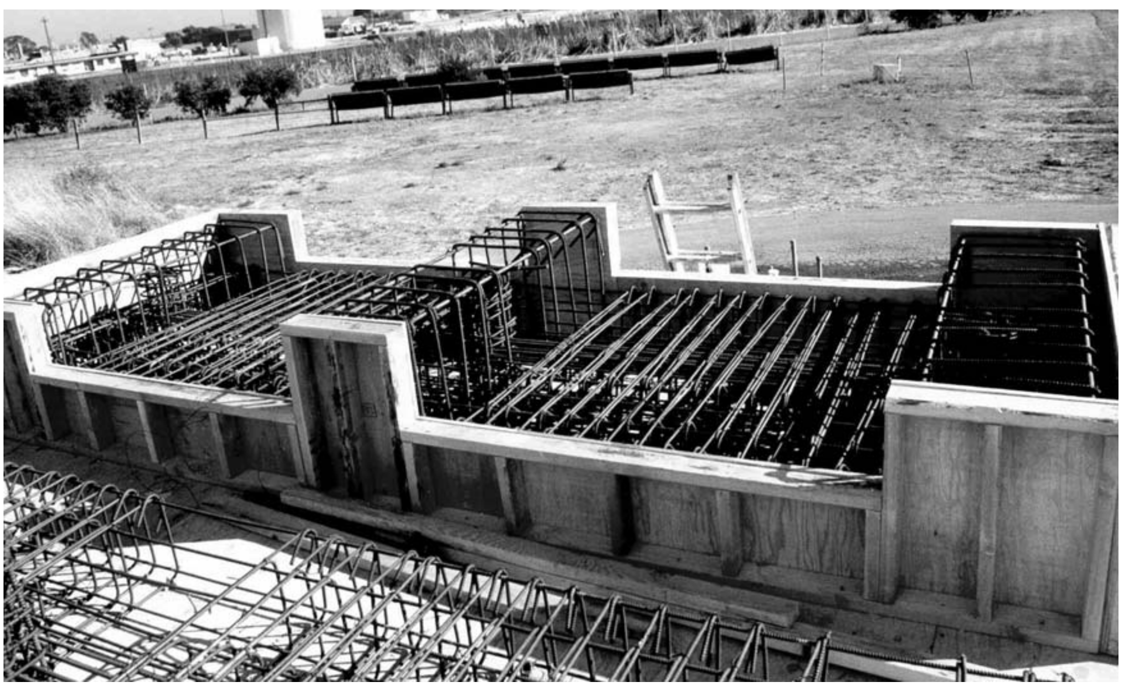

Figure A-20. Beam reinforcement

Figure A-21. Column and beam casting

Figure A-22. Moving specimens to laboratory

Appendix B: Experimental Setup, Procedures, and Data Reduction

B.1 INTRODUCTION

The experimental setup, shown in Figure B-1, was designed to facilitate the observation of load redistribution in the event of axial failure of the center column and to ensure that the out-of-plane movement of the specimen mass was restricted during testing. The following paragraphs describe the installation of the test specimens and the experimental setup.

A 2″-thick steel base plate was prestressed to the shake table using high-strength rods threaded into tapped holes in the base plate. Hydrostone was placed between the base plate and the shake table to ensure a level surface. Six triaxial force transducers (described in Section B.4.2) were bolted to the base plate. The force transducers were located directly above the prestressing rods attaching the base plate to the table in order to maximize the stiffness of the end condition. Hydrostone was placed between the force transducers and the base plate to ensure that the transducers were level and to maximize the bearing surface. After the hydrostone cured, the bolts attaching the force transducers to the base plate were torqued to achieve a frictional force of approximately 25 kips between each transducer and the base plate.

After installation of the force transducers, the test specimen was lifted into position on the shake table and aligned with the intended shaking direction. The specimen was leveled and then supported on screw jacks 1/4″ above the force transducers, while hydrostone was placed between the footings and the top plate of the transducers. After the hydrostone was cured, 3/4″ high-strength rods passing through 1″ EMT pipe cast into the footings were used to firmly secure the specimen to the force transducers and to achieve a frictional force of approximately 25 kips between the footings and each transducer. Four-by-four wood posts were shimmed under each corner of the beam

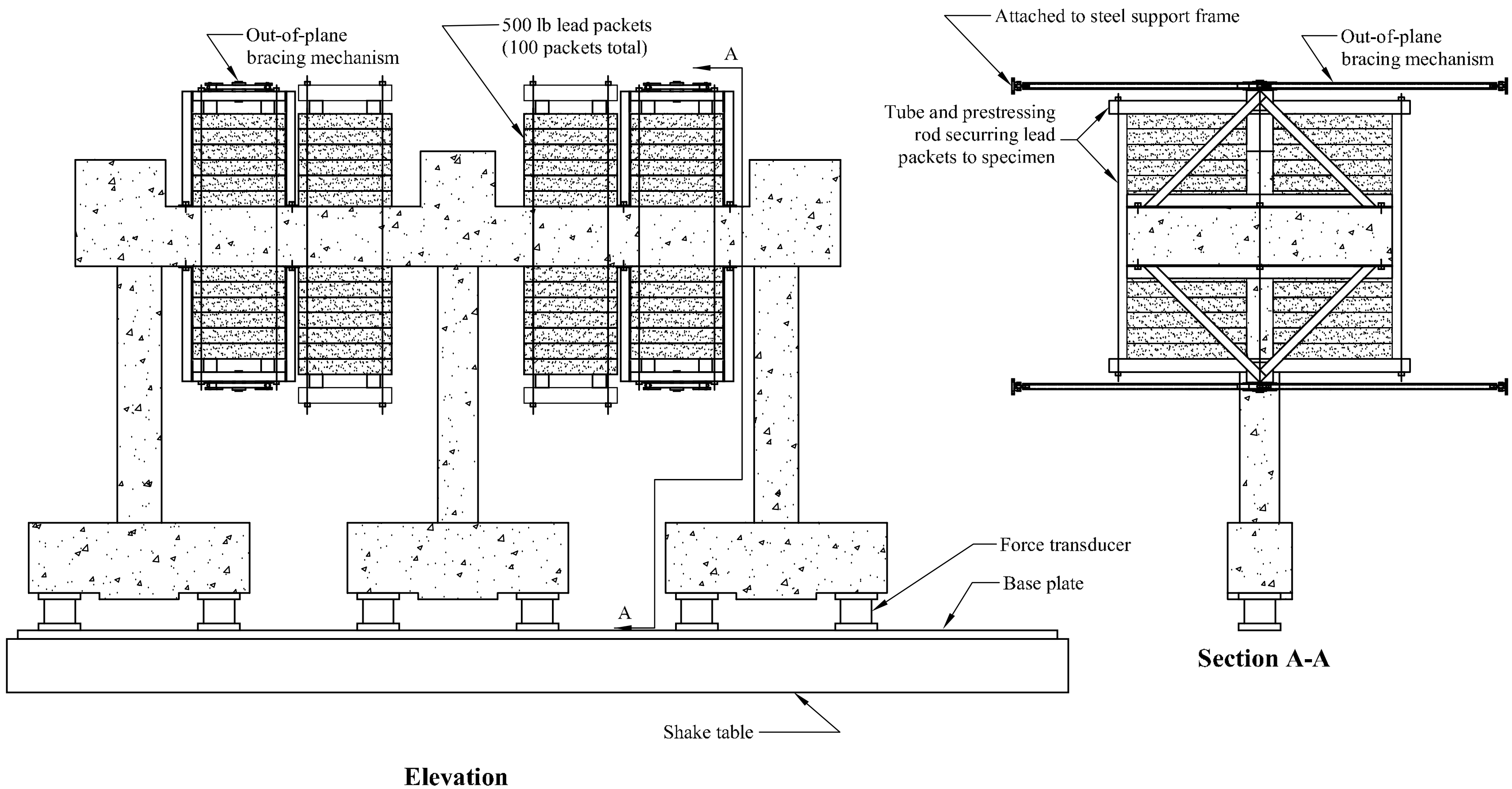

Figure B-1. Loaded specimen

to restrict the out-of plane movement of the specimen while the lead packets were loaded onto the specimen.

The lead packets, consisting of five 100 lb. lead ignots tied together by steel straps, were weighed and loaded onto the beam of the test specimen carefully to avoid causing a load unbalance that would crack the center column. The lead packets were supported at one end on a steel shim to fix the position and at the other end on a rubber shim to allow deformation of the concrete test specimen beneath the lead packets. The lead packets below the beam, shown in Figure B-2, were first placed onto the support tubes resting on wood blocking between the columns of the test specimen. The stacks of lead packets were then lifted by the support tubes and secured into position by stressing 3/4″ high-strength prestressing rods to achieve a frictional force of approximately 5 kips between the stack of lead packets and the beam. Figure B-3 and Table B-1 give the distribution of weight due to the lead packets secured to the specimen.

After the lead packets were mounted on the specimen, the out-of-plane bracing mechanisms, described in Section B.2, were installed over each of the outside stacks of lead packets as shown in Figure B-1. The steel frame designed to support the ends of each of the bracing mechanisms was lifted over the test specimens and aligned with the intended direction of shaking, then secured to the shake table. Figure B-4 shows the loaded specimen and support frame on the shake table just before testing.

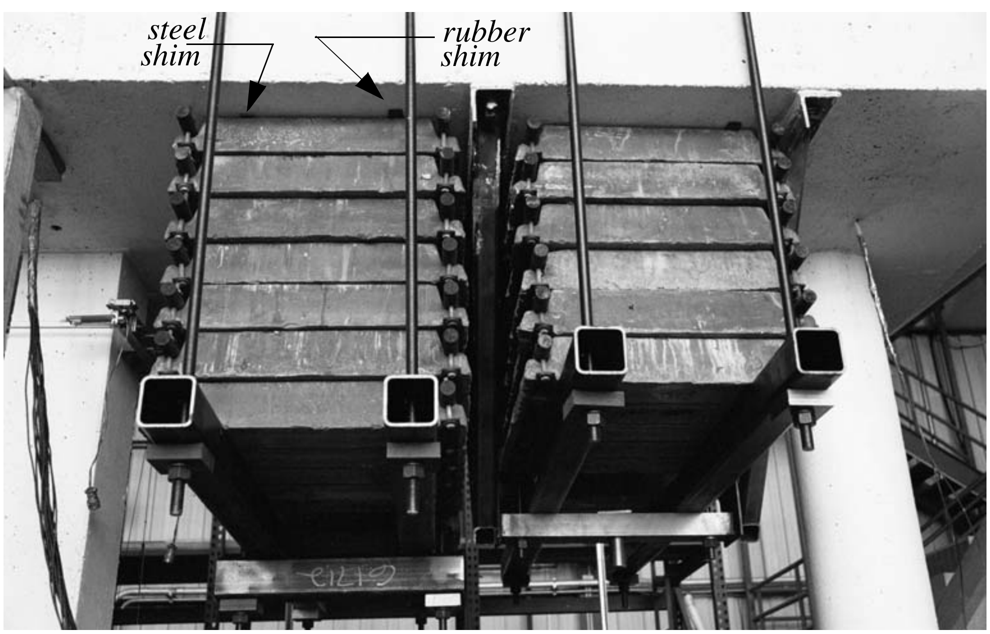

Figure B-2. Lead packets secured to the underside of the beam

Table B-1. Weight of lead packet stacks (see Figure B-3 for location key)

Location	*Weight (lbs)*
1 Top	3014
2 Top	3014
3 Top	3005
4 Top	3019
5 Top	3037
6 Top	3037
7 Top	3009
8 Top	3010
1 Bottom	3014
2 Bottom	3019
3 Bottom	3516
4 Bottom	3544
5 Bottom	3526
6 Bottom	3558
7 Bottom	2953
8 Bottom	2963
Total	**50238**

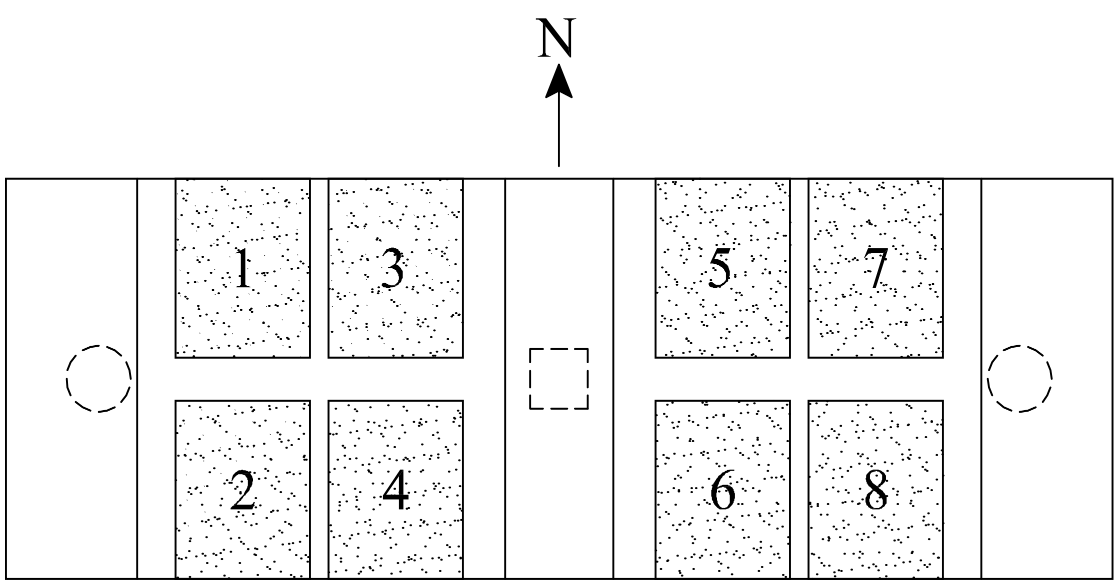

Figure B-3. Plan of lead weight layout on specimen

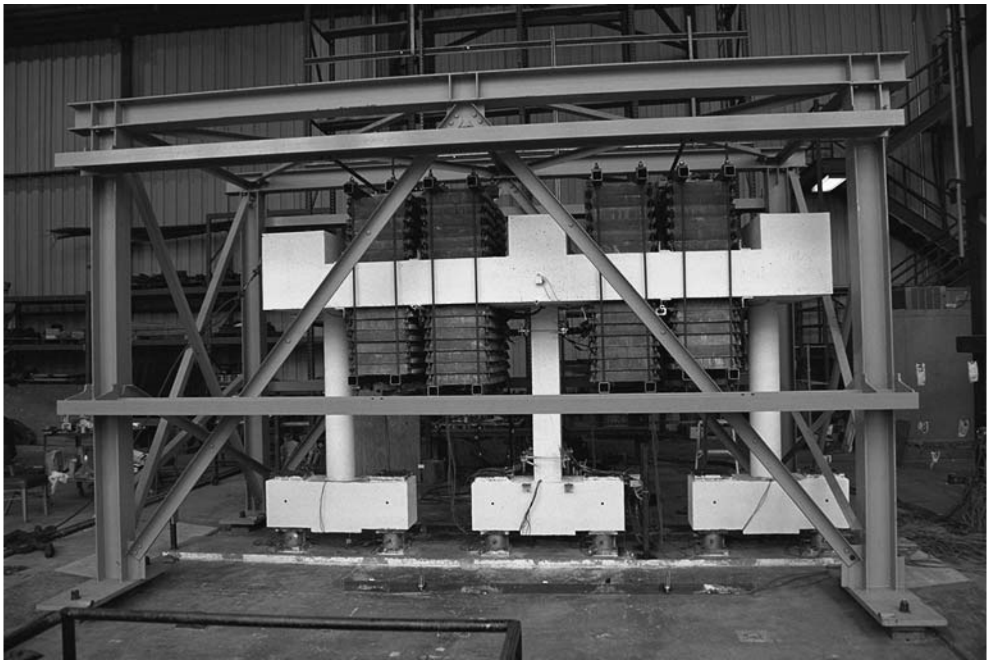

Figure B-4. Loaded specimen and support frame on shake table

B.2 OUT-OF-PLANE BRACING

The planar frame specimens were subjected to unidirectional horizontal ground motions. An out-of-plane bracing mechanism (shown in Figure B-5), commonly known as a pantograph, was designed to restrain the specimen mass in the out-of-plane direction while allowing unrestrained movement in the direction of the table motion. The mechanism was connected to the specimen through the 1-1/2″ center pin. Four such mechanisms were attached to the specimen, one over each of the exterior lead weight stacks using the diagonal bracing steel shown in the elevation view of Figure B-5. The distance between the mechanisms enabled them to provide torsional restraint to the specimen mass. As shown in Figure B-6, the ends of the 1″ pipe arms were connected to a steel support frame through a 1/2″ clevis pin.

If the specimen mass tries to move in the out-of-plane direction, one of the 1″ pipe arms goes into compression while the other goes into tension. The pipe arms and the steel support frame were designed to provide enough stiffness to all but eliminate the out-of-plane movement of the specimen mass relative to the shake table.

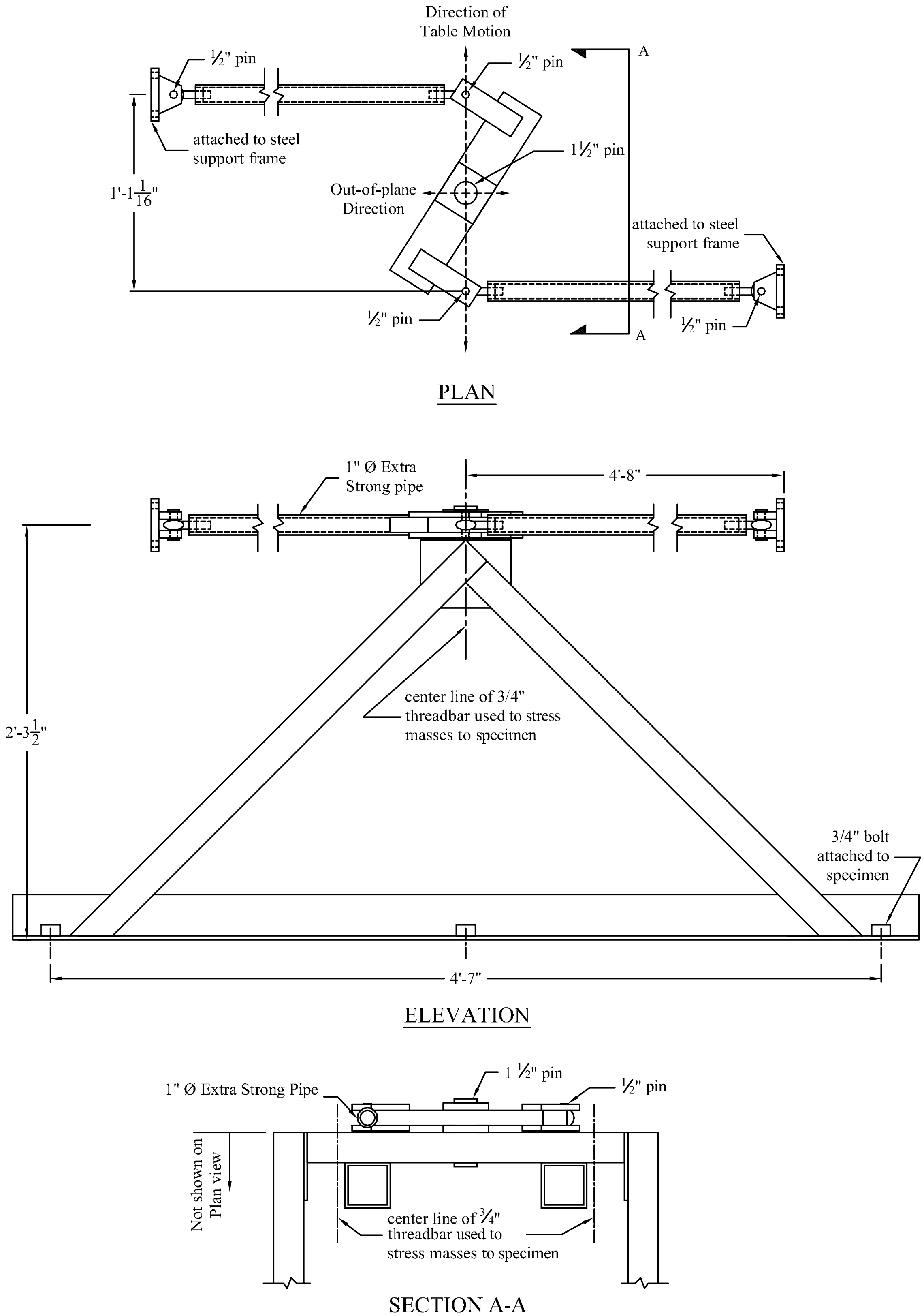

Figure B-5. Out-of-plane bracing mechanism

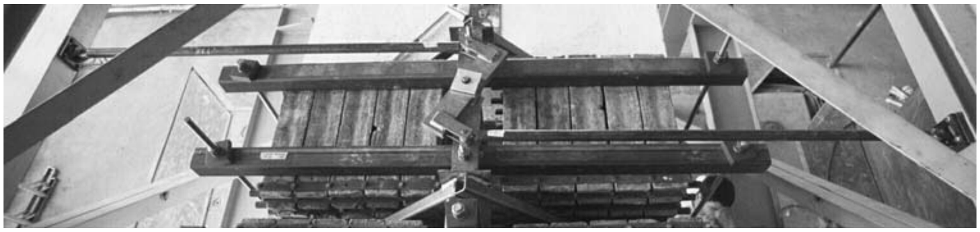

Figure B-6. Out-of-plane bracing mechanism installed on specimen

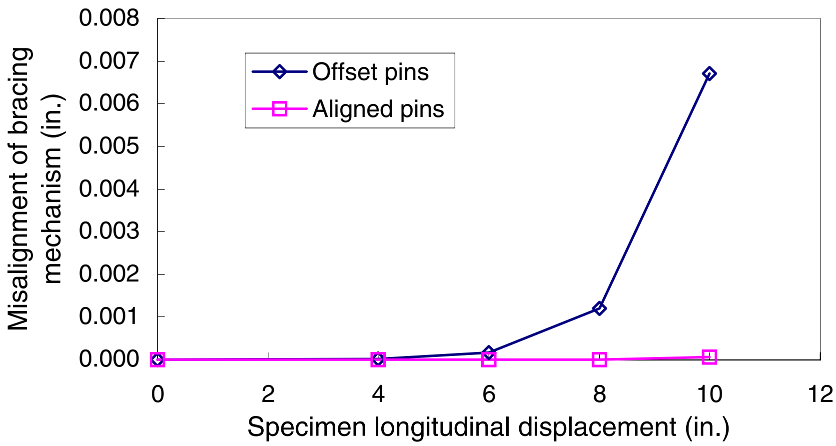

Figure B-7. Performance of bracing mechanism with aligned and offset pins

As the specimen mass moves relative to the table in the direction of the table motion, the 1-1/2″ center pin moves with the specimen. The steel support frame, which is well-braced in both directions and secured to the shake table, experiences negligible movement relative to the shake table. The 1″ pipe arms will rotate about the 1/2″ clevis pins attached to the steel support frame, causing the center plate to rotate about the 1-1/2″ center pin. For small relative displacements of the specimen mass, the mechanism allows for unrestrained movement in the direction of the table motion. For larger displacements, the arcs traced out by the rotation of the 1″ pipe arms and the center plate do not match perfectly. However, if the pins attached to the center plate are initially aligned with the direction of the table motion (as shown in Figure B-5), then the misalignment of the arcs for large displacements is minimized. Figure B-7 illustrates the difference in the performance of the mechanism for the case of pins aligned with the direction of the table motion and the case of the center plate aligned with the direction of the table motion (i.e., offset pins).

B.3 PRESTRESSING APPARATUS

The two specimens were nominally identical except for the axial load on the columns. Since the shake table could not reliably control a significantly larger mass than that used for Specimen 1, the additional axial load for Specimen 2 was attained by prestressing using a pneumatic jack on each side of the center column, as shown in Figure B-8. A 10″ x 10″ x 5/8″ tube was placed on a hydro-stone pad on top of the center column transverse torsional beam. A clevis pin, aligned with the intended direction of shaking, was installed on each end of the tube. A high-strength threaded rod was used to attach the clevis pin to the pneumatic jack which was secured to the shake table with another clevis pin, also aligned with the intended direction of ground shaking.

In the event of axial shortening of the center column, the prestress force applied by the pneumatic jacks will decrease in proportion to the increase in volume of the pressurized chamber in the pneumatic jacks. For Specimen 2, a 7″-long pressurized chamber resulted in a 14% loss of prestress force when the center column shortened by 1″ (i.e., 1″/7″ = 14%). The prestress force from the pneumatic cylinders before, during, and after testing is shown in Figure B-9. The prestress force is distributed to the three column (based on the force transducers: 72% of the force to the center column and 14% to each of the outside columns).

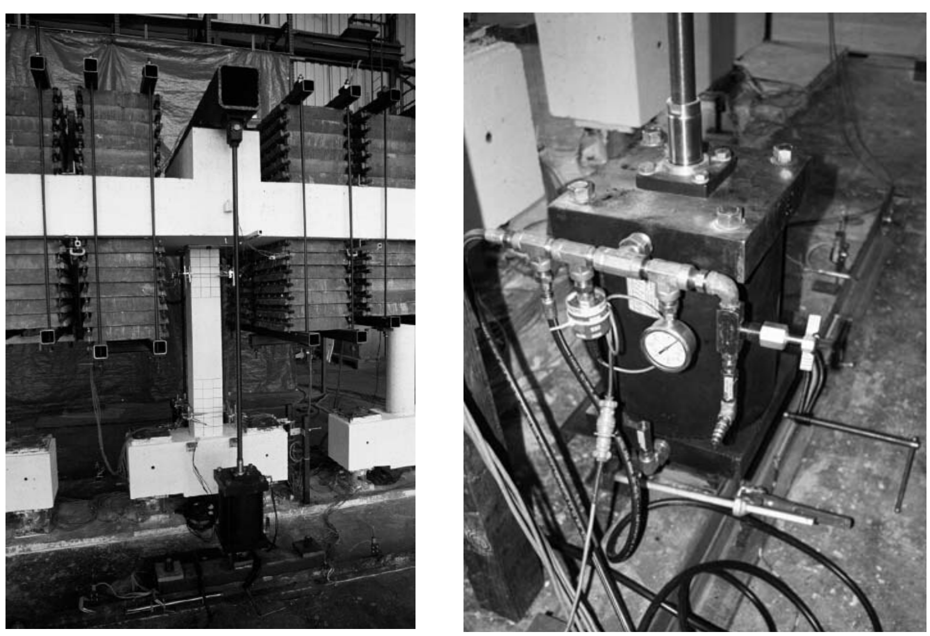

Figure B-8. Pneumatic cylinders for adding axial load to center column

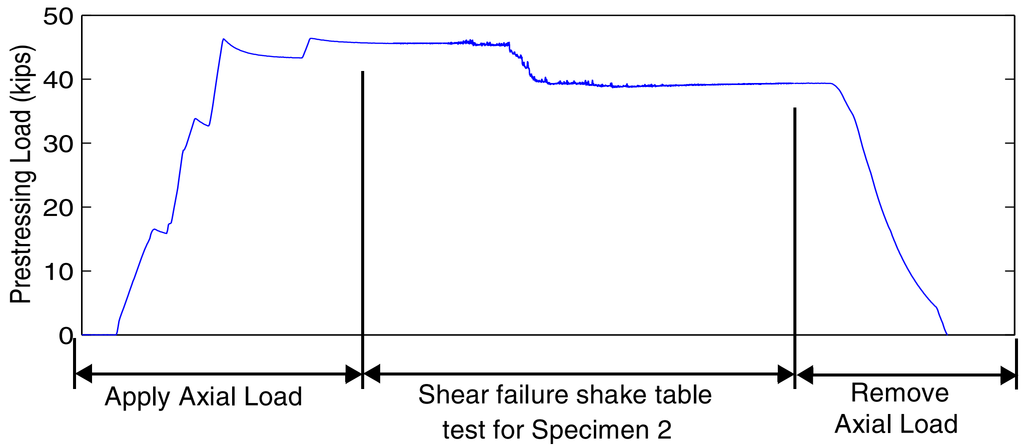

Figure B-9. Prestressing force from pneumatic cylinders

B.4 INSTRUMENTATION

The instrumentation can be grouped into the following categories:

- table instruments to measure the displacement and acceleration of the table,
- force transducers to measure the reactions at the base of the columns,
- strain gages to measure the strain in the reinforcement,
- accelerometers to measure the acceleration of the mass,
- displacement transducers to measure the deformations of the center column, and
- displacement transducers to measure the global displacements of the specimen.

Tables B-2 and B-3 list the instruments used for Specimens 1 and 2.

Table B-2. Instrumentation list for Specimen 1

Channel #	*Instrument Type*	*Description*	*Name*
1	Table Displacements	Table Stroke Horz 1	H1O STROKE
2	Table Displacements	Table Stroke Horz 2	H20 STROKE
3	Table Displacements	Table Stroke Horz 3	H3O STROKE
4	Table Displacements	Table Stroke Horz 4	H4O STROKE
5	Table Displacements	Table Stroke Vert 1	V1O STROKE
6	Table Displacements	Table Stroke Vert 2	V2O STROKE
7	Table Displacements	Table Stroke Vert 3	V3O STROKE
8	Table Displacements	Table Stroke Vert 4	V4O STROKE
9	Table Accelerations	Table Acceleration Horz 1	H1-2 ACC

Table B-2. ***(continued)*** **Instrumentation list for Specimen 1**

Channel #	*Instrument Type*	*Description*	*Name*
10	Table Accelerations	Table Acceleration Horz 2	H3-4 ACC
11	Table Accelerations	Table Acceleration Horz 3	H4-1 ACC
12	Table Accelerations	Table Acceleration Horz 4	H2-3 ACC
13	Table Accelerations	Table Acceleration Vert 1	1V ACC
14	Table Accelerations	Table Acceleration Vert 2	2V ACC
15	Table Accelerations	Table Acceleration Vert 3	3V ACC
16	Table Accelerations	Table Acceleration Vert 4	4V ACC
17	Force Transducer	Axial Column 1 West	COL1WAXIAL
18	Force Transducer	In-plane Moment Column 1 West	COL1WM1
19	Force Transducer	In-plane Shear Column 1 West	COL1WS1
20	Force Transducer	Out-of-plane Moment Column 1 West	COL1WM2
21	Force Transducer	Out-of-plane Shear Column 1 West	COL1WS2
22	Force Transducer	Axial Column 1 East	COL1EAXIAL
23	Force Transducer	In-plane Moment Column 1 East	COL1EM1
24	Force Transducer	In-plane Shear Column 1 East	COL1ES1
25	Force Transducer	Out-of-plane Moment Column 1 East	COL1EM2
26	Force Transducer	Out-of-plane Shear Column 1 East	COL1ES2
27	Force Transducer	Axial Column 2 West	COL2WAXIAL
28	Force Transducer	In-plane Moment Column 2 West	COL2WM1
29	Force Transducer	In-plane Shear Column 2 West	COL2WS1
30	Force Transducer	Out-of-plane Moment Column 2 West	COL2WM2
31	Force Transducer	Out-of-plane Shear Column 2 West	COL2WS2
32	Force Transducer	Axial Column 2 East	COL2EAXIAL
33	Force Transducer	In-plane Moment Column 2 East	COL2EM1
34	Force Transducer	In-plane Shear Column 2 East	COL2ES1
35	Force Transducer	Out-of-plane Moment Column 2 East	COL2EM2
36	Force Transducer	Out-of-plane Shear Column 2 East	COL2ES2
37	Force Transducer	Axial Column 3 West	COL3WAXIAL
38	Force Transducer	In-plane Moment Column 3 West	COL3WM1
39	Force Transducer	In-plane Shear Column 3 West	COL3WS1
40	Force Transducer	Out-of-plane Moment Column 3 West	COL3WM2
41	Force Transducer	Out-of-plane Shear Column 3 West	COL3WS2
42	Force Transducer	Axial Column 3 East	COL3EAXIAL

Table B-2. *(continued)* Instrumentation list for Specimen 1

Channel #	*Instrument Type*	*Description*	*Name*
43	Force Transducer	In-plane Moment Column 3 East	COL3EM1
44	Force Transducer	In-plane Shear Column 3 East	COL3ES1
45	Force Transducer	Out-of-plane Moment Column 3 East	COL3EM2
46	Force Transducer	Out-of-plane Shear Column 3 East	COL3ES2
47	Strain Gage	Column 1 Longitudinal Top West	SG 1LTW
48	Strain Gage	Column 1 Longitudinal Top East	SG 1LTE
49	Strain Gage	Column 1 Longitudinal Bottom West	SG 1LBW
50	Strain Gage	Column 1 Longitudinal Bottom East	SG 1LBE
51	Strain Gage	Column 2 Longitudinal Top West	SG 2LTW
52	Strain Gage	Column 2 Longitudinal Top East	SG 2LTE
53	Strain Gage	Column 2 Longitudinal Top Extra	SG 2LT.2
54	Strain Gage	Column 2 Longitudinal Middle Top West	SG 2LMTW
55	Strain Gage	Column 2 Longitudinal Middle Top East	SG 2LMTE
56	Strain Gage	Column 2 Longitudinal Middle West	SG 2LMW
57	Strain Gage	Column 2 Longitudinal Middle East	SG 2LME
58	Strain Gage	Column 2 Longitudinal Middle Bottom West	SG 2LMBW
59	Strain Gage	Column 2 Longitudinal Middle Bottom East	SG 2LMBE
60	Strain Gage	Column 2 Longitudinal Bottom West	SG 2LBW
61	Strain Gage	Column 2 Longitudinal Bottom East	SG 2LBE
62	Strain Gage	Column 2 Longitudinal Bottom Extra	SG 2LB.2
63	Strain Gage	Column 3 Longitudinal Top West	SG 3LTW
64	Strain Gage	Column 3 Longitudinal Top East	SG 3LTE
65	Strain Gage	Column 3 Longitudinal Bottom West	SG 3LBW
66	Strain Gage	Column 3 Longitudinal Bottom East	SG 3LBE
67	Strain Gage	Column 2 Hoop Top South	SG 2STS
68	Strain Gage	Column 2 Hoop Top North	SG 2STN
69	Strain Gage	Column 2 Hoop Middle Top South	SG 2SMTS
70	Strain Gage	Column 2 Hoop Middle Top North	SG 2SMTN
71	Strain Gage	Column 2 Hoop Middle South	SG 2SMS
72	Strain Gage	Column 2 Hoop Middle North	SG 2SMN
73	Strain Gage	Column 2 Hoop Middle Bottom South	SG 2SMBS
74	Strain Gage	Column 2 Hoop Middle Bottom North	SG 2SMBN
75	Strain Gage	Column 2 Hoop Bottom South	SG 2SBS

Table B-2. *(continued)* Instrumentation list for Specimen 1

Channel #	*Instrument Type*	*Description*	*Name*
76	Strain Gage	Column 2 Hoop Bottom North	SG 2SBN
77	Strain Gage	Beam Longitudinal Underside West Bay	BF BLU1
78	Strain Gage	Beam Longitudinal Underside Column 2 West	BF BLU2W
79	Strain Gage	Beam Longitudinal Underside Column 2 East	BF BLU2E
80	Strain Gage	Beam Longitudinal Underside East Bay	BF BLU3
81	Accelerometer	Longitudinal CG Mass over Column 1 South	AL CGC1
82	Accelerometer	Longitudinal CG Mass over Column 2 South	AL CGC2S
83	Accelerometer	Longitudinal CG Mass over Column 2 North	AL CGC2N
84	Accelerometer	Longitudinal CG Mass over Column 3 South	AL CGC3
85	Accelerometer	Longitudinal West Bay Mass Top	AL B1MT
86	Accelerometer	Longitudinal West Bay Mass Bottom	AL B1MB
87	Accelerometer	Longitudinal East Bay Mass Top	AL B2MT
88	Accelerometer	Longitudinal East Bay Mass Bottom	AL B2MB
89	Accelerometer	Longitudinal Base of Column 2	AL BC2
90	Accelerometer	Transverse CG Mass over Column 1 South	AT CGC1
91	Accelerometer	Transverse CG Mass over Column 2 South	AT CGC2
92	Accelerometer	Transverse CG Mass over Column 3 South	AT CGC3
93	Accelerometer	Vertical West Bay Mass Top	AV B1MT
94	Accelerometer	Vertical West Bay Mass Bottom	AV B1MB
95	Accelerometer	Vertical CG Mass over Column 2 South	AV CGC2S
123	Accelerometer	Vertical CG Mass over Column 2 North	AV CGC2N
97	Accelerometer	Vertical East Bay Mass Top	AV B2MT
98	Accelerometer	Vertical East Bay Mass Bottom	AV B2MB
99	Local Deformations	Vertical North West Top	LDV NWT
100	Local Deformations	Vertical North West Middle	LDV NWM
101	Local Deformations	Vertical North West Bottom	LDV NWB
102	Local Deformations	Vertical North East Top	LDV NET
103	Local Deformations	Vertical North East Middle	LDV NEM
104	Local Deformations	Vertical North East Bottom	LDV NEB
105	Local Deformations	Horizontal North Top	LDH NT
106	Local Deformations	Horizontal North Bottom	LDH NB
107	Local Deformations	Diagonal North Top	LDD NT
108	Local Deformations	Diagonal North Middle	LDD NM

Table B-2. *(continued)* Instrumentation list for Specimen 1

Channel #	*Instrument Type*	*Description*	*Name*
109	Local Deformations	Diagonal North Bottom	LDD NB
110	Local Deformations	Vertical South West Top	LDV SWT
111	Local Deformations	Vertical South West Middle	LDV SWM
112	Local Deformations	Vertical South West Bottom	LDV SWB
113	Local Deformations	Vertical South East Top	LDV SET
124	Local Deformations	Vertical South East Middle	LDV SEM
115	Local Deformations	Vertical South East Bottom	LDV SEB
116	Local Deformations	Horizontal South Top	LDH ST
117	Local Deformations	Horizontal South Bottom	LDH SB
118	Local Deformations	Diagonal South Top	LDD ST
119	Local Deformations	Diagonal South Middle	LDD SM
120	Local Deformations	Diagonal South Bottom	LDD SB
121	Global Displacements	Longitudinal LVDT North	GDL LVDTN
122	Global Displacements	Longitudinal LVDT South	GDL LVDTS
125	Global Displacements	Longitudinal Redundant Table Displ Lower	GDL RTDL
126	Global Displacements	Longitudinal Redundant Table Displ Upper	GDL RTDU
127	Global Displacements	Longitudinal Top of Column 2 Side of Beam North	GDL TC2SBN
128	Global Displacements	Longitudinal Top of Column 2 Side of Beam South	GDL TC2SBS
129	Global Displacements	Longitudinal CG at End of Beam	GDL CGEB
130	Global Displacements	Longitudinal West Mass Top	GDL WMT
131	Global Displacements	Longitudinal West Mass Bottom	GDL WMB
144	Global Displacements	Longitudinal Base of Column 2 North	GDL BC2N
145	Global Displacements	Longitudinal Base of Column 2 South	GDL BC2S
146	Global Displacements	Longitudinal CG at End of Beam (DCDT)	GDLCGEBDCD
132	Global Displacements	Transverse CG of Mass over Column 1	GDT CGC1
133	Global Displacements	Transverse Top of Beam at Column 2	GDT TBC2
134	Global Displacements	Transverse CG of Mass over Column 1	GDT CGC3
135	Global Displacements	Transverse Top of Column 2	GDT TC2
136	Global Displacements	Vertical Beam Underside at Column 1 South	GDV BUC1S
137	Global Displacements	Vertical Beam Underside at Column 3 South	GDV BUC3S
147	Global Displacements	Vertical Mid span Bay 1 North	GDVMSB1N
139	Global Displacements	Vertical Mid span Bay 1 South	GDV MSB1S

Table B-2. ***(continued)*** **Instrumentation list for Specimen 1**

Channel #	*Instrument Type*	*Description*	*Name*
140	Global Displacements	Vertical Mid span Bay 2 North	GDV MSB2N
141	Global Displacements	Vertical Mid span Bay 2 South	GDV MSB2S
142	Global Displacements	Vertical Beam Underside at Column 2 North	GDV BUC2N
143	Global Displacements	Vertical Beam Underside at Column 2 South	GDV BUC2S

Table B-3. Instrumentation list for Specimen 2

Channel #	*Category*	*Description*	*Name*
1	Table Displacements	Table Stroke Horz 1	H1O STROKE
2	Table Displacements	Table Stroke Horz 2	H20 STROKE
3	Table Displacements	Table Stroke Horz 3	H3O STROKE
4	Table Displacements	Table Stroke Horz 4	H4O STROKE
5	Table Displacements	Table Stroke Vert 1	V1O STROKE
6	Table Displacements	Table Stroke Vert 2	V2O STROKE
7	Table Displacements	Table Stroke Vert 3	V3O STROKE
8	Table Displacements	Table Stroke Vert 4	V4O STROKE
9	Table Accelerations	Table Acceleration Horz 1	H1-2 ACC
10	Table Accelerations	Table Acceleration Horz 2	H3-4 ACC
11	Table Accelerations	Table Acceleration Horz 3	H4-1 ACC
12	Table Accelerations	Table Acceleration Horz 4	H2-3 ACC
13	Table Accelerations	Table Acceleration Vert 1	1V ACC
14	Table Accelerations	Table Acceleration Vert 2	2V ACC
15	Table Accelerations	Table Acceleration Vert 3	3V ACC
16	Table Accelerations	Table Acceleration Vert 4	4V ACC
17	Force Transducer	Axial Column 1 West	COL1WAXIAL
18	Force Transducer	In-plane Moment Column 1 West	COL1WM1
19	Force Transducer	In-plane Shear Column 1 West	COL1WS1
20	Force Transducer	Out-of-plane Moment Column 1 West	COL1WM2
21	Force Transducer	Out-of-plane Shear Column 1 West	COL1WS2
22	Force Transducer	Axial Column 1 East	COL1EAXIAL
23	Force Transducer	In-plane Moment Column 1 East	COL1EM1
24	Force Transducer	In-plane Shear Column 1 East	COL1ES1
25	Force Transducer	Out-of-plane Moment Column 1 East	COL1EM2
26	Force Transducer	Out-of-plane Shear Column 1 East	COL1ES2

Table B-3. *(continued)* Instrumentation list for Specimen 2

Channel #	*Category*	*Description*	*Name*
27	Force Transducer	Axial Column 2 West	COL2WAXIAL
28	Force Transducer	In-plane Moment Column 2 West	COL2WM1
29	Force Transducer	In-plane Shear Column 2 West	COL2WS1
30	Force Transducer	Out-of-plane Moment Column 2 West	COL2WM2
31	Force Transducer	Out-of-plane Shear Column 2 West	COL2WS2
32	Force Transducer	Axial Column 2 East	COL2EAXIAL
33	Force Transducer	In-plane Moment Column 2 East	COL2EM1
34	Force Transducer	In-plane Shear Column 2 East	COL2ES1
35	Force Transducer	Out-of-plane Moment Column 2 East	COL2EM2
36	Force Transducer	Out-of-plane Shear Column 2 East	COL2ES2
37	Force Transducer	Axial Column 3 West	COL3WAXIAL
38	Force Transducer	In-plane Moment Column 3 West	COL3WM1
39	Force Transducer	In-plane Shear Column 3 West	COL3WS1
40	Force Transducer	Out-of-plane Moment Column 3 West	COL3WM2
41	Force Transducer	Out-of-plane Shear Column 3 West	COL3WS2
42	Force Transducer	Axial Column 3 East	COL3EAXIAL
43	Force Transducer	In-plane Moment Column 3 East	COL3EM1
44	Force Transducer	In-plane Shear Column 3 East	COL3ES1
45	Force Transducer	Out-of-plane Moment Column 3 East	COL3EM2
46	Force Transducer	Out-of-plane Shear Column 3 East	COL3ES2
47	Strain Gage	Column 1 Longitudinal Top West	SG 1LTW
48	Strain Gage	Column 1 Longitudinal Top East	SG 1LTE
49	Strain Gage	Column 1 Longitudinal Bottom West	SG 1LBW
50	Strain Gage	Column 1 Longitudinal Bottom East	SG 1LBE
51	Strain Gage	Column 2 Longitudinal Top West	SG 2LTW
52	Strain Gage	Column 2 Longitudinal Top East	SG 2LTE
53	Strain Gage	Column 2 Longitudinal Top Extra	SG 2LT.2
54	Strain Gage	Column 2 Longitudinal Middle Top West	SG 2LMTW
55	Strain Gage	Column 2 Longitudinal Middle Top East	SG 2LMTE
56	Strain Gage	Column 2 Longitudinal Middle West	SG 2LMW
57	Strain Gage	Column 2 Longitudinal Middle East	SG 2LME
58	Strain Gage	Column 2 Longitudinal Middle Bottom West	SG 2LMBW
59	Strain Gage	Column 2 Longitudinal Middle Bottom East	SG 2LMBE

Table B-3. ***(continued)*** **Instrumentation list for Specimen 2**

Channel #	*Category*	*Description*	*Name*
60	Strain Gage	Column 2 Longitudinal Bottom West	SG 2LBW
61	Strain Gage	Column 2 Longitudinal Bottom East	SG 2LBE
62	Strain Gage	Column 2 Longitudinal Bottom Extra	SG 2LB.2
63	Strain Gage	Column 3 Longitudinal Top West	SG 3LTW
64	Strain Gage	Column 3 Longitudinal Top East	SG 3LTE
65	Strain Gage	Column 3 Longitudinal Bottom West	SG 3LBW
66	Strain Gage	Column 3 Longitudinal Bottom East	SG 3LBE
67	Strain Gage	Column 2 Hoop Top South	SG 2STS
68	Strain Gage	Column 2 Hoop Top North	SG 2STN
69	Strain Gage	Column 2 Hoop Middle Top South	SG 2SMTS
70	Strain Gage	Column 2 Hoop Middle Top North	SG 2SMTN
71	Strain Gage	Column 2 Hoop Middle South	SG 2SMS
72	Strain Gage	Column 2 Hoop Middle North	SG 2SMN
73	Strain Gage	Column 2 Hoop Middle Bottom South	SG 2SMBS
74	Strain Gage	Column 2 Hoop Middle Bottom North	SG 2SMBN
75	Strain Gage	Column 2 Hoop Bottom South	SG 2SBS
76	Strain Gage	Column 2 Hoop Bottom North	SG 2SBN
77	Strain Gage	Beam Longitudinal Underside West Bay	BF BLU1
78	Strain Gage	Beam Longitudinal Underside Column 2 West	BF BLU2W
79	Strain Gage	Beam Longitudinal Underside Column 2 East	BF BLU2E
80	Strain Gage	Beam Longitudinal Underside East Bay	BF BLU3
81	Accelerometer	Longitudinal CG Mass over Column 1 South	AL CGC1
82	Accelerometer	Longitudinal CG Mass over Column 2 South	AL CGC2S
83	Accelerometer	Longitudinal CG Mass over Column 2 North	AL CGC2N
84	Accelerometer	Longitudinal CG Mass over Column 3 South	AL CGC3
85	Accelerometer	Longitudinal West Bay Mass Top	AL B1MT
86	Accelerometer	Longitudinal West Bay Mass Bottom	AL B1MB
87	Accelerometer	Longitudinal East Bay Mass Top	AL B2MT
88	Accelerometer	Longitudinal East Bay Mass Bottom	AL B2MB
89	Accelerometer	Longitudinal Base of Column 2	AL BC2
90	Accelerometer	Transverse CG Mass over Column 1 South	AT CGC1
91	Accelerometer	Transverse CG Mass over Column 2 South	AT CGC2
92	Accelerometer	Transverse CG Mass over Column 3 South	AT CGC3

Table B-3. ***(continued)*** **Instrumentation list for Specimen 2**

Channel #	*Category*	*Description*	*Name*
93	Accelerometer	Vertical West Bay Mass Top	AV B1MT
94	Accelerometer	Vertical West Bay Mass Bottom	AV B1MB
95	Accelerometer	Vertical CG Mass over Column 2 South	AV CGC2S
123	Accelerometer	Vertical CG Mass over Column 2 North	AV CGC2N
97	Accelerometer	Vertical East Bay Mass Top	AV B2MT
98	Accelerometer	Vertical East Bay Mass Bottom	AV B2MB
99	Local Deformations	Vertical North West Top	LDV NWT
100	Local Deformations	Vertical North West Middle	LDV NWM
101	Local Deformations	Vertical North West Bottom	LDV NWB
102	Local Deformations	Vertical North East Top	LDV NET
103	Local Deformations	Vertical North East Middle	LDV NEM
104	Local Deformations	Vertical North East Bottom	LDV NEB
105	Local Deformations	Horizontal North Top	LDH NT
106	Local Deformations	Horizontal North Bottom	LDH NB
107	Local Deformations	Diagonal North Top	LDD NT
108	Local Deformations	Diagonal North Middle	LDD NM
109	Local Deformations	Diagonal North Bottom	LDD NB
110	Local Deformations	Vertical South West Top	LDV SWT
111	Local Deformations	Vertical South West Middle	LDV SWM
112	Local Deformations	Vertical South West Bottom	LDV SWB
113	Local Deformations	Vertical South East Top	LDV SET
124	Local Deformations	Vertical South East Middle	LDV SEM
115	Local Deformations	Vertical South East Bottom	LDV SEB
116	Local Deformations	Horizontal South Top	LDH ST
117	Local Deformations	Horizontal South Bottom	LDH SB
118	Local Deformations	Diagonal South Top	LDD ST
119	Local Deformations	Diagonal South Middle	LDD SM
120	Local Deformations	Diagonal South Bottom	LDD SB
121	Global Displacements	Longitudinal LVDT North	GDL LVDTN
122	Global Displacements	Longitudinal LVDT South	GDL LVDTS
148	Global Displacements	Longitudinal Redundant Table Displ Lower	GDL RTDL
149	Global Displacements	Longitudinal Redundant Table Displ Upper	GDL RTDU

Table B-3. *(continued)* Instrumentation list for Specimen 2

Channel #	*Category*	*Description*	*Name*
127	Global Displacements	Longitudinal Top of Column 2 Side of Beam North	GDL TC2SBN
128	Global Displacements	Longitudinal Top of Column 2 Side of Beam South	GDL TC2SBS
129	Global Displacements	Longitudinal CG at End of Beam	GDL CGEB
130	Global Displacements	Longitudinal West Mass Top	GDL WMT
131	Global Displacements	Longitudinal West Mass Bottom	GDL WMB
144	Global Displacements	Longitudinal Base of Column 2 North	GDL BC2N
145	Global Displacements	Longitudinal Base of Column 2 South	GDL BC2S
146	Global Displacements	Longitudinal CG at End of Beam (DCDT)	GDLCGEBDCD
132	Global Displacements	Transverse CG of Mass over Column 1	GDT CGC1
133	Global Displacements	Transverse Top of Beam at Column 2	GDT TBC2
134	Global Displacements	Transverse CG of Mass over Column 1	GDT CGC3
135	Global Displacements	Transverse Top of Column 2	GDT TC2
136	Global Displacements	Vertical Beam Underside at Column 1 South	GDV BUC1S
137	Global Displacements	Vertical Beam Underside at Column 3 South	GDV BUC3S
147	Global Displacements	Vertical Mid span Bay 1 North	GDVMSB1N
139	Global Displacements	Vertical Mid span Bay 1 South	GDV MSB1S
140	Global Displacements	Vertical Mid span Bay 2 North	GDV MSB2N
141	Global Displacements	Vertical Mid span Bay 2 South	GDV MSB2S
142	Global Displacements	Vertical Beam Underside at Column 2 North	GDV BUC2N
143	Global Displacements	Vertical Beam Underside at Column 2 South	GDV BUC2S
126	Global Displacements	Vertical Under Column 2 Footing	C2FOUNVRT
125	Axial Cylinders	Prestress force from both cylinders	AXIAL PNUE

B.4.1 SHAKE TABLE INSTRUMENTATION

As shown in Tables B-2 and B-3, the shake table was instrumented with 4 horizontal displacement transducers, 4 vertical displacement transducers, 4 horizontal accelerometers, and 4 vertical accelerometers. The layout of the instruments was such that one could determine the three-dimensional movement of the table. The unidirectional horizontal displacements in the intended direction of shaking can be found by averaging channels 2 and 4. The unidirectional horizontal accelerations in the direction of shaking can be found by averaging channels 11 and 12.

Although the table motion was intended to be unidirectional, some out-of-plane and vertical displacements were detected, but all were within tolerable limits. The output from the table instruments was checked by two displacement transducers measuring the total displacements of the steel support frame. These instruments were also used to confirm that the pitch of the table during testing was negligible.

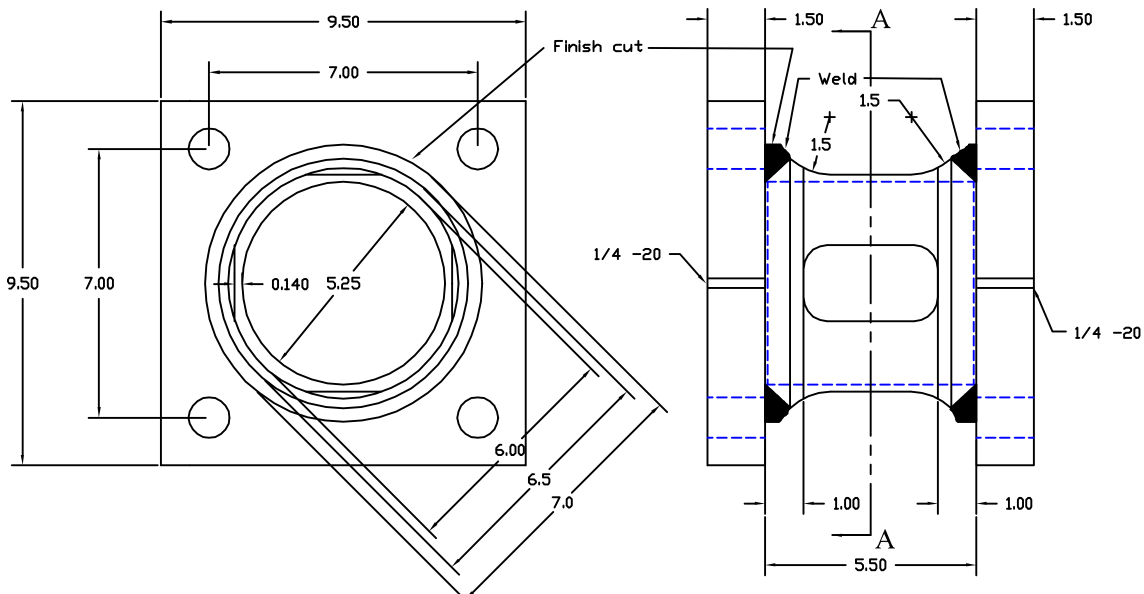

Figure B-10. Force transducers

B.4.2 FORCE TRANSDUCERS

Force transducers were used in pairs under each of the columns to monitor the redistribution of shear and axial load during testing. Each force transducer is capable of measuring orthogonal shears and moments in the horizontal plane, in addition to axial load. Moments are measured about midheight of the transducers. Tables B-2 and B-3 specify the channels measuring the in-plane and out-of plane forces.

The force transducers were made from 4140 steel. They were machined, welded, and then heat treated to maximum hardness and a proportional limit of 130 ksi. Dimensions for the transducers are shown in Figure B-10. The strain gages measuring shears and moments are mounted on the 0.14″ reduced sections parallel to the sides of the end plates. The strain gages measuring axial load are mounted on the 3/8″-thick rounded section at 45° to the sides of the end plates.

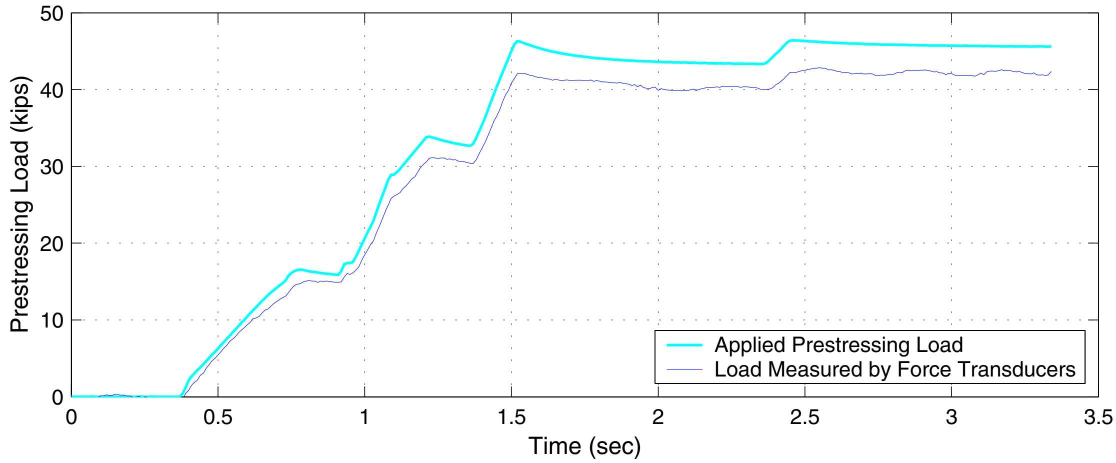

Figure B-11. Error in force transducer measurements

Some cross talk between the shear and axial load measurements has been identified during calibration of the force transducers. However, no single correction factor could be determined to correct the measurements. During loading of the pneumatic cylinders for Specimen 2 (Figure B-11), it was noted that the sum of the axial loads from the force transducers was 92% of the prestress force from the pneumatic cylinders.

B.4.3 ACCELEROMETERS

Accelerometers were mounted using high-strength epoxy in nine locations, as shown in Figure B-12, to determine the acceleration of the specimen mass and base. When acceleration in more than one direction was required at a single location, the accelerometers were mounted on 2″ x 2″ x 2″ aluminum blocks. The accelerometers mounted on the side of the beam were located at the center of gravity for the beam and the lead weights (i.e., 6.75″ above the beam soffit).

The longitudinal accelerations from the base of the specimen matched the accelerations from the table instruments.

B.4.4 STRAIN GAGES

The strain gages were mounted on the reinforcement and distributed throughout the specimen, as shown in Figure B-13. The strain gages mounted on the longitudinal reinforcement were located on the inside face of the bars to protect the gages from being damaged during installation of the

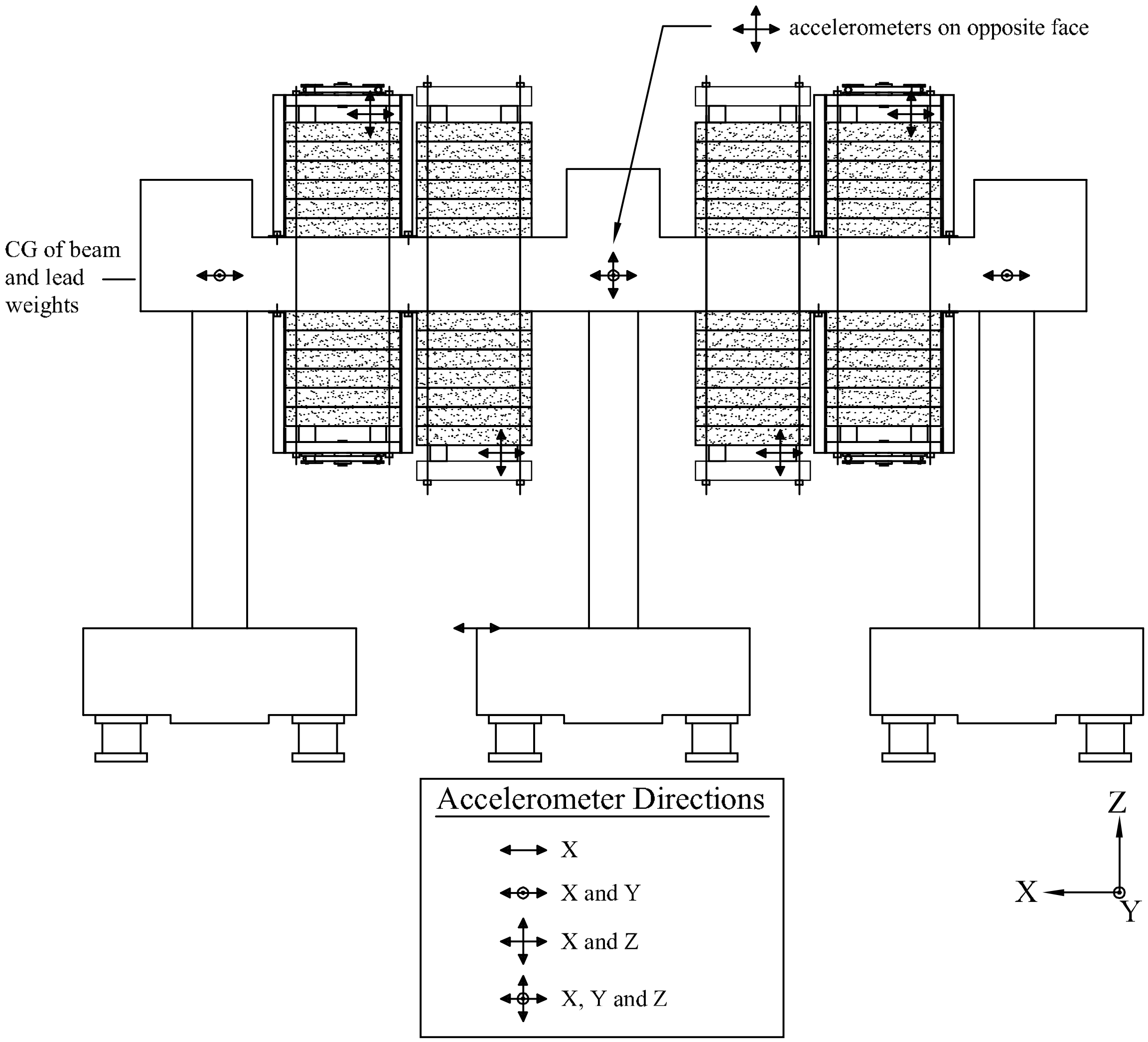

Figure B-12. Location of accelerometers (south side of specimen shown)

transverse reinforcement. The strain gages mounted on the transverse reinforcement were located on the top or bottom face of the reinforcing wire. The strain gages require several protective coatings to ensure that they are not damaged during the concrete pour. The following procedure was followed for the installation of each strain gage:

- File down deformations without reducing minimum cross section. Clean surface with degreaser, conditioner, neutralizer, and isopropyl alcohol.
- Glue on strain gage and terminal using CN high-strength adhesive
- Apply M-coat B protective sealant to strain gage.
- Solder strain gage wires and instrumentation cables to terminals.
- Apply M-coat B protective sealant to strain gage, terminals and exposed wires.

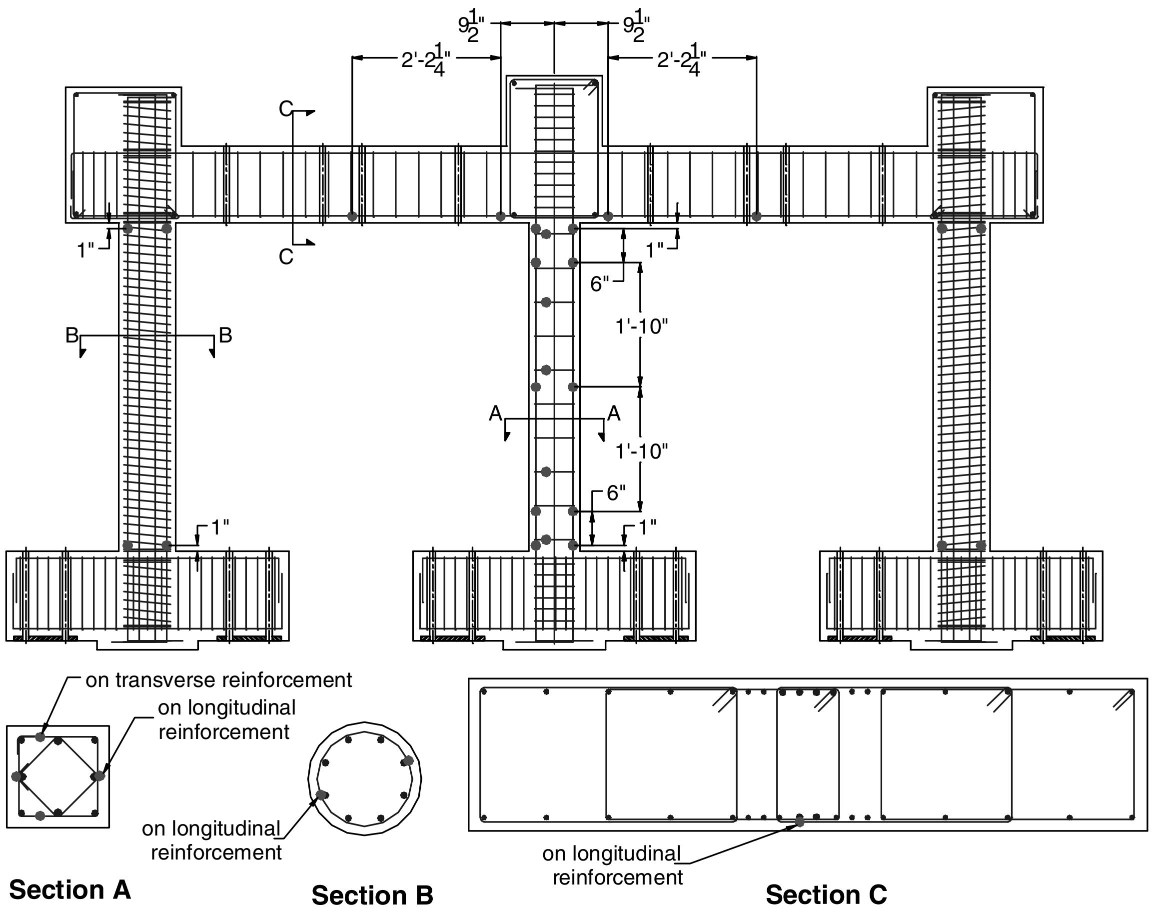

Figure B-13. Strain gage locations

- Apply wax coating to area covered by M-coat B.
- Apply M-coat J3 to area covered by wax.
- Cover affected region with vinyl mylar tape.

The strain gage mounted to the south side of the center column top hoop of Specimen 2 was damaged during construction and did not provide any output during the test. The gains for the strain gage readings were inadvertently set too high for the shear failure test for Specimen 2, resulting in readings that exceed the capacity of the data acquisition system shortly after yield of the reinforcement.

B.4.5 CENTER COLUMN INSTRUMENTS

The local deformations of the center column were recorded by direct current displacement transducers (DCDTs) mounted to the center column as shown in Figures B-14 and B-15. The DCDTs

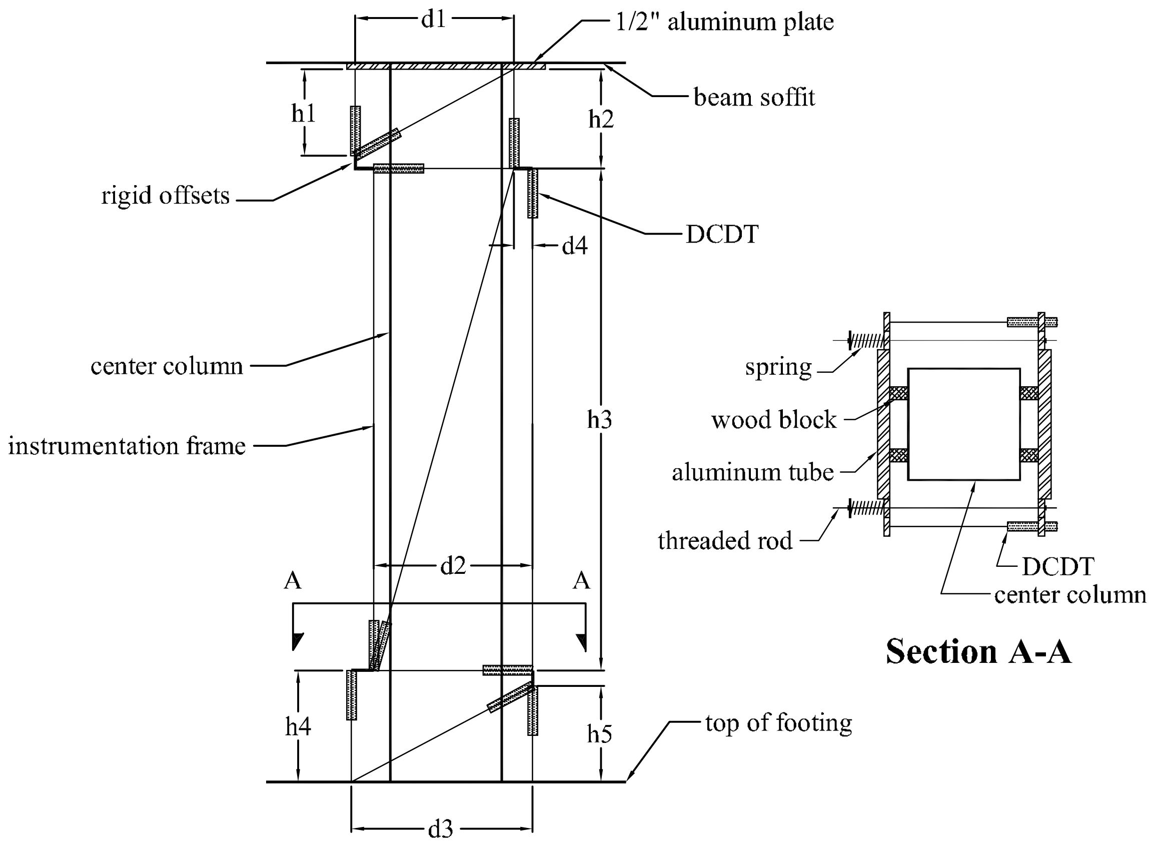

Figure B-14. Center column instrumentation (for dimensions see Table B-4)

Table B-4. Center column instrumentation dimensions

Dimension (see Figure B-14)	*Specimen 1 South*	*Specimen 1 North*	*Specimen 2 South*	*Specimen 2 North*
d1	13 1/8″	13″	12 7/8″	12 7/8″
d2	13 1/8″	12 3/4″	12 7/8″	12 5/8″
d3	14 3/4″	14 1/4″	14 5/8″	14 1/4″
d4	1 1/2″	1 1/2″	1 1/2″	1 1/2″
h1	7″	7 1/4″	7″	7″
h2	8 3/8″	8 5/8″	8 1/2″	8 1/2″
h3	40 1/2″	40 1/2″	40 1/2″	40 1/2″
h4	9 1/8″	9 1/8″	8 7/8″	9″
h5	8 1/4″	8″	7 3/4″	8″

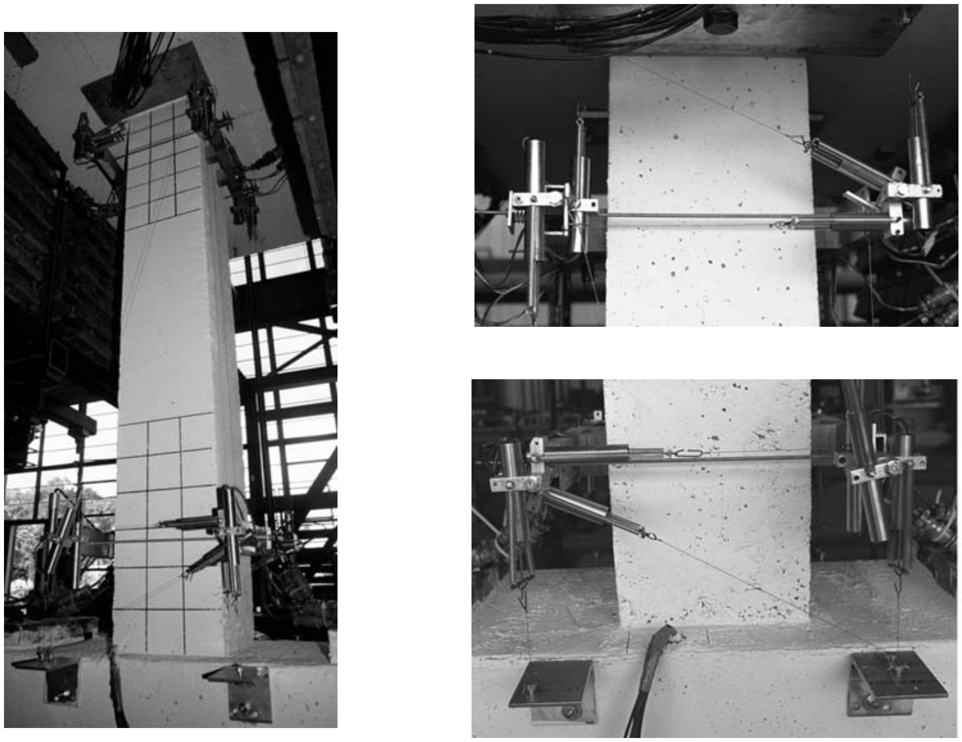

Figure B-15. Center column instruments and close-up view of top and bottom of column

were rigidly attached to 10″ x 2″ aluminum tubes that were secured to the column using spring tensioned threaded rods. Each aluminum tube was offset from the column face by two 10″ x 2″ x 1.5″ wood blocks. The tip of a concrete screw protruded from one wood block per tube and was set into a predrilled hole in the column face, thereby fixing the position of the instruments. The other wood block was held in place by friction to allow for unrestrained dilation of the concrete column between the blocks.

The truss configuration of the instruments allows for calculation of deformations based on the principle of virtual forces. For more details see Section B.6.

Owing to interference from spalling cover concrete and severe distortion of the center column during the shear failure test, data from the center column instruments can be used only for times before shear failure of the center column (see Sections 6.3.2 and B.6 for more details).

B.4.6 GLOBAL DISPLACEMENT INSTRUMENTS

Displacement transducers were used to measure the global vertical, longitudinal, and transverse displacements of the specimens, as shown in Figures B-16 through B-18. Transducers mounted to the instrumentation frames off the shake table measured the total displacements (i.e., including the displacement of the shake table). Transducers mounted to the shake table (including GDL LVDTN and GDL LVDTS) measured the displacement of the specimens relative to the shake table.

Transverse displacements were recorded to confirm that the out-of-plane bracing mechanism was maintaining the unidirectional response of the specimens. All transverse displacements were below tolerable limits.

To avoid conflict between the lead weight stacks and the vertical and longitudinal instrumentation wires, aluminum tubes with attachments for the instrumentation wires were cantilevered from the sides of the specimen beam. The longitudinal displacements of the center column were recorded by linear variable differential transformers (LVDTs) mounted flat on the shake table surface (GDL LVDTN and GDL LVDTS). The instrumentation wires from the LVDTs passed through a pulley mounted to the shake table and extended up at an angle to the cantilever tubes attached to the specimen beam (Figure B-17). The vertical displacements of the center column were recorded in a similar manner.

B.5 EXPERIMENTAL PROCEDURES

After the instrumentation was installed and calibrated for each specimen, a "channel check" was performed, wherein the data acquisition system recorded the readings from each of the instruments for several seconds without any induced movement of the specimen. This allowed for a check of the electronic noise on each of the channels. Resistors were used to reduce electronic noise where necessary.

As described in Section 5.6, the experimental program for each specimen consisted of free-vibration tests, a low-level earthquake simulation test, and a "shear-failure" earthquake simulation test. Four digital camcorders were used to film each of the earthquake simulation tests. One camcorder filmed the center column from a stand mounted on the shake table. The other three camcorders, mounted on stands off the shake table, filmed the whole frame, and the top and bottom of the center column, respectively. Filming was started immediately before each of the earthquake simulation tests. An audio signal from the shake table operator was recorded by the camcorders when the data acquisition system was activated. This allowed for the approximate synchronization of the video and recorded data. After each of the earthquake simulation tests, the specimens were

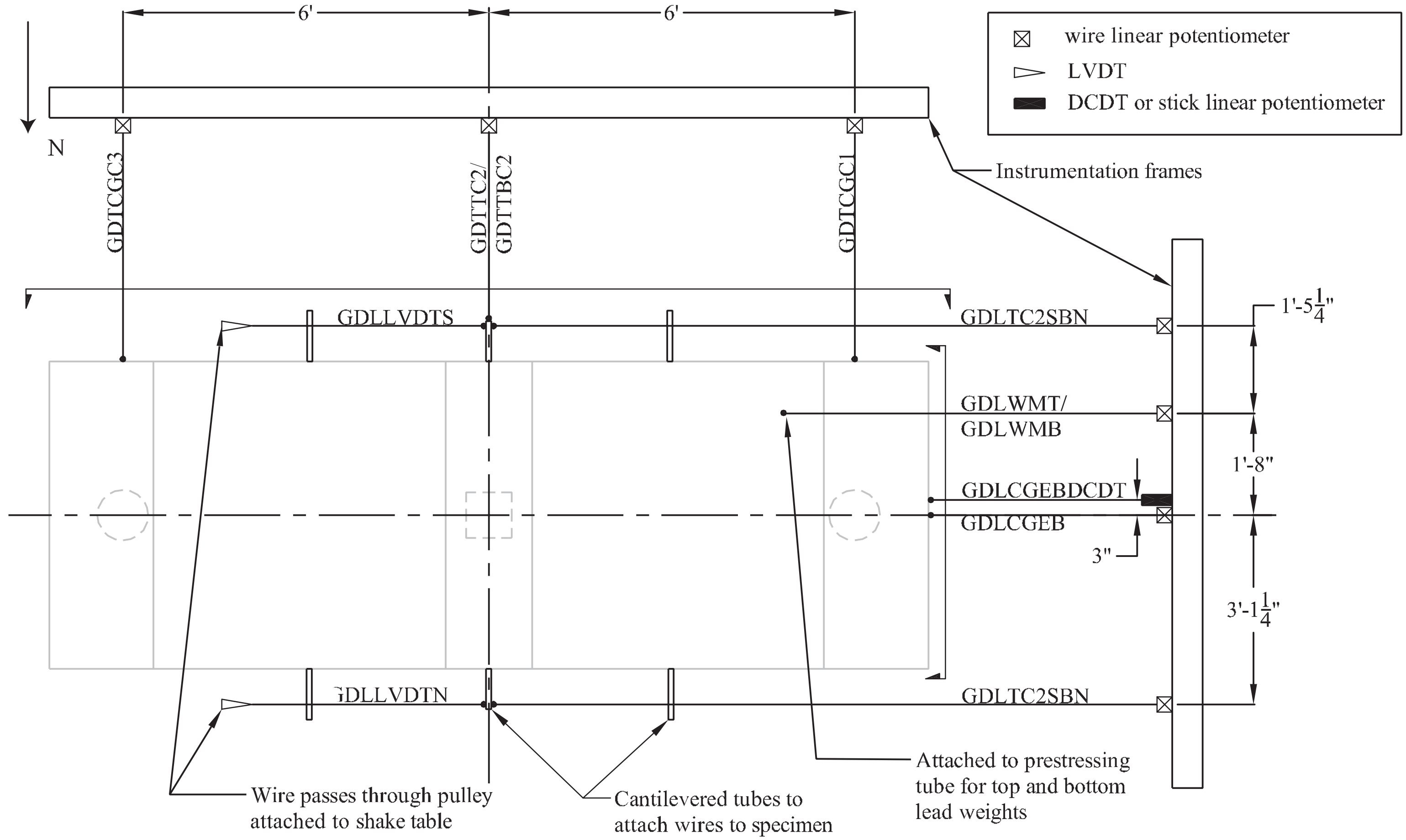

Figure B-16. Plan view of global displacement instruments (longitudinal and transverse instruments shown)

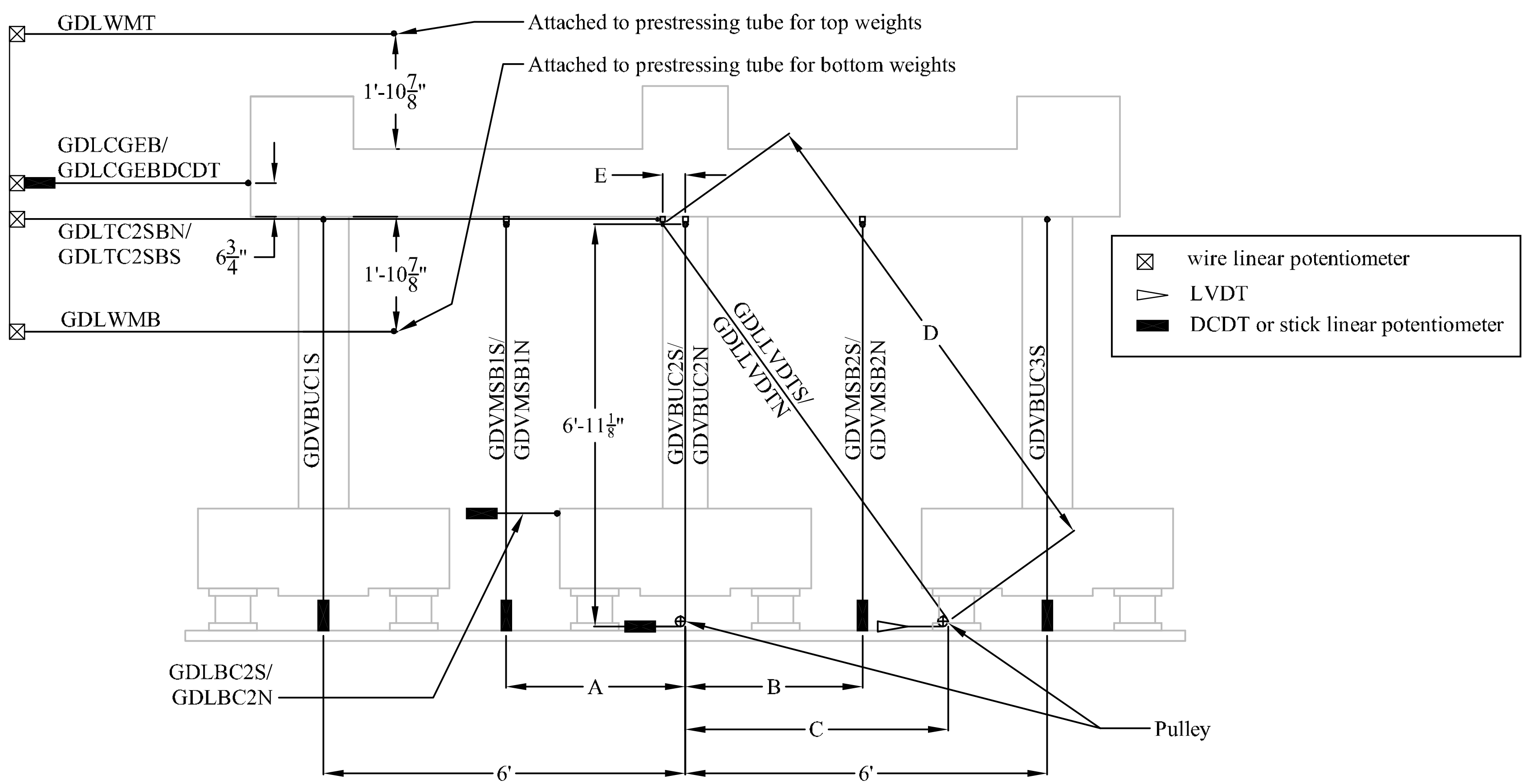

Figure B-17. Elevation view of global displacement instruments (longitudinal and vertical instruments shown)

Table B-5. Dimensions for Figure B-17

Dimension	*Specimen 1 North Side*	*Specimen 1 South Side*	*Specimen 2 North Side*	*Specimen 2 South Side*
A	2′ - 11 7/8″	2′ - 11 5/8″	2′ - 11 1/2″	2′ - 11 1/8″
B	2′ - 11 3/8″	2′ - 11 1/4″	2′ - 11 1/2″”	2′ - 11 1/2″
C	4′ - 4 1/4″	4′ - 4 1/4″	4′ - 3 1/2″	4′ - 3 1/2″
D	8′ - 2 3/16″	8′- 2 3/16″	8′ - 4 1/4″	8′ - 4 1/″
E	0	0	4 1/2″	4 1/2″

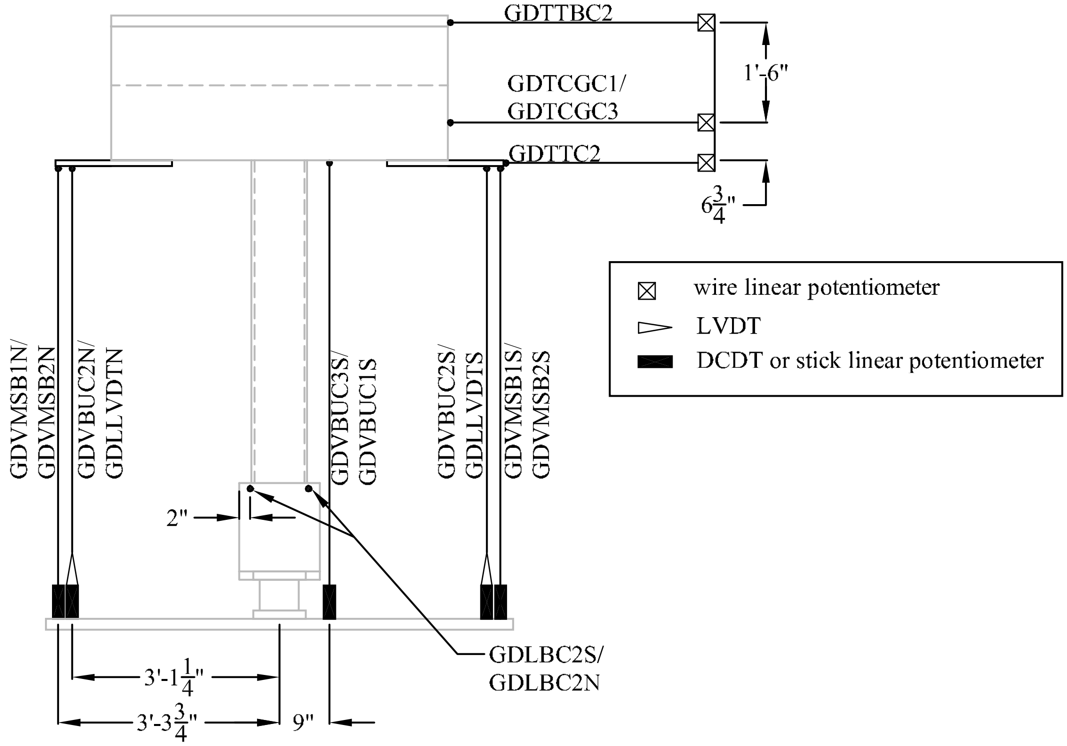

Figure B-18. End view of global displacement instruments (transverse and vertical instruments shown)

inspected for cracks. Videos from each of the tests document the progression of damage and the distribution of cracks during the shear-failure tests (see Appendix E).

B.6 DATA REDUCTION

This section summarizes the procedures used to reduce the recorded data to the results presented in Chapter 6.

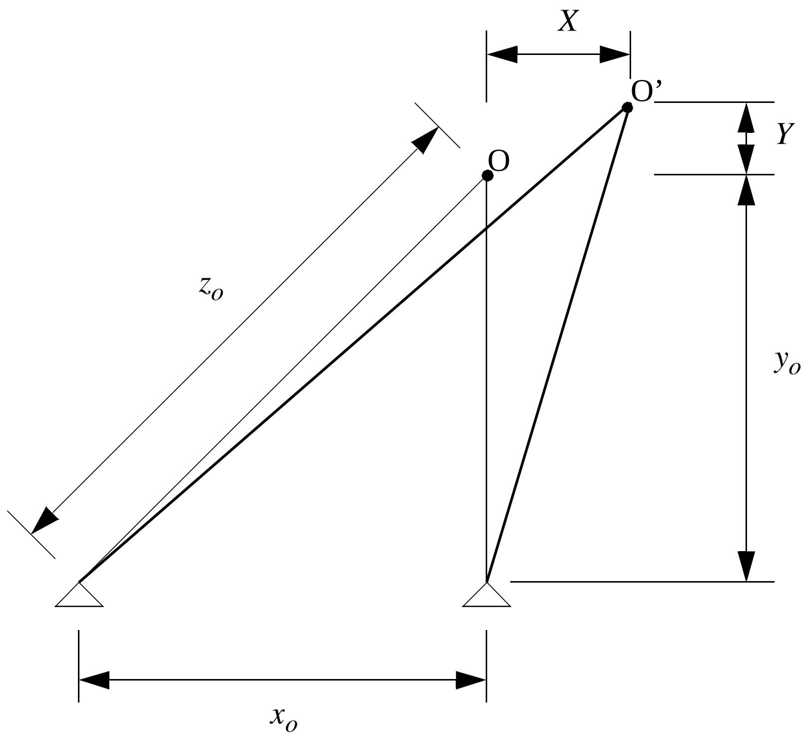

Figure B-19. Correction for large displacements

Longitudinal and vertical displacements at center column: The longitudinal displacements were recorded by several instruments including the diagonal LVDTs, GDL LVDTN and GDL LVDTS. The results from the LVDTs were compared with the output from other instruments to confirm that the pulley system (Figure B-17) produced accurate data.

The triangularized setup of GDL LVDTN and GDV BUC2N on the north side and GDL LVDTS and GDV BUC2S on the south side was used to correct for large displacements in the longitudinal and vertical recordings. With reference to Figure B-19, the following equations can be written for the position of node O:

$$(z_o + \Delta z)^2 = (x_o + X)^2 + (y_o + Y)^2 \tag{B.1}$$

$$(y_o + \Delta y)^2 = X^2 + (y_o + Y)^2 \tag{B.2}$$

where Δz and Δy are the changes in the lengths of wires z and y (i.e., the recorded data from the diagonal and vertical instruments, respectively). There are only two unknowns, the corrected longitudinal and vertical displacements (X and Y). The unknowns can be determined by iteration as follows:

1. Y is assumed equal to Δy
2. X is evaluated using Equation B.1
3. Y is evaluated using Equation B.2 and the current value for X
4. X is re-evaluated using Equation B.1 and the current value for Y
5. Steps 3 and 4 are repeated until the change from one iteration to the next is negligible

A converged solution is attained after only five iterations. The maximum difference between the corrected and uncorrected results was 0.035″.

The corrected longitudinal and vertical displacements from the north and south sides of the specimen are averaged to get the longitudinal displacements shown in Figure 6-5 and the vertical displacements shown in Figure 6-14. These corrected longitudinal displacements are used for any plots in Chapter 6 requiring the longitudinal displacements of the beam or the tops of the columns.

Base shear and inertial forces: The base shear plotted in Figures 6-5, 6-6, and 6-7 was determined by summing the shears recorded by the force transducers. As discussed in Section 6.3.1, the base shear should be approximately equal, and opposite in sign, to the longitudinal inertial forces. The longitudinal inertial forces were calculated by two methods:

- F_i = (total beam and lead weight mass)*(average longitudinal acceleration recorded by ALCGC2S and ALCGC2N)
- F_i = Σ(mass of each lead weight stack)*(acceleration of the closest stack with accelerometer) + (concrete beam mass)*(average longitudinal acceleration recorded by ALCGC2S and ALCGC2N)

Both methods produced very similar results, although high-frequency oscillations of the accelerations recorded on the lead weight stacks resulted in a maximum difference between the two methods of 4.77 kips. Inertial forces from method 2 were used in the fourth plot of Figure 6-5.

Overturning moments: The overturning moments were defined as the base moment resulting from axial loads in the columns. The overturning moments plotted in Figures 6-5, 6-8, and 6-9 were calculated by summing the moments caused by the column axial loads about the base of the center column as follows:

$$OTM = P_{Wcol}6' + P_{Ecol}6' \qquad \text{(B.3)}$$

As noted in Section 6.3.1, the noise in the overturning moment plots is caused by high-frequency pitching of the shake table. If these frequencies are filtered out and the overturning moments, summed with the column base moments, are divided by the recorded base shear, the result is approximately 64.75″, or the height of the center of gravity above the base of the columns.

Center column shear: The center column shear plotted in Figures 6-14, 6-15, and 6-16, was determined by summing the in-plane shear data from the two force transducers under the center column.

Center column axial load: The change in the center column axial load during the tests was determined by summing the axial load data from the two force transducers under the center column. The initial axial load in the center column was determined using two readings from the force transducers: one just before the test, and another before the specimen was installed on the table in the fully unloaded condition. Since the clamping force from the bolts and threadbars securing the force transducers to the base plate and specimen appeared to affect the readings, the bolts and threadbars were loosened before taking the reading before the test. The clamping force did not influence the results during the test, since the clamping force remained constant during testing.

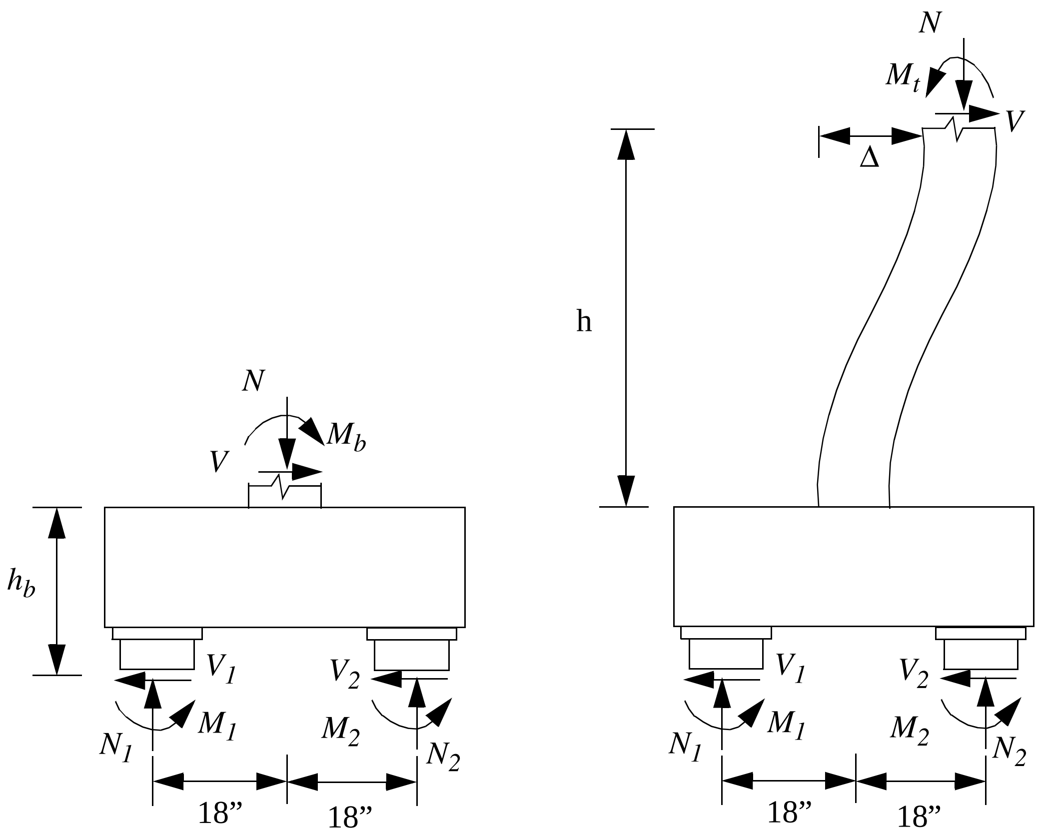

Figure B-20. Free-body diagrams for calculating column moments (Reactions recorded at midheight of the force transducers)

Center column moments: The center column moments plotted in Figures 6-14, and 6-22, through 6-27, were determined using the output from the force transducers and the free-body diagrams shown in Figure B-20. Based on the free-body diagrams, and ignoring the inertial force from the column and footings, the top and bottom column moments were calculated as follows:

$$M_b = M_1 + M_2 - 18N_1 + 18N_2 - h_b(V_1 + V_2) \tag{B.4}$$

$$M_t = h(V_1 + V_2) - M_b + \Delta(N_1 + N_2) \tag{B.5}$$

Note that Equation B.5 can be used to calculate the moment at any column section at a height *h* above the bottom of the column given that the longitudinal displacements at a height *h* are known.

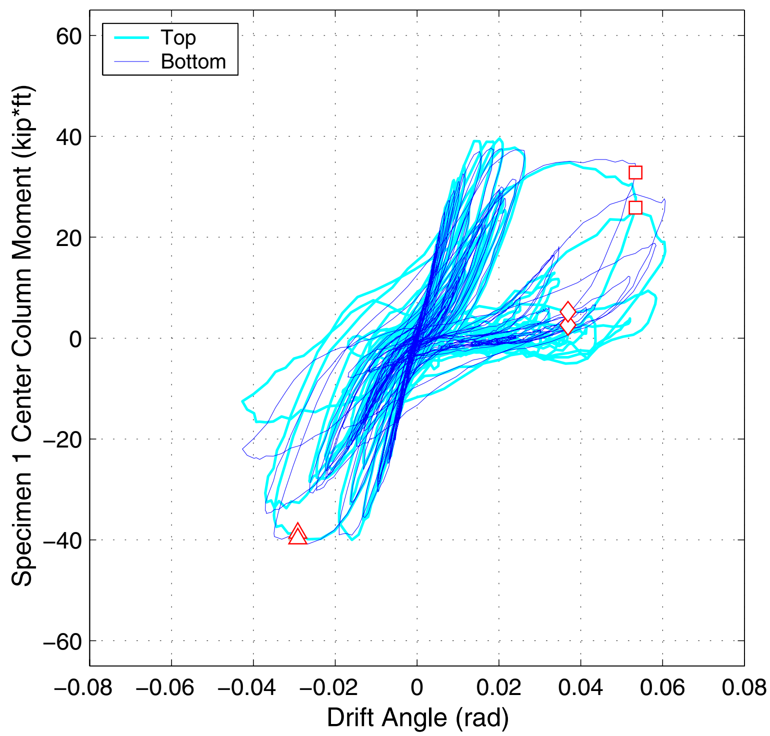

Figure B-21. Specimen 1 center column moment hysteretic response with $\alpha_V = 0.89$ and $\alpha_N = 1.0$

Figures 6-22 through 6-27 plot the center column moment hysteretic response. According to the plots, the yield strength at the top of the column appears to be approximately 50% higher than that at the bottom of the column. Although some discrepancy in the top and bottom yield strength should be expected due to slight variation in the reinforcement location and pockets of

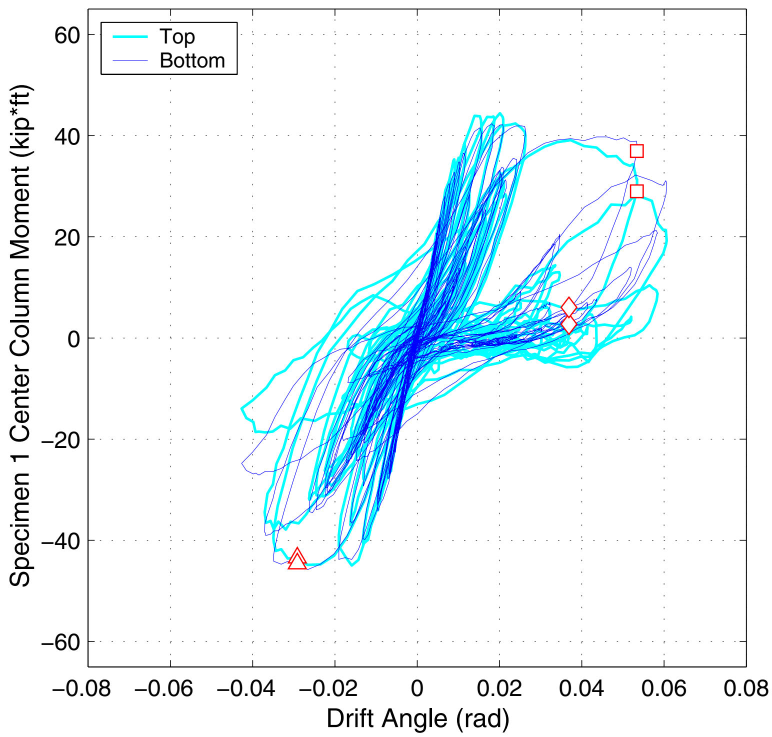

Figure B-22. Specimen 1 center column moment hysteretic response with $\alpha_V = 1.0$ and $\alpha_N = 1.12$

aggregates at the base of the column, one would not expect this discrepancy to be more than approximately 10%. It was concluded, therefore, that an error exists in the force transducer output used to calculate the moments. Since the moment readings from the force transducers were very small, the discrepancy in the top and bottom moments could result from errors in the axial load readings, the shear readings, or both. To investigate the magnitude of the possible errors, the shears and axial loads from the force transducers in Equations B.4 and B.5 were factored as follows:

$$M_b = M_1 + M_2 + 18\alpha_N(N_2 - N_1) - h_b\alpha_V(V_1 + V_2) \tag{B.6}$$

$$M_t = h\alpha_V(V_1 + V_2) - M_b + \Delta\alpha_N(N_1 + N_2) \tag{B.7}$$

Figures B-21 and B-22 show close agreement between the top and bottom yield moments for the Specimen 1 center column using $(\alpha_V,\alpha_N) = (0.89,1.0)$ or $(\alpha_V,\alpha_N) = (1.0,1.12)$. Since the sum of all the shear readings is in close agreement with the inertial forces (see Figure 6-5), and the axial load readings from the force transducers do not agree with the prestressing force from the pneumatic cylinders (see Figure B-11), it is expected that the discrepancy in the unfactored yield moments primarily results from errors in the axial load readings.

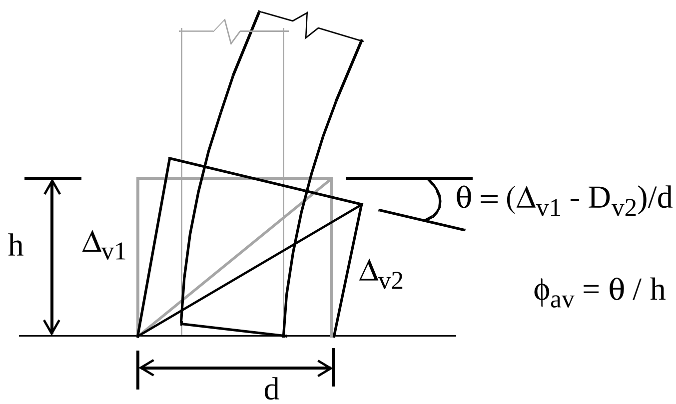

Figure B-23. Calculation of rotations and average curvatures

Rotations and average curvatures: The rotations and average curvatures plotted in Figures 6-24 through 6-27 were calculated using the center column instruments described in Section B.4.5. The rotations were calculated by taking the difference of the two vertical instruments in a single panel of the instrumentation truss and dividing by the distance between the instruments, as illustrated for the bottom panel in Figure B-23. The rotations calculated from the instruments on the north and south faces of the column were averaged to arrive at the rotations shown in Figures 6-24 and 6-25. The average curvature over the panel, ϕ_{av}, is defined as the rotation divided by the height of the panel. The rotation of the beam relative to the footing, shown in Figure 6-28, was determined by summing the rotations calculated for each panel of the instantiation frame. Note that the rotation and average curvature include both flexural and slip deformations.

Displacements based on center column instruments: Longitudinal displacements for the center column can be calculated from the center column instrument data by applying the Principle of Complementary Virtual Work (also known as the Principle of Virtual Forces). Specifically for a truss, the Principle can be stated in the following form:

$$\Delta\delta P = \sum \Delta_i \delta f_i \tag{B.8}$$

where Δ is the real displacement of the truss at the location and in the direction of interest, Δ_i is the real deformation in the i^{th} truss member, δP is a virtual force applied to a compatible virtual truss system at the location and in the direction of displacement Δ, and δf_i is the virtual force in the i^{th}

member of the compatible virtual truss system. Any virtual system can be chosen as long as all the virtual forces within the system, δf_i, including reactions, are multiplied by the associated real deformations. By selecting a unit load for δP, the displacement at any node in the truss, and in any direction, can be determined by applying Equation B.8.

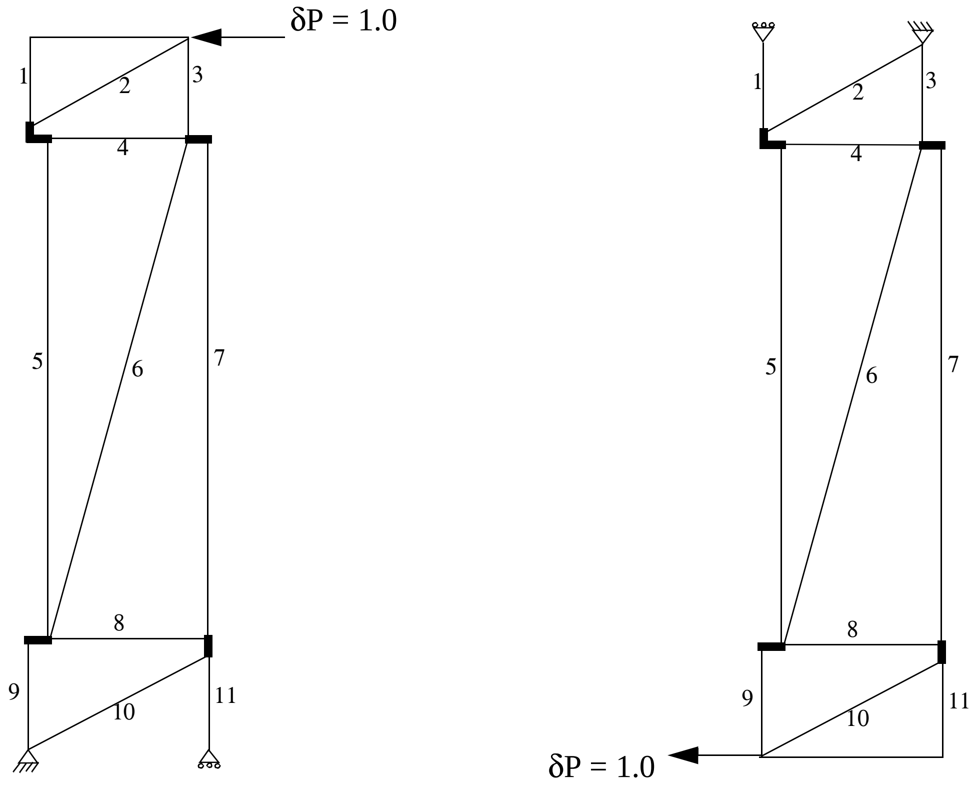

Figure B-24. Virtual truss systems used to calculate the longitudinal displacement of the center column

The center column instrumentation frame can be considered as a truss, and the readings from the instruments provide the real deformations, Δ_i. The longitudinal displacement of the column can be determined by selecting a virtual truss system with members in place of the instruments in the instrumentation frame and applying a horizontal virtual unit load at the top or bottom of the virtual truss, as shown in Figure B-24. The rigid offsets between the center lines of the instruments cause virtual moments at the joints of the virtual truss systems. These moments must be accounted for in the internal virtual work by rewriting Equation B.8 as follows:

$$\Delta = \sum_i \Delta_i \delta f_i + \sum_j \theta_j \delta M_j \qquad \text{(B.9)}$$

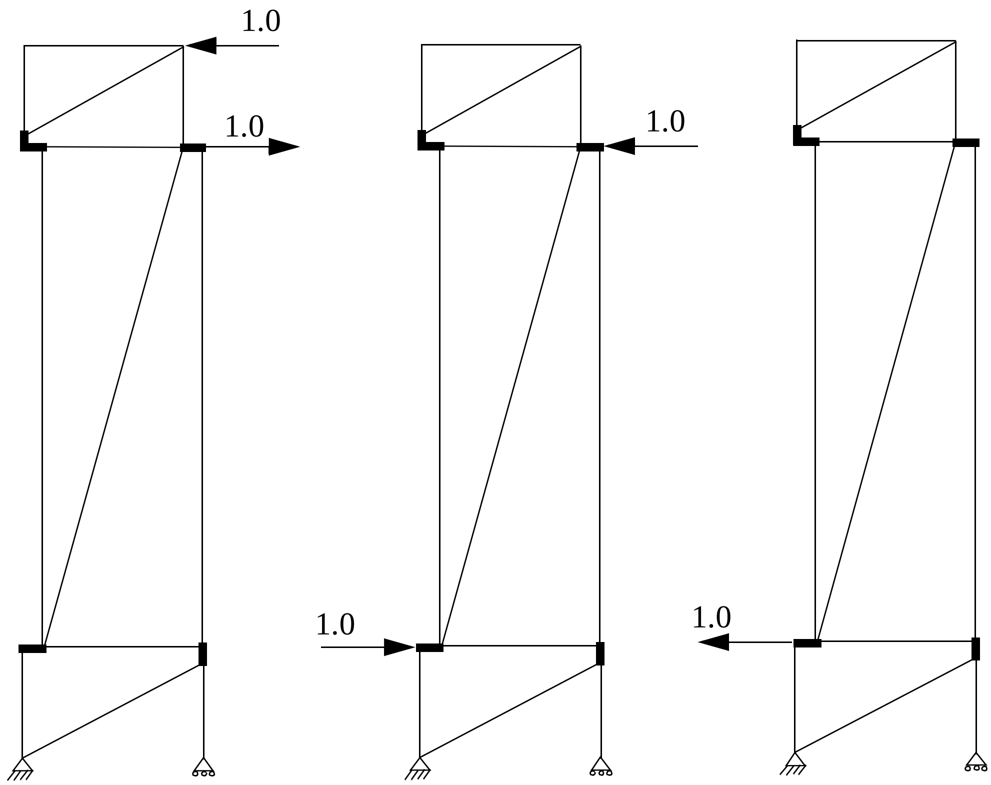

Figure B-25. External virtual forces used to calculate the contribution of the deformations within each panel to the longitudinal displacements

where θ_j is the real rotation of the column at the level of the j^{th} joint, and δM_j is the virtual moment at the j^{th} joint due to the rigid offsets. The virtual moments can be considered to be resisted at the joints by virtual flexural springs. Since the virtual truss systems are statically determinate, the virtual forces and moments resulting from the unit loads can be determined by basic statics.

Equations B.8 and B.9 assume that the displacements at the locations of the boundary conditions in the virtual truss systems are negligible. In other words, when applying Equation B.9 to virtual system A shown in Figure B-24, the rotation of the footing is neglected. Similarly, when using virtual system B the rotation of the beam is neglected. Virtual system A was used to calculate the displacements shown in the upper plot of Figures 6-29 and 6-30, and virtual system B was used to calculated the displacements shown in the middle plot of Figures 6-29 and 6-30.

The longitudinal displacements shown in Figures 6-31 and 6-32 were calculated using the average of the results from virtual system A and B. The average produced better agreement with the longitudinal displacements measured by the global instruments. The contributions of the deformations in each panel to the longitudinal displacement were determined using the external virtual forces shown in Figure B-25. Although shown here applied to virtual system A, similar external virtual forces were applied to both virtual systems and the results were averaged.

A description of the method used to calculate the panel deformations without rigid body rotations can be found in Section 6.3.2.

Outside column initial forces: The force transducers were unable to monitor the column reactions accurately over an extended period of time, such as the one week required to install the specimen and mount the masses. Furthermore, unlike the center column, the dead-load shear present in the outside columns required that the threadbars and bolts securing the force transducers to the footings and the base plate remain tightened to ensure that no slip occurred between the specimen and the base plate. In effect, the only dead-load reaction recorded from the force transducers with reasonable accuracy was the initial axial load on the center column. The initial moments and shears on the center column were assumed to be negligible. The remaining reactions (i.e., shear, moment, and axial load on the outside columns) were determined from the dead-load model for the loaded specimen described in Section 8.2.3. The initial loads on the outside columns, summarized in Table B-6, are used in Figures 6-36 through 6-49.

Table B-6. Initial loads on outside columns based on final dead-load model

Load Type	*Specimen 1*	*Specimen 2*
Axial load	19.4 kips	21.5 kips
Shear	1.15 kips	1.39 kips
Moment (Top of Column)	76.3 kip in	92.1 kip in
Moment (Bottom of Column)	9.2 kip in	11.1 kip in

Outside column moments: The outside column moments shown in Figures 6-36, 6-37, and 6-46 through 6-49 were calculated according to the procedures described above for the center column and using Equations B.4 and B.5.

As noted in Section 6.3.3, for positive displacement cycles the yield strength at the top of the west column appears to be approximately 50% higher than the yield strength at the bottom of the column, while the top and bottom yield strengths for negative cycles for the west column and both cycles for the east column appear to be within expected tolerances. It should be noted that water damage to the solo-tube forms used for the outside columns resulted in a reduction of the cover at the base of both Specimen 1 outside columns. Although this would result in a slightly lower moment capacity for the base of the column relative to the top of the column, it is not expected to account for the large discrepancy in yield strengths observed in the data. Furthermore, the reduction in the cover concrete should influence the strength of both the east and west columns of Specimen 1, not just the west column of both specimens as seen in the data. It is concluded, therefore, that, as with the center column, the discrepancy in the yield strengths for the west column is most likely due to errors in the axial load readings from the force transducers.

Outside column shear and axial loads: The shear and axial loads in the outside columns plotted in Figures 6-36 and 6-37 were determined by summing the shear and axial load data from the two force transducers under each column. The initial shear and axial loads were determined as described above.

Outside column vertical displacements: The outside column vertical displacements plotted in Figures 6-36 and 6-37 were based directly on the data from instruments GDV BUC1S for the west column and GDV BUC3S for the east column.

Total vertical load: Two methods were used to calculate the total vertical load acting on the specimen:

1. The total weight of the beam and lead packets (67.9 kips) was added to the recorded prestress force. The result of this method is denoted in Figure 6-55 as the “Total Gravity Load.”
2. The axial loads from each column (based on the force transducer data) were added to the vertical inertial forces, calculated based on the vertical accelerations measured on the beam over the center column (average of data from instruments AVCGC2S and AVCGC2N) and the total mass of the beam and lead packets. (All frequencies above 25 hz were removed from the recorded accelerations.) The result of this method is denoted in Figure 6-55 as $\Sigma P_{col} + ma_{vert}$.

The results from the second method exhibit some high-frequency axial load oscillations, which may be attributed to the broader range of frequency content recorded by the accelerometers compared with the force transducers. At the end of the test there was a difference of 2.5 kips between the “Total Gravity Loads” and the sum of the column axial loads.

B.7 DERIVATION OF BAR SLIP MODEL

When a reinforced concrete column is subjected to lateral forces, slip of the reinforcing bars within the anchor blocks will result in lateral displacements in addition to those caused by flexural defor-

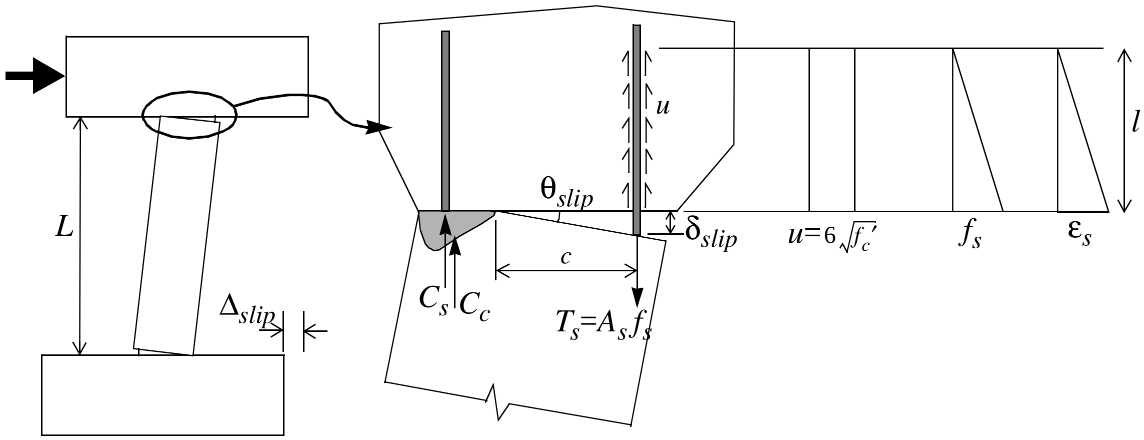

Figure B-26. Slip of longitudinal reinforcement from anchorage block

mation of the column. This section describes the derivation of Equation 7.3 used to estimate the lateral displacement due to bar slip before yielding of the longitudinal reinforcement.

Moments at the anchored end of a reinforced concrete column may cause tension in the anchored reinforcing bars as shown in Figure B-26. The tension force, T_s, must be resisted by the bond stress, u, between the reinforcement and the anchorage block concrete. This results in the following equilibrium equation, if the bond stress is approximately constant:

$$A_s f_s = \pi d_b l u \tag{B.10}$$

where A_s is the area of one longitudinal reinforcing bar, f_s is the stress in the reinforcing bar (less than or equal to the yield stress), d_b is the nominal diameter of a reinforcing bar, and l is the length over which the bond stress acts as shown in Figure B-26. The slip of the reinforcing bar, δ_{slip}, can be found by integrating the strain diagram shown in Figure B-26:

$$\delta_{slip} = \frac{1}{2}\varepsilon_s l \tag{B.11}$$

where ε_s is the strain in the reinforcing bar corresponding to the stress f_s. Using Equation B.10 to find the length l, Equation B.11 can be rewritten as follows:

$$\delta_{slip} = \frac{\varepsilon_s d_b f_s}{8u} \tag{B.12}$$

The rotation at the anchorage due to slip of the reinforcing bars, θ_{slip}, is given by the ratio of δ_{slip} to the distance from the reinforcement to the neutral axis, c. Using Equation B.12, and recognizing that (ε_s/c) is equal to the curvature at the section, ϕ, the rotation can be expressed as follows:

$$\theta_{slip} = \frac{d_b f_s \phi}{8u} \tag{B.13}$$

Finally, the lateral displacement of a column of length L due to slip of the reinforcement from the anchorage block is given by:

$$\Delta_{slip} = \frac{L d_b f_s \phi}{8u} \tag{B.14}$$

For the slip displacement at yield, f_s and ϕ in Equation B.14 are replaced by f_y and ϕ_y, respectively, as shown in Equation 7.3. The slip displacement beyond yield can be estimated using a similar model presented by Sezen (2002).

Appendix C: Experimental Results from Low-level Tests

This appendix documents selected recorded results for the low-level shake table tests performed before each of the shear-failure tests described in Chapter 6. The experimental setup for the low-level tests is identical to that described in Chapter 5 and Appendices A and B for the shear-failure tests.

The results indicate that column longitudinal reinforcement did not yield during the low-level tests. Only limited cracking of the outside columns was observed after the tests.

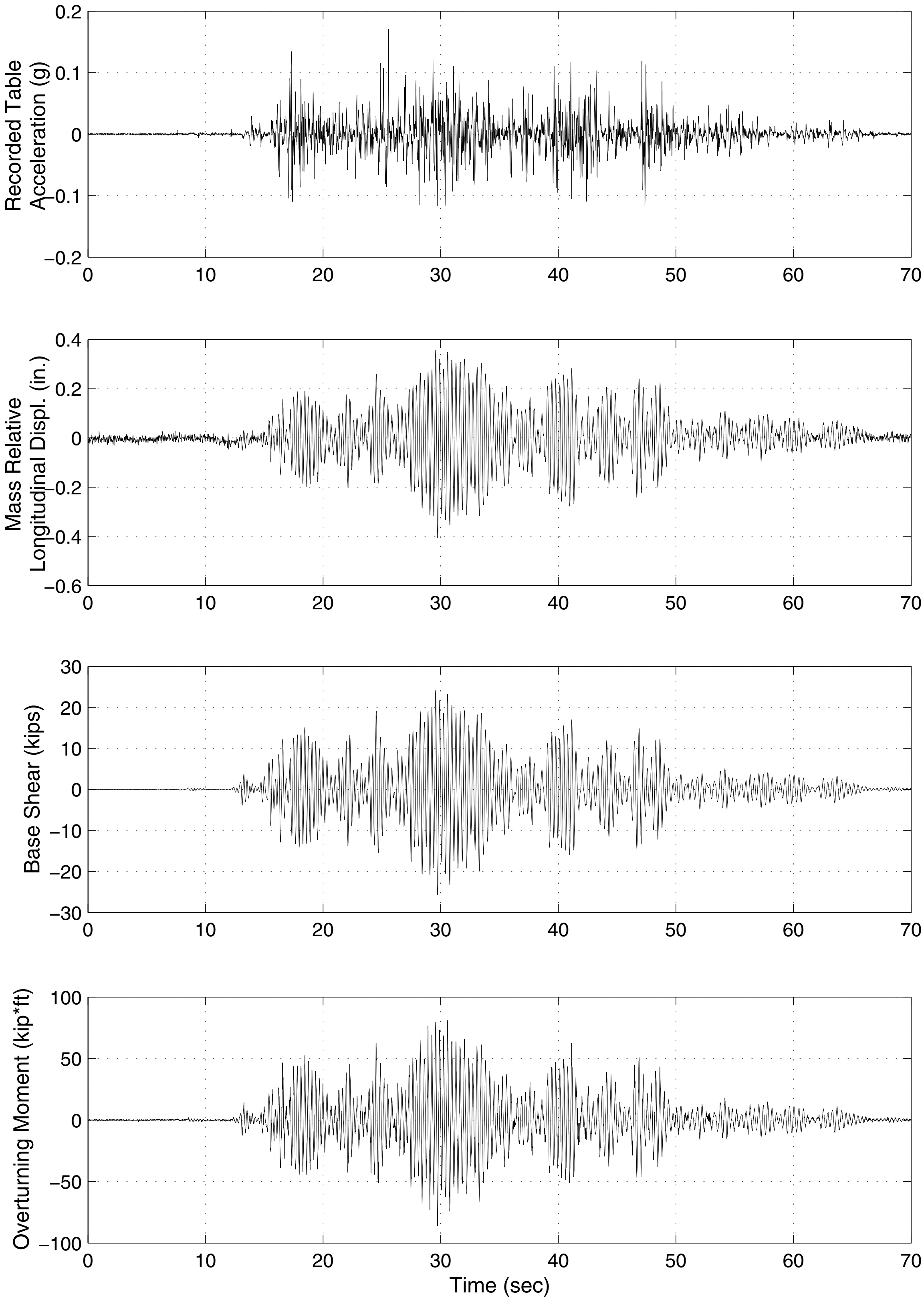

Figure C-1. Global response histories for low-level test — Specimen 1

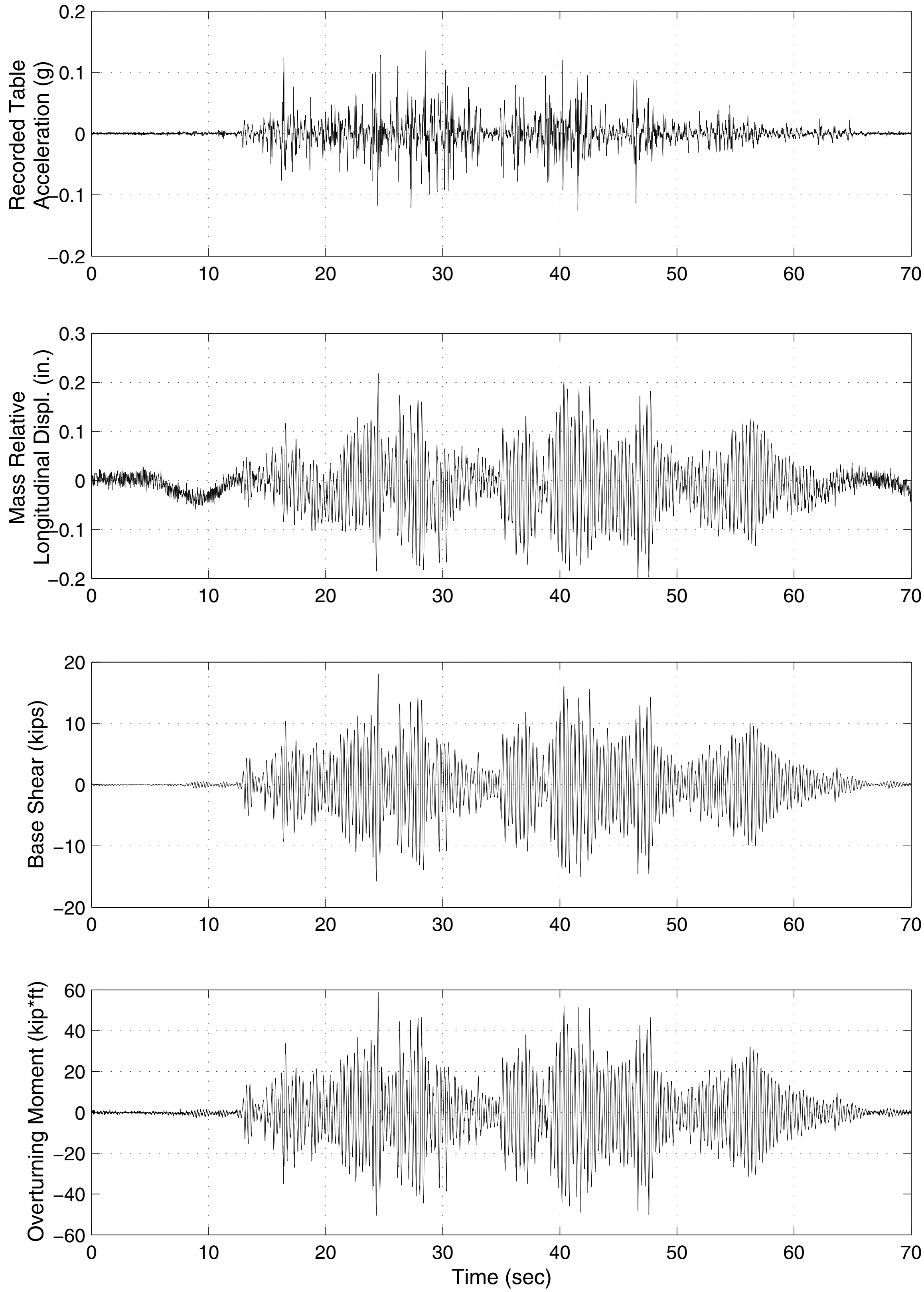

Figure C-2. Global response histories for low-level test — Specimen 2

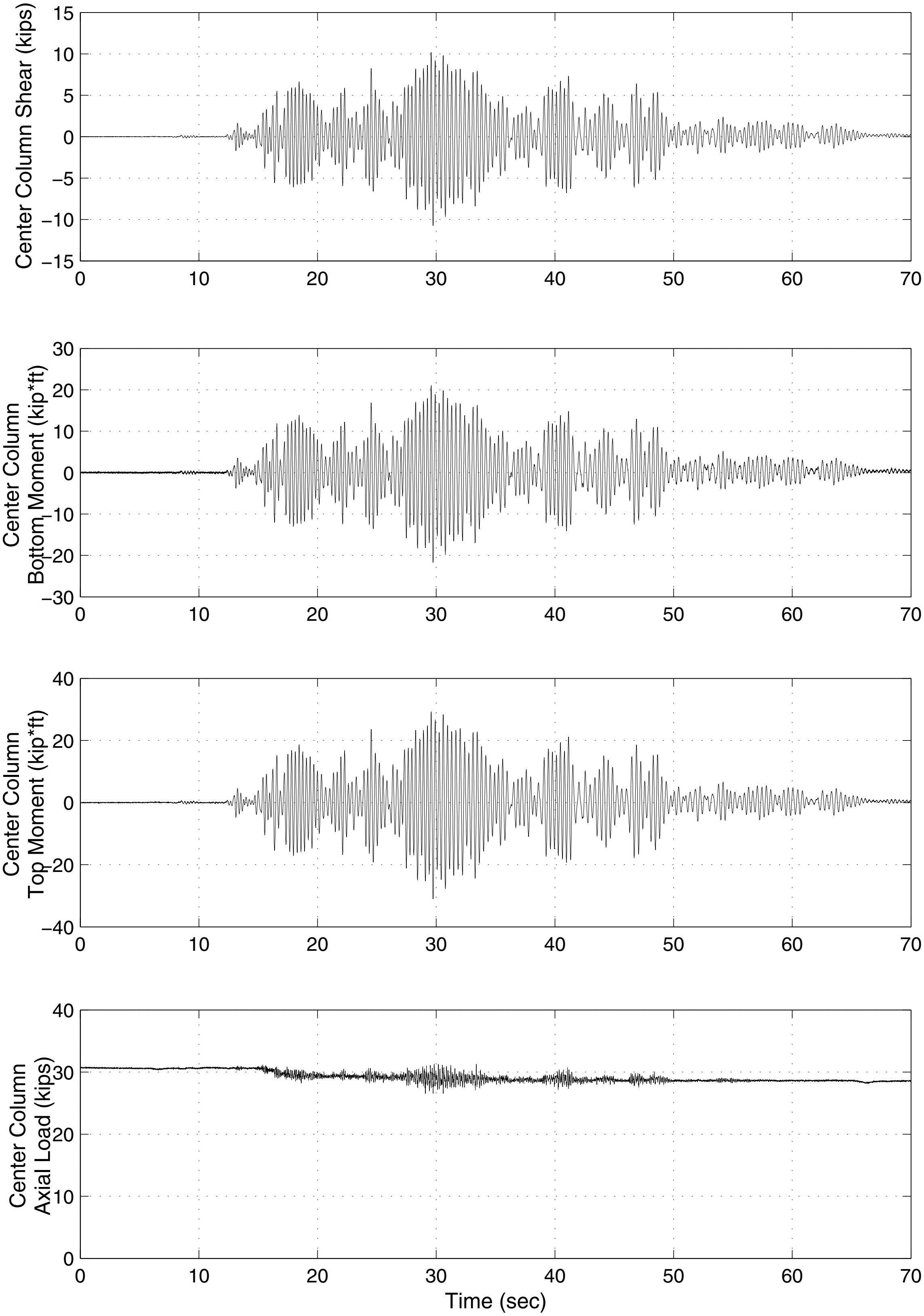

Figure C-3. Center column response histories for low-level test — Specimen 1

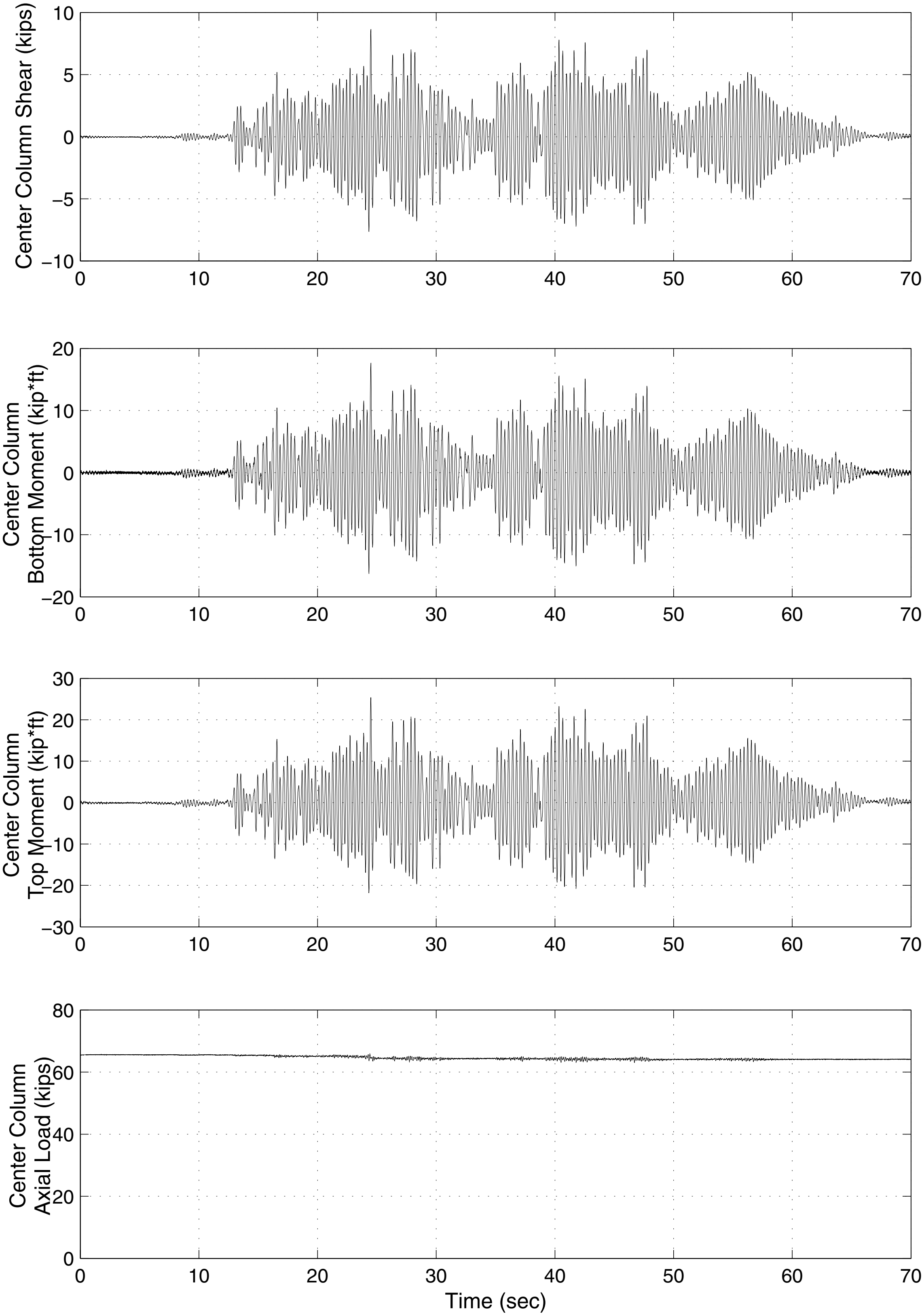

Figure C-4. Center column response histories for low-level test — Specimen 2

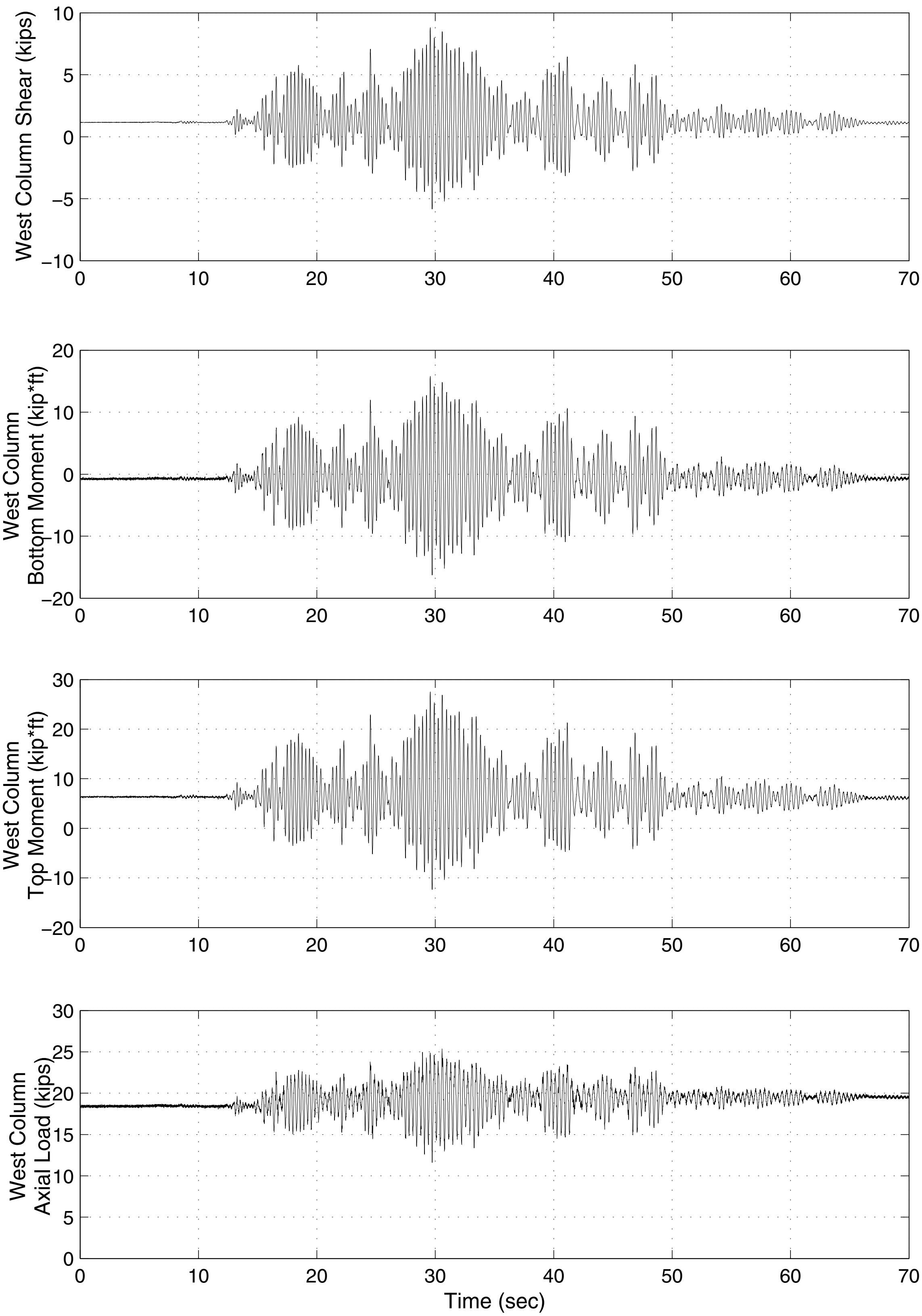

Figure C-5. West column response histories for low-level test — Specimen 1

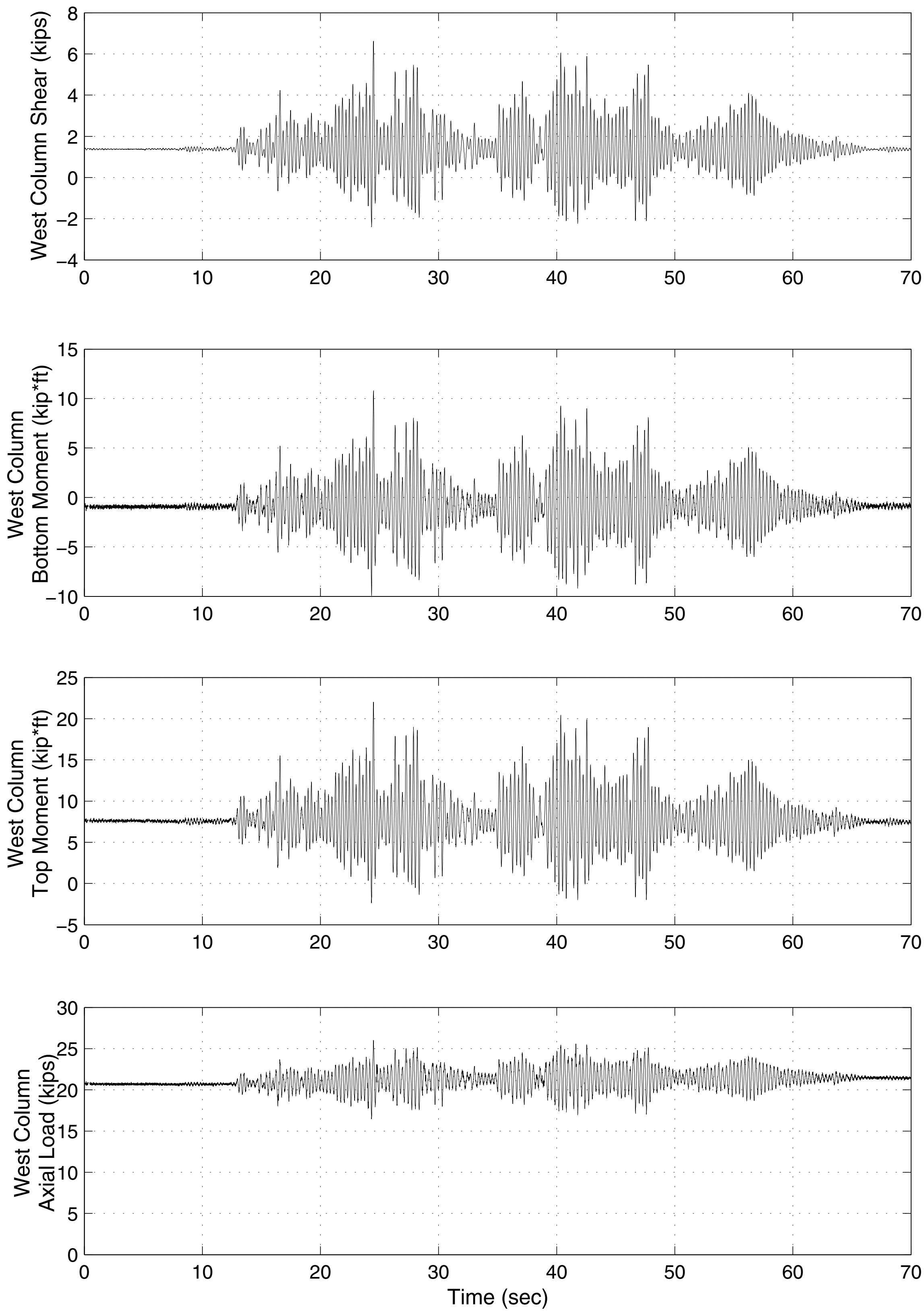

Figure C-6. West column response histories for low-level test — Specimen 2

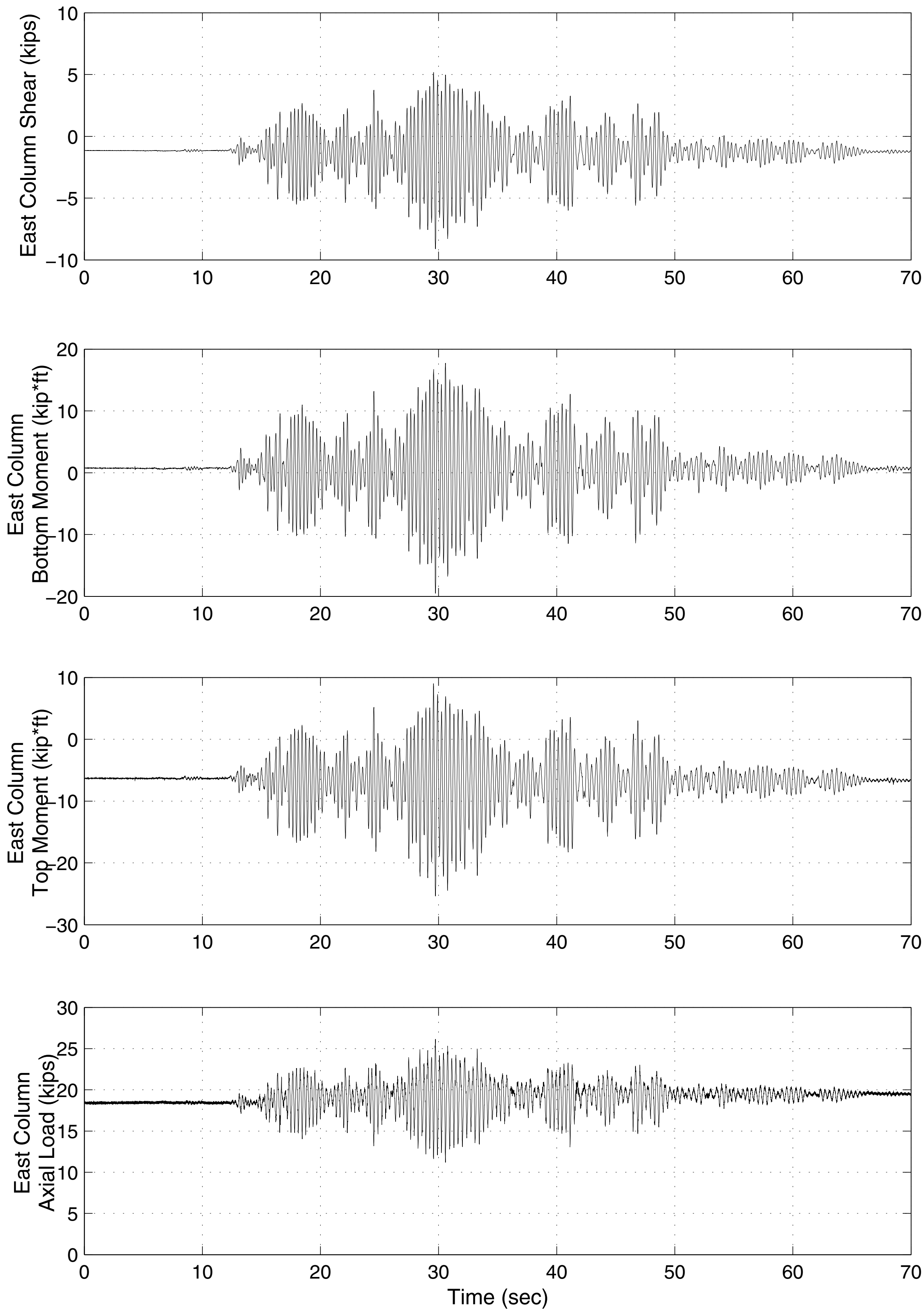

Figure C-7. East column response histories for low-level test — Specimen 1

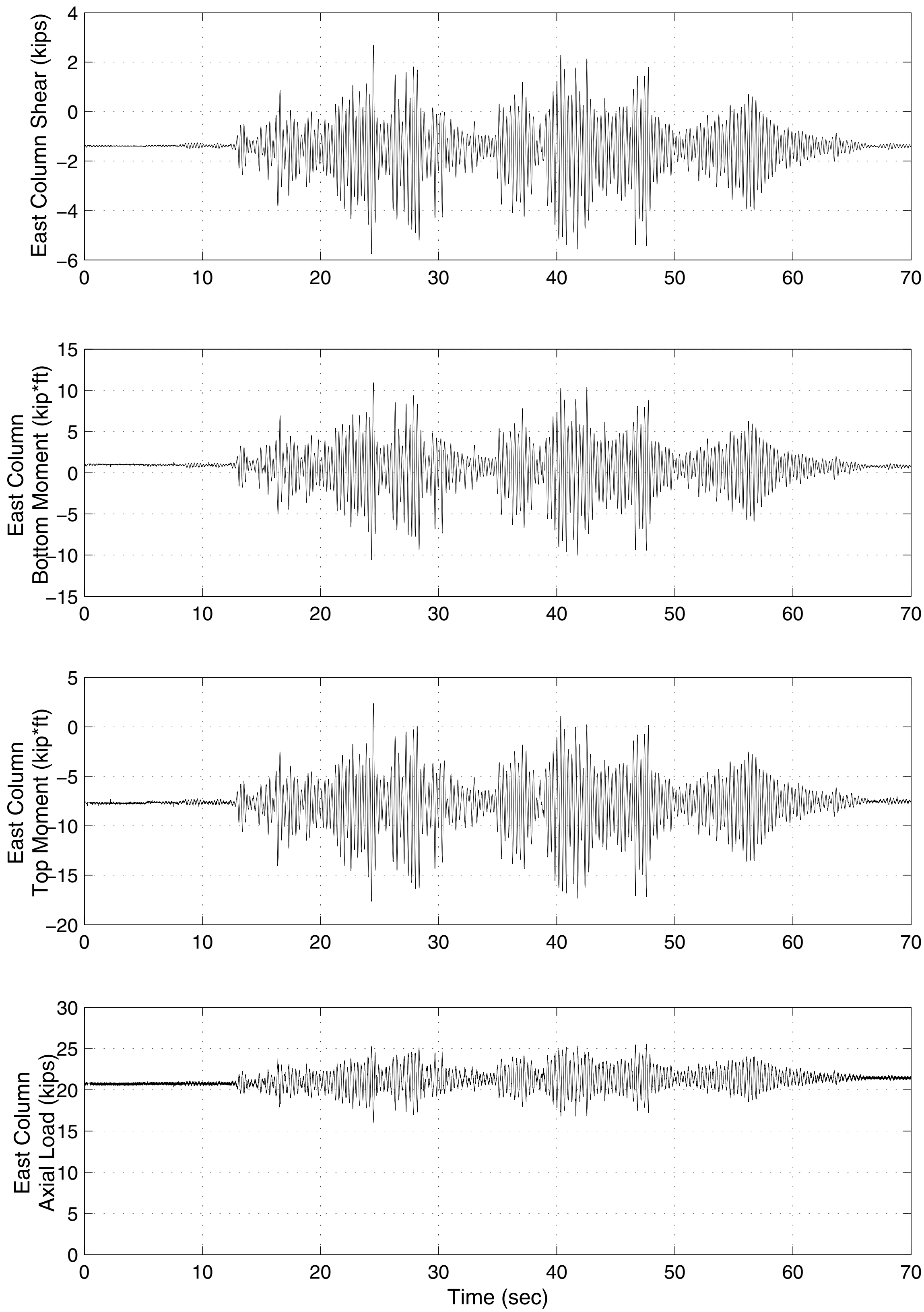

Figure C-8. East column response histories for low-level test — Specimen 2

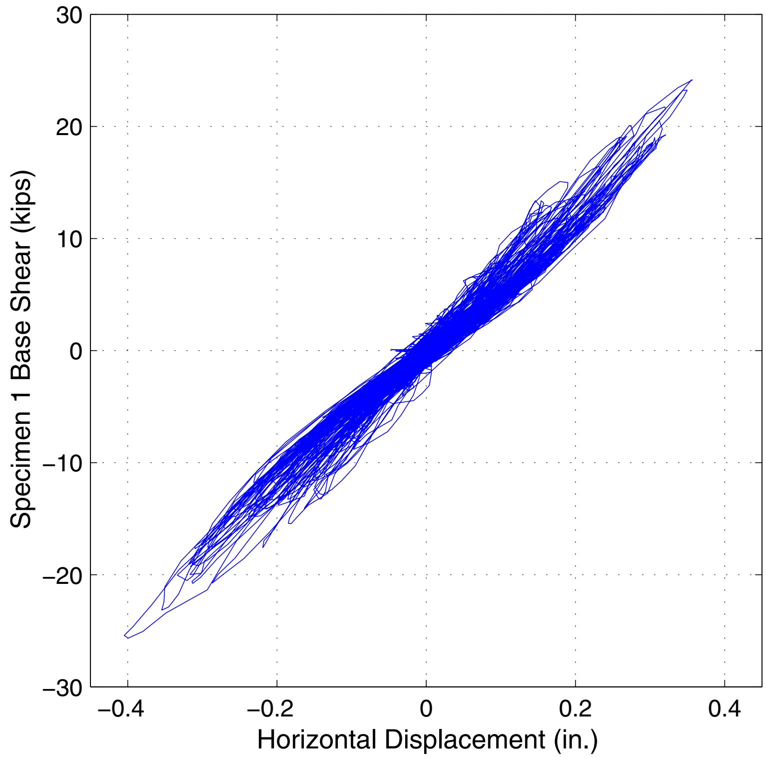

Figure C-9. Specimen 1 base shear hysteretic response for low-level test

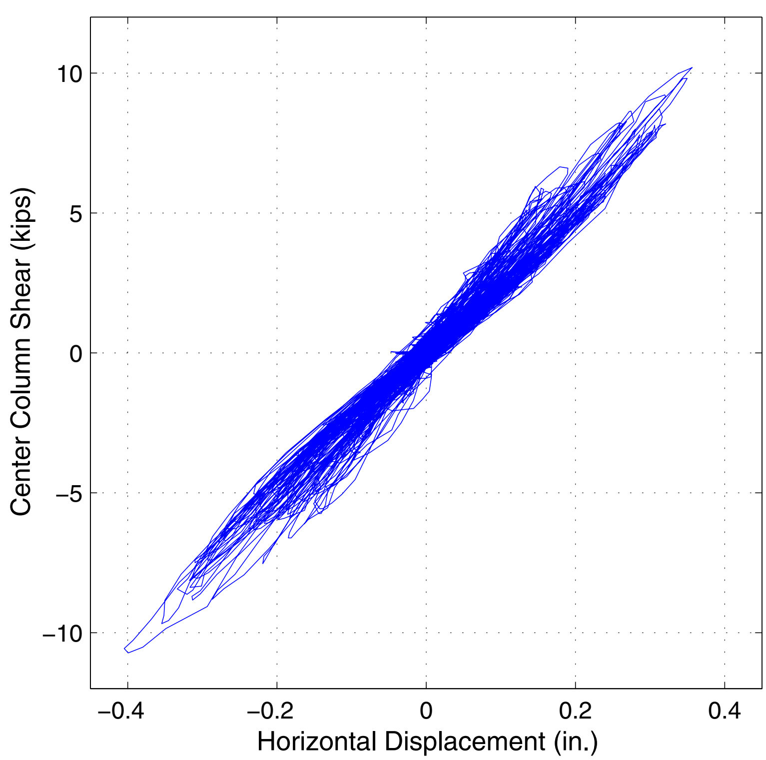

Figure C-10. Specimen 1 center column shear hysteretic response for low-level test

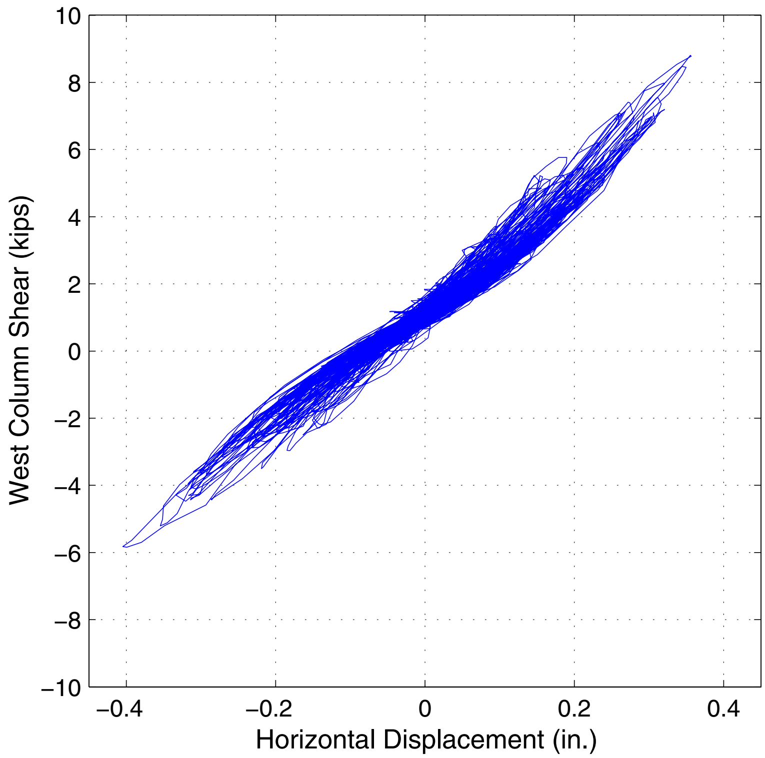

Figure C-11. Specimen 1 west column shear hysteretic response for low-level test

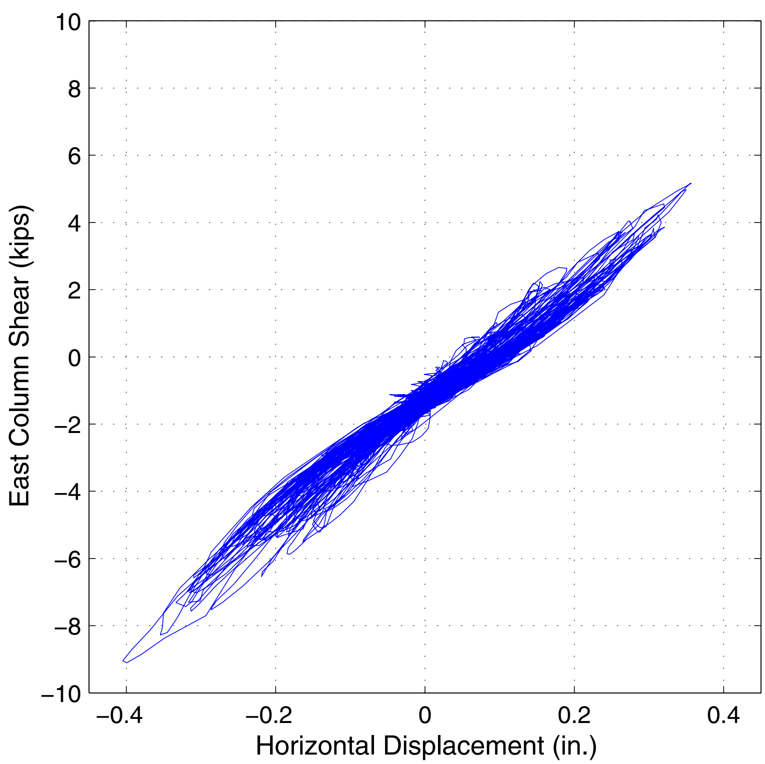

Figure C-12. Specimen 1 east column shear hysteretic response for low-level test

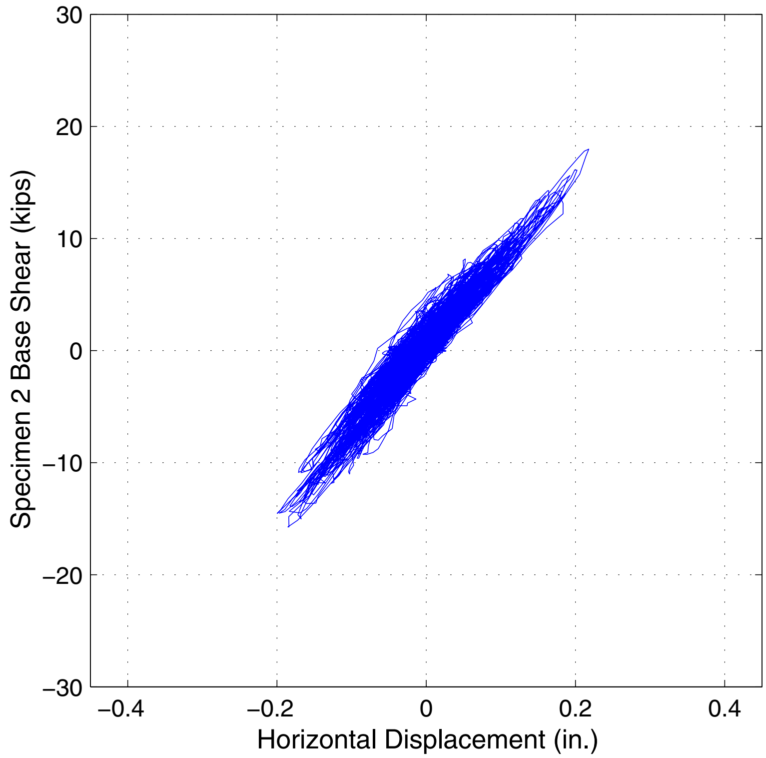

Figure C-13. Specimen 2 base shear hysteretic response for low-level test

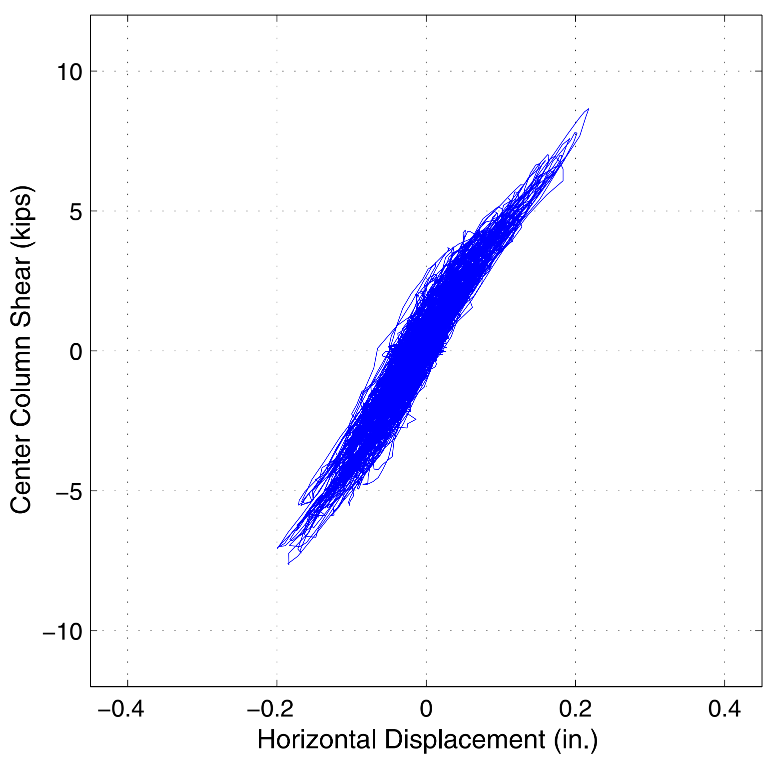

Figure C-14. Specimen 2 center column shear hysteretic response for low-level test

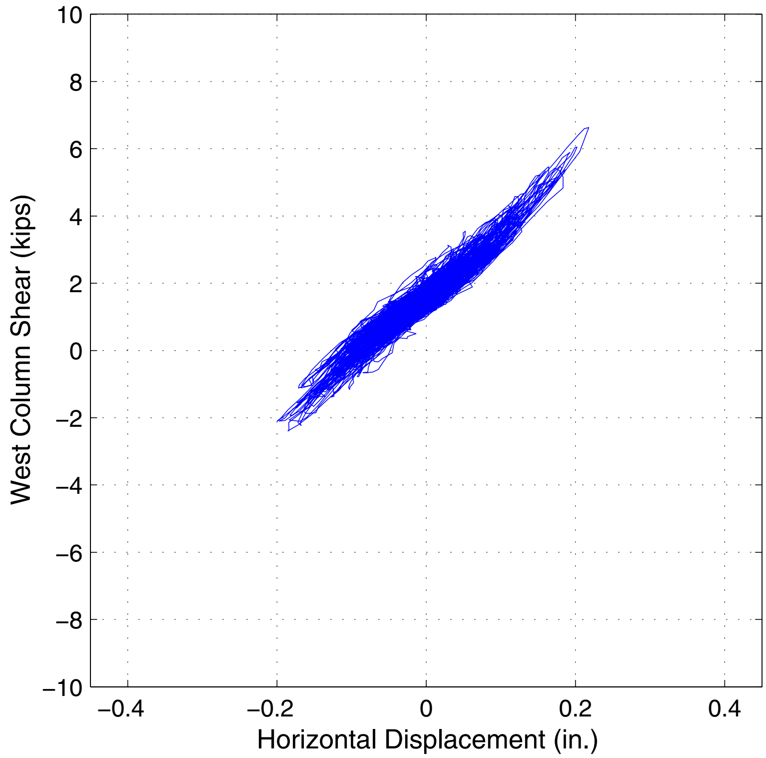

Figure C-15. Specimen 2 west column shear hysteretic response for low-level test

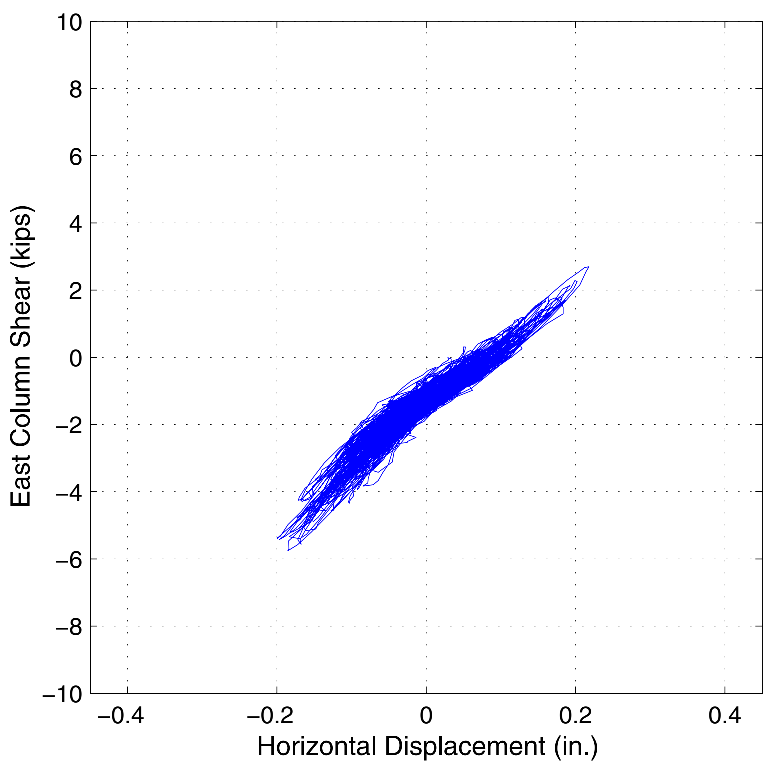

Figure C-16. Specimen 2 east column shear hysteretic response for low-level test

Appendix D: C++ Implementation of Limit State Failure Model

D.1 CLASS STRUCTURE FOR LIMIT STATE FAILURE MODEL

This section will describe the classes required for the new uniaxial material model described in Chapter 4, and their interaction with existing OpenSees classes. The new material model will be referred to as "LimitStateMaterial." Further information on OpenSees and object-oriented finite-element programing can be found in OpenSees (2002) and McKenna (1997).

The LimitStateMaterial class is a subclass of UniaxialMaterial, as shown in Figure D-1. It is based on the HystereticMaterial class and uses the same hysteretic rules (see Section D.4 for more information on HystereticMaterial). As described in Chapter 4, the LimitStateMaterial changes its backbone when the appropriate force-deformation response intersects the limit curve. Since the shape of this curve is different for the shear and axial failure models (see Figures 4-1 and 4-2), new classes AxialCurve and ShearCurve (used for the axial and shear-failure models, respectively) have been created to define the limit curve and determine when it is exceeded. A third subclass, ThreePointCurve, has also been created to define a general-purpose limit curve. These subclasses inherit from a new base class LimitCurve, which is aggregated with the LimitStateMaterial class (Figure D-1). If a LimitCurve is not aggregated with LimitStateMaterial, then the behavior of LimitStateMaterial is the same as HystereticMaterial.

Deformation measures such as chord rotations are known only by the Elements, and displacements are known only by the Nodes, in the OpenSees framework. Hence, the LimitCurve requires information from either the associated beam-column element or the associated nodes to determine when the limit curve is reached. To achieve this, the beam-column element class (e.g., BeamWithHinges) and the Node class are made component classes of each of the LimitCurve sub-

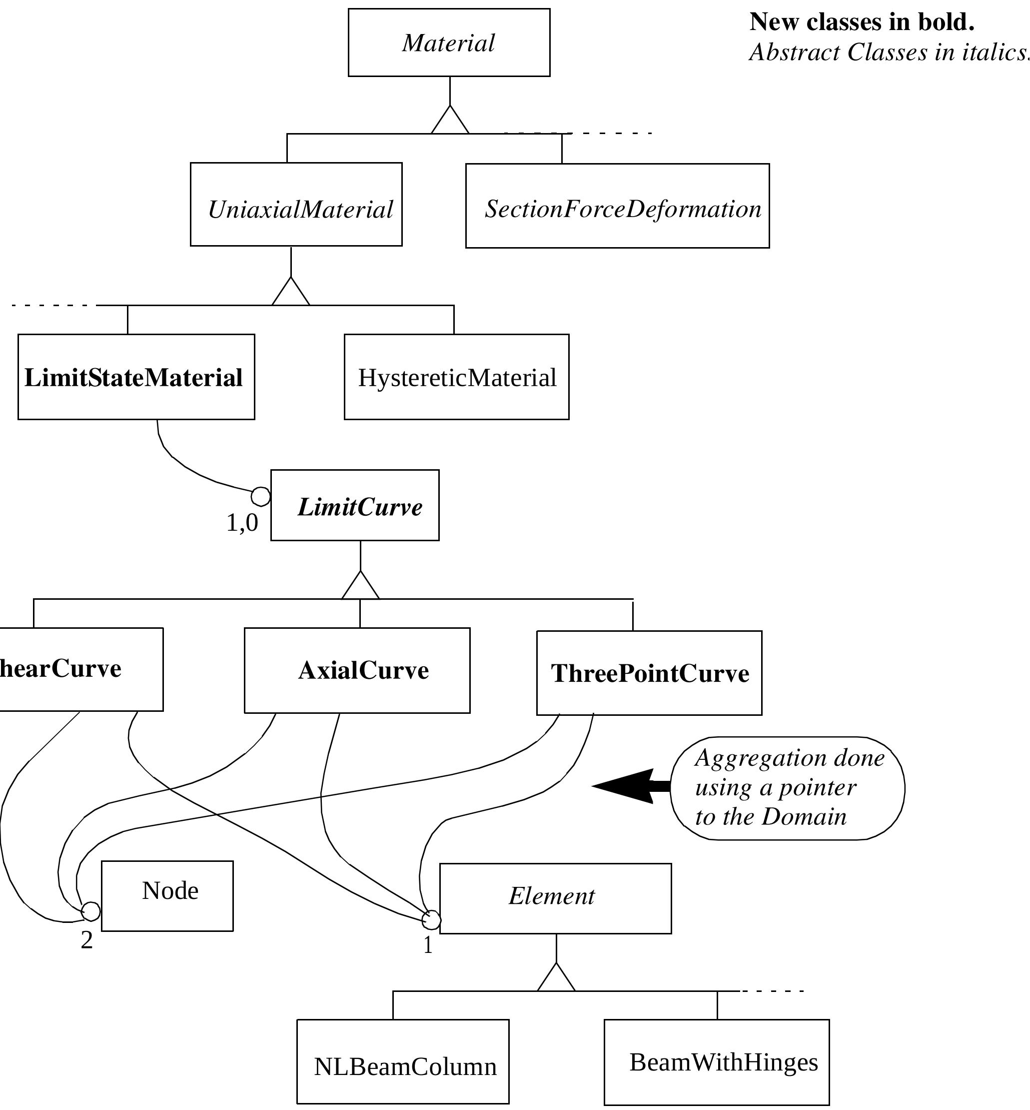

Figure D-1. Partial OpenSees Class Diagram including LimitStateMaterial and LimitCurve

classes, as shown by the "has-a" relationship in Figure D-1. Since the materials are created by the OpenSees ModelBuilder before the elements are created, it is necessary to form the aggregation between the LimitCurve subclasses and the element after the material class has been constructed. This is done by passing a pointer to the Domain into the LimitCurve subclass and then asking the Domain to provide a copy of the appropriate element to the LimitCurve. The aggregation between the nodes and the LimitCurve subclasses is done in a similar manner.

D.2 TCL INTERFACE FOR LIMIT STATE FAILURE MODEL

The scripting language Tcl is used to enter commands in OpenSees. The following section, describing the syntax of the new Tcl commands, can be used as a "User's Guide" for the limit state failure model in OpenSees.

The input command for LimitStateMaterial is given in Table D-1. All of the input variables except for the last two are the same as those for HystereticMaterial and are defined in Section D.4. The input command for AxialCurve is given in Table D-2. The limit curve is based on the axial failure model from Chapter 3:

$$\frac{\Delta}{L} = \frac{4}{100}\frac{1 + (\tan\theta)^2}{\tan\theta + \dfrac{P}{F_{sw}\tan\theta}} \tag{D.1}$$

where $\theta = 65°$ and P is the axial load in the associated beam-column element. The drift ratio, Δ/L, can be determined based on the displacements of nodes I and J or approximated by the maximum beam-column chord rotation. The input variable $delta can be used to shift the limit curve, as shown in Figure D-2, to evaluate the influence of variability in the position of the limit curve.

The input command for ShearCurve is given in Table D-3. Note that all input variables for the OpenSees model are assumed to be in kips and inches, except for the concrete compressive strength, f_c', which must be specified in psi. The limit curve is based on the empirical drift capacity model from Chapter 2:

$$\frac{\Delta}{L} = \frac{3}{100} + 4\rho'' - \frac{1}{500}\frac{V/(bd)}{\sqrt{f_c'}} - \frac{1}{40}\frac{P}{bhf_c'} \geq \frac{1}{100} \text{ (psi units)} \tag{D.2}$$

where P and V are the axial load and shear in the associated beam-column element, respectively. Similar to the AxialCurve, the drift ratio, Δ/L, can be determined based on the displacements of nodes I and J or approximated by the maximum beam-column chord rotation, and the input variable *$delta* can be used, as shown in Figure D-2, to shift the limit curve to evaluate the influence of variability in the position of the limit curve.

The input command for ThreePointCurve is given in Table D-4. Any failure model that can be reasonably approximated by the trilinear surface shown in Figure D-3, and does not depend on

Table D-1. OpenSees input command for LimitStateMaterial

Limit State Material

This command is used to construct a uniaxial hysteretic material object with pinching of force and deformation, damage due to ductility and energy, and degraded unloading stiffness based on ductility. Failure of the material is defined by the associated limit curve.

uniaxialMaterial LimitState $matTag $s1p $e1p $s2p $e2p $s3p $e3p $s1n $e1n $s2n $e2n $s3n $e3n $pinchX $pinchY $damage1 $damage2 $beta $curveTag $curveType.

$matTag		unique material object integer tag
$s1p	**$e1p**	stress and strain (or force & deformation) at first point of the envelope in the positive direction
$s2p	**$e2p**	stress and strain (or force & deformation) at second point of the envelope in the positive direction
$s3p	**$e3p**	stress and strain (or force & deformation) at third point of the envelope in the positive direction (optional)
$s1n	**$e1n**	stress and strain (or force & deformation) at first point of the envelope in the negative direction*
$s2n	**$e2n**	stress and strain (or force & deformation) at second point of the envelope in the negative direction*
$s3n	**$e3n**	stress and strain (or force & deformation) at third point of the envelope in the negative direction (optional)*
$pinchX		pinching factor for strain (or deformation) during reloading
$pinchY		pinching factor for stress (or force) during reloading
$damage1		damage due to ductility: $D_1(\mu-1)$
$damage2		damage due to energy: $D_2(E_i/E_{ult})$
$beta		power used to determine the degraded unloading stiffness based on ductility, $\mu^{-\beta}$ (optional, default=0.0)
$curveTag		an integer tag for the LimitCurve defining the limit surface
$curveType		an integer defining the type of LimitCurve (0 = no curve, 1 = axial curve, all other curves can be any other integer)

***NOTE:** negative backbone points should be entered as negative numeric values

Table D-2. OpenSees input command for AxialCurve

Axial Limit Curve

This command is used to construct an axial limit curve object that is used to define the point of axial failure for a LimitStateMaterial object. Point of axial failure based on model from Chapter 3. After axial failure response of LimitStateMaterial is forced to follow axial limit curve.

limitCurve Axial $curveTag $eleTag $Fsw $Kdeg $Fres $defType $forType <$ndI $ndJ $dof $perpDirn $delta>.

$curveTag	unique limit curve object integer tag
$eleTag	integer element tag for the associated beam-column element
$Fsw	floating point value describing the amount of transverse reinforcement ($F_{sw} = A_{st} f_{yt} d_c / s$)
$Kdeg	floating point value for the slope of the third branch in the post-failure backbone, assumed to be negative (see Figure 4-6)
$Fres	floating point value for the residual force capacity of the post-failure backbone (see Figure 4-6)
$defType	integer flag for type of deformation defining the abscissa of the limit curve 1 = maximum beam-column chord rotations 2 = drift based on displacment of nodes ndI and ndJ
$forType	integer flag for type of force defining the ordinate of the limit curve* 0 = force in associated limit state material 1 = shear in beam-column element 2 = axial load in beam-column element
$ndI	integer node tag for the first associated node (normally node I of $eleTag beam-column element)
$ndJ	integer node tag for the second associated node (normally node J of $eleTag beam-column element)
$dof	nodal degree of freedom to monitor for drift**
$perpDirn	perpendicular global direction from which length is determined to compute drift**
$delta	drift (floating point value) used to shift axial limit curve

NOTE: * Options 1 and 2 assume no member loads.
** 1 = X, 2 = Y, 3 = Z

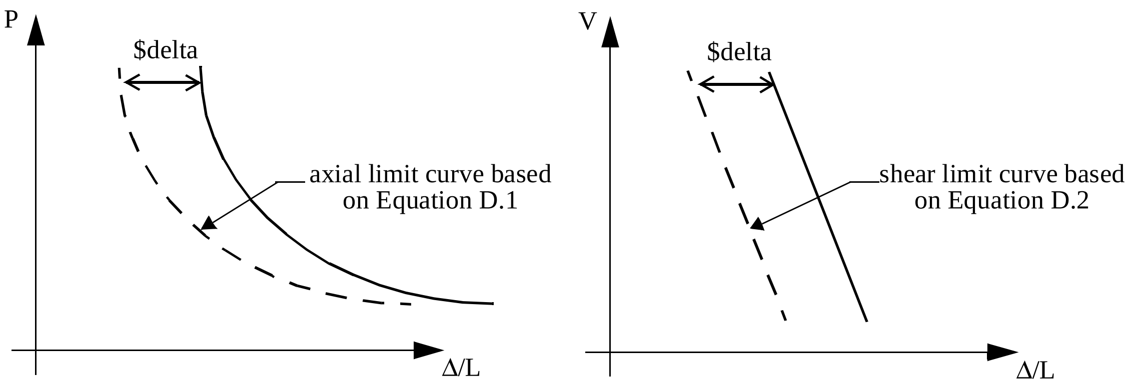

Figure D-2. Shifting of limit curve using $delta input variable

quantities which may vary during the analysis (such as beam-column shear or axial load), can be modeled using ThreePointCurve.

D.3 C++ CODE FOR LIMIT STATE FAILURE MODEL

This section describes select portions of the C++ implementation for the limit state failure model. The complete code can be found at *http://opensees.berkeley.edu*.

D.3.1 LimitStateMaterial

Upon convergence of each time step a material commits the current state of the history variables within `commitState`. The following code was added to `commitState` to check if the limit curve, defined by `theCurve`, had been exceeded in that time step.

```
// check element state if using limit curve option
// and not beyond residual capacity (CstateFlag == 4)
if (curveType != 0 && CstateFlag != 4)
{
        // Check state of element relative to the limit state surface.
        // Note that steps should be kept small to minimize error
        // caused by committed state being far beyond limit state surface
        int stateFlag = theCurve->checkElementState(Cstress);

        // If beyond limit state surface for first time,
        // get the new final slope and residual capacity
        // for this LimitState material
        if (stateFlag == 1)
        {
                // get backbone in current direction
                result += getNewBackbone(stateFlag);

                // if not an axial curve, cause failure in both directions
                if (curveType != 1)
                        result += mirrorBackbone();
        }
```

Table D-3. OpenSees input command for ShearCurve

Shear Limit Curve

This command is used to construct a shear limit curve object that is used to define the point of shear failure for a LimitStateMaterial object. Point of shear failure based on empirical drift capacity model from Chapter 2.

limitCurve Shear $curveTag $eleTag $rho $fc $b $h $d $Fsw $Kdeg $Fres $defType $forType <$ndI $ndJ $dof $perpDirn $delta>.

$curveTag	unique limit curve object integer tag
$eleTag	integer element tag for the associated beam-column element
$rho	transverse reinforcement ratio (A_{st}/bh)
$fc	concrete compressive strength (psi)
$b	column width (in.)
$h	full column depth (in.)
$d	effective column depth (in.)
$Fsw	floating point value describing the amount of transverse reinforcement ($F_{sw} = A_{st}f_{yt}d_c/s$)
$Kdeg	If positive: unloading stiffness of beam-column element (K_{unload} from Figure 4-8) if negative: slope of third branch of post-failure backbone (see Figure 4-6)
$Fres	floating point value for the residual force capacity of the post-failure backbone (see Figure 4-6)
$defType	integer flag for type of deformation defining the abscissa of the limit curve 1 = maximum beam-column chord rotations 2 = drift based on displacment of nodes ndI and ndJ
$forType	integer flag for type of force defining the ordinate of the limit curve 0 = force in associated limit state material 1 = shear in beam-column element
$ndI	integer node tag for the first associated node (normally node I of $eleTag beam-column element)
$ndJ	integer node tag for the second associated node (normally node J of $eleTag beam-column element)
$dof	nodal degree of freedom to monitor for drift
$perpDirn	perpendicular global direction from which length is determined to compute drift
$delta	drift (floating point value) used to shift shear limit curve

Table D-4. OpenSees input command for ThreePointCurve

Three-Point Limit Curve

This command is used to construct a three-point limit curve object that is used to define the point of failure for a LimitStateMaterial object.

limitCurve ThreePoint $curveTag $eleTag $x1 $y1 $x2 $y2 $x3 $y3 $Kdeg $Fres $defType $forType <$ndI $ndJ $dof $perpDirn>.

$curveTag	unique limit curve object integer tag
$eleTag	integer element tag for the associated beam-column element
$x1 $y1	coordinates for the first point on the limit curve (see Figure D-3)
$x2 $y2	coordinates for the second point on the limit curve (see Figure D-3)
$x3 $y3	coordinates for the third point on the limit curve (see Figure D-3)
$Kdeg	floating point value for the slope of the third branch in the post-failure backbone, assumed to be negative (see Figure 4-6)
$Fres	floating point value for the residual force capacity of the post-failure backbone (see Figure 4-6)
$defType	integer flag for type of deformation defining the abscissa of the limit curve 1 = maximum beam-column chord rotations 2 = drift based on displacment of nodes ndI and ndJ
$forType	integer flag for type of force defining the ordinate of the limit curve* 0 = force in associated limit state material 1 = shear in beam-column element 2 = axial load in beam-column element
$ndI	integer node tag for the first associated node (normally node I of $eleTag beam-column element)
$ndJ	integer node tag for the second associated node (normally node J of $eleTag beam-column element)
$dof	nodal degree of freedom to monitor for drift**
$perpDirn	perpendicular global direction from which length is determined to compute drift**

NOTE: * Option 1 assumes no member loads.
** 1 = X, 2 = Y, 3 = Z

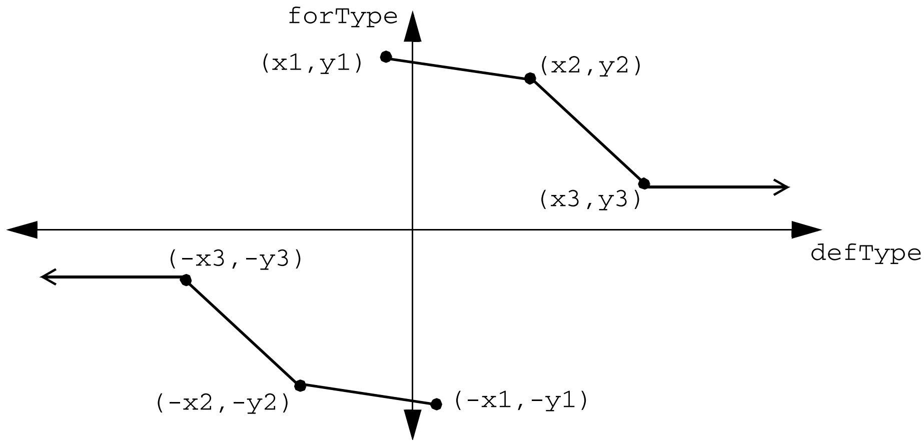

Figure D-3. Definition of limit curve for ThreePointCurve

First, the `checkElementState` function of the LimitCurve object, `theCurve`, is used to determine if the limit curve has been exceeded. This function returns an integer flag, `stateFlag`, indicating the current state of the material (0 = initial state before hitting curve for first time, 1 = limit curve reached for first time, 2 = on limit curve, 3 = off limit curve, 4 = at residual capacity). (Note that `stateFlag` = 1, 2, 3, and 4 are used to define the behavior of the material after axial failure, but are equivalent for the ShearCurve and ThreePointCurve). Then the post-failure backbone is defined in the direction of motion by the `getNewBackbone` function. For the shear-failure limit curve, the post-failure backbone is reflected in the opposite direction, since shear failure is assumed to reduce the capacity in both directions.

To define the behavior after axial failure (as described in Section 4.5.3), the following code is added to the `commitState` function:

```
// special functions for axial curve
if (curveType == 1) {

        // If on surface, get axial load lost
        if (stateFlag == 1 || stateFlag == 2 || stateFlag == 4) {
                Ploss += theCurve->getUnbalanceForce();
        }
        // if moving off surface, get new backbone with 1/100elastic 3rd slope
        if (CstateFlag == 2 || CstateFlag == 1) {
                if (stateFlag == 3) {
                        result += getNewBackbone(stateFlag);
                }
        }
        // if moving onto surface then get new backbone with degrading slope
        if (CstateFlag == 3) {
                if (stateFlag == 2) {
                        result += getNewBackbone(stateFlag);
                }
        }
        // if forceSurface governed by residual capacity set new flat backbone
        // do not allow backbone to be changed again.
```

```
			if (stateFlag == 4) {
				result += getNewBackbone(stateFlag);
			}
		}
		// commit the current state if needed outside commitState
		CstateFlag = stateFlag;
}
```

The `getUnbalanceForce` function from AxialCurve provides the axial load required to return the material to the limit curve at the same displacement. This force, `Ploss`, is used to determine the stress and strain in the material for the next time step. The `getNewBackbone` function is used twice to redefine the post-failure backbone such that the material responds with a stiffness equivalent to 1/100 times the elastic stiffness when it is off the limit curve and to restore the degrading slope when the response returns the material to the limit curve. Once the axial capacity has degraded down to the residual capacity, the column is assumed to have lost a significant amount of core concrete, and, hence can no longer sustain axial loads above the residual capacity. To achieve this the backbone is redefined with a flat slope at the residual capacity, and the `CstateFlag` variable is set to 4 to ensure that the backbone is not redefined in future load steps.

All uniaxial materials must provide the functions `getStrain`, `getStress`, and `getTangent` in order for the elements to determine the current state of the materials. In LimitStateMaterial these functions must be adapted as shown below to account for the behavior of the material after axial failure.

```
double
LimitStateMaterial::getStrain(void)
{
	// Return trail strain plus strain due to loss of axial load.
	// Ploss will be zero if no axial failure or not using AxialCurve.
	// Ploss is always positive.
	// E3 set to any number if not using limit curve,
	// otherwise should be negative for axial curve.
	double strain;
	double E3;

	if (curveType != 0)
		E3 = theCurve->getDegSlope();
	else
		E3 = 1.0;

	if (Tstrain < 0.0)
		strain = Tstrain + Ploss/E3;
	else
		strain = Tstrain - Ploss/E3;

	return strain;
}

double
LimitStateMaterial::getStress(void)
{
	// Return trail stress minus the loss of axial load.
```

```
	// Ploss will be zero if no axial failure or not using AxialCurve.
	// Ploss is always positive.
	// For axial failure Tstress is negative in compression
	double stress;

	stress = Tstress + Ploss;

	return stress;
}

double
LimitStateMaterial::getTangent(void)
{
	// If on the limit state surface use degrading slope,
	// but if beyond third corner point use approx zero slope (axial curve only)
	if (curveType == 1)
	{
		double E3 = theCurve->getDegSlope();

		if (CstateFlag == 1 || CstateFlag == 2) {
			if (Tstrain > 0.0) {
				if (Tstrain > rot3p) {
					Ttangent = E1p*1.0e-9;
				} else {
					Ttangent = E3p;
				}
			} else {
				if (Tstrain < rot3n) {
					Ttangent = E1p*1.0e-9;
				} else {
					Ttangent = E3n;
				}
			}
		}
	}
	return Ttangent;
}
```

The trial strain, stress, and tangent variables (`Tstrain`, `Tstress`, and `Ttangent`) are determined by the hysteretic rules of HystereticMaterial. The trial strain and stress are modified using `Ploss` to account for any unbalance forces needed to return the response of the material to the limit curve. To ensure that a loss of axial load is accompanied by an increase in vertical displacements, the trial tangent is set equal to the degrading slope (or zero slope if degraded to residual capacity) if the response of the LimitStateMaterial is on the axial limit curve.

For an axial limit state material, `Ploss` is defined when a load step is committed. Hence, when the `getStress` or `getStrain` functions are called by the recorder before the start of the next step, the stress or strain provided by the LimitStateMaterial will include the effect of `Ploss`. Since `Ploss` is not, in fact, applied to the material until the next load step, the stress and strain from the recorder will be in error. This problem can be averted by recording the axial force in the beam-column element and the node displacements.

D.3.2 ShearCurve

The `checkElementState` function is used by the LimitStateMaterial to determine if the beam-column element response has exceeded the limit curve. The following section of code finds the beam-column element that is associated with this instantiation of LimitCurve:

```
// check if limit state surface has been reached
int
ShearCurve::checkElementState(double springForce)
{
	// find associated beam-column element on first visit
	if (theElement == 0)
	{
		theElement = theDomain->getElement(eleTag);

		if (theElement == 0)
			g3ErrorHandler->fatal("WARNING ShearCurve -
				no element with tag %i exists in Domain",eleTag);
// find length between nodes if drift is desired
		if (defType == 2)
		{
			Node *nodeI = theDomain->getNode(ndI);
			Node *nodeJ = theDomain->getNode(ndJ);

			const Vector &crdI = nodeI->getCrds();
			const Vector &crdJ = nodeJ->getCrds();

			oneOverL = 1.0/fabs(crdJ(perpDirn) - crdI(perpDirn));
		}
	}
```

If a copy of the beam-column element is not yet available (i.e., the first time `checkElementState` is called), the Domain is asked the make a copy of the element with the user-provided element tag `eleTag`. A fatal error is displayed if a copy cannot be created. This procedure was done outside the constructor because OpenSees creates the material objects before the element objects. If the abscissa of the limit curve is defined by interstory drift (`defType` = 2), then the Domain is also asked to make a copy of the nodes with the user-provided node tags `ndI` and `ndJ`. The height of the beam-column element is determined by finding the coordinates of the nodes and finding the projection of the element along the axis defined by `perpDirn`.

The `checkElementState` function continues to determine if the beam-column response has exceeded the limit curve:

```
if (defType == 1) // maximum chord rotations for x-axis of limit curve
{
	Response *theRotations =0; // integer element returns in setResponse
	char *r[1] = {"basicDeformations"}; // must be implemented in element
	Information*rotInfoObject =0;
	Vector *rotVec; //vector of chord rotations at beam-column ends

	// set type of beam-column element response desired
	theRotations = theElement->setResponse(r, 1, *rotInfoObject);
```

```
		// put element response in the vector of "myInfo"
		result = theRotations->getResponse();

		// access the myInfo vector containing the response (new for Version 1.2)
		rotVec = (theRotations->myInfo.theVector);

		//use larger of two end rotations
		deform = (fabs((*rotVec)(1)) > fabs((*rotVec)(2))) ?
				fabs((*rotVec)(1)) : fabs((*rotVec)(2));
}
else if (defType == 2) // interstory drift for x-axis of limit curve
{
		// find associated nodes
		Node *nodeI = theDomain->getNode(ndI);
		Node *nodeJ = theDomain->getNode(ndJ);

		// get displacements
		const Vector &dispI = nodeI->getTrialDisp();
		const Vector &dispJ = nodeJ->getTrialDisp();

		// calc drift
		double dx = fabs(dispJ(dof)-dispI(dof));
		deform = dx*oneOverL;
}
else {
		g3ErrorHandler->fatal("Deformation type flag %i not implemented",defType);
}
// get beam-column local forces
Response *theForces =0;
char *f[1] = {"localForce"}; // does not include influence of P-delta
							// for P-delta use forType = 0
Information*forInfoObject =0;
Vector *forceVec; //vector of basic forces from beam column

// set type of beam-column element response desired
theForces = theElement->setResponse(f, 1, *forInfoObject);

// put element response in the vector of "myInfo"
result += theForces->getResponse();

// access the myInfo vector containing the response (new for Version 1.2)
forceVec = (theForces->myInfo.theVector);

// Force for y-axis of limit curve
if (forType == 0)
		force = fabs(springForce);	// force in associated LimitState material
else if (forType == 1)
		force = fabs((*forceVec)(1)); // shear
else if (forType == 2)
		force = fabs((*forceVec)(0)); // axial
else {
		g3ErrorHandler->fatal("Force type flag %i not implemented",forType);
}
// axial load at shear failure
P = fabs((*forceVec)(0));

// Determine if (deform,force) is outside limit state surface.
//
// Use absolute value of deform and force
double forceSurface = findLimit(deform); // force on surface at deform

if (stateFlag == 0) //prior to failure
{
		if (force >= forceSurface) // on/outside failure surface
		{
```

```
				stateFlag = 1;
				//set degrading slope based on drift at axial failure
				setDegSlope(force, deform);
			}
			else // inside failure surface
			{
				stateFlag = 0;
			}
		}
		else //after failure
		{
			if (force >= forceSurface) // on/outside failure surface
			{
				stateFlag = 2;
			}
			else // inside failure surface
			{
				stateFlag = 3;
			}
		}
		return stateFlag;
}
```

The strings “basicDeformations” and “localForce” are passed to the `setResponse` function for `theElement` to let the element know which response quantities are requested. The `getResponse` functions are used to place the response quantities selected by `setResponse` in a vector of `myInfo`, a public object defined for each `Response` object. Finally, the vector of selected response quantities are obtained from `myInfo.theVector` for each `Response` object.

The `defType` and `forType` flags are used to determine which response quantities define the limit surface space. Element chord rotations (`defType` = 1) or interstory drift (`defType` = 2) can be selected as deformations. The force in the associated LimitStateMaterial (`forType` = 0), the column shear (`forType` = 1), or column axial load (`forType` = 2) can be used as forces. For the ShearCurve, it assumed that `forType` is equal to 0 or 1.

The `findLimit` function, shown below, is used to determine the force on the limit surface at the deformation `deform`. The limit surface is defined by the empirical drift capacity model from Chapter 2. The drift capacity model requires all input variables for the OpenSees model to be specified in kips and inches, with the exception of the concrete compressive strength which must be given in psi.

```
double
ShearCurve::findLimit(double DR)
{
		double V = 0.0; //Shear in kips!!

		if (DR < 0.01)
			V = 9.9e9; //no shear failure below drift ratio of 1%
		else
			V = 500*(0.03+delta+4*rho-DR-0.025*P/b/h/(fc/1000))*(b*d*sqrt(fc)/1000);
```

```
        if (V < 0.0)
                V = 0.0;

        return V;
}
```

Based on the force returned by `findLimit` to `checkElementState`, an if-statement is used to set the `stateFlag` variable indicating whether or not the limit surface has been exceeded. For ShearCurve, only the first change of state results in any change in behavior (i.e., when failure is detected and `stateFlag` changes from 0 to 1 resulting in the redefinition of the backbone by LimitStateMaterial). When failure is detected, the degrading slope of the new backbone is determined by the `setDegSlope` function shown below.

```
void
ShearCurve::setDegSlope(double V, double Dshear)
{
        if (Kdeg > 0.0)
        {
                // Calculate degrading slope based on point of shear failure and
                // calculated deformation at axial failure based on current axial
                // load and axial failure model by Elwood (2002).
                // If positive, Kdeg is assumed equal to the flexural stiffness

                double theta = 65.0*PI/180.0;
                double Daxial;

                Daxial = 0.04*(1+tan(theta)*tan(theta))/(tan(theta)+P/Fsw/tan(theta));

                if (defType == 2)
                {
                        double K = -V/(Daxial-Dshear)*oneOverL;
                        Kdeg = 1/(1/K - 1/Kdeg);
                }
                else
                        g3ErrorHandler->fatal("Must use defType = 2 for calculated Kdeg");
        }
}
```

If the user-specified `Kdeg` is positive, the setDegSlope function is used to determine the degrading slope of the new backbone based on the axial failure model from Chapter 3. The specified value for `Kdeg` is assumed to be equal to the unloading stiffness of the flexural component. If the user-specified `Kdeg` is negative, the setDegSlope function does nothing and `Kdeg` is left unchanged.

D.3.3 AxialCurve

The `checkElementState` function for AxialCurve is the same as that for ThreePointCurve except that if the response of the material is beyond the limit curve, then the unbalance force to return the response of the material to the limit curve is calculated as follows:

```
dP = force - forceSurface
```

Also note that the AxialCurve does not take the absolute value of the `force` variable, since failure occurs only in compression. The `checkElementState` function assumes that the `force` variable will be positive for compression (valid if using `forType` = 2 and a vertical column element).

The `findLimit` function shown below is based on the axial failure model developed in Chapter 3. The function defining the limit curve requires only the constant `Fsw`, describing the amount of transverse reinforcement. An optional variable, `delta,` may also be specified to shift the limit curve to higher or lower drift values.

```
double
AxialCurve::findLimit(double x)
{
	double y = 0.0;

	if (x < 0 || x > 0.08)
		g3ErrorHandler->warning("Warning: Outside limits of AxialCurve");

	double theta = 65.0*PI/180.0;
	double d = x-delta;

	if (d <= 0.0)
		d = 1.0e-9;

	// positive for compression
	y = ((1+tan(theta)*tan(theta))/(25*d)-tan(theta))*Fsw*tan(theta);

	//Do not allow axial load to be reduced below residual capacity (may be zero)
	//Input as positive
	if (y < Fres) {
		y = Fres;
	}
	return y;
}
```

D.4 HYSTERETIC UNIAXIAL MATERIAL

This section describes the Hysteretic uniaxial material available in OpenSees to model a piece-wise linear constitutive relationship including strength degradation, stiffness degradation, and pinching. The LimitState uniaxial material described in this chapter, and used to define the response of the shear and axial failure springs described in Chapters 4 and 8, was developed based on Hysteretic material. The Hysteretic material model in OpenSees was developed based on a similar material model implemented in the finite-element library FEDEAS (Filippou and Spacone, 1996).

The input command for Hysteretic material is given in Table D-5. The backbone parameters are defined in Figure D-4. The pinching parameters are defined in Figure D-5. The unloading stiffness parameter is defined in Figure D-6. The damage parameters are not used in the study described in this report. Given $p_x = 1.0$, $p_y = 1.0$, $\beta = 0.0$, $D_1 = 0.0$, $D_2 = 0.0$ (i.e., no effect from damage parameters), Hysteretic material will obey Clough-type hysteretic laws (Clough, 1966).

Figure D-7 illustrates the response of Hysteretic material for the parameters used for the center column shear spring model described in Chapter 8 (i.e., $p_x = 0.5$, $p_y = 0.4$, $\beta = 0.4$, $D_1 = 0.0$, $D_2 = 0.0$).

Table D-5. OpenSees input command for Hysteretic uniaxial material (OpenSees, 2002)

Hysteretic Material

This command is used to construct a uniaxial hysteretic material object with pinching of force and deformation, damage due to ductility and energy, and degraded unloading stiffness based on ductility.

uniaxialMaterial Hysteretic $matTag $s1p $e1p $s2p $e2p <$s3p $e3p> $s1n $e1n $s2n $e2n <$s3n $e3n> $pinchX $pinchY $damage1 $damage2 <$beta>.

$matTag		unique material object integer tag
$s1p	**$e1p**	stress and strain (or force & deformation) at first point of the envelope in the positive direction
$s2p	**$e2p**	stress and strain (or force & deformation) at second point of the envelope in the positive direction
$s3p	**$e3p**	stress and strain (or force & deformation) at third point of the envelope in the positive direction (optional)
$s1n	**$e1n**	stress and strain (or force & deformation) at first point of the envelope in the negative direction*
$s2n	**$e2n**	stress and strain (or force & deformation) at second point of the envelope in the negative direction*
$s3n	**$e3n**	stress and strain (or force & deformation) at third point of the envelope in the negative direction (optional)*
$pinchX		pinching factor for strain (or deformation) during reloading
$pinchY		pinching factor for stress (or force) during reloading
$damage1		damage due to ductility: $D_1(\mu-1)$
$damage2		damage due to energy: $D_2(E_i/E_{ult})$
$beta		power used to determine the degraded unloading stiffness based on ductility, $\mu^{-\beta}$ (optional, default=0.0)

***NOTE:** negative backbone points should be entered as negative numeric values

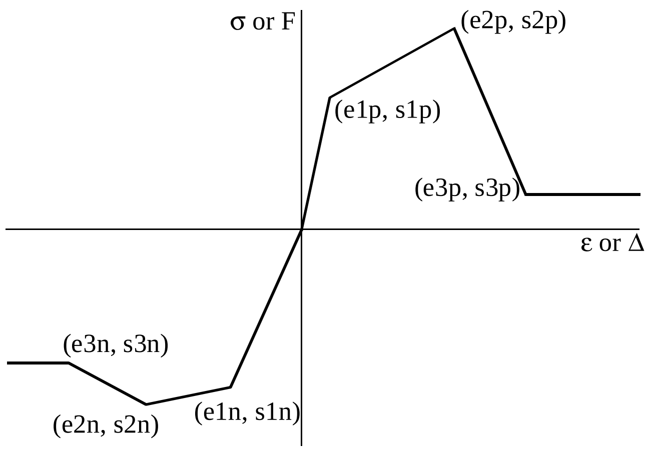

Figure D-4. Definition of backbone parameters for Hysteretic material

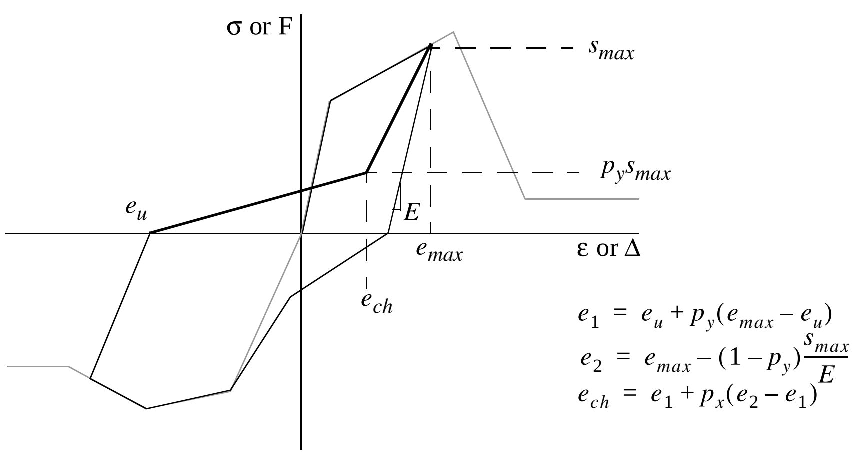

Figure D-5. Definition of pinching parameters for Hysteretic material (adapted from Scott, 2003)

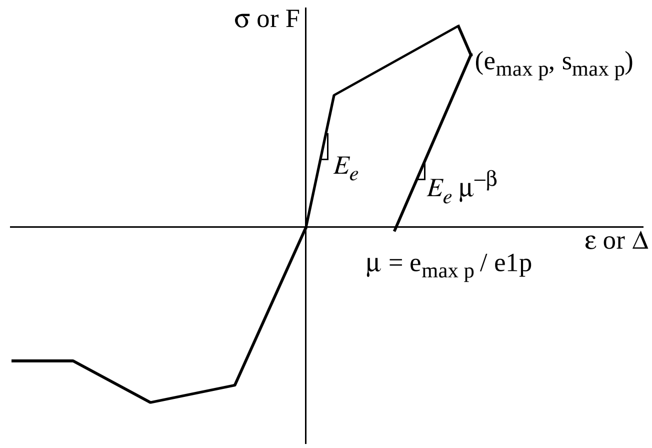

Figure D-6. Definition of unloading parameter for Hysteretic material

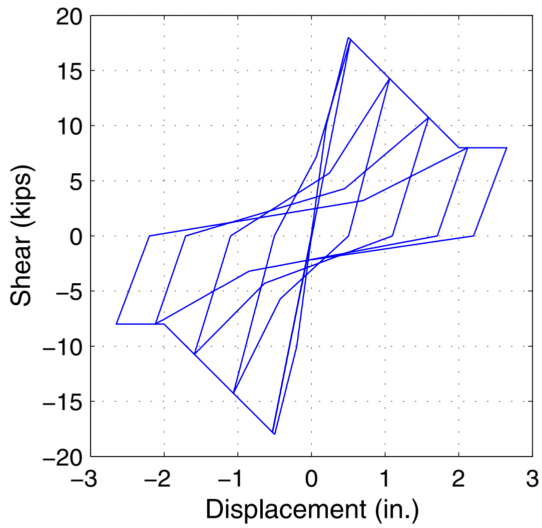

Figure D-7. Example of Hysteretic material response with pinching and unloading stiffness degradation parameters (p_x = 0.5, p_y = 0.4, β = 0.4, D_1 = 0.0, D_2 = 0.0)

Appendix E: Videos from Shear-Failure Shake Table Tests

The attached compact disk contains processed videos from the shear-failure shake table tests described in Chapter 6. The videos are approximately synchronized with data plots, allowing for comparison of the damage states of the specimens with measured response quantities. The synchronization was achieved by aligning an audio signal from the shake table operator with the start of the recorded data. Synchronization was further improved by matching the observed peaks in displacement with the significant peaks in the recorded data.

The videos are provided in two formats: AVI and MPEG. The AVI files provide higher quality images but require significantly more disk space. The contents of each file is described in Table E-1.

Table E-1. Description of video files

Filename	*File Type*	*Description*
Spec1_25fps	AVI, MPEG	Shear hysteretic response using relative displacements for Specimen 1 (Figure 6-15) synchronized with: Video of full frame (total displacements) Video of center column (relative displacements) Video of top of center column (total displacements)
Spec2_25fps	AVI, MPEG	Shear hysteretic response using relative displacements for Specimen 2 (Figure 6-16) synchronized with: Video of full frame (total displacements) Video of center column (relative displacements) Video of top of center column (total displacements)
Spec2_axial	AVI, MPEG	Relations from Figure 6-19 using relative displacements for Specimen 2 synchronized with: Video of top of center column (total displacements)
axial_compare	AVI, MPEG	Center column axial load histories from Figure 6-14 synchronized with: Video of top of center column (Specimen 1) Video of top of center column (Specimen 2)
fullcolumn_splitscreen	AVI	Videos of center column from both specimens synchronized.
dataPlots	HTML	Comparison of lateral drift response (Figure 6-5) with state of center columns at 0.0, 16.7, 24.9, 29.8, 70.0 seconds. Roll mouse over symbols to see changes to center column.

PEER REPORTS

PEER reports are available from the National Information Service for Earthquake Engineering (NISEE). To order PEER reports, please contact the Pacific Earthquake Engineering Research Center, 1301 South 46th Street, Richmond, California 94804-4698. Tel.: (510) 231-9468; Fax: (510) 231-9461.

PEER 2003/06 *Performance of Circular Reinforced Concrete Bridge Columns under Bidirectional Earthquake Loading.* Mahmoud M. Hachem, Stephen A. Mahin, and Jack P. Moehle. February 2003

.

PEER 2003/05 *Response Assessment of Nonstructural Building Elements*. Shahram Taghavi and Eduardo Miranda. September 2003.

PEER 2003/03 *Probabilistic Response Assessment for Building-Specific Loss Estimation.* Eduardo Miranda and Hesameddin Aslani. September 2003.

PEER 2003/02 *Software Framework for Collaborative Development of Nonlinear Dynamic Analysis Program.* Jun Peng and Kincho H. Law. September 2003.

PEER 2003/01 *Shake Table Tests and Analytical Studies on the Gravity Load Collapse of Reinforced Concrete Frames.* Kenneth John Elwood and Jack P. Moehle. November 2003.

PEER 2002/24 *Performance of Beam to Column Bridge Joints Subjected to a Large Velocity Pulse.* Natalie Gibson, André Filiatrault, and Scott A. Ashford. April 2002.

PEER 2002/23 *Effects of Large Velocity Pulses on Reinforced Concrete Bridge Columns.* Greg L. Orozco and Scott A. Ashford. April 2002.

PEER 2002/22 *Characterization of Large Velocity Pulses for Laboratory Testing.* Kenneth E. Cox and Scott A. Ashford. April 2002.

PEER 2002/21 *Fourth U.S.-Japan Workshop on Performance-Based Earthquake Engineering Methodology for Reinforced Concrete Building Structures*. December 2002.

PEER 2002/20 *Barriers to Adoption and Implementation of PBEE Innovations.* Peter J. May. August 2002.

PEER 2002/19 *Economic-Engineered Integrated Models for Earthquakes: Socioeconomic Impacts.* Peter Gordon, James E. Moore II, and Harry W. Richardson. July 2002.

PEER 2002/18 *Assessment of Reinforced Concrete Building Exterior Joints with Substandard Details.* Chris P. Pantelides, Jon Hansen, Justin Nadauld, and Lawrence D. Reaveley. May 2002.

PEER 2002/17 *Structural Characterization and Seismic Response Analysis of a Highway Overcrossing Equipped with Elastomeric Bearings and Fluid Dampers: A Case Study.* Nicos Makris and Jian Zhang. November 2002.

PEER 2002/16 *Estimation of Uncertainty in Geotechnical Properties for Performance-Based Earthquake Engineering.* Allen L. Jones, Steven L. Kramer, and Pedro Arduino. December 2002.

PEER 2002/15 *Seismic Behavior of Bridge Columns Subjected to Various Loading Patterns.* Asadollah Esmaeily-Gh. and Yan Xiao. December 2002.

PEER 2002/14 *Inelastic Seismic Response of Extended Pile Shaft Supported Bridge Structures.* T.C. Hutchinson, R.W. Boulanger, Y.H. Chai, and I.M. Idriss. December 2002.

PEER 2002/13 *Probabilistic Models and Fragility Estimates for Bridge Components and Systems.* Paolo Gardoni, Armen Der Kiureghian, and Khalid M. Mosalam. June 2002.

PEER 2002/12 *Effects of Fault Dip and Slip Rake on Near-Source Ground Motions: Why Chi-Chi Was a Relatively Mild M7.6 Earthquake.* Brad T. Aagaard, John F. Hall, and Thomas H. Heaton. December 2002.

PEER 2002/11 *Analytical and Experimental Study of Fiber-Reinforced Strip Isolators*. James M. Kelly and Shakhzod M. Takhirov. September 2002.

PEER 2002/10 *Centrifuge Modeling of Settlement and Lateral Spreading with Comparisons to Numerical Analyses***.** Sivapalan Gajan and Bruce L. Kutter. January 2003.

PEER 2002/09 *Documentation and Analysis of Field Case Histories of Seismic Compression during the 1994 Northridge, California, Earthquake.* Jonathan P. Stewart, Patrick M. Smith, Daniel H. Whang, and Jonathan D. Bray. October 2002.

PEER 2002/08 *Component Testing, Stability Analysis and Characterization of Buckling-Restrained Unbonded Braces™.* Cameron Black, Nicos Makris, and Ian Aiken. September 2002.

PEER 2002/07 *Seismic Performance of Pile-Wharf Connections.* Charles W. Roeder, Robert Graff, Jennifer Soderstrom, and Jun Han Yoo. December 2001.

PEER 2002/06 *The Use of Benefit-Cost Analysis for Evaluation of Performance-Based Earthquake Engineering Decisions*. Richard O. Zerbe and Anthony Falit-Baiamonte. September 2001.

PEER 2002/05 *Guidelines, Specifications, and Seismic Performance Characterization of Nonstructural Building Components and Equipment*. André Filiatrault, Constantin Christopoulos, and Christopher Stearns. September 2001.

PEER 2002/04 *Consortium of Organizations for Strong-Motion Observation Systems and the Pacific Earthquake Engineering Research Center Lifelines Program: Invited Workshop on Archiving and Web Dissemination of Geotechnical Data, 4–5 October 2001*. September 2002.

PEER 2002/03 *Investigation of Sensitivity of Building Loss Estimates to Major Uncertain Variables for the Van Nuys Testbed.* Keith A. Porter, James L. Beck, and Rustem V. Shaikhutdinov. August 2002.

PEER 2002/02 *The Third U.S.-Japan Workshop on Performance-Based Earthquake Engineering Methodology for Reinforced Concrete Building Structures*. July 2002.

PEER 2002/01 *Nonstructural Loss Estimation: The UC Berkeley Case Study. Mary C. Comerio and John C. Stallmeyer.* December 2001.

PEER 2001/16 *Statistics of SDF-System Estimate of Roof Displacement for Pushover Analysis of Buildings.* Anil K. Chopra, Rakesh K. Goel, and Chatpan Chintanapakdee. December 2001.

PEER 2001/15 *Damage to Bridges during the 2001 Nisqually Earthquake.* R. Tyler Ranf, Marc O. Eberhard, and Michael P. Berry. November 2001.

PEER 2001/14 *Rocking Response of Equipment Anchored to a Base Foundation.* Nicos Makris and Cameron J. Black. September 2001.

PEER 2001/13 *Modeling Soil Liquefaction Hazards for Performance-Based Earthquake Engineering.* Steven L. Kramer and Ahmed-W. Elgamal. February 2001.

PEER 2001/12 *Development of Geotechnical Capabilities in OpenSees.* Boris Jeremic. September 2001.

PEER 2001/11 *Analytical and Experimental Study of Fiber-Reinforced Elastomeric Isolators*. James M. Kelly and Shakhzod M. Takhirov. September 2001.

PEER 2001/10 *Amplification Factors for Spectral Acceleration in Active Regions.* Jonathan P. Stewart, Andrew H. Liu, Yoojoong Choi, and Mehmet B. Baturay. December 2001.

PEER 2001/09 *Ground Motion Evaluation Procedures for Performance-Based Design.* Jonathan P. Stewart, Shyh-Jeng Chiou, Jonathan D. Bray, Robert W. Graves, Paul G. Somerville, and Norman A. Abrahamson. September 2001.

PEER 2001/08 *Experimental and Computational Evaluation of Reinforced Concrete Bridge Beam-Column Connections for Seismic Performance*. Clay J. Naito, Jack P. Moehle, and Khalid M. Mosalam. November 2001.

PEER 2001/07 *The Rocking Spectrum and the Shortcomings of Design Guidelines.* Nicos Makris and Dimitrios Konstantinidis. August 2001.

PEER 2001/06 *Development of an Electrical Substation Equipment Performance Database for Evaluation of Equipment Fragilities*. Thalia Agnanos. April 1999.

PEER 2001/05 *Stiffness Analysis of Fiber-Reinforced Elastomeric Isolators.* Hsiang-Chuan Tsai and James M. Kelly. May 2001.

PEER 2001/04 *Organizational and Societal Considerations for Performance-Based Earthquake Engineering.* Peter J. May. April 2001.

PEER 2001/03 *A Modal Pushover Analysis Procedure to Estimate Seismic Demands for Buildings: Theory and Preliminary Evaluation.* Anil K. Chopra and Rakesh K. Goel. January 2001.

PEER 2001/02 *Seismic Response Analysis of Highway Overcrossings Including Soil-Structure Interaction.* Jian Zhang and Nicos Makris. March 2001.

PEER 2001/01 *Experimental Study of Large Seismic Steel Beam-to-Column Connections.* Egor P. Popov and Shakhzod M. Takhirov. November 2000.

PEER 2000/10 *The Second U.S.-Japan Workshop on Performance-Based Earthquake Engineering Methodology for Reinforced Concrete Building Structures.* March 2000.

PEER 2000/09 *Structural Engineering Reconnaissance of the August 17, 1999 Earthquake: Kocaeli (Izmit), Turkey.* Halil Sezen, Kenneth J. Elwood, Andrew S. Whittaker, Khalid Mosalam, John J. Wallace, and John F. Stanton. December 2000.

PEER 2000/08 *Behavior of Reinforced Concrete Bridge Columns Having Varying Aspect Ratios and Varying Lengths of Confinement.* Anthony J. Calderone, Dawn E. Lehman, and Jack P. Moehle. January 2001.

PEER 2000/07 *Cover-Plate and Flange-Plate Reinforced Steel Moment-Resisting Connections.* Taejin Kim, Andrew S. Whittaker, Amir S. Gilani, Vitelmo V. Bertero, and Shakhzod M. Takhirov. September 2000.

PEER 2000/06 *Seismic Evaluation and Analysis of 230-kV Disconnect Switches.* Amir S. J. Gilani, Andrew S. Whittaker, Gregory L. Fenves, Chun-Hao Chen, Henry Ho, and Eric Fujisaki. July 2000.

PEER 2000/05 *Performance-Based Evaluation of Exterior Reinforced Concrete Building Joints for Seismic Excitation.* Chandra Clyde, Chris P. Pantelides, and Lawrence D. Reaveley. July 2000.

PEER 2000/04 *An Evaluation of Seismic Energy Demand: An Attenuation Approach.* Chung-Che Chou and Chia-Ming Uang. July 1999.

PEER 2000/03 *Framing Earthquake Retrofitting Decisions: The Case of Hillside Homes in Los Angeles.* Detlof von Winterfeldt, Nels Roselund, and Alicia Kitsuse. March 2000.

PEER 2000/02 *U.S.-Japan Workshop on the Effects of Near-Field Earthquake Shaking.* Andrew Whittaker, ed. July 2000.

PEER 2000/01 *Further Studies on Seismic Interaction in Interconnected Electrical Substation Equipment.* Armen Der Kiureghian, Kee-Jeung Hong, and Jerome L. Sackman. November 1999.

PEER 1999/14 *Seismic Evaluation and Retrofit of 230-kV Porcelain Transformer Bushings*. Amir S. Gilani, Andrew S. Whittaker, Gregory L. Fenves, and Eric Fujisaki. December 1999.

PEER 1999/13 *Building Vulnerability Studies: Modeling and Evaluation of Tilt-up and Steel Reinforced Concrete Buildings.* John W. Wallace, Jonathan P. Stewart, and Andrew S. Whittaker, editors. December 1999.

PEER 1999/12 *Rehabilitation of Nonductile RC Frame Building Using Encasement Plates and Energy-Dissipating Devices.* Mehrdad Sasani, Vitelmo V. Bertero, James C. Anderson. December 1999.

PEER 1999/11 *Performance Evaluation Database for Concrete Bridge Components and Systems under Simulated Seismic Loads.* Yael D. Hose and Frieder Seible. November 1999.

PEER 1999/10 *U.S.-Japan Workshop on Performance-Based Earthquake Engineering Methodology for Reinforced Concrete Building Structures.* December 1999.

PEER 1999/09 *Performance Improvement of Long Period Building Structures Subjected to Severe Pulse-Type Ground Motions*. James C. Anderson, Vitelmo V. Bertero, and Raul Bertero. October 1999.

PEER 1999/08 *Envelopes for Seismic Response Vectors.* Charles Menun and Armen Der Kiureghian. July 1999.

PEER 1999/07 *Documentation of Strengths and Weaknesses of Current Computer Analysis Methods for Seismic Performance of Reinforced Concrete Members.* William F. Cofer. November 1999.

PEER 1999/06 *Rocking Response and Overturning of Anchored Equipment under Seismic Excitations.* Nicos Makris and Jian Zhang. November 1999.

PEER 1999/05 *Seismic Evaluation of 550 kV Porcelain Transformer Bushings.* Amir S. Gilani, Andrew S. Whittaker, Gregory L. Fenves, and Eric Fujisaki. October 1999.

PEER 1999/04 *Adoption and Enforcement of Earthquake Risk-Reduction Measures.* Peter J. May, Raymond J. Burby, T. Jens Feeley, and Robert Wood.

PEER 1999/03 *Task 3 Characterization of Site Response General Site Categories*. Adrian Rodriguez-Marek, Jonathan D. Bray, and Norman Abrahamson. February 1999.

PEER 1999/02 *Capacity-Demand-Diagram Methods for Estimating Seismic Deformation of Inelastic Structures: SDF Systems*. Anil K. Chopra and Rakesh Goel. April 1999.

PEER 1999/01 *Interaction in Interconnected Electrical Substation Equipment Subjected to Earthquake Ground Motions.* Armen Der Kiureghian, Jerome L. Sackman, and Kee-Jeung Hong. February 1999.

PEER 1998/08 *Behavior and Failure Analysis of a Multiple-Frame Highway Bridge in the 1994 Northridge Earthquake.* Gregory L. Fenves and Michael Ellery. December 1998.

PEER 1998/07 *Empirical Evaluation of Inertial Soil-Structure Interaction Effects.* Jonathan P. Stewart, Raymond B. Seed, and Gregory L. Fenves. November 1998.

PEER 1998/06 *Effect of Damping Mechanisms on the Response of Seismic Isolated Structures.* Nicos Makris and Shih-Po Chang. November 1998.

PEER 1998/05 *Rocking Response and Overturning of Equipment under Horizontal Pulse-Type Motions.* Nicos Makris and Yiannis Roussos. October 1998.

PEER 1998/04 *Pacific Earthquake Engineering Research Invitational Workshop Proceedings, May 14–15, 1998: Defining the Links between Planning, Policy Analysis, Economics and Earthquake Engineering.* Mary Comerio and Peter Gordon. September 1998.

PEER 1998/03 *Repair/Upgrade Procedures for Welded Beam to Column Connections.* James C. Anderson and Xiaojing Duan. May 1998.

PEER 1998/02 *Seismic Evaluation of 196 kV Porcelain Transformer Bushings.* Amir S. Gilani, Juan W. Chavez, Gregory L. Fenves, and Andrew S. Whittaker. May 1998.

PEER 1998/01 *Seismic Performance of Well-Confined Concrete Bridge Columns.* Dawn E. Lehman and Jack P. Moehle. December 2000.